

This document is confidential and is proprietary to the American Chemical Society and its authors. Do not copy or disclose without written permission. If you have received this item in error, notify the sender and delete all copies.

Recent advances in triboelectric nanogenerators: from technological progress to commercial applications

Journal:	ACS Nano
Manuscript ID	nn-2022-12458y.R5
Manuscript Type:	Review
Date Submitted by the Author:	20-Apr-2023
Complete List of Authors:	<p>Choi, Dongwhi; Kyung Hee University, Mechanical Engineering (Integrated Engineering Program)</p> <p>Lee, Younghoon; Massachusetts Institute of Technology</p> <p>Lin, Zong-Hong; National Tsing Hua University, Institute of Biomedical Engineering</p> <p>Cho, Sumin; Kyung Hee University, Mechanical Engineering</p> <p>Kim, Miso; Sungkyunkwan University College of Engineering, Materials Science and Engineering</p> <p>Soh, Siowling; National University of Singapore,</p> <p>Ao, Chi Kit; National University of Singapore, Department of Chemical and Biomolecular Engineering</p> <p>Jeong, Chang Kyu; Jeonbuk National University, Division of Advanced Materials Engineering</p> <p>Sohn, Changwan; Jeonbuk National University, Division of Advanced Materials Engineering</p> <p>Lee, Minbaek; Inha University</p> <p>Lee, Jeongwan ; Inha University</p> <p>Ryu, Jungho; Yeungnam University, School of Materials Science and Engineering</p> <p>Lee, Seungah; Yeungnam University</p> <p>Parashar, Parag; National Tsing Hua University, Institute of Biomedical Engineering</p> <p>Kim, Il-Doo; Korea Advanced Institute of Science and Technology, Dept. of Materials Science and Engineering;</p> <p>Ahn, Jaewan; Korea Advanced Institute of Science and Technology, Materials Science and Engineering</p> <p>Cho, Yujang; Korea Advanced Institute of Science and Technology</p> <p>Lee, Pooi See; Nanyang Technological University, School of Materials Science and Engineering;</p> <p>Jiang, Feng; Nanyang Technological University</p> <p>Kim, Sang-jae; Jeju National University, Mechatronics Engineering</p> <p>Khandelwal, Gaurav; Jeju National University</p> <p>Song, Hyun-Cheol; Korea Institute of Science and Technology, Center for Electronic Materials</p> <p>Kim, Hyun Soo; Korea Institute of Science and Technology</p> <p>Nah, Jungghyo; Chungnam National University, Electrical Engineering</p> <p>Kim, Minje; Chungnam National University, Dept. of Electrical Engineering</p> <p>Kim, Wook; Sungkyunkwan University College of Engineering</p> <p>Park, Yong Tae; Myongji University - Natural Science Campus, Mechanical Engineering</p> <p>MENGE, HABTAMU GEBEYEHU; Myongji University - Natural Science</p>

1	
2	
3	
4	Campus, Mmechanical Engineering
5	Hao, Jianhua; The Hong Kong Polytechnic University
6	Xu, Wei; The Hong Kong Polytechnic University
7	Lee, Ju-Hyuck; Daegu Gyeongbuk Institute of Science and Technology,
8	Department of Energy Science and Engineering
9	Park, Hyosik; Daegu Gyeongbuk Institute of Science and Technology,
10	Department of Energy Science and Engineering
11	Kim, Sang-Woo; Sungkyunkwan University, School of Advanced
12	Materials Science and Engineering
13	Lee, Dong-Min ; Sungkyunkwan University
14	Park, Ji Young; Sungkyunkwan University, School of Advanced Materials
15	Science and Engineering, College of Engineering
16	Zhang, Haixia; Peking University
17	Zi, Yunlong; The Hong Kong University of Science and Technology -
18	Guangzhou Campus, Sustainable Energy and Environment
19	Guo, Ru; The Hong Kong University of Science and Technology
20	Cheng, Jia; Tsinghua University, Mechanical Engineering
21	Yang, Ze; Tsinghua University, Department of Mechanical Engineering
22	Xie, Yannan; Nanjing University of Posts and Telecommunications
23	Institute of Advanced Materials, Institute of Advanced Materials
24	Lee, Sangmin; Chung-Ang University,
25	Chung, Jihoon; Kumoh National Institute of Technology
26	Oh, Il-Kwon; Korea Advanced Institute of Science and Technology,
27	School of Mechanical, Aerospace and Systems Engineering
28	Kim, Ji-Seok; Korea Advanced Institute of Science and Technology
29	Cheng, Tinghai; Chinese Academy of Sciences, Beijing Institute of
30	Nanoenergy and Nanosystems
31	Gao, Qi; Chinese Academy of Sciences
32	Cheng, Gang; Henan University, Key lab for special functional materials
33	Gu, Guangqin; Henan University, Key Lab for Special Functional
34	Materials
35	Shim, Minseob; Gyeongsang National University
36	Jung, Jeehoon; Ulsan National Institute of Science and Technology
37	Yun, Changwoo ; Ulsan National Institute of Science and Technology
38	Zhang, Chi; Chinese Academy of Sciences
39	Liu, Guoxu; Institute of Nanoenergy and Nanosystems Chinese Academy
40	of Sciences
41	Chen, Yufeng; Massachusetts Institute of Technology
42	Kim, Suhan; Massachusetts Institute of Technology
43	Chen, Xiangyu ; Beijing Institute of Nanoenergy and
44	Nanosystems, Chinese Academy of Sciences,
45	Hu, Jun; CAS
46	Pu, Xiong; Beijing Institute of Nanoenergy and Nanosystems, Chinese
47	Academy of Sciences, Beijing Institute of Nanoenergy and Nanosystems
48	Guo, Zi Hao; Beijing Institute of Nanoenergy and Nanosystems, Chinese
49	Academy of Sciences, Beijing Institute of Nanoenergy and Nanosystems
50	Wang, Xudong; University of Wisconsin-Madison
51	Chen, Jun; University of California Los Angeles, Bioengineering
52	Xiao, Xiao; University of California Los Angeles
53	Xie, Xing; Georgia Institute of Technology, Civil and Environmental
54	Jarin, Mourin; Georgia Institute of Technology, Civil and Environmental
55	Engineering
56	Zhang, Hulin; Taiyuan University of Technology, College of Information
57	and Computer
58	Lai, Ying-Chih; National Chung Hsing University, Department of materials
59	science and engineering
60	He, Tianyiyi; National University of Singapore
	Kim, Hakjeong; Sungkyunkwan University College of Engineering
	Park, Inkyu; Korea Advanced Institute of Science and Technology
	(KAIST), Mechanical Engineering
	Ahn, Junseong; Korea Advanced Institute of Science and Technology,

	<p>Mechanical Engineering Huynh, Nghia Dinh; Sungkyunkwan University College of Engineering Yang, Ya; Institute of Nanoenergy and Nanosystems Chinese Academy of Sciences, Wang, Zhong Lin; Georgia Institute of Technology, School of Materials Science and Engineering, Baik, Jeong Min; Sungkyunkwan University Choi, Dukhyun; Sungkyunkwan University College of Engineering, Department of Mechanical Engineering</p>

SCHOLARONE™
Manuscripts

Recent advances in triboelectric nanogenerators: from technological progress to commercial applications

Dongwhi Choi^{1,†}, Younghoon Lee^{2,3,4,†}, Zong-Hong Lin^{1,5,6,†}, Sumin Cho¹, Miso Kim^{7,8}, Chi Kit Ao⁹, Siowling Soh⁹, Changwan Sohn^{10,11}, Chang Kyu Jeong^{10,11}, Jeongwan Lee¹², Minbaek Lee¹², Seungah Lee¹³, Jungho Ryu¹³, Parag Parashar⁵, Yujang Cho¹⁴, Jaewan Ahn¹⁴, Il-Doo Kim¹⁴, Feng Jiang^{15,16}, Pooi See Lee¹⁵, Gaurav Khandelwal^{17,18}, Sang-Jae Kim¹⁷, Hyun Soo Kim^{19,20}, Hyun-Cheol Song^{19,21}, Minje Kim²², Junghyo Nah²², Wook Kim²³, Habtamu Gebeyehu Menge²⁴, Yong Tae Park²⁴, Wei Xu²⁵, Jianhua Hao²⁶, Hyosik Park²⁷, Ju-Hyuck Lee²⁷, Dong-Min Lee⁷, Sang-Woo Kim^{7,8,28,29}, Ji Young Park⁷, Haixia Zhang³⁰, Yunlong Zi³¹, Ru Guo³¹, Jia Cheng³², Ze Yang³², Yannan Xie³³, Sangmin Lee³⁴, Jihoon Chung³⁵, Il-Kwon Oh³⁶, Ji-Seok Kim³⁶, Tinghai Cheng³⁷, Qi Gao³⁷, Gang Cheng³⁸, Guangqin Gu³⁸, Minseob Shim³⁹, Jeehoon Jung⁴⁰, Changwoo Yun⁴⁰, Chi Zhang^{41,42}, Guoxu Liu^{41,42}, Yufeng Chen², Suhan Kim², Xiangyu Chen^{42,43}, Jun Hu^{42,43}, Xiong Pu^{42,43}, Zi Hao Guo^{42,43}, Xudong Wang⁴⁴, Jun Chen⁴⁵, Xiao Xiao⁴⁵, Xing Xie⁴⁶, Mourin Jarin⁴⁶, Hulin Zhang⁴⁷, Ying-Chih Lai^{48,49,50}, Tianyiyi He⁵¹, Hakjeong Kim²³, Inkyu Park⁵², Junseong Ahn⁵², Nghia Dinh Huynh²³, Ya Yang^{41,42,53}, Zhong Lin Wang^{37,42,54,*}, Jeong Min Baik^{7,8,21,*}, Dukhyun Choi^{8,23,*}

¹Department of Mechanical Engineering (Integrated Engineering Program), Kyung Hee University, Gyeonggi 17104, South Korea.

²Department of Electrical Engineering and Computer Science, Massachusetts Institute of Technology, 77 Massachusetts Avenue, Cambridge, MA, 02139 USA.

³Department of Mechanical Engineering, Soft Robotics Research Center, Seoul National University, Seoul, 08826, South Korea.

⁴Department of Mechanical Engineering, Gachon University, Seongnam 13120, Korea

⁵Department of Biomedical Engineering, National Taiwan University, Taipei 10617, Taiwan

⁶Frontier Research Center on Fundamental and Applied Sciences of Matters, National Tsing Hua University, Hsinchu 30013, Taiwan

⁷School of Advanced Materials Science & Engineering, Sungkyunkwan University, Suwon, 16419, Republic of Korea.

1
2
3
4
5
6
7
8
9
10
11
12
13
14
15
16
17
18
19
20
21
22
23
24
25
26
27
28
29
30
31
32
33
34
35
36
37
38
39
40
41
42
43
44
45
46
47
48
49
50
51
52
53
54
55
56
57
58
59
60

⁸SKKU Institute of Energy Science and Technology (SIEST), Sungkyunkwan University, 2066, Seobu-ro, Jangan-gu, Suwon, Gyeonggi 16419, South Korea.

⁹Department of Chemical and Biomolecular Engineering, National University of Singapore, 4 Engineering Drive 4, Singapore 117585, Singapore.

¹⁰Division of Advanced Materials Engineering, Jeonbuk National University, 567 Baekje-daero, Deokjin-gu, Jeonju, Jeonbuk 54896, South Korea.

¹¹Department of Energy Storage/Conversion Engineering of Graduate School (BK21 FOUR), Jeonbuk National University, 567 Baekje-daero, Deokjin-gu, Jeonju, Jeonbuk 54896, South Korea.

¹²Department of Physics, Inha University, 100 Inha-ro, Michuhol-gu, Incheon, 22212, South Korea.

¹³School of Materials Science & Engineering, Yeungnam University, Gyeongsan, Gyeongbuk 38541, South Korea.

¹⁴Department of Materials Science and Engineering, Korea Advanced Institute of Science and Technology (KAIST), 291 Daehak-ro, Yuseong-gu, Daejeon 34141, Republic of Korea.

¹⁵School of Materials Science and Engineering, Nanyang Technological University, 50 Nanyang Avenue, Singapore 639798, Singapore.

¹⁶Institute of Flexible Electronics Technology of Tsinghua, Zhejiang, Jiaxing 314000, China.

¹⁷Nanomaterials and System Lab, Major of Mechatronics Engineering, Faculty of Applied Energy System, Jeju National University, Jeju 632-43, South Korea.

¹⁸School of Engineering, University of Glasgow, Glasgow G128QQ, U. K.

¹⁹Electronic Materials Research Center, Korea Institute of Science and Technology (KIST), Seoul, 02792, Republic of Korea.

²⁰Department of Physics, Inha university, Incheon 22212, Republic of Korea.

²¹KIST-SKKU Carbon-Neutral Research Center, Sungkyunkwan University (SKKU), Suwon 16419, Republic of Korea.

²²Department of Electrical Engineering, College of Engineering, Chungnam National University, 34134, Daehak-ro, Yuseong-gu, Daejeon 34134, South Korea.

²³School of Mechanical Engineering, College of Engineering, Sungkyunkwan University, 2066, Seobu-ro, Jangan-gu, Suwon, Gyeonggi 16419, South Korea.

²⁴Department of Mechanical Engineering, College of Engineering, Myongji University, 116 Myongji-ro, Cheoin-gu, Yongin, Gyeonggi 17058, Republic of Korea.

²⁵Research Centre for Humanoid Sensing, Zhejiang Lab, Hangzhou 311100, P.R. China.

²⁶Department of Applied Physics, The Hong Kong Polytechnic University, Hong Kong, P.R. China.

1
2
3
4
5
6
7
8
9
10
11
12
13
14
15
16
17
18
19
20
21
22
23
24
25
26
27
28
29
30
31
32
33
34
35
36
37
38
39
40
41
42
43
44
45
46
47
48
49
50
51
52
53
54
55
56
57
58
59
60

²⁷Department of Energy Science and Engineering Daegu Gyeongbuk Institute of Science and Technology (DGIST) Daegu 42988, Republic of Korea.

²⁸Samsung Advanced Institute for Health Sciences & Technology (SAIHST), Sungkyunkwan University, 115, Irwon-ro, Gangnam-gu, Seoul 06351, South Korea.

²⁹SKKU Advanced Institute of Nanotechnology (SAINT), Sungkyunkwan University, 2066, Seobu-ro, Jangan-gu, Suwon, Gyeonggi 16419, South Korea.

³⁰National Key Laboratory of Science and Technology on Micro/Nano Fabrication; Beijing Advanced Innovation Center for Integrated Circuits, School of Integrated Circuits, Peking University, Beijing 100871, China.

³¹Thrust of Sustainable Energy and Environment, The Hong Kong University of Science and Technology (Guangzhou), Nansha, Guangdong 511400, China.

³²State Key Laboratory of Tribology in Advanced Equipment, Department of Mechanical Engineering, Tsinghua University, Beijing, 100084, China.

³³College of Automation & Artificial Intelligence, State Key Laboratory of Organic Electronics and Information Displays & Institute of Advanced Materials, Jiangsu Key Laboratory for Biosensors, Jiangsu National Synergetic Innovation Center for Advanced Materials, Nanjing University of Posts and Telecommunications, Nanjing, Jiangsu 210023, China.

³⁴School of Mechanical Engineering, Chung-ang University, 84, Heukseok-ro, Dongjak-gu, Seoul 06974, South Korea.

³⁵Department of Mechanical Design Engineering, Kumoh National Institute of Technology (KIT), 61 Daehak-ro, Gumi, Gyeongbuk 39177, South Korea.

³⁶National Creative Research Initiative for Functionally Antagonistic Nano-Engineering, Department of Mechanical Engineering, School of Mechanical and Aerospace Engineering, Korea Advanced Institute of Science and Technology (KAIST), Daejeon 34141, South Korea.

³⁷Beijing Institute of Nanoenergy and Nanosystems, Chinese Academy of Sciences, Beijing 101400, China.

³⁸Key Lab for Special Functional Materials, Ministry of Education, National & Local Joint Engineering Research Center for High-efficiency Display and Lighting Technology, School of Materials Science and Engineering, and Collaborative Innovation Center of Nano Functional Materials and Applications, Henan University, Kaifeng 475004, China.

³⁹Department of Electronic Engineering, College of Engineering, Gyeongsang National University, 501, Jinjudae-ro, Gaho-dong, Jinju 52828, South Korea.

⁴⁰Department of Electrical Engineering, College of Information and Biotechnology, Ulsan National Institute of Science and Technology (UNIST), 50, UNIST-gil, Eonyang-eup, Ulju-gun, Ulsan 44919, South Korea.

1
2
3
4
5
6
7
8
9
10
11
12
13
14
15
16
17
18
19
20
21
22
23
24
25
26
27
28
29
30
31
32
33
34
35
36
37
38
39
40
41
42
43
44
45
46
47
48
49
50
51
52
53
54
55
56
57
58
59
60

⁴¹CAS Center for Excellence in Nanoscience, Beijing Key Laboratory of Micro-nano Energy and Sensor, Beijing Institute of Nanoenergy and Nanosystems, Chinese Academy of Sciences, Beijing 101400, China.

⁴²School of Nanoscience and Technology, University of Chinese Academy of Sciences, Beijing 100049, China.

⁴³CAS Center for Excellence in Nanoscience, Beijing Institute of Nanoenergy and Nanosystems, Chinese Academy of Sciences, 100083, Beijing, China.

⁴⁴Department of Materials Science and Engineering, University of Wisconsin–Madison, Madison, WI 53706, USA.

⁴⁵Department of Bioengineering, University of California, Los Angeles, Los Angeles, CA 90095, USA.

⁴⁶School of Civil & Environmental Engineering, Georgia Institute of Technology, Atlanta, GA, 30332, USA.

⁴⁷College of Information and Computer, Taiyuan University of Technology, Taiyuan, 030024 P. R. China.

⁴⁸Department of Materials Science and Engineering, National Chung Hsing University, Taichung, 40227, Taiwan.

⁴⁹i-Center for Advanced Science and Technology, National Chung Hsing University, Taichung, 40227, Taiwan.

⁵⁰Innovation and Development Center of Sustainable Agriculture, National Chung Hsing University, Taichung, 40227, Taiwan.

⁵¹Department of Electrical and Computer Engineering, National University of Singapore, 4 Engineering Drive 3, Singapore, 117576, Singapore.

⁵²Department of Mechanical Engineering, Korea Advanced Institute of Science and Technology (KAIST), Daejeon 34141, Republic of Korea.

⁵³Center on Nanoenergy Research, School of Physical Science and Technology, Guangxi University, Nanning 530004, PR China.

⁵⁴School of Materials Science and Engineering, Georgia Institute of Technology, Atlanta, GA, 30332, USA.

† Dongwhi Choi, Younghoon Lee, and Zong-Hong Lin contributed equally to this work.

*To whom all correspondence should be addressed.

Email: zhong.wang@mse.gatech.edu (Prof. Z. L. Wang)

1
2
3
4
5
6
7
8
9
10
11
12
13
14
15
16
17
18
19
20
21
22
23
24
25
26
27
28
29
30
31
32
33
34
35
36
37
38
39
40
41
42
43
44
45
46
47
48
49
50
51
52
53
54
55
56
57
58
59
60

Email: jbaik97@skku.edu (Prof. J. M. Baik)

Email: bred96@skku.edu (Prof. D. Choi)

Abstract

Serious climate changes and energy-related environmental problems are currently critical issues in the world. In order to reduce carbon emissions and save our environment, renewable energy harvesting technologies will serve as a key solution in near future. Among them, triboelectric nanogenerators (TENGs), which is one of the most promising mechanical energy harvesters by means of contact electrification phenomenon, are explosively developing due to abundant wasting mechanical energy sources and a number of superior advantages in a wide availability and selection of materials, relatively simple device configurations, and low-cost processing. Significant experimental and theoretical efforts have been achieved toward understanding fundamental behaviors and a wide range of demonstrations since its report in 2012. As a result, the considerable technological advancement has been exhibited and it advances the timeline of achievement in the proposed roadmap. Now, the technology has reached the stage of prototype development with verification of performance beyond the lab scale environment toward its commercialization. In this review, distinguished authors in the world worked together to summarize the state of the art in theory, materials, devices, systems, circuits, and applications in TENG fields. The great research achievements of researchers in this fields around the world over the past decade are expected to play a major role in coming to fruition of unexpectedly accelerated technological advances over the next decade.

Keywords

Triboelectric nanogenerator, tribomaterials, device designs, mechanical systems, circuits, applications, energy harvesting, mechanical energy

Table of Contents



1. Introduction

1.1 Wasting Mechanical Energies

1.1.1 Various mechanical energy sources for energy harvesting

Energy harvesting is a technology through which ambient energy in nature or everyday life, otherwise wasted, can be converted into useful electrical energy, offering a sustainable power generation solution for various practical applications. Such ambient energies include wind, solar, fluid, thermal, and mechanical energies, as shown in Figure 1a, being invaluable input sources for power generation when converted. Depending on the input energy harvesting sources, it is possible to select and explore each distinctive energy harvesting technology, ranging from wind power plants, solar (or photovoltaic) cells, and thermal, mechanical, and biological energy harvesting. These various energy harvesting technologies are not competing with one another; rather, they can provide complementary power solutions depending on the operating environment and their potential power levels, as indicated in the bottom arrowed line of Figure 1a. For example, wind power can be a viable solution for mega-watts level power generation, while being quite impractical for milli-watts level power solutions as they entail additional devices or components for reducing the high-level power to several magnitudes lower of level powers. In this case, harvesting technology utilizing mechanical energy sources would be more suitable. Therefore, each energy harvesting technology can be selectively utilized depending on the target applications and their required power levels.

Mechanical energies are abundant, and moreover advantageous as they are not limited to any environmental condition such as weather. These mechanical energy sources range from ocean waves, structural noises and vibrations, sounds, and ultrasounds, as illustrated in Figure

1
2
3
4 1b as a function of the frequency. In general, it is useful to characterize mechanical energy
5 sources by their frequencies, amplitudes, and/or acceleration levels, based on which potential
6 power generation levels can be estimated.¹⁻³ To convert mechanical energies into electricity,
7 energy conversion mechanisms such as piezoelectric, triboelectric, and electromagnetic
8 effects can be usefully adopted. Piezoelectricity is a phenomenon where mechanical stress
9 induces electrical potentials or vice versa in a certain class of crystalline materials with non-
10 centrosymmetry. The triboelectric effect, on the other hand, induces charge generation from
11 friction mainly due to the coupling effect of contact electrification and electrostatic induction
12 between two oppositely surface-charged materials. In electromagnetic devices,
13 electromagnetic induction is the key to converting mechanical energy into electrical energy.
14 Depending on the energy conversion in use, energy harvesting devices are commonly defined
15 as piezoelectric nanogenerators (PENGs),⁴⁻⁶ triboelectric nanogenerators (TENGs),⁷⁻⁸
16 electromagnetic generators (EMGs), or hybrid nanogenerators consisting of two or more
17 mechanisms.⁹ These mechanical-to-electrical conversion mechanisms can offer a great
18 platform for sensors and energy harvesting applications, as they can produce renewable clear
19 electrical energy using mechanical input sources available from the environment.
20
21
22
23
24
25
26
27
28
29
30
31
32
33
34
35
36
37
38
39
40
41

42 **1.1.2 Mechanical Energy Source-based TENGs**

43
44

45 TENGs deliver a number of advantages in a wide availability and selection of materials,
46 relatively simple device configurations, and low-cost processing, thus are regarded as an
47 effective technology for harvesting a broad range of ambient mechanical energies. Wind or
48 even light breezes proved to be an invaluable input source to generate electricity via an ultra-
49 stretchable TENG, as shown in Wen *et al.*'s work (Figure 2a).¹⁰ Harvesting wind energy
50
51
52
53
54
55
56
57
58
59
60

1
2
3
4 generated by high-speed trains through a TENG offers a great powering strategy for large-
5
6
7
8 scale signal and sensor networks,¹¹ in addition to various types of wind-based TENG
9
10
11 demonstrations.¹²⁻¹⁶ Meanwhile, ocean wave harvesting via TENGs has been intensively
12
13
14 studied as a renewable power solution.¹⁷⁻²⁰ Active resonance TENGs proposed by Zhang *et al.*
15
16
17 are one of the recently reported TENG examples of ocean wave harvesting, where a flexible
18
19
20 ring structure was explored to tackle the challenging characteristics of low frequencies and
21
22
23 random varying directions of the ocean waves (Figure 2b).²¹ Besides, numerous intriguing
24
25
26 TENG designs for ocean wave energy harvesting have been proposed in the past years,
27
28
29 including a seesaw equal-arm lever structured TENG,²² a multiple-frequency TENG based on
30
31
32 a water balloon,¹⁸ a tubular TENG with hollow ball buoy,²³ and a spherical TENG based on
33
34
35 spring-assisted multilayered structure for multidirectional functionality.¹⁷ Recently,
36
37
38 ultrasound has been re-visited as a promising way to deliver power safely into implanted
39
40
41 medical devices. TENGs proved to play a crucial role in converting externally applied
42
43
44 ultrasound into internal electricity inside the body, eliminating the need for replacement
45
46
47 batteries that entail additional surgery (Figure 2c).²⁴⁻²⁸ Sound is another green energy source
48
49
50 for harvesting that exists everywhere. Various concepts of TENGs for sound energy
51
52
53
54
55
56
57
58
59
60 harvesting have been reported, including an acoustic core-shell resonance harvester for the

1
2
3
4 application of artificial cochleae based on the piezo-triboelectric effect (Figure 2d),²⁹ a dual-
5
6
7
8 tube Helmholtz resonator-based TENG,³⁰ an integrated TENG with an electrospun polymer
9
10
11 tube,³¹ and a 3D-printed acoustic TENG for a self-powered edge sensing system.³² Structural
12
13
14 vibration, a type of mechanical motion, exists everywhere in our daily life from vehicles,
15
16
17
18 railways, buildings, and bridges as well as in industrial environments, offering ubiquitous
19
20
21 sources for harvesting.³³ A variety of TENG devices for structural vibration harvesting and
22
23
24 applications have been demonstrated, including a free-fixed TENG for train wheel energy
25
26
27
28 harvesting and monitoring (Figure 2e),³⁴ a multiple-mode TENG for harvesting the freight
29
30
31 train carriage joints and self-powered freight train monitoring,³⁵ and a self-powered vibration
32
33
34 TENG based on electrospinning nanofibers for rail fasteners tightness safety detection.³⁶ On
35
36
37
38 the other hand, human motion energy is also an indispensable energy source for wearable and
39
40
41 biomedical harvesting applications.³⁷⁻³⁹ Human gesture sensing and real-time clinical human
42
43
44 vital sign monitoring have been successfully realized via various kinds of TENGs, including
45
46
47
48 a waterproof fabric-based multifunctional TENG (Figure 2f)^{37, 40} and a hierarchically
49
50
51 designed high-performance stretchable TENG using ferroelectric barium-titanate-coupled 2D
52
53
54 MXene ($\text{Ti}_3\text{C}_2\text{T}_x$) nanosheets,⁴¹ to name a few. As seen from the example cases mentioned
55
56
57
58 above, TENGs offer a promising platform for sustainable power generation via converting
59
60

1
2
3
4 various kinds of mechanical energy sources from wind, ocean waves, ultrasound and sound,
5
6
7
8 structural vibrations, and human motions.
9
10
11
12
13
14
15
16
17
18
19
20
21
22
23
24
25
26
27
28
29
30
31
32
33
34
35
36
37
38
39
40
41
42
43
44
45
46
47
48
49
50
51
52
53
54
55
56
57
58
59
60

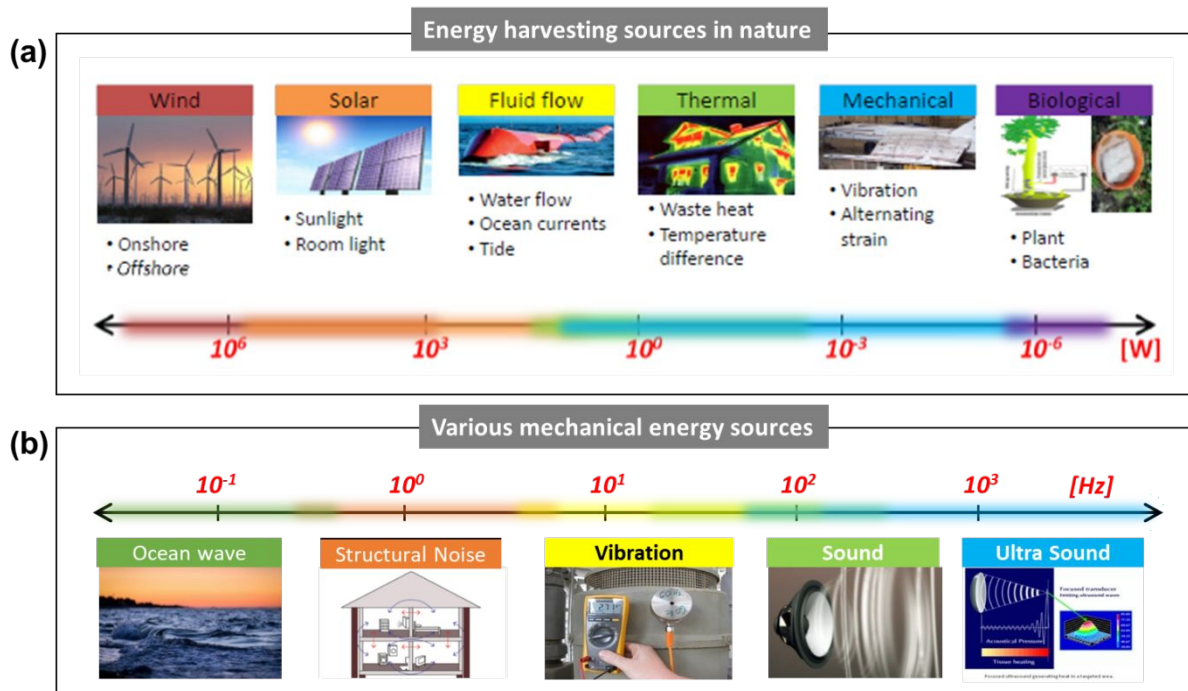


Figure 1. (a) Energy harvesting sources in nature and potential power levels (bottom) corresponding to each source, (b) various kinds of mechanical energy sources as a function of frequencies.

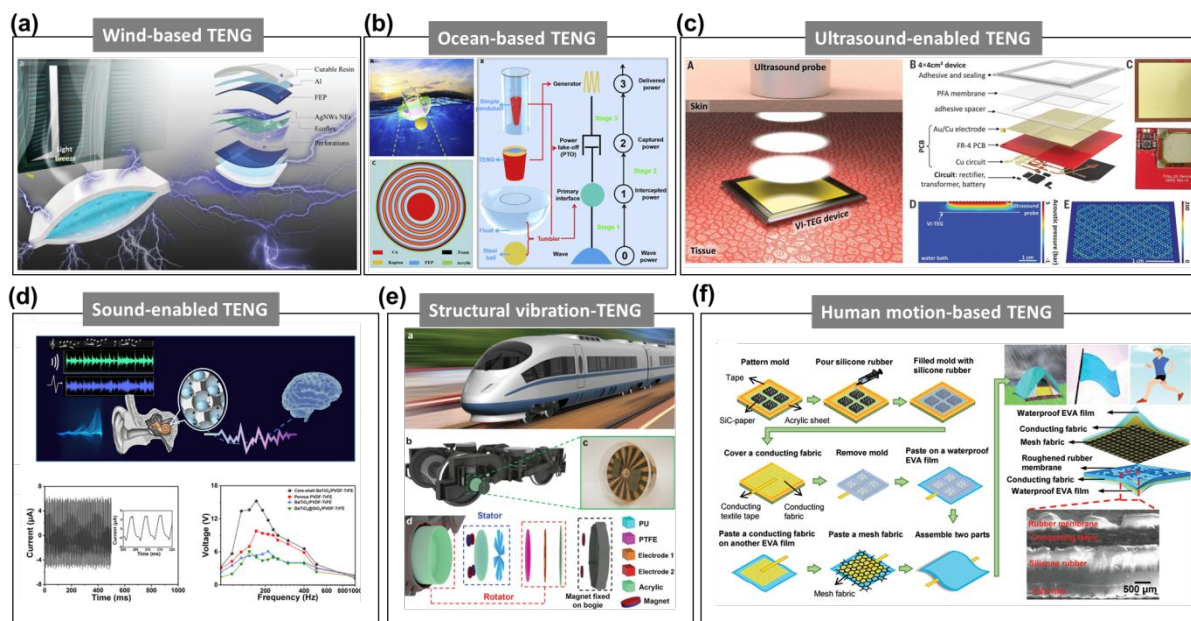


Figure 2. Designs of TENGs for harvesting various mechanical energy sources: (a) Wind-based TENG. Reprinted with permission from ref. 10, Copyright 2020, Wiley. (b) Ocean wave-based TENG. Reprinted with permission from ref. 21, Copyright 2021, Elsevier. (c) Ultrasound-enabled TENG. Reprinted with permission from ref. 28, Copyright 2019, American Association for the Advancement of Science. (d) Sound-enabled TENG. Reprinted with permission from ref. 29, Copyright 2021, American Chemical Society. (e) Structural vibration-based TENG. Reprinted with permission from ref. 34, Copyright 2021, Wiley. (f) Human motion-based TENG. Reprinted with permission under a Creative Commons CC BY license from ref. 37, Copyright 2019, John Wiley and Sons.

1.2 Fundamentals of TENGs

The TENG working modes can be distinguished into four fundamental modes such as, contact-separation, single-electrode, lateral sliding, and free-standing mode⁴²⁻⁴⁴. Among these mentioned working modes, the contact-separation modes are the most common design, as shown in Figure 3. Almost all materials in our daily life have triboelectrification effects, such as silk, plastic, metal, polymers, and wood. As a result, most of them can be utilized as a tribo-material-based TENGs. In this section, the basic TENG structure with vertical contact-separation working mode is displayed. It is composed of two tribo-materials and two electrodes. To control the TENG's output performance, there are various parameter controls that are being investigated from the beginning of the TENGs discovery, such as the material selection, material surface roughness, material thickness, gap between two tribo-materials, contact area, applied force, applied velocity, and input frequency. In this schematic diagram, the basic structure of a contact-separation TENG uses dielectric-to-dielectric materials including dielectric material 1 (D1) assembled to metal electrode 1 (M1) located in the top, and dielectric material 2 (D2) attached to metal electrode 2 (M2) at the bottom. As show in Figure 3, the surface charges on both dielectric materials are equal in density (σ_{sc}) due to contact electrification. Afterward, the separation of these tribo-materials results in

1
2
3
4 electrostatic induction. Therefore, the opposite charges localize on both surfaces causing an
5
6
7
8 electric field on tribo-materials D1 and D2, thus activating charge separation due to
9
10
11 electrostatic induction. This phenomenon leads to the potential difference between both tribo-
12
13
14 materials. If metal electrodes M1 and M2 are electrically connected by a conductive wire, the
15
16
17 repelled electrons in the negative dielectric material D2 flow to M1, producing an alternating
18
19
20 current (AC) during a periodic applied force from the external mechanical source. At the
21
22
23
24 balanced state of TENGs, the device turns back to the initial state.
25
26

27
28 Furthermore, the theoretical TENG mechanism is explained by Gauss's theorem. In this
29
30
31 description, the relationships among voltage-charge-motion ($V - Q - x$) are exhibited as a
32
33
34 time correlation. Both tribo-materials D1 and D2 have thicknesses of d_1 and d_2 with
35
36
37 relative electric constants of ϵ_{r1} and ϵ_{r2} , respectively. With the periodic applied force from
38
39
40 the external source, the distance x is changed with time. At the time when D1 and D2 are
41
42
43 brought into contact with each other when an external force is applied, the inner surfaces
44
45
46 produced opposite static charges with a charge density of σ_{sc} . Afterward, the release of the
47
48
49 external force led to the separation of the two tribo-materials, producing a potential difference
50
51
52 (V) between both electrodes. The number of transferred charges between M1 and M2 is Q ,
53
54
55 i.e., $-Q$ and Q , respectively. By using Gauss's theorem, the voltage difference between both
56
57
58 electrodes is finalized across D1-D2 and the air gap as shown in equation 1:
59
60

$$V(t) = E_1 d_1 + E_2 d_2 + E_{air} x \quad (1)$$

The relationships of $V - Q - x$ are then described by substituting σ_{sc} into equation (1), as shown below.

$$V(t) = -\frac{Q}{S\epsilon_0} \left(\frac{d_1}{\epsilon_{r1}} + \frac{d_2}{\epsilon_{r2}} + x(t) \right) + \frac{\sigma_{sc}}{\epsilon_0} x(t) \quad (2)$$

From equation (2), because of the open circuit condition the charges do not move on the electrode, so the current then becomes zero, and the open circuit voltage (V_{oc}) can be derived as:

$$V_{oc}(t) = \frac{\sigma_{sc}}{\epsilon_0} x(t) \quad (3)$$

In addition, at the short circuit condition, the voltage potential difference becomes zero ($V(t) = 0$). The transfer charges Q_{sc} and short circuit current I_{sc} are exhibited as:

$$Q_{sc} = \left[\frac{S\sigma_{sc}x(t)}{\left(\frac{d_1}{\epsilon_{r1}} + \frac{d_2}{\epsilon_{r2}} + x(t)\right)} \right] \quad (4)$$

$$I_{sc} = \frac{dQ_{sc}}{dt} = \frac{d}{dt} \left[\frac{S\sigma_{sc}x(t)}{\left(\frac{d_1}{\epsilon_{r1}} + \frac{d_2}{\epsilon_{r2}} + x(t)\right)} \right] = \frac{S\sigma_{sc} \left(\frac{d_1}{\epsilon_{r1}} + \frac{d_2}{\epsilon_{r2}}\right) v(t)}{\left(\frac{d_1}{\epsilon_{r1}} + \frac{d_2}{\epsilon_{r2}} + x(t)\right)^2} \quad (5)$$

For better understanding of the TENG's working mechanism, Maxwell's displacement current for the TENGs and the expanded Maxwell's equations form are presented. We discuss the fundamental form of Maxwell's equations, which are a set of partial differential equations. These equations exhibit fluctuations in the electromagnetic fields, i.e., waves propagate at a stable speed c ($\sim 3 \times 10^8$ m/s in a vacuum), as exhibited below.

$$\text{(Gauss's law)} \quad \nabla \cdot \mathbf{D}' = \rho_f \quad (6)$$

$$\nabla \cdot \mathbf{B} = 0 \quad (7)$$

(Gauss's law correlated to magnetism)

1
2
3
4 (Faraday's law)
$$\nabla \times E = -\frac{\partial B}{\partial t} \quad (8)$$

5
6
7

8 (Ampère – Maxwell law)
$$\nabla \times H = J_f + \frac{\partial D'}{\partial t} \quad (9)$$

9
10
11

12 where D is the displacement field

13 ρ_f is the free electric charge density

14 B is the magnetic field

15 E is the electric field

16 H is the magnetizing field

17 J_f is the free electric current density.

18
19
20
21
22
23
24
25
26
27 The above differential form of Maxwell's equations is applied to systems that involve fixed
28 boundaries and volumes of dielectric media. Thus, they are time independent. Moreover, in
29 this expression, the law is generated and transmitted in terms of electromagnetic waves in
30 stationary media. A difficult challenge is exhibited in the cases of moving charged media
31 systems and time dependent configurations. A discussion related to Maxwell's equations is
32 presented in some articles by Professor Wang from 2017 and 2021⁴⁵⁻⁴⁶. In 2022, the full
33 understanding of this situation was figured out by Professor Wang. That is, he solved this
34 problem from general theory, including mathematical solutions to TENGs applications, the so
35 called the expanded Maxwell's equations⁴⁷⁻⁴⁸.
36
37
38
39
40
41
42
43
44
45
46

47 The expanded form of Maxwell's equations is derived from the addition of a polarization
48 density term P_s correlated to the displacement vector. In this case, electrostatic charges
49 appear on medium surfaces due to triboelectrification, leading to the fundamental theory of
50 TENGs. Both electromagnetic interactions, power generation, and their coupling are involved
51 in the expanded Maxwell's equations. Additionally, the energy conservation for the expanded
52 Maxwell's equations and displacement current is derived in terms of the TENG's output
53
54
55
56
57
58
59
60

power. As a result of the triboelectric or piezoelectric effect, the electrostatic charges are located on surfaces like the nanogenerators case. The modified displacement vector is showed by adding the term P_s , which is related to polarization due to the electrostatic pre-charges on the media surface, so the modified displacement vector is given as:

$$D = \varepsilon_0 E + P + P_s = D' + P_s \quad (10)$$

where $\varepsilon_0 E$ is the field established by the free charge, the so-called external electric field

P is the medium polarization charge vector induced by the external electric field E

P_s is the added term due to the presence of surface/volume electrostatic charges with the variation time in boundary shapes (independent of E).

Finally, the general approach of the expanded Maxwell's equations in the case of moving charge media is described below.

$$\nabla \cdot D' = \rho_f - \nabla \cdot P_s \quad (11)$$

$$\nabla \cdot B = 0 \quad (12)$$

$$\nabla \times E = - \left(\frac{\partial}{\partial t} + v \cdot \nabla \right) B \quad (13)$$

$$\nabla \times H = J_f + \left(\frac{\partial}{\partial t} + v \cdot \nabla \right) (P_s + D') \quad (14)$$

where v is the movement velocity of the medium.

In summary, from the original differential form of Maxwell's equations with the fixed medium volumes and boundary, the differential form of the expanded Maxwell's equations is derived for the movement of medium as a translated rigid object in space. A comparison of the Maxwell's equations for stationary media and moving charged media is illustrated as a

tree in Figure 4. By accounting for the presence of surface electrostatic charges induced by triboelectrification, the modified equations are presented in various expressions using the displacement current. Through this, the expanded Maxwell's equations contribute to the fundamental theory of nanogenerators.

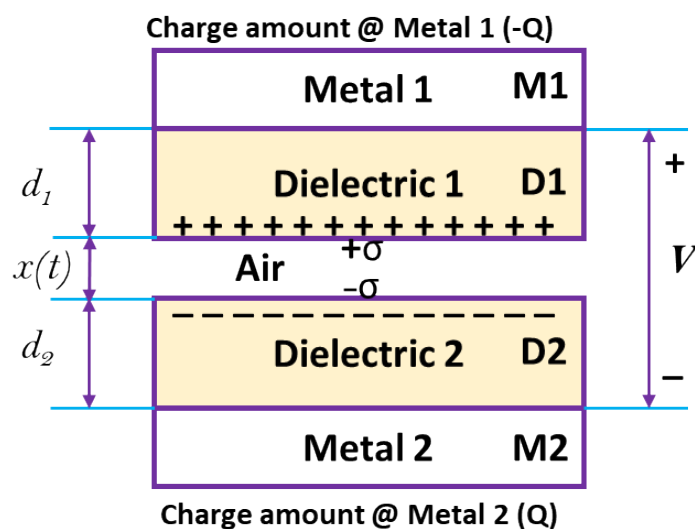


Figure 3. Schematic diagram showing the working principle of the vertical contact-separation fundamental mode.

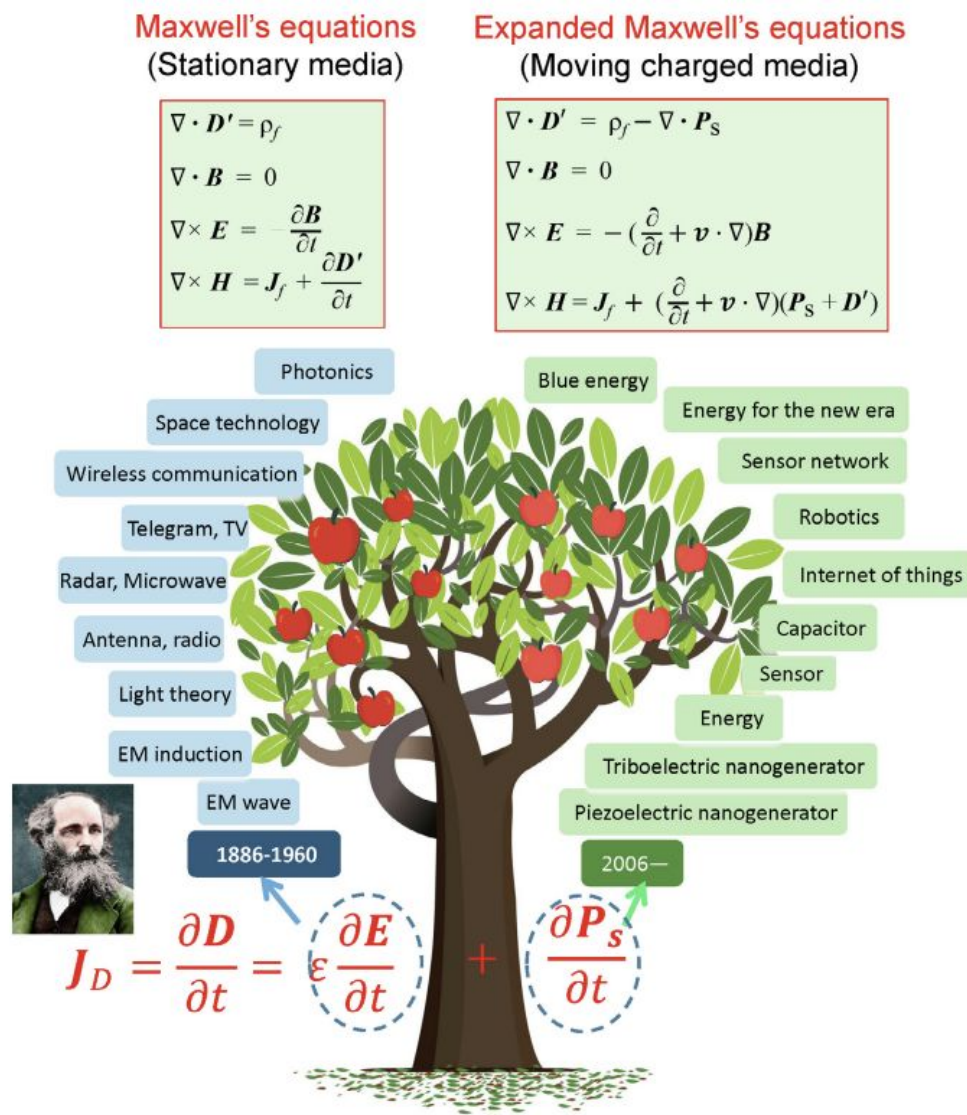


Figure 4. A comparison of Maxwell's equations for stationary media and moving charged media. Schematic diagram showing the contribution of the displacement current proposed by Maxwell as a term of time-variation of electric field and how it contributes to the development of electromagnetic field theory. The term $\left(\frac{\partial P_s}{\partial t}\right)$ in the expanded Maxwell equation introduced by Wang is the foundation of TENGs, which is called the Wang term. **Reprinted with permission from ref. 48, Copyright 2022, ELSEVIER SCI LTD.**

1.3. Recent Trends of Triboelectric Nanogenerators

Since the milestone research on triboelectric nanogenerators (TENGs) was reported in 2012⁴⁹, the research field of triboelectric nanogenerators has been spotlighted as a promising energy harvesting technology. With the advantages of TENGs including high power generation, diverse material selection, simple structure, and cost-efficient fabrication processes, the research field of TENGs has been widely extended by its applications such as self-powered touch sensors⁵⁰⁻⁵², power sources for robotics⁵³⁻⁵⁵, medical rehabilitation⁵⁶⁻⁵⁸, and human-machine interaction^{51, 59-60}. The numbers of articles and countries researching TENGs have dramatically increased during the last ten years (Figure 5a). Especially, research on triboelectric materials has been tremendous for maximizing power generation by enhancing contact electrification (Figure 5b)^{51, 61-62}. Furthermore, there has been a notable development on flexible^{49, 63-64}, stretchable^{51, 65-66}, and transparent^{51, 61, 66} material based-TENGs to meet the requirement of human-machine interfaces. Triboelectric material design innovations have contributed to the research scope of TENGs toward systemization and ultimately toward industrialization^{62, 67-68}. In accordance with the trend of commercialization, research on mechanical conversion systems and power management is gradually being spotlighted (Figure 5c) and can provide promising opportunities for sustainability and industrialization.

According to roadmaps proposed by Prof. Wang's group, who is a pioneer in the research field of TENGs⁶⁹⁻⁷⁰, there have been worldwide studies of TENGs over the last ten years (Figure 6a)⁶⁹. Along with these roadmaps, many researchers have made tremendous efforts for TENGs to be commercialized. As a result, systemization and prototype production are already underway even though these were originally expected to occur around 2024 (Figure 6b)⁷⁰. Triboelectric applications have focused on energy harvesting and self-powered touch

1
2
3
4 sensing. Recently, its applications are expanding to wider research fields such as biomedical
5
6 ⁵⁶⁻⁵⁸ and robotic⁵³⁻⁵⁵ applications. As the research field of TENGs has grown dramatically in a
7
8 short period of 10 years, it is expected that its growth will far exceed our expectations in the
9
10 upcoming 10 years. The purpose of this work is to provide a review of triboelectric research
11
12 to help prepare the next 10 years of research toward industrialization. This paper will provide
13
14 overviews of the fundamentals of TENGs and discuss the development of TENGs through
15
16 five major research branches: materials, devices, mechanical systems, electrical circuits, and
17
18 applications. We will also cover defining challenges and perspectives for commercialization
19
20
21
22
23 of TENGs.
24
25
26
27
28
29
30
31
32
33
34
35
36
37
38
39
40
41
42
43
44
45
46
47
48
49
50
51
52
53
54
55
56
57
58
59
60

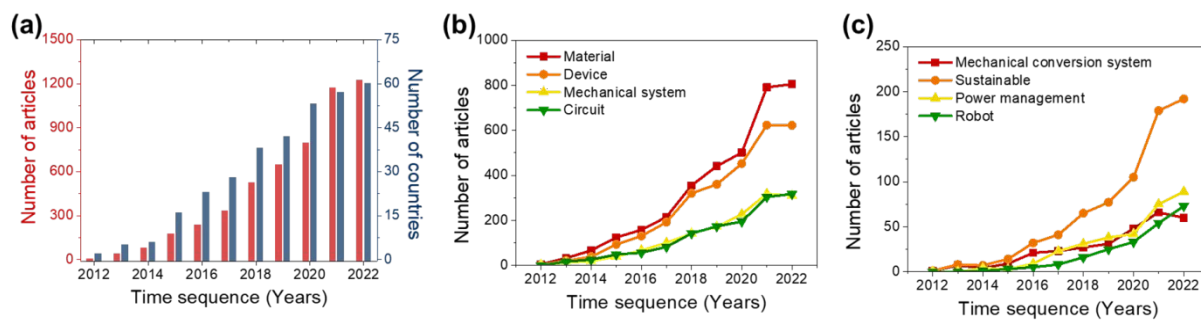


Figure 5. (a) Annual trends in the number of published articles and the number of countries in the research field of triboelectric nanogenerators. The last eleven years of publication related to (b) materials, devices, mechanical systems, circuits, (c) mechanical conversion systems, sustainable aspects, power management, and robots was extracted from the Web of Science.

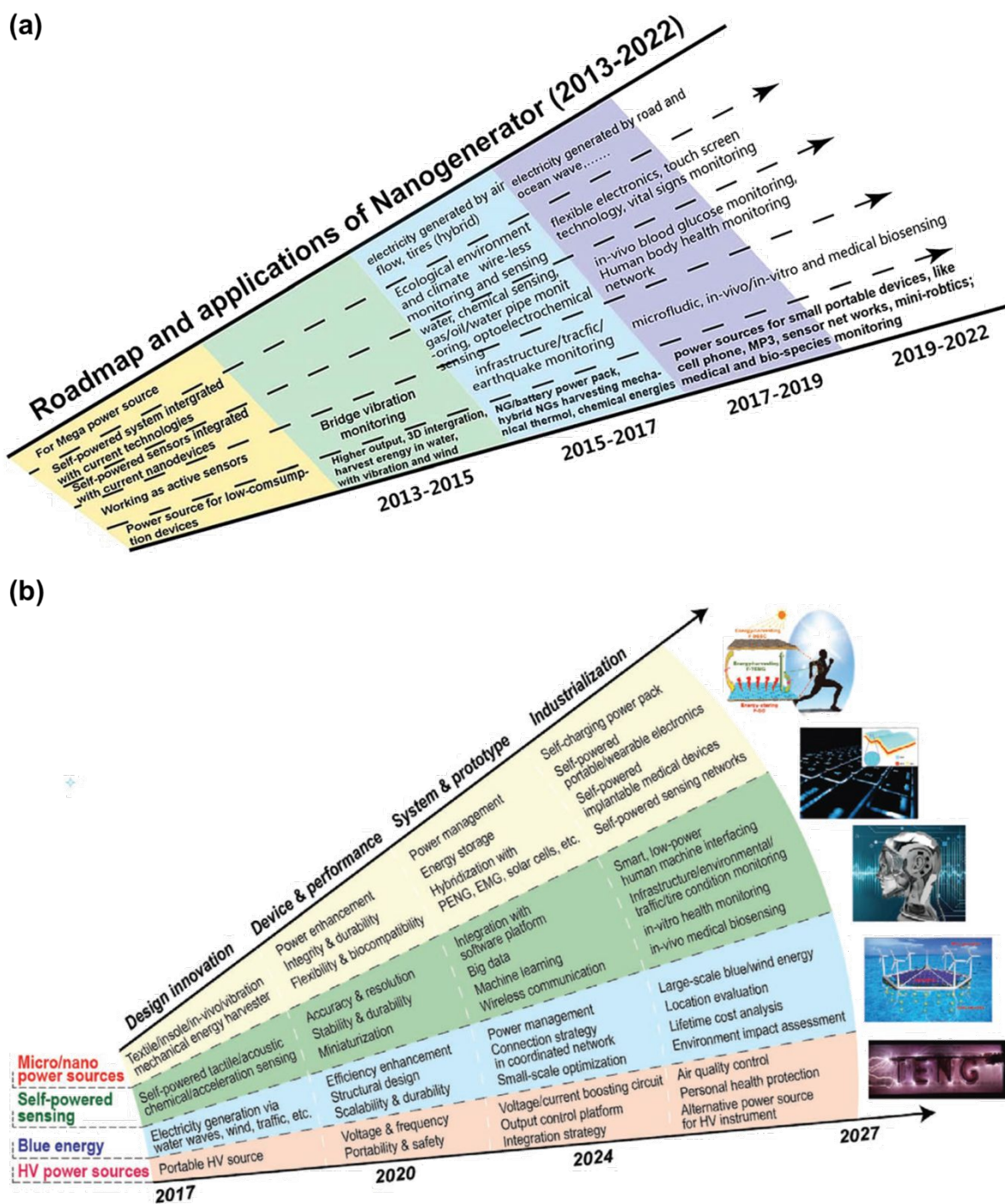


Figure 6. A proposed roadmap of TENGs (a) from 2013 to 2022 Reprinted with permission from ref. 69. Copyright 2014, ROYAL SOC CHEMISTRY. (b) from 2017 to 2027 toward industrialization of TENGs. Reprinted with permission from ref. 70. Copyright 2017, John Wiley and Sons.

2. Triboelectric materials for TENGs

In this chapter, we review a range of triboelectric materials, starting from the fundamentals of the charge transfer mechanism occurring on the surfaces of two materials during the physical contact to the governing strategies of key material technologies to maximize the charge densities created on the surfaces. Charge transfer is commonly explained via the transfer of electrons, ions, and materials, or two mores, and the contact electrification of a solid surface and a liquid was also reviewed. To increase the charge density, many studies on physical surface modifications by developing various nanostructures via etching processes and patterning processes have been conducted. Chemical surface modification such as plasma treatment, neutral beam irradiation, ultraviolet/ozone treatment, and chemical functionalization is also a good way to enhance the output performance of a triboelectric nanogenerator. Besides surface modification, material modification such as the dielectric constant, as well as mechanical properties, could significantly change the performance of TENGs. Here, various composites such as polymer-metal inorganic nanomaterial composites, polymer-2D nanomaterial composites, ferroelectric polymer-inorganic nanomaterial composites, and flexible/stretchable composites are reviewed. In addition to surface and bulk modifications, intermediate layer engineering via electron trapping layers and electron

1
2
3
4 blocking layers /functional interlayers show a promising approach for increasing the outputs
5
6
7
8 of TENGs. A layer-by-layer self-assembly approach was also reviewed, based on covalent
9
10
11 bonding and weak electrostatic interactions.
12

13
14 What should be overcome in TENGs may be the stability of the materials and the noise
15
16 during operation. As functional tribomaterials, self-healing polymer materials for TENGs are
17
18 suggested to improve the durability of devices. To reduce noise during operation, noise-
19
20 canceling TENG technologies were reported by introducing porous metallic sponges. Finally,
21
22 biological materials for TENGs are reviewed as energy sources for electronic devices such as
23
24
25
26
27
28
29
30
31
32 wearable, implantable, and environmentally friendly devices.
33
34
35
36
37

38 **2.1 Fundamentals of surface charge generation**

39
40

41 In principle, triboelectric nanogenerators (TENGs) generate an electrical energy from
42
43 surrounding mechanical energy due to the coupling effect of contact electrification and
44
45 electrostatic induction.⁷¹ The contact electrification is physically the result of charge transfer
46
47
48 when two different materials are charged after contact and separation.⁷² This can occur
49
50
51
52 between two pieces of the chemically same material because the surfaces are not commonly
53
54
55
56
57
58
59
60 uniform. Such a situation is common in nature and human life and is also responsible for

1
2
3
4 lightning in thunderstorms. Thus, a detailed understanding of contact electrification that
5
6
7
8 occurs at certain interfaces such as solid-solid and solid-liquid interfaces is critical.
9

10
11 While the principle of contact-electrification has long been studied for over 2600
12
13
14 years, the charge transfer mechanism is still unclear. Recently, the importance of surface
15
16
17
18 electronic states was reported and electron cloud/potential models have also been employed
19
20
21 to explain electron transfer between two contacted materials. However, they are limited to
22
23
24 only metal-semiconductors and metal-insulators, and not currently compatible with metal-
25
26
27
28 polymers or polymers-polymers. Except for electron transfer, ions' and materials' transfers
29
30
31 are suggested to contribute to charge transfer, especially for systems related to polymers.
32
33
34 Thus, contact-electrification may be explained via a complex interplay of physical or
35
36
37
38 chemical interactions in realistic material systems.
39
40

41
42 In general, strategies to enhance the output performance of TENGs are based on the
43
44
45 increase of charge density transferred during physical contact because the open-circuit
46
47
48 voltage and the short-circuit current are strongly dependent on the charge surface density.
49
50
51 The charge surface density was considered to be mainly affected by the intrinsic material
52
53
54 properties of the two contacted materials. Thus, lots of strategies have relied on the choice of
55
56
57
58 materials in the triboelectric series, along with chemical and physical modifications, such as
59
60

1
2
3
4 work-function differences, stretchability, dielectric constant, surface roughness, and
5
6
7
8 functionalization. However, despite much effort, the maximum charge density obtained was
9
10
11 about $260 \mu\text{C m}^{-2}$ and $283 \mu\text{C m}^{-2}$ in TENGs fabricated with single-layered film and multi-
12
13
14 layered film, respectively.
15
16
17
18
19
20

21 **2.1.1 Triboelectric series**

22
23
24
25 The most effective way to increase the charge density is to find the best pair for the positive
26
27
28 and negative charged materials in the triboelectric series. Here, the triboelectric series is a list
29
30
31 that ranks the various materials according to their tendency to gain or lose electrons,
32
33
34 suggested by Johan Carl Wilcke in 1757 (Figure 7).⁷³ In the series, materials on the upper left
35
36
37 side tend to have a greater affinity to give electrons than those on the lower right side. When
38
39
40 two different materials far away from each position are contacted, the one on the lower right
41
42
43 side releases electrons, transferred to materials on the upper left side. This makes two
44
45
46 surfaces have opposite charges and when two materials are separated, an electric potential is
47
48
49 generated between them. For example, Al and polytetrafluoroethylene (PTFE) have been
50
51
52 commonly used as a pair in TENGs. However, the material choice according to the
53
54
55 triboelectric series is still insufficient to generate the highest output power for TENGs. To
56
57
58
59
60

1
2
3
4 understand this, many theories have been suggested, but the reasons are still not sufficiently
5
6
7
8 supported theoretically or experimentally, and thus no convincing results can be found.
9
10
11
12
13
14
15
16
17
18
19
20
21
22
23
24
25
26
27
28
29
30
31
32
33
34
35
36
37
38
39
40
41
42
43
44
45
46
47
48
49
50
51
52
53
54
55
56
57
58
59
60

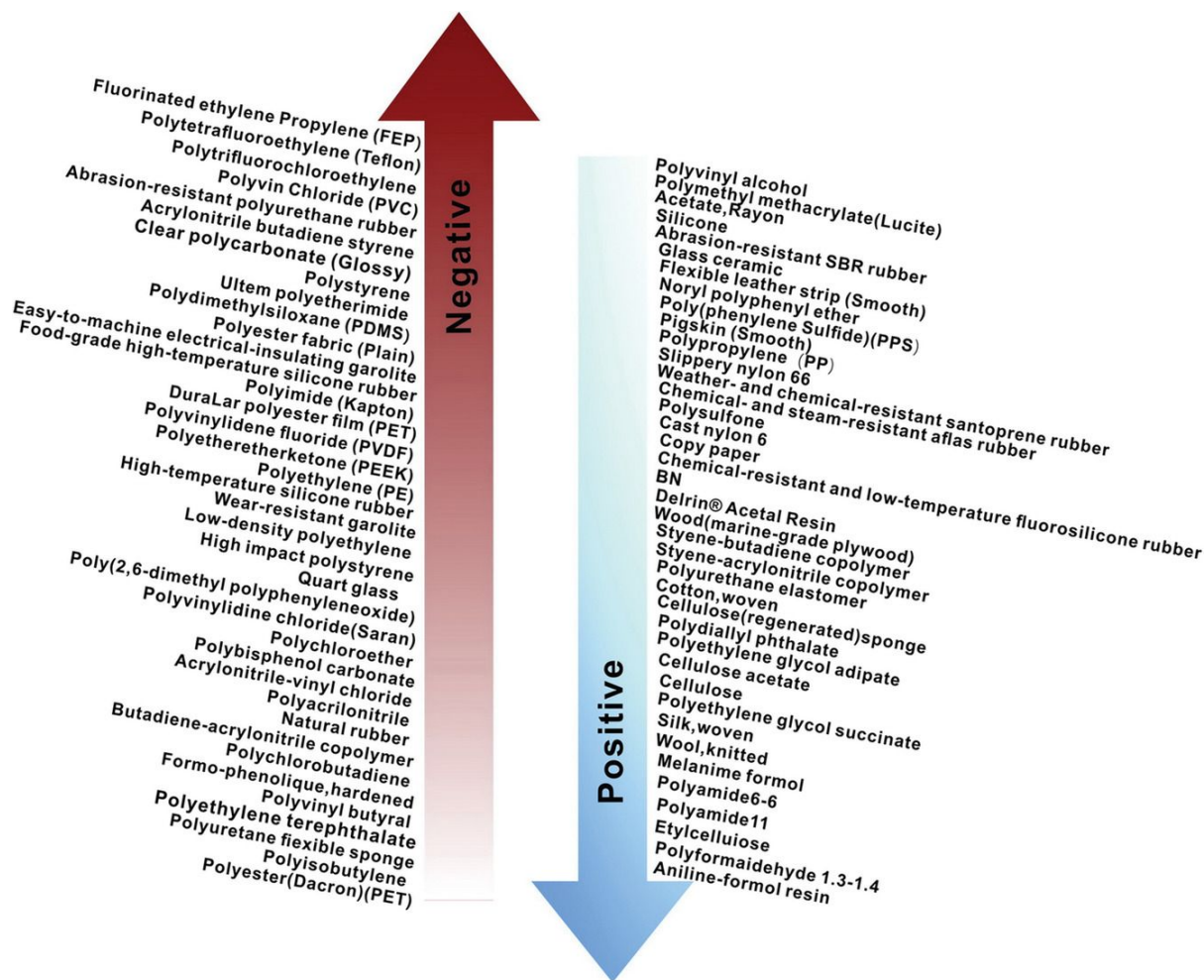


Figure 7. The triboelectric series. Reprinted with permission from ref. 73, Copyright 2020, Wiley.

2.1.2 Electron transfer model

The electron transfer model proposes that electrons are the charge carriers that are transferred from one surface to the other surface during contact electrification (Figure 8(a)), thus charging both surfaces. For the contact electrification of two metals, strong evidence has been reported in previous studies that electron transfer is the fundamental mechanism for charging the surfaces. Previous studies have found that the amount of charge generated by contact electrification is proportional to the difference between the work functions of the contacting metals.⁷⁴⁻⁷⁵ The surface with a lower work function is found to charge positively, whereas the surface with a higher work function is found to charge negatively. The work function is the minimum energy required to remove an electron from a solid surface. Hence, these results indicated that electrons are the charge carriers that are transferred from the surface with a lower work function to the surface with a higher work function.

For contact electrification of a metal and a dielectric material, it is probable that electron transfer is also the fundamental mechanism for charging the surfaces. Results from experiments involving contacting a variety of metals with a reference polymer showed a good correlation between the amount of charge generated by contact electrification and the work function of the contacting metal (i.e., similar to the case of metal-metal contact).⁷⁶⁻⁷⁷ Besides

1
2
3
4 the work function of the metal, correlations were also found between the amount of charge
5
6
7
8 generated by contact electrification (i.e., of a metal and a dielectric material) and properties
9
10
11 of the dielectric material that relate to electron transfer; these properties include the electronic
12
13
14 properties (e.g., the LUMO energy level) and electron affinity (i.e., Hammett substituent
15
16
17 constant of aromatic compounds).⁷⁸⁻⁷⁹ Another study investigated the effects of electric
18
19
20 potential on the contact electrification of a Pt-coated AFM tip and a dielectric material (e.g.,
21
22
23 Parylene).⁸⁰ Results showed that the polarity and amount of charge generated were controlled
24
25
26
27 by the bias voltage applied to the metal tip. Because the bias voltage determined the
28
29
30 concentration of electrons at the metallic tip, this result indicated that electrons were
31
32
33 transferred between the metal and the dielectric material.
34
35
36
37

38 Wang and coworkers showed that the fundamental mechanism of contact
39
40
41 electrification is based on the electron transfer model via the thermionic emission effect.⁸¹⁻⁸³
42
43
44 The experiment involved contacting a metal with a dielectric material (e.g., Al₂O₃ and SiO₂)
45
46
47 and then monitoring the dissipation of charge from the dielectric material at different
48
49
50 temperatures with time. Results showed that the charge decayed at a faster rate at a higher
51
52
53 temperature.⁸¹⁻⁸³ Thermionic emission is the release of electrons from a surface at high
54
55
56
57
58 temperature. Therefore, these results suggested that electrons are the charge carriers of
59
60

1
2
3
4 contact electrification. Besides monitoring the dissipation of charge, another study
5
6
7 investigated the effect of temperature during contact electrification.⁸¹ The experiment
8
9
10 involved contacting an Au-coated AFM tip heated to elevated temperatures and a dielectric
11
12 material (e.g., SiO₂ or Si₃N₄) maintained at a low temperature of 313 K (Figure 8(b)). In
13
14
15 general, results showed that the contact electrification charged the dielectric material more
16
17
18 negatively (or less positively) when the metal-coated tip was heated to a higher temperature.
19
20
21
22 For the case of Si₃N₄, its polarity switched from positive to negative when the temperature of
23
24
25 the metal-coated tip increased beyond around 403 K. These results indicated that contact
26
27
28 electrification is based on thermionic emission: more electrons are transferred from the
29
30
31
32 metallic surface to the dielectric material at a higher temperature. Hence, these results
33
34
35 showed that electron transfer is the mechanism for the contact electrification of a metal and a
36
37
38 dielectric material.
39
40
41
42
43
44

45 The mechanism of contact electrification between a dielectric material and another
46
47 dielectric material is complex and still under debate among researchers. For explaining the
48
49 general phenomenon of contact electrification for all types of materials—including the
50
51 contact electrification of two dielectric materials—Wang and coworkers have proposed the
52
53
54 general overlapped electron cloud model (Figure 8(c)). The model involves two surfaces that
55
56
57
58
59
60

1
2
3
4 are far apart. In this case, the electron clouds of the atoms at one surface are separated from
5
6
7
8 the electron clouds of the atoms at the other surface; hence, the electrons remain localized
9
10
11 (Figure 8(c)-(i)). Subsequently, the surfaces are brought into contact (i.e., with a compressive
12
13
14 force) for contact electrification to occur. At this stage, the electron clouds of some of the
15
16
17 atoms of both surfaces could overlap and form an asymmetric double-well potential. Because
18
19
20 of the lower energy barrier due to the overlapping electron clouds, electrons can transfer from
21
22
23 a higher energy state of one atom at one surface to a lower energy state of the other atom at
24
25
26 another surface (Figure 8(c)-(ii)). This transfer of electrons causes both surfaces to charge.
27
28
29 When the two surfaces are separated, the electron clouds of the atoms of the surfaces do not
30
31
32 overlap anymore and are separated again (Figure 8(c)-(iii)), thus preventing electrons from
33
34
35 transferring back to their original surface (Figure 8(c)-(iv)). The separated surfaces thus gain
36
37
38 charges permanently by contact electrification due to the transfer of electrons. In addition,
39
40
41 defects on surfaces could provide favorable surface states of electrons within the bandgap and
42
43
44 facilitate the transfer of electrons from one dielectric material to the other.^{75, 84-85}
45
46
47
48
49
50

51 Thermionic emission is also observed for the contact electrification of two dielectric
52
53 surfaces.⁸⁴ The experiment involved the contact electrification between two dielectric
54
55 materials (i.e., SiO₂ and Al₂O₃) and then monitoring the charge dissipation of Al₂O₃ after
56
57
58
59
60

1
2
3
4 contact. Similar to the contact electrification of a metal and a dielectric material, the charge
5
6
7
8 of the Al_2O_3 decayed faster at a higher temperature. Results showed the exponential decay of
9
10
11 charge with time that is predicted by theory of thermionic emission of electrons in all tests
12
13
14 (Figure 8(d)). Hence, the charge carrier of contact electrification may be due to the transfer of
15
16
17 electrons. A recent interesting study investigated the emission of light due to the contact
18
19
20 electrification of two dielectric materials (e.g., FEP and acrylic) in a low-pressure
21
22
23 environment (i.e., within 10 to 1000 Pa).⁸⁶ The emission spectra obtained may possibly be
24
25
26 due to the transfer of electrons during contact electrification and then the relaxation of the
27
28
29 electrons from their excited states.
30
31
32
33
34
35
36
37
38
39
40
41
42
43
44
45
46
47
48
49
50
51
52
53
54
55
56
57
58
59
60

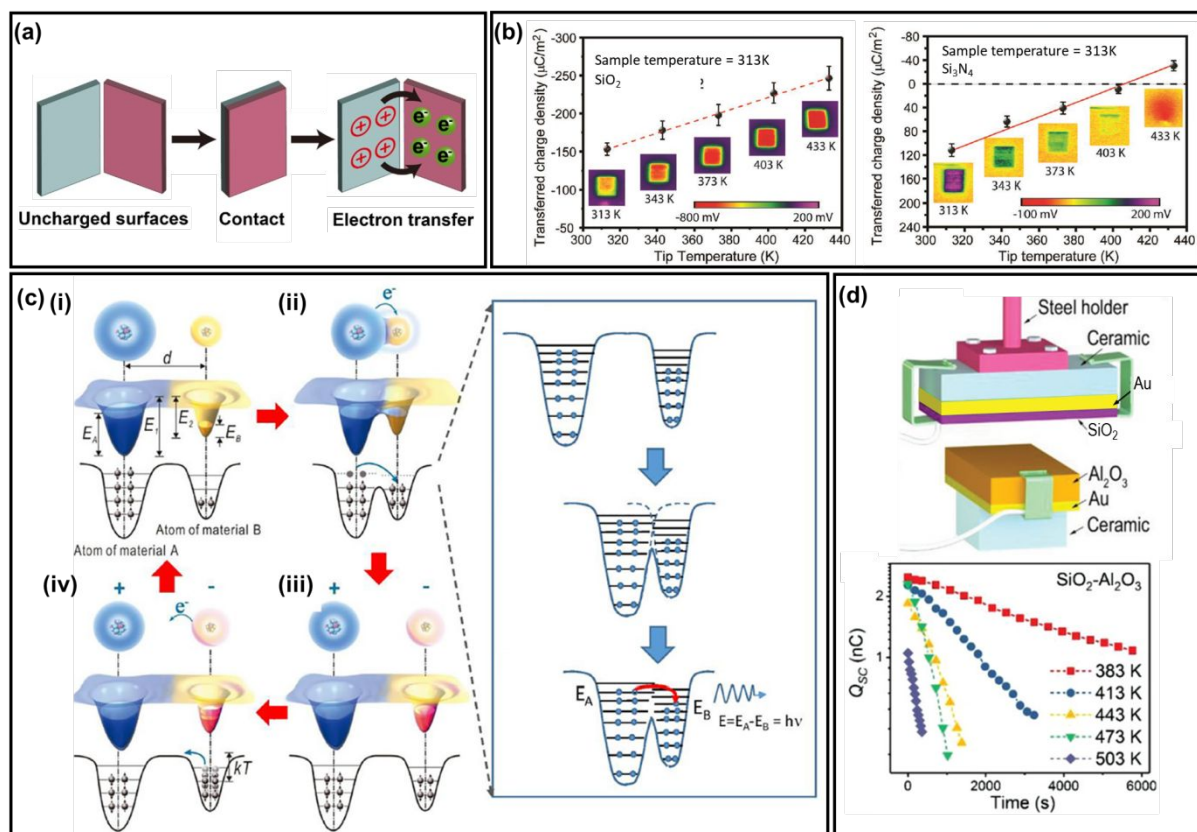


Figure 8. Electron transfer model. (a) The scheme illustrates the transfer of electrons between two solid surfaces due to contact electrification. **Reproduced with permission from ref. 87** (b) Contact electrification between an Au-coated tip and the surface of a dielectric material depends on the temperature of the metal tip. The plot on the left shows the case when the dielectric material is SiO₂. The plot on the right shows the case when the dielectric material is Si₃N₄. **Reproduced with permission from ref. 81, Copyright 2019, Wiley.** (c) The overlapped electron cloud model is proposed for explaining contact electrification between all types of materials, including the contact of two dielectric materials. The scheme illustrates the electron clouds and potential energy profiles of two atoms from the materials A and B (i) before contact, (ii) during contact, and (iii-iv) after contact. Electron transfer occurs at (ii) when the electron clouds of the two atoms overlap. **Reproduced with permission from ref. 85** (d) A TENG device that involved the contact electrification of SiO₂ and Al₂O₃ was used to investigate the effect of thermionic emission. The plot shows the effect of temperature on the dissipation of charge of the contact-charged Al₂O₃. **Reproduced with permission from ref. 84**

1
2
3
4 Wang and coworkers have proposed a revised model of the formation of the electric double
5
6
7
8 layer (EDL) that involves the transfer of electrons during the contact electrification of a solid
9
10
11 surface and a liquid (Figure 9(a)). This revised model consists of two steps. The first step
12
13
14 involves the fresh contact between the surface and the liquid. In this step, the liquid
15
16
17 molecules may impact onto the solid surface due to thermal motion or pressure from the flow
18
19
20 of the liquid (Figure 9(a)-(i)). These collisions of the molecules lead to the overlap of electron
21
22
23 clouds between the liquid molecules and molecules on the surface. Subsequently, electrons
24
25
26 transfer through the overlapping electron clouds due to the lowered potential barrier, thus
27
28
29 charging the surface and the liquid. In the second step, the free ions in the liquid (i.e.,
30
31
32 including the ions formed during the electron transfer in the first step and other ions present
33
34
35 in the liquid) are attracted to the charged solid surface and form the diffuse layer (Figure 9(a)-
36
37
38
39
40
41 (ii)).
42
43
44

45
46 A number of studies showed experimentally the involvement of electrons in the
47
48 contact electrification of a solid surface and a liquid. In one recent study, the experiment
49
50
51 involved sandwiching a liquid droplet between two solid surfaces (i.e., made of PTFE).⁸⁸ The
52
53
54 contact electrification was carried out by bringing the top surface into contact with the liquid
55
56
57 that rested on the bottom surface and then separating the top surface from the liquid droplet.
58
59
60

1
2
3
4
5 After being fully separated from the liquid, the surface potential of the top surface was
6
7
8 measured. The experiment was performed by using either water or non-polar transformer oil
9
10
11 as the liquid droplet. The results showed the same order of magnitude of charge on the PTFE
12
13
14 surface regardless of whether it contacted with the drop of non-polar transformer oil or drop
15
16
17 of water (Figure 9(b)). Because there were no ions in the non-polar transformer oil, this result
18
19
20 suggested that electrons transferred during the contact electrification of the solid and liquid
21
22
23 instead of ions.
24
25
26
27

28 The involvement of electrons during contact electrification is also investigated via the
29
30
31 thermionic emission effect (i.e., similar to the investigation of the contact electrification of
32
33
34 two solid surfaces).⁸⁹⁻⁹⁰ One of the studies performed experiments that involved the contact
35
36
37 electrification of water droplets and a dielectric material (e.g., SiO₂, MgO, Si₃N₄, HfO₂,
38
39
40 Al₂O₃, or AlN) and then monitoring the dissipation of charge of the dielectric material with
41
42
43 time (Figure 9(c)).⁸⁹ For SiO₂, results showed that about three-fourths of the charge was
44
45
46 found to dissipate from its surface at a high temperature of above 433 K (Figure 9(d)).
47
48
49 Varying amounts of charge were found to dissipate for other types of dielectric materials.
50
51
52 Based on the principle of thermionic emission, electrons dissipate at elevated temperatures,
53
54
55 whereas ions (i.e., the “sticky charge”) remain on the surface. Hence, the charge carriers may
56
57
58
59
60

1
2
3
4 be both electrons and ions for the solids investigated. It is reported that whether electron
5
6
7
8 transfer or ion transfer dominates as the mechanism of contact electrification depends on the
9
10
11 properties of the liquid (e.g., concentration of ions) and the solid surface (e.g.,
12
13
14 hydrophilicity). Another study investigated the thermionic emission of surfaces that were
15
16
17 coated with organic functional groups after contact-charging them with a non-polar organic
18
19
20 liquid (e.g., cyclohexane).⁹⁰ The results showed that most charge dissipated with time (Figure
21
22
23 9(e)); hence, the charge carrier of contact electrification of the surface and a non-polar
24
25
26 organic liquid was primarily electrons.
27
28
29
30

31
32 In another study, the authors compared the contact-charging behaviors of water and a
33
34 metal.⁹¹ The experiment involved contact-charging different types of polymers (i.e., with
35
36
37 functional groups that had different electron-withdrawing abilities) with a reference metal
38
39
40 (i.e., Al). The authors then repeated the experiment by using water as the reference substance
41
42
43 instead of metal. Their results showed that the amounts of charge generated by the contact
44
45
46 electrification of the different polymers and the reference metal generally had the same trend
47
48
49 as that of the different types of polymers and the reference water. As discussed in the
50
51
52 previous section (2.1.2), the mechanism of contact electrification that involved a metal as at
53
54
55 least one of the contacting materials is based on electron transfer. Therefore, the results
56
57
58
59
60

1
2
3
4 indicated that the contact electrification of the polymers and water is also based on electron
5
6
7
8 transfer (i.e., due to the similar charging behavior of water and metal).
9
10
11
12
13
14
15
16
17
18
19
20
21
22
23
24
25
26
27
28
29
30
31
32
33
34
35
36
37
38
39
40
41
42
43
44
45
46
47
48
49
50
51
52
53
54
55
56
57
58
59
60

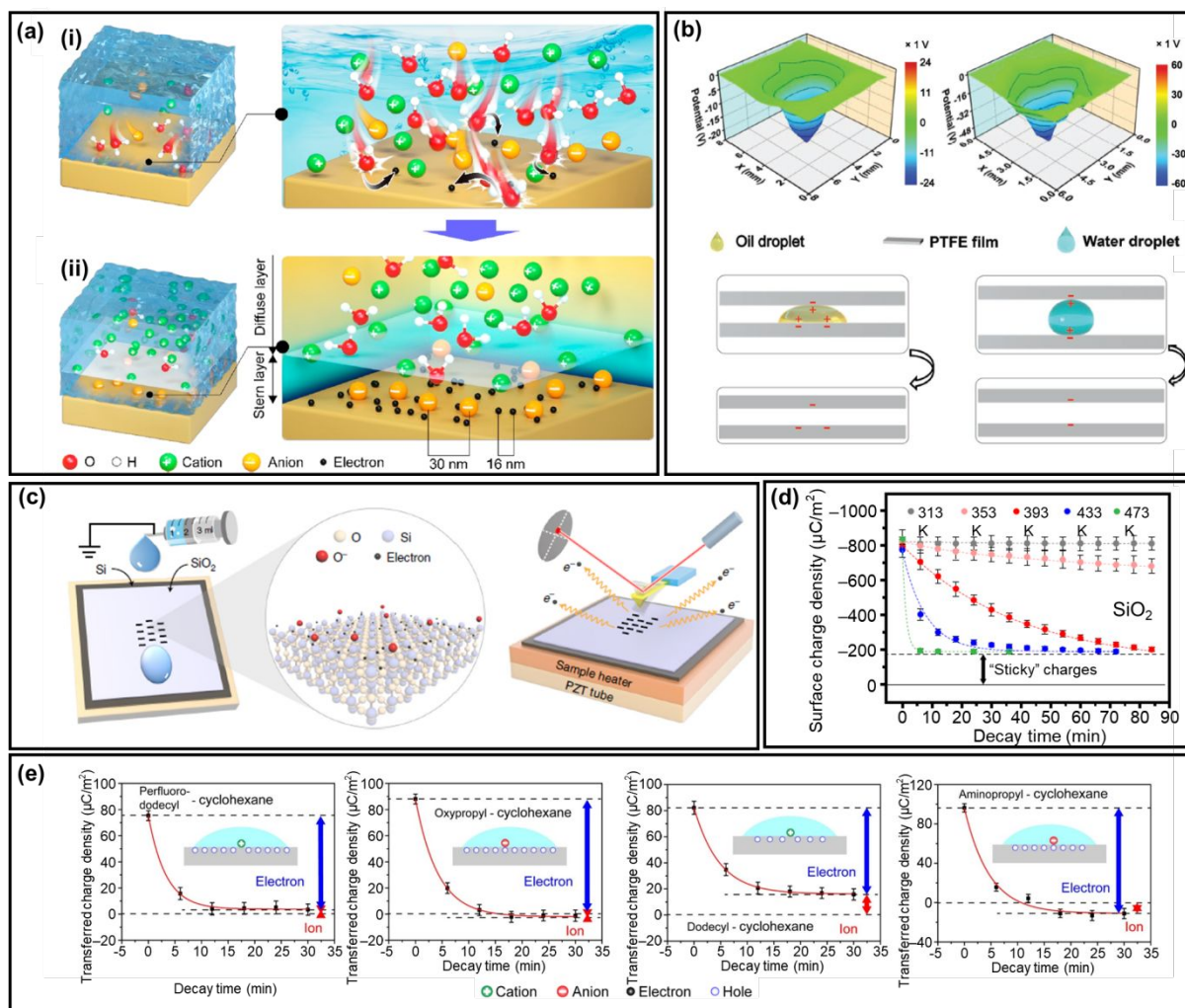


Figure 9. Electron transfer model at the liquid–solid interface. (a) The scheme illustrates a revised two-step model of the formation of the electric double layer (EDL). (a)-(i) The first step involves the transfer of electrons due to the collision of the liquid molecules and the solid surface, thus charging the surface. (a)-(ii) The free ions in the liquid are subsequently attracted to the charged surface in the second step for forming the diffuse layer. **Reproduced with permission from ref. 92** (b) Charge generated due to the contact electrification of an oil droplet and a PTFE film was found to be similar to that of a water droplet and a PTFE film. **Reproduced with permission from ref. 88** (c) Scheme illustrates the setup used for investigating the decay of charge of solid surfaces under different temperatures. The surfaces were first charged by sliding water droplets across them. (d) Charge decay of SiO₂ (i.e., after contacting with water droplets) with time at different temperatures. The large amount of decay indicated that the charged species transferred during contact electrification were mostly

1
2
3
4
5 electrons. **(c, d) Reprinted with permission under a Creative Commons CC BY License**
6 **from ref. 89, Copyright 2020, Springer Nature. (e) Charge decay of surfaces coated with**
7 different organic functional groups with time after contacting with droplets of cyclohexane at
8 413 K. The large amount of decay indicated that the charged species that transferred during
9 the contact electrification of a non-polar organic liquid and a dielectric surface were mainly
10 electrons. **Reproduced with permission from ref. 90**
11
12
13
14
15
16
17
18
19
20
21
22
23
24
25
26
27
28
29
30
31
32
33
34
35
36
37
38
39
40
41
42
43
44
45
46
47
48
49
50
51
52
53
54
55
56
57
58
59
60

2.1.2 Ion transfer model

Another possible mechanism of contact electrification involves the transfer of ions from one surface to another during contact electrification; thus, one surface becomes positively charged, whereas the other surface becomes negatively charged (Figure 10(a)). This ion transfer model has been proposed to be the fundamental mechanism of the contact electrification of two dielectric materials. Whitesides and coworkers have devised a model system that involved functionalization of the surfaces (i.e., microspheres) with molecules that had ionic functional groups.⁹³ The experiment involved the contact electrification of microspheres coated with different types of ionic functional groups and glass beads. The results showed that the polarity of the charge of the coated microspheres after contact electrification was always the same as the polarity of the ionic functional group on the microspheres. In addition, the amount of charge generated was found to be proportional to the surface area coated with the ionic functional groups (Figure 10(b)). Other studies that worked on other types of materials that are similarly coated with molecules that have ionic functional groups (e.g., acidic and basic groups) also reported similar results.⁹⁴⁻⁹⁷ Therefore, the mechanism seems to involve the transfer of the mobile counterions of the ionic functional groups from one surface to the other during contact electrification.

1
2
3
4
5 The ion transfer model is also proposed to be responsible for the contact
6
7
8 electrification between two dielectric surfaces that do not have any ionic functional groups.

9
10
11 One possibility is based on the tendency of surfaces (i.e., including both hydrophilic and
12
13
14 hydrophobic surfaces) to adsorb water from the surrounding atmosphere. Whitesides
15
16
17 hypothesized that the contact electrification between two insulating materials (i.e., without
18
19
20 any ionic functional groups) is due to the transfer of aqueous ions (e.g., H^+ and OH^- ions) of
21
22
23 the adsorbed water from one surface to other.⁹⁸ The polarity and amount of charge generated
24
25
26 by contact electrification of two solid surfaces is found to correlate with the zeta potential of
27
28
29 the surfaces immersed in water.⁹⁸ Because the zeta potential may indicate the tendency of the
30
31
32 surfaces to adsorb aqueous ions, this correlation supported the mechanism that the contact
33
34
35 electrification of insulating surfaces is due to the preferential adsorption of the aqueous ions
36
37
38 (e.g., OH^- ions) from one surface to the other. Besides ions generated by water adsorbed on
39
40
41 surfaces, ions may also be generated by the heterolytic cleavage of molecular bonds during
42
43
44 contact electrification (i.e., ions that may subsequently transfer from one surface to
45
46
47 another).⁹⁹⁻¹⁰⁴ Other studies showed that the polarities of charge produced by the contact
48
49
50 electrification between two dielectric materials are determined by the Lewis acidity/basicity
51
52
53 of the contacting materials. This correlation between the Lewis acidity/basicity and the
54
55
56
57
58
59
60

1
2
3
4 polarities of charge was established by contact-charging multiple pairs of polymers and
5
6
7
8 comparing their polarities and Lewis acidity/basicity (Figure 10(c)).¹⁰⁵⁻¹⁰⁷ The Lewis
9
10
11 acidity/basicity is the ability of the molecule to share electrons with another molecule or ion.
12
13
14 Therefore, the correlation indicated that Lewis acidity/basicity is the property that determines
15
16
17 the preferential adsorption of ions; in other words, the mechanism of contact electrification is
18
19
20 due to the transfer of ions between the surfaces of the dielectric materials.
21
22
23
24
25
26
27

28 The transfer of ions is another mechanism that underlies the contact electrification of a
29
30
31 solid and a liquid. Ions may transfer at the liquid–solid interface via a few ways. One way
32
33
34 involves a solid surface that has ionic functional groups. The mobile counterions of the ionic
35
36
37 functional groups may dissociate from the surface and move into the liquid, thus leading to
38
39
40 the separation of charge.¹⁰⁸ Another common way involves the adsorption of ions that are
41
42
43 present in the liquid (e.g., hydroxide ions in water) onto the solid surface. Results from a
44
45
46 previous study found that the zeta potential of a surface was more negative when the surface
47
48
49 was in contact with a basic solution and more positive when the surface was in contact with
50
51
52 an acidic solution.¹⁰⁹ These results indicated that the surface became charged due to the
53
54
55 adsorption of either the hydronium or hydroxide ions from the aqueous solutions. In addition,
56
57
58
59
60

1
2
3
4 results from a number of studies that performed computational simulation showed that there
5
6
7
8 is the preferential adsorption of hydroxide ions over hydronium ions at the solid-water
9
10
11 interface.¹¹⁰⁻¹¹² This preferential adsorption of hydroxide ions explains the experimental
12
13
14 observations that many surfaces charge negatively, whereas the water charges mainly
15
16
17
18 positively.
19
20
21
22
23
24
25
26
27
28
29
30
31
32
33
34
35
36
37
38
39
40
41
42
43
44
45
46
47
48
49
50
51
52
53
54
55
56
57
58
59
60

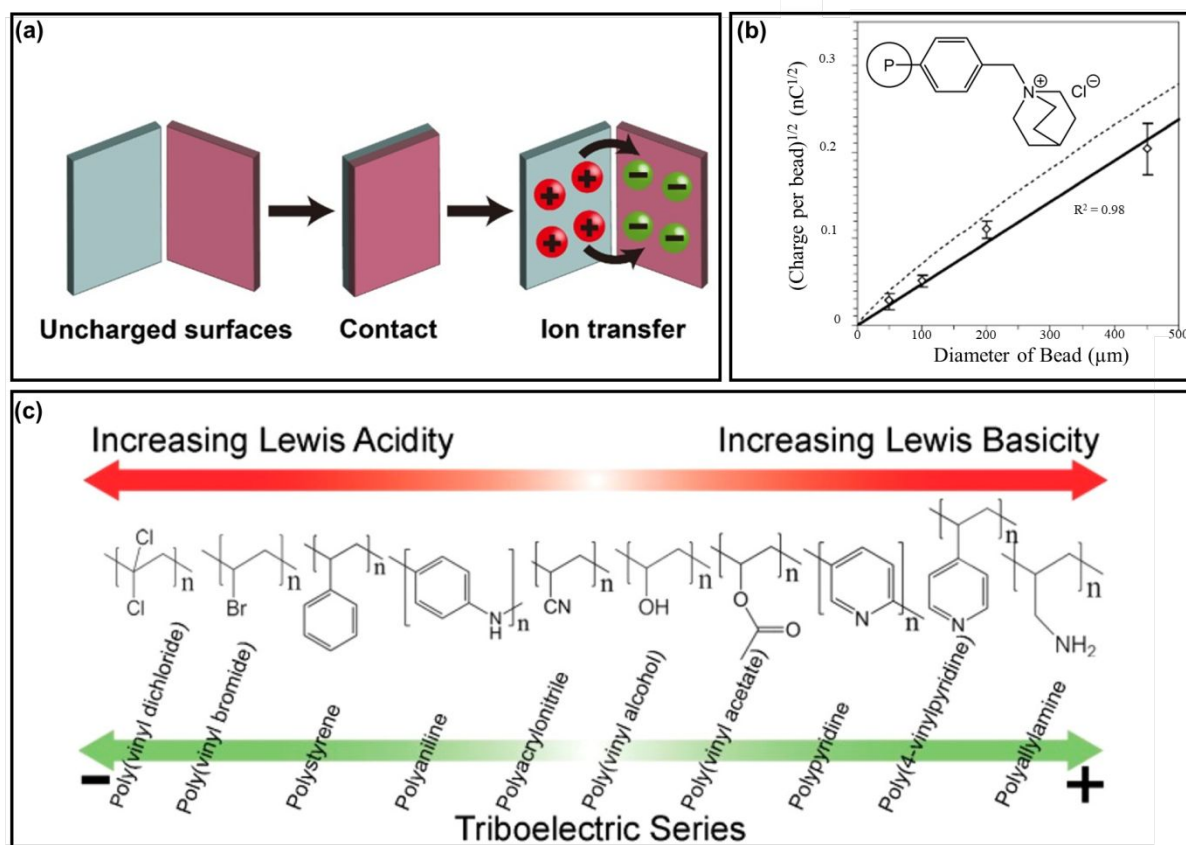


Figure 10. Ion transfer model. **(a)** The scheme illustrates the transfer of ions between two solid surfaces due to contact electrification. **Reproduced with permission from ref. 87** **(b)** The plot shows the charge of microspheres coated with molecules that had ionic functional groups after contact electrification with glass beads. The dashed line represents the maximum possible amount of charge that can be accumulated on the microsphere without dielectric breakdown of air. **Reproduced with permission from ref. 93** **(c)** Experimental results showed that there is a correlation between the Lewis acidity/basicity of polymers and the polarity of charge generated by contact electrification (i.e., the triboelectric series). **Reproduced with permission from ref. 107**

2.2 Surface Modifications

2.2.1 Physical surface modification

Since TENGs are based on the electric charge transfer between the contact surface of materials, the surface condition of constituent materials of TENGs is one of the crucial factors for high output performance TENGs. For example, it is reported that the output voltage of contact-mode TENGs is defined by equations (1) – (3).¹¹³⁻¹¹⁵ To enhance the output performance of TENGs based on these fundamentals, various research on physical^{114, 116-131} and chemical¹³²⁻¹⁴⁶ surface modifications to control contact surface morphology has been conducted by many research groups during the last decade. Tailoring the surface topography into nanometer or micrometer scales by physical and chemical modifications has previously been reported to achieve advanced triboelectrification. Physical surface morphology modifications such as direct patterning¹¹⁷, designing pattern template¹¹⁸, mechanical nanoparticles impacting the surface¹¹⁴, laser treatment¹²⁶⁻¹²⁸, surface attached nanoparticles¹³¹, inverse opal structures¹²⁵, plasma treatment¹²⁹⁻¹³⁰, and lifting out the material to form a porous sponge structure¹²³ are mostly focused on enlarging the active friction area and roughness of the contact materials, while chemical modification such as ion doping¹³⁵⁻¹³⁷, functionalized groups or molecules¹³⁸⁻¹⁴⁰, chemically modified nanowires¹³³⁻¹³⁴, anodic

1
2
3
4 aluminum oxides^{132, 146}, and polymer dry-etching¹⁴⁵ are mainly focused on enhancement of
5
6
7
8 the electron affinity and enlarging the surface area. Recently, Xenon flash lamps with
9
10
11 strong photon energy for a short time (in the millisecond range) have been employed for
12
13
14 light-material interactions (LMIs), where a nano composite is embedded into the material,
15
16
17
18 which can significantly affect improvement of the surface electrification and increase
19
20
21 triboelectrification¹²⁸. Table 1 and Figure 11 show the TENG performance (output voltage,
22
23
24 current, and power density) with various noticeable surface morphology modifications.
25
26
27
28
29
30
31
32
33
34
35
36
37
38
39
40
41
42
43
44
45
46
47
48
49
50
51
52
53
54
55
56
57
58
59
60

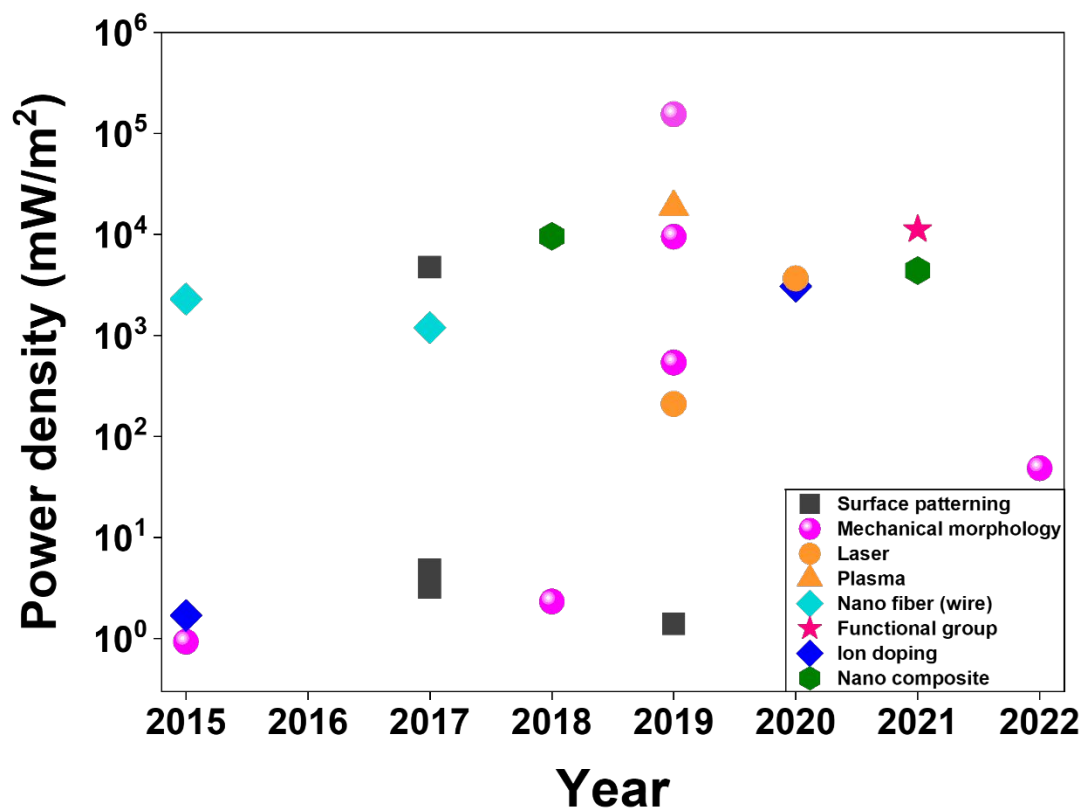


Figure 11. Reported power density of TENGs with surface modification methods over publication year. Each data point is taken from the following references: surface patterning¹¹⁶⁻¹¹⁹, mechanical morphology control^{114, 120-125}, laser treatment¹²⁶⁻¹²⁸, plasma treatment¹²⁹, nano fiber¹³²⁻¹³⁴, ion doping^{135, 137}, chemical functional group¹³⁸, and nano composite embedding^{141, 143}

1
2
3
4
5 Many studies about physical surface modifications have been conducted to improve the
6
7
8 output of TENG devices.^{52, 147} Figure 12(a) shows TENGs with a sandpaper-assisted
9
10
11 micropattern on its surface,¹⁴⁸ which easily and cost-effectively enlarged the surface contact
12
13
14 area, thus enhancing output performance. A morphology-controllable wrinkled micro/nano
15
16
17 hierarchical structure was also developed by integrating multiscale poly(vinyl alcohol) (PVA)
18
19
20 architectures (Figure 12(b)).¹⁴⁹ Additionally, superhydrophobic characteristics were imparted
21
22
23 by the PVA structure,¹⁵⁰ resulting in the signal rapidly recovering after hard humid spraying.
24
25
26
27
28 By mimicking the surface structures of skin (Figure 12(c)), a hierarchical nanoporous and
29
30
31 interlocked microridge structured polymer-based TENG was fabricated without a spacer.¹⁵¹
32
33
34
35 The gradient elastic modulus between the interlock-structured poly(vinylidene fluoride-co-
36
37
38 trifluoroethylene) (P(VDF-TrFE)) and porous polydimethylsiloxane (PDMS) layers
39
40
41 significantly enhanced the output performance in terms of bending and pressing input
42
43
44 conditions. As shown in Figure 12(d), dry etching was applied on the polymer surface to
45
46
47 create vertical and rough nanowires.¹⁵² Enhanced surface roughness by forming polyimide
48
49
50 (PI) nanowires with a dry etching process leads to high triboelectric output. Figure 12(e)
51
52
53 presents the schematics and SEM images of the wet etching method for PI film.¹⁵³ In contrast
54
55
56 to the dry etching method, it has the advantage of being able to modify the surface
57
58
59
60

1
2
3
4 morphology in a short time.¹⁵⁴ Because of the uniform honeycomb-patterned surface of the PI
5
6
7
8 film, the current output of the TENG was increased by more than 4 times.
9

10
11 Laser direct patterning is a facile method to fabricate micro/nanostructures in ambient
12
13
14 conditions due to its ultrashort irradiation period.¹⁵⁵ Figure 12(f) shows the direct laser
15
16
17 patterning on the Cu surface and PDMS using a femtosecond (fs) laser.¹³⁰ Single fs laser
18
19
20 scanning was initially processed on the Cu film surface, resulting in micro-cone patterns.
21
22
23
24 Then, the fs laser pulse was irradiated to the PDMS, thus fabricating the micro-bowl
25
26
27 structures. This specific morphology improved the effective contact area and surface
28
29
30 roughness, which can be used for higher triboelectric output performance. Figure 12(g)
31
32
33
34 presents a study about simultaneous surface modification with materials synthesis.¹⁵⁶ When
35
36
37 the laser was irradiated onto the precursor ($(\text{NH}_4)_2\text{MoS}_4$) on a substrate, this leads to heating
38
39
40 the precursor above a thermal threshold, which synthesized MoS_2 layers. Interestingly, by
41
42
43
44 controlling the laser irradiating fluence (i.e., power range), the synthesized MoS_2 surface
45
46
47 becomes three-dimensionally distorted and highly crumpled MoS_2 . The increase of surface
48
49
50 roughness of MoS_2 using laser-direct synthesis led to improved triboelectric performance.
51
52
53
54 Moreover, the surface crumpling of MoS_2 induced a change of the work function, which can
55
56
57
58 lead to efficient contact electrification.
59
60

1
2
3
4
5
6
7
8
9
10
11
12
13
14
15
16
17
18
19
20
21
22
23
24
25
26
27
28
29
30
31
32
33
34
35
36
37
38
39
40
41
42
43
44
45
46
47
48
49
50
51
52
53
54
55
56
57
58
59
60

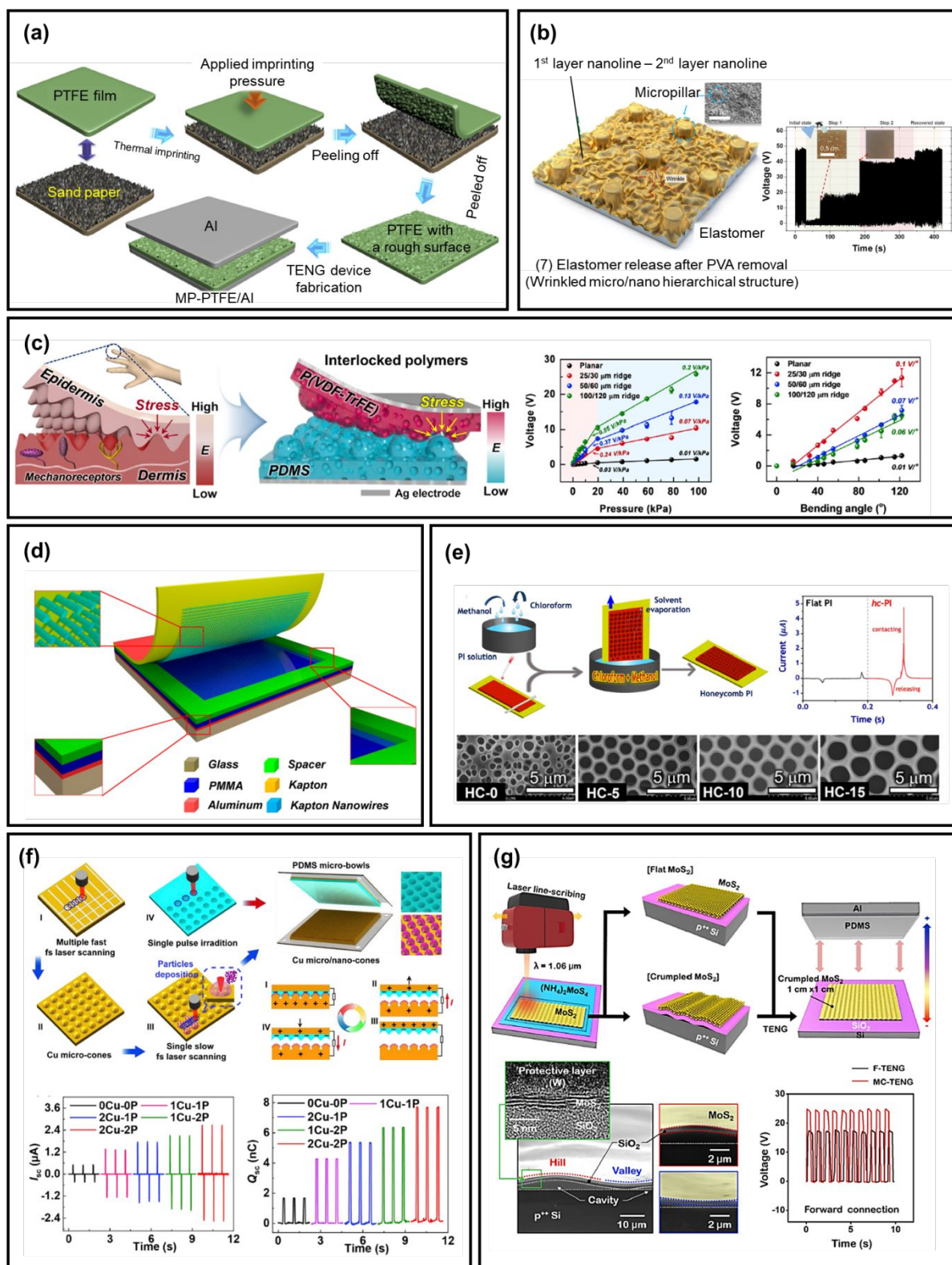


Figure 12. (a) Fabricating process of a sandpaper-assisted TENG. Reprinted with permission from ref. 148, Copyright 2018, Elsevier. (b) Schematics of nano/micro hierarchical structure TENG and SEM images of an inclined view of the fabricated TENG. The right panel shows the results of a water spraying test during contact and separation

1
2
3
4 processes of the TENG. **Reprinted with permission from ref. 149, Copyright 2021,**
5 **Elsevier.** (c) Structural characteristics of human skin and a schematic of the skin-inspired
6 triboelectric sensor. The right panels present the sensitivity of the triboelectric voltage
7 followed by the pressure and bending angle. **Reprinted with permission from ref. 151,**
8 **Copyright 2018, American Chemical Society.** (d) Sketch of the Kapton nanowire-based
9 TENG. **Reprinted with permission from ref. 152, Copyright 2012, American Chemical**
10 **Society.** (e) Fabrication of the honeycomb-patterned PI-TENG and surface morphology
11 variation with various methanol contents. Current signal generated compared between the flat
12 and honeycomb-patterned PI-TENG (right panel). **Reprinted with permission from ref. 153,**
13 **Copyright 2022, American Chemical Society.** (f) Schematic diagrams for the fabrication
14 process, structure and principle of micro/nano-structured TENGs. Triboelectric signal of
15 TENGs with different micro/nanostructures. **Reprinted with permission from ref. 130,**
16 **Copyright 2019, Elsevier.** (g) Schematic illustration of laser-directed patterning of MoS₂ on
17 an SiO₂ wafer and illustration of the crumpled MoS₂-based TENG structure. The down panels
18 show SEM images of crumpled MoS₂ and V_{oc} generated from F-MoS₂ and MC-MoS₂-based
19 TENGs. **Reprinted with permission from ref. 156, Copyright 2020, Elsevier.**
20
21
22
23
24
25
26
27
28
29
30
31
32
33
34
35
36
37
38
39
40
41
42
43
44
45
46
47
48
49
50
51
52
53
54
55
56
57
58
59
60

2.2.2 Chemical Surface modification

Since the invention of triboelectric nanogenerators (TENGs) in 2012, special emphasis has been paid on manipulating the surface chemistry of the friction layers through chemical modifications for improving the TENG's performance. Chemical modifications improve the output performance by enhancing the triboelectric surface charge density on the material surfaces. This technique also facilitates the possibility of fabricating TENGs by incorporating diverse material surfaces irrespective of their original triboelectric properties, thereby increasing the material selectivity choices for designing TENGs. Furthermore, the chemical modification method also improves the flexibility of the TENG's structural design for practical applications by incorporating additional functionalities (hydrophobicity), reducing the encapsulation process, and retaining the material's original excellent characteristics and strong chemical bond connections which stabilize the chemical groups on its surface, thereby increasing its wear resistance.⁷³ Chemical modification can broadly be segregated into ligand functionalization and surface treatment methods.

Sometimes, chemical surface modification can be better than physical modification for TENGs because chemical methods can change the inherent surface material properties. For example, there are plasma, neutral beam (NB), ultraviolet/ozone (UVO), and chemical

1
2
3
4
5 functionalization techniques.^{144, 157-160} Figure 13(a) shows C_4F_8 plasma applied onto the outer
6
7
8 surface of a polymer film,¹⁶¹ which coated the fluorocarbon layers. It is well known that CF_n
9
10
11 functional groups have low surface energy and hydrophobic characteristics compared to other
12
13
14 functional groups.¹⁶² Additionally, the fluorine-based plasma treatment can lead to improving
15
16
17 the performance of TENG devices since the fluoro-based materials are typically positioned
18
19
20 on extremely charged triboelectric series.¹⁶³
21
22
23

24
25 NB treatment was highlighted due to its advantages with preventing defects.¹⁶⁴ Figure 13(b)
26
27
28 illustrates the NB surface treatment for PDMS, thermoplastic polyurethane (TPU), and
29
30
31 related triboelectric output.¹⁶⁵ Depending on the utilized gas types, nitrogen ambient NB (N-
32
33
34 NB) and oxygen ambient NB (O-NB) can be formed. Through NB treatments depending on
35
36
37 the surface types (PDMS or TPU), the surface triboelectric potential can be increased via the
38
39
40 attached oxygen or nitrogen functional groups on the triboelectric charging surface.
41
42
43
44 Interestingly, NB-treated TENG devices showed higher output than the plasma-treated
45
46
47 TENGs, which indicates that NB can be an excellent approach. Figure 13(c) presents UVO
48
49
50 treatment-based chemical modification for PDMS surfaces.¹⁶⁶ Non-treated PDMS surfaces
51
52
53 mainly consist of Si- CH_3 bonds, whereas the UVO-irradiated PDMS surface is composed of
54
55
56 Si-O, Si-OH and Si-COOH bonds converted from broken Si- CH_3 bonds. Because of the polar
57
58
59
60

1
2
3
4 features of oxygen functional groups, UVO-treated TENG devices generated higher
5
6
7
8 triboelectric output. Atomic oxygen (AO) irradiation is another kind of ion-plasma treatment
9
10
11 for enhancing triboelectrification. Figure 13(d) shows a schematic process and enhanced
12
13
14 triboelectric signals of TENG devices after AO irradiation to the PDMS.¹⁶⁷ The original Si-C
15
16
17 bonds are destroyed and Si-O bonds appear on the PDMS surface using AO irradiation.
18
19
20
21 Furthermore, Si-O bonds increased with more irradiation time, which leads to improved
22
23
24 surface potential, similar to Figure 13(c).¹⁶⁶
25
26
27

28 Laser-based processes can be utilized for chemical modification as well as physical
29
30
31 patterning. A laser-induced graphene (LIG)-based TENG was proposed (Figure 13(e)).¹⁶⁸
32
33
34 When CO₂ laser was irradiated on a PI film, the graphene layers were synthesized on the
35
36
37 surface. Long carbon fiber-dominant/LIG (LF-LIG), short carbon fiber/LIG (SF-LIG), and
38
39
40 porous LIG were formed according to the conditions of CO₂ laser irradiation. Lots of
41
42
43 graphitic nitrogen (N) components are contained in the LIG, which prefers to transfer the
44
45
46 outer electrons to the surrounding carbon atoms. These carbon atoms decrease the work
47
48
49 function via electron donation. Particularly, long chain structured LF-LIG contains more
50
51
52 graphitic N components and results in a larger work function, which is a key factor to
53
54
55 enhancing triboelectric device performance.¹⁶⁹
56
57
58
59
60

1
2
3
4
5
6
7
8
9
10
11
12
13
14
15
16
17
18
19
20
21
22
23
24
25
26
27
28
29
30
31
32
33
34
35
36
37
38
39
40
41
42
43
44
45
46
47
48
49
50
51
52
53
54
55
56
57
58
59
60

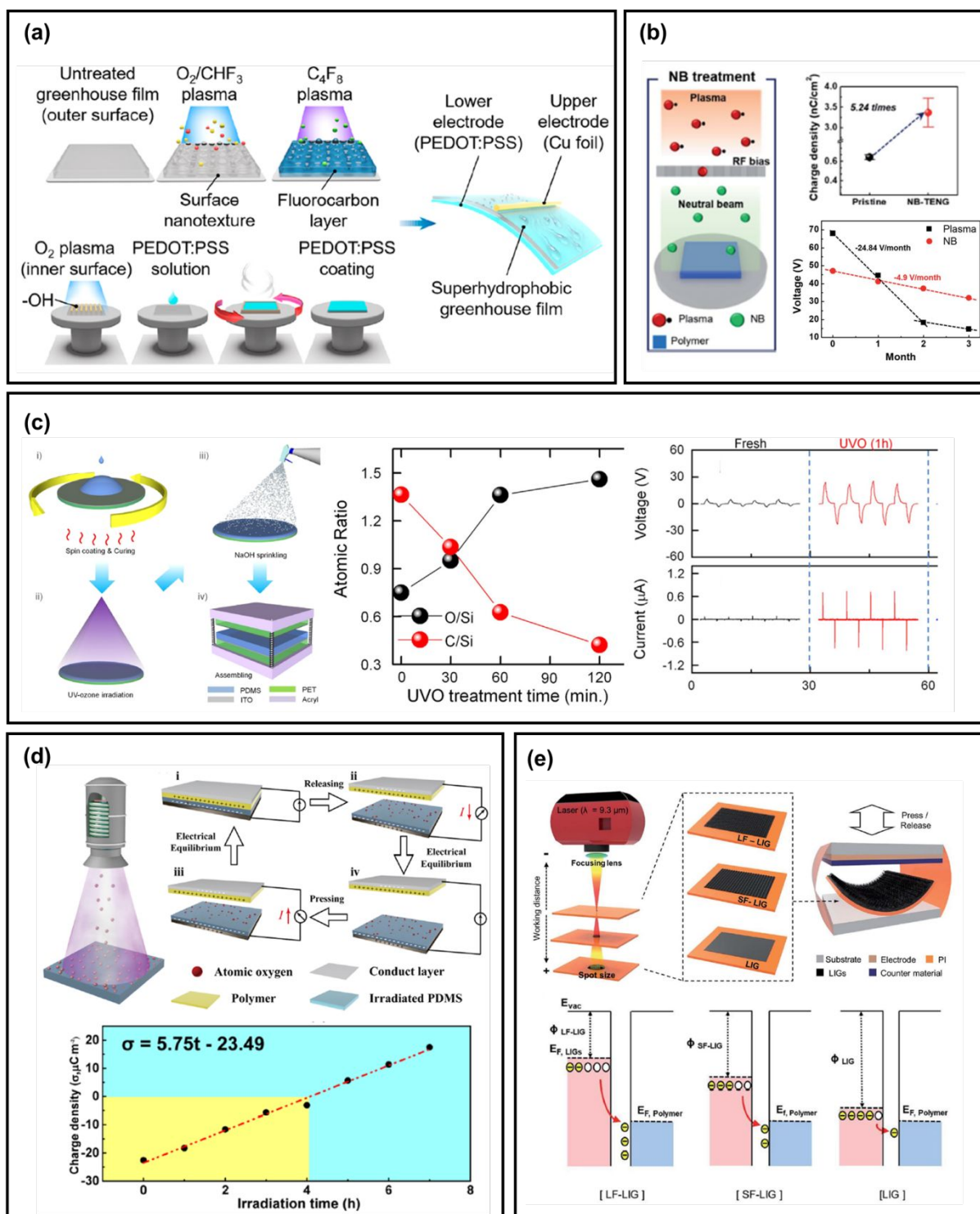


Figure 13. (a) Schematic illustration of the fabrication process TENG, utilizing O_2/CHF_3 plasma and C_4F_8 plasma. Reprinted with permission from ref. 161, Copyright 2021, American Chemical Society. (b) Process of NB treatment on the polymer surface. The right panel presents triboelectric performance and long-term stability of NB treated TENG. Reprinted with permission from ref. 165, Copyright 2019, Royal Society of Chemistry. (c) Process of surface treatment utilizing UV-O treatment on a PDMS surface and effect on

1
2
3
4 atomic ratio of PDMS. The right panels present enhanced open-circuit voltage of UV-O
5 treated PDMS-based TENG. **Reprinted with permission from ref. 166, Copyright 2015,**
6 **Elsevier.** (d) Illustration of AO modification and working mechanism of AO irradiated
7 TENGs. Correlation of charge density and AO irradiation time (down panel of Figure 2d).
8 **Reprinted with permission from ref. 167, Copyright 2021, American Chemical Society.**
9 (e) Process of the laser direct LIG synthesis and energy band diagram of LIG, SF-LIG, LF-
10 LIG when contact with PMMA. **Reprinted with permission from ref. 168, Copyright 2020,**
11 **Royal Society of Chemistry.**
12
13
14
15
16
17
18
19
20
21
22
23
24
25
26
27
28
29
30
31
32
33
34
35
36
37
38
39
40
41
42
43
44
45
46
47
48
49
50
51
52
53
54
55
56
57
58
59
60

1
2
3
4 Ion implantation has been one popular method to modify the surface of triboelectric
5 materials. The experimental process of He⁺-ion irradiation is shown in Figure 14(a). In this
6
7
8
9
10
11
12
13
14
15
16
17
18
19
20
21
22
23
24
25
26
27
28
29
30
31
32
33
34
35
36
37
38
39
40
41
42
43
44
45
46
47
48
49
50
51
52
53
54
55
56
57
58
59
60

Ion implantation has been one popular method to modify the surface of triboelectric materials. The experimental process of He⁺-ion irradiation is shown in Figure 14(a). In this study, a low-energy ion beam of 50 keV is utilized to irradiate the target sample for protection of the target polymer from crystallization and carbonization during the irradiation process.

For irradiated Kapton, a C–H bond and an N–H bond are formed Figure 14(a)-(ii)., i.e., the –NHCOR bond is established, which is an electron donating group. The electron donating ability of a functional group can be determined by the inductive and conjugation effects. As an example, the C=O in the –NHCOR bond is an electron withdrawing group, while the –NHCOR bond is a medium electron donating group. This is a typical example of an induction effect. On the other hand, when the –NHCOR fragment is bonded to a group containing a π bond (p electron), a conjugation effect occurs. Therefore, the electron donating effect of the –NHCOR bond could be largely enhanced by bonding with the benzene ring, which is a sort of conjugation effect (Figure 14(a)-(ii)). A polymer containing strong electron donating groups can be a good candidate for positive triboelectric materials. When irradiated Kapton film (KAPTON1E16) was matched with a film of fluorinated ethylene propylene (FEP), more electrons can be transferred owing to this conjugation effect (Figure 14(a)-(iii)).¹⁷⁰

1
2
3
4
5 Aside from the adjustment of existing chemical bonding, introduction of elements in the
6
7
8 original polymer matrix can be a useful means for increasing its triboelectric performance.

9
10
11 Figure 14(b)-(i) represents an interstitial replacement of N in the PTFE by N-ion
12
13
14 implantation.¹⁷¹ This study proposed the following mechanism to describe the modification
15
16
17
18 process.

19
20
21 At the lower implantation dose (PTFE-1E14, PTFE-5E14 in Figure 14(b)-(ii), the bonds
22
23
24 with lower chemical bond energy, i.e., C-C bonds, are preferentially destroyed and leave lots
25
26
27 of terminal ($\cdot\text{CF}_2\text{-CF}_2\cdot$) radicals. Such radicals are readily combined with implanted N ions
28
29
30 to form chemical bonds (C=N and C \equiv N) at the chain ends. Meanwhile, some of the F atoms
31
32
33 could be detached by the collision of N ions and become free atoms. Interstitial defects
34
35
36 consist of N induced polar groups and unsaturated bonds, which can break the spatial
37
38
39 structural symmetry of the PTFE. Such rearrangement in a polymeric matrix improved the
40
41
42 polarity and electronegativity of groups, which altered them into polar polymers. This in turn
43
44
45 enriched the overlap of the electron cloud to enhance the electron-withdrawing capability.
46
47
48 Furthermore, the sp^3 hybridization changed to sp^2 and sp hybridizations, which led to the
49
50
51 larger role of s orbitals in hybrid orbitals, resulting in stronger attraction of the electrons.
52
53
54
55 Especially, the C \equiv N groups have larger electron cloud density and higher electron affinity
56
57
58
59
60

1
2
3
4 than those of the -F groups. In fact, the cyanogroups can result in a shorter molecular distance
5
6
7
8 and strengthen the overlap of the electronic cloud. Thus, it had stronger electron-withdrawing
9
10
11 capability and facilitated the surface charge transfer process during contact with other tribo-
12
13
14 materials.¹⁷²⁻¹⁷³

15
16
17
18 In the case of high dose implantation, the collision cascade between N ions and the chemical
19
20
21 chains in the near-surface region increases. A number of F ions were released from the C-F
22
23
24 bond and formed F free atoms and inter-chain middle (-CF₂-·CF-CF₂-) radicals. Such
25
26
27 processes also led to numerous small molecular chains with low molecular weight, which
28
29
30 could increase the probability of secondary reactions with radicals. This may result in polar
31
32
33 bonds, unsaturated bonds, molecular fluorine, and fluoromethane. The detachment,
34
35
36 recombination, and escape of F atoms occurred in higher doses (PTFE-1E15, PTFE-1E16 in
37
38
39
40
41 Figure 14(b)-(i), which reduced the content of -F, resulting in weakened EW ability.
42
43
44
45 Furthermore, focused energy density in a beam due to high-dose ions caused surface
46
47
48 carbonization, which decreased the surface charge transfer process of materials, leading to
49
50
51 lower performance compared to PTFE-1E14. Therefore, the triboelectric and electrical
52
53
54 performance of implanted PTFE first increases and then decreases with increasing ion doses
55
56
57
58 (Figure 14(b)-(ii)).
59
60

1
2
3
4
5
6
7
8
9
10
11
12
13
14
15
16
17
18
19
20
21
22
23
24
25
26
27
28
29
30
31
32
33
34
35
36
37
38
39
40
41
42
43
44
45
46
47
48
49
50
51
52
53
54
55
56
57
58
59
60

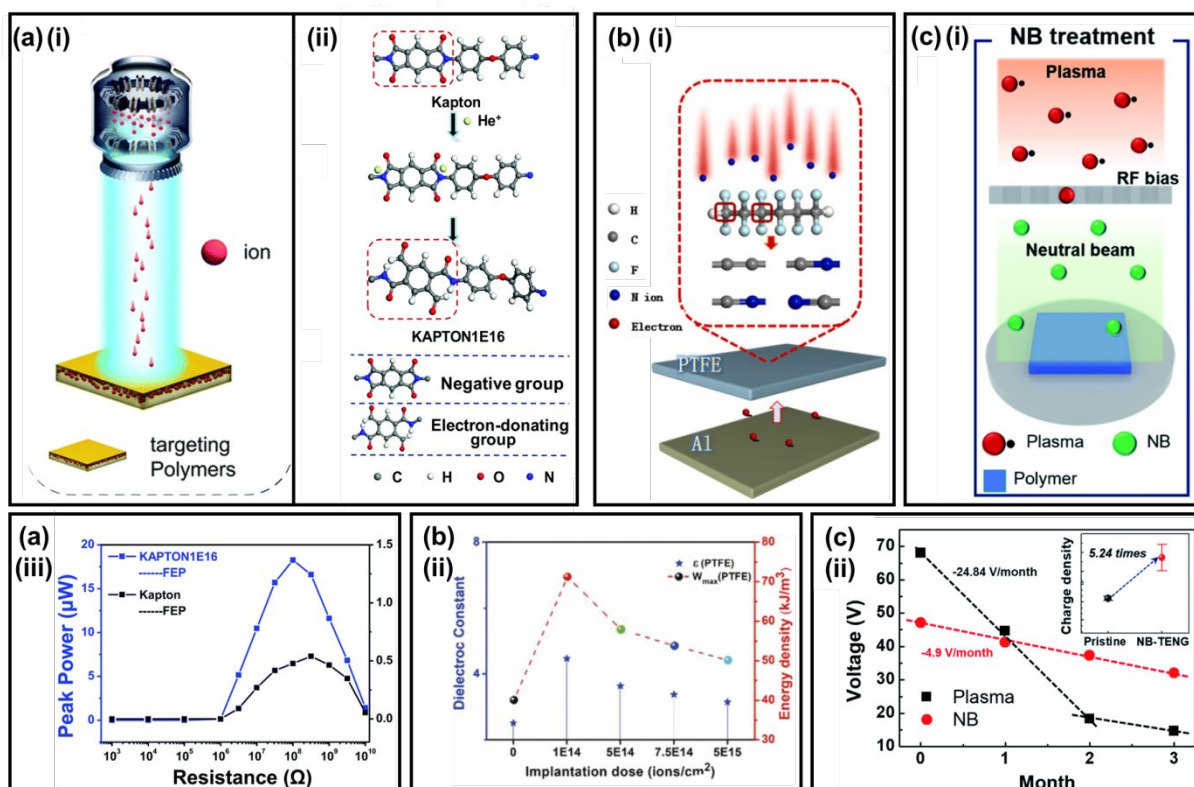


Figure 14. (a) Schematic diagram of He⁺-ion irradiation on the target polymer (Kapton) surface. (a)-(ii) Schematic diagram depicting the change of the molecular structure and formula of Kapton by He⁺ ion irradiation. (a)-(iii) Power comparison of TENGs based on Kapton and FEP with and without He⁺-ion irradiation. **Adapted from ref. 170, Copyright 2020 The Royal Society of Chemistry.** (b) Schematic diagram depicting a TENG based on modified PTFE with N-ion implantation. (b)-(ii) The calculated maximum energy storage density of the PTFE films depending on of the implantation dose. **Adapted from ref. 171, Copyright 2021 Elsevier.** (c) Schematic of the NB treatment process. (c)-(ii) Time-dependent degradation of voltage outputs from TENGs treated by plasma or NB for a three-month period. All voltage outputs were measured in a controlled environment (RH 40%, 25 °C). **Adapted from ref. 165, Copyright 2019 The Royal Society of Chemistry.**

1
2
3
4
5
6
7 TENG performance can be enhanced by functionalizing different ligand groups with the
8
9
10 ability to gain or lose electrons on the contact material surfaces. Therefore, selecting
11
12
13 materials with good triboelectric properties is a crucial factor to improve the surface charge
14
15
16 density of TENGs. Shin et al. reported a facile method to tune the triboelectric properties of
17
18
19 the polyethylene terephthalate (PET) substrate by atomic-level chemical functionalization
20
21
22 using electron-accepting halogens and electron-donating aminated molecules (Figure
23
24
25
26 15(a)).¹⁵⁹ Significant variations in transferred charge density are reported with aminated-PET
27
28
29 surfaces generating a positive charge density, while halogenated-PET surfaces generated
30
31
32 negative charge density. In addition to halogens, sulfur (S) also possesses a large electron
33
34
35 affinity. Therefore, extremely negative triboelectric material can be designed due to sulfur's
36
37
38 high electron affinity and hypervalency. Lee et al. reported sulfur backbone-based inorganic
39
40
41 polymers synthesized by the inverse-vulcanization process of elemental sulfur (Figure
42
43
44 15(b)).¹⁷⁴ Triboelectric energy output for the fluorinated polymeric sulfur significantly
45
46
47 improved with a 6-times voltage enhancement in comparison to the polytetrafluoroethylene
48
49
50 (PTFE)-based TENG. Jian et al. reported 2D MXenes materials with high electron-
51
52
53 withdrawing capabilities due to the presence of fluorine and oxygen functional groups, for the
54
55
56
57
58
59
60

1
2
3
4 preparation of nanofiber films with a 1087.6 mW/m² maximum peak power density.⁶³
5
6
7

8 MXenes are flexible, environmentally friendly, and large-scale manufacturable, making them
9
10 quite suitable for flexible electronics.
11
12
13

14 In the last few years, research related to controlling the triboelectric charge density of
15
16 biodegradable natural materials, such as cellulose, has gained momentum in the field of
17
18 TENGs. As depicted in Figure 15(c), the surface tailoring of cellulose nanofibrils (CNFs) has
19
20
21
22
23
24
25 been done to tune the triboelectric charge density to enhance the performance of TENGs.¹⁷⁵
26
27

28 Based on the functional group introduced (-CF₂CF₃, -CN, -SH, or -NH₂), the CNFs surface
29
30
31
32
33
34
35
36
37
38
39
40
41
42
43
44
45
46
47
48
49
50
51
52
53
54
55
56
57
58
59
60
chemical compositions changes, and the materials exhibit different polarities. A renewable
high-performance cellulose-based TENG was developed by synthesizing allicin-grafted CNF
(Alc-S-CNF) by “thiol-ene” click chemistry to enhance the triboelectric properties of bare
CNFs.¹⁷⁶

The current density and power density of modified cellulose film were enhanced by 6 times
and 41 times, respectively, compared to the original cellulose film, owing to a higher dipolar
nature of the sulfoxide group (-S=O) and good polarization of the disulfide bonds in allicin.

Furthermore, in recent years, ligand functionalization has emerged as an effective
method to develop triboelectric nanosensors (TENSs) for label-free and rapid analysis of

1
2
3
4 pathogenic microorganisms. Jung et al. used intermolecular recognition interactions for the
5
6
7
8 development of an aptamer-based self-powered triboelectric biosensor for the detection of
9
10
11 thrombin.¹⁷⁷ By assembling thiol-modified anti-thrombin aptamers on Au nanoparticles
12
13
14 (NPs), the sensor showed enhanced electrical signals after incubation with thrombin, with a
15
16
17 detection limit of 0.41 nM. Pao et al. functionalized D-mannose-thiol on Au NPs and
18
19
20 developed a solid-liquid-based TENS to study the carbohydrate-protein interactions.¹⁷⁸ In
21
22
23 particular, concanavalin A (Con A) protein and Escherichia coli (E. coli) are detected by D-
24
25
26 mannose-thiol functionalized Au nanoparticles (m-Au NPs). Attachment of Con A or E.coli
27
28
29 decreases the work function of the solid triboelectric sensing layer, thereby reducing the
30
31
32 surface potential barrier and providing a key physical phenomenon responsible for sensing.
33
34
35 Furthermore, a Con A modified m-Au NP solid contact layer underwent a sequential contact-
36
37
38 separation operation with PBS buffer solution to generate the triboelectric effect.
39
40
41
42 Interestingly, as the Con A concentration increases over m-Au NPs, the output voltage also
43
44
45 increases steadily (Figure 15(d)).
46
47
48
49
50
51
52
53
54
55
56
57
58
59
60

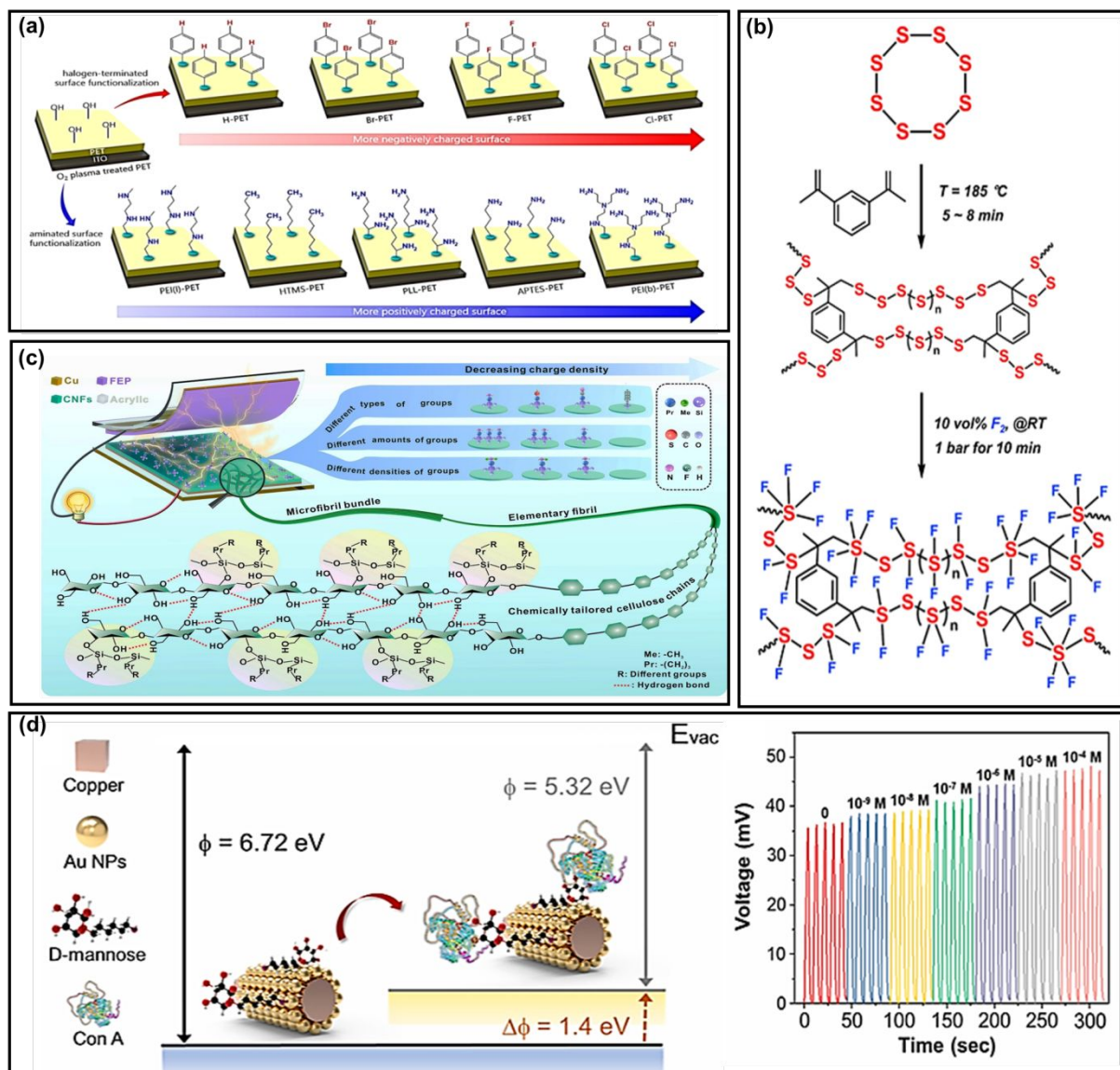


Figure 15. Chemical surface modification by ligand functionalization. **(a)** Schematic illustration showing the introduction of halogen and aminated containing functional groups to a PET surface. **Reprinted with permission from ref. 159, Copyright 2017 American Chemical Society.** **(b)** Synthesis scheme of fluorinated sulfur copolymers. **Reprinted with permission from ref. 174, Copyright 2019 Elsevier.** **(c)** Schematic diagram of chemical functional groups tailored CNFs for manipulating the charge density. **Reprinted with permission from ref. 175, Copyright 2021 Elsevier.** **(d)** Schematic of change in work function with the attachment of Con A over m-Au NPs and corresponding voltage shift with increasing concentration of Con A over m-Au NPs. **Reprinted with permission from ref. 178, Copyright 2021 Elsevier.**

1
2
3
4
5
6
7 Surface treatment methods have also been explored quite extensively for enhancing surface
8
9
10 charge density of the materials. Fan et al. proposed an ultraviolet-ozone (UVO) irradiation
11
12
13 mechanism for the PDMS surface-induced molecular structure change.¹⁷⁹ The reactive O
14
15
16 radicals convert the methyl groups (Si-CH₃) to silanol groups (Si-OH) upon exposure,
17
18
19 thereby changing the surface structure (Figure 16(a)). This led to stabilized output
20
21
22 performance of the TENG. Similarly, significant improvement in the performance of a TENG
23
24
25 has been achieved by altering the PDMS frictional layer surface charge density by UVO
26
27
28 irradiation and NaOH treatment (Figure 16(b)).¹⁶⁶ The surface charge sequentially increased
29
30
31 when fresh PDMS was treated with UVO and UVO+NaOH. The short-circuit current and
32
33
34 open-circuit voltage were reported as 1.16 μA and 49.3 V, respectively, an approximately 15-
35
36
37 fold enhancement when compared to the untreated fresh PDMS. In addition to UVO
38
39
40 irradiation, single-step fluorocarbon plasma treatment technology for functionalizing fluorine
41
42
43 groups onto the material surface has also been used for enhancing surface charge density.
44
45
46
47 Zhang et al. demonstrated a high-performance TENG with enhanced energy density via a
48
49
50 single-step fluorocarbon plasma treatment method.¹⁸⁰ The power density of the TENG
51
52
53
54 increased by 2.78 times after chemical modification, with a peak output voltage of 265 V and
55
56
57
58
59
60

1
2
3
4 a current density of $18.3 \mu\text{A}/\text{cm}^2$. Lee et al. analyzed the PDMS surface structure and
5
6
7
8 chemical properties after a two-step reactive ion etching (RIE) plasma treatment to
9
10
11 understand its effect on the output performance.¹³³ A surface interface engineered PDMS
12
13
14 (SIE-PDMS) is reported by implementing Ar plasma and CF_4+O_2 plasma individually on the
15
16
17 PDMS surface (Figure 16(c)). The power density measurements for the TENG revealed that
18
19
20 plasma-treated PDMS-based TENG achieved $18.8 \text{ W}/\text{m}^2$ power density (at 25 W RIE power),
21
22
23 an almost 4-times enhancement compared to untreated PDMS-based TENGs. Similarly, a
24
25
26 surface modification of a PET film via inductive-coupled plasma etching has been reported
27
28
29 by using a mixture of carbon tetrafluoride (CF_4) and O_2 gases.¹⁸¹ TENGs based on the
30
31
32 modified PET exhibit approximately 300% enhancement in open-circuit voltage, short-circuit
33
34
35 current, and induced charge quantity. Recently, neutral beam (NB) technology, an advanced
36
37
38 plasma-based etching technique, has gained much attention. This technology provides a high
39
40
41 degree of control over the energy of the collimated neutral beam by suppressing the incident
42
43
44 charged particles and high-energy photons, thereby controlling surface states with high
45
46
47 precision and preventing defects at the atomic-layer level.^{165, 182} Typically, for large contact
48
49
50 electrification, surface treatment is done separately for both the positive and negative
51
52
53
54
55
56
57
58
59
60

1
2
3
4 material. Kim et al. introduced a system that uses a neutral beam (NB) for both positive and
5
6
7
8 negative triboelectric materials for enhancing TENG performance (Figure 16(d)).¹⁶⁵
9

10
11 In addition to the aforementioned methods, other surface treatment methods such as
12
13
14 ionized air injection¹³⁶, corona charging¹⁸³, and ion implantation¹⁷¹ also have been widely
15
16
17
18 employed to enhance the performance of TENGs. Among these, the ion implantation
19
20
21
22 technique can precisely control the concentration and distribution of dopant atoms in the
23
24
25 material, thereby generating favorable intrinsic point defects and various functional groups.
26
27
28 Fan et al. implanted N ions with high kinetic energy (100 keV) to form polar bonds among
29
30
31 the atoms of triboelectric layers (PTFE, FEP, and Kapton) (Figure 16(e)).¹⁷¹ A triboelectric
32
33
34 series of various films before and after implantations with N ions implantation doses of
35
36
37
38 1×10^{14} (1E14) and 5×10^{14} ions/cm² (5E14) has been established. With this implantation,
39
40
41 PTFE and FEP films exhibited stronger negative triboelectric polarity with high surface
42
43
44
45 charge density. Similarly, Li et al. irradiated He ions with 1×10^{16} ions/cm² concentration on
46
47
48 four polymers surfaces namely, Kapton, PET, PTFE, and FEP, and assembled a TENG with
49
50
51 Al foil as the other frictional layer.¹⁷⁰ Before and after irradiation, the output voltage related
52
53
54
55 to the Kapton film-based TENG device changed from 2.2 to -2 V, indicating a change in
56
57
58 polarity.
59
60

Though significant results have been achieved through chemical surface modifications, research related to different functional groups' internal mechanisms needs to be further explored. As stated earlier, chemically-modified TENGs offer distinct advantages such as material selection choices, high wear resistance, and added functionalities while retaining the characteristics of the material itself. Therefore, the applicability of chemically-modified TENGs can further be extended for developing emerging fields such as human-machine interaction (HMI), wearable electronics, and implantable medical devices.

Surface modification method		Process	Output voltage (V) and current (μA)	Power/Power density (mW/m^2)	Ref.
Physical	Surface pattering	3D print		$1.4 \text{ mW}/\text{m}^2$	116
		Graphene sheet	530 V, 21 μA	$4.8 \text{ mW}/\text{m}^2$	117
		Wafer scale nanogrates of multistep pattern	256.6 V	$3.2 \text{ mW}/\text{m}^2$	118
		PDMS Nanopillar	440 V, 3.6 μA	$4.75 \cdot 10^3 \text{ mW}/\text{m}^2$	119
	Mechanical morphology	Spraying nano bullet	685 V, 277 μA	21 mW $9.545 \cdot 10^3 \text{ mW}/\text{m}^2$	114
		Paper-based hierarchical honeycombs structure	76.3 V	$48.6 \text{ mW}/\text{m}^2$	120
		Octopus surface from hydrogel sheet	139 V	2.7 mW	121

		Porous polymer	60.6 V, 7.7 μA	2.33 mW/m^2	122
		Hydrophobic sponge structure	130 V, 100 $\mu\text{A}/\text{cm}^2$		123
		Mesoporous film + Au NP	150 V, 0.62 $\mu\text{A}/\text{cm}^2$	13 mW 0.93 mW/m^2	124
		Nanosphere with inverse opal nanostructure	242 V	155.12 10^3 mW/m^2	125
	Laser treatment	Laser pattern	36 V	8 mW/m^2	126
		Femtosecond laser	22.04 V	210 mW/m^2	127
		Flash lamp + CuO particle layer	870 V, 145 μA	8.1 mW 3.68 10^3 mW/m^2	128
	Plasma treatment	Chemically-engineered polydimethylsiloxane layer	256.5 V, 22.4 μA	1.64 mW 18.8 $\cdot 10^3$ mW/m^2	129
		Wrinkle pattern	685 V, 165 μA		130
chemical	Nano fiber	Functionalize the nanowires PP (AAO template)	1900 V 19 $\cdot 10^3$ $\mu\text{A}/\text{m}^2$		132
		Electrospinning (nanofiber)	340 V 78 μA	2.3 10^3 mW/m^2	133
		Nanowire TiO ₂ - PDMS (hydrothermal reaction)	740 mV -> 1.6 10^3 μA	1.2 10^3 mW/m^2	134
	Ion doping	Doping Ba ₂ p into CsPbBr ₃	220V, 22.8 10^3 $\mu\text{A}/\text{m}^2$	3.07 $\cdot 10^3$ mW/m^2	135
		Ion injection	~1000V, 900 10^6 $\mu\text{A}/\text{m}^2$	315 $\cdot 10^3$ mW/m^2	136
		Doping polymer	3.1 V, 5.5 $\mu\text{A}/\text{cm}^2$	1.7 mW/m^2	137
	Functional group	MXene-functionalized PVDF	724 V, 163.3 μA	11.213 $\cdot 10^3$ mW/m^2	138
		Nanostructure embedded	~200 V, 14 μA	~2.8 mW	139
		Molecular functionalization	240 V, 1.75 10^3 $\mu\text{A}/\text{m}^2$		140
	Nano composite	3D layer	800 V	27 mW 4.4 $\cdot 10^3$ mW/m^2	141
		MoS ₂ -embedded PVDF	200 V, 11.8 μA	0.07 mW/m^2	142
		Surface texture (CCTO)-embedded PDMS	390 V, 170 10^3 $\mu\text{A}/\text{m}^2$	9.6 10^3 mW/m^2	143
		BMF+ CCTO particle-induced	268 V, 25.8 10^3 $\mu\text{A}/\text{m}^2$		144

Table 1. Energy harvesting properties reported for TENGs with various surface modification methods.

1
2
3
4
5
6
7
8
9
10
11
12
13
14
15
16
17
18
19
20
21
22
23
24
25
26
27
28
29
30
31
32
33
34
35
36
37
38
39
40
41
42
43
44
45
46
47
48
49
50
51
52
53
54
55
56
57
58
59
60

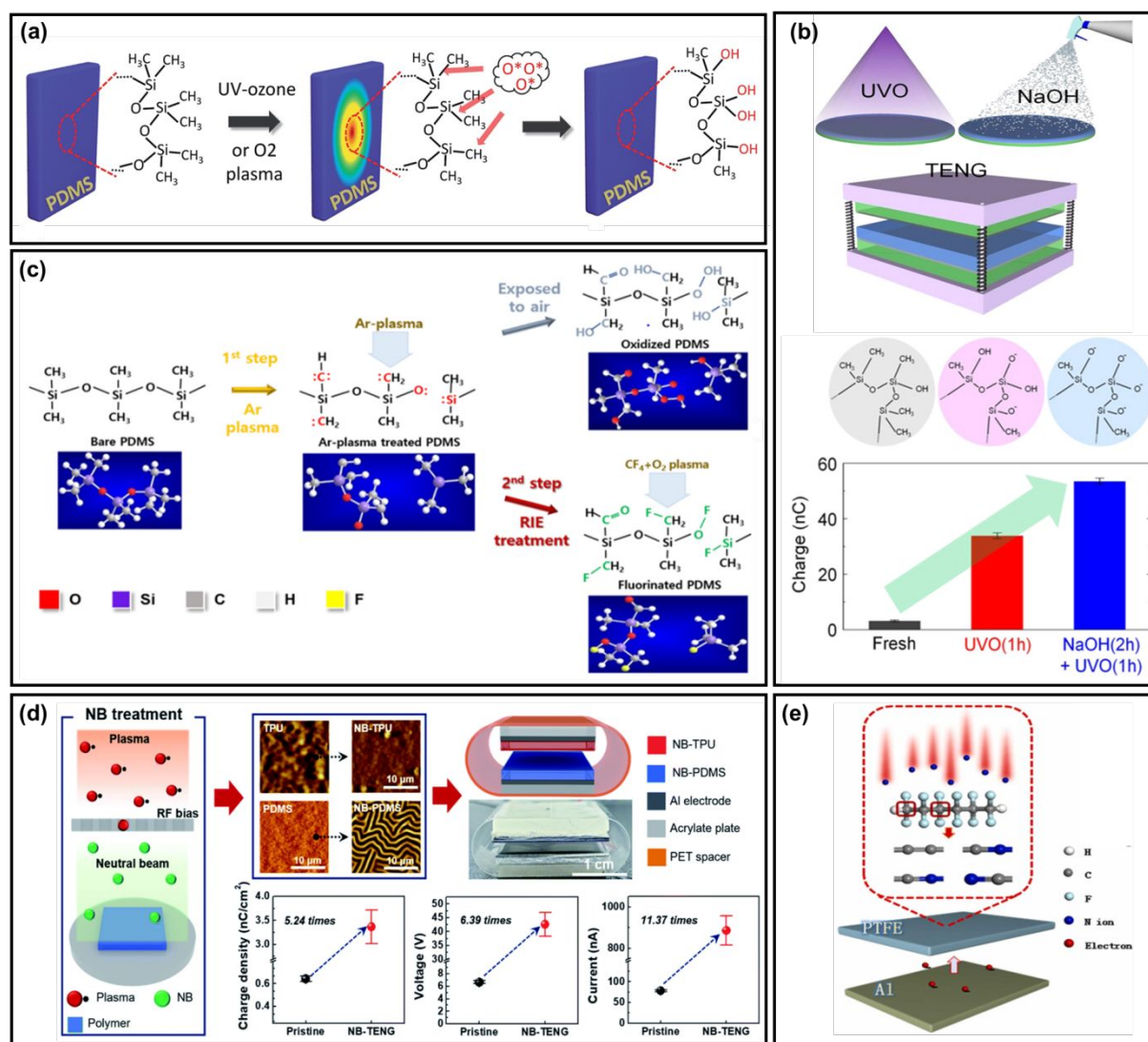


Figure 16. Surface treatment methods. **(a)** Schematic illustration of a plausible mechanism showing the change in the molecular structure of a PDMS surface after ultraviolet-ozone (UVO) irradiation. **Reprinted with permission under a Creative Commons CC BY 3.0 License from ref. 179, Copyright 2014, Royal Society of Chemistry.** **(b)** Schematic of surface treatment of a PDMS film-based TENG device and changes of molecular structure and charges before and after UVO, NaOH treatment. **Reprinted with permission from ref. 166, Copyright 2015 Elsevier.** **(c)** Possible mechanism for chemical modification of PDMS surfaces by one-step Ar-only plasma treatment and two-step process with consecutive Ar and CF₄ + O₂ plasmas. **Reprinted with permission for ref. 133, Copyright 2019 Elsevier.** **(d)** Neutral Beam (NB) treatment process and NB-treated TENG. **Reprinted with permission from ref. 165, Copyright 2019 Royal Society of Chemistry.** **(e)** Schematic diagram of TENG comprised of Al and PTFE modified by ion implantation. **Reprinted with permission from ref. 171, Copyright 2021 Elsevier.**

2.3 Bulk Modifications

2.3.1 Pore structures

In capacitor-type structures, the charges between two electrodes are dependent on the potential and capacitance as functions of time. However, two materials are contacted and separated as a function of time by external force. This indicates that the transferred charges through the external circuit are also strongly dependent on the change in potential and capacitance with time, as follows:

$$I = C \frac{\delta V}{\delta t} + V \frac{\delta C}{\delta t} \quad (15)$$

where I is the output current, C is the capacitance, and V is the potential generated. Thus, the compressible properties of the materials should be considered to maximize the output currents. As one of the interesting methods to fabricate compressible materials, porous films will be an example by introducing pores to the film.

K. Y. Lee et al. fabricated hydrophobic sponge structured polydimethyl-siloxane (PDMS) film as a negative charged material (Figure 17(a)).¹²³ Polystyrene (PS) spheres with diameters of 0.5, 1, 3, and 10 μm was used to fabricate the PDMS inverse opal-structured film. After many layers of PS spheres were stacked, the PDMS solution was poured into the PS spheres and solidified. The PS spheres were removed by soaking in acetone for 24 h. When the film was contacted with Al, the electrical outputs of the TENG fabricated with the film having pores size of 0.5 μm were enhanced by 2.6 times in terms of the output voltages,

1
2
3
4 compared with one with flat film. As the pore size increases up to 10 μm , the output voltage
5
6
7
8 was decreased due to the decrease in the contacted surface area with the increase of pore
9
10
11 diameter. Interestingly, the TENG showed less-sensitive outputs to the relative humidity (RH)
12
13
14 and it was clearly seen that the TENG with porous film at 80% RH showed a higher electrical
15
16
17 output performance than the TENG with flat film at 20% RH. *Y. Liu et al.* reported an elastic
18
19
20 TENG based on conductive elastic sponge, in which polyaniline (PANI) nanowires were
21
22
23 fabricated on the surface of polyurethane sponge, followed by removal of the sponge after
24
25
26 dilute solution chemical polymerization (Figure 17(b)).¹⁸⁴ As the chemical polymerization
27
28
29 time increased to 24 h, the PANI nanowire grew up to a length of 100 nm and the film
30
31
32 became quite porous. The electric outputs of output voltage, current, and charge density also
33
34
35 increased as the polymerization time increased.
36
37
38
39
40
41

42
43 *Z. Haider et al.* proposed a tribopositive material composed of porous polymer
44
45 cryogel and the fabrication of TENGs in conjunction with PDMS as a negative charged
46
47
48 material. The cryogel was synthesized using lauryl acrylate (LA) by a polymerization
49
50
51 procedure named cryo-polymerization.¹⁸⁵ The highest porosity of 73% was obtained with a
52
53
54 monomer concentration of 0.3 M in the porous cryogel films. As the concentration increased,
55
56
57
58 the porosity decreased to 49%. The highest electric outputs were obtained at the sample with
59
60

1
2
3
4 the highest porosity, indicating that the high performance is attributed to the creation of extra
5
6
7
8 charges on the surface of the pores.
9
10
11
12
13
14
15
16
17
18
19
20
21
22
23
24
25
26
27
28
29
30
31
32
33
34
35
36
37
38
39
40
41
42
43
44
45
46
47
48
49
50
51
52
53
54
55
56
57
58
59
60

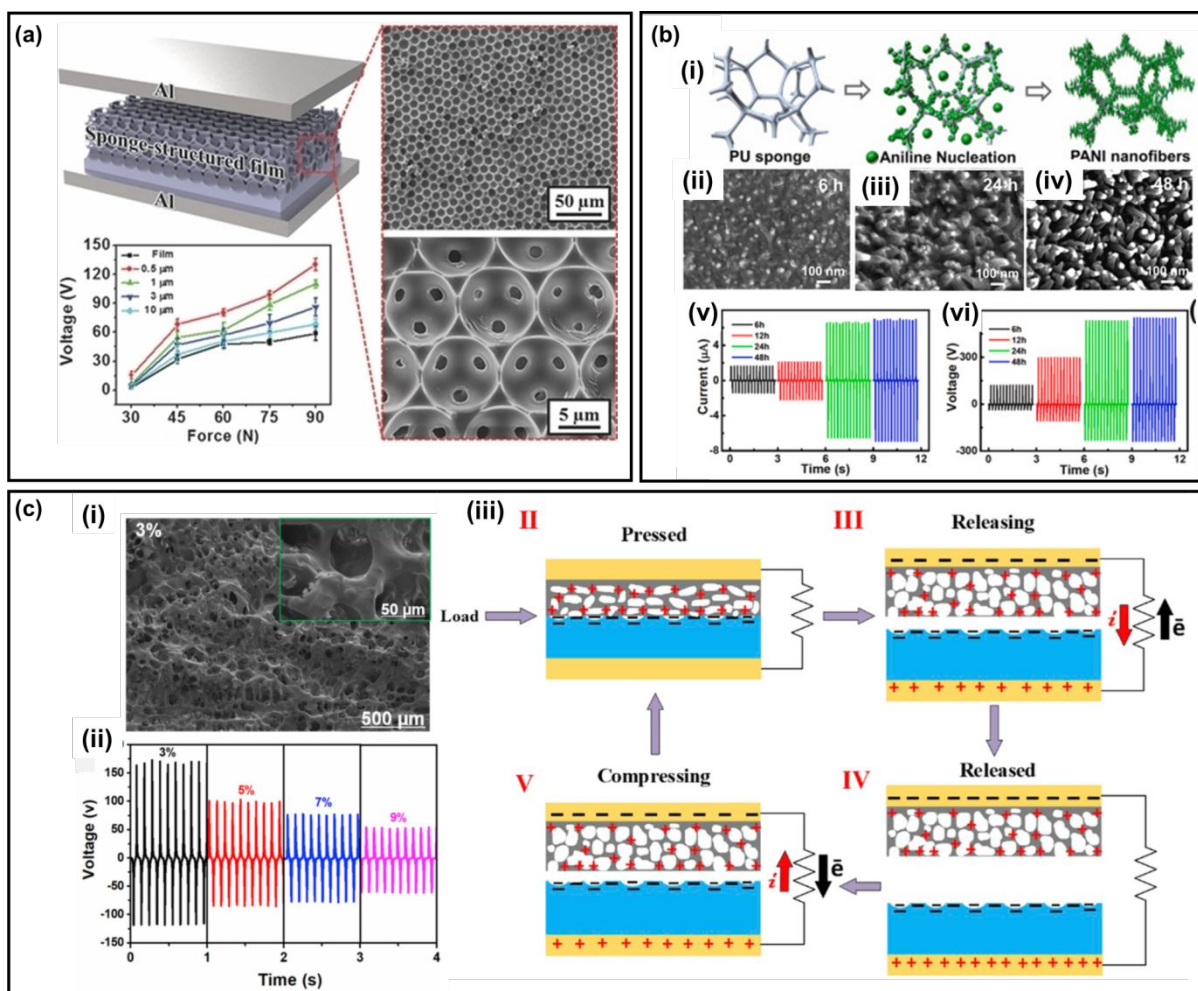


Figure 17. Porous structures. (a) Sponge-structured PDMS film and TENG performance. **Reprinted with permission from ref. 123, Copyright 2014 John Wiley and Sons.** (b) Schematic illustration of the preparation process of conductive elastic sponge by a dilute chemical polymerization method (i). SEM images of PANI nanowires with polymerization time (ii), (iii), (iv). Output performance of ES-TENG with different polymerization times (v) (vi). **Reprinted with permission from ref. 184, Copyright 2021 Elsevier.** (c) SEM image of the surfaces of porous cryogel films (i) and output voltages of TENGs of various concentrations of crosslinker in the porous cryogel films (ii). Mechanism for high performance of TENGs (iii). **Reprinted with permission from ref. 185, Copyright 2020 Elsevier.**

2.3.2 Dielectric constants

In this section, we discuss how the output performance of triboelectric nanogenerators (TENG) is influenced by the dielectric properties of the active layer, and the different strategies to engineer their dielectric properties toward improving TENG performance. It is imperative to focus on the dielectric properties because triboelectricity is induced by contact charging and electrostatic induction between dissimilar triboelectric materials, each with different dielectric properties. In this context, the dielectric constant (or relative permittivity) is the central parameter that describes how efficiently the active material is polarized when subjected to an electric field, and is calculated by the equation:¹⁸⁶

$$\varepsilon = \frac{C \times d}{\varepsilon_0 \times A} \quad (16)$$

where ε is the dielectric constant, C is the capacitance, d is the thickness of the active layer, A is the area of the active layer, and ε_0 is the dielectric constant of a vacuum (8.854×10^{-12} pF m⁻¹).

In the metal-insulator system, the surface charge transfer between the two layers can be induced as follows:

$$\sigma = \frac{(W - E_0)/e}{1/\left(\frac{\varepsilon + 1}{t + z}\right)\varepsilon_0 + 1/\overline{N_s(E)}e^2} \quad (17)$$

where σ is the surface charge density on the dielectric surface, W is the work function of the metal, E_0 is the effective work function, ε is the relative permittivity, t is the thickness of the insulator, z is the separation distance between the metal and insulator layer, ε_0 is the permittivity of a vacuum, e is the elementary charge, and $\overline{N_s(E)}$ is the average surface density of states for the dielectric layer.⁸⁰ Equation (17) indicates that the conditions of a

1
2
3
4 thinner dielectric layer and larger ε/t can result in a higher surface charge density. Therefore,
5
6 among the various parameters related to the surface charge density, the permittivity of the
7
8 bulk insulator may have the most significant influence on contact electrification. The
9
10 permittivity of the bulk insulator can be modulated by inserting a layer of high-k material or
11
12 by containing high-k particles. In addition, the high-k material can function as a charge-
13
14 trapping layer to improve surface charge retention. In this section, we will mainly discuss
15
16 bulk modifications to improve contact electrification by adjusting the permittivity of the
17
18 insulator.
19
20
21

22
23 The electric displacement field (D) means the electric field in the material, which can
24
25 be expressed as follows:
26

$$27 \quad \mathbf{D} = \varepsilon_0 \mathbf{E} + \mathbf{P} \quad (18)$$

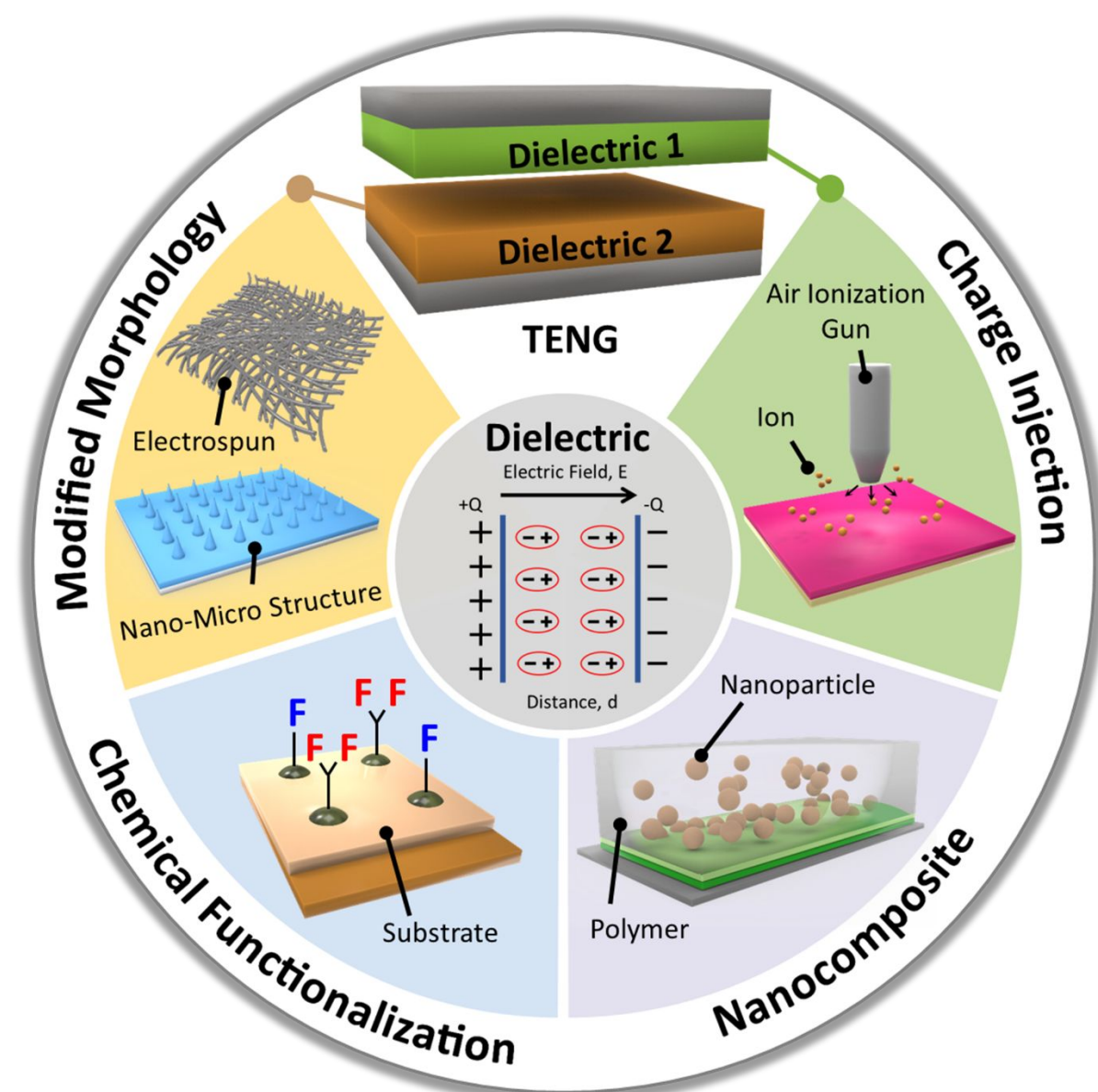
28
29 where ε_0 is the permittivity of the vacuum, E is the electric field, and P is the electric dipole
30
31 moments in the material. In general, the electric dipole is proportional to the external electric
32
33 field and changing the electric displacement field can be expressed as follows:
34
35

$$36 \quad \mathbf{P} = \varepsilon_0 \chi \mathbf{E} \quad (19)$$

$$37 \quad \mathbf{D} = \varepsilon_0 \mathbf{E} + \varepsilon_0 \chi \mathbf{E} = \varepsilon_0 (\mathbf{1} + \chi) \mathbf{E} = \varepsilon \mathbf{E} \quad (20)$$

38
39 where χ is the electric susceptibility. In general, ferroelectric materials with electric dipoles
40
41 have a very large permittivity. Thus, it is established that a triboelectric material with a higher
42
43 permittivity induces a larger displacement current.¹⁸⁷⁻¹⁸⁸ Therefore, the output efficiency of
44
45 TENGs can be enhanced by modulating the dielectric constant through a rational design of
46
47 the physicochemical properties of the active layer. In fact, recent studies show that the
48
49 performance of TENGs can be effectively improved by amplifying the net dielectric constant
50
51
52
53
54
55
56
57
58
59
60

1
2
3
4 to maximize the dielectric polarization.¹⁸⁹⁻¹⁹³ Specifically, herein we discuss the four
5
6
7
8 strategies that can maximize the dielectric polarization: (i) modification of the morphology of
9
10
11 the dielectric material; (ii) surface activation by attaching functional groups to the surface; (iii)
12
13
14 introduction of dielectric additives to form nanocomposites; and (iv) forced external charge
15
16
17
18 injection (Figure 18).



1
2
3
4
5 **Figure 18.** Schematic illustration of modification methods of dielectric constant for high-
6 performance TENGs.
7
8
9
10
11
12
13
14
15
16
17
18
19
20
21
22
23
24
25
26
27
28
29
30
31
32
33
34
35
36
37
38
39
40
41
42
43
44
45
46
47
48
49
50
51
52
53
54
55
56
57
58
59
60

1
2
3
4 To facilitate this discussion, we must establish a specific theoretical model for the
5 TENG that can be used to rationalize the correlation between the dielectric constant of the
6 material and its triboelectric performance (Figure 19). In this context, S. Niu *et al.*
7 systematically demonstrated the fundamental working principles of a model TENG system
8 through simulations. The parallel-plate contact mode TENG, which is the simplest
9 configuration for TENGs, can be further subdivided into two categories depending on their
10 operating principle: dielectric-to-dielectric mode and conductor-to-dielectric mode (Figure
11 19(a)-(c)). In the former, two dielectric plates with dielectric constants ϵ_1 and ϵ_2 and
12 thicknesses of d_1 and d_2 , respectively, are separated by a distance (x) that can vary with an
13 external mechanical force. Upon contact, the inner surfaces of the two plates are
14 electrostatically charged (tribo-charges) with the same charge density (σ) and opposite
15 polarity. Subsequently, when the two plates start to separate, a potential difference (V)
16 between the two electrodes is generated according to how much positive (+ Q) and negative (-
17 Q) charges have been transferred across the interface. In the latter, a metallic plate (“metal
18 1”) contacts the dielectric plate in a similar fashion. In this structure, the generation of
19 triboelectric charge is concomitant with charge transfer across the two electrodes (- Q), and
20 thus the total charge on the metallic plate amounts to $S\sigma-Q$. Considering these two contact
21 modes, the relationship between V , Q , and x (V - Q - x) and the intrinsic output characteristics
22 (V_{OC} , I_{SC} , Q_{SC} , C) of TENG can be derived as equations (10) – (13) and follows.

$$C = \frac{\epsilon_0 S}{d_0 + x(t)} \quad (21)$$

23
24
25
26
27
28
29
30
31
32
33
34
35
36
37
38
39
40
41
42
43
44
45
46
47
48
49
50
51
52
53 According to Equations (10) and (11), the surface charge density (σ) directly correlates to the
54 TENG output performance. Therefore, the aforementioned surface modification strategies
55 such as modification of surface morphology,^{130, 194-195} chemical functionalization of the
56
57
58
59
60

1
2
3
4 surface of active layer,^{159, 175, 196} formation of nanocomposites with tunable dielectric
5 properties,^{186, 197-198} and direct charge injection^{136, 199} can be highly effective in amplifying the
6
7 triboelectric polarity to increase the surface charge density on the dielectric, ultimately
8
9 improving the TENG performance.
10
11

12
13 In Equation (12), the effective dielectric thickness d_0 is defined as the sum of the total
14 dielectric thickness (d_i) between the two metal electrodes normalized by the relative effective
15 dielectric thickness ($\epsilon_{er,i}$). The V-Q-x relationship can be derived from equations (10) – (13)
16
17 based on the electrostatic induction mechanism, which, together with Gauss' theorem,
18 represents the foundational working principle of TENGs. Equation (21) shows that higher
19 values of the dielectric constant lead to a greater capacitance (C). Specifically, C is directly
20 proportional to the ratio of the dielectric constant to thickness (ϵ/d), with the contact area (S)
21 as the scaling factor. Note that the surface charge density also increases with higher ϵ/d . For
22 example, when the dielectric layer of a TENG is based on nanofiber-based or otherwise
23 porous materials, the TENG output is improved compared to those based on bulk solid layers
24 because the nanostructure induces a higher dielectric constant and an increase in the ϵ/d ratio
25 upon contraction by an external force.
26
27

28
29 Zhong Lin Wang, a pioneer of TENG technology, postulated that the theoretical working
30 principle of the nanogenerator originates from Maxwell's displacement current (Figure 19(d)).
31 In TENGs, the displacement current represents the current generated by an intrinsic internal
32 driving force, the practical expression of which in the external circuit is represented by the
33 capacitive conduction current. The displacement current caused by triboelectric charge was
34 represented by the term $\left(\frac{\partial P_s}{\partial t}\right)$, through which Wang elucidated how dielectric polarization
35 governs the operation of TENGs.²⁰⁰ In terms of the dielectric layer, there is a direct
36 correlation with the material's dielectric constant and the induced displacement current, as
37
38
39
40
41
42
43
44
45
46
47
48
49
50
51
52
53
54
55
56
57
58
59
60

1
2
3
4 well as between the displacement current and the conduction current produced by the device.
5

6 Taken together, the dielectric property of the triboelectric active layer determines the
7 performance of TENG, and through appropriate surface modification, the dielectric constant
8 can be tuned to achieve the optimal TENG performance. Here, a comprehensive discussion
9 regarding the strategies to modify the dielectric properties of the active material are provided
10 through the context of the theoretical working mechanism of TENGs. Specifically, we
11 present examples of conceptual prototypes demonstrated in the literature as case studies of
12 the effective strategies for improving the dielectric properties and how they can enhance
13 TENG performance.
14
15
16
17
18
19
20
21
22
23
24
25
26
27
28
29
30
31
32
33
34
35
36
37
38
39
40
41
42
43
44
45
46
47
48
49
50
51
52
53
54
55
56
57
58
59
60

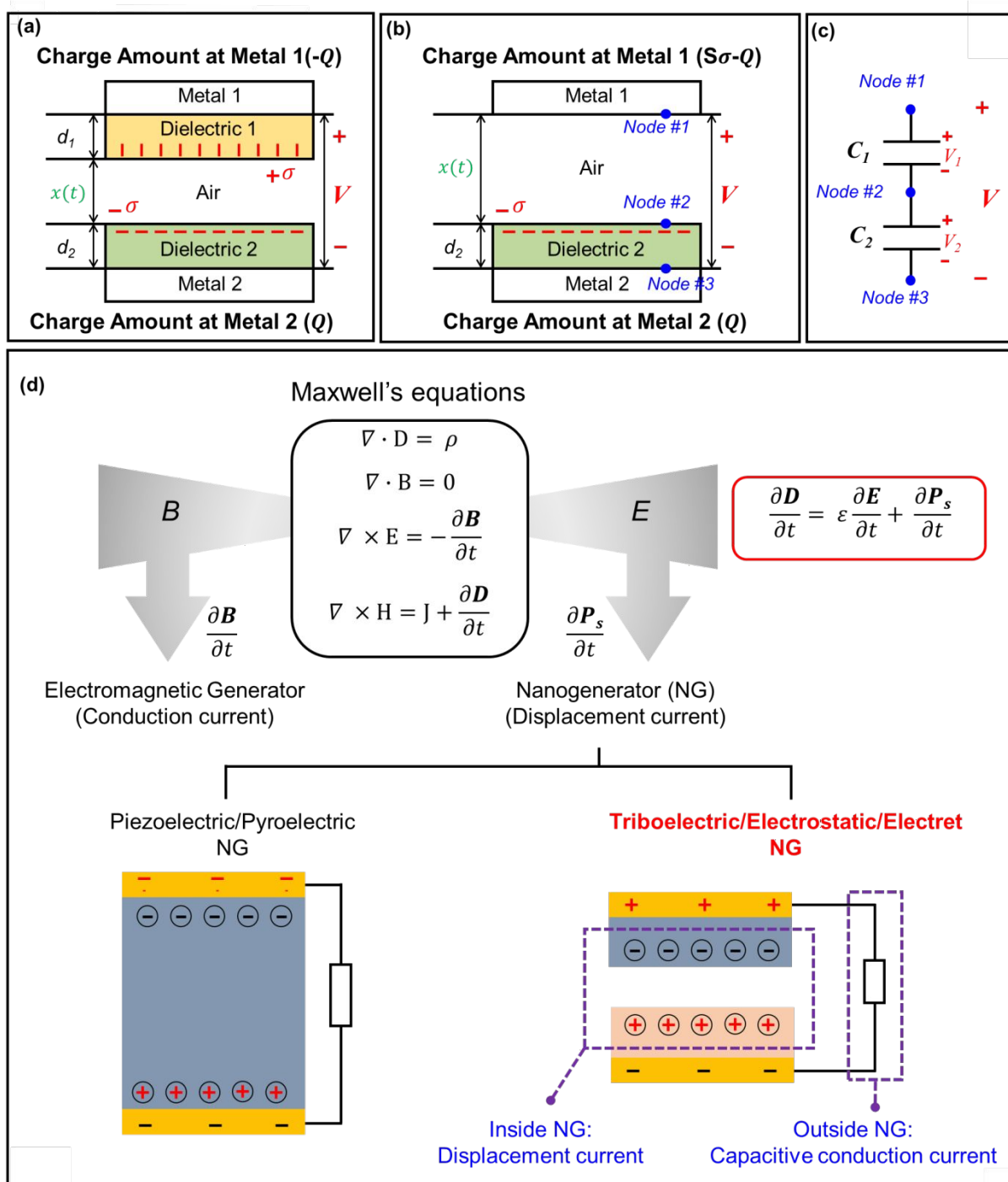


Figure 19. Schematic illustration of fundamentals of triboelectric nanogenerators (TENGs). Theoretical models for attached-electrode parallel-plate contact mode TENGs. (a) Dielectric-to-dielectric and (b) conductor-to-dielectric. (c) Schematic illustration of an equivalent circuit for conductor-to-dielectric attached-electrode parallel-plate contact mode TENGs. **Reprinted with permission from ref. 113, Copyright 2013, Royal Society of Chemistry.** (d) Schematic illustration of the displacement current-dominated nanogenerators based on the piezoelectric/pyroelectric, triboelectric/electrostatic/electret effects, and the conduction

1
2
3
4 current-dominated electromagnetic generator. **Reprinted with permission from ref. 188,**
5 **Copyright 2020, Elsevier.**

6
7 As elucidated, the friction-induced surface charge density and effective contact area both
8 directly affect the output performance of TENGs. Therefore, many researchers have focused
9
10 on designing the surface structure of the active material with those considerations to improve
11
12 the triboelectric charge surface density. Various material processing methods have been used
13
14 to fabricate complex and functional surface morphologies, such as electrospinning,^{142, 201-202}
15
16 nano-micro structure,²⁰³⁻²⁰⁵ photolithography,²⁰⁶⁻²⁰⁸ and patterning.²⁰⁹⁻²¹¹ While the
17
18 morphological engineering of the active triboelectric layers may not affect its intrinsic
19
20 dielectric constant, the bulk dielectric behavior in the context of the final TENG device can
21
22 be considerably improved.
23
24
25
26
27
28

29 In one example, S. Chen *et al.* fabricated a ferroelectric polymer-metal nanowire
30 composite nanofiber membrane as a triboelectric active layer for use in high-performance
31 TENGs. The electrospinning process induces a spontaneous alignment of the PVDF polymer
32 chains along the length of the resultant nanofiber, leading to the formation of PVDF
33 nanofibers with a highly oriented and crystalline β -phase. By incorporating Ag nanowires
34 (NW) into the electrospinning solution, PVDF-AgNW composite nanofiber membranes could
35 be obtained. Figure 20(a) shows a schematic diagram of a TENG that can be fabricated by
36 assembling the electrospun PVDF-AgNW membrane together with electrospun nylon
37 nanofibers as the respective dielectric layers. The morphologies of the as-spun PVDF-AgNW
38 composite nanofibers (3 wt%, AgNWs) and the nylon nanofibers were analyzed through
39 scanning electron microscopy (SEM) (Figure 20(b)). The electric field applied during the
40 electrospinning process promoted the alignment of AgNWs in parallel to the direction of the
41 nanofiber (insert in Figure 20(b)). Kelvin probe force microscopy (KPFM) analysis clearly
42 showed the shift in the surface charge potential of the nanofibers, which can be attributed to
43
44
45
46
47
48
49
50
51
52
53
54
55
56
57
58
59
60

1
2
3
4 the presence of AgNWs (Figure 20(c)). The authors confirmed that the nanofiber structure of
5
6 the triboelectric layer increases the effective surface area and, as confirmed by equation (21),
7
8 improves the ϵ/d ratio when mechanical compression is applied, thus improving the TENG
9
10 output in comparison to spin-coated film analogs of the PVDF-AgNW nanocomposite.
11
12

13
14 Nanofiber-based TENGs can also be fabricated into various form factors, each with
15
16 practical implications. For instance, L. Ma *et al.* proposed the yarn-type TENG, which could
17
18 be incorporated into consumer textiles and fabric for wearable applications. The ultralight
19
20 nano-micro hybridized core-shell structured yarn exhibited excellent triboelectric
21
22 performances owing to the increased friction-induced capacitance (Figure 20(d)). This is
23
24 specifically due to the fact that the nanofibers are packed much more tightly in a yarn
25
26 structure compared to the case of randomly oriented nanofiber membranes. These single-
27
28 electrode triboelectric yarns showed potential for development into a variety of wearable
29
30 hypotonic fabrics.
31
32

33
34 The fabrication of nano-micro structures is another practical approach among methods for
35
36 amplifying the performance of TENGs through surface morphology modification. J. Huang *et*
37
38 *al.* reported the fabrication of TENG based on active layers with surface nano-micro
39
40 structures for enhanced output performance compared to unstructured active layers. A
41
42 femtosecond laser direct writing method was used to fabricate two dielectric layers, each
43
44 decorated with PDMS microbowls and Cu micro/nanocones, to serve as the active
45
46 triboelectric layers (Figure 20(e)). As shown in Figure 20(f), SEM images and 3D digital
47
48 optical microscope images confirm that the nano-micro double-scale structures of stripes and
49
50 cones could be formed on the Cu surface, respectively (Figure 20(g)). The nano-micro
51
52 surface structure of the two dielectric layers can significantly increase the effective contact
53
54 area and surface roughness when the layers are rubbed against each other. As a result, both
55
56 dielectric layers generate more triboelectric charge during contact and improve the effective
57
58
59
60

1
2
3
4 dielectric properties, which helps bolster the output performance of TENGs. Figure 20(h)
5
6 shows the mechanical endurance of the nano-micro structured TENG, indicating that the
7
8 nano-micro structure is suitable for promoting efficient TENG operations. In summary, the
9
10 specific study of surface shape control can significantly promote the practicality of TENGs
11
12 by modulating the bulk dielectric properties that are induced in the triboelectric layer during
13
14
15 friction.
16
17
18
19
20
21
22
23
24
25
26
27
28
29
30
31
32
33
34
35
36
37
38
39
40
41
42
43
44
45
46
47
48
49
50
51
52
53
54
55
56
57
58
59
60

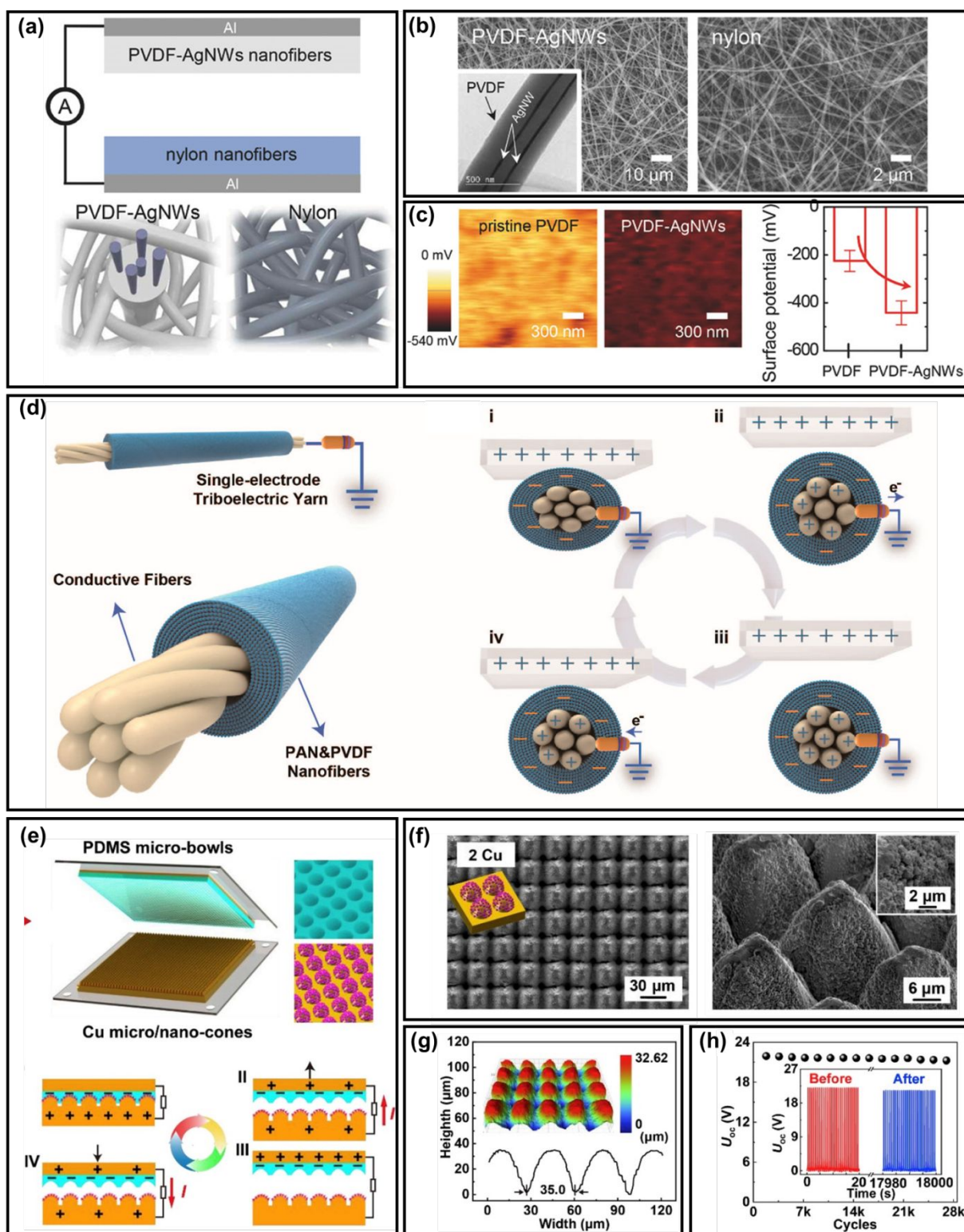


Figure 20. Schematic illustration of modified surface morphology for high-dielectric properties. **(a)** Schematic illustration of the PVDF-AgNW composite-based TENGs and nylon nanofibers. **(b)** SEM images of the electrospun PVDF-AgNW composite and nylon nanofibers (insert an image: TEM image of the PVDF-AgNW composite nanofibers). **(c)** KPFM images of the surface of the pristine PVDF and PVDF-AgNW composite nanofibers.

1
2
3
4 **Reprinted with permission from ref. 194, Copyright 2018, Wiley-VCH. (d)** Schematic
5 illustration of the single-electrode triboelectric yarn (SETY) and working principle of SETY.
6 **Reprinted with permission from ref. 195, Copyright 2020, American Chemical Society.**
7 **(e)** Schematic illustration of the fabricated TENG based on Cu film with nano-micro
8 structured and PDMS film with micro-bowls structure and working principle of the TENG in
9 contact-separation mode. **(f)** SEM image of TENG based on nano-micro structure (top-view
10 and 30° tilted view) and **(g)** 3D surface topography. **(h)** Stability of the TENG (insert: UOC
11 of the TENG before and after). **Reprinted with permission from ref. 130, Copyright 2019,**
12 **Elsevier.**
13
14
15
16
17
18
19
20
21
22
23
24
25
26
27
28
29
30
31
32
33
34
35
36
37
38
39
40
41
42
43
44
45
46
47
48
49
50
51
52
53
54
55
56
57
58
59
60

1
2
3
4 In a different approach from the aforementioned morphological modification strategies in
5
6 designing the active triboelectric layer, the intrinsic dielectric constant of the triboelectric
7
8 material could be chemically tuned to achieve an increase in the TENG performance, in
9
10 particular by modifying the functional groups of the polymer chain.^{176, 212-213} In this regard,
11
12 the grafting of various functional groups and the self-assembly of organic molecules on the
13
14 surface of a polymer-based triboelectric layer have been shown to be effective in modifying
15
16 the surface potential of the triboelectric layer, artificially increasing its dielectric constant.^{205,}
17
18
19
20
21
22
23
24
25
26
27
28
29
30
31
32
33
34
35
36
37
38
39
40
41
42
43
44
45
46
47
48
49
50
51
52
53
54
55
56
57
58
59
60

214-215 Y. Liu *et al.* reported the chemically-tailored molecular surface modification of cellulose nanofibrils (CNF) for amplifying the surface charge density (Figure 21(a)). The surface of CNFs could be chemically modified with a silane coupling agent with the same main chain but different terminal functional groups. As a result, the surface charge density of the cellulose nanofibrils could be altered in different ways by introducing functional groups (NH₂-, SH-, CN-, and CF₂CF₃-) with varying degrees of electron-withdrawing or electron-donating tendencies (Figure 21(b)). By controlling the number and density of functional groups, the range of charge density can be more specifically tuned. Utilizing a similar approach, S. Nie *et al.* could produce surface-modified CNFs that exhibited excellent triboelectric charge density and hydrophobicity (Figure 21(c)). With the introduction of aminosilane on the CNF surface (3-(2-aminoethylamino)-propyldimethoxymethylsilane (AEAPDMS)-CNF), the modified CNF film showed a more efficient removal of electrons, consequently resulting in a more positive surface charge which increased the triboelectric charge density of TENG (Figure 21(d)). The insights provided in these studies unfold numerous possibilities for different surface modification approaches, ultimately toward the development of a designed synthesis of surface-modified CNFs and further improved TENGs derived from such active materials.

1
2
3
4 The self-assembled monolayer (SAM) method, which exploits the phenomenon of the
5 spontaneous molecular assembly of chemisorbed surfactants on a solid surface, is another
6 effective method toward chemical surface modification.²¹⁴ S.-H. Shin *et al.* reported a facile
7 SAM method for achieving atomic-level chemical functionalization, which would alter the
8 dielectric property of a polymeric surface (Figure 21(e)). SAMs were prepared in series on a
9 polyethylene terephthalate (PET) substrate *via* a series of halogens and amines. First, the
10 surface of the PET substrate was functionalized with hydroxyl groups (-OH) through
11 treatment with oxygen plasma. The hydroxyl groups would serve as the intermediate layer
12 that facilitates the formation of chemical bonds with the target functional molecules. The OH-
13 covered layer was then functionalized with halogen (Br, F, and Cl)-terminated phenyl
14 derivatives (tribo-negative materials) and several amination molecules (tribo-positive
15 materials) to triboelectrically induce negative or positive properties, respectively, in the PET
16 substrate. As a result, the aminated PET substrate showed strong tribo-positive materials
17 properties while the halogenated PET substrate induced strong tribo-negative materials
18 properties. By forming a contact pair between the samples with opposite triboelectric
19 polarities, such as in the case of PEI(b)-PET/Cl-PET, to construct the TENG, high voltage
20 outputs of 300 V and 200 V, respectively for each layer, could be observed. Taken together,
21 the atomic-level chemical functionalization strategy provides a simple and effective pathway
22 for widening the design flexibility with regard to the type of polymer substrate that could be
23 employed for the construction of a high-performance TENG.
24
25
26
27
28
29
30
31
32
33
34
35
36
37
38
39
40
41
42
43
44
45
46
47
48
49
50
51
52
53
54
55
56
57
58
59
60

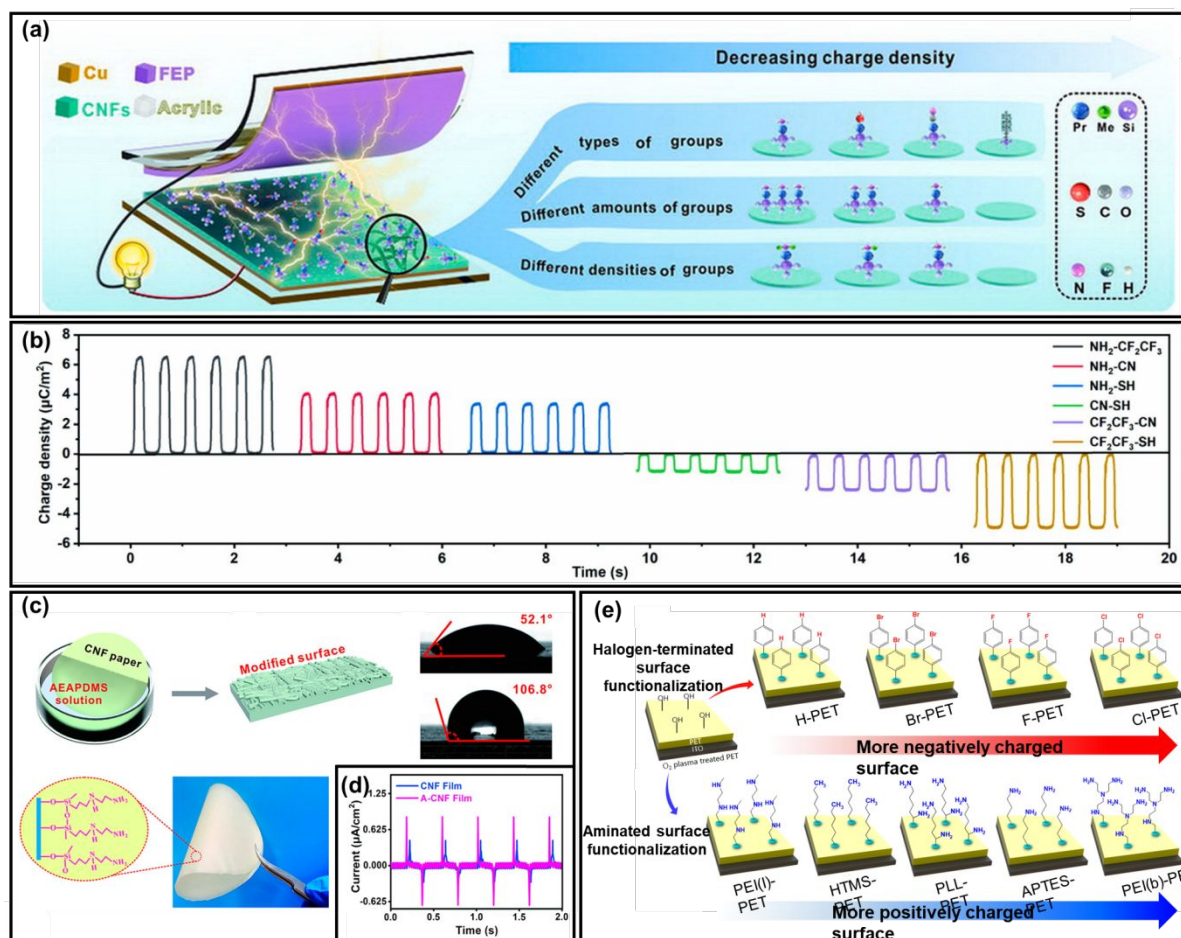


Figure 21. Schematic illustration of chemically functionalized surface for high-dielectric properties. (a) Schematic illustration of chemical functional groups tailored CNFs for manipulating the charge density. (b) Surface charge density according to various functional groups. Reprinted with permission from ref. 175, Copyright 2021, Elsevier. (c) Schematic illustration of the surface modification on CNF paper. (d) The output current of the CNF-based TENG. Reprinted with permission from ref. 196, Copyright 2020, American Chemical Society. (e) Schematic illustration of the surface functionalized negative and positive PETs with adopted molecules. Reprinted with permission from ref. 159, Copyright 2017, American Chemical Society.

2.3.2.4. Triboelectric Nanocomposites based on High-Dielectric Nanoparticles and Conductive Fillers

Directly modulating the intrinsic dielectric constant of the active triboelectric layer represents another approach to maximize the dielectric polarization across the triboelectric layers and produce high-performance TENGs. Due to the limited selection of ferroelectric polymers (*e.g.*, PVDF, PVDF-copolymer, nylon)²¹⁶⁻²¹⁹ applicable for TENGs, the choice of materials alone only allows a small window of design flexibility for preparing a triboelectric layer. As such, the triboelectric layer can be prepared as nanocomposites comprising high-dielectric metal oxide nanoparticles (NP) (*e.g.*, BaTiO₃, BiFeO₃, CCTO)²²⁰⁻²²² dispersed within the matrix of the ferroelectric polymers to effectively raise the material's dielectric constant. In detail, the high-dielectric NPs increase the surface charge density of the triboelectric layer, thus improving the output performance of the TENG. To this end, J. Chen *et al.* demonstrated that the surface charge density and amount of charge transfer are closely related to the relative dielectric constant and porosity of triboelectric materials (Figure 22(a)). In their work, the authors fabricated a polydimethylsiloxane (PDMS) layer with NaCl-induced porosity, incorporating the high-dielectric SrTiO₃ NPs into the PDMS matrix to amplify the TENG output performance. The nanocomposite PDMS film-based TENG containing 10 wt% SrTiO₃ nanoparticles (~100 nm size) and 15 vol% pores provided a power improvement of more than 5-fold from that of the pure PDMS film-based TENG at a working frequency of 2.5 Hz. The high dielectric constant of the nanocomposite, and therefore its high ϵ/d ratio, induced stronger TENG output when the nanocomposite was contracted by an external force (refer to Equation (21)).

Similarly, J. Kim *et al.* reported a composite triboelectric layer based on butylated melamine formaldehyde (BMF) and high-dielectric CaCuTi₄O₁₂ (CCTO) NPs for facilitating

1
2
3
4 the design of a high-output TENG with stable performance (Figure 22(c)). CCTO NPs have a
5 considerably high dielectric constant of 7500, which induces a substantial dielectric
6 polarization at the composite triboelectric layer to promote an efficient charge induction at
7 the counter electrode, improving the TENG output performance. The dielectric constant of
8 the BMF-CCTO composite layer (1 wt%) was measured to be 21.74, which was about 3-fold
9 higher than pristine BMF, BMF-Al₂O₃, and BMF-TiO₂. As shown in Figure 22(d), the
10 relationship between permittivity and electrical polarization is expressed as
11
12
13
14
15
16
17
18
19

$$\vec{P} = \epsilon_0 (\epsilon_r - 1) \vec{E} \quad (22)$$

20
21 where \vec{P} is the electrical polarization within a material, ϵ_0 is the permittivity of free space
22 ($8.854 \times 10^{-12} \text{ F m}^{-1}$), ϵ_r is the relative permittivity, and \vec{E} is the applied electric field.²²³
23
24
25
26
27
28
29

30 According to Equation (22), the higher the dielectric constant, the stronger the internal
31 polarization under the electric field. Consequently, the BMF-CCTO could provide high
32 TENG performance, as demonstrated by rotation-type TENGs in a freestanding mode
33 fabricated with the BMF-CCTO composite layers, as schematically shown in Figure 22(e).
34
35
36
37
38
39
40
41
42
43

44 Introducing conductive fillers can be another way to improve the output performance of
45 TENG, particularly in consideration of its capacitor-like mechanism. X. He *et al.* investigated
46 the enhancement of triboelectric performance in PDMS by mixing in graphite particles (GP)
47 as conductive fillers. As seen in Equation (12), the charge density increases in proportion to
48 the capacitance and voltage. However, when a conductive filler is introduced, the capacitance
49 is reduced as the conductive pathway facilitates charge transfer to the surface of the layer.
50 This reduced conductivity C^* can be expressed as:
51
52
53
54
55
56
57
58
59
60

$$C^* = \frac{\epsilon S}{d-r} \quad (23)$$

where $d - r$ indicates the reduction of the effective thickness of the whole capacitive layer (d) by the effective thickness of the conductive fillers (r).

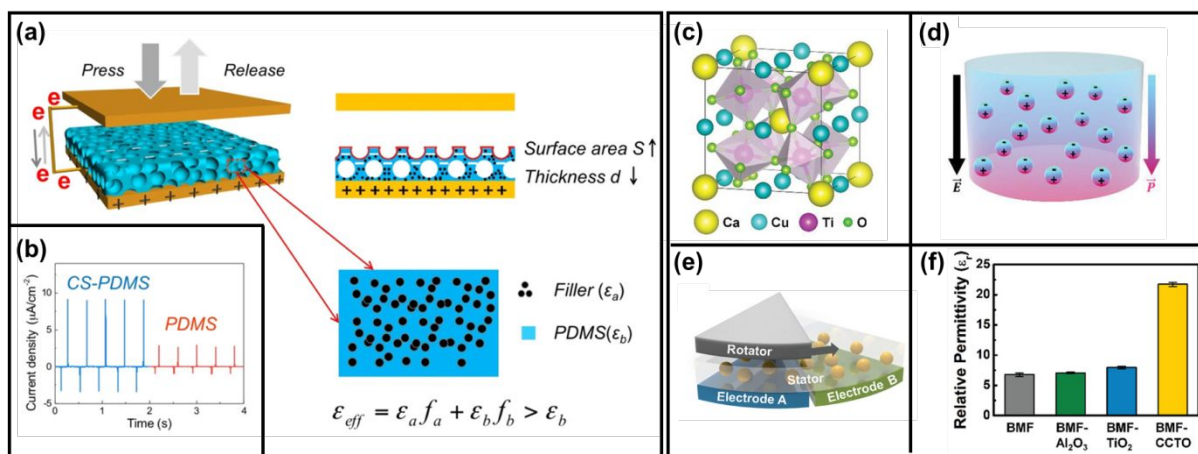


Figure 22. Schematic illustration of the tribo-material nanocomposite. (a) Schematic illustration of the composite sponge PDMS-based TENG (CS-TENG). (b) The current density of the pristine PDMS-based TENG and CS-TENG. **Reprinted with permission from ref. 197, Copyright 2016, American Chemical Society.** (c) Chemical structure of CCTO and (d) relationship between the relative permittivity and electrical polarization within material under the electric field. (e) Schematic illustration of BMF-CCTO-based rotation-type TENG. (f) The relative permittivity of various composite. Schematic illustration of composite film nanogenerator (CFNG) **Reprinted with permission from ref. 186, Copyright 2020, Wiley-VCH.**

1
2
3
4
5 Adding the conductive GP fillers to the PDMS matrix decreases the effective layer
6
7 thickness as a function of the amount of GP fillers, thus increasing the effective capacitance
8
9 and the charge density compared to the case of pristine PDMS (Figure 23(a)-(b))¹⁹⁸. The
10
11 increased capacitance translates to an increase in the dielectric constant of the layer. As a
12
13 result, the GP-infused PDMS film-based TENG showed a high output performance of about
14
15 2-fold or more compared to that based on pristine PDMS (Figure 23(c)). Altogether, the
16
17 presence of appropriate additives provides an opportunity to directly influence the intrinsic
18
19 dielectric properties of the triboelectric layer.
20
21
22
23
24
25
26
27
28
29

30 Polyvinylidene fluoride (PVDF) is a ferroelectric polymer, which can be combined with
31
32 various functional groups to significantly change its physical properties. *Lee et al.* found that
33
34 TENG controlled the dielectric constant by mixing PVDF and poly(tert-butylacrylate) (PtBA)
35
36 can markedly increase the output power.²²⁴ The PVDF copolymers were mainly composed of
37
38 α phases with an enhanced dipole moment by π -bonding and polar characteristics of the ester
39
40 functional groups in the PtBA. As the PtBA grafting ratio increased to 18 mol%, the
41
42 permittivity of PVDF increased from 8.6 to 16.5, and the output power was improved by 20-
43
44 fold compared to pristine PVDF-based TENG.
45
46
47
48
49
50

51 Polymer-based ferroelectric materials such as polyvinylidene difluoride (PVDF) are
52
53 also employed in wearable energy harvesting devices and can also be fabricated by mixing
54
55 powder with high dielectric constant to improve their properties. *Jin et al.* reported active-
56
57 carbon-doped PVDF with high permittivity for to high-performance wearable TENGs.²²⁵
58
59
60

1
2
3
4 After mixing active-carbon with a PVDF solution, a film was prepared by a blade coating
5 method, and the dielectric constant was increased by about 35% according to the weight
6 percent of active-carbon. Through the of dielectric constant, the voltage, current, and power
7 of the PVDF film-based TENG were improved by 2.5, 3.5, and 9.8 times, respectively. *Chen*
8 *et al.* also developed a high dielectric triboelectrics by filling high dielectric nanoparticles
9 into sponge PDMS film, which is most commonly used as a triboelectric material.¹⁹⁷ The
10 sponge-structured PDMS film was formed by mixing PDMS with NaCl particles and washing
11 out NaCl particles with water. The high dielectric nanoparticles of SiO₂, TiO₂, BaTiO₃, or
12 SrTiO₃ were mixed with the PDMS in proportion, and 15 vol% SrTiO₃ exhibited the highest
13 output performance. By optimizing both the dielectric properties and the porosity of the
14 triboelectric material, the best output performance of TENG were obtained at 10 vol% SrTiO₃
15 nanoparticles and 15 vol% pores. It is worth noting that the porosity to increase the surface
16 area and the high dielectric particle content to increase the permittivity should be optimized at
17 the same time.
18
19
20
21
22
23
24
25
26
27
28
29
30
31
32
33
34
35
36
37
38
39
40
41
42
43
44
45
46
47
48
49
50
51
52
53
54
55
56
57
58
59
60

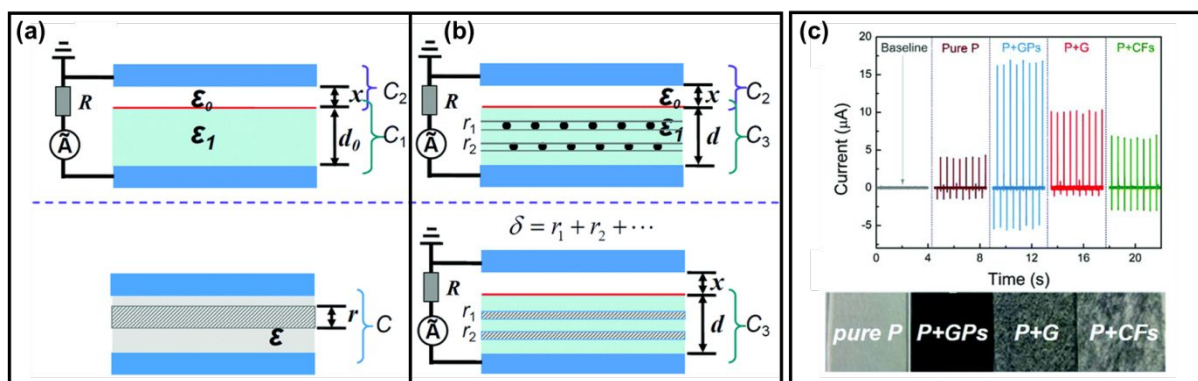


Figure 23. (a) Pure PDMS film and (b) PDMS@GPs thin film. (c) The output current of various composite and SEM images. Reprinted with permission from ref. 198, Copyright 2015, Royal Society of Chemistry.

1
2
3
4 One of the major issues of triboelectric contact electrification is the short retention time of the
5 surface charge. If the inside of the triboelectric layer is porous or another dielectric layer is
6 inserted, the charges can be trapped and held for a longer period of time.²²⁶⁻²²⁹ *Kim et al.*
7 reported that the charge trap interlayer between a charge generation layer and an electrode
8
9 can conserve the surface charges for a long period of time and increase the surface
10 potential.²³⁰ The PDMS was utilized in the charge trapping interlayer, which greatly
11 enhanced the output power density of TENGs as shown in Figure 24. Triboelectric electrons
12 can be trapped at the interface between the triboelectric and PDMS charge trapping layers,
13 which can prevent the loss of the surface charge. Although the charge loss decreased in
14 proportion to the thickness of the inserted charge trapping layer, a very thick interlayer may
15 not induce enough opposite charges in the electrode, resulting in low output performance of
16 TENG as described in Figure 24(c).
17
18
19
20
21
22
23
24
25
26
27
28
29
30
31
32
33
34
35
36
37
38
39
40
41
42
43
44
45
46
47
48
49
50
51
52
53
54
55
56
57
58
59
60

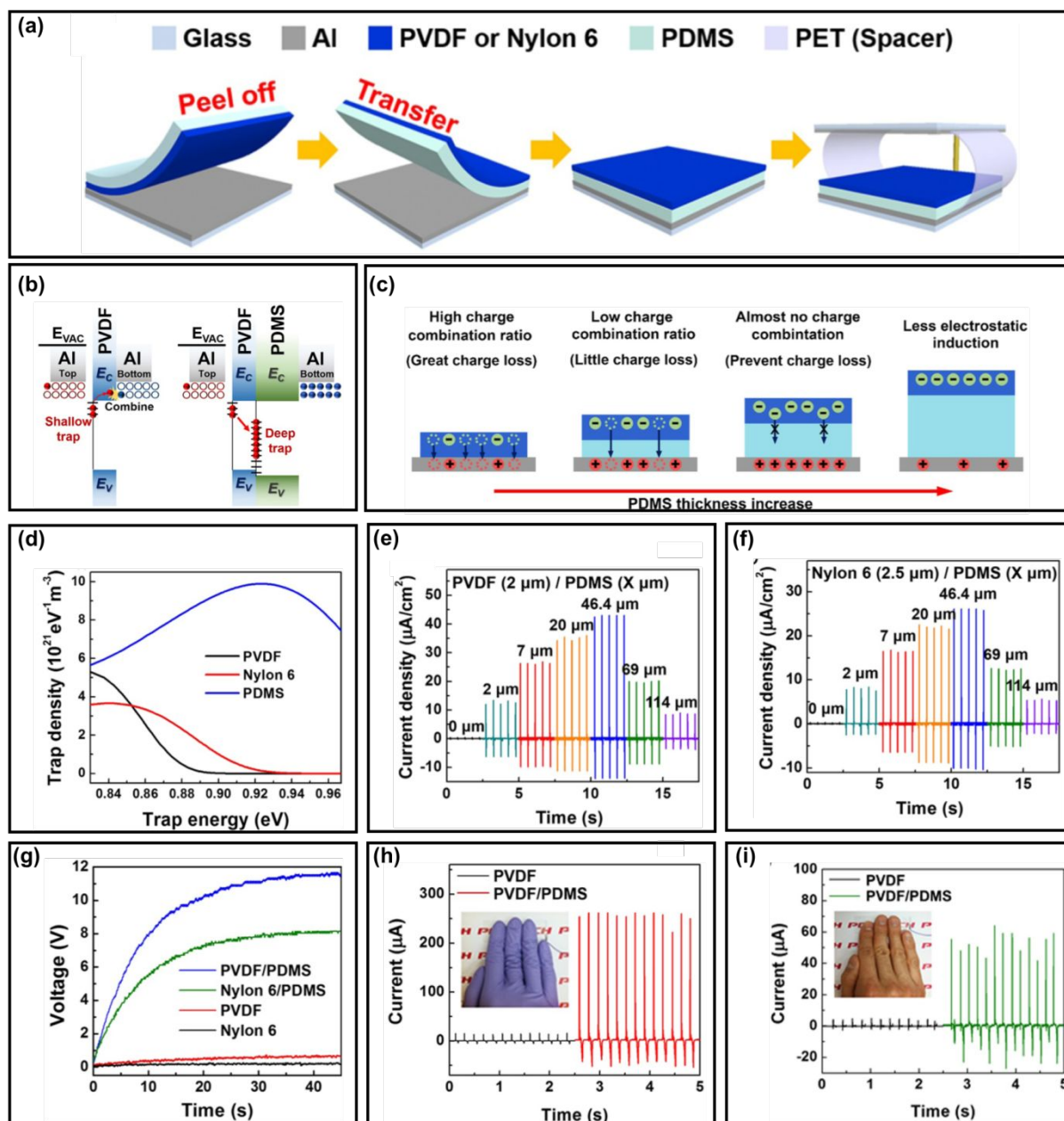


Figure 24. Deep-trap interlayer triboelectric nanogenerator. (a) Schematic description for fabricating TENGs made of a PVDF/PDMS double layer and Nylon 6/PDMS double layer. (b) Schematic charge trapping mechanism of the PVDF single-layer TENG and PVDF/PDMS double-layer TENG. (c) Schematic illustration of the charge combination and electrostatic potential induction according to the thickness of the PDMS interlayer. (d) Calculated charge trap energy distribution of PVDF, Nylon 6 and PDMS. (e)-(f) Current densities of the (e) PVDF/PDMS double-layer TENG and (f) Nylon 6/PDMS double-layer TENG with various thicknesses of the PDMS interlayer. (g) Superior capacitor charging properties of the double-layer TENGs. (h)-(i) Comparison of short-circuit current between the PVDF single-layer S-TENG and PVDF/PDMS double-layer S-TENG by gently tapping

1
2
3
4 each S-TENG with **(h)** latex gloves and **(i)** bare fingers. **Reprinted with permission from**
5 **ref. 230, Copyright 2018 Elsevier.**
6

7
8 For biomechanical energy harvesting, the skin-touch-actuated textile-based TENG has
9
10 been developed to improve both durability and performance by coating an electron-trapping
11 layer.²³¹ Black phosphorus (BP) encapsulated with hydrophobic cellulose oleoyl ester
12
13 nanoparticles (HCOENPs) was employed as a synergetic electron-trapping coating. The
14
15 textile-based TENG constituted the three layers stack of the triboelectric fabric composed of
16
17 BP and HCOENPs coated on PET fabric, fabric electrode, and waterproof fabric. It showed a
18
19 high output of 200 V or more even in various situations caused by skin contact or rubbing,
20
21 and it also can be operated in various motions such as folding, twisting, and stretching.
22
23
24
25
26
27
28
29

30 *Park et al.* conducted a study on improving the surface charge density by inserting an
31
32 electron blocking layer (EBL) between the negative triboelectric material and the electrode as
33
34 shown in Figure 25.²³² EBL with high permittivity dramatically increased the surface charge
35
36 by forming polarization as well as blocking the electron. The TiO₂ EBL layer was deposited
37
38 by RF-sputtering, and oxygen vacancies created inside TiO₂ played an important role in the
39
40 electron charge trap. The optimum thickness of the EBL layer was obtained at 100 nm, and
41
42 the output peak power from the TENG with a TiO_x EBL reached about 2.5 mW, which is 25
43
44 times larger than that of a TENG without an EBL.
45
46
47
48
49
50
51
52
53
54
55
56
57
58
59
60

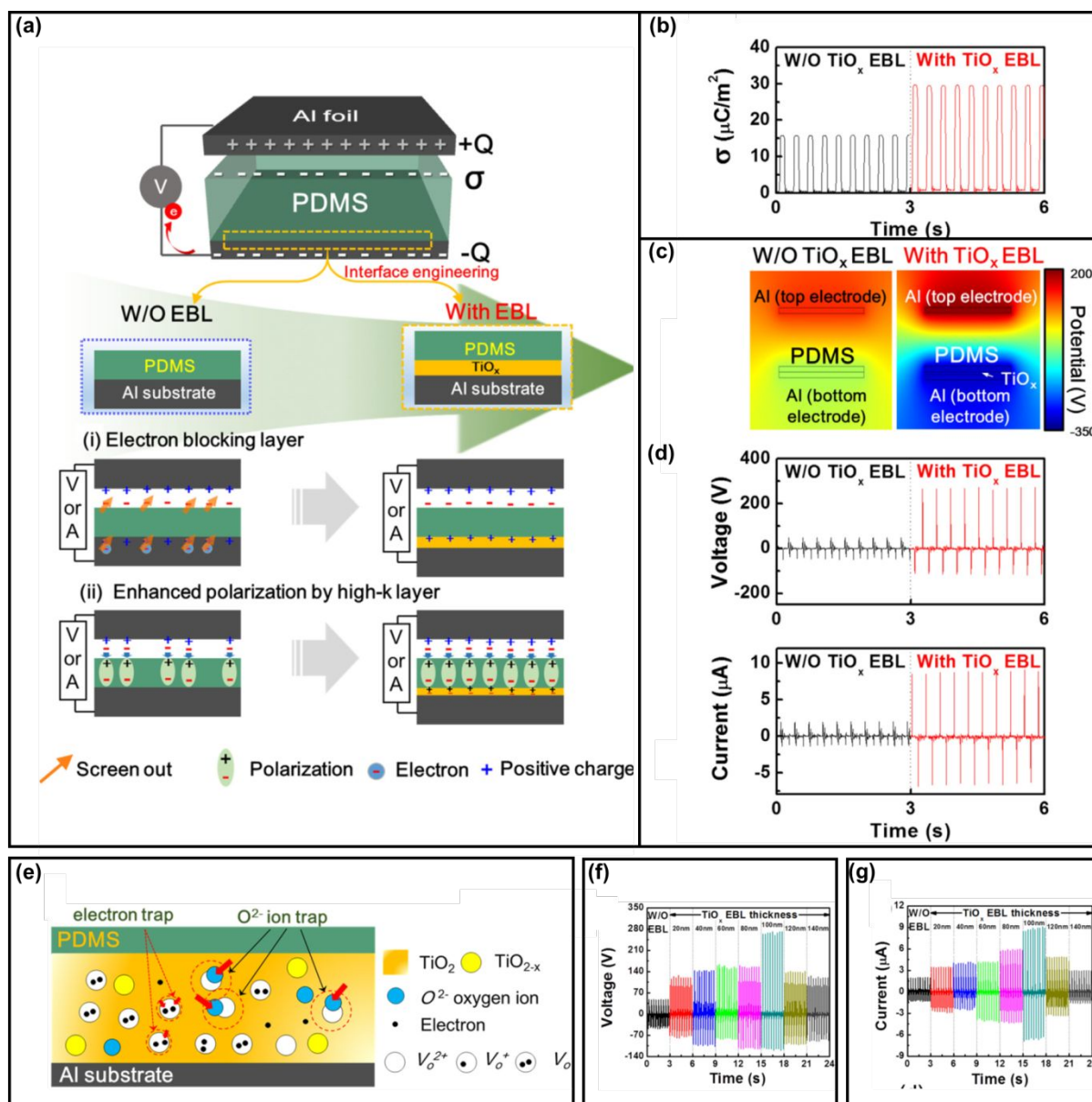


Figure 25. Electron blocking layer-based triboelectric nanogenerators. (a) Schematic illustration of the working principle of TENGs and the role of the multifunctional TiO_x EBL. (b) Charge density, (c) COMSOL Multiphysics simulation results, and (d) output voltage and current of the TENGs with and without the TiO_x EBL. (e) Schematic illustration of the electron trap mechanism according to the oxygen vacancies. (f) Output voltage and (g) Current of the TENGs with a TiO_x EBL as a function of the TiO_x EBL thickness. **Reprinted with permission from ref. 232, Copyright 2018 Elsevier.**

2.3.2.5. Direct Charge Injection into the Dielectric Surface Layer

Directly injecting electric charge into the surface of a dielectric layer is an intuitive yet highly effective method to dramatically improve the surface charge density. To this end, the dielectric layer is subjected to a strong external electromagnetic driving force to generate a dipole electret with permanent electrostatic bias,²³³ for which the specific methods include ionized air injection,²³⁴ plasma polarization,²³⁵ and high-voltage corona charging.²³⁶⁻²³⁸ In one case study, S. Wang *et al.* reported on the improvement of the output performance of TENGs through ionized air injection of fluorinated ethylene propylene (FEP) film by an air ionization gun (Figure 26(a)). The electret film (FEP film) formed by ion implantation maintained a surface charge density ($\Delta\sigma_{SC}$) of about $\sim 200 \mu\text{C}/\text{m}^2$ for 160 days, and the loss rate was only 16.6%. As a result, the ionized FEP film-based TENG increased the short-circuit current density and open-circuit voltage by 5-fold compared to the case of the non-treated FEP film (Figure 26(b)). However, when charge is induced between the dielectric contact surface and the electrode, the induced electric field in the dielectric generates an opposite charge at the electrode, resulting in stray charges on the dielectric surface. These stray charges inhibit the inflow of new charges, ultimately limiting the maximum achievable charge density on the dielectric surface through the ionized air injection method.^{230, 239-241}

In another case study, Y. Cho *et al.* proposed a method to improve the surface charge density of the dielectric layer further by applying the charge injection process on a gradient charge-confinement layer based on electrospun nanofibers, with each consecutive nanofibrous layer from the inside out containing a progressively larger sized population of mesoporous carbon spheres (mCS), as schematically shown in Figure 26(c). The mCSs facilitate charge transport from the outermost surface, which is bombarded by the charge injection process, all the way down to the deeper parts of the nanofibrous layer, while at the same time mitigating charge loss through charge confinement. The sequential arrangement of

1
2
3
4 the mCS along the depth gradient leads to an overall high space charge density of the charge-
5 injected composite layer (Figure 26(d)). Upon charge injection in presence of a strong
6 external field of 7 kV, the surface charge density on the gradient charge-confinement layer
7 was about 7.5 times higher compared to the case without the presence of mCSs. As a result,
8 the output voltage, which was initially 15.2 V before the charge injection, could be
9 dramatically increased to 600 V after the high voltage charge injection. Taken together, the
10 charge injection method, when coupled with proper structural engineering of the dielectric
11 layer to facilitate an efficient injection, has great potential as a powerful strategy to produce
12 high-performance TENGs.
13
14
15
16
17
18
19
20
21
22
23
24
25
26
27
28
29
30
31
32
33
34
35
36
37
38
39
40
41
42
43
44
45
46
47
48
49
50
51
52
53
54
55
56
57
58
59
60

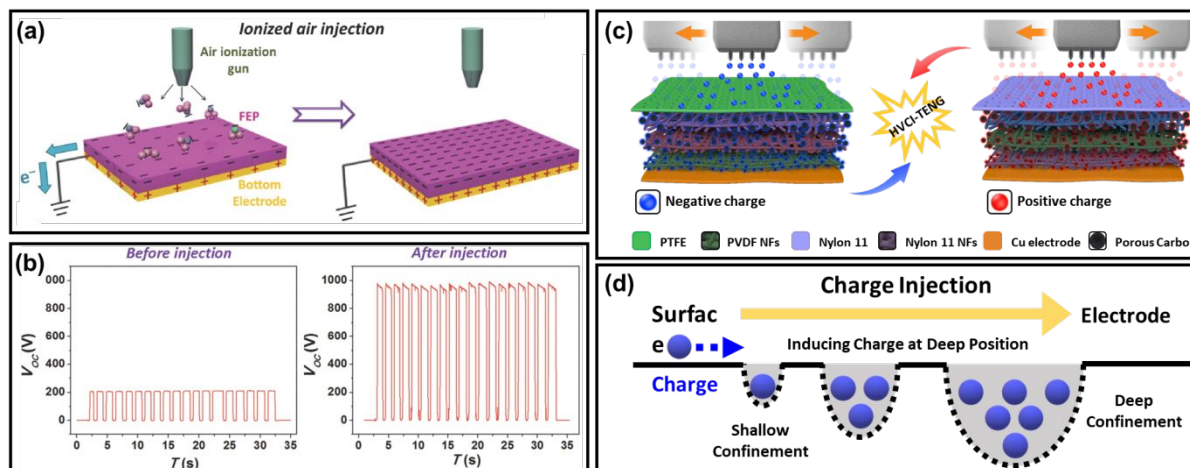


Figure 26. Schematic illustration of the charge injection method. (a) Schematic illustration of the basic process of ion injection onto the FEP film. (b) Open-circuit voltages of the TENG before and after the injection process. **Reprinted with permission from ref. 136, Copyright 2014, Wiley-VCH.** (c) Schematic illustration of the negative and positive charge-injection process to PTFE and Nylon 11, including the gradient confinement layer. (d) Schematic illustration of the charge transport and confinement from the surface to the electrode based on the charge confinement layer. **Reprinted with permission from ref. 199, Copyright 2022, Wiley-VCH.**

2.3.3 Composites

With the rapid development of flexible electronics, soft robotics, and distributed sensor networks, the requirements for wearable and portable power sources are increasing sharply. Thus, designing flexible/stretchable TENGs with excellent deformability and high electric performance is highly desirable, which provides an efficient and convenient way to endow the wearable energy harvesters with good comfortability, portability and biocompatibility. To ensure outstanding flexibility, stretchability and electric output of TENGs, massive efforts have been conducted to develop intrinsically flexible/stretchable composites by mixing the flexible/stretchable matrix and different functional fillers.²⁴² Typically, elastic polymers and hydrogels are selected as flexible/stretchable matrix networks considering their distinguished flexibility, deformability, biocompatibility and transparency. However, the triboelectric performance of these soft materials is often lackluster, not being able to satisfy the escalating demands of energy consumption. Therefore, a myriad of functional materials, such as graphene oxide (GO)²⁴³, carbon nanotubes (CNTs)²⁴⁴, black phosphorus (BPs)²³¹, MXenes²⁴⁵ and halide perovskites²⁴⁶⁻²⁴⁷, have been developed to modify the physical and chemical properties of the stretchable matrix, which can substantially improve the electrical output of stretchable TENGs.

1
2
3
4 The main strategy to promote the output performance of flexible/stretchable TENGs is to
5
6
7
8 enhance the charge trapping capacity and reduce the internal impedance of composite by
9
10
11 adding active materials with strong charge-storing ability or high electrical conductivity.

12
13
14 From this aspect, Kang et al. reported a poly(dimethylsiloxane) (PDMS) / GO / sodium
15
16
17 dodecyl sulfate (SDS) composite-based TENG with high electric output (Figure 27(a)).²⁴³ For
18
19
20
21 this composite, GO serves as a strong negative charge trapping material in view of its large
22
23
24 number of oxygen functional groups on the surface, while SDS surfactant not only promotes
25
26
27 the emulsification and dispersion of GO in the PDMS matrix, but also provides sufficient
28
29
30 anionic head groups to further boost the negative charges in the composite. After the
31
32
33 concentration and ratio optimization, a maximum electrical output of 438 V and 11 $\mu\text{A}/\text{cm}^2$
34
35
36
37 can be obtained, which is over three times higher than a pure PDMS-based TENG device.

38
39
40
41 Similarly, Ping et al. adopted a PDMS / MXene composite film as triboelectric negative
42
43
44 material.²⁴⁵ The introduction of MXene improved both the electron trapping ability and the
45
46
47 electrical conductivity of the composite film, which enhanced the tribonegativity and reduced
48
49
50 the interfacial impedance of the TENG device. The optimum electrical output voltage and
51
52
53 current of PDMS / MXene film are ~119 V and 11 μA , respectively, which is 7 times greater
54
55
56
57 than the pure PDMS TENGs. To further enhance the charge trapping capacity of triboelectric
58
59
60

1
2
3
4 materials, Lee's group also developed a series of flexible/stretchable nanocomposites,
5
6
7 including hydrophobic cellulose oleoyl ester nanoparticles (HCOENPs) / black phosphorus
8
9
10
11 (BPs) / polyethylene terephthalate (PET) textile²³¹, poly(vinylidene fluoride-co-
12
13
14 hexafluoropropylene) (PVDF-HFP) / fluorinated carbon nanotubes (F-CNT) film²⁴⁴, and
15
16
17 PVDF-HFP / styrene-ethylene-butylene-styrene (SEBS) / Cs₃Bi₂Br₉ nanofiber composite²⁴⁶.
18
19
20
21 The HCOENPs/BPs/PET textile was prepared via a dip-coating or spray-coating method, and
22
23
24 BPs significantly improved the triboelectric performance owing to their strong electron
25
26
27 accepting properties and high specific surface area (Figure 27(b)).²³¹ Meanwhile, HCOENPs
28
29
30 also promoted the electron trapping process and protected BPs from degradation. Owing to
31
32
33
34 the synergistic charge trapping mechanism of BPs and HCOENPs, a maximum electrical
35
36
37 output voltage and current density were enhanced up to 880 V and 1.1 $\mu\text{A}/\text{cm}^2$, respectively,
38
39
40
41 which could easily drive over 150 LEDs in series. Furthermore, a PVDF-HFP / F-CNT
42
43
44 nanofiber film was also fabricated through an electrospinning method (Figure 27(c)).²⁴⁴ The
45
46
47 addition of F-CNT microspheres not only intensified the tribonegativity but also the surface
48
49
50 roughness of the nanocomposite, resulting in an enhanced electric performance as well as
51
52
53 excellent hydrophobicity of the nanofiber film. The prepared flexible TENGs also displayed a
54
55
56 strong electrostatic adhesion, which made them easily attach on the surface of plant leaves,
57
58
59
60

1
2
3
4 enabling them to harvest mechanical energy from ambient environment such as wind and rain
5
6
7
8 energy, as shown in Figure 27(c). To further improve the stretchability and electrical output
9
10
11 of nanofiber composite, a PVDF-HFP/SEBS/Cs₃Bi₂Br₉ nanofiber composite was also
12
13
14 prepared through an in-situ electrospinning method (Figure 27(d)).²⁴⁶ SEBS microspheres can
15
16
17 serve as stretchable binders and hydrophobic agents, endowing the composite with excellent
18
19
20 stretchability and waterproofness, while the incorporation of Cs₃Bi₂Br₉ perovskites can
21
22
23 function as effective electron acceptors that improved the charge trapping capacity of the
24
25
26 composite. The excellent energy level matching between PVDF-HFP nanofibers and
27
28
29 perovskites also reinforced the electron transfer efficiency and decreased the charge loss,
30
31
32 further boosting the output performance. Due to these promising advantages, this nanofiber
33
34
35 composite-based mechanical energy harvester shows exceptional electric output of 400 V and
36
37
38 1.63 $\mu\text{A}/\text{cm}^2$, setting a record of output voltage among all halide perovskite-based mechanical
39
40
41 energy harvesters. The device also exhibited outstanding durability, deformation resistance,
42
43
44 and mechanical stability, which can sustain stable electric output after various physical
45
46
47 deformations (washing, folding and crumpling).
48
49
50
51
52
53
54
55
56
57
58
59
60

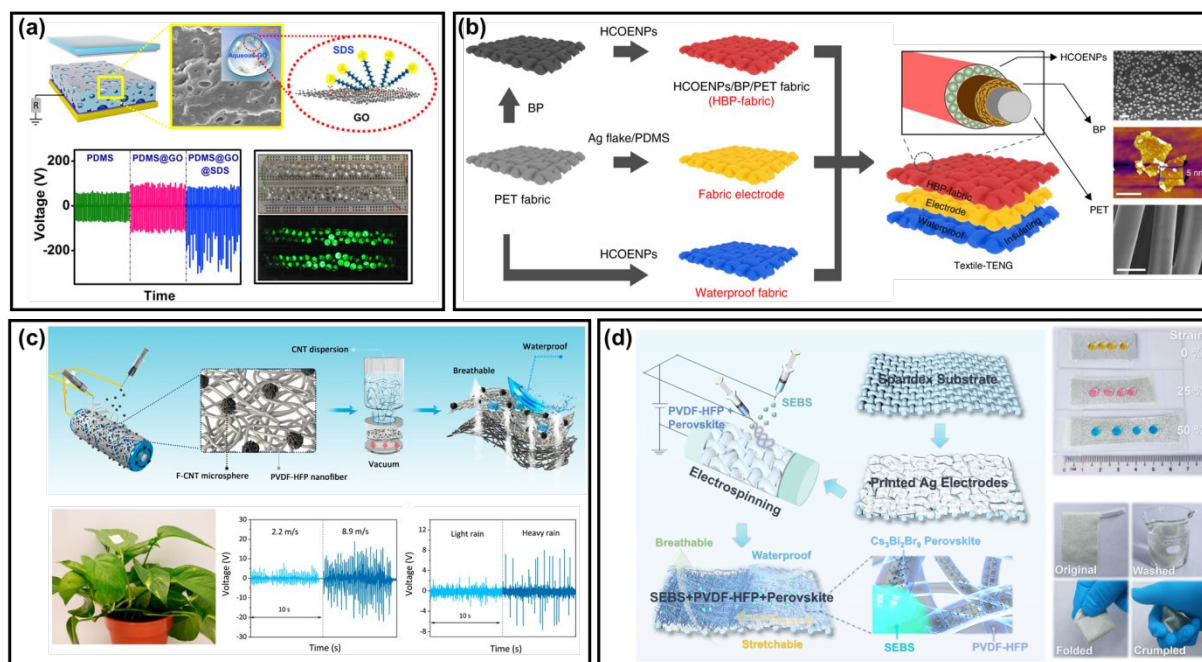


Figure 27. Flexible/stretchable composites for TENGs. **(a)** Schematic diagram of the PDMS/GO/SDS composite-based TENG and its output voltage compared to pure PDMS and PDMS/GO composite-based TENG. **Reprinted with permission from ref. 243, Copyright 2018, American Chemical Society.** **(b)** Schematic of the fabrication process of HCOENPs/BPs/PET textile based TENG. **Reprinted with permission under a Creative Commons CC BY license from ref. 231, Copyright 2018, Springer Nature.** **(c)** Schematic of fabrication process of PVDF-HFP / F-CNT nanofiber film-based TENG. The TENG device can be attached to a plant leaf for energy harvesting from the ambient environment, including wind energy under different air flow speed and rain energy under different rainfall intensity. **Reproduced from ref. 244, Copyright 2021, American Chemical Society.** **(d)** Schematic of fabrication process of PVDF-HFP/SEBS/Cs₃Bi₂Br₉ nanofiber composite-based TENG. The TENG device shows excellent stretchability, waterproofness, breathability, and mechanical stability after extreme deformations. **Reproduced from ref. 246, Copyright 2022, John Wiley and Sons.**

1
2
3
4
5
6
7 In the case of metal-oxide (MO)-organic composites, zinc oxide (ZnO) and titanium
8
9
10 oxide (TiO₂) are the most used fillers. ZnO nanostructures are piezoelectric in nature,
11
12
13 meaning they have the ability to be polarized in the presence of force, leading to changes in
14
15
16 the surface potential of the composite film (Figure 28(a)). The presence of metal-oxides in
17
18
19 polyvinylidene fluoride (PVDF) also improves the β -phase, thereby leading to better
20
21
22 polarization in the composite layer. Moreover, the introduction of metal-oxides improves the
23
24
25 dielectric properties and surface roughness of the composite films ²⁴⁸⁻²⁵¹. Carbon based
26
27
28 materials like carbon nanotubes (CNTs), graphene, graphene oxide, and reduced graphene
29
30
31 oxide were also used as fillers in polymer matrix to improve the TENG performance. The
32
33
34 CNTs not only improve the electrical conductivity but also enhances the mechanical
35
36
37 properties for designing stretchable and durable TENGs ²⁵²⁻²⁵³. Graphene has excellent
38
39
40 electrical conductivity with optical transparency and its introductions in PDMS increases the
41
42
43 capacitance and reduces the dielectric loss. The presence of graphene in PVDF improves the
44
45
46 β -phase content and electron trapping sites to improve the TENGs performance ^{117, 254}. In this
47
48
49 regard, the graphene-PVDF TENG shown in Figure 28(b) produced an excellent output
50
51
52 voltage of 1511 V and current density of 189 mA m⁻² ¹¹⁷. Recently, an MXene (Ti₃C₂T_x) was
53
54
55
56
57
58
59
60

1
2
3
4 reported to exhibit triboelectric negativity similar to that of PTFE. MXenes can improve the
5
6
7
8 surface charge density and electrical conductivity of the composite films. Similar to other
9
10
11 materials, MXenes can also improve the dielectric properties and polymers crystallinity.
12
13
14 $Ti_3C_2T_x$ was mixed with PTFE to improve the mechanical properties and surface charge
15
16
17 density. The use of MXene leads to 450% enhancement in the tensile property, while the
18
19
20
21 TENG fabricated with an MXene-PTFE active layer showed 4- and 6-times enhancement in
22
23
24 terms of the voltage (397 V) and current (21 μA), respectively ²⁵⁵. Similarly, porous
25
26
27
28 PDMS/MXene and PVA/MXene electrospun nanofibers were used for improving the TENG
29
30
31 performance ^{63, 245}. The introduction of MXenes in PDMS improves the surface potential of
32
33
34 PDMS from about -95 V to about -301 V, leading to a 7-fold enhancement in voltage (119 V)
35
36
37 and current ($\sim 11\mu A$) ²⁴⁵. MXene was also introduced in polyvinyl alcohol (PVA) hydrogel to
38
39
40 improve its stretchability by promoting crosslinking. MXene nanosheets also enhance the
41
42
43 conductivity and improve the ionic transport for enhancing the TENG output ²⁵⁶.
44
45
46
47

48 Similarly, metal-organic composites fabricated by using gold (Au) and silver (Ag)
49
50
51 nanostructures exhibited high performance when used as the active layer in TENGs. In this
52
53
54 regard, Au nanoparticles were introduced in polytetrafluoroethylene (PTFE), resulting in a 70%
55
56
57
58 increment in current compared to pristine PTFE film ²⁵⁷. The enhancement in performance
59
60

1
2
3
4 was due to improvements in the material capacitance, leading to effective charge trapping. In
5
6
7
8 other work, the introduction of Au nanoparticles in mesoporous PDMS led to a 5-fold
9
10
11 improvement in power via dipole alignment ¹²⁴. In the case of silver, nanowires used as a
12
13
14 filler in polymers is well documented, which improves the conductivity, surface potential,
15
16
17 and lowers the fermi energy of the composite film for enhancing the TENG output ²⁵⁸⁻²⁶⁰.
18
19
20
21 One such example is shown in Figure 28(c), where the surface potential of PVDF changes
22
23
24 from -225 mV to -441 mV when 3 wt.% silver nanowires were mixed in the polymer ²⁵⁹.
25
26
27
28 Ferroelectric materials like barium titanate (BTO), calcium copper titanate (CCTO), and zinc
29
30
31 sulfite (ZnSO_3) are an excellent choice of fillers in a polymer to improve the TENG
32
33
34 performance. The majority of ferroelectric materials have a high dielectric constant and can
35
36
37 increase the surface charge density (σ) of the composite film ²⁶¹⁻²⁶². Similar to other materials,
38
39
40
41 the use of ferroelectric polymers can also improve the polymer crystallinity. In this regard,
42
43
44
45 high dielectric materials like BTO and CCTO were introduced in P(VDF-TrFE) and butylated
46
47
48 melamine formaldehyde (BMF), respectively ^{141, 263}. The TENG based on 5 wt. % BTO
49
50
51 showed an output of 330 V and 0.3 mA ²⁶³. The use of 1 wt.% CCTO in BMF leads to a
52
53
54 voltage of 268 V and current density of 25.8 mA m⁻² ¹⁴¹ (Figure 28(d)). Ferroelectric
55
56
57
58 materials were also used to tune the dipole alignment for enhanced performance of TENGs
59
60

1
2
3
4 and ferroelectric polymer below the active layer for TENGs operating in contactless mode ²⁶⁴⁻
5
6
7
8 ²⁶⁵.

9
10
11 In 2019, metal-organic frameworks (MOFs) were explored as fillers in polymer for
12
13
14 improving TENG performance. The use of HKUST-1 in PDMS as a charge trapping material
15
16
17
18 with better trapping capabilities at high relative humidity (RH) solves the issue of RH
19
20
21 influence on TENG output ²⁶⁶. Similarly, fluorinated KAUST-8 in PDMS enhances its charge
22
23
24 trapping and charge-inducing properties, leading to 11 times improvement in power density
25
26
27
28 ²⁶⁷. In another approach, ionic liquid was mixed with block copolymer as self-healing
29
30
31 material for TENGs ²⁶⁸. The ionic liquid was also mixed with PVDF-HFP for enhancing the
32
33
34 output of fluid-based TENGs (Figure 28(e)). The ionic liquid/PVDF-HFP TENG showed 212%
35
36
37
38 higher power density (26.1 mW m^{-2}) compared to pristine polymer ²⁶⁹. However, composites
39
40
41 using different materials are widely explored for improving TENG performance; still,
42
43
44
45 significant efforts are required in theory for predicting composite dielectric constants,
46
47
48 polymer modifications, and use of eco-friendly materials.
49
50
51
52
53
54
55
56
57
58
59
60

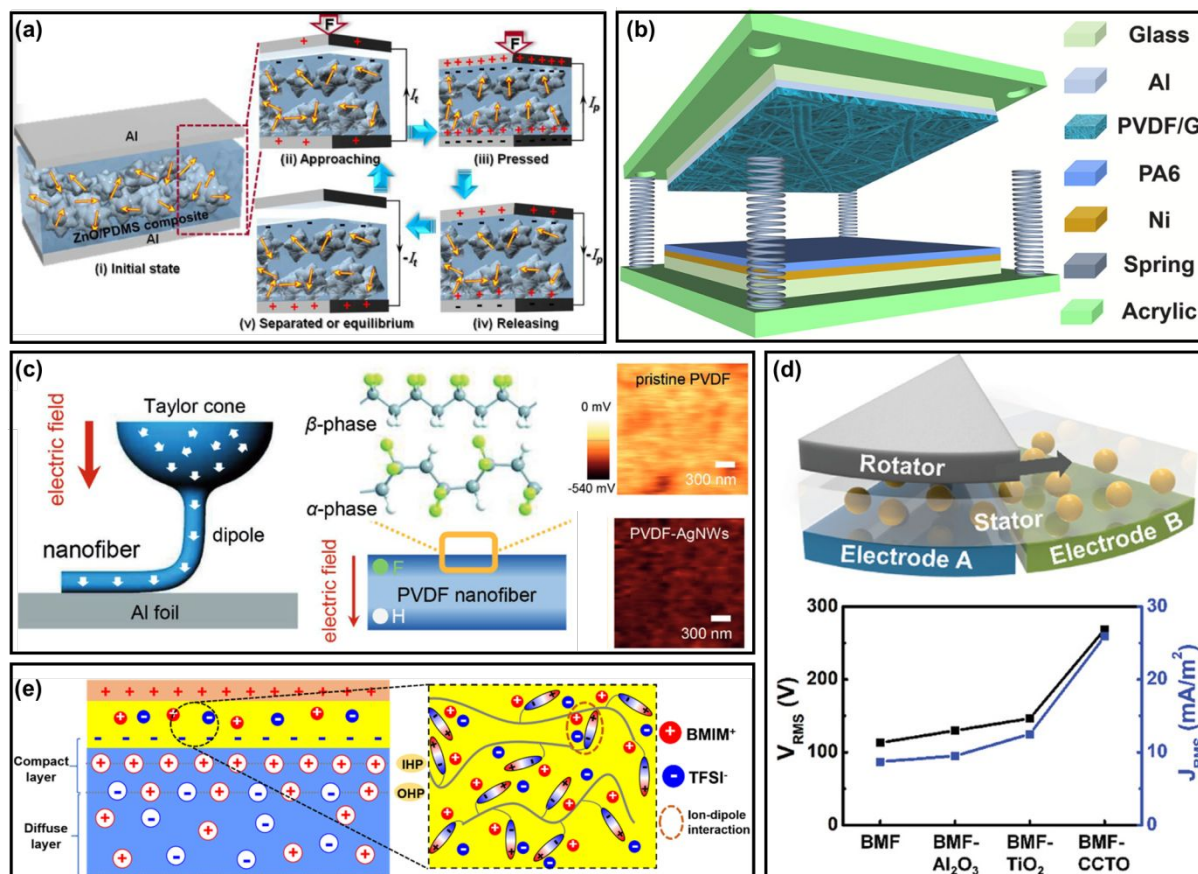


Figure 28. (a) Schematic illustration for the working mechanism of ZnO incorporated PDMS-based TENG devices. **Reproduced with permission. 249 Copyright 2018, American Chemical Society.** (b) 3D depiction of graphene-PVDF TENG comprised of PVDF/G and PA6 active layers. **Reproduced with permission. 254 Copyright 2021, Elsevier.** (c) Electrospinning process of PVDF and KPFM images of surface potential for pristine PVDF and silver nanowire incorporated PVDF. **Reproduced with permission. 259 Copyright 2018, John Wiley and Sons.** (d) Design of stator-rotator TENG based on CCTO-BMF and the output value of the device with different fillers. **Reproduced with permission. 141 Copyright 2020, John Wiley and Sons.** (e) Electrical double layer formation at the solid-liquid interface for enhanced output of the fluid-based TENG. **Reproduced with permission. 269 Copyright 2021 John Wiley and Sons.**

1
2
3
4
5
6
7 Recently, 2D nanomaterials have attracted attention in various fields due to their
8
9
10 inherent structural and electrical characteristics. In TENGs, they have also been used as
11
12
13 fillers to form composite layers. For instance, MXenes, a family of 2D transition metal
14
15
16 carbides and carbonitrides, have excellent electrical and mechanical properties. Thanks to -F,
17
18
19 -OH, -O and other functional groups, its surfaces can be easily functionalized. Due to surface
20
21
22 groups of -F, -O, and -OH, MXenes exhibit highly electronegative properties.²⁷⁰ These
23
24
25 functional groups on the surface also make MXenes hydrophilic²⁷¹⁻²⁷² and facilitate
26
27
28 composite formation. In Figure 29, the TENG fabricated with electrospun PVDF/MXene
29
30
31 composites achieved a peak power density 1.6 times higher than that of pristine PVDF
32
33
34 nanofibers attributed to the electrostatic attraction between the H or F atoms in the PVDF
35
36
37 polymer and the functional groups of MXenes. Therefore, MXene-polymer composites
38
39
40 demonstrated enhanced electronegativity and thus functioned as good negative friction layers
41
42
43 in TENGs.^{63, 273-274} Depending on their work function, 2D semiconductors exhibit slightly
44
45
46 different triboelectric properties.²⁷⁵ Among them, nanoflake MoS₂²⁷⁶⁻²⁷⁷ and bulk MoS₂²⁷⁸⁻²⁷⁹
47
48
49 have been extensively used in TENGs. When composited with the polymers, MoS₂
50
51
52 composites demonstrate triboelectrically negative properties and work as a charge trapping
53
54
55
56
57
58
59
60

1
2
3
4 reservoir.^{277, 280} Similar to metal oxide filler, these 2D materials also effectively increase the
5
6
7
8 permittivity of the friction layers. By doping and controlling layer thickness of these 2D
9
10
11 materials, symmetry in their crystal structure can be disturbed to modify their inherent
12
13
14 properties, inducing inherent dipole moment, increasing electronegativity, and trapping
15
16
17 charges.²⁸¹⁻²⁸² Therefore, further investigation is needed to exploit 2D-polymer composites
18
19
20
21 for TENGs.
22
23
24
25
26
27
28
29
30
31
32
33
34
35
36
37
38
39
40
41
42
43
44
45
46
47
48
49
50
51
52
53
54
55
56
57
58
59
60

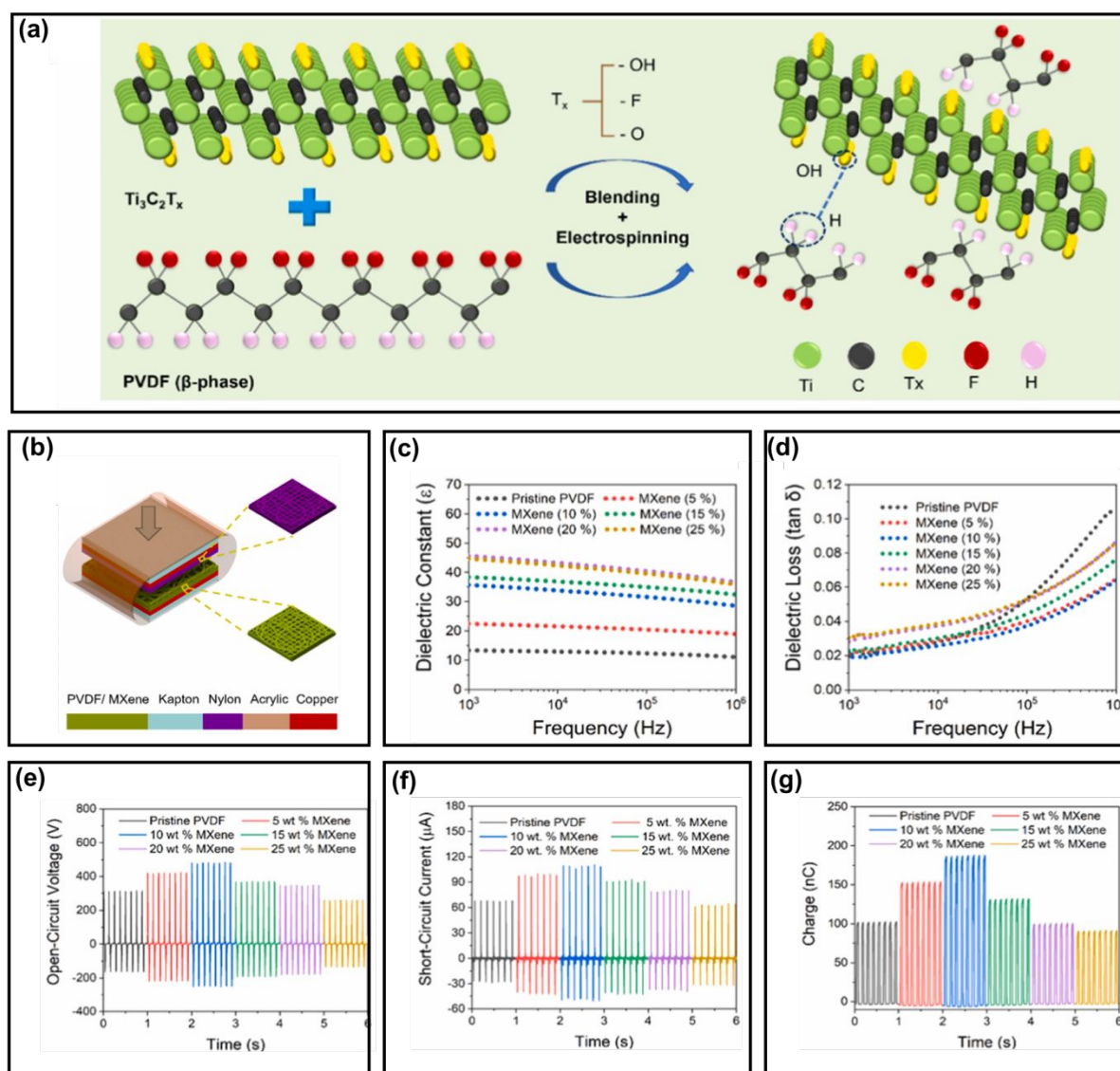


Figure 29. (a) Chemical structure and the schematics illustrating the influence of MXene blending into the PVDF matrix to form H-bonding. (b) Schematic device structure of as-fabricated TENGs. (c) Dielectric constant as a function of measurement frequency. (d) Dielectric loss as a function of measurement frequency. (e) Open-circuit voltages (V_{oc}) and (f) short circuit current (I_{sc}) (g) charge of the TENG for different wt.% of MXenes in PVDF. Reproduced from ref. 142, Copyright 2021, Elsevier.

1
2
3
4
5 Ferroelectric polymers Nylon 11 and PVDF-TrFE are triboelectrically high positive
6
7
8 and negative polymers, respectively. They have been widely used as friction materials
9
10
11 because of their intrinsic ferroelectric properties.²⁸³⁻²⁸⁸ To improve the ferroelectric properties
12
13
14 of ferroelectric polymers, various fillers such as metal oxides,²⁸⁹⁻²⁹⁰ 2D materials,^{278, 291-292}
15
16
17 and ferroelectric materials^{285, 287} are composited with these polymers. In particular,
18
19
20 ferroelectric fillers such as BaTiO₃,^{285, 287} PZT,²⁹³⁻²⁹⁴ and MAPbI₃²⁹⁵⁻²⁹⁶ induce additional
21
22
23 polarization into the composite material and thus demonstrated high output performance.
24
25
26
27 Among them, BaTiO₃ is a lead-free material with high dielectric constant and excellent
28
29 ferroelectric properties, and is widely used as a ferroelectric filler for TENGs.²⁹⁷⁻²⁹⁸ In the
30
31
32 case of TENGs with ferroelectric composite layers, electrical polarization can be applied to
33
34
35 further improve the ferroelectric properties of the friction layers, inducing rearrangement of
36
37
38 the dipoles inside the composite through externally applied electric field.²⁹⁹⁻³⁰⁰ Effective
39
40
41 polarization of each composite can be achieved by appropriate electric field, temperature, and
42
43
44 process time, which are determined by its coercive field, insulation resistance, Curie
45
46
47 temperature, etc.³⁰¹⁻³⁰² In addition to optimizing the poling process, the direction of
48
49
50 polarization must be carefully decided to boost the polarity of the friction surface as shown in
51
52
53 Figure 30. Consequently, the dielectric properties and triboelectric friction surface can be
54
55
56
57
58
59
60

1
2
3
4 modulated through electrical polarization of the ferroelectric composite materials to improve
5
6
7
8 the performance of TENGs. Besides, the polarized dipoles inside the composite layer also
9
10
11 affect the movement of the charge carriers, further enhancing the triboelectric output.^{284, 303-}
12
13

14 304
15
16
17
18
19
20
21
22
23
24
25
26
27
28
29
30
31
32
33
34
35
36
37
38
39
40
41
42
43
44
45
46
47
48
49
50
51
52
53
54
55
56
57
58
59
60

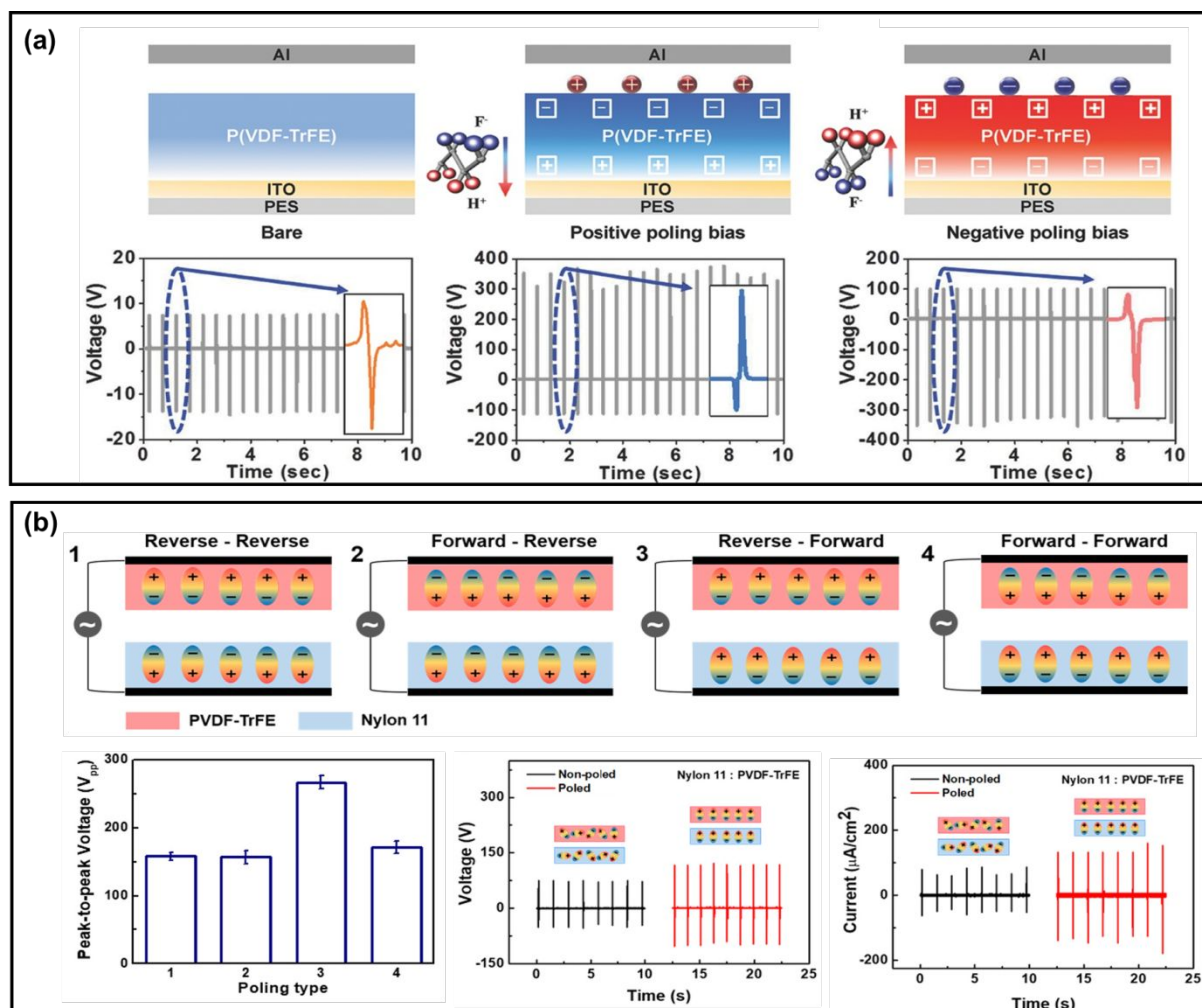


Figure 30. Optimization of the poling process for TENGs. (a) Controllable charge transfer by ferroelectric polarization. Reproduced from ref. 284, Copyright 2016, WILEY-VCH Verlag GmbH & Co. KGaA, Weinheim. (b) Output performance dependence on the polarization direction of both ferroelectric polymer layers. Reproduced from ref. 278, Copyright 2019, American Chemical Society.

2.4 Interlayer modifications

As well as surface and bulk modifications, intermediate layer engineering is a promising approach for achieving improved triboelectric performance. As its name suggests, the interlayer modifications are usually treated between tribo-materials and electrodes. The interlayer modifications are able to control the interfacial properties based on physical characteristics of the interlayer materials. On the technical background, there are two major issues of surface charge decay and electrostatic induction hindrance by the charge recombination at electrodes.^{232, 305} The surface charges exposed in air can be naturally reduced because the electric field of the charge attracts ions, which are always present in the atmosphere.^{75, 306} In addition, the surface charges can be reduced by a drift process caused by the electric field and a diffusion process caused by the concentration gradient of electrons.³⁰⁵ Therefore, the surface charge decay induces the reduction of triboelectric performance. The electrostatic induction hindrance can occur at the interface between tribo-materials and electrodes. In electrodes, there are numerous free electrons and they are able to nullify the electrostatic induction due to recombination.²³² The suppression of electrostatic induction negatively affects the triboelectric behavior, and the corresponding triboelectric performance can be reduced. Therefore, to reduce the negative effects and enhance the triboelectric

1
2
3
4 performance, interfacial engineering methods were widely investigated. In this section, we
5
6
7
8 review the interfacial engineering approaches according to two categories: electron trapping
9
10
11 layers (ETLs) and electron blocking layers (EBLs)/functional interlayers.
12

13
14 The electron trapping layers (ETLs) or charge trapping layers (CTLs) has been investigated
15
16
17 to minimize the surface charge decay issue and to improve the triboelectric performance.
18
19
20
21 Based on the dynamic behavior of the triboelectric charges under the incident of external
22
23
24 electric field, *Cui et al.*³⁰⁵ demonstrated and suggested the three-layered friction layer. In this
25
26
27 research, the polyvinylidene fluoride (PVDF) was utilized as a negative friction layer and Al
28
29
30 was utilized as both a counter friction layer and electrode. To form a charge storage layer,
31
32
33 polystyrene (PS) was selected due to its relatively low electron mobility and carrier density
34
35
36 compared to PVDF (Figure 31(a)-(i)). In addition, for the improved charge storage capability,
37
38
39 the utilization of composites with conductive materials was suggested. In this research,
40
41
42 carbon nanotubes (CNTs)/PS composites were utilized and the total triboelectric charge
43
44
45 density was improved over 11 times, compared to PVDF monolayer-based TENG devices
46
47
48 (Figures 31(a)-(ii), (iii)). Based on this friction layer design approach, various forms of
49
50
51 friction layer were suggested and demonstrated.
52
53
54
55
56
57
58
59
60

1
2
3
4
5 *Feng et al.*²²⁸ demonstrated the effectiveness of the polymeric interlayer for enhanced
6
7
8 triboelectric performance. Polyimide (PI) was utilized as the intermediate layer called the
9
10
11 “charge storage layer.” The charge storage layer was deposited between a negative tribo-
12
13
14 material (i.e., PVDF) and an electrode (i.e., Cu). The PVDF collects the negative surface
15
16
17 charges by triboelectrification with the nylon and the PI layer stores the negative charges in it
18
19
20 due to its high negative polarity. Compared to the PVDF monolayer-based TENG, the
21
22
23 triboelectric outputs were improved over 9 times. *Kim et al.*²³⁰ also proposed a polymeric
24
25
26 intermediate layer called the “deep-trap interlayer” (Figure 31(b)-(ii)). The PVDF and Al
27
28
29 were utilized as a negative tribo-material and an electrode, respectively, and a
30
31
32 polydimethylsiloxane (PDMS) interlayer was inserted between them (Figure 31(b)-(i)). The
33
34
35 electron trapping effect is based on charge trapping theory, in which charges can be captured
36
37
38 by physical and chemical trapping sites in the amorphous phase of polymers, the crosslinking
39
40
41 networks and the functional groups.^{226, 307-308} With the PDMS interlayer, the triboelectric
42
43
44 performance can be improved by approximately 48 times compared to the pristine PVDF-
45
46
47 based TENG device (Figure 31(b)-(iii)). *Kim et al.*³⁰⁹ demonstrated the advanced design of a
48
49
50 polymeric interlayer-based TENG. In this study, the electrospun polyvinylidene fluoride co
51
52
53 trifluoroethylene (PVDF-TrFE) and PDMS were utilized as a negative tribo-material and a
54
55
56
57
58
59
60

1
2
3
4 charge trapping layer, respectively (Figures 31(c)-(i), (ii)). The interfused charge trapping
5
6
7
8 layer was proposed to effectively capture the triboelectric charges in the PDMS interlayer
9
10
11 (Figure 31(c)-(ii)). The interfused structure can improve the contact between PVDF-TrFE and
12
13
14 PDMS and it can enhance the charge transport from PVDF-TrFE to PDMS. Thereby, the
15
16
17 charge trapping capability of the PDMS layer can be improved, corresponding to
18
19
20 enhancement of the triboelectric performance by approximately 2 times and 6 times
21
22
23 compared to the PVDF-TrFE-based TENG and the simple bonded PVDF-TrFE/PDMS
24
25
26
27
28 TENG, respectively (Figure 31(c)-(iii)).
29
30
31
32
33
34
35
36
37
38
39
40
41
42
43
44
45
46
47
48
49
50
51
52
53
54
55
56
57
58
59
60

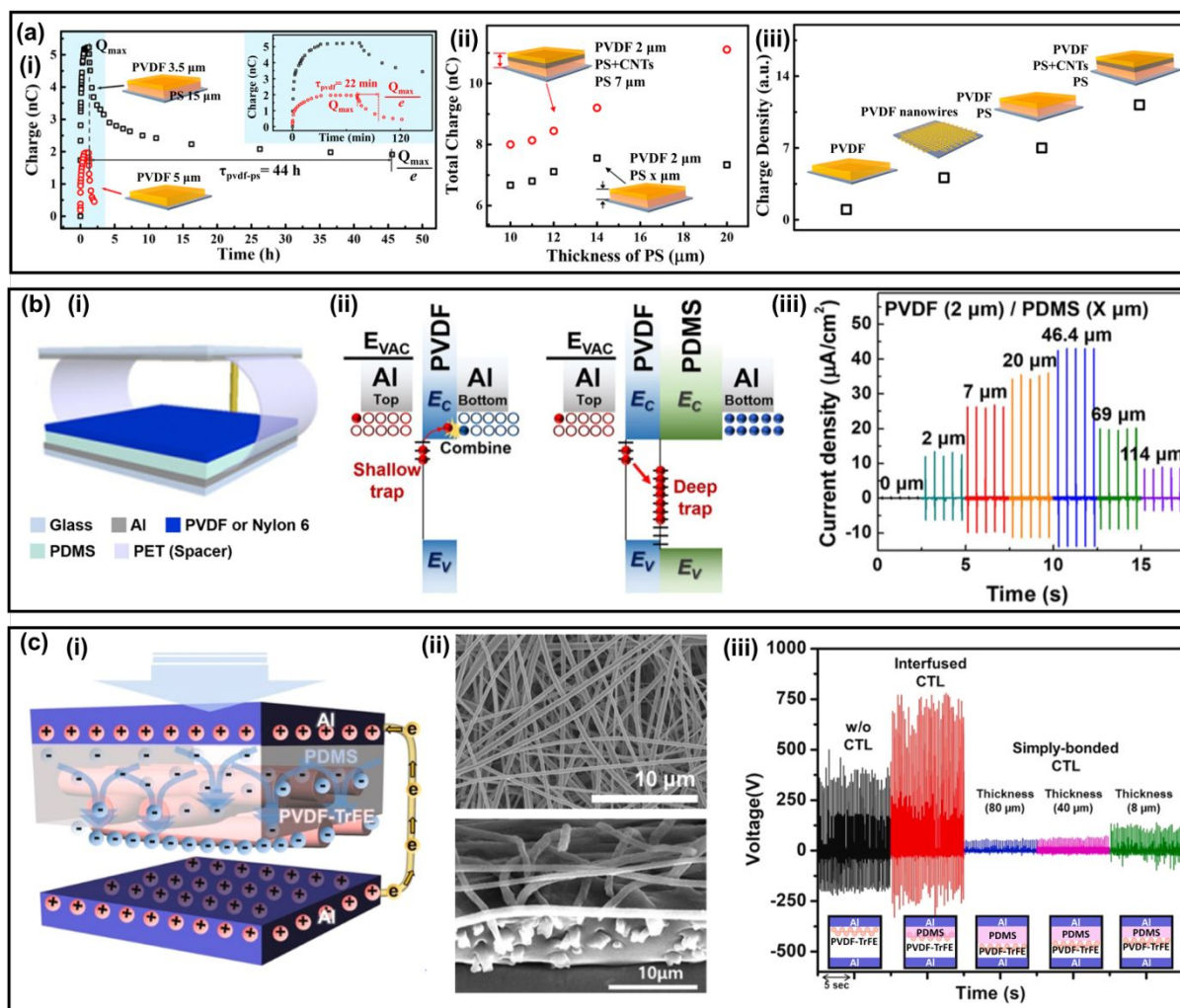


Figure 31. Charge trapping layer designs and their effects on the triboelectric performance. **(a)-(i)** Charge accumulation and decay properties of the PVDF single layer TENG and PVDF/PS double layer TENG. **(a)-(ii)** Measured total surface charge with and without the PS/CNTs composite layer. **(a)-(iii)** Friction layer structures and their maximum charge density. **Reprinted with permission from ref. 305, Copyright 2016, American Chemical Society.** **(b)-(i)** Schematic of the interface engineered TENG with the PDMS intermediate layer. **(b)-(ii)** Schematic of the charge trapping mechanism of the PVDF-monolayer TENG and PVDF/PDMS-multilayer TENG. **(b)-(iii)** Current densities of PVDF/PDMS-multilayer TENGs with various PDMS thicknesses. **Reprinted with permission from ref. 230, Copyright 2018, Elsevier.** **(c)-(i)** Schematic diagram of the TENG device with an interfused charge trapping layer. **(c)-(ii)** FE-SEM images of an electrospun PVDF layer and an interfused PVDF/PDMS friction layer. **(c)-(iii)** Effects of interlayer thickness and structure on the triboelectric voltage. **Reprinted with permission from ref. 309, Copyright 2022, Elsevier.**

1
2
3
4
5 Advanced conductive materials/polymer composites-based charge trapping layers have
6
7
8 been investigated. *Wu et al.*³¹⁰ demonstrated reduced graphene oxide (rGO)-based ETL for
9
10
11 enhanced triboelectric behavior (Figure 32(a)-(i)). Polyimide (PI) was utilized as a negative
12
13
14 tribo-material and a PI/rGO composite layer was deposited inside of the PI layer as an
15
16
17 electron storage layer. The rGO also modifies the interfacial energy band alignment (Figure
18
19
20 32(a)-(ii)); this energy band alignment provides the electron trapping capability. Due to the
21
22
23 electron trapping effect, the triboelectric performance was improved over 3 times compared
24
25
26 to a pristine PI-based TENG device (Figure 32(a)-(iii)). *Jiang et al.*³¹¹ also investigated an
27
28
29 advanced rGO-based intermediate layer. PVDF and Al were utilized as a negative friction
30
31
32 layer and an electrode, respectively. Here, as well as for the rGO, Ag nanoparticles (NPs)
33
34
35 were used to form an intermediate layer that has the improved dielectric property. Due to the
36
37
38 abundant charge carriers in Ag NPs, the polarization effect can be enhanced and the
39
40
41 corresponding triboelectric performance can be improved. Therefore, by using the rGO/Ag
42
43
44 NPs composites, the 5-fold triboelectric outputs were obtained.
45
46
47
48
49
50
51

52 Based on the energy band alignment control, *Hwang et al.*³¹² investigated the
53
54
55 optimized ETL for polydimethylsiloxane (PDMS)-based TENG devices (Figure 32(b)-(i)).
56
57
58 The negative tribo-material was PDMS and various carbon nanomaterials such as graphene
59
60

1
2
3
4
5 oxide (GO) and graphite were selected to compare their charge trapping capability (Figure
6
7
8 32(b)-(ii)). The largest enhancement was achieved by the GO with abundant oxygen defects
9
10
11 (ETL-R) and the enhancement factor for the triboelectric performance was 3.5 (Figure 32(b)-
12
13
14 (iii)). Due to the charge trapping by oxygen defects and huge modification of interfacial
15
16
17 energy band alignment called the “band-well structure,” the charging trapping capability can
18
19
20 be formed in the GO/PDMS composite layer, compared to the graphite/PDMS composite
21
22
23 intermediate layer (Figures 32(b)-(iv), (v)). *Li et al.*³¹³ also demonstrated the carbon black-
24
25
26 based ETL. The polyethersulfone (PES) was utilized as a negative tribo-material and PS was
27
28
29 utilized as a charge storage material. To improve the charge transport capability, the
30
31
32 PS/carbon black composite film was utilized. Due to the improved electron transport and
33
34
35 storage capability, the triboelectric outputs were improved by approximately 3 times
36
37
38 compared to the PES-monolayer-based TENG device. As well as carbon nanomaterials-based
39
40
41 ETLs, the 2D material-based ETL was proposed. *Wu et al.*²⁷⁷ investigated the molybdenum
42
43
44 disulfide (MoS₂)-based ETL for the enhanced triboelectric performance. In this study, the PI
45
46
47 was utilized as a negative tribo-material and MoS₂ monolayer/PI composite was utilized as an
48
49
50 electron trapping layer. By modifying the interfacial energy band alignment, it is able to trap
51
52
53 the electrons in MoS₂. With the MoS₂-intermediate layer, the triboelectric power density can
54
55
56
57
58
59
60

1
2
3
4 be improved by over 120 times compared to PI-monolayer-based TENG device. *Xiong et*
5
6
7
8 *al.*²³¹ presented that black phosphorus (BP) can be utilized as an intermediate material for the
9
10
11 enhanced electron trapping capability. The cellulose-derived hydrophobic nanoparticles
12
13
14 (HCOENPs) plays a role as a negative tribo-material. Compared to the HCOENPs-based
15
16
17 TENG device, the triboelectric performance was enhanced by approximately 3 times. The
18
19
20
21 MXene composites can be utilized as an electron trapping layer. *Chen et al.*³¹⁴ investigated
22
23
24 how ETL consists of MXene/titanium dioxide (TiO₂) composite. The mixed cellulose esters
25
26
27 (MCE) and Cu were the negative and positive tribo-materials, respectively. The counter tribo-
28
29
30
31 material was Cu. Based on how oxygen vacancies can trap the electrons, the heavily oxidized
32
33
34 MXene (HO-Ti₃C₂T_x) was utilized. TiO₂ nanoparticles also have abundant electron trap sites.
35
36
37
38 The composite film was deposited between MCE and the Cu electrode. Due to the numerous
39
40
41
42 electron trapping sites, the enhanced electron trapping capability was acquired. Furthermore,
43
44
45 the polarization can be improved because the TiO₂ layer provides high relative permittivity.
46
47
48
49 Due to the electron trapping effect and the enhanced polarization, the corresponding
50
51
52 triboelectric performances were improved by over 5 times. *Salauddin et al.*³¹⁵ presented the
53
54
55 laser-carbonized MXene/ZiF-67 (LC-MXene/ZiF-67) composite-based intermediate layer
56
57
58
59 with a silicone friction layer. Due to the presence of abundant charge trapping sites originated
60

1
2
3
4 from the chemical structure and the porous structure, the LC-MXene/ZiF-67 intermediate
5
6
7
8 layer can have a great charge trapping property. Thereby, the triboelectric performance was
9
10
11 improved by over 9 times.
12
13
14
15
16
17
18
19
20
21
22
23
24
25
26
27
28
29
30
31
32
33
34
35
36
37
38
39
40
41
42
43
44
45
46
47
48
49
50
51
52
53
54
55
56
57
58
59
60

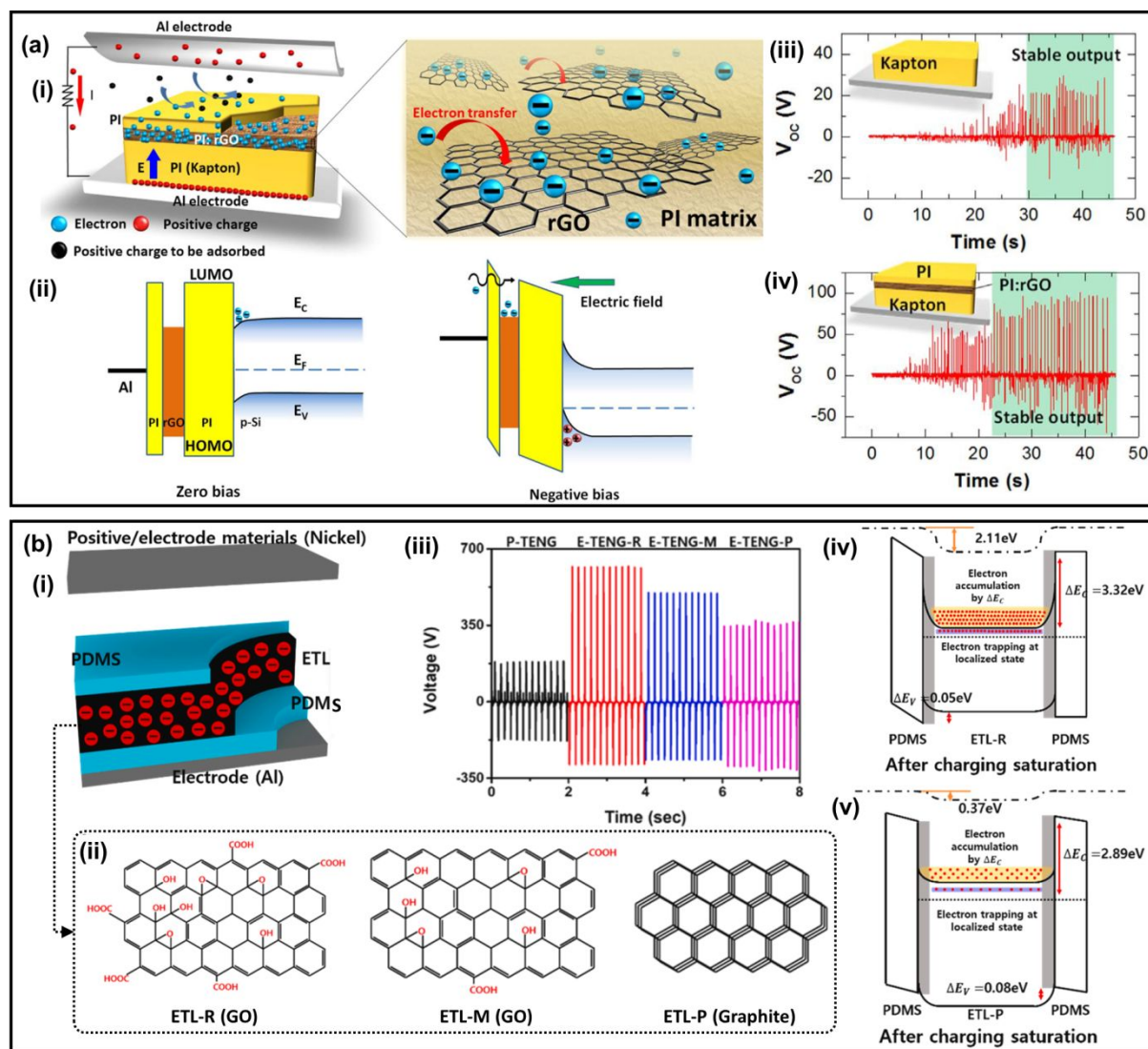


Figure 32. Charge trapping layer designs using the polymer/nanomaterial composites. **(a)-(i)** Schematic of the PI/rGO multilayer TENG. **(a)-(ii)** Schematic of the energy band diagram without and with a negative bias. Measured open-circuit voltages (V_{OC}) and charging characteristics of **(iii)** the PI monolayer TENG and **(iv)** the PI/rGO multilayer TENG. **Reproduced from ref. 310, Copyright 2017, Elsevier.** **(b)-(i)** Schematic illustration of the GO-ETL-based TENG device. **(b)-(ii)** Molecular structure of three different organic nanomaterials for the charge trapping capability comparison. **(b)-(iii)** Measured triboelectric voltages of TENG devices with different charge trapping layers. Energy band diagram of **(iv)** the ETL-R embedded friction layer and **(v)** the ETL-P merged friction layer. **Reproduced from ref. 312, Copyright 2021, Elsevier.**

1
2
3
4
5 Electron blocking layers (EBLs) have been investigated to suppress the electrostatic
6
7
8 induction hindrance at the interface between tribo-materials and electrodes. *Park et al.*²³²
9
10
11 introduced and reported the EBL using a sputtered titanium oxide (TiO_x) layer (Figure 33(a)-
12
13
14 (i)). Here, the friction layer was polydimethylsiloxane (PDMS) and the electrode was Al film.
15
16
17
18 The electron blocking mechanism is based on the free electron capture capability of oxygen
19
20
21 vacancies in the TiO_x layer (Figure 33(a)-(ii)). Since the oxygen vacancies are electrically
22
23
24 positive defects, it is able to capture the free electrons in Al electrode under the external
25
26
27
28 electric field. The electron blocking capability of the TiO_x layer is directly related to the
29
30
31 amount of oxygen vacancies. Therefore, it is important to increase the ratio of oxygen
32
33
34 vacancies in the interlayer. However, the interlayer affects not only the electron blocking
35
36
37
38 property but also the device capacitance. Since the device capacitance and electrostatic
39
40
41 induction can be reduced with the increment of material thickness, it is required to form an
42
43
44 interlayer with an optimal thickness. With the electron blocking effect, the 25-fold enhanced
45
46
47
48 triboelectric performances were obtained (Figure 33(a)-(iii)). Based on the electron blocking
49
50
51 capability of the TiO_x layer, *Hwang et al.*³¹⁶ demonstrated the EBLs for both positive and
52
53
54 negative tribo-material. Here, the positive friction layer was a thermoplastic polyurethane
55
56
57
58 (TPU) and the counter friction layer was a polytetrafluoroethylene (PTFE). The TiO_x
59
60

1
2
3
4 interlayers were formed beneath both friction layers. This work demonstrated that the EBL
5
6
7
8 technique is valid for obtaining an enhanced triboelectric behavior of both positive and
9
10
11 negative tribo-materials. For positive tribo-materials, the TiO_x interlayer prevents
12
13
14 recombination of the surface positive charges and free electrons in a top electrode. In the case
15
16
17 of negative tribo-materials, the TiO_x interlayer captures the free electrons in electrode and
18
19
20 preserves the electrostatically induced positive charges in a bottom electrode. By adapting
21
22
23 electron blocking layers on both positive and negative tribo-materials, the triboelectric
24
25
26 performance was improved by approximately 12 times compared to the pristine PTFE-TPU-
27
28
29 based TENG device. As well as TiO_x , graphite has an electron blocking capability. *Xin et*
30
31
32 *al.*³¹⁷ also demonstrated the electron blocking capability of a graphite paper (Figure 33(b)-(i)).
33
34
35 Here, the graphite paper was inserted between a positive friction layer (Cu) and an electrode
36
37
38 (Ni) (Figure 33(b)-(ii)). The graphite is a multilayered graphene and the graphene is able to
39
40
41 prevent electrons from drifting and diffusing due to the sp^2 -hybridized structure. Thereby, the
42
43
44 electron blocking capability can be formed in the graphite paper. The electron blocking
45
46
47 effects of different interlayers consisting of various materials such as Gp, Ti, paper, and
48
49
50 rubber were compared and the Gp interlayer showed the largest accumulated charges (Figure
51
52
53 33(b)-(iii)). The self-assembled monolayers (SAMs) are also valid intermediate materials to
54
55
56
57
58
59
60

1
2
3
4 improve the triboelectric performance. *Kim et al.*³¹⁸ presented the SAM-based intermediate
5
6
7
8 layer and its mechanism. The PDMS was utilized as a negative friction layer and Au was
9
10
11 utilized as an electrode. The thiolate SAMs, such as 4-aminobenzenethiol (ABT), 2,3,4,5,6-
12
13
14 pentafluorothiophenol (PFBT), and benzenethiol (BT), were deposited between PDMS and
15
16
17 the Au electrode. The working mechanism is based on the matching of an electrostatic
18
19
20 induction direction of PDMS and a dipole moment of SAM. The SAMs with a positive
21
22
23 functional group (e.g., -NH₂) can boost up the electrostatic induction of a negatively charged
24
25
26 PDMS by providing dipole momentum in the same direction. On the other hand, the SAMs
27
28
29 with a negative functional group (e.g., -F) can hinder the electrostatic induction of negatively
30
31
32 charged PDMS due to their dipole moment in the opposite direction. For the positively
33
34
35 charged PDMS, the negative SAM is utilizable but the increased work function of Au
36
37
38 electrode negatively affects the triboelectric performance. The triboelectric performance of
39
40
41 ABT-TENG was improved by 2.5 times compared to the PDMS-monolayer-based TENG.
42
43
44
45
46
47

48
49 Due to the rapid development of microscale electronic devices, such as nanorobots
50
51 and microelectromechanical devices, in recent years, layer-by-layer (LbL) self-assembly has
52
53 been considered for the demand for ultra-thin devices. This LbL assembly technology not
54
55 only successfully overcomes the thickness problem in performance improvement and
56
57 applications of TENG, but also presents a low-cost, eco-friendly process and large-scale
58
59
60

1
2
3
4 production. This review highlights recent advances in the development of LbL-based
5
6 tribomaterials for TENGs, demonstrating their potential in the field of energy harvesting
7
8 devices reviewed to date. Finally, we briefly present a perspective on LbL assembly
9
10 orientations for various ultra-thin TENG implementations.
11
12
13
14
15
16
17
18
19
20
21
22
23
24
25
26
27
28
29
30
31
32
33
34
35
36
37
38
39
40
41
42
43
44
45
46
47
48
49
50
51
52
53
54
55
56
57
58
59
60

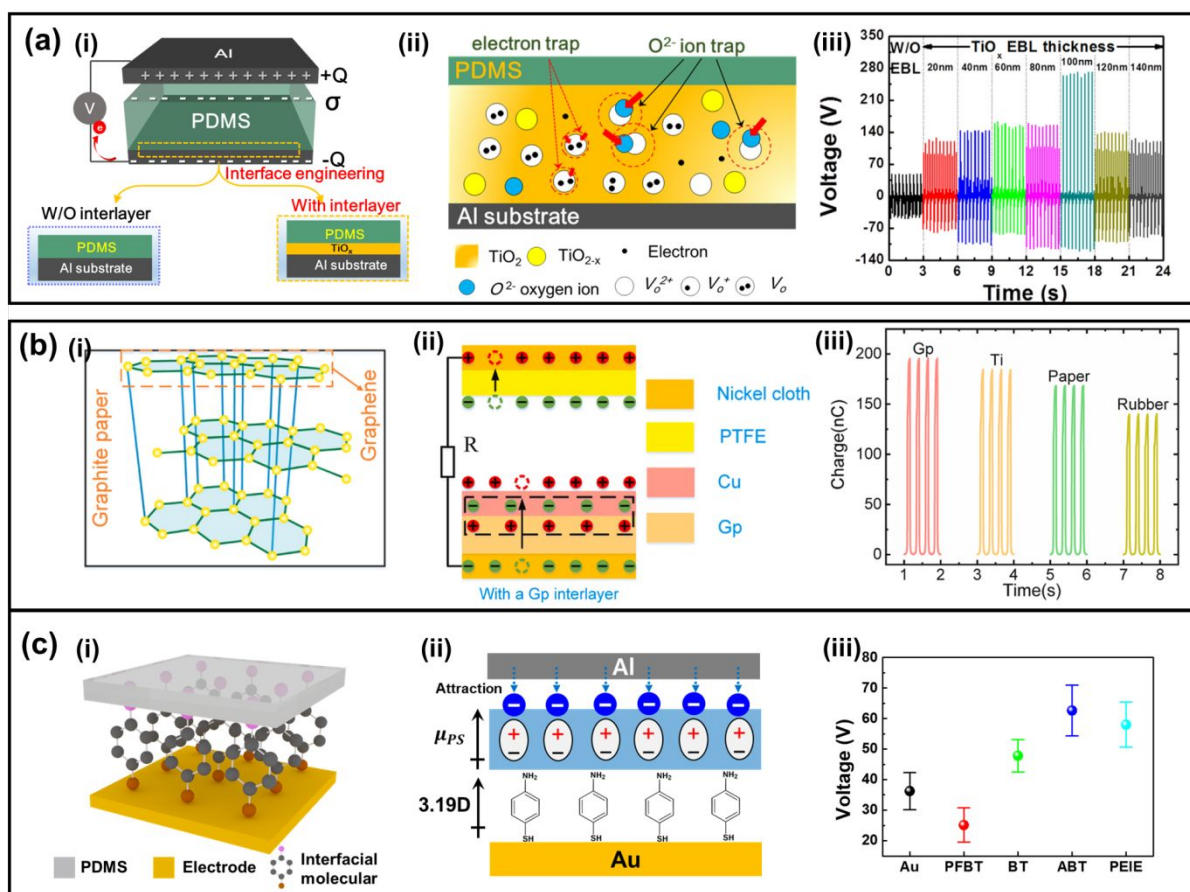


Figure 33. Electron blocking layer designs and the enhancement in the triboelectric performance. **(a)** Schematic diagram of **(i)** an interface engineered TENG with the TiO_x intermediate layer and **(ii)** the electron blocking mechanism of the TiO_x interlayer. **(a)-(iii)** Measured triboelectric voltages with various thicknesses of the TiO_x intermediate layer. **Reprinted with permission from ref. 232, Copyright 2018, Elsevier.** **(b)-(i)** Molecular structure of graphite paper. **(b)-(ii)** Schematic diagram of the Gp-interlayer-formed TENG device and its electron blocking effect. **(b)-(iii)** Measured total surface charge on Cu with different intermediate materials of Gp, Ti, paper, and rubber. **Reproduced from ref. 317, Copyright 2022, Elsevier.** **(c)** Schematic of **(i)** SAM-based interface engineered TENG device and **(ii)** working mechanism. **(c)-(iii)** Obtained triboelectric voltages produced by TENGs with the SAM-intermediate layer. **Reprinted with permission from ref. 318, Copyright 2022, Elsevier.**

1
2
3
4 Through decades of innovation, LbL self-assembly has emerged as one of the most versatile
5 fabricating methods used to develop multifunctional thin-film coatings.³¹⁹⁻³²⁰ LbL assembly
6
7 is a method used to create ultrathin multifunctional films by alternatively immersing a
8
9 substrate in solutions containing positive and negative polyelectrolytes. In terms of charges,
10
11 polyelectrolyte can be classified into three categories: polycations, polyanions, and
12
13 polyampholytes. Polyampholytes are ionic polymers that have both positively and negatively
14
15 charged groups, resulting in dense conformation due to the attraction between opposite
16
17 charged groups. On the other hand, polycations and polyanions have positively and negatively
18
19 charged groups, respectively, and take the form of extended chains owing to the repulsive
20
21 force between charged groups.
22
23
24
25
26
27

28 *Kim et al.* introduced LbL assembly-induced TENGs that exhibit high electric output
29
30 under a wide range of humidity conditions using replicas of nano/microporous multilayer
31
32 film (Figure 34).²⁰⁵ In this study, a cationic poly(allylamine hydrochloride)/anionic
33
34 poly(acrylic acid) multilayer film was prepared using electrostatic LbL-assembly, and then
35
36 sequentially immersed in acidic water to form a nano/micro-porous multilayer. The porosity
37
38 of the multilayer was controlled by the solution concentration of the polyelectrolyte (for
39
40 multilayer deposition) and the solution pH (for acidic treatment). When the porous multilayer
41
42 was used as a mold for the fabrication of triboelectric PDMS films, the replicated PDMS
43
44 films exhibited enhanced hydrophobic properties due to the formation of the nano/micro-
45
46 structured bumps and the relatively low surface energy of PDMS. The film device displayed
47
48 high electric outputs of 242 V and 16 $\mu\text{A}/\text{cm}^2$ (for comparison, the outputs of the flat PDMS
49
50 film were 75 V and 6.1 $\mu\text{A}/\text{cm}^2$) under a compressive force of 90 N at 20% relative humidity.
51
52 The output voltage was maintained at 194 V (for comparison, the output voltage of the flat
53
54 PDMS film was 14 V) under a high humidity condition of 80% relative humidity. Given that
55
56
57
58
59
60

1
2
3
4 the surface morphology and modification of the triboelectric film can be easily and delicately
5 controlled through electrostatic LbL assembly and additional fluorination treatment, this
6 approach can provide a facile, versatile, and cost-effective tool for designing large-area
7 TENGs with excellent electric output and high humidity resistance.
8
9
10
11
12
13
14
15
16
17
18
19
20
21
22
23
24
25
26
27
28
29
30
31
32
33
34
35
36
37
38
39
40
41
42
43
44
45
46
47
48
49
50
51
52
53
54
55
56
57
58
59
60

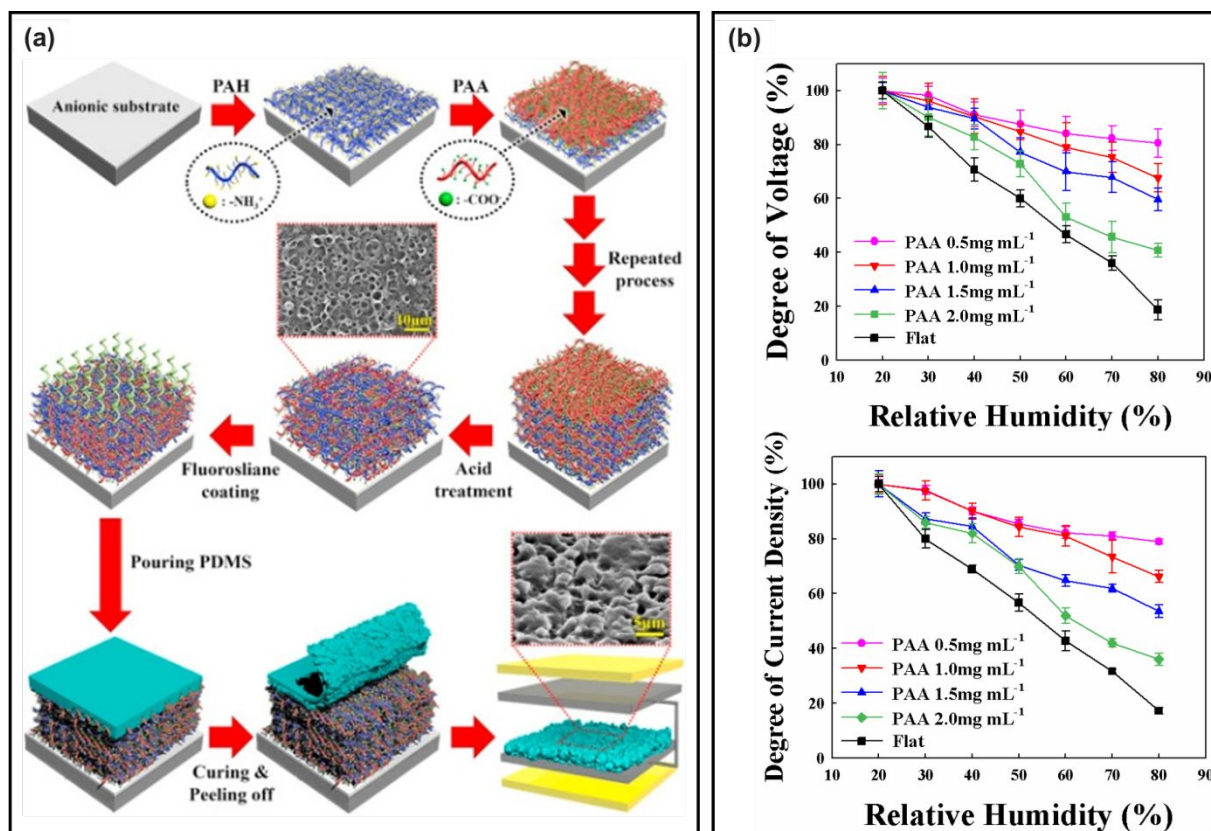


Figure 34. (a) Schematic for the preparation of triboelectric PDMS films with hierarchically embossed structures using porous PE-multilayered templates. (b) The degree of the triboelectric output for the flat PDMS and four different LbL-TENGs as a function of the RH. Reprinted with permission from ref. 205, Copyright 2017, Elsevier.

1
2
3
4 Menge et al. reported a designable functional polymer nanocomposite layer via an LbL
5 assembly process to manage highly deformable TENGs (Figure 35(a)).³²¹ To enhance the
6 output of the TENG, a high dielectric titanium (IV) oxide (TiO₂)-based nanocomposite
7 interlayer was used between the negative tribomaterial and the electrode. The functional
8 interlayer was designed with a multilayer of TiO₂ nanoparticles and poly(4-styrene-sulfonic
9 acid) through the LbL process. The achieved output performance was approximately 3.8- and
10 5.7-times higher than those without the functional nanocomposite layer owing to the effects
11 of the functional layer, i.e., improved polarizability and increased surface roughness. Guo et
12 al. investigated how contact electrification can be controlled by polyelectrolyte films.³²² The
13 selected substrate is polyimide (Kapton), which is used in both the electronic packaging
14 industry and in triboelectric nanogenerators. Chung et al. prepared a flexible graphene-based
15 ultrathin tribomaterial using LbL assembly from poly(4-styrene-sulfonic acid)-modified
16 graphene nanoplatelets, where the strong hydrogen bonding with poly(vinyl alcohol) plays an
17 important role in LbL deposition (Figure 35(b)).³²³ Poly(4-styrene-sulfonic acid), which is
18 known to be effective in dispersing graphene in water, was used to enhance the surface charge
19 of graphene to improve the dispersion and surface adhesion of graphene. The growth trend
20 confirmed the successful combination and constant composition of poly(vinyl alcohol) and
21 graphene. Interestingly, the multilayered thin film TENG containing three graphene layers
22 showed a maximum output voltage of 100 V and a current of 5 mA. Lee et al. reported a
23 wrinkled elastomer with bulk metal-like conductivity, high electrical stability, and large
24 electrode surface without further treatment process by in situ cooperation of solvent swelling
25 and metal nanoparticle assembly (Figure 35(c)).³²⁴ The authors layer-by-layer assembled
26 tetraoctylammonium bromide-stabilized Au nanoparticles dispersed in toluene on a thiol-
27 functionalized PDMS film with tris(2-aminoethyl)amine in ethanol. With this ligand-
28 exchange LbL process, TENGs with Au nanoparticle-based elastomeric electrodes were

1
2
3
4 fabricated. The authors also investigated the change in electrical output of various types of
5
6 TENGs (i.e., combinations of rigid or elastomeric electrode with planar or embossed PDMS)
7
8
9 under repeated compressive force at 5 Hz application frequency and 20% relative humidity.
10
11
12
13
14
15
16
17
18
19
20
21
22
23
24
25
26
27
28
29
30
31
32
33
34
35
36
37
38
39
40
41
42
43
44
45
46
47
48
49
50
51
52
53
54
55
56
57
58
59
60

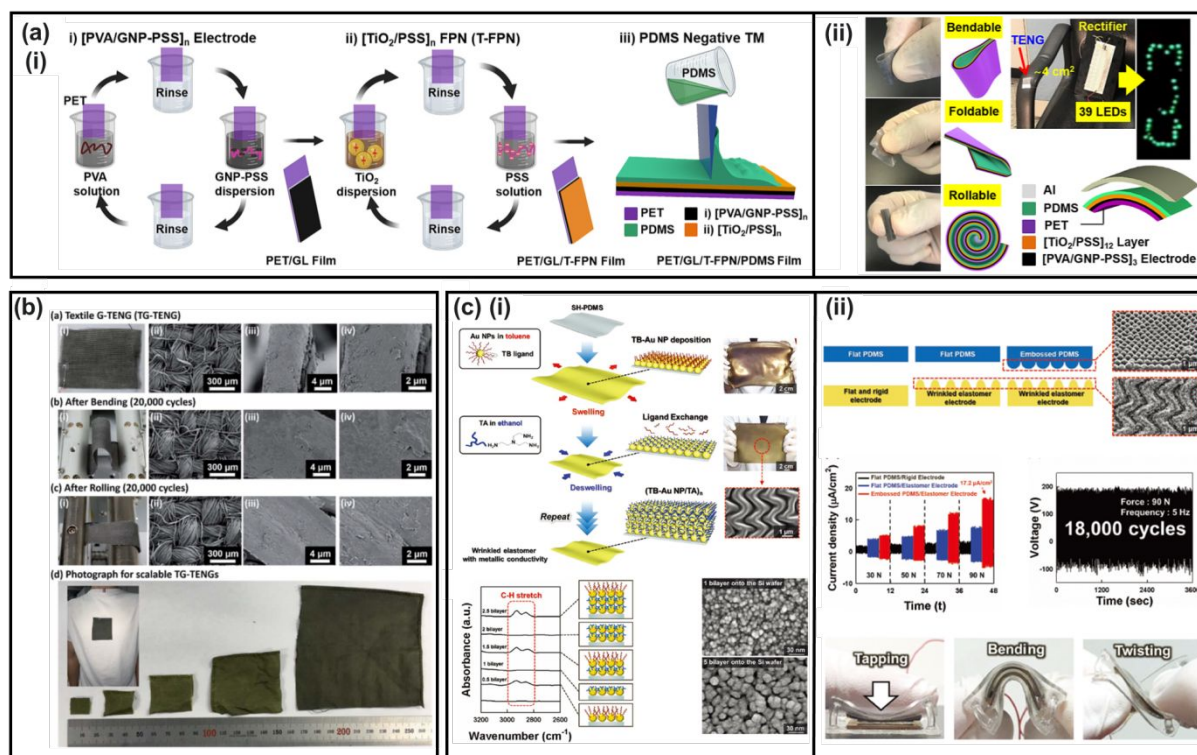


Figure 35. (a)-(i) Schematic of LbL dipping assembly process of PET/GL/T-FPN/PDMS multilayers. (a)-(ii) Extremely high bendability, foldability, and rollability of the PET/GL/T-FPN/PDMS TENG. Photograph of 39 green LEDs lit by the T-FPN-based TENG attached to the curved part of the chair. Reprinted with permission from ref. 321, Copyright 2022, Elsevier. (b) Photograph and FE-SEM of a cotton-based 3 BL TG-TENG before and after 20,000 cycle bending and rolling tests. TG-TENGs on various cotton fabrics with different sizes. Reprinted with permission from ref. 323, Copyright 2016, RCS. (c)-(i) Schematic of the fabrication process and FTIR spectra of wrinkled (TB-Au NP/TA)_n elastomeric electrodes. (c)-(ii) Schematic and performances of TENGs with three different electrodes. Reprinted with permission from ref. 324, Copyright 2019, Wiley.

2.5 Functional tribomaterials

2.5.1 Self-healing materials

In this section, we review the application of self-healing polymer materials to TENGs, which aims to improve the durability of devices. As mechanical energy harvesting-based devices, TENGs must frequently suffer from various mechanical impacts. Such interaction inevitably accelerates devices fracture, leading to degradation in durability and lifespan of the device³²⁵⁻³²⁷. The combination of self-healing polymers with TENGs is a straightforward method to overcome the above challenges in TENGs³²⁷⁻³³⁰. The self-healing polymer is one type of smart material allowing fractures to restore to their original state³³¹⁻³³². The acquisition of this healability is attributed to the existence of some special bonds, including dynamic covalent bonds, reversible covalent bonds, and non-covalent bonds in the molecular structures of self-healing polymers^{331, 333}. From a molecular level (Figure 36(a)), mechanical damage may cause polymer chain cleavage, and further generate some reactive end-groups. Compared to traditional polymers, the reactive end-groups generated in self-healing polymers possess the special ability to reassemble at the broken site, leading to the reformation of broken chemical bonds. Meanwhile, the mobility of cleaved polymer segments, including conformation changes and diffusion, contributes to the molecular network rearrangements around the fracture area. Their cooperation results in the recovery in molecular structural integrity, arriving at the material's repair^{331, 334}. Both the reformation of bonds and the mobility of molecular segments are strongly affected by the external stimuli. Self-healing polymers therefore can be categorized as autonomous (healing occurs without stimuli) and non-autonomous (healing requires external stimuli)³³².

By employing self-healing polymers as constituent materials, the resultant self-healing TENGs are endowed with the ability to repair the device's structure (Figure 36(b)) and

1
2
3
4 electrical performance (Figure 36(c)) once mechanical damage is occurred^{242, 335}, which
5 technically improves the lifespan, durability, and reliability of devices. Additionally, by
6 means of the healing process, self-healing TENGs also present shape-tailorability and adapt
7 readily to various application occasion (Figure 36(d))^{326, 336}. Currently, most self-healing
8 TENGs consist of a self-healing polymer contact layer and the conductive filler as electrodes.
9 Herein, the healing of the polymer layer not only guarantees mechanical property restoration
10 of the devices, but also assists the recontact of broken electrodes for their conductivity
11 recovery^{327, 337}. The full healing of TENGs is therefore achieved. Note that the recovery of
12 the output performance of TENGs mainly depends on the healing of electrodes
13 conductivity³²⁷. Some intrinsic self-healing electrodes have also been developed based on
14 conductive self-healing polymers, such as hydrogel³³⁸⁻³³⁹, organohydrogel³⁴⁰⁻³⁴¹, and ion-
15 conducting elastomer³⁴². Among them, self-healing hydrogel is the most representative self-
16 healing electrode material used in TENGs, which possesses the advantages of transparency,
17 stretchability, and biocompatibility^{338, 343}. Recently, the self-healing organohydrogel
18 electrodes is attracting increased attention (Figure 36(e)) due to its superior freezing-
19 resistance compared to hydrogel, which is beneficial for devices operating under harsh
20 environments³⁴⁰.

21
22
23
24
25
26
27
28
29
30
31
32
33
34
35
36
37
38
39
40
41
42
43
44
45
46
47
48
49
50
51 Even though a series of self-healing TENGs have been developed, some limitations still
52 exist especially when these devices are extended into practical operation. One of the obstacles
53 is the conflict between bulk strength and healability³⁴⁴⁻³⁴⁵. In Figure 36(f), we summarize the

1
2
3
4 healing ratio and the mechanical strength of numerous self-healing polymers used in
5
6
7
8 TENGs^{327, 336, 341, 346-353}. It was found that TENGs based on autonomous-self-healing
9
10
11 polymers perform good healability under ambient conditions but low inherent mechanical
12
13
14 strength. This implies that these autonomous-self-healing TENGs are liable to be damaged,
15
16
17 and possibly show worse durability than regular TENGs. In contrast, TENGs based on non-
18
19
20 autonomous-self-healing polymers usually can arrive at higher strength. However, their
21
22
23 healing requires external stimuli (e.g., temperature and light illumination), which can be
24
25
26 inconvenient. Hence, the development of some non-autonomous-self-healing polymers that
27
28
29 can be triggered by mild and ubiquitous stimuli from the operation environment may be a
30
31
32 compromise solution to obtain self-healing devices with more comprehensive properties
33
34
35 towards practical application. Another challenge for most self-healing TENGs is their
36
37
38 relatively low electrical output. On the one hand, the dynamic or reversible bonds in self-
39
40
41 healing polymers are usually relatively weak. This may cause larger dissipation in
42
43
44 mechanical energy input and therefore lower energy conversion efficiency compared to that
45
46
47 of regular polymers. Besides, the triboelectric property of current self-healing polymers is
48
49
50 usually not located at extreme positions of the triboelectric material series, which also leads
51
52
53 to the degradation in the electrical output. Therefore, the strategy of material's design is still
54
55
56
57
58
59
60

1
2
3
4 considered as the main method for realizing the output performance improvement of self-
5
6
7
8 healing devices. Accompanying with the continuous progress in self-healing polymers, it is
9
10
11 foreseen that more advanced self-healing TENGs with expected performance and application
12
13
14 advantages will be emerging devices.
15
16
17
18
19
20
21
22
23
24
25
26
27
28
29
30
31
32
33
34
35
36
37
38
39
40
41
42
43
44
45
46
47
48
49
50
51
52
53
54
55
56
57
58
59
60

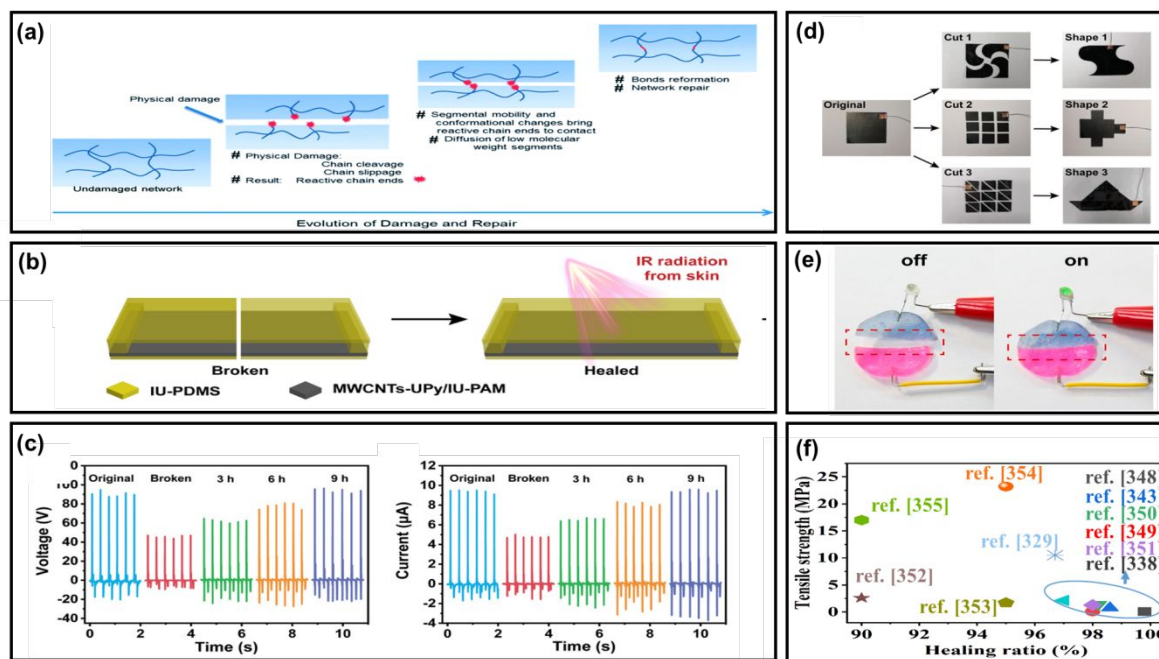


Figure 36. (a) Schematic of damage–repair process in self-healing polymers. **Reprinted with permission under a Creative Commons CC BY License from ref. 334, Copyright 2020, Royal Society of Chemistry.** (b) Schematic of the IR-triggered healing process of one previously reported self-healing TENG (IU-TENG). (c) The electrical output healing of the IU-TENG. (d) Optical images of the shape-tailorable process of the IU-TENG. **Reproduced with permission from ref. 336, Copyright 2020, WILEY.** (e) Breakage and healing of a PAAM-Clay organohydrogel electrode. **Reproduced with permission from ref. 340, Copyright 2021, Elsevier.** (f) Comparison in strength and healability of a series of representative self-healing polymers employed in TENGs. Herein, the data in the blue circle come from some autonomous-self-healing TENGs, and the other data are from the non-autonomous-self-healing TENGs.

1
2
3
4 Polyurethane (PU), one of the shape memory polymers (SMP), was proposed as a
5
6
7
8 triboelectric material based on its relatively low glass transition temperature (T_g) of 55 °C
9
10
11 (Figure 37(a)).³⁵⁴ In this work, the PU triboelectric layer forms a pyramid-patterned
12
13
14 microstructure (width and height: 10 μm) to achieve high triboelectric output performances of
15
16
17
18 ~60 V open-circuit voltage. In addition, a theoretical study to understand the self-healing
19
20
21 property was explored through the following constitutive mechanical equation:
22

$$S = S_e(C(t)) + \int_0^t F(G(t-s), s; C(t)) ds \quad (24)$$

23
24
25
26
27
28
29 where S represents the second Piola-Kirchhoff stress tensor, S_e represents the elastic second
30
31
32 Piola-Kirchhoff stress tensor, C is the Cauchy tensor, and F represents a general tensor-
33
34
35 valued function determined by the variables of $G(t-s)$ and s (t : the current time, s : the
36
37
38 historical time). When the mechanical characteristics of PU were considered to solve
39
40
41 equation (24) above, it can be found that PU generally follows the stress-strain curve that
42
43
44 exhibits elasticity, hyperelasticity, and plasticity. Therefore, PU is known to be more resistant
45
46
47 to any permanent mechanical deformations. The mechanically deformed SMP-based TENGs
48
49
50
51 were electrically characterized with a temperature variation from 25 °C to 65 °C. When the
52
53
54 temperature reached 55 °C, the TENG was recovered and generated open-circuit voltage
55
56
57
58 output of 83 V. Its stability and repeatability were further confirmed through 30 cycles of
59
60

1
2
3
4 deformation and healing process, demonstrating the strong reliability of the SMP-based
5
6
7
8 TENG operation.
9

10
11 Polyurethane acrylate (PUA) film was also adopted as a self-healable triboelectric
12 material (Figure 37(b)).³⁵⁵ The self-healing property of the PUA was realized through the
13 application of T_g temperature by recovering the breakage of intermolecular hydrogen bonds
14 and covalent bonds (type I: [-NH \cdots O=C-]; type II: [-NH \cdots O=C-O-]). After treating at 100
15 °C for 24 hours, the bifurcated pieces of the PUA were mechanically healed with an
16 efficiency of 45.1%. The energy harvesting performance of the PUA-based TENG remained
17 unchanged after the healing process compared to the original performance of the TENG.
18
19
20
21
22
23
24
25
26

27 PDA-CNTs/PVA hydrogel was also introduced as a triboelectric material that shows
28 a complete healing process at room temperature within 10 minutes (Figure 37(c)).³⁵⁶ This
29 hydrogel was synthesized by combining sodium borate, polyvinyl alcohol (PVA), and the
30 poly(dopamine) (PDA)-modified carbon nanotubes (CNTs). The catechol and amino
31 functional groups in PDA materials act as hydrogen bonding sites with the hydroxyl
32 functional groups in PVA, improving its self-healing performance. The major contribution to
33 the self-healing property was made by sodium borate. The borate ions provide the binding
34 site with the hydroxyl functional groups in PVA, exploiting the dehydration reaction. These
35 PDA-CNTs/PVA hydrogel-based TENG were attached to the human body, such as the wrist
36 and elbow joints. Despite the sizeable bending angle of each joint, the stable electrical
37 outputs of the joint-adhered TENGs imply their excellent self-healing ability.
38
39
40
41
42
43
44
45
46
47
48
49
50
51
52
53
54
55
56
57
58
59
60

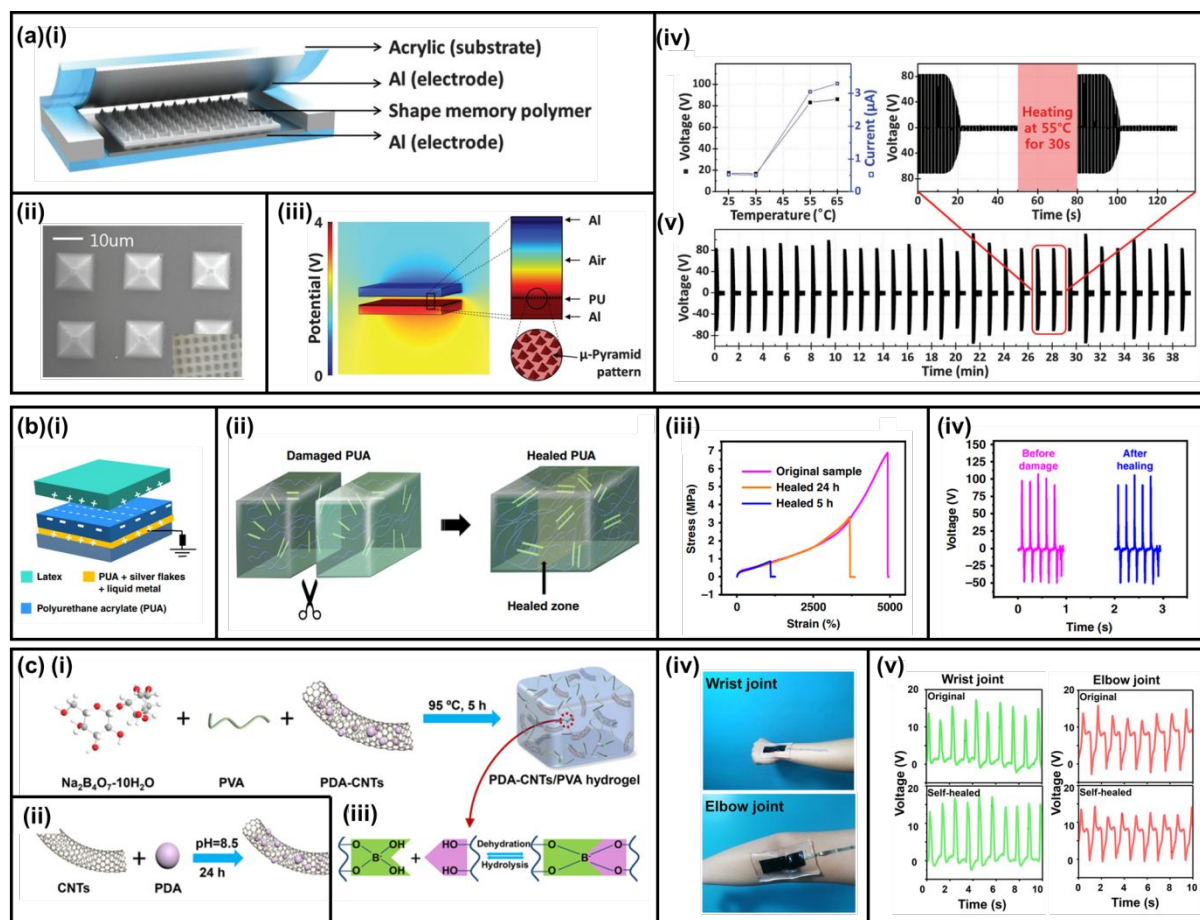


Figure 37. Material design and characterization for self-healing material-based TENGs. (a)-(i) Schematic illustration of the SMP-based TENG. (a)-(ii) SEM image that shows micro-scale pyramid pattern of the PU layer. (a)-(iii) FEM simulation result that expresses the potential distribution upon contact-electrification. (a)-(iv) Electrical characterization of the SMP-based TENG upon various healing temperatures. (a)-(v) Extended electrical characterization with repetitive deformation and healing cycles. **Reprinted with permission from ref. 354, Copyright 2015, Royal Society of Chemistry.** (b)-(i) Schematic of the PUA-based TENG. (b)-(ii) Illustration showing self-healing property of the PUA. Demonstration of the self-healing performance with (b)-(iii) a stress-strain curve and (b)-(iv) triboelectric output performances. **Reprinted with permission under a Creative Commons CC BY license from ref. 355, Copyright 2019, Springer Nature.** Schematic illustration showing the material synthesis of (c)-(i) the PDA-CNTs/PVA hydrogel and (c)-(ii) the PDA-CNTs. (c)-(iii) Chemical structure displaying the self-healing mechanism of the PDA-CNTs/PVA hydrogel. (c)-(iv) Demonstration of the hydrogel adherence. (c)-(v) Electrical

1
2
3
4 characterization of the joint-adhered TENGs to demonstrate their self-healable
5 function. **Reprinted with permission from ref. 356, Copyright 2021, American Chemical**
6
7
8 **Society.**
9
10
11
12
13
14
15
16
17
18
19
20
21
22
23
24
25
26
27
28
29
30
31
32
33
34
35
36
37
38
39
40
41
42
43
44
45
46
47
48
49
50
51
52
53
54
55
56
57
58
59
60

2.5.2 Noise-canceling material

This section discusses the noise-canceling TENG that can significantly reduce the noise level during its operation (Figure 38).³⁵⁷ The framework of the TENG was fabricated using 3D printing technology, allowing its facile fabrication. Poly(dimethylsiloxane) (PDMS) balls, easily synthesized using a 3D printed master mold, acted as an electron-accepting material. To develop the noise-canceling TENG, the silver nanowire (Ag NW) embedded PU sponge covered the inner surface of the 3D printed cylindrical structure, which generated open-circuit voltage output of 78 V and short-circuit current of 0.75 mA. The noise-canceling performance of this TENG was compared with an Al electrode-based cylindrical TENG. During TENG operation, the Al-based cylindrical TENGs emitted a noise level ranging from 67 to 75 dB, while the TENG with the Ag NW embedded PU sponge showed a noise level ranging from 45 to 52 dB that is comparable to that of a normal conversation. The reduced noise level resulted from the compressive and recovery characteristics of the conductive sponge.

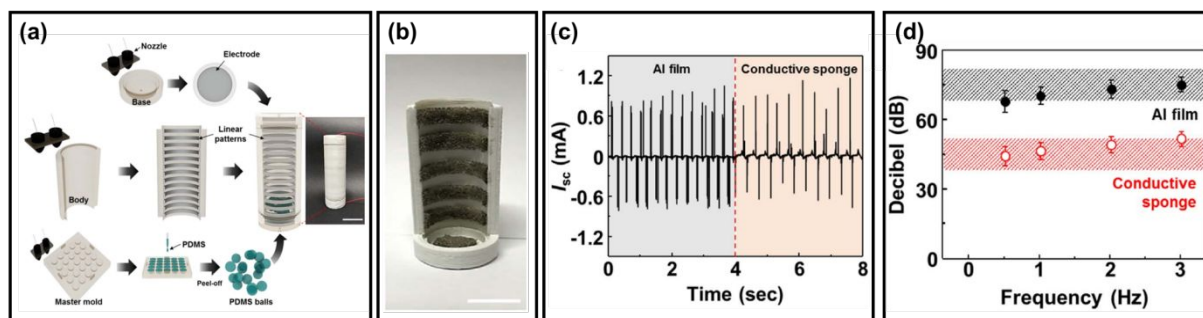


Figure 38. Material design and characterization for a noise-canceling TENG. (a) Schematic illustration showing the fabrication process of the noise-canceling TENG. (b) Real image of the noise-canceling TENG. (c) Electrical characterization of the 3D printed cylindrical TENG with different electrode materials. (d) The measured noise level during the operation of the 3D printed TENGs. **Reprinted with permission from ref. 357, Copyright 2017, Elsevier.**

2.5.3 2D nanomaterials

2D nanomaterials (e.g., transition metal dichalcogenides and graphene) gained great attention due to their material characteristics compared to bulk materials (Figure 39(a)).²⁷⁵ For example, 2D nanomaterials have in-plane mechanical stability due to their strong covalent bonds. At the same time, there is a merely infinitesimal interaction in the vertical direction that enables their facile exfoliation from the bulk. Especially, their electronic properties, such as charging polarities, provide an exceptional option for selecting triboelectric materials. Figure 39(a) describes the surface charging mechanism of 2D nanomaterials under contact-electrification with polymer materials. Here, the direction of electron transfer can be determined by comparing their effective work function values; the electron will be transferred to the empty electronic states from the filled electronic states. Kelvin-probe force microscopy (KPFM) was used to measure the quasi-Fermi level of the 2D nanomaterials. The effective work function of 2D nanomaterials (Φ_{2D}) can be calculated based on the following equation:

$$\Phi_{2D} = \Phi_{probe} - eV_{CPD} \quad (25)$$

where Φ_{probe} represents the work function of the probe, e represents the electronic charge, and V_{CPD} is the measured value of CPD (contact potential difference). It was noteworthy that

1
2
3
4 MoS₂ has the highest value of the effective work function, 4.85 eV. Meanwhile, WSe₂
5
6
7
8 showed a relatively low value of the effective work function, 4.45 eV. Based on this
9
10
11 microscopic analysis, the triboelectric series of the 2D nanomaterials was established, as
12
13
14 shown in Figure 39(a).
15
16

17
18 Another characteristic of 2D nanomaterials can be found in the localization of
19
20
21 electric charges (Figure 39(b)).³⁵⁸ When a defective graphene layer was rubbed with a Pt-
22
23
24 coated AFM tip, the triboelectric charges generated at the interface of the graphene and the
25
26
27 AFM tip tunnel through the defective sites of the graphene. Then, the tunneled triboelectric
28
29
30 charges remained trapped underneath the graphene layer. These tunneled triboelectric charges
31
32
33 lasted for several days, which cannot be seen in conventional triboelectric materials. Based
34
35
36 on this finding, this work demonstrated the fabrication of both p/p⁺ and p/n⁺ junctions (sub-
37
38
39 micrometer scale) with the variation in the AFM tip bias. Also, these junctions can be
40
41
42 enlarged, reduced, and removed according to the CMOS analog/digital circuits or MEMS
43
44
45 design.
46
47
48
49
50
51
52
53
54
55
56
57
58
59
60

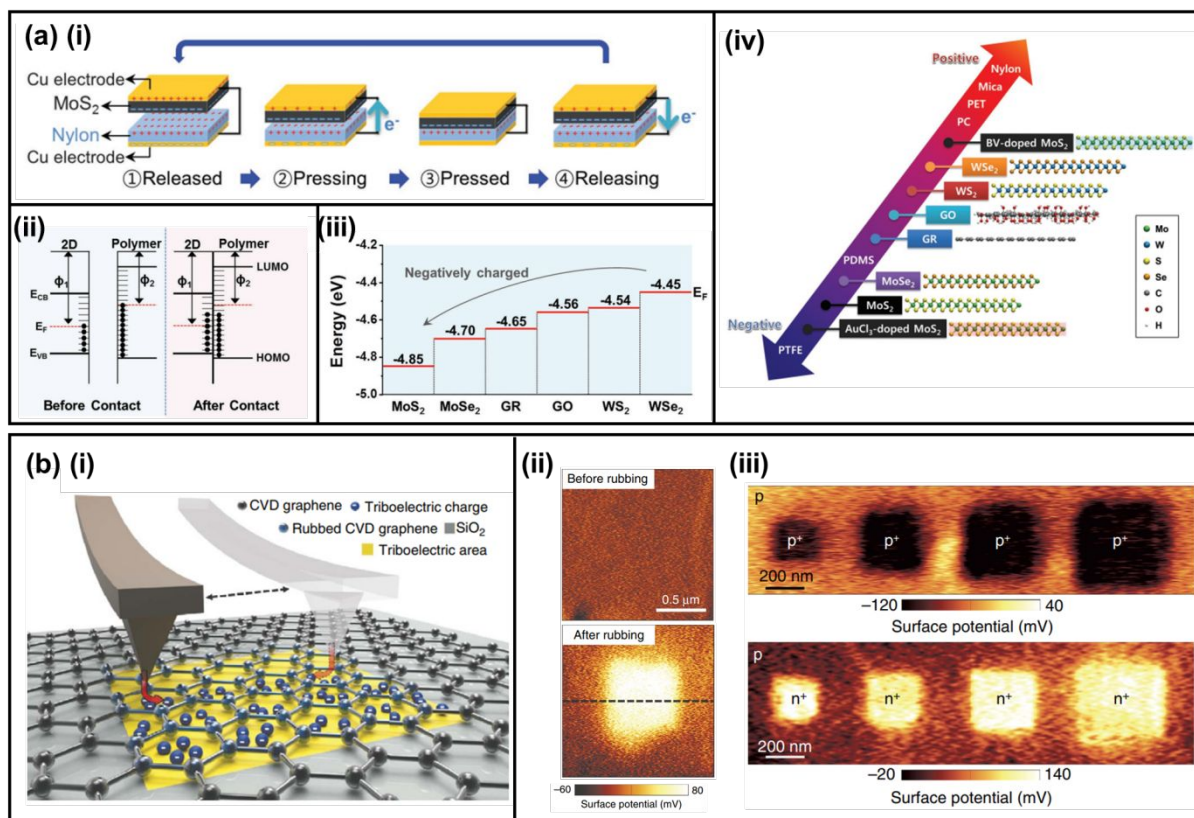


Figure 39. Material characterization of 2D nanomaterials and electronic properties. **(a)-(i)** Schematic illustration showing the triboelectric mechanism of the 2D nanomaterial-based TENG. **(a)-(ii)** Illustration of the charge transfer mechanism. **(a)-(iii)** Measured effective work function of the 2D nanomaterials. **(a)-(iv)** Triboelectric series of the 2D nanomaterials. **Reprinted with permission from ref. 275, Copyright 2018, Wiley.** **(b)-(i)** Schematic illustration of the contact electrification between defective graphene and an AFM tip. **(b)-(ii)** Measured surface potential of graphene before/after rubbing with the AFM tip. **(b)-(iii)** KPFM images of graphene displaying p/p⁺ and p/n⁺ junctions with different dimensions. **Reprinted with permission under a Creative Commons CC BY license from ref. 358, Copyright 2017, Springer Nature.**

2.5.4 Biological material based TENGs

This section will introduce biological materials for TENGs used as energy sources for electronic devices such as attachable³⁵⁹⁻³⁶⁰, wearable³⁶¹⁻³⁶⁴, implantable³⁶⁵⁻³⁶⁶, and environmentally friendly devices. TENGs for biological applications require biocompatibility and biodegradability to minimize infection, inflammation, and secondary surgery.³⁶⁵⁻³⁶⁸ In addition, biodegradable TENGs are advantageous for use in natural energy harvesting applications such as wind, rainwater, and waves due to their environmentally-friendly properties that are naturally eliminated. Materials typically used in TENGs, such as nylon³⁶⁹⁻³⁷⁰, polyvinyl chloride (PVC)³⁷¹⁻³⁷², perfluoroalkoxy alkane (PFA)³⁷³⁻³⁷⁴, polytetrafluoroethylene (PTFE)³⁷⁵⁻³⁷⁶, and aluminum (Al)^{370, 377}, show strong output performance but are not biocompatible or biodegradable, making them unsuitable for biological applications in TENGs. Therefore, biocompatible and biodegradable materials are being actively developed for TENGs. Here we divide the biological materials into natural and artificial materials and biocompatible and biocompatible/biodegradable materials. The biocompatible natural materials refer to biocompatible materials that can be obtained from human, animal or plant such as silk³⁷⁸⁻³⁸¹, chitosan^{359, 382-384}, cellulose^{361, 385-388}, plants³⁸⁹⁻³⁹¹, gelatin³⁹²⁻³⁹³, polypeptide³⁹⁴⁻³⁹⁵, paper³⁹⁶⁻³⁹⁸, rice paper³⁹⁹, wood⁴⁰⁰, and alginate⁴⁰¹.

1
2
3
4 Biocompatible artificial materials are materials that have been artificially processed through
5
6
7 industrial processing such as polyvinylidene fluoride (PVDF)^{244, 362}, polydimethylsiloxane
8
9
10 (PDMS)^{364-365, 402-403}, polyvinyl alcohol (PVA)^{363, 404-405}, poly(lactic-co-glycolic acid)
11
12
13 (PLGA)^{360, 366-367}, and polylactic acid (PLA)⁴⁰⁶⁻⁴⁰⁹, poly-caprolactone (PCL)³⁶⁶. In particular,
14
15
16 silk, cellulose, plant, gelatin, polypeptide, and alginate in natural materials and PVA, PLGA,
17
18
19 PLA, and PCL in artificial materials are biodegradable and are used in body implantable
20
21
22 electronics because they can be removed naturally from the human body.
23
24
25
26
27

28 In 2020, Niu, Q. et al. reported a natural biocompatible material silk-based TENG
29
30 (Figure 40(a)).³⁷⁹ TENGs were fabricated using an initial silk nanoribbon film (SNRF) and a
31
32
33 regenerated silk fibroin film (RSFF) with Mg electrodes, as shown in Figure 40(a)-(i). Cell
34
35
36
37 viability tests were performed to assess the biocompatibility of SNRF and RSFF for days 2, 4,
38
39
40
41 and 6, showing faster growth in SNRF and RSFF than controls cultured on glass coverslips
42
43
44 (Figure 40(a)-(ii)). In 2022, S. Hu et al. reported a natural biocompatible/biodegradable
45
46
47 bacterial cellulose (BC) based TENG with carbon nanotubes (CNT), and polypyrrole (PPy)
48
49
50 based microfiber (Figure 40(b)-(i)).³⁶¹ The degradability of BC/CNT/PPy macro fibers was
51
52
53
54 evaluated using an enzymatic digestion method. Figure 40(b)-(ii) shows photographic and
55
56
57
58 SEM images of the real-time degradation process every 48 h, showing the gradual
59
60

1
2
3
4 degradation of BC/CNT/PPy macro fibers in the cellulase solution. In 2018, Yao, G. et al.
5
6
7
8 reported an artificial biocompatible polydimethylsiloxane (PDMS)-based TENG (Figure
9
10
11 40(c)).³⁶⁵ The TENG is implanted in mice and connected to nerves, and it generates electrical
12
13
14 energy from mechanical energy (Figure 40(c)-(i)). To confirm the biocompatibility of the
15
16
17 TENG, mouse cells were cultured on the surface of the encapsulated TENG and in a
18
19
20 reference culture dish for 4 days to investigate and compare cell adhesion, proliferation, and
21
22
23 morphology (Figure 40(c)-(ii)). Cells in both media exhibited similar densities and equivalent
24
25
26 morphology. These results confirmed the non-toxicity and biocompatibility of the
27
28
29 encapsulated TENG. In 2020, Peng, X. et al. reported artificial biocompatible/biodegradable
30
31
32 PLGA- and PVA-based TENGs.³⁶⁰ In contact with PTFE film, both types of biodegradable
33
34
35 film-based TENGs produced strong output power. In addition, a biodegradation test was
36
37
38 performed, and the results showed that PVA exhibited rapid autocatalytic hydrolysis and bulk
39
40
41 degradation after 3 days of incubation, and its weight loss was up to 90%. Unlike PVA,
42
43
44 PLGA has strong resistance to weight loss and water absorption in the early stages (days 0-21)
45
46
47 but slightly shrinkage and curl due to hydrolytic cleavage of the polymer backbone.
48
49
50
51
52
53
54
55
56
57
58
59
60

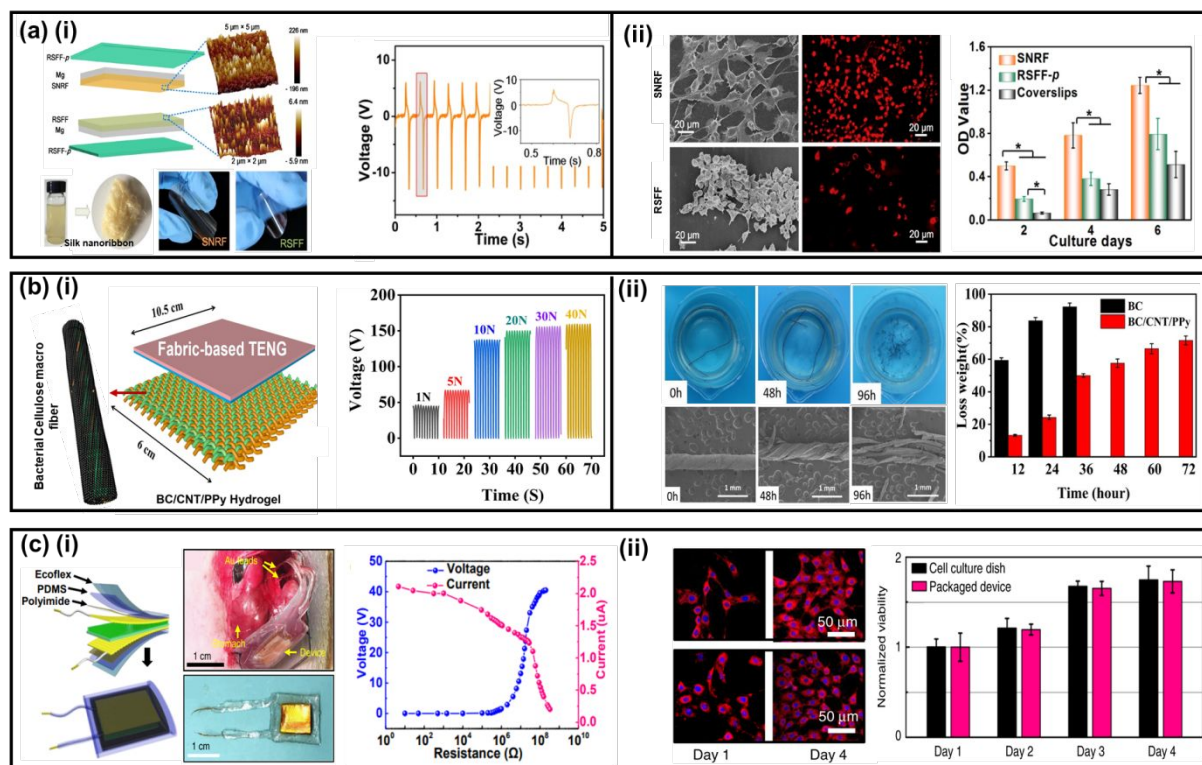


Figure 40. Bio-TENG based on biological materials. (a)-(i) Schematic illustration of the silk-based TENG and its output voltage. (a)-(ii) Cell viability after 2, 4, and 6 days of culture on different substrates. Reprinted with permission from ref. 379, Copyright 2020, Elsevier. (b)-(i) Schematic diagram of fabric based TENG structure and its output voltage. (b)-(ii) The photographs and SEM images of the degradation experiment of BC and BC/CNT/PPy macro fiber and loss weight. Reprinted with permission under a Creative Commons CC BY license from ref. 361, Copyright 2022, Springer Nature. (c)-(i) Schematic illustration of the encapsulated TENG and its output voltage and current. (c)-(ii) Cell viability test on the surface of the TENG, and comparison of normalized cell viability for 4 days. Reprinted with permission under a Creative Commons CC BY license from ref. 365, Copyright 2018, Springer Nature.

1
2
3
4 For the practical application of TENGs using these biological materials, there are still
5
6
7
8 challenge issues to overcome, such as low output performance, limited materials option,
9
10
11 mechanical properties, encapsulation, and control of biodegradability. The output
12
13
14 performance of the TENGs using biological materials still needs to be improved. For high-
15
16
17 performance TENGs, the friction material should have a large surface area, high surface
18
19
20 charge density, high dielectric constant, and high positive or negative triboelectric properties.
21
22
23

24 However, there are many limitations in satisfying all conditions using biocompatible and
25
26
27 biodegradable materials. Recently, efforts to develop high-output bio-TENGs using
28
29
30 modification methods such as functional chemical groups^{359, 410-411}, structures⁴¹²⁻⁴¹⁴, and
31
32
33 charge storing⁴¹⁵⁻⁴¹⁷ have been reported. Kim, J.-N. et al. reported a high-output TENG based
34
35
36 on diatom-silica embedded in chitosan film (Figure 41(a)).⁵ Diatoms greatly helped increase
37
38
39 the charge density generated on the chitosan surface, resulting in the output of the TENG
40
41
42 producing a maximum output voltage and RMS current of 150 V and 1.02 μ A, respectively.
43
44
45
46
47

48 Another challenging issue is the degradation control of the TENG. The degradation rate
49
50
51 should not be too fast or slow, and it is necessary to degrade at the desired time after the
52
53
54 service is finished. The biodegradation rate is generally controlled by controlling the
55
56
57 thickness of the biodegradable material, but this is not sufficient for future practical
58
59
60

1
2
3
4 applications. Recently methods such as material methanol treatment³⁹⁹, NIR³⁶⁷, and
5
6
7
8 ultrasound control²⁶ have been used to regulate the degradation of TENGs. D.-M. Lee et al.
9
10
11 reported a poly(3-hydroxybutyrate-co-3-hydroxyvalerate) (PHBV)-based TENG that controls
12
13
14 biodegradation using ultrasound.²⁶ The TENG can generate electrical outputs under low
15
16
17
18 ultrasound intensity (0.5 W/cm²), while a higher intensity of 3.0 W/cm² ultrasound triggers
19
20
21 the molecular level degradation (i.e., hydrolysis). This TENG can be easily triggered to
22
23
24 initiate a transient process by tuning ultrasound power and, therefore, no need for device
25
26
27
28 removal methods.

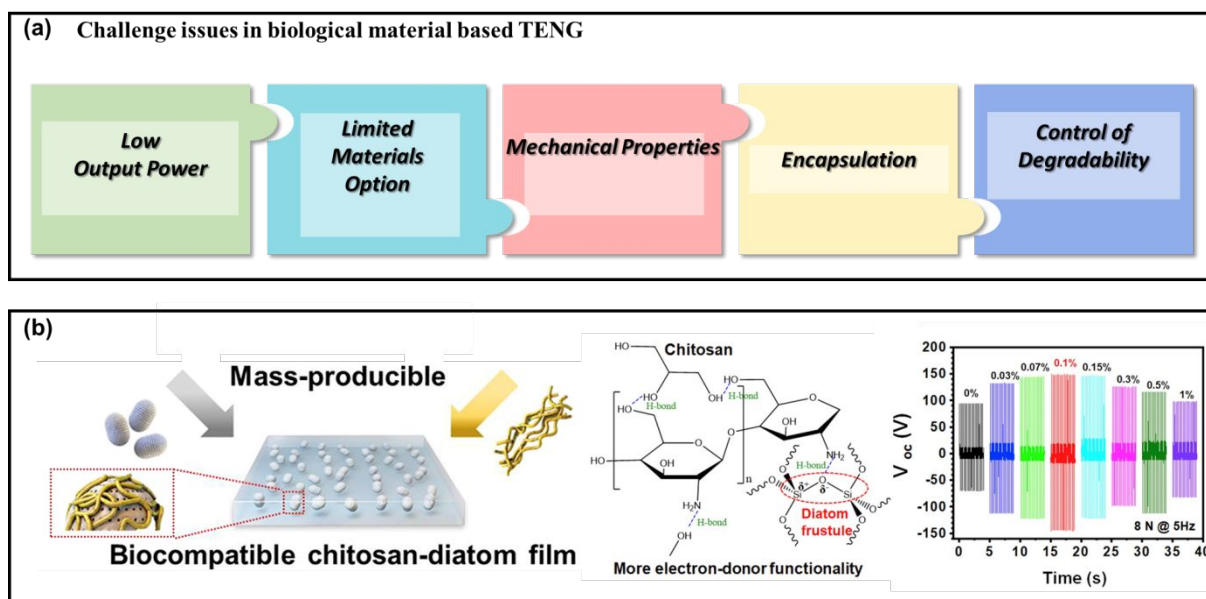


Figure 41. (a) Challenge issues of bio-TENG. (b) Enhanced output power with modification chemical structure of chitosan adding diatom. Reprinted with permission from ref. 359, Copyright 2020, Elsevier.

1
2
3
4
5 Figure 42 represents an implantable TENG, of which the triboelectric layer is based
6
7
8 on the natural bioresorbable polymers (NBPs) (e.g., cellulose, chitin, egg white, etc.).³⁹⁹ A
9
10
11 pair of the selected NBPs was assembled to measure the resulting triboelectric output
12
13
14 performances. Through these measurements, the triboelectric series of the NBPs was settled,
15
16
17 indicating that the egg white exhibited the most tribo-positive property while the rice paper
18
19
20 showed the most tribo-negative property. In this work, the bioresorbable property of the
21
22
23 NBP-based TENGs was identified through in-vitro and in-vivo experiments. Both
24
25
26
27
28 experiments suggested that the TENGs could be fully degraded in 84 days.
29
30
31

32
33 Next, artificially synthesized biodegradable polymers (BDPs) were also adopted as
34
35
36 triboelectric materials to constitute an implantable TENG.³⁶⁶ In this work, the following
37
38
39 BDPs were rationally chosen since they are low cost, commercially available, and solution
40
41
42 processible: poly(L-lactide-co-glycolide) (PLGA), poly(3-hydroxybutyric acid-co-3-
43
44
45 hydroxyvaleric acid) (PHB/V), poly(caprolactone) (PCL), and poly(vinyl alcohol) (PVA).
46
47
48
49 Electrical characterization of the BDP-based TENGs was identified by measuring transferred
50
51
52 charges upon repetitive contact-separation with Kapton membranes. Based on this electrical
53
54
55 characterization, PLGA showed the highest electron-donating property among the other
56
57
58 BDPs. In addition, the BDP-based TENG was immersed in PBS (phosphate-buffered saline)
59
60

1
2
3
4 solution (pH 7.4, 37 °C). The device suffered a severe mass loss after 40 days and eventually
5
6
7
8 underwent complete degradation after 90 days.
9

10
11 The time-transient performance of the bioresorbable and implantable TENGs
12 mentioned above relies on a passive operation system, in which the device lifetime is already
13 determined by the material dimension and mechanical/chemical characteristics. In contrast, D.-
14
15
16 M. Lee et al. represented a fully biodegradable and implantable TENG (FBI-TENG) that
17
18
19 exploits an active operation system, which its transience is determined by a well-defined
20 triggering event.²⁶ The FBI-TENG generates ultrasound-driven triboelectric outputs upon a
21
22
23 low-intensity ultrasound (probe power: $\leq 1.0 \text{ W cm}^{-2}$), while it exhibits mechanical
24
25
26 disintegration to trigger its biodegradation upon a high-intensity ultrasound (HIU; probe
27
28
29 power: $\geq 3.0 \text{ W cm}^{-2}$). The poly(3-hydroxybutyrate-co-3-hydroxyvalerate) (PHBV) polymer
30
31
32 membrane enabled this ultrasound-mediated transience. In addition, its porous microstructure
33
34
35 facilitates the localization of the ultrasound-driven acoustic pressure, as demonstrated using a
36
37
38 Finite Element Method (FEM) simulation. Moreover, the ultrasound-mediated transience was
39
40
41 confirmed through an ex-vivo study. After the device insertion into a porcine tissue, the
42
43
44 ultrasound-driven triboelectric output was measured. The device generated stable output
45
46
47 performance upon the ultrasound with 0.5 W cm^{-2} , while it ceased functioning upon the HIU
48
49
50
51
52
53
54
55
56
57
58
59
60 (3.0 W cm⁻²).

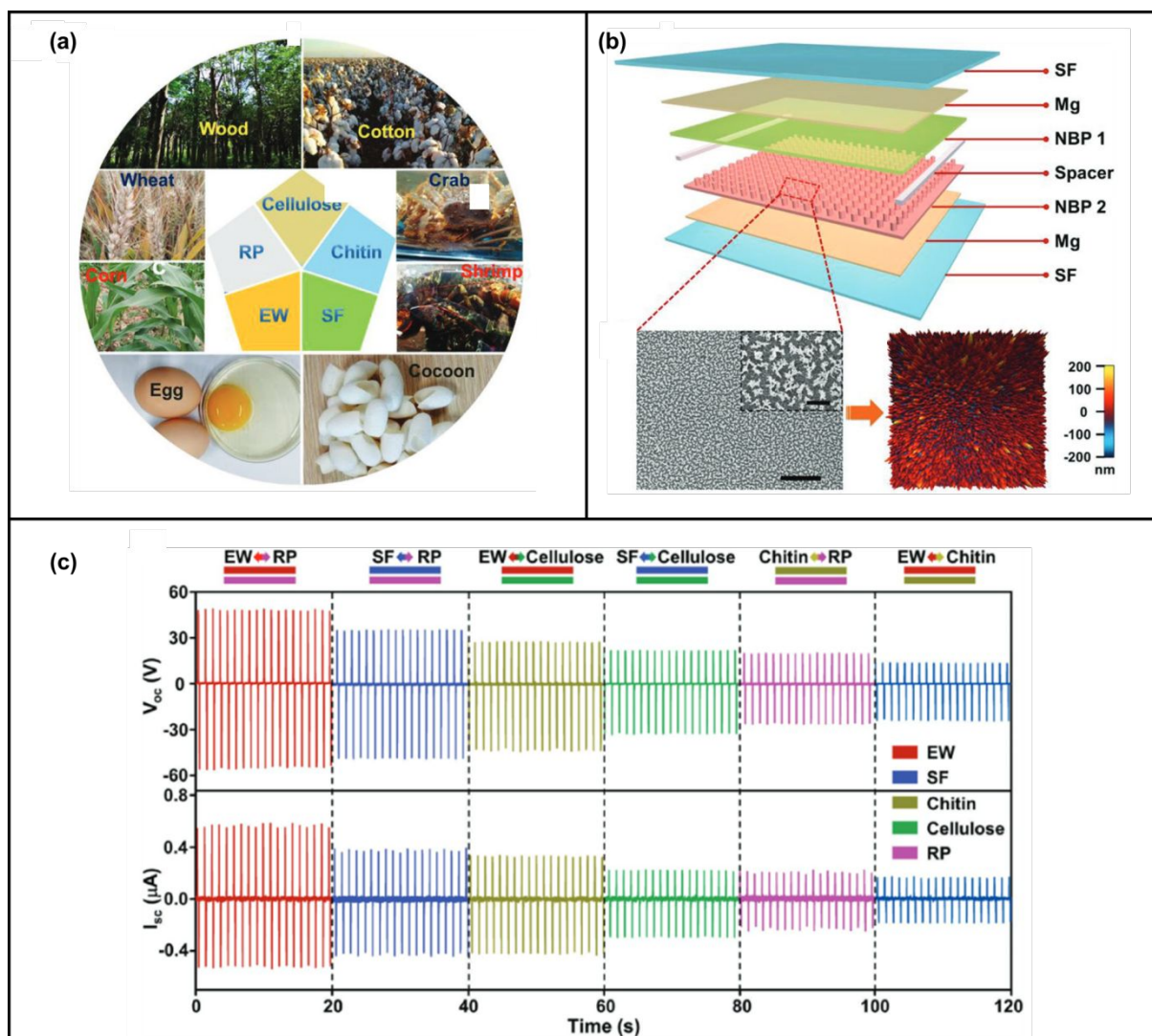


Figure 42. Material design and characterization for bioresorbable material-based TENGs (a) Various types of NBPs and their natural resources. (b) Schematic illustration of the NBP-based TENG. The inset displays the microscopic morphology of the NBP membrane. (c) Electrical characterization of a pair of the selected NBPs. **Reprinted with permission from ref. 399, Copyright 2018, Wiley.**

3. Triboelectric devices

3.1. Operation Mechanisms of TENGs

Triboelectric nanogenerators (TENGs) are based on a combination of triboelectrification effects and electrostatic induction⁴¹⁸, which can be classified into four main types based on different operating mechanisms, as shown in Figure 43.

3.1.1. Contact-Separation (CS) Mode

Contact-Separation (CS) mode TENGs are the contact separation mode proposed in 2012 by the Zhonglin Wang group in Georgia Tech⁴⁹. At the initial stage, there is no electric charge on the surface of the two friction layers. As the friction layers become in contact with each other normally in the vertical direction, based on the electrification effect, the negative and positive surface will be charged equally, and it will stay on the surface stably. When the two friction layers start separating, the charge on the surface will be introduced to the electrodes on the top, this charge flow between two electrodes transfer the mechanical energy into electric energy eventually. This mode of TENGs is widely utilized in environments with strong low frequency mechanical contact, such as, floors, keyboards, and waves.

3.1.2. Relative-Sliding (RS) Mode

The Relative-Sliding (RS) mode TENGs were developed in April 2013 by the ZL Wang group to overcome the shortcomings of frequency limitation that exist in the CS mode TENGs⁴¹⁹, and subsequently several optimized RS mode TENGs were implemented to obtain rotational energy as well as air-flow energies^{420,421}.

The difference of RS mode TENGs from the former mode is that the device is working along the horizontal direction, in which two friction layers start to stack. Based on the

1
2
3
4 electrification effect, this overlapping area will introduce the charge re-distribution on the
5
6 electrodes which will realize the energy transformation from mechanical to electrical.

7
8
9 The most attractive advantage of RS mode TENG is applicable for high-frequency
10
11 applications and then generating continuous output electricity. However, this operation
12
13 method of relatively sliding also poses a severe challenge to friction damage on the surfaces
14
15 of triboelectric pairs. Although several studies have reported the considerable reliability of
16
17 RS mode TENGs, the long-term stability in practical applications remain a major problem.
18
19

20 21 **3.1.3. Single-Electrode (SE) Mode**

22
23 The Single-Electrode (SE) mode was invented by the Haixia Zhang group in Peking
24
25 University⁴²² in August 2013, which is also named Single-Friction (SF) mode in some
26
27 cases^{423,424}.

28
29 In SE mode, only one electrode directly interacts with the moving triboelectric layer, while
30
31 the other electrode is just a reference electrode working as a source for electrons, which can
32
33 be a large conductor or just the ground. The major advantage of this SE/SF mode TENG is its
34
35 simple structure which is suited for many applications with single surfaces, like cellphones
36
37 and walls.
38
39

40 41 **3.1.4. Freestanding (FS) Mode**

42
43 The Freestanding mode (FS) TENG was proposed in January 2014 by the Zhonglin Wang
44
45 group; the operating principle is similar to that of the RS mode TENG except continuous
46
47 sliding friction is utilized^{425,426}. It can harvest energy from a free-moving triboelectrically
48
49 charged object and generate an alternative output when the outer object moves between the
50
51 two electrodes.
52
53

54
55 Since electrostatic induction acts more importantly than the electrification effect, the energy
56
57 conversion efficiency of FS mode TENG can achieve up to 100% theoretically, which makes
58
59 it applicable as active sensors with rich information and high sensitivity/ However, the free-
60

standing design of movable triboelectric layer makes it difficult to integrate with other electronic devices and systems.

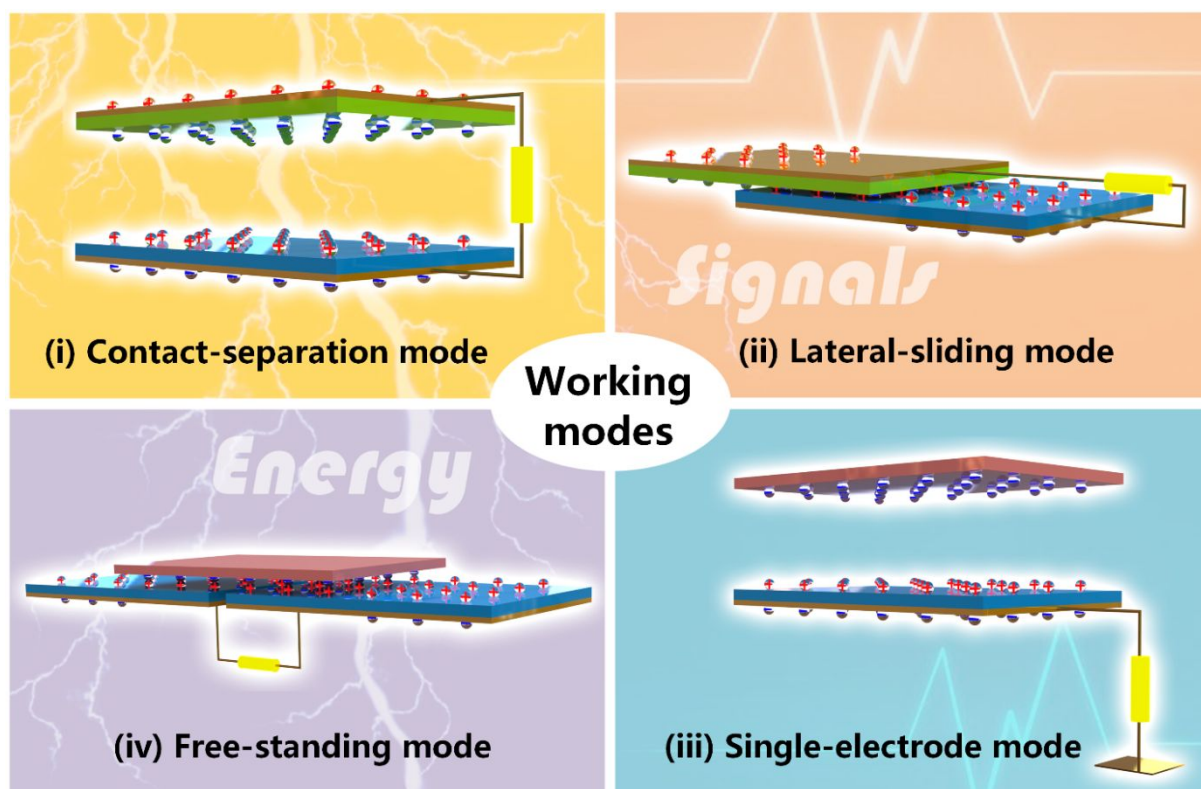


Figure 43. Four operation mechanism of triboelectric nanogenerators (TENGs).

3.2. Instantaneous discharged device designs

In this part, we will discuss instantaneous discharged device designs. Here, the structures and working mechanisms in previous research are discussed, including TENGs based on solid-solid and liquid-solid interfaces. Here, we emphasize its characteristics of high peak voltage generation. Finally, the brief challenges and future direction of instantaneous discharged device are discussed.

3.2.1. The solid-solid based instantaneous discharged TENG

By virtue of advantages of ultrafast discharging characteristic of TENGs, various types of solid-solid based instantaneous discharged devices have been developed to elevate the electrical power output performance⁴²⁷. An ultrahigh instantaneous power density (over 10 MW/m² at 1 Hz) triboelectric nanogenerator was developed by leveraging the opposite-charge-enhancement effect and the transistor-like device design⁴²⁸. The structure of OCT-TENG mainly includes a stator substrate and a slider. The stator contains fluorinated ethylene propylene (FEP), polycarbonates (PC) and four electrodes (E_1 , E_2 , E_L and E_R). The slider contains a sheet electrode E_3 coated on a thin FEP film. Analogously, E_1 and E_2 could be regarded as the “source” (S) and E_3 as dynamic “drain” (D). E_L and E_R are the “gate” (G). The working mechanisms of the OCT-TENG are shown in Figure 44(a). In detail, the operation and power generation processes are divided into the following four parts. At stage 1, electrode E_3 contacts the left floating electrode to make the “ON” state of the left “transistor”. When the slide moves towards the PC side (before contact with E_R , state 2), the transistor is at the “OFF” state. Further moving the slide to make E_3 touch the E_R electrode, the right “transistor” is in the “ON” state (state 3). Then, the “OFF” stage occurred again when sliding back to the FEP side before contacting the E_L electrode. At each stage, electrons transferred between the corresponding electrodes and balanced the established potential

1
2
3
4 difference. Benefitting from the opposite-charge enhancement effect and the transistor-like
5 structure, at the "ON" state (stages 1 and 3), large amounts of charges (Q_2-Q_1) quickly
6
7 transferred from the "source" to the "drain", leading to sharp and high current peaks for high
8
9 energy generation. Lee et al. reported an ion-enhanced field emission triboelectric
10 nanogenerator (IEFE-TENG), which consists of a charge accumulation layer and a metal-to-
11 metal contact point. The structure of IEFE-TENG includes five layers (top electrode, charge-
12 generation layer, IEFE-inducing layer, dielectric layer, and bottom electrode), as shown in
13 Figure 44(b)⁴²⁹. In the initial state, the positive charge is generated in the top electrode due to
14 the triboelectrification and charge separation. Polymer dielectric layer is polarized owing to
15 the electric field between the charge-accumulation layer and bottom electrode. The free
16 electrons in the charge-accumulating layer tend to concentrate on the metal-to-metal contact
17 point due to the attraction of positive charges on the top electrode and the repel of negative
18 charges on the bottom electrode. As the top electrode approaches the metal-to-metal contact
19 point in a microscale gap of 1-10 μm , the field emission is dominant for the gas breakdown
20 due to quantum-mechanical tunneling. The IEFE occurs when positive ions in between this
21 microscale gap could enhance field emissions by lowering the potential barrier. As the top
22 electrode continues to move and contact with the metal-to-metal point, the electrons can
23 directly flow to the top electrode to keep electrical potential difference, which generates high
24 voltage and current output compared to conventional TENG owing to the smaller energy loss.
25
26 Furthermore, Baik et al. reported a type of slide-mode TENG with outstanding output
27 enhancement via direct metal-to-metal contact with the ground-connection⁴³⁰, as shown in
28 Figure 44(c). The key feature of the TENG is bottom plates including three parts: PTFE/Al
29 (electrode 1), middle Al film (grounded) and Al (electrode 2). The working mechanism is
30 investigated from the physical movement at each stage. At the initial state, the negative and
31
32
33
34
35
36
37
38
39
40
41
42
43
44
45
46
47
48
49
50
51
52
53
54
55
56
57
58
59
60

1
2
3
4 positive charges are generated on the surface of PTFE film and Al layer due to the
5 triboelectrification and electrostatic induction. When the top Al further moves to the Al film
6
7 with ground, the positive charges in the top Al layer induce the electrons through Al from the
8
9 ground, while the negative charges in PTFE induce the positive charges on electrode 1,
10
11 leading to electron flow through the external circuit. Finally, the electrons go through the Al
12
13 to the ground when the top layer contacted with the right part. Additionally, the obviously
14
15 increased electric potential difference via COMSOL simulation between two electrodes in the
16
17 grounded TENG facilitate driving the current flow during sliding, which also supports the
18
19 working mechanism and enhances the output performance. Besides, Kim et al. proposed a
20
21 serrated electrode-based TENG (SE-TENG) that generates ultrahigh power output based on
22
23 the spark discharge to drive high voltage operating devices directly⁴³¹. As shown in Figure
24
25 44(d), due to the triboelectrification and electrostatic induction, spark discharge occurs in the
26
27 gap between the serrated electrode and metal wire, which makes a large number of electrons
28
29 transfer at a rapid speed. Consequently, a higher triboelectric output voltage peak and root-
30
31 mean-square value are observed in spark discharge SE-TENG.
32
33
34
35
36
37
38
39
40
41
42
43
44
45
46
47
48
49
50
51
52
53
54
55
56
57
58
59
60

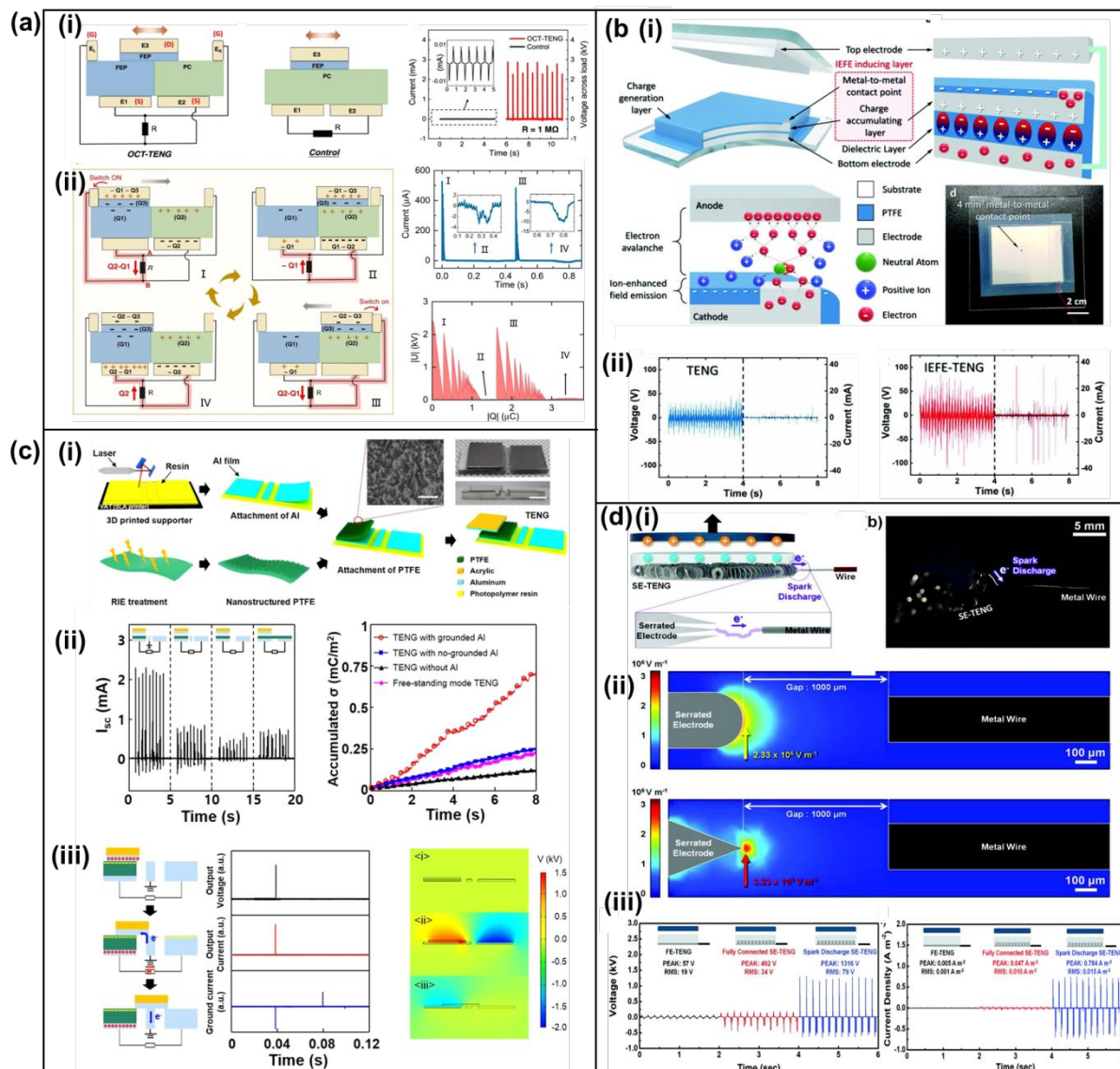


Figure 44. (a) The opposite-charge enhanced transistor-like triboelectric nanogenerator (OCT-TENG). (a)-(i) Schematic of the cross section, comparison of current output of OCT-TENG and the control device. (a)-(ii) Working principle of the OCT-TENG. The generated current and U-Q plot of the OCT-TENG during one cycle of operation. **Reprinted with permission under a Creative Commons CC BY license from ref. 428, Copyright 2021, Springer Nature.** (b) The ion-enhanced field emission triboelectric nanogenerator (IEFE-TENG). (b)-(i) Schematic illustration of IEFE-TENG). IEFE mechanism between top electrode and metal-to-metal contact point. (b)-(ii) Open-circuit voltage and closed-circuit current of IEFE-TENG and control TENG. **Reproduced from ref. 429, Copyright 2019, Wiley-VCH.** (c) Sliding-mode triboelectric nanogenerator through direct metal-to-metal contact with the ground. (c)-(i) Structure schematic, (c)-(ii) short circuit currents (I_{sc}), accumulative charge density, (c)-(iii) working mechanism and COMSOL simulations of the TENGs. **Reproduced from ref. 430, Copyright 2019, Elsevier.** (d) Triboelectric nanogenerator based on serrated electrode via spark discharge. (d)-(i) A schematic illustration of SE-TENG, serrated electrode and FE-SEM image of serrated electrode. (d)-(ii) schematic

1
2
3
4 illustration of mechanism in which spark discharge occurs in a gap between the serrated
5 electrode and metal wire. FEM simulation results for electric field distribution. **(d)-(iii)**
6 Triboelectric output the FE-TENG, the SE-TENG, and the spark discharge SE-TENG.
7 **Reproduced from ref. 431. Copyright 2020, Wiley-VCH.**
8
9
10
11
12
13
14
15
16
17
18
19
20
21
22
23
24
25
26
27
28
29
30
31
32
33
34
35
36
37
38
39
40
41
42
43
44
45
46
47
48
49
50
51
52
53
54
55
56
57
58
59
60

3.2.2 The liquid/solid based instantaneous discharged TENG

Apart from the above mentioned solid-solid contact based instantaneous discharged TENG, the droplet-based electricity generation based on liquid/solid interface has attracted significant attention, which is capable of generating higher instantaneous electric power density⁴³². Wang et al. developed a droplet-based electricity generator (DEG) by using a structure that comprises a PTFE film on an ITO substrate and an Al electrode⁴³³. The open-circuit voltage (~ 143.5 V) and short-circuit current (~ 270.0 μA) obtained in this DEG are around 295.0 and 2,600.0 times higher than that of the control device. The circuit model of the device is shown in Figure 45(a). The spreading droplet can be regarded as a transistor and the PTFE as a capacitor C_p . Before the droplet contacts PTFE surface, the device is in a “switch off” state. As the droplet spreads to contact the Al electrode, the DEG device is in a “switch on” state. The instantaneous peak output voltage and current occur when the charges transfer from the ITO electrode to the Al electrode. After the droplet leaves Al electrode, the positive charges flow back to the ITO electrode. It is worth mentioning that DEG possesses a good output charge stability due to the combination of continuous droplet impinging and the good charge-carrying capability of PTFE. An universal single electrode droplet-based electricity generator (SE-DEG) is proposed by a special configuration that is located on the electrode on the top of dielectric material rather than under as in the conventional triboelectric nanogenerator⁴³⁴. The diagrams of the working mechanism are separately discussed and shown in Figure 45(b). For example, as a droplet falls and spreads on the negatively charged surface, an electric double layer (EDL) is formed at the solid-liquid interface. The water droplet injects negative charges on the surface and keeps positive charges itself. Further contacting toward the single electrode, the droplet connects the solid surface and electrode by bridging each of them. In this state, the potential balance between the single electrode and ground is broken due to a directional flow with positive and negative

1
2
3
4 charges towards the solid surface and single electrode, respectively, thus generating
5 instantaneous output voltage and current. Compared with conventional TENGs, special
6 configuration of the electrode can effectively harness the triboelectric charges generated
7 without going through the electrostatic induction process between the bottom electrode and
8 the surface. In addition, charge contribution of two surfaces simulated by COMSOL verifies
9 the established electric field on the water droplet interface, which are the driving force for the
10 charge accumulation and transfer. In equivalent circuit model, spreading droplets are
11 regarded as a resistor for the circuit analysis. Inspired by thunderbolt, Dong et al.
12 demonstrated a high-voltage direct-current droplet-based electricity generator (DC-DEG).
13 The DC-DEG is comprised of PTFE plate, two metal electrodes and a charge collector needle
14 attached to the top electrode⁴³⁵. As shown in Figure 45(c), the top electrode collects the
15 negative charges while the bottom electrode returns electrons back to the droplet (i.e., collects
16 positive charges) to recover the neutrality of the droplet. A DC electricity with two pulse
17 peaks from a single droplet is shown through these two electrodes via an external load. The
18 working mechanism and equivalent circuit of DC-DEG are divided into four steps. Step 1,
19 charge separation perpendicular to the surface of PTFE. Step 2, negative charge transfer from
20 the water to the needle and then the top electrode. Step 3, positive charge collection due to
21 hydrophobicity of PTFE and the gravity. Step 4, positive charge transfer from the water to the
22 bottom electrode. Wu et al. demonstrated a fully biodegradable TENG (FBD-TENG), where
23 the ion-conductivity tissue served as the bottom electrode and the leaf cuticle employed as the
24 dielectric capacitor and tribo-materials, as shown in Figure 45(d)⁴³⁶. When a drop of water
25 contacts the conductive wire, the water will be employed as the top electrode and connect the
26 external circuit for electricity generation. The mechanism of current generation is
27 demonstrated as following: (a) Step 1, an electrode double layer was formed at the leaf/water
28 interface when a droplet touches the charged leaf surface. Step 2, the droplet bridges the leaf
29

1
2
3
4 surface with external circuit as it spreads and contacts the conductive wire. The electric
5
6 potential difference will force the electrons to move from the plant tissue to the water droplet.
7
8 Step 3, As the droplet shrinks, the water/leaf interface area and electric double layer
9
10 decreases, leading to the electrons moving back to the plant issue. Step 4, when the droplet
11
12 disconnects with the wire, the current reduces to zero. The current generated from FBD-
13
14 TENG is much higher compared to the conventional single electrode TENG for water droplet
15
16 energy harvesting^{437,389}.
17
18
19
20
21
22

23 **3.2.3 Challenges and future direction**

24
25 Although instantaneous discharged TENG devices have made great progress in structure
26
27 design and technology application, there are still some problems to be solved. The output
28
29 performance of instantaneous discharged TENG is at a relatively low level, which poses a
30
31 challenge to the advancement of related fields. Exploring more potential strategies including
32
33 materials, structures, and working principles is necessary to boost the outperformance and
34
35 wide practical application of TENGs in the future.
36
37
38
39
40
41
42
43
44
45
46
47
48
49
50
51
52
53
54
55
56
57
58
59
60

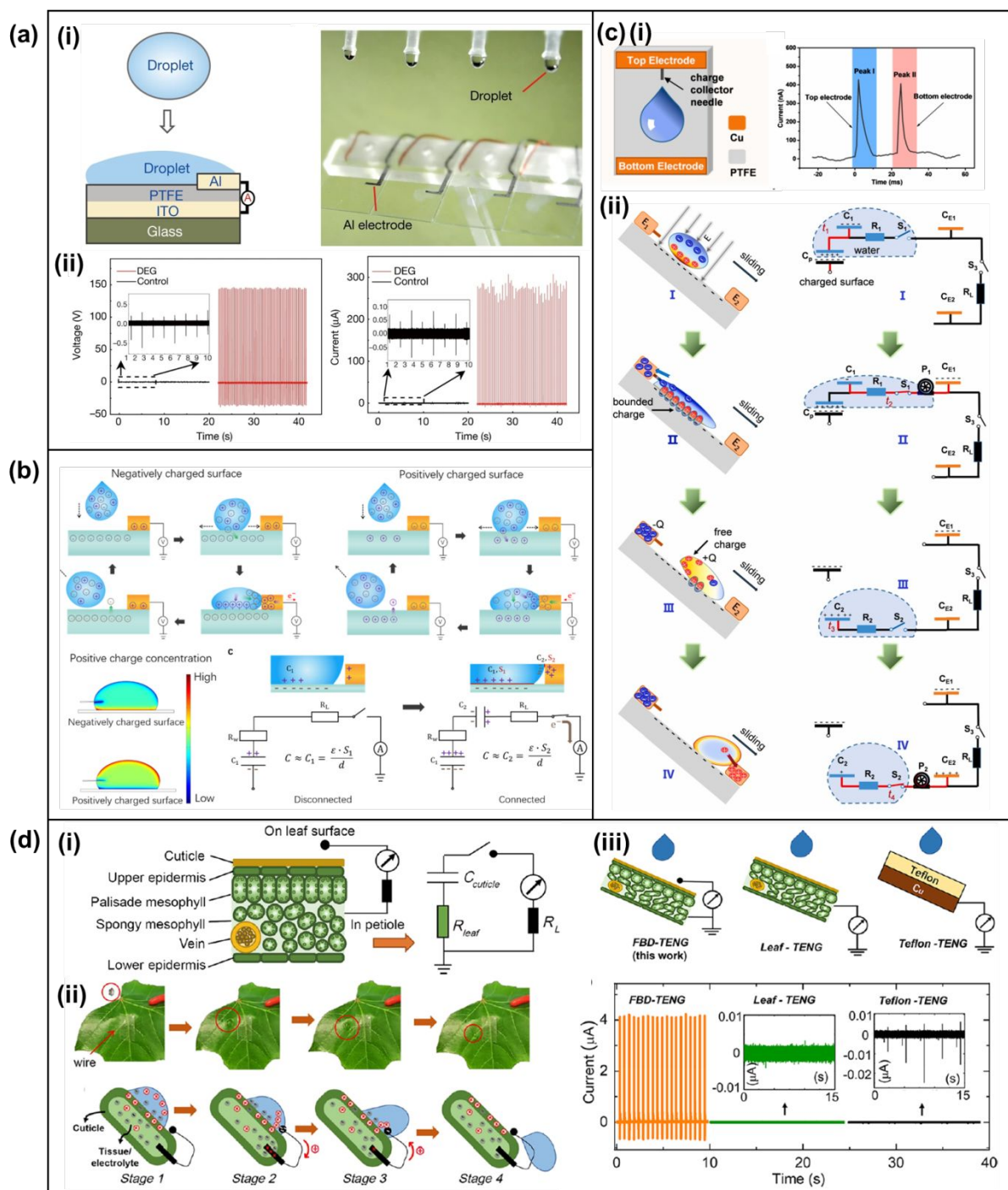


Figure 45. (a) A droplet-based electricity generator (DEG) with high instantaneous power. (a)-(i) Schematic diagram and optical image of DEG devices. (a)-(ii) the output voltage and current of DEG compared with control device. (a)-(iii) Circuit model of DEG. **Reproduced from ref. 435. Copyright 2020, Elsevier.** (b) The single electrode droplet-based electricity generator (SE-DEG). (b)-(i) The working mechanism of negatively charged surface and positively charged surface. (b)-(ii) The simulations of positive charge concentration corresponding to the negatively charged surface and positively charged surface when the droplet contacts the single electrode. (b)-(iii) The equivalent circuit model of SE-DEG. **Reproduced from ref. 436. Copyright 2021, Elsevier.** (c) The direct current droplet-based

1
2
3
4 electricity generator (DC-DEG) inspired by thunderbolts. **(c)-(i)** Structure of the DC-DEG.
5 **(c)-(ii)** The working mechanism and equivalent circuit of the DC-DEG. **Reproduced from**
6 **ref. 437. Copyright 2021, Elsevier. (d)** A biodegradable TENG (FBD-TENG) Based on
7 Leaves of Living Plants. **(d)-(i)** Schematic of the cross section of leaves and equivalent
8 circuit of the FBD-TENG. **(d)-(ii)** Schematic of the working mechanism of the FBD-TENG.
9 **(d)-(iii)** Current generated from the droplet impact onto the FED-TENG, leaf-based TENG,
10 and Teflon-based TENG. **Reproduced from ref. 389. Copyright 2020, American Chemical**
11 **Society.**
12
13
14
15
16
17
18
19
20
21
22
23
24
25
26
27
28
29
30
31
32
33
34
35
36
37
38
39
40
41
42
43
44
45
46
47
48
49
50
51
52
53
54
55
56
57
58
59
60

3.3. Charge pumping designs (Sub-TENG for main TENG)

To improve the output of TENGs⁴³⁸, the traditional methods are focused on structure optimization^{439,440}, material selection⁴⁴¹, surface modification^{442,443}, and environment control⁴⁴⁴. Although great progress has been made by those methods, there is still room for improvement^{445,446,447}. For example, the charge pumping technology emerging recently can bring the TENG further improved output performance through breaking the bottleneck of charge density enhancement⁴⁴⁸. In general charge pumping design, there is usually a main TENG and a pump TENG (Sub-TENG) with different functions, namely the pump TENG generates charges while the main TENG stores and releases charges^{449,450}. Accordingly, the basic working principle is that injected charges from the pump TENG unidirectionally flow into the main TENG to elevate its charge density, increasing the number of flowing and transferring charges within one motion cycle for a larger electricity output^{451,452,453}.

In recent years, several charge-pumping TENG systems with different structure components, movement types, and power management circuits are proposed to elevate the charge density and promote the output performance of TENG. For instance, a self-improving TENG (SI-TENG) with high charge density of $490 \mu\text{C m}^{-2}$ was put forward by Cheng et al. in 2018⁴⁵⁴, as is shown in Figure 46(a), which had a main TENG with double-layer metal

1
2
3
4 electrodes. One layer of its electrodes was used to store charges from pump TENGs and thus
5
6 to enhance the inner electric field intensity while the other one for the electricity output.
7
8 Created in the same year, an integrated self-charge-pumping TENG with a floating metal
9
10 layer structure is proposed by Xu et al. (Figure 46(b))⁴⁵⁵, which adopted a floating layer to
11
12 accumulate and bind charges and finally achieve an ultrahigh surficial charge density of 1020
13
14 $\mu\text{C m}^{-2}$. Moreover, Liu et al. reported a charge excitation TENG system with a voltage-
15
16 multiplying circuit (VMC) in 2019⁴⁵⁶ which realized the external charge excitation (ECE) and
17
18 self-charge excitation (SCE) in a TENG system shown in Figure 46(c). It used the VMC both
19
20 to boost the terminal voltage of the main TENG and to serve as a circuit for charge excitation,
21
22 and the obtained charge density was up to 1250 $\mu\text{C m}^{-2}$. In 2020, a contact-separated charge
23
24 pumping TENG with shuttling charges was proposed by Wang et al. (Figure 46(d))⁴⁵⁷. It
25
26 utilized the shuttling charges to output electricity, which flowed between the main TENG and
27
28 a buffer capacitor. Owing to the quasi-symmetrical domains and working mechanism, an
29
30 ultrahigh charge density of 1850 $\mu\text{C m}^{-2}$ was achieved. Following this research, a charge-
31
32 pumped sliding TENG system with shuttling charges was demonstrated by Yang et al. in
33
34 2021 as shown in Figure 46(e)⁴⁵⁸, which adopted the sliding movement to promote charge
35
36 generation and the VMC for the terminal voltage enhancement of main TENG. As for the
37
38 rotary sliding TENG, Bai et al., in 2020 reported a charge pumping TENG system with the
39
40 concentric main TENG and pump TENG (Figure 46(f))⁴⁵⁹. With the charge pumping strategy,
41
42 an ultrahigh average power density of 1.66 kW m^{-3} was achieved under the drive frequency of
43
44 2 Hz. In addition, Yang et al. proposed a decoupled charge pumping TENG system with a
45
46 discharge tube in 2022 (Figure 46(g))⁴⁶⁰, and it adopted the pump TENG of freestanding
47
48
49
50
51
52
53
54
55
56
57
58
59
60

1
2
3
4 mode and the main TENG of contact-separation mode to enhance the charge generation and
5
6
7
8 transfer efficiency. With a discharge tube, the instantaneous current had a 1171.2-fold
9
10
11 increase, showing great improvement for the output current of TENGs.
12
13

14
15 The primary purpose of charge pumping designs is to elevate the charge density and thus
16
17
18 to increase the participated charges for electricity output. Accordingly, more attention in the
19
20
21 future could be paid to the special electrode made by excellent materials and preferred
22
23
24 configuration, the working environment including the insulation and vacuum, the method of
25
26
27 electricity output such as charge shuttling and pulse discharge, etc. Moreover, the matched
28
29
30 motion between the pump TENG and main TENG is also important to elevate the efficiency
31
32
33 of charge generation and transfer, namely choosing suitable synchronous or decoupled
34
35
36 movement as needed.
37
38
39
40
41
42
43
44
45
46
47
48
49
50
51
52
53
54
55
56
57
58
59
60

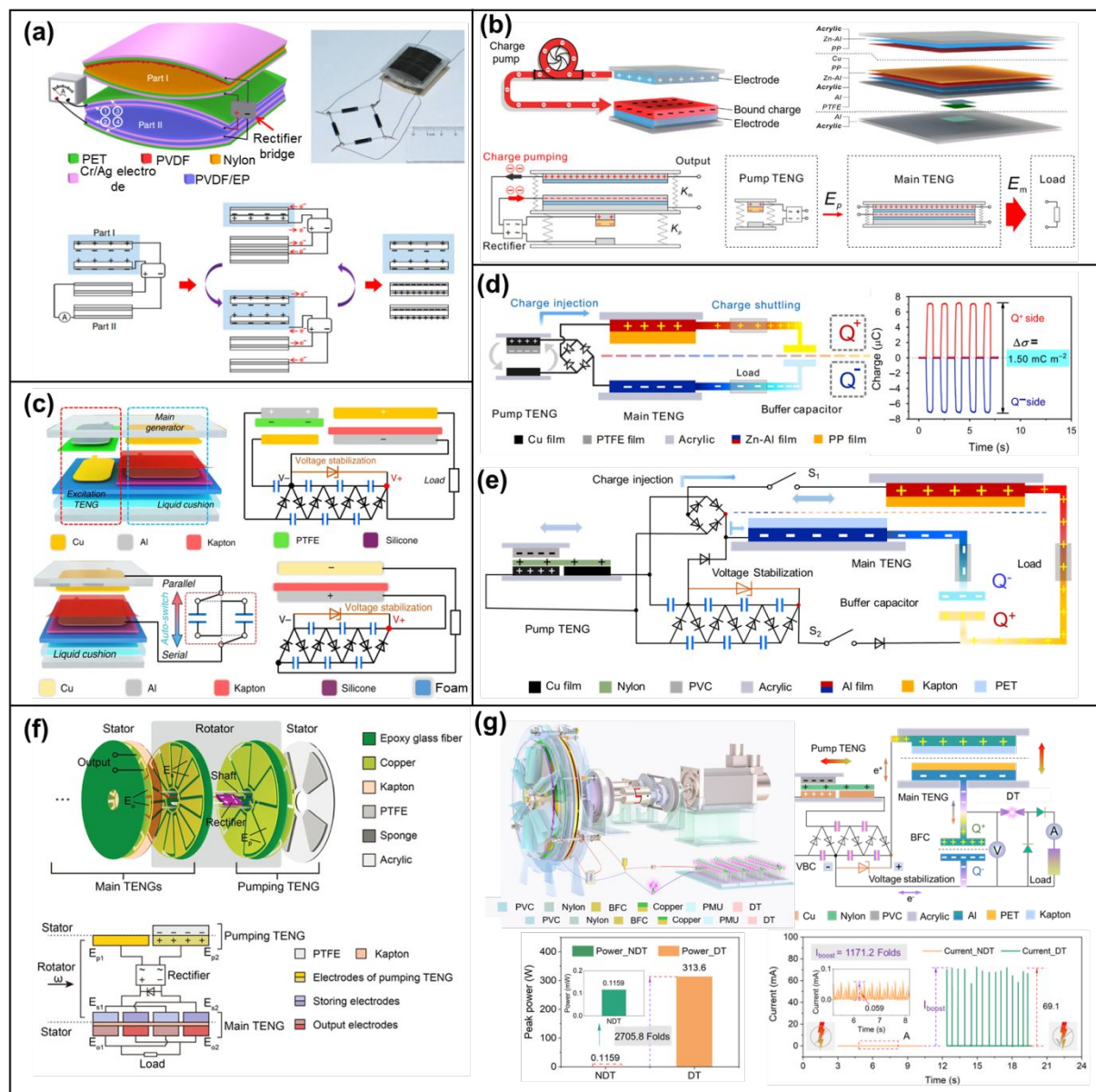


Figure 46. Charge pumping technologies for the enhancement of charge density of triboelectric nanogenerators (TEGs). (a) A self-improving TENG (SI-TENG) with high charge density. Reprinted with permission under a Creative Commons CC BY license from ref. 454, Copyright 2018, Springer Nature. (b) An integrated self-charge-pumping TENG with a floating metal layer structure. Reprinted with permission from ref. 455, Copyright 2018, Elsevier. (c) A charge excitation TENG system with a voltage-multiplying circuit (VMC). Reprinted with permission from ref. 456, Copyright 2019, Springer. (d) A contact-separated charge pumping TENG with shuttling charges. Reprinted with permission under a Creative Commons CC BY license from ref. 457, Copyright 2020, Springer Nature. (e) A charge-pumped sliding TENG system with shuttling charges. Reprinted with permission from ref. 458, Copyright 2021, Wiley. (f) A rotary sliding TENG system with a charge pumping strategy. Reprinted with permission from ref. 459, Copyright 2020,

1
2
3
4 **Wiley. (g) A decoupled charge pumping TENG system with a discharge tube. Reprinted**
5 **with permission from ref. 460, Copyright 2022, Elsevier.**
6
7
8
9
10
11
12
13
14
15
16
17
18
19
20
21
22
23
24
25
26
27
28
29
30
31
32
33
34
35
36
37
38
39
40
41
42
43
44
45
46
47
48
49
50
51
52
53
54
55
56
57
58
59
60

3.4. Direct current (DC) TENGs

Though TENGs have great potential for providing promising solutions to growing energy consumption, the alternating current pulsed outputs obstruct their extensive applications. To address the above issue, TENGs with constant DC output have been proposed and become hugely significant. In this regard, various types of DC-TENGs with distinct working mechanisms, such as dielectric breakdown, phase coupling, and tribovoltaic effect^{85,461}, will be discussed and summarized in detail as follows.

3.4.1. Dielectric Breakdown

Yang et al.⁴⁶² proposed the DC-TENG based on dielectric breakdown. As shown in Figure 47(a), the DC-TENG consists of two rotating wheels, a belt which connects them, and two electrodes. The wheels and belt are three triboelectric materials with different ability to gain electrons ($\alpha_{III} < \alpha_I < \alpha_{II}$). Electrode E_2 is close to wheel II, and electrode E_1 is in contact with wheel III. According to the triboelectric sequence, when the wheels rotate, the electrons in wheel III will continue to transfer to the belt I. The electrons in belt I will also continue to transfer to the wheel II, resulting in the continuous accumulation of positive charges on wheel III and negative charges on wheel II. Due to electrostatic induction, positive charges will also accumulate at electrode E_2 . When the electric field between wheel II and electrode E_2 reaches the air breakdown limit, electrical breakdown occurs between them, driving the electron transfer from wheel II to E_2 . The above process generates a DC signal in the external circuit. The DC-TENGs were fabricated with PTFE, Al, and rubber, where PTFE corresponds to wheel II, Al corresponds to wheel III, and rubber corresponds to belt I (Figure 47(b)). Figure 47(c) shows that when the proposed DC-TENG rotates at a speed of $600 \text{ r}\cdot\text{min}^{-1}$, the surface potential of electrodes E_1 and E_2 are 2100 V and -1100 V, respectively, and the output

1
2
3
4 voltage between the two electrodes is 3200 V (V_{OC}). Moreover, the open-circuit voltage of
5
6 the device increases with speed (Figure 47(d)). When the speed is $100 \text{ r}\cdot\text{min}^{-1}$, the output
7
8 current of the DC-TENG is about $6 \mu\text{A}$ (I_{SC}). The amplified current-time curve shows that the
9
10 maximum width of the current pulse is about 5 ms (Figure 47(e)).
11
12
13
14
15
16
17
18
19
20
21
22
23
24
25
26
27
28
29
30
31
32
33
34
35
36
37
38
39
40
41
42
43
44
45
46
47
48
49
50
51
52
53
54
55
56
57
58
59
60

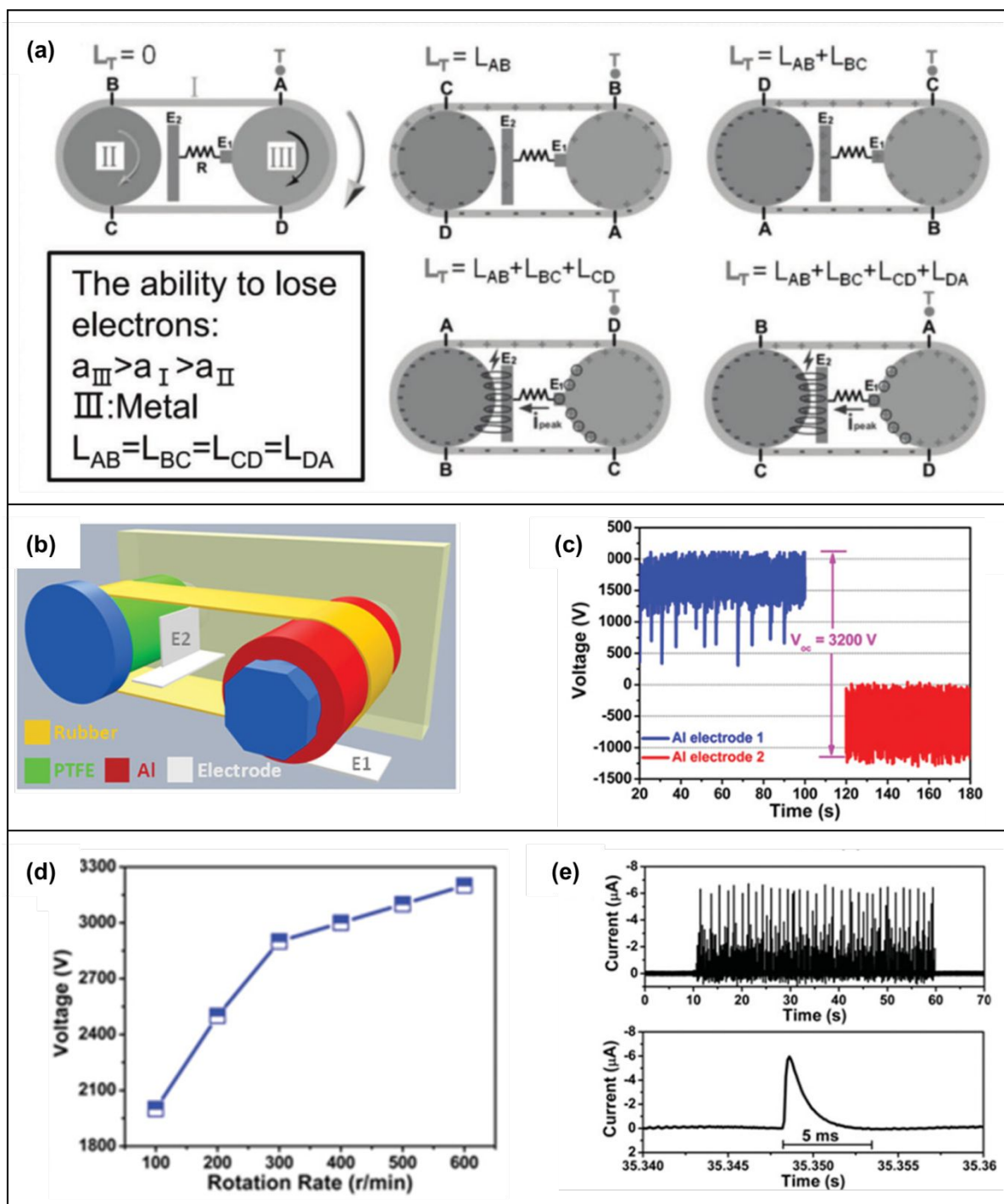


Figure 47. Structure, working mechanisms, and output characteristics of the insulator-based DC-TENG by dielectric breakdown. **(a)** Working mechanisms of the DC-TENG. **(b)** Schematic of the double-wheel designed DC-TENG. **(c)** The measured surface electric potential of electrodes during working. **(d)** Open-circuit voltage of the DC-TEG at different rotational speeds. **(e)** Short-circuit current of the DC-TEG at a rotational speed of 100 r•min⁻¹. Reprinted with permission from ref. 462, Copyright 2022, Wiley.

1
2
3
4 Liu et al.⁴⁶³ designed a DC-TENG based on the electrostatic breakdown. This device is made
5
6 up of three parts, a charge collecting electrode (CCE), a frictional electrode (FE), and a
7
8 triboelectric layer. Particularly, the CCE layer is attached to the side of the sliding acrylic
9
10 substrate and keeps a certain distance with the triboelectric layer, which is favorable for
11
12 electrostatic breakdown. Both CCE and FE are fabricated with copper. A PTFE film, as
13
14 another triboelectric layer, is attached to the acrylic plate below. In the beginning, FE is
15
16 placed on the friction layer and aligned to the left, and two opposite charges are generated on
17
18 PTFE and FE due to the triboelectrification effect. Moreover, PTFE is an electret, which can
19
20 keep the charge from dissipating. When FE slides to the right, CCE will accumulate a
21
22 positive charge and an intense electrostatic field will be established between CCE and PTFE.
23
24 When the strength of this electrostatic field is higher than the breakdown threshold of the air
25
26 between them, electrostatic breakdown will occur, which will lead to electron transfer from
27
28 PTFE to CCE. In summary, through triboelectrification and electrostatic breakdown,
29
30 electrons are transferred from FE to PTFE, then to CCE, and finally back to FE, forming a
31
32 complete current loop. As long as FE has been sliding, there will always be a DC signal in the
33
34 external circuit. Yi et al.⁴⁶⁴ proposed that oxygen atmosphere could enhance both contact
35
36 electrification and electrostatic breakdown through investigating the impact of various
37
38 atmospheres on the above two processes. Furthermore, an optimized DC-TENG (Figure
39
40 48(a)) was prepared to integrate with controlled oxygen atmosphere, and achieved a greatly
41
42 enhanced output performance, which was 8 times larger than that in atmospheric air (Figure
43
44 48(b)). Based on triboelectrification effect and electrostatic breakdown, Gao et al.⁴⁶⁵
45
46 proposed a rolling DC TENG (R-DC-TENG) consisting of a rolling frictional electrode
47
48 (RFE), a triboelectric layer (PTFE) and the charge collecting layer (CCE) (Figure 48(c)).
49
50 When the device rolls, the electron is transferred from RFE to PTFE via triboelectrification
51
52 effect, which is then transferred to CCE via electrostatic breakdown. Finally, the electron
53
54
55
56
57
58
59
60

1
2
3
4 flows back to RFE through the external circuit. When the speed reaches 1000 rpm, the crest
5
6 factor of the device can be reduced to 1.02.
7
8
9
10
11
12
13
14
15
16
17
18
19
20
21
22
23
24
25
26
27
28
29
30
31
32
33
34
35
36
37
38
39
40
41
42
43
44
45
46
47
48
49
50
51
52
53
54
55
56
57
58
59
60

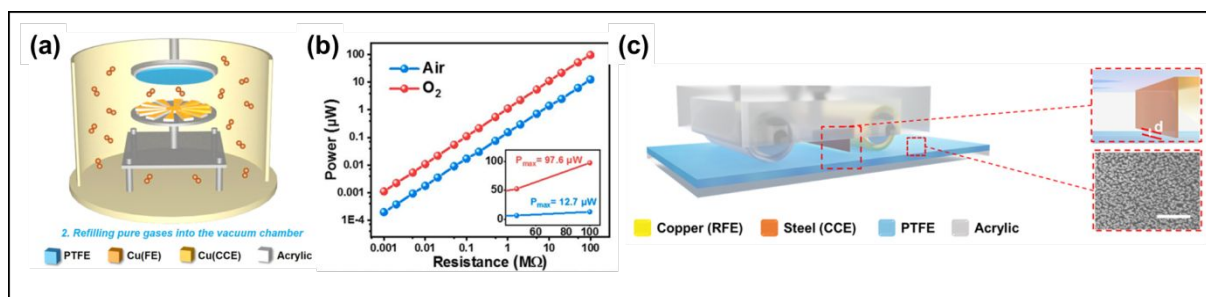


Figure 48. (a) Schematic illustration of TENGs in the measurement system. (b) The output power of the rotatory DC-TENG with various loads in atmospheric air and oxygen at $200 \text{ r}\cdot\text{min}^{-1}$, inset is the zoom-in of maximum values. **Reprinted with permission from ref. 464, Copyright 2021, Elsevier.** (c) Structural design and working principle of the R-DC-TENG. **Reprinted with permission from ref. 465, Copyright 2021, Elsevier.**

3.4.2 Phase coupling

The DC-TENG based on phase coupling, as shown in Figure 49(a) and 49(b), consists of a stator with fluorinated propylene film (FEP) and a rotor with Cu⁴⁶⁶. The stator is divided into three phases, each of which consists of three groups. The working mechanism of the DC-TENG is similar to freestanding triboelectric-layer working mode (Figure 49(c)). During rotation, the relative position of Cu and FEP changes periodically, and the pulse DC signal is generated after rectification. The designed phase difference couples the electrical signals of the three-phase TENG to obtain a constant DC signal with a low crest factor. Hu et al⁴⁶⁷. utilized 3D printing technology to fabricate a phase coupling DC-TENG (Figure 49(d)) with low crest factor and long service life, which successfully achieved accurate phase control and the structure with adaptable contact mode. The device is composed of a rotor and a stator. The rotor is a ring-like support with several gaps which can be inserted with triboelectric layers (FEP). The stator is supported by two inner and outer ring devices, the walls of which are affixed with Cu electrodes. The working mechanism of a single TENG is shown in Figure 49(e). During the process of rotation, the induced charge is transferred between the two electrodes owing to the coupling of triboelectrification effect and electrostatic induction. Then a current signal is formed on the external circuit. After optimizing parameters such as the pair number of the electrode, thickness of triboelectric layer, and distances, a crest factor of 1.07 and a service life of 1.2 million cycles were obtained. In addition, Chen et al.⁴⁶⁸ designed a DC multiphase TENG with high stability and high power through electrode dislocation and circuit connection. By superimposing various TENG units with different phases in parallel, an ultra-low peak coefficient of 1.05 and an average power increase of 40.1% compared to the single-phase TENG can be achieved in the multiphase DC-TENG.

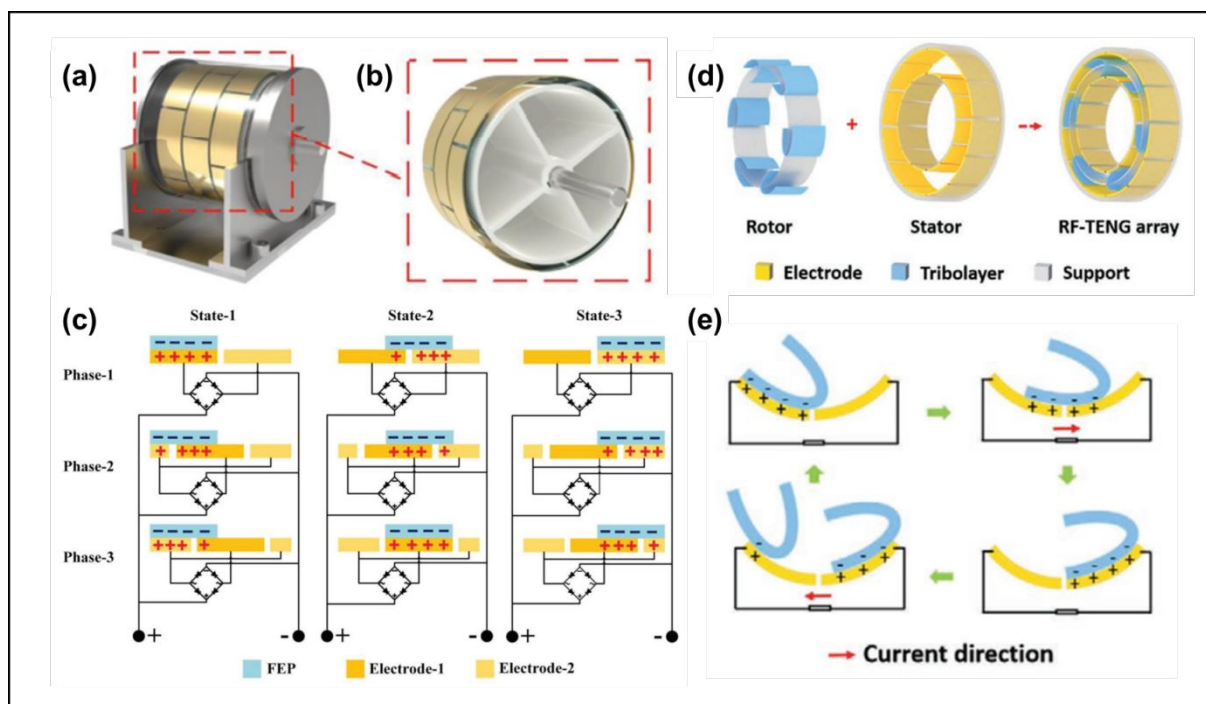


Figure 49. (a) Schematic diagram showing the monolithic construction of the DC-TENG. (b) Partial enlargement drawing of the triboelectric power-generating unit. (c) Schematic working principle of DC-TENG at three states. **Reprinted with permission from ref. 466, Copyright 2020, Wiley-VCH.** (d) Structure schematic of RF-TENG array. (e) Working mechanism of the RF-TENG array. **Reprinted with permission from ref. 467, Copyright 2020, AIP publishing.**

3.4.3 Semiconductor-Based DC-TENG with tribovoltaic effect

The phenomenon of DC generation based on semiconductor heterojunctions was demonstrated in squeezing metal/conducting polymer⁴⁶⁹ and sliding metal/semiconductor systems^{461, 470, 471}. A DC output was generated in Schottky contacts by sliding metal/MoS₂⁴⁷¹, which reached a current density as high as 10⁶ A•m⁻² (Figure 50(a)). Such phenomenon was further explained at the nanoscale by detecting three adjacent MoS₂ crystal grains (Figure 50(b)), which responded differently to triboelectric current ($I_{\text{grain 2}} > I_{\text{grain 3}} > I_{\text{grain 1}}$). The diode feature with different rectification effect between grain 1 and grain 2 was revealed in Figure 50(c), which explained the key role of Schottky contacts in DC generation phenomenon.

After the DC output generated from sliding metal/semiconductor was proposed, traditional TENGs encountered new opportunities to achieve the high impedance and alternating current output. Zhang et al.⁴⁶¹ proposed investigating the triboelectric properties between metal and semiconductors through studying the electrical output generated from sliding n-type silicon/stainless steel (Figure 50(d)). When the stainless steel was sliding over the n-type silicon substrate, a voltage of 20 mV and a current of 20 μA with low impedance of 620 Ω were achieved. The tribovoltaic effect (like photovoltaic effect) is proposed to be responsible for the DC output. Once rubbed, the dynamic electrons in metal and electron-hole pairs in semiconductor will be excited by triboelectricity and move directionally under the built-in electric field. Therefore, such a TENG can transfer mechanical energy into electrical energy with DC output. Lin et al.⁴⁷² proposed that sliding water droplets on the surface of silicon wafer could generate tribo-voltage and DC tribo-current by exploring contact electrification at the solid-liquid interface (Figure 50(e)). A syringe filled with DI water and equipped with a conductive needle was placed 0.25mm above the silicon surface. Similar to the DC

1
2
3
4 generation from the Schottky sliding contact, the droplet/semiconductor interface contact
5
6 could be capable of generating an output of 200 mV (V_{OC}) and 40 nA (I_{SC}) (Figure 50(f)).
7
8

9
10 The basic mechanisms of semiconductor-based DC-TENG with tribovoltaic effect has been
11
12 systemically illustrated, marvelous progress has been achieved to provide solutions for self-
13
14 powered wearable devices and IoTs network owing to the features of low impedance and
15
16 high current density. Moreover, constructing DC generation systems based on multi-physics
17
18 coupling effects (e.g., tribo-photovoltaics coupling⁴⁷³ and tribo-thermoelectric coupling⁴⁷⁴)
19
20 provide ideas to expend the potential applications of self-powered sensing and energy
21
22 harvesting based on TENG.
23
24
25
26
27
28
29
30
31
32
33
34
35
36
37
38
39
40
41
42
43
44
45
46
47
48
49
50
51
52
53
54
55
56
57
58
59
60

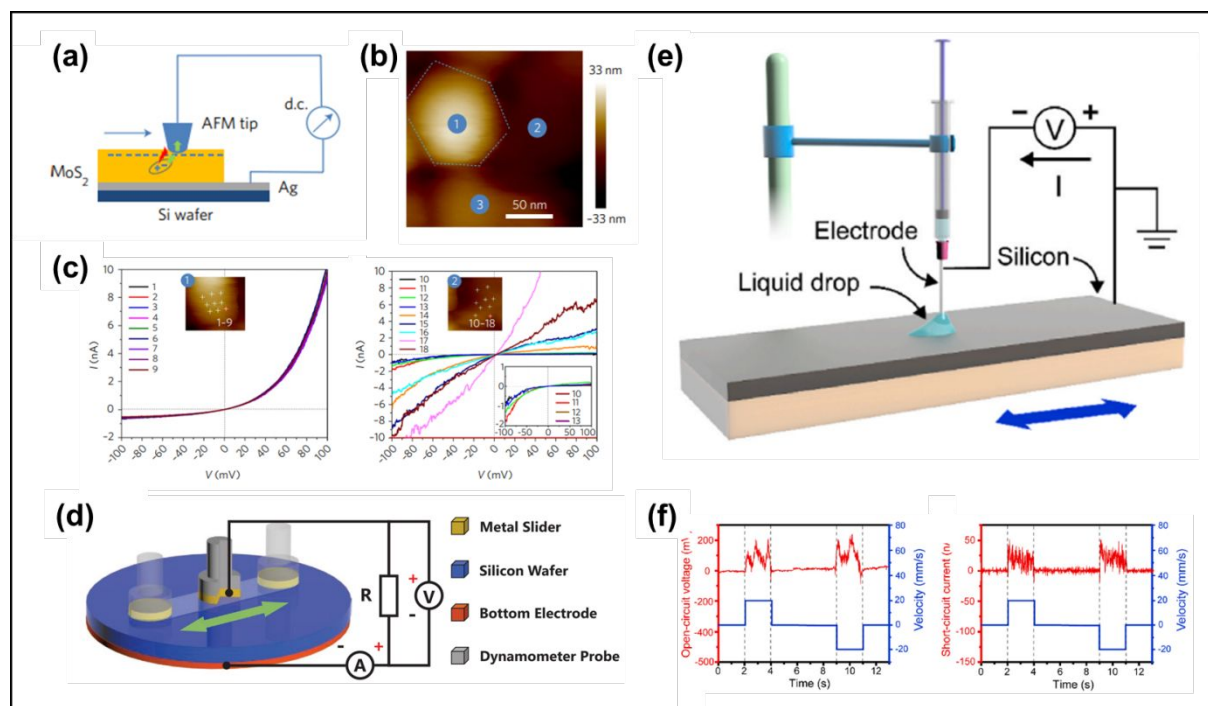


Figure 50. (a) Schematic of nanoscale d.c. harvesting. An MoS₂ thin film is deposited on Ag by PLD. A Pt/Ir-coated AFM tip slides in contact mode on the sample surface, which induces electronic excitation and carrier conduction. (b) AFM topographic image of three adjacent MoS₂ crystal grains marked 1, 2, and 3, respectively. (c) C-AFM *I–V* spectra for grains, 1 and 2. C-AFM *I–V* spectra for grains 1 (left) and 2 (right). Inset, nine data points marked on the topographic image. **Reprinted with permission from ref. 471, Copyright 2018, Springer Nature.** (d) The 3D schematic illustrations of the measurement setup and the external circuit. **Reprinted with permission from ref. 461, Copyright 2020, Wiley-VCH.** (e) The setup of the tribovoltaic experiments and the external circuit. (f) (left) The oscillogram of open-circuit voltage when a DI water droplet slides on the P-type silicon wafer (0.1 Ω cm) at 20 mm/s, and the droplet static contact diameter is 2.5 mm. (right) The oscillogram of short-circuit current when a DI water droplet slides over the P-type silicon wafer (0.1 Ω cm) at 20 mm/s, and the droplet static contact diameter is 2.5 mm. **Reprinted with permission from ref. 472, Copyright 2020, Elsevier.**

3.5 Durable device designs

In this section, we review lubrication-based TENGs that can increase the mechanical lifespan as well as the electrical output of the generators. As TENGs essentially require friction to generate surface charge on the triboelectric materials, the ways to enhance the limited mechanical lifespan of TENGs have been developed^{475,476,326,477}. Especially by utilizing traditional ways to reduce friction between surfaces, such as utilizing lubrication, TENGs can have a longer lifespan by reducing frictional wear as well as increase its electrical output by suppressing electrons escaping from the surfaces of triboelectric materials.

From a mechanical perspective, utilizing lubricant decreases the friction force between two contacting surfaces which leads to less wear during operation. When liquid lubricant is applied between the surfaces, it forms three primary regimes of boundary lubrication, elastohydrodynamic lubrication, and hydrodynamic lubrication depending on the thickness of lubricant film formed⁴⁷⁸. As the thickness of lubricant film increases, the friction coefficient decreases until it reaches the hydrodynamic lubrication regime, where lubricant liquid introduces a drag to the surface. With the right thickness of lubricant liquid film, two surfaces contacting during TENG operation would have significantly reduced friction force.

1
2
3
4
5 In electrical perspective, the lubricant liquid fully covers the surface of triboelectric
6
7
8 materials, which would prevent electrons from escaping due to air breakdown and field
9
10
11 emission^{429,479,480,481}. As materials with high surface charge are being used and discovered to
12
13
14 be utilized as triboelectric layers for TENGs^{482,170}, there have been increasing studies that
15
16
17 point out the upper limitations due to these phenomena⁴⁸⁰. As lubricant liquid has
18
19
20 significantly higher breakdown voltage compared to air, it can prevent the electrons
21
22
23 exchanged from contact electrification from escaping into air. With higher surface charge,
24
25
26 lubricant-based TENGs produce higher electrical output compared to conventional TENGs
27
28
29 that operate without lubricant.
30
31
32
33

34
35 Figure 51 shows various designs of TENGs that utilizes lubricant to ensure longer
36
37
38 mechanical lifespan and higher electrical output. As shown in Figure 51(a), lubricant can be
39
40
41 applied to TENGs with vertical contact separation modes⁴⁸³. An oleic-acid doped polystyrene
42
43
44 (OA-PS) is synthesized, and spin coated on the surface of conductive polyimide (PI) substrate.
45
46
47 Nylon-11 layer was used as a counter triboelectric material. This device has been utilized as a
48
49
50 vertical contact separation mode TENG. The electrical output has shown to improve by 9
51
52
53 times compared to the conventional TENG when charging a capacitor.
54
55
56
57
58
59
60

1
2
3
4
5 Considering that friction wear occurs more severely in horizontal sliding TENGs, sliding
6
7
8 and rotating type TENGs could benefit more from utilizing lubricant liquid. As shown in
9
10
11 Figure 51(b), various lubricant liquids are applied in between the PI and aluminum surface⁴⁸⁴.
12
13
14
15 The main electrical potential difference occurs due to the friction between the PI and
16
17
18 aluminum electrode. TENGs in this study have a typical sliding mode to compare the
19
20
21 electrical output depending on various liquids and influence of different loads given to the
22
23
24
25 system. In this work, the open-circuit voltage (V_{oc}) and closed-circuit current (I_{cc}) of
26
27
28 squalene applied sliding TENGs have shown 3 times more output compared to conventional
29
30
31 TENGs. In addition, as shown in Figure 51(c), liquid lubricant was applied in between the PI
32
33
34 and electrode surface, which can enhance the output and mechanical lifespan of both sliding-
35
36
37 mode AC-TENGs and sliding-mode DC-TENGs⁴⁸⁵. In this work, sliding type TENGs with
38
39
40 liquid lubricant produced 1.5 times more output than conventional TENGs, and have shown
41
42
43 similar output even after 500,000 operation cycles.
44
45
46
47

48 Figure 51(d) shows sliding type TENG with lubricant liquid in between two surfaces, and
49
50
51 the main electrical potential difference is due to friction between PTFE and electrode⁴⁸⁶.
52
53
54
55 Although it follows the conventional sliding mode TENG design of two parallel electrodes
56
57
58 with triboelectric material sliding on the top, it reports a working mechanism considering the
59
60

1
2
3
4 air breakdown and field emission effect occurring from electrode (aluminum) surface when
5
6
7
8 lubricant liquid is pushed by the dielectric material on top. Through this working mechanism,
9
10
11 lubricant-based TENGs can produce high electrical current output over a milliampere. When
12
13
14 lubricant liquid with high breakdown voltage fully covers the aluminum electrode, the
15
16
17 electrons cannot escape from electrode to the liquid. However, when liquid lubricant is
18
19
20 removed from the surface, the aluminum surface is exposed to air and the triboelectric charge
21
22
23 is enough to cause air breakdown. Since negative surface charge of polytetrafluoroethylene
24
25
26 (PTFE) is continuously inducing electrons to flow from the aluminum electrode that is in
27
28
29 contact with PTFE to the counter electrode that is exposed in air, it can produce higher
30
31
32 electrical output due to more electrons flowing from electrode to another. This work shows
33
34
35 that there is TENG mechanisms yet to be discovered by utilizing lubricant, which could
36
37
38 benefit TENGs in both mechanical and electrical perspective.
39
40
41
42
43
44

45 As lubricant is a traditional way of reducing friction effectively, the application of TENGs
46
47
48 can be expanded to various mechanical components. In Figure 51(e), TENG is designed as a
49
50
51 rotating shaft that can produce electrical output through inner PTFE pipe rotating⁴⁸⁷. This
52
53
54 work submerged the whole TENG inside lubricant liquid and utilized a rotating cylinder to
55
56
57 further decrease the friction wear during operation. The liquid submerged TENG consists of 5
58
59
60

1
2
3
4 parts; PMMA substrate, rolling electrode, plate electrode, and inner PTFE pipe. As the
5
6
7
8 rotating rod electrode around the TENG rotates along with the PTFE pipe inside, it contacts
9
10
11 the patterned plate electrode. When it contacts the patterned plate electrode, the electrons can
12
13
14 flow directly from the rod electrode and the plate electrode, which can enhance the electrical
15
16
17 output. In addition, as shown in Figure 51(f), a bearing-type TENG that utilizes semi-solid
18
19
20 lubricant in between two surfaces⁴⁸⁸. In this work, a commercial semi-solid lubricant was
21
22
23
24 utilized inside, and bearing was composed of PTFE and steel sphere. Even when the bearing
25
26
27 TENG was rotated continuously over 12 hours, the electrode surface did not show critical
28
29
30 damage, while the electrode surface of conventional TENG had electrode debris around the
31
32
33 rotating path of the spheres from friction wear. The lubricant was also shown to further
34
35
36 reduce the operating temperature of the TENG, where the temperature of the TENG with
37
38
39 lubricant increased by only 1.2 °C over 12 hours.
40
41
42
43
44
45
46
47
48
49
50
51
52
53
54
55
56
57
58
59
60

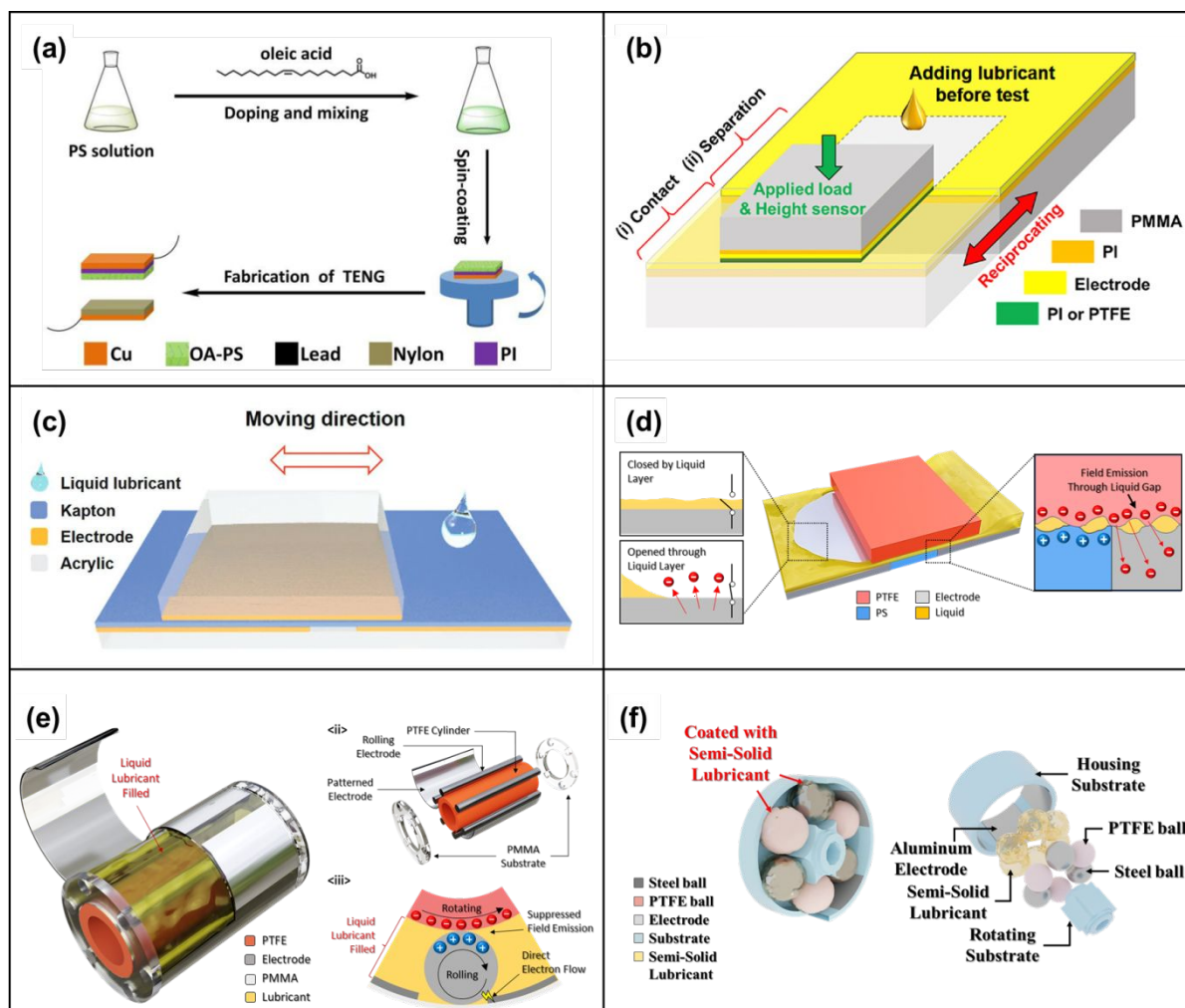


Figure 51. Lubricant based triboelectric nanogenerators. **(a)** Oleic-acid doped polystyrene (OA-PS) based TENG. Reprinted with permission from ref. 483, Copyright 2020, Elsevier. **(b)** Sliding-type TENG under lubricated conditions. Reprinted under a Creative Commons license from ref. 484, Copyright 2020, Elsevier. **(c)** Schematics of sliding freestanding TENG where 50 μL of liquid lubricant is applied in between surfaces. Reprinted with permission from ref. 485, Copyright 2020, Wiley-VCH. **(d)** Sliding mode TENG that utilize the electrical behavior of electrons during liquid lubricant flow. Reprinted with permission from ref. 486, Copyright 2021, Elsevier. **(e)** Rotating shaft-type TENG that is submerged inside lubricant liquid. Reprinted with permission from ref. 487, Copyright 2021, Wiley-VCH. **(f)** Bearing-type TENG with semi-solid lubricant applied on

1
2
3
4 the surface. **Reprinted with permission from ref. 488, Copyright 2022, Elsevier.**
5
6
7
8
9
10
11
12
13
14
15
16
17
18
19
20
21
22
23
24
25
26
27
28
29
30
31
32
33
34
35
36
37
38
39
40
41
42
43
44
45
46
47
48
49
50
51
52
53
54
55
56
57
58
59
60

1
2
3
4 Figure 52(a) shows a schematic of non-lubricated and lubricated conditions of TENGs and
5
6
7
8 the non-polar lubricant liquid increasing the electrical output⁴⁸⁷. When the TENG is under
9
10
11 polar liquid conditions such as water, the polar liquid molecule has polarity itself. Due to the
12
13
14 surface charge of dielectric materials used in the TENG, the polar liquid molecules orient
15
16
17 themselves⁴⁸⁹. Due to this phenomenon, the Debye length, which is the length of charge
18
19
20 screening, is considerably shorter compared to non-polar liquids. For example, the Debye
21
22
23 length of water is reported to be less than 20 nm⁴⁹⁰. This indicates that even when the
24
25
26 electrode is placed further than the short Debye length, charge transfer cannot affect the
27
28
29 electrode by electrostatic induction. In contrast, when the TENG surface is under non-polar
30
31
32 liquid conditions, the non-polar liquid can be polarized by the surface charge of the
33
34
35 triboelectric material. A Debye length of non-polar liquid is over a μm , which is typically
36
37
38 longer than that of polar liquid⁴⁹¹. This indicates that higher surface charge can be inducted to
39
40
41
42
43
44
45 the counter electrode, producing higher electrical output.

46
47
48
49 Figure 52(b) is the V_{OC} and I_{CC} output of TENG depending on air and lubricant
50
51
52 conditions⁴⁸⁷. By utilizing both metal-to-metal contact and having lubricant in between
53
54
55 triboelectric materials, the electrical output can increase drastically. As shown in the plot, the
56
57
58
59 V_{OC} and I_{CC} output are shown to be around 200 V and 40 mA, respectively, in air conditions,
60

1
2
3
4 while that of air condition is around 20 V and 3 mA, respectively. In addition, as shown in
5
6
7
8 Figure 52(c), the friction coefficient has shown to decrease when various liquid is applied on
9
10
11 the TENG surface⁴⁹². As polyalphaolefin 4(PAO 4) and perfluoropolyether (PFPE) are
12
13
14 applied on the surface, the friction coefficient decreased more than half, while electrical
15
16
17
18 output increased.
19

20
21 For lubricant liquids to be further utilized in TENGs, future studies are required to
22
23
24 optimize the lubricant needed for each design and applications. One of the important
25
26
27
28 parameters for optimization is choosing the right lubricant liquid for the design. Figure 52(d)
29
30
31 shows electrical output of TENG depending various liquids in between TENG surfaces⁴⁸⁴. As
32
33
34 shown in the plot, the electrical output when TENG is exposed to squalene, paraffin oil, PAO
35
36
37
38 16 has shown to increase compared to the dry conditions, and when TENG is exposed to
39
40
41 olive oil, rapeseed oil, pluriol A 500 PE, 1-ethyl-3-methylimidazolium bis(trifluoromethyls
42
43
44 ulfonyl)imide, PEG 200, and water have decreased compared to dry condition. For further
45
46
47
48 optimization, examining quantitative relationship between TENG and lubricating materials,
49
50
51 structural design of TENG considering lubricant, and utilizing commercial lubrication
52
53
54 material is essential for lubrication based TENGs. We believe that continuous research efforts
55
56
57
58 of lubrication based TENGs have great potential for utilizing TENGs in various industries.
59
60

1
2
3
4
5
6
7
8
9
10
11
12
13
14
15
16
17
18
19
20
21
22
23
24
25
26
27
28
29
30
31
32
33
34
35
36
37
38
39
40
41
42
43
44
45
46
47
48
49
50
51
52
53
54
55
56
57
58
59
60

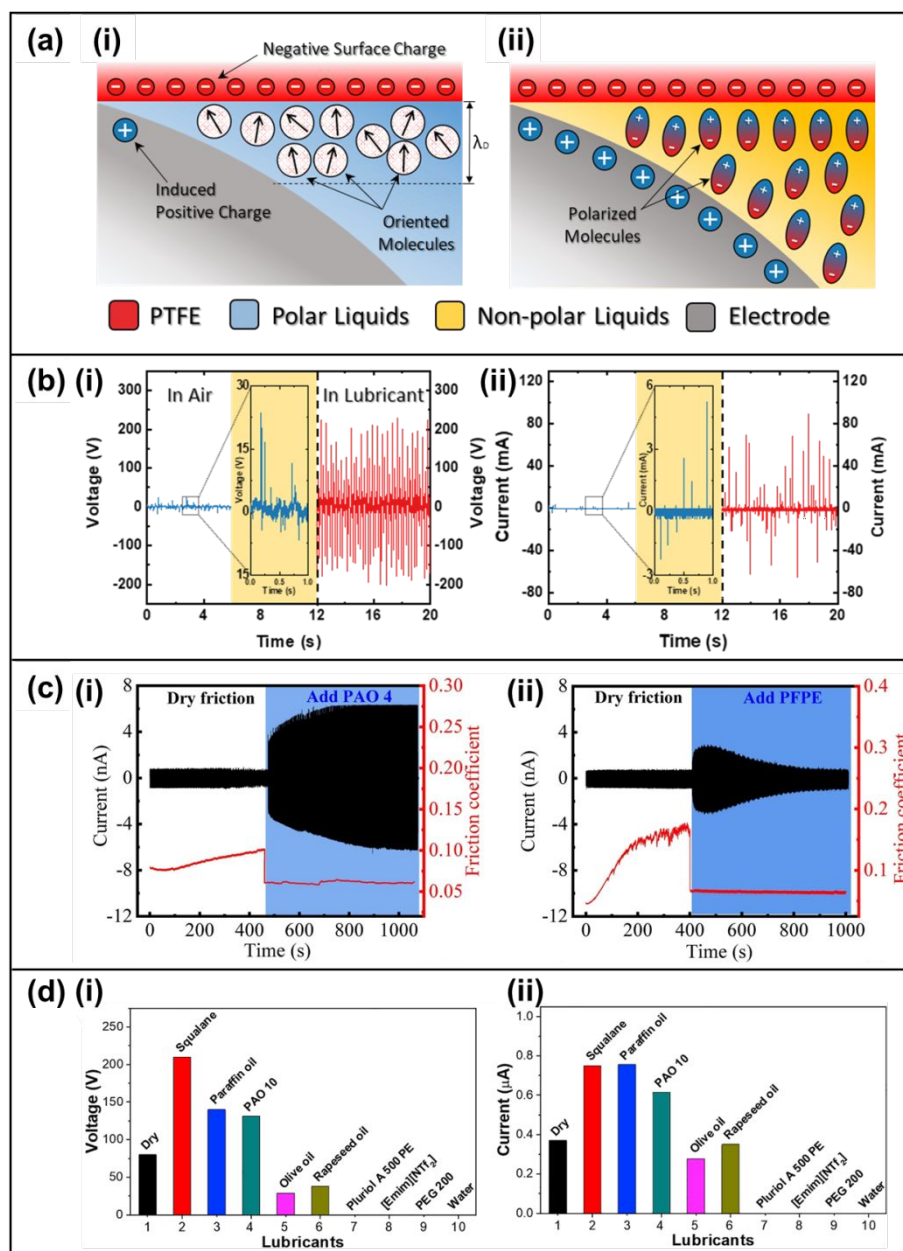


Figure 52. Mechanism schematics and electrical output of lubricant based TENGs. (a) Schematics of Debye length and induced charge depending on (a)-(i) non-lubricant and (a)-(ii) lubricant condition. (b)-(i) Open-circuit voltage and (b)-(ii) closed-circuit current comparison when TENG is operating in air and in lubricant conditions. Reprinted with permission from ref. 487, Copyright 2021, Wiley-VCH. (c) Friction coefficient and current output comparison of a sliding type TENG in dry and lubricated surfaces ((c)-(i) PAO4, (c)-(ii) PFPE). Reprinted with permission from ref. 492, Copyright 2021, Elsevier. (d)-(i) Open-circuit voltage and (d)-(ii) closed-circuit current output depending on various lubricant liquids. Reprinted under a Creative Commons license from ref. 484, Copyright 2020, Elsevier.

4. Mechanical Systems for TENGs

In this section, we review various types of rationally designed mechanical systems with the TENGs integrated with the mechanical elements for the effective generation of electrical energy.⁴⁹³⁻⁴⁹⁷ Due to the simplicity of the working principle of tribo-electrification, which is based on the contact-separation of dissimilar materials as mentioned above, the TENG can be created in a variety of ways by employing various mechanical elements.⁴⁹⁸⁻⁵⁰² In this regard, the mechanical systems enable the TENG to convert various mechanical movements that are difficult-to-harvest around us into easy-to-harvest forms for the TENG. Therefore, this review focus on the motion transformation of the mechanical movements to fulfill the intended purpose in the various mechanical TENG systems.

4.1 Kinematic Systems

Kinematics (i.e., velocities as inputs) are composed of one or more mechanisms, such as involving an analysis of the geometry of motion.^{13, 68} In detail, kinematic design is considered the motion of points, bodies, and systems. A representative kinematic system as a one of mechanical elements is a gear-train, which can change the rotation speed, torque, and direction of input power on purpose.⁵⁰³⁻⁵⁰⁸ Given that, the transformed movements are able to

1
2
3
4 effectively improve output performance, functionality, and mechanical properties. In this
5
6
7
8 regard, we briefly introduce various kinematically designed mechanical TENG systems,
9
10
11 which are based on the simple working principle of triboelectrification.
12
13
14
15
16
17

18 **4.1.1 Linear to rotational motion transformation**

19
20

21 Due to the rapid development of electricity-based technologies, energy demand is rapidly
22
23
24 increasing, and the energy crisis caused by an imbalance in energy supply and demand is
25
26
27 becoming more serious. Hence, energy harvesting technologies are significantly getting
28
29
30 worldwide attention for their characteristic ability to harvest mechanical energy from the
31
32
33 environment as the sustainable energy sources, such as ocean, wind, and vibration energy in
34
35
36 the ambient. Given that, the mechanical TENG system considering input mechanical
37
38
39 characteristics should be designed to achieve its desired output performance.⁵⁰⁹⁻⁵¹³ First,
40
41
42
43
44
45 linear motion, one of the various mechanical movements in the environment, is inappropriate
46
47
48 in the point of view of having to produce a large amount of energy output due to the low
49
50
51 output frequency. Therefore, to effectively harvest mechanical energy from the linear
52
53
54 movements in the fields of mechanical TENG systems, the above problem can be solved by
55
56
57
58 using a mechanical component such as a gear-train. Therefore, we introduce the mechanically
59
60

1
2
3
4 designed TENG systems, which enable to effectively convert the mechanical movement with
5
6
7
8 the low frequency in the around us into the high frequency rotation for high output
9
10
11 performance energy harvesting.
12

13
14 In this regard, *Y. Xu et al.* present a graded energy harvesting triboelectric nanogenerator
15
16
17
18 (GEH-TENG) incorporating the primary transmission elements, such as flywheel, gear, and
19
20
21 incomplete gear, that can effectively harvest ocean energy by adjusting the number of the
22
23
24 generation unit depending on the magnitude of the external input waves (Figure 53(a)-(i)).⁵¹⁴
25
26
27

28 The operation mechanism of the GEH-TENG is mainly determined by the incomplete gear,
29
30
31 which is partially fabricated gear teeth. Thus, when a small wave pushes the pendulum, the
32
33
34 generation unit I operates by the incomplete gear, which can transform into a high frequency
35
36
37 rotation. Meanwhile, when the large waves impact the pendulum, the swing angle of the
38
39
40 pendulum is high, thereby generation unit II can generate the electrical output in conjunction
41
42
43 with the generation unit I (Figure 53(a)-(ii)). According to this mechanical design, the
44
45
46 incomplete gear of the GEH-TENG is capable of mechanical modulation by controlling the
47
48
49 number of the generation unit, which affects the required initial torque to operate. Therefore,
50
51
52 the GEH-TENG can effectively produce the output performance depending on the magnitude
53
54
55 of the external waves due to the incomplete gear system (Figure 53(a)-(iii)).
56
57
58
59
60

1
2
3
4
5 In the case of the wind energy harvesting, *Y. Luo et al.* propose a travel-controlled
6
7
8 approach employing a tunable cam switch for stable and automatic mode transition to
9
10
11 enhance the stability and durability of the TENG (travel-controlled TENG, TC-TENG) for
12
13
14 efficient breeze wind energy harvesting (Figure 53(b)-(i)).⁵¹⁵ In particular, not only the
15
16
17 transmission unit incorporating the gear-train can dramatically enhance the output
18
19
20 performance, but also the cam switch of the TC-TENG plays an important role in the mode
21
22
23 transition, which enables improvement of the durability of the TC-TENG by preventing the
24
25
26 abrasion of the friction area. Therefore, the output performance of the TC-TENG was tested,
27
28
29 as a result, the output voltage and the transferred charged of the TC-TENG can be measured
30
31
32 depending on the automatic mode transition, respectively (Figures 53(b)-(ii) and 53(b)-(iii)).
33
34
35
36
37
38 Consequently, in order to demonstrate in the view of long-term durability, the TC-TENG was
39
40
41 evaluated, indicating that the TE-TENG has outstanding electrical stability of attenuation 10%
42
43
44
45 in the operation for 80 hours compared with the constant contact modes (Figure 53(b)-(iv)).
46
47

48 To effectively harvest random vibration excitation energy in the ambient, *W. Yang et al.*
49
50
51 exhibit a travel switch integrated mechanical regulation triboelectric nanogenerator (TSMR-
52
53
54 TENG) with linear-rotational motion transformation mechanism (Figure 53(c)-(i)).⁵¹⁶ The
55
56
57 combination of the one-way clutch, spring, and linear-rotational motion transformation
58
59
60

1
2
3
4 mechanism unit can convert the mechanical energy of the vibration motion into electrical
5
6
7
8 energy. The travel switch, which plays an important role in the working mechanism of the
9
10
11 TSMR-TENG, anchors the inertia wheel, and all rotation energy is stored in the spiral spring
12
13
14 (Figure 53(c)-(ii)). As a result, the locking plate begins to rotate and releases the travel switch,
15
16
17
18 thereby generating the electrical output. In this paper, the open-circuit voltage of the TSMR-
19
20
21 TENG is evaluated by changing the inertia wheels with various masses, respectively (Figure
22
23
24 53(c)-(iii)). This means that a larger inertia force can store more mechanical energy of the
25
26
27
28 vibration motion and produce more electrical output over a long period of time.
29
30
31
32
33
34
35
36
37
38
39
40
41
42
43
44
45
46
47
48
49
50
51
52
53
54
55
56
57
58
59
60

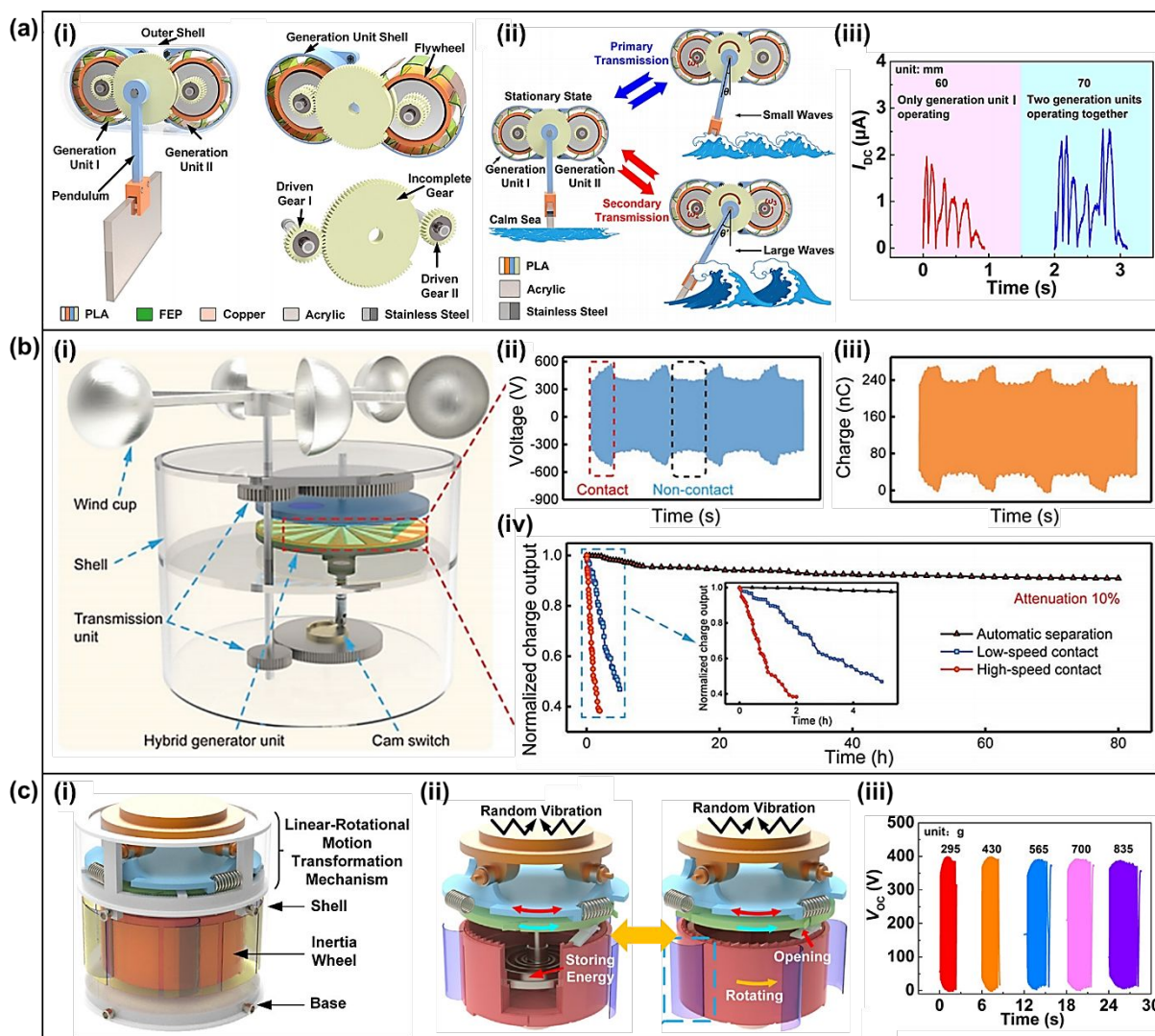


Figure 53. Mechanical TENG system designs to convert the linear motion of ocean, wind, and vibration energy into rotational motion. **(a)-(i)** Schematic diagram of the GEH-TENG. **(a)-(ii)** The operation mechanism depending on the wave types. **(a)-(iii)** The direct current output graph under the number of units of the VR-TENG. **Reproduced with permission from ref. 514, Copyright 2021 American Chemical Society.** **(b)-(i)** The illustration of the TC-TENG equipped with the EMG. **(b)-(ii)** The output voltage and **(b)-(iii)** charge graph of the TC-TENG at 300 rpm and 0.05 N. **(b)-(iv)** The durability comparison during long-term operation for different modes. **Reproduced with permission from ref. 515, Copyright 2022 Wiley-VCH.** **(c)-(i)** The entire structure of the TSMR-TENG including gear-train and mechanical elements. **(c)-(ii)** The working mechanism of the TSMR-TENG. **(c)-(iii)** The open-circuit voltage and running time for TSMR-TENG with different inertia wheel weight. **Reproduced with permission from ref. 516, Copyright 2020 Elsevier B. V.**

1
2
3
4 Recently, many studies on electricity-based applications (e.g., electronic devices, water
5 sterilization, etc.) have been reported. In addition, to supply the electrical power,
6
7
8 biomechanical energy harvesting capable of overcoming temporal/spatial limitations has been
9
10
11
12
13
14
15 proposed as a significantly promising technology.

16
17
18
19 Given that, *Il. W. Tcho et al.* proposed a disk-based TENG, called a linear-to-rotational
20
21
22 TENG (LR-TENG), driven by abundant linear mechanical energy from human motion
23
24
25 (Figure 54(a)-(i)).⁵¹⁷ A well-designed gear system can also transform linear into rotational
26
27
28
29 mechanical energy to effectively generate tribo-electricity. Among various human motions,
30
31
32 the stepping motion is adopted for the downward force to the LR-TENG (Figure 54(a)-(ii)).
33
34
35 Hence, due to the integration of various mechanical elements, such as the one-way bearing,
36
37
38
39 gear, and rack, the LR-TENG can generate electrical energy. To compare the electrical output
40
41
42 of the LR-TENG and the vertical contact-separation TENG (V-TENG), the open-circuit
43
44
45 voltage of the V-TENG was measured under the same applied force. (Figure 54(a)-(iii)).
46
47
48 Therefore, the maximum electrical output energy of 194 μJ of the LR-TENG was achieved
49
50
51 with the gear system, which is approximately 100 times compared to the TENG without the
52
53
54 gear system.

55
56
57 To fabricate the wearable devices of the mechanical TENG systems, *Y. Yun et al.*
58
59
60 proposed a mechanical TENG system in which the exo-shoe TENG (ES-TENG) is a

1
2
3
4 reasonably designed power transmission unit for wearable device incorporating the bi-
5
6
7
8 directional gear-train and one-way clutch (Figure 54(b)-(i)).⁵¹⁸ In this case, the ES-TENG can
9
10
11 convert the linear motion, which is based on the reciprocating stepping motion with a high
12
13
14 force, short displacement, and low frequency, into the TENG-friendly motion with a low
15
16
17 force, large displacement, and high-frequency thanks to the mechanical system. In addition,
18
19
20 the combination of the torsion spring and the one-way clutch can successfully work to
21
22
23 produce electricity continuously with the unidirectional operation regardless of the rotation
24
25
26 direction of the lever (Figure 54(b)-(ii)). In the absence of a mechanical gear system of the
27
28
29 ES-TENG, the maximum output is similarly output voltage, but the amount of generated
30
31
32 energy is significantly reduced due to the intermittent contact/separation (Figure 54(b)-(iii)).
33
34
35
36
37
38 In contrast, the open-circuit voltage of the ES-TENG was measured and calculated as the
39
40
41 RMS value of 160 V, indicating that the ES-TENG is capable of generating a voltage of 160
42
43
44 V from the biomechanical energy during daily walking (Figure 54(b)-(iv)).
45
46
47

48
49
50
51
52
53
54
55
56
57
58
59
60
There are straightforward linear motions in the actual environment, but there are also linear motions with several degrees of freedom that are difficult to harvest, such as biomechanical movements. To overcome the abovementioned limitation, *S. Cho et al.* introduce a type of mechanical TENG system with an incorporated transmission unit for converting linear to

1
2
3
4 rotational motion. Among the various mechanical components, a string serves the most
5
6
7
8 crucial role in freely transferring power regardless of direction and displacement of various
9
10
11 linear motions at each joint of the body (Figure 54(c)-(i)).⁵¹⁹ Thanks to the inherent flexibility
12
13
14 of the string, the present direction-switchable triboelectric nanogenerator (STRING) can
15
16
17 universally harvest multi-directional and multi-displacement motions of diverse joints.
18
19
20
21 Moreover, the STRING also adopted a gear-train with a gear ratio of $N (= 1:44)$ to enhance
22
23
24 the output performance. The operation mechanism including the unidirectional rotation of the
25
26
27 STRING (Figure 54(c)-(ii)). Briefly, when an external force is applied to the string, which is
28
29
30 wound around the converter, the shaft combined with the converter and driving gear rotate.
31
32
33
34 Due to the high gear ratio, the shaft integrated with the driven gear rotates at high speed,
35
36
37 resulting in the enhancement of the output performance of the STRING. The superiority of
38
39
40 the STRING, indicating that biomechanical energy can be effectively harvested except for
41
42
43 energy losses due to inevitable string-housing friction for omnidirectional linear motion
44
45
46
47
48 (Figure 54(c)-(iii)).
49

50
51 Recently, a more developed biomechanical energy harvester that can be easily carried as a
52
53
54 portable device are also proposed. *Y. Gai et al.* reported a fitness gyroscope nanogenerator
55
56
57 (fg-NG) that can effectively harvest the biomechanical energy with a low-frequency human
58
59
60

1
2
3
4 movement to charge batteries and power portable electronics as an auxiliary power source
5
6
7
8 (Figure 54(d)-(i)).⁵²⁰ The internal flywheel of gyroscope of the fg-NG can dramatically
9
10
11 surpass 8,000 rpm with hand operation, increasing the frequency by more than 280 times.
12
13
14 The working principle of the fg-NG is based on the precession whirling of the flywheel
15
16
17 spinning at high speed (Figure 54(d)-(ii)). Thus, the continuous output voltage and current of
18
19
20 the fg-NG during hand operation were measured (Figure 54(d)-(iii)). With the produced
21
22
23
24 electrical energy, the feasibility of the fg-NG can be verified by supplying electrical power to
25
26
27
28 wearable electronics, such as smart bracelets and mobile phones.
29
30
31
32
33
34
35
36
37
38
39
40
41
42
43
44
45
46
47
48
49
50
51
52
53
54
55
56
57
58
59
60

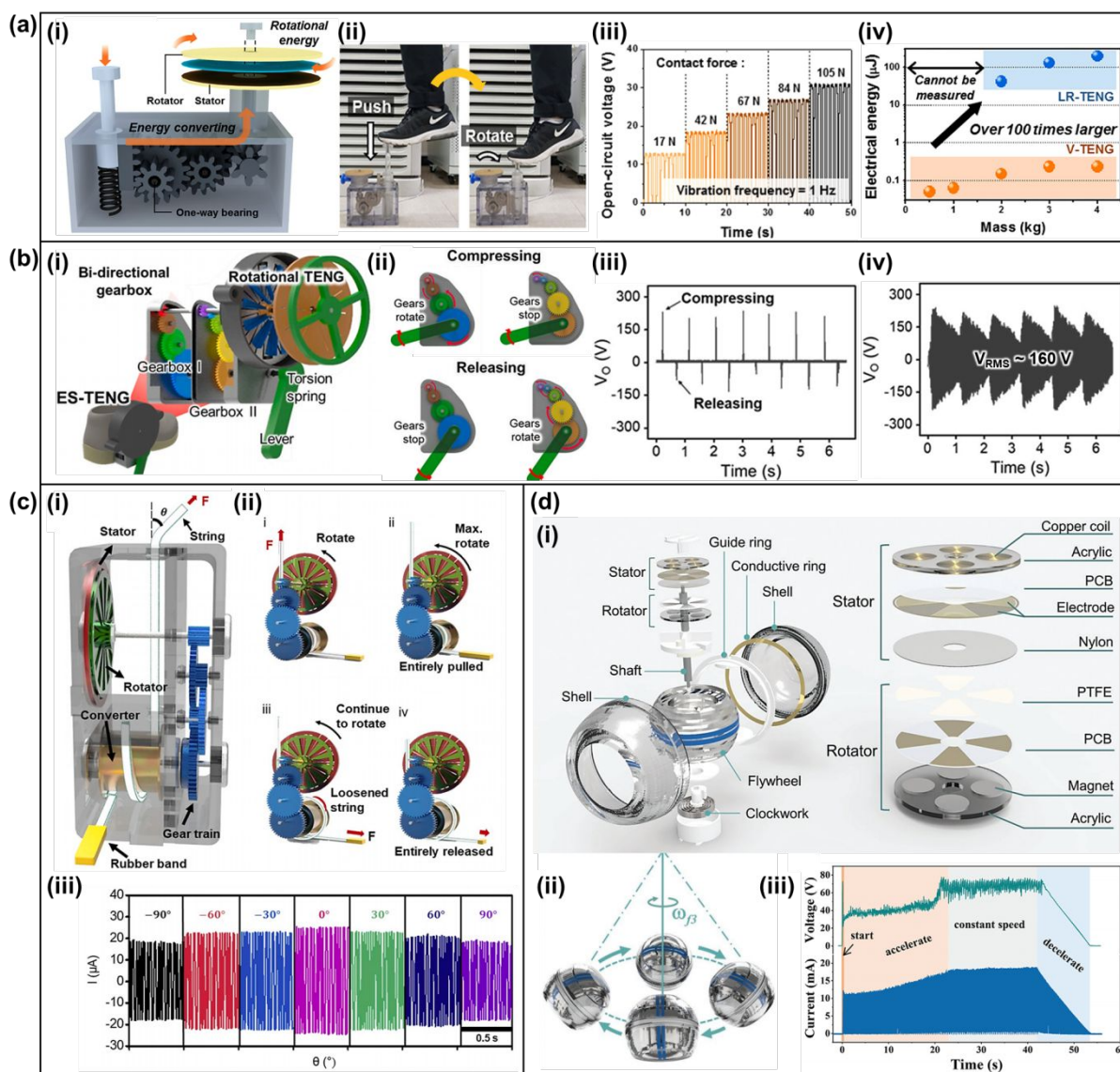


Figure 54. Mechanical TENG systems designs to convert the linear motion of biomechanical energy into rotational motion. **(a)-(i)** Schematic illustration of the LR-TENG. **(a)-(ii)** The photograph of the operation with the LR-TENG in real. **(a)-(iii)** The short-circuit current of the LR-TENG. **(a)-(iv)** The comparison of the output electrical energy of the LR-TENG with/without gear system. **Reproduced with permission from ref. 517, Copyright 2018 Elsevier B. V.** **(b)-(i)** The illustration of the ES-TENG equipped with the gear-train. **(b)-(ii)** The working mechanism of the gear-train in the ES-TENG. The open-circuit voltage of the ES-TENG **(b)-(iii)** without the gear-train and **(b)-(iv)** without the gear-train. **Reproduced with permission from ref. 518, Copyright 2021 Elsevier B. V.** **(c)-(i)** Schematic diagram of the STRING. **(c)-(ii)** The operation mechanism of the STRING including the gear-train and one-way clutch. **(c)-(iii)** The output current graph of the STRING under different angles of the input force. **Reproduced with permission from ref. 519, Copyright 2020 Elsevier B. V.** **(d)-(i)**

1
2
3
4 Structural design of the fg-NG. **(d)-(ii)** Trajectory of the gyroscopic device during the
5 operation by hand. **(d)-(iii)** The continuously generated output voltage and current of the fg-
6 NG during the operation by hand. **Reproduced with permission from ref. 520, Copyright 2022**
7
8
9 **Wiley-VCH.**
10
11
12
13
14
15
16
17
18
19
20
21
22
23
24
25
26
27
28
29
30
31
32
33
34
35
36
37
38
39
40
41
42
43
44
45
46
47
48
49
50
51
52
53
54
55
56
57
58
59
60

4.1.2 Rotational to linear motion transformation

Many studies on mechanical TENG systems based on the sliding mode for harvesting rotational movements, which is one of the operating mechanisms in the TENG, have been reported. Although the aforementioned mechanical TENG systems enable effectively producing sufficient output performance, these kinds of rotational TENGs with sliding mechanisms have a critical limitation in long-term use and persistent high energy conversion efficiency due to the high number of contact-separation and friction.⁵²¹⁻⁵²⁴ Hence, it is necessary to transform rotational motion into vertical linear motion by employing various mechanical elements. In this regard, *T. Cheng et al.* proposed a cam and a movable frame-based triboelectric nanogenerator (CMF-TENG) that can transform rotational into linear motion for vertical contact-separation TENG (Figure 55(a)-(i)).⁵²⁵ The CMF-TENG can consistently generate the output performance by linearly moving the movable frame from the rotation of the cam. Thus, the open-circuit voltage and the short-circuit current were measured under different rotation speeds. Consequently, the CMF-TENG is durable even after 86,400 contact-separation (Figure 55(a)-(ii)). Therefore, the mechanical design that converts the rotational motion into linear motion is essential to maintain a long lifespan and consistent output performance. Similarly, *T. Cheng et al.* present a ratchet-like wheel-based

1
2
3
4 and spring-assisted sustainable triboelectric nanogenerator (RS-TENG) to harvest rotational
5
6
7
8 mechanical energy (Figure 55(b)-(i)).⁵²⁶ The RS-TENG consists of a ratchet and a pawl,
9
10
11 which are often used to form a one-way intermittent feed in machine tools, indicating that this
12
13
14 mechanical design of RS-TENG is mainly expected to reduce the abrasion between the
15
16
17 interfacial friction layers by transforming the rotational into linear motion. Thus, the open-
18
19
20 circuit voltage of the RS-TENG was evaluated depending on the structural designs of the
21
22
23 ratchet-like wheels with 6, 9, and 12 teeth, so that the electrical output frequency can be
24
25
26
27
28 adjusted on the purpose (Figure 55(b)-(ii)).
29
30

31
32 In another way to transform rotational into linear motion, *K. Han et al.* presented radial
33
34 engine-shaped TENGs inspired by the piston motion of an automobile engine for self-
35
36
37 powered NO_x absorption (Figure 55(c)-(i)).⁵²⁷ Since the radial engine-shaped TENG includes
38
39
40
41 five gas chambers in a plane. Hence, a piston-like stacked structure with eight TENGs in
42
43
44 parallel can also generate electricity by converting rotational motion into linear motion
45
46
47 (Figure 55(c)-(ii)). With the radial engine-shaped TENG, the output performance of five
48
49
50 stacked TENGs, such as output voltage and current, can be steadily generated at the rotation
51
52
53 frequency of 3 Hz, indicating that the linear motion of the presented mechanical TENG
54
55
56
57
58 system has also the benefit of high durability (Figures 55(c)-(iii) and 55(c)-(iv)).
59
60

1
2
3
4
5 In the other case, *J. Qian et al.* reported a seesaw-structured triboelectric nanogenerator
6
7
8 (S-TENG) integrated with the rotating machinery for long-term, sustainable, and durable
9
10
11 operation (Figure 55(d)-(i)).⁵²⁸ The permanent magnets were affixed to the side plane of each
12
13
14 circular disk at a particular distance from the bottom of the S-TENG. In accordance with the
15
16
17 magnetic-coupling force, the rotating magnets on the disk enable the S-TENG to operate by
18
19
20 transforming a periodic rotational motion into linear motion, resulting in the vertical contact-
21
22
23 separation for electricity generation. The electrical output performance of the S-TENG with
24
25
26 the pyramid-type PDMS, which is a method to improve output performance due to the higher
27
28
29 charge density and increased contact area, was measured at a rotation speed of 300 rpm
30
31
32 (Figures 55(d)-(ii) and 55(d)-(iii)). To characterize the relation between rotation speed and
33
34
35 output power density, they conducted an experiment by varying the rotation speed and
36
37
38 magnetic field strengths (Figure 55(d)-(iv)). Since the contact force between the pyramid-
39
40
41 PDMS and electrode of the S-TENG was reduced with an increased rotation rate, the average
42
43
44 output power density was decreased slightly. However, the polymer morphology of the
45
46
47 pyramid-PDMS can be maintained for a long time thanks to the transformed linear contact
48
49
50 and separation, resulting in a significant improvement in durability and reliability of the S-
51
52
53
54
55
56
57
58 TENG.
59
60

1
2
3
4
5
6
7
8
9
10
11
12
13
14
15
16
17
18
19
20
21
22
23
24
25
26
27
28
29
30
31
32
33
34
35
36
37
38
39
40
41
42
43
44
45
46
47
48
49
50
51
52
53
54
55
56
57
58
59
60

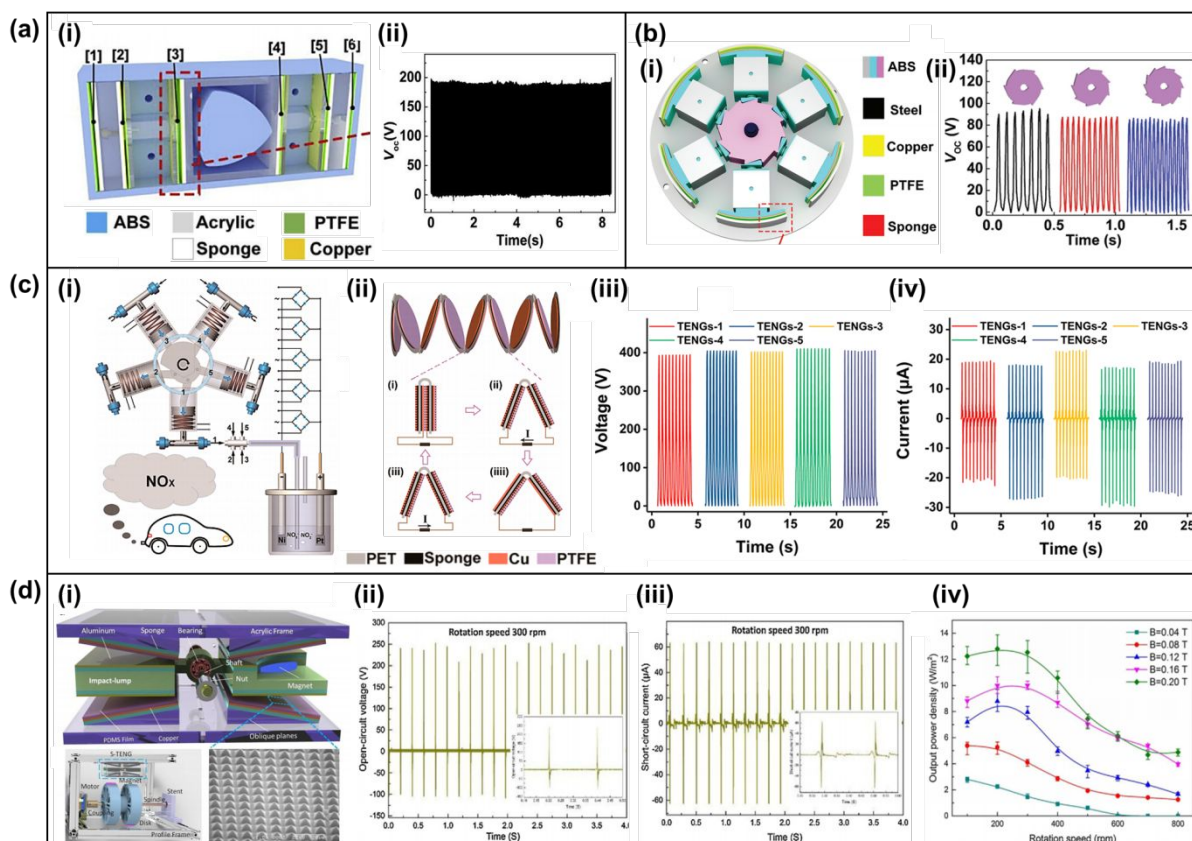


Figure 55. Mechanical TENG systems designs to convert the rotational into linear motion. **(a)-(i)** Illustration of the CMF-TENG. **(a)-(ii)** The open-circuit voltage graph to demonstrate outstanding robustness and durability of the CMF-TENG. **Reproduced with permission from ref. 525, Copyright 2019 Elsevier B. V.** **(b)-(i)** Scheme of the constructional design of the RS-TENG. **(b)-(ii)** The open-circuit voltage of the RS-TENG under the 6-, 9-, and 12-tooth ratchet-like wheels at 150 rpm. **Reproduced with permission from ref. 526, Copyright 2019 Wiley-VCH** **(c)-(i)** Schematic of the radial-engine-shaped TENG. **(c)-(ii)** The operation mechanism of the stacked TENGs in the unit of the radial-engine-shaped TENG. The output measurement of **(c)-(iii)** open-circuit voltage and **(c)-(iv)** short-circuit current of each TENG unit. **Reproduced with permission from ref. 527, Copyright 2020 American Chemical Society** **(d)-(i)** Schematic diagram of the S-TENG. **(d)-(ii)** Open-circuit voltage and **(d)-(iii)** short-circuit measurement of the S-TENG at 300 rpm. **(d)-(iv)** The output power density under various rotation speeds. **Reproduced with permission from ref. 528, Copyright 2017 Elsevier B. V.**

4.2 Frequency Regulation Systems

In this section, we introduce frequency regulation systems for efficiently harvesting wasted mechanical energy with low-frequency, irregular, and random signal characteristics. Most studies of TENGs from abundant wasted energy such as biomechanical motions,⁵²⁹⁻⁵³⁰ ocean tidal waves,⁵³¹⁻⁵³² air/water flows,⁵³³ and structural vibrations⁵³⁴ have inevitable limitations; output performances of TENGs are highly dependent on operating frequencies, but natural wasted energy is mostly low-frequency, irregular, and random.⁵³⁵⁻⁵³⁶ Therefore, the development of a mechanical system to regulate irregular mechanical motion into steady and regular motion is a challenging issue for practical applications of TENGs.

To address the aforementioned problem, *Oh et al.* suggested a long-lasting and steady TENG system using an escapement mechanism (EM-TENG).⁵³⁷ The EM-TENG utilizes the resonance effect to amplify the input movement, and a frequency regulating system based on the escapement mechanism to effectively modulate the output frequency of the movement because the resonance effect occurs only at the near resonance frequency. Figure 56(a) shows a schematic diagram, operating mechanism, and outperformance improvement of the EM-TENG. Figure 56(a)-(i) depicts the concept of frequency regulating systems. The EM-TENG consists of an energy storage part, an escapement mechanism part, and a rotational TENG

1
2
3
4 part. The energy storage part stores external rotational energy in a torsional hair spring and
5
6
7
8 rotates the gear to transfer the energy to the escapement mechanism part, preventing
9
10
11 unwanted energy loss by using a clutch bearing that can inhibit the rotation in the opposite
12
13
14 direction. When the hair spring is fully wound, torque is transferred to the escapement
15
16
17 mechanism part. The escapement wheel hits a pallet fork to induce rotational resonance of the
18
19
20 hair spring in the rotational TENG because the pallet fork marked as the yellow dashed box is
21
22
23 attached on the top side of the rotational TENG as shown in Figure 56(a)-(ii). The
24
25
26 comparison between the EM-TENG and R-TENG without the escapement mechanism was
27
28
29 conducted in an extremely low-frequency rotational motion of 0.067 Hz. The output voltage
30
31
32 and current of the EM-TENG were greatly improved over 100 times with the escapement
33
34
35 mechanism because the output characteristics of rotational TENGs are highly dependent on
36
37
38 the revolution speed. (Figures 56(a)-(iii) and 56(a)-(iv)) Most importantly, the EM-TENG
39
40
41 can be operated for 110 s even under only 5 s of short input rotational motion. In addition, to
42
43
44 prevent the expected wear problems in the rotational sliding mode TENG, a non-contact
45
46
47 rotating sliding mode TENG with freestanding interdigitated electrodes was applied to the
48
49
50 suggested rotational TENG part. Interdigitated electrodes induced a relatively higher
51
52
53 frequency of the output electrical signal than the input rotational motion of the rotor.
54
55
56
57
58
59
60

1
2
3
4 Therefore, the proposed EM-TENG can generate long-lasting and steady electricity even
5
6
7
8 under extremely low-frequency and deficient mechanical motion.
9

10
11 *He et al.* reported a mechanical regulator using a principle of auto-winding mechanical
12
13 watch for operating the TENG with constant alternating current (AC) output (CO-TENG)
14
15 even under low-frequency and irregular excitation.⁵³⁸ The suggested mechanical regulator-
16
17 based CO-TENG consists of a rack gear, a spiral spring, an escapement lever, a ratchet, and
18
19 sliding mode TENGs as shown in Figure 56(b)-(i). The mechanical energy of random linear
20
21 excitation in the natural environment can be collected as potential energy in a spiral spring
22
23 using the rack gear. Thus, the spiral spring drives the rotor of the sliding mode TENG with a
24
25 regular release of the rotational motion controlled by the escapement-spring-leaf mechanism.
26
27
28 (Figure 56(b)-(ii)) The ratchet rotates clockwise under the external excitation and transmits
29
30 the external force to the escapement lever, breaking the balance of the spring leaf system and
31
32 driving the escapement lever and mass block to rotate clockwise. When the escapement lever
33
34 and mass block reach the equilibrium position, and finally the spring leaf is totally relieved.
35
36
37 In this stage, the restoring moment is zero and the angular velocity is at its maximum. Finally,
38
39 the escapement lever and mass block rotate counterclockwise until they reach the left limit.
40
41
42
43
44
45
46
47
48
49
50
51
52
53
54
55
56
57
58 Notably, the rotating speed of the rotor of the TENG can be controlled by the vibration
59
60

1
2
3
4 frequency of the spring leaf and the number of the ratchet teeth, which induces a controllable,
5
6
7
8 stable, and continuous output speed of the rotor regardless of the external excitation.
9

10
11 Therefore, the constant and continuous energy harvesting performance was obtained by using
12
13
14 the sliding mode TENG by using a rotational motion of the rotor as shown in Figure 56(b)-

15
16
17
18 (iii). The constant AC output signals from mechanical excitation such as water wave, water
19
20
21 flow, and wind were also demonstrated to verify the potential application of energy
22
23
24 harvesting in random, irregular, and low-frequency wasted energy in natural environments.
25

26
27
28 To consider the hands-free operation of a frequency regulating mechanical system, *Pham*
29
30
31 *et al.* suggested an automatic switchable mechanical frequency regulator integrated with a
32
33
34 TENG (ASMFR-TENG).⁵³⁹ ASMFR-TENGs are comprised of gear-trains, a spiral-spring
35
36
37 (mainspring), a blocker-stopper unit, a TENG with a vertical contact-separation mode, and a
38
39
40 governor as shown in Figure 56(c)-(i). Importantly, gear-trains increase the input torque from
41
42
43
44 external energy to effectively wind the high-stiffness mainspring that temporarily stores
45
46
47
48 mechanical energy as potential energy and regularly releases energy toward the blocker-
49
50
51 stopper unit. The driven torque for winding the mainspring was designed to have 8.5 times
52
53
54 the input torque by selecting specific gear ratios in the gear-trains. Figure 56(c)-(ii) shows the
55
56
57
58 operating mechanism of automatic switching in the proposed mechanical system. In the
59
60

1
2
3
4 initial state, the stopper is stationary while the blocker connected to the input side shaft is
5
6
7
8 continuously rotating until the mainspring is fully charged. Thereafter, the notch in the
9
10
11 blocker enables the stopper to start rotating, thus the mainspring steadily releases the energy.
12
13
14 The output side shaft rotates and consequently operates the TENG at a regulated frequency
15
16
17 due to the cam connected to the output side shaft. For the cyclic operation of the frequency
18
19
20 regulating system, after the mainspring fully releases the energy, the blocker and stopper
21
22
23 reach their initial positions. At the bottom side, the graph shows the charging time of the
24
25
26 mainspring (t_{MC}) and TENG operating time (t_{TO}), and they vary depending on the rotational
27
28
29 input and the governor design, respectively. Figure 56(c)-(iii) depicts the detailed and
30
31
32 simplified structure of the governor. The authors systematically analyzed the effects of the
33
34
35 radius (r_G) and mass (M_G) of the total governor on the operating frequency and time of the
36
37
38 TENG considering the moment of inertia of the governor and the torque on the output side
39
40
41 shaft. Therefore, the frequency regulating mechanical systems take advantage of multiplying
42
43
44 operating frequencies and effective torque or force transfer to greatly enhance the output
45
46
47 performance of the TENG. In particular, frequency regulating mechanical systems should be
48
49
50 considered and applied in the mass production of TENG-based products for industrialization
51
52
53
54
55
56
57
58
59 as the next-generation future application of renewable energy harvesting technology.
60

1
2
3
4
5
6
7
8
9
10
11
12
13
14
15
16
17
18
19
20
21
22
23
24
25
26
27
28
29
30
31
32
33
34
35
36
37
38
39
40
41
42
43
44
45
46
47
48
49
50
51
52
53
54
55
56
57
58
59
60

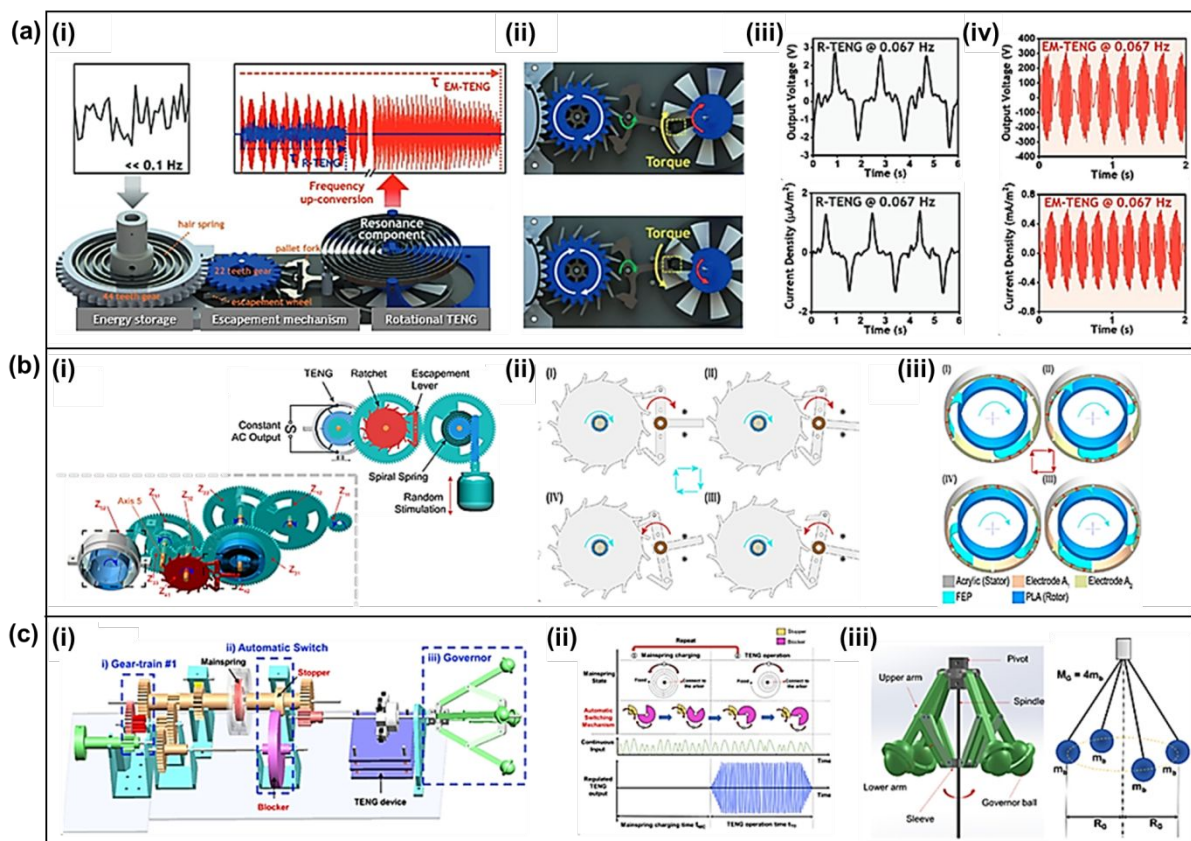


Figure 56. Frequency regulating mechanical systems based TENGs and their operating mechanisms. (a)-(i) Schematic diagram of EM-TENG, (a)-(ii) operating mechanism of the EM-TENG, and comparison of output performance between (a)-(iii) R-TENG without escapement mechanism and (a)-(iv) EM-TENG. Reprinted with permission from ref. 537, Copyright 2021, John Wiley and Sons. (b)-(i) Schematic diagram of CO-TENG, (b)-(ii) schematic illustration of escapement-spring-leaf mechanism, and (b)-(iii) operating mechanism of sliding mode TENGs. Reprinted with permission from ref. 538, Copyright 2021, Elsevier. (c)-(i) Schematic diagram of ASMFR-TENG, (c)-(ii) operating principle of blocker and stopper, and (c)-(iii) design parameters of governor for optimization of operating time of TENG. Reprinted with permission from ref. 539, Copyright 2021, Elsevier.

4.3 Resonant Systems

The definition of resonance is that a physical system vibrates at specific frequencies and wavelengths, called resonant frequencies and resonant wavelengths,⁵⁴⁰ with greater amplitude than other frequencies and wavelengths. The very small periodic vibrations with resonant frequencies and resonant wavelengths can produce large vibrations due to the storage of the system kinetic energy. When the resistance is very small, the resonant frequency and wavelength are approximately equal to the intrinsic frequency and wavelength of the system, which are the frequencies and wavelengths at free oscillation.⁵⁴¹

The resonance phenomenon has some negative effects in some environments, while it is more convenient for human life. In terms of the mechanical system, when the excitation frequency reaches the intrinsic frequency, the system amplitude increases significantly, absorbing more energy from the surrounding environment. At this time, the excitation input energy reaches its largest value, and the system exhibits obvious displacement resonance, which provides great convenience for the recycling of energy.⁵⁴²⁻⁵⁴³ The essence of resonance in a circuit system is that the energy of the electric field in the capacitor and the energy of the magnetic field in the inductor are converted to each other, increasing and decreasing to fully compensate for each other.⁵⁴⁴⁻⁵⁴⁵ The distinctive feature of resonant circuits is their ability to select frequencies allowing useful frequency components to be retained and useless ones to be filtered out. It is extremely suitable for signal transmission and is indispensable in various radio devices, equipment, and measuring instruments. Therefore, the resonance principle has been well applied in the field of energy capture and signal transmission.

4.3.1 Energy harvesting based on resonant assisted system

4.3.1.1 Acoustic energy harvesters

To collect high entropy energy from the environment, Wang et al. developed an acoustic core-shell resonant harvester based on the piezoelectric triboelectric effect that can be used in cochlear implants using piezoelectric ceramic particles and porous piezoelectric polymers, as shown in Figure 57.²⁹ This acoustically driven resonant acquisition device greatly increases the short-circuit current and open-circuit voltage and plays a key role in smart cochlear and acoustic wave acquisition. Xie et al. developed a nanogenerator (ANG) with integrated piezoelectric and triboelectric effects for broadband acoustic energy harvesting.³² The device has an operating bandwidth from 110 Hz to 400 Hz and is capable of directly illuminating 7 LEDs in series. The energy collector has a simple and effective mechanical structure design, which realizes flexible and stable acoustic energy collection. It provides an effective solution to further realize the efficient collection of acoustic waves. Xu et al. proposed a triboelectric nanogenerator (MH-TENG) based on a multi-tube parallel Helmholtz resonator,⁵⁴⁶ which can harvest acoustic energy in low-frequency noise environments. The core materials of the device are aluminum, FEP film, and carbon, which have good power generation performance and can power low-power components in environments such as machine shops, railroads, and computer rooms.

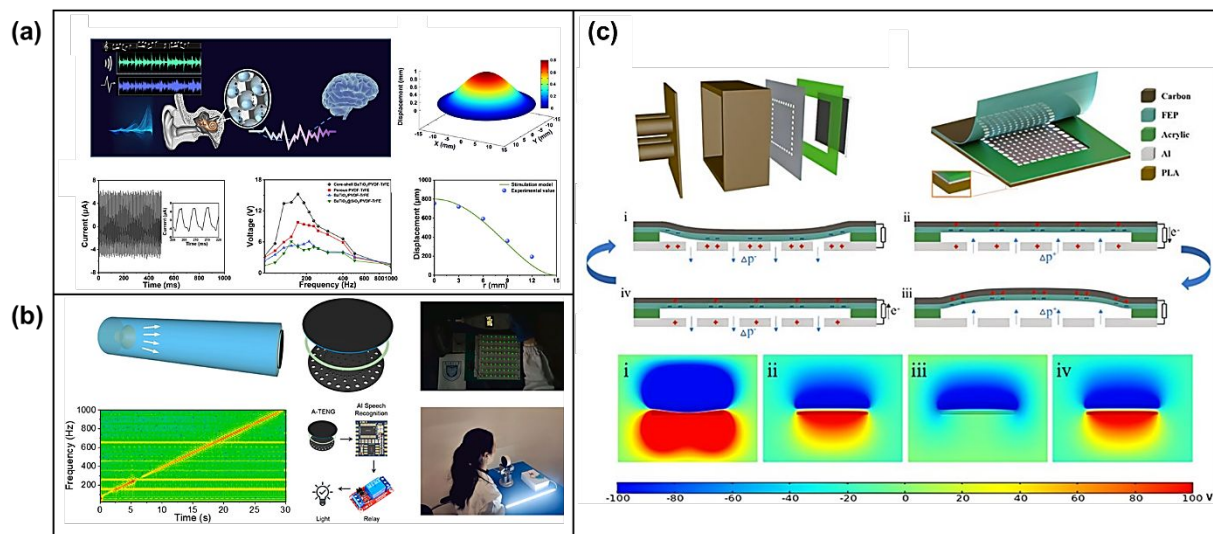


Figure 57. Harvesting acoustic energy using resonance principle (a) Acoustic harvest membrane working mechanism schematic diagram for use as an artificial cochlea. **Reprinted with permission from ref. 29, Copyright 2021, American Chemical Society.** (b) Schematic diagram of the acoustic energy harvesting system. **Reprinted with permission from ref. 32, Copyright 2022, Elsevier.** (c) Multi-tube Helmholtz resonator triboelectric nanogenerator schematic diagram for harvesting broadband acoustic energy. **Reprinted with permission under a Creative Commons CC BY license from ref. 546, Copyright 2022, Frontiers.**

4.3.1.2 Other energy harvesters

Vibration is ubiquitous in life and has become an attractive target for energy harvesting, and TENGs have made great achievements in vibration energy harvesting and self-powered sensing. As shown in Figure 58, *Xu et al.* developed a MFM based on triboelectric nanogenerators (TENGs).⁵⁴⁷ Its open circuit voltage is as high as 287.4 V, and the short-circuit current amplitude is 76.8 μA . The peak power density is 726.1 MWm^{-2} , which can effectively extract energy from ordinary environmental vibrations, including automobile engines and household furniture. In water wave energy harvesting, *Zhang et al.* designed a resonant triboelectric nanogenerator.²¹ It is composed of a single pendulum, a rotating drum, and a flexible ring. Due to the high damping motion of the single pendulum, the system has an excellent ability to capture low-frequency water wave energy. At the same time, due to the resonance effect and the shielding effect on water, the system can not only achieve all-around energy collection but provide a solution for the capture of large-scale blue energy. In terms of wearable devices, multi-functional metamaterials have an excellent ability in collecting vibration energy.⁵⁴⁸ *Xu et al.* Proposed a MFM based on triboelectric nanogenerators, composed of a local resonator, integrated contact separation mode TENG and spiral connecting beam. By establishing multiple physical models, theoretical analysis was carried out, and the ability of the structure to capture low-frequency vibration energy was further verified by experiments. It provides a theoretical model and analysis method for the design of a vibration energy capture device based on TENGs.

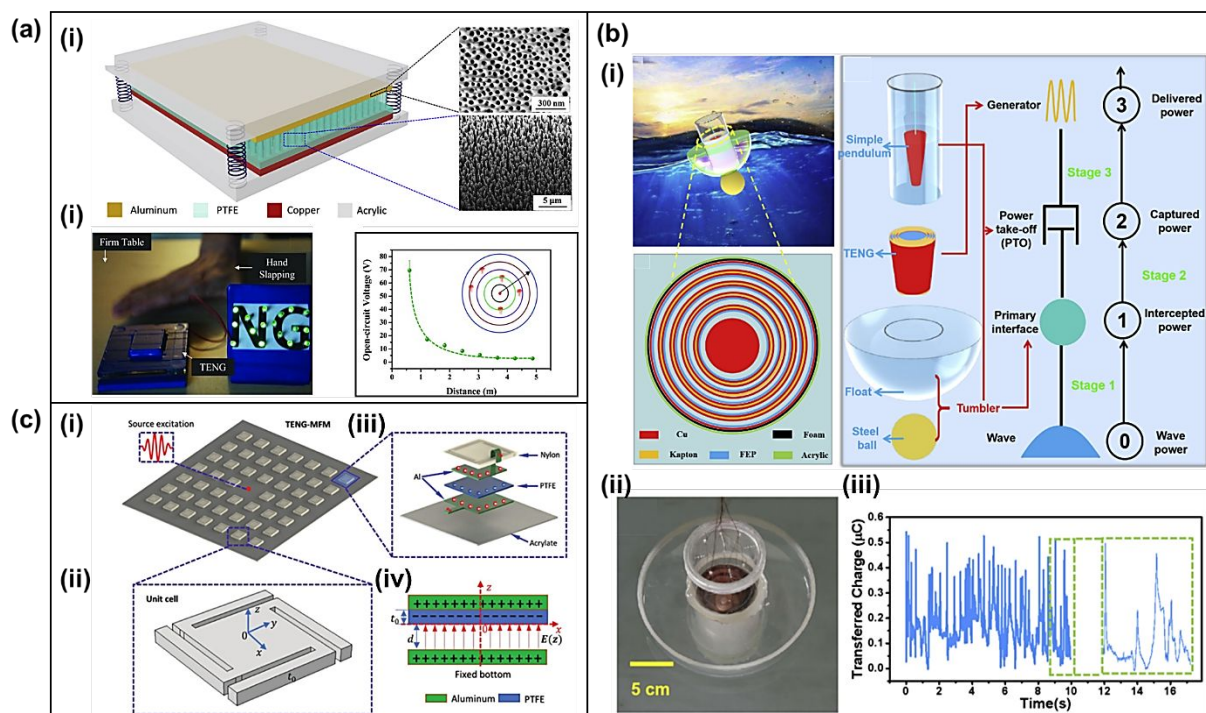


Figure 58. Vibration energy capture device based on TENG. **(a)-(i)** Harmonic-resonator-based triboelectric nanogenerator **(a)-(ii)** Collect desk vibration energy to light commercial LEDs **(a)-(iii)** Distance measurement and environmental vibration detection. **Reprinted with permission from ref. 547, Copyright 2022, Wiley.** **(b)-(i)** Structural design of AR-TENG system **(b)-(ii)** Photo of AR-TENG system in the water tank. **(b)-(iii)** Transferred charges of AR-TENG system in simulative water waves. **Reprinted with permission from ref. 21, Copyright 2022, Elsevier.** **(c)-(i)** Diagram of the TENG-MFM resonator array **(c)-(ii)** Geometric figure of the individual resonator. **(c)-(iii)** An illustration of the unit cell's layered structure. **(c)-(iv)** Schematic diagram of the working mode. **Reprinted with permission from ref. 548, Copyright 2022, Wiley.**

1
2
3
4 TENGs can not only capture the vibration energy in the environment to power micro nano-
5
6 electronic devices but also act as a self-powered vibration sensors to monitor the surrounding
7
8 environment. As shown in Figure 59, *Wang et al.* proposed a contact separation mode
9
10 triboelectric nanogenerator for quantitative measurement of amplitudes (CF-TENG).⁵⁴⁹ The
11
12 structure consists of acrylic acid as the substrate, 8 springs as the connection support, and
13
14 aluminum electrodes and FEP as the contact materials. Through this contact separation mode,
15
16 the sensed vibration of the external environment is converted into electrical signal output, to
17
18 achieve the purpose of monitoring amplitude. CF-TENG can feel very subtle vibration with
19
20 amplitude as low as 3.5 μm . Captured vibrational energy can also be used to monitor
21
22 cracks.⁵⁵⁰ The paper studied a wire-type triboelectric resonator (WTER) for monitoring
23
24 cracks. The structure converts the vibration of the metal wire on the dielectric film into a
25
26 triboelectric electric signal, which has a good matching relationship with the resonance
27
28 frequency the effects of tension, linear density, and wire length on the resonance frequency of
29
30 WTER were studied. The results show that the sensitivity of the sensor is mainly influenced
31
32 by the length and tension of the wire. The researchers developed an independent WTER
33
34 system based on this. Under the condition of using 30 cm wide and 0.967 g/m linear density,
35
36 the sensitivity was 300 Hz/mm, and the elongation was less than 1 mm, which proved that the
37
38 resolution of A-WTER was less than 100 μm . In the future, the A-WTER system could be
39
40 used to monitor cracks on a structural level using self-powered sensors.
41
42
43
44
45
46
47
48
49
50
51
52
53
54
55
56
57
58
59
60

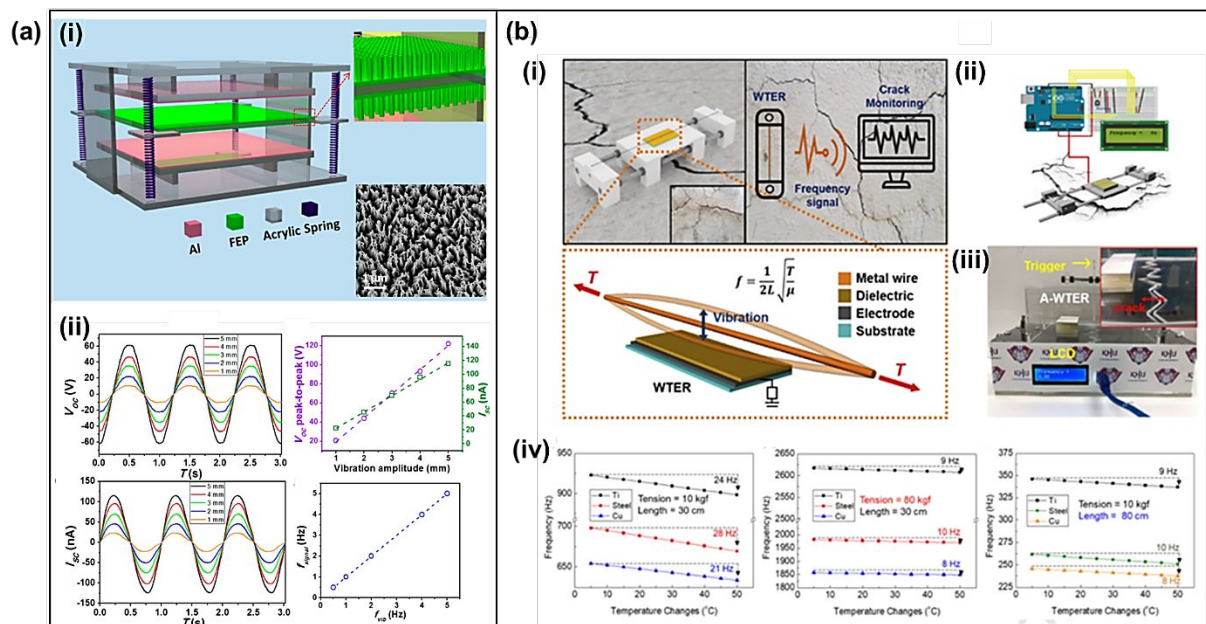


Figure 59. Environmental monitoring structure based on TENG. **(a)-(i)** Structural diagram of triboelectric nanogenerator in contact-separation mode. **(a)-(ii)** Output characteristic curve of the system driven by a linear motor. Reprinted with permission from ref. 549, Copyright 2014, American Chemical Society. **(b)-(i)** Concept and structural design of the WTER used to monitor a crack. **(b)-(ii)** Integrated System Schematic (A-WTER). **(b)-(iii)** A-WTER integrated crack model photograph. **(b)-(iv)** Environmental stability of the A-WTER. Reprinted with permission from ref. 550, Copyright 2022, Elsevier.

4.3.2 Signal transmission based on resonant assisted system

Wireless sensor systems that are self-powered have become very popular in the information age and are widely used in many applications. As shown in Figure 60, *Tang et al.* proposed a wireless traffic monitoring system based on fully self-powered triboelectric nanogenerator (TENG) for real-time monitoring of traffic conditions on sidewalks or non-motorized lanes.⁵⁵¹ Wireless traffic monitoring is capable of accurately identifying pedestrians and electric motorcycles and calculating foot traffic on sidewalks. It can also monitor the speed of motorcycles with an accuracy rate of over 94%. *Tan et al.* developed a passive wireless triboelectric sensor (PWTES) using a triboelectric nanogenerator (TENG) and a surface acoustic wave resonator (SAWR).⁵⁵² PWTES demonstrated wireless transmission of sensing signals over a distance of 2 m, with a sensitivity of 23.75 kHz/V in the 0-5 V voltage range of TENG and a measurement update rate of 12 kHz, fully utilizing TENG's sensing capabilities. advantages, and the great potential of SAWR in wireless communications. *Le et al.* proposed a parsimonious multimodal contactless interface that simultaneously detects stable and instantaneous finger movements.⁵⁵³ Triboelectric sensors can quickly reflect multi-directional finger movements by outputting different voltage waveforms from their two electrodes, while humidity sensors can provide a stable and continuous real-time response to finger movements through changes in their resonant frequency. Using this fusion of technologies, a touchless interface can be designed with minimal configuration, multimodal sensing capabilities, and high-dimensional response. It has been successfully applied to the control of VR cars and the entry of 3D passwords utilizing intuitive finger interaction.

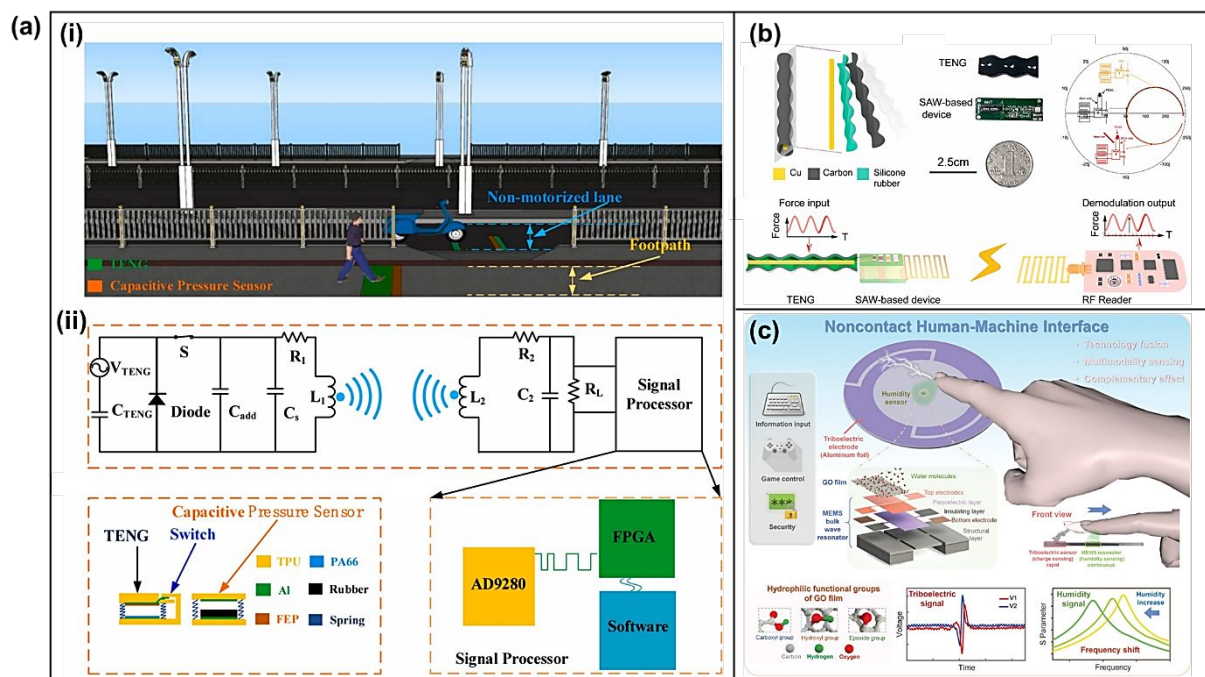


Figure 60. (a)-(i) Schematic diagram of the application of the TENG-based wireless traffic monitoring system. (a)-(ii) Equivalent circuit diagram of the wireless sensor system. Reprinted with permission from ref. 551, Copyright 2022, Elsevier. (b) Schematic diagram of PWTES structure. Reprinted with permission from ref. 552, Copyright 2022, Elsevier. (c) Schematic illustration of the HMI consisting of a MEMS bulk wave resonant humidity sensor and a triboelectric sensor. Reprinted with permission under a Creative Commons CC BY license from ref. 553, Copyright 2022, John Wiley and Sons.

4.3.3 Design criteria and its guideline for resonance occurrence

1
2
3
4
5
6
7
8
9
10
11
12
13
14
15
16
17
18
19
20
21
22
23
24
25
26
27
28
29
30
31
32
33
34
35
36
37
38
39
40
41
42
43
44
45
46
47
48
49
50
51
52
53
54
55
56
57
58
59
60

Triboelectric nanogenerators based on the resonance principle can be utilized as an energy trap or sensor due to the intrinsic frequency closing to the ambient excitation frequency. The definition of intrinsic frequency is the displacement of an object that vibrates freely with time according to a sine or cosine law, independent of the initial conditions and related to the intrinsic properties of the system. Therefore, the designer needs to understand what factors can influence the system's intrinsic frequency for the system to achieve a more ideal operating condition in a particular environment. The dimensions of the resonant body or resonant cavity (e.g., elasticity, area, length, etc.), material properties (texture, lattice structure), temperature, hardness, and environmental reference or pivot point can affect the system's intrinsic frequency. The vibration of matter is a complex science, and the mysteries of theory and application need to be explored by more researchers.

5. Power management for TENGs

Triboelectric nanogenerators (TENGs) have large input impedance ($\sim M\Omega$) due to the existence of intrinsic capacitance. TENG output characteristics typically offer high voltage, a few hundred volts, and low output current at $\sim \mu A$ level, thereby rendering their direct usage for either powering conventional low-impedance electronics applications or charging energy-storage units.⁵⁵⁴ Therefore, designing an efficient power management circuit is of great importance for the TENGs toward providing practical solutions for self-powered microsystems-based applications. In this direction, several strategies of power management have been extensively explored, such as inductive and capacitive transformers, switched-capacitors convertors, and MOSFET power convertors.

5.1 Inductive and capacitive transformers

In this section, we review inductive and capacitive transformers for TENGs. Inductive transformers are widely used in the power industry can effectively reduce the output impedance of TENG. Capacitive transformers can reduce the open circuit voltage and improve the transferred charge of TENG multiple times. Hence, the inductive and capacitive transformers can improve energy utilization efficiency.

5.1.1 Inductive transformers

In 2014, Zhu *et al.* developed a radial-arrayed rotary TENG (Figure 61(a)-(i)).⁵⁵⁵ The central angle of each sector unit is 3° , and the rotator has a total of 60 units, which can increase the rotation frequency by 60 times. At a rotation rate of 3,000 rpm, the radial-arrayed rotary TENG has a high output power of 1.5 W at an efficiency of 24%. Through a power management circuit consisting of an inductive transformer, a rectifier, a voltage regulator, and capacitors (Figure 61(a)-(ii)), the output of the radial-arrayed rotary TENG can be regulated in a DC output at a constant voltage of 5 V in less than 0.5 s after the radial-arrayed rotary TENG starts to operate, as shown in Figure 61(a)-(iii). The radial-arrayed rotary TENG can be applied not only to self-powered electronics but also possibly to power generation at a large scale. In 2015, Han *et al.* prepared a disk-structured TENG based on printed circuit board (PCB) technology.⁵⁵⁶ The TENG is operated at a rotation rate of 1,000 rpm and produced a high output power density of 267 mW/cm². With an inductive transformer, the output power can be managed and be used to charge a battery for a smart phone directly.

With the reduced output voltage and increased output current, inductive transformers have been used to charge batteries.⁵⁵⁷⁻⁵⁵⁹ For example, in 2015, Pu *et al.* demonstrated feasible and efficient charging of Li-ion batteries by a rotating TENG with an inductive transformer.⁵⁵⁸

1
2
3
4 The circuit diagram is shown in Figure 61(b)-(i). With the increase of the transformer coil
5
6
7
8 ratio, the output current increases gradually (Figure 61(b)-(ii)). With a transformer coil ratio
9
10
11 of 36.7, about 72.4% of the power generated by the TENG at 250 rpm can be stored in a
12
13
14 $\text{LiFePO}_4\text{-Li}_4\text{Ti}_5\text{O}_{12}$ battery (Figure 61(b)-(iii)). Considering the readily scaled-up capability
15
16
17
18 of TENG, promising applications in personal electronics can be anticipated.
19
20
21
22
23
24
25
26
27
28
29
30
31
32
33
34
35
36
37
38
39
40
41
42
43
44
45
46
47
48
49
50
51
52
53
54
55
56
57
58
59
60

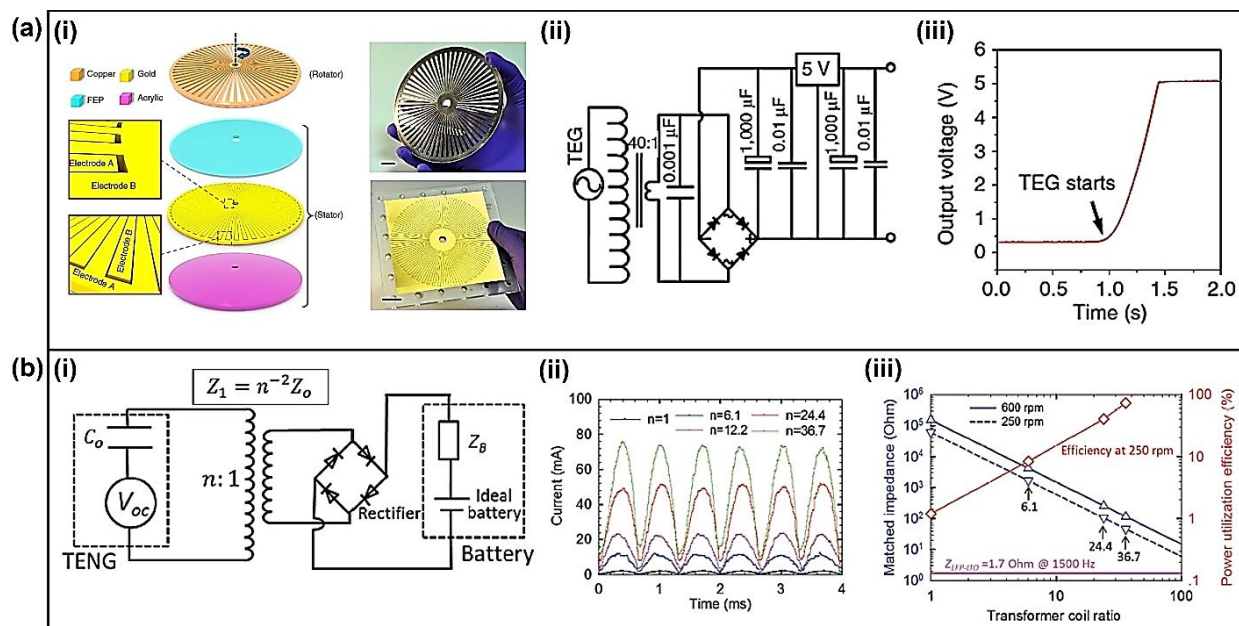


Figure 61. Inductive transformer for TENG. **(a)-(i)** Schematic illustrations of the radial-arrayed rotary TENG. **(a)-(ii)** Circuit diagram of the complete power-supplying system that consists of a triboelectric generator and a power management circuit. **(a)-(iii)** Output voltage of the system reaches a constant value of 5V in less than 0.5 s as the triboelectric generator starts to rotate at 3,000 r/min. **Reprinted with permission from ref 555. Copyright 2014 Springer Nature.** **(b)-(i)** The equivalent circuit of battery charging by the TENG with the aid of a transformer and a rectifier. **(b)-(ii)** Rectified currents of the TENG at the same rotating speed (250 rpm) but with different transformers ($n = 1, 6, 12, 24,$ and 36). **(b)-(iii)** The effect of the transformer coil ratio on matched impedances of the TENG, and the power utilization efficiency of the TENG at 250 rpm when charging an LFP–LTO full cell. **Reprinted with permission under a Creative Commons CC BY license from ref. 558, Copyright 2015, John Wiley and Sons.**

1
2
3
4
5
6 In 2021, Wang *et al.* proposed an ultrahigh-voltage energy management unit consisting of
7
8
9 a spark switch and a matched home-made transformer.⁴²⁷ The circuit diagram and a photo
10
11
12 image of the energy management unit are shown in Figure 62-(i) and Figure 62-(ii),
13
14
15 respectively. With the tunable auto-spark switch, an ultrahigh voltage of over 7.5 kV was
16
17
18 established, which guarantees energy accumulation and fast release. With this energy
19
20
21 management unit, TENG can continuously power a wireless sensors network at 1 Hz (Figure
22
23
24 62-(iii)). The fast release of energy increases the frequency. The average output power in
25
26
27 constant mode at 1 Hz with the energy management unit at 200 k Ω is 78.5% of output power
28
29
30 without the energy management unit at 35 G Ω (Figure 62-(iv)). This work would greatly
31
32
33 promote TENGs toward extensive practical applications. Though inductive transformers have
34
35
36 shown immense potential, but their relatively large size and the intrinsic requirement for a
37
38
39 higher working frequency restricts their use for a wider range of TENG-based applications.
40
41
42
43
44
45
46
47
48
49
50
51
52
53
54
55
56
57
58
59
60

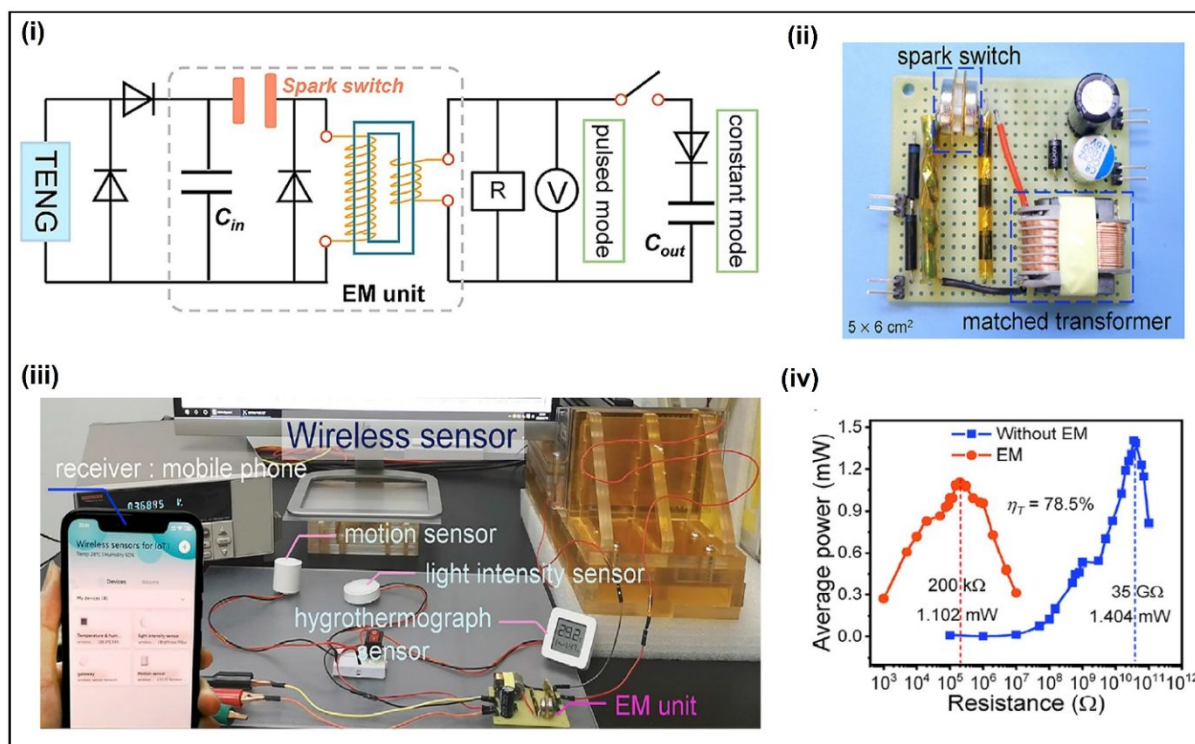


Figure 62. Inductive transformer for TENG with a spark switch. **(i)** Circuit diagram for TENG to drive external load at a pulsed mode or a constant mode. **(ii)** Image of the integrated matched energy management unit. **(iii)** Demonstration of the wireless transmission. **(iv)** Comparison of average output power with and without energy management unit. **Reprinted with permission from ref 427. Copyright 2021 Elsevier.**

5.1.2 Capacitive transformers

Different from the inductive transformer's requirement for the TENGs to operate at high frequency, the power management circuit based on capacitive transformer is independent of the working frequency. In 2014, Tang *et al.* designed a power-transformed-and-managed triboelectric nanogenerator (PTM-TENG), as depicted in Figure 63-(i) and Figure 63-(ii).⁵⁶⁰ The design is based on a synchronized mechanical agitation that not only drives the TENG but also switches the connections for the capacitors. The capacitors are in serial when be charged and in parallel during discharging. The experimental results are in agreement with the theoretical analysis, which means the output voltage be reduced N (the capacitor number) times while the output charges be enhanced N times (Figure 63-(iii) and Figure 63-(iv).). Moreover, the power supply efficiency is significantly improved when charging a 10 μF capacitor (Figure 63-(v)).

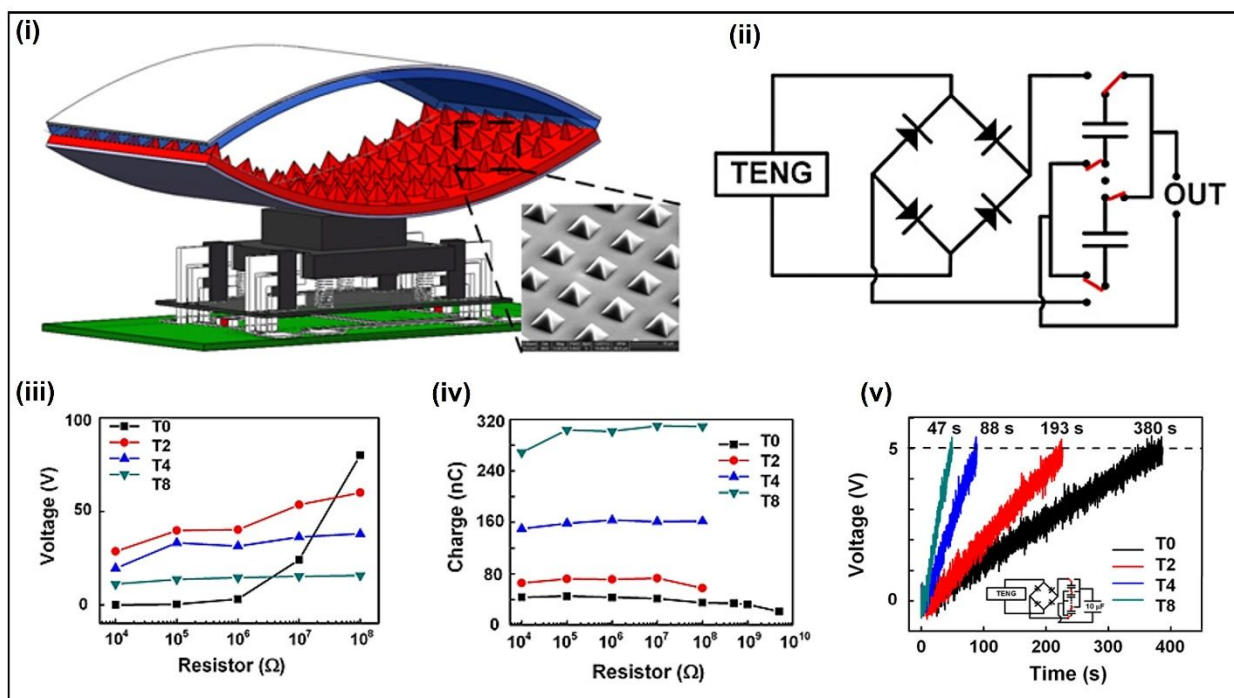


Figure 63. Capacitive transformers for TENGs. **(i)** 3D structure of the PTM-TENG. **(ii)** The equivalent circuit diagram of the PTM-TENG. **(iii)** Output voltages and **(iv)** charges of the T0, T2, T4, and T8 under various load resistances. **(v)** Time-dependent plot of charging a $10 \mu\text{F}$ capacitor to 5 V. Reprinted with permission from ref 560. Copyright 2014 Institute of Physics.

5.2 Switched-capacitor converters

TENG is a representative AC energy source with a relatively high voltage and low current characteristic compared to other energy harvesters. Therefore, both the low-current consumption and the proper voltage conversion ratio are necessary for the power management system that consists of an AC/DC converter for rectification and a DC/DC converter for supplying the energy to batteries or other applications. Especially, the DC/DC converter has more design issues than AC/DC converter because of its complex structure and operation.

There are three types of DC-DC converters as shown in Figure 64(a). A low dropout regulator⁵⁶¹ (linear regulator) can be easily implemented because of its simple structure however, it is not suitable for the power management system that requires a high voltage conversion ratio because the high dropout voltage degrades the power conversion efficiency.

As explained in the last section, inductive switching converter⁵⁶²⁻⁵⁶³ is widely used for the energy harvesting system owing to the high-power conversion efficiency and the wide voltage conversion ratio range. However, a bulky inductor and an electromagnetic noise are obvious disadvantages of the inductive power converter. On the other hand, a switched-capacitor (SC) converter changes the voltage ratio by using the series/parallel connection

1
2
3
4 among capacitors and it can not only achieve a small form factor with board-level design but
5
6
7
8 also integrate whole components on the small chip. Therefore, SC converter⁵⁶⁴ can be an
9
10
11 effective solution to overcome the limitations of the output characteristics of the TENGs.
12
13
14
15
16
17
18
19
20
21
22
23
24
25
26
27
28
29
30
31
32
33
34
35
36
37
38
39
40
41
42
43
44
45
46
47
48
49
50
51
52
53
54
55
56
57
58
59
60

5.2.1 Maximum power point of TENG and switched-capacitor converter

Every energy harvester has an optimal voltage and current value, which is called a maximum power point⁵⁶² (MPP), at which the largest energy can be extracted from the harvester in the same harvesting environment. Therefore, an SC converter topology that has many voltage conversion ratios is required because the power conversion efficiency is also maximized when the voltage conversion ratio of the SC converter is matched to the ratio between the MPP voltage and the target output voltage of the SC converter (Figure 64(b)).

Figure 64(c) shows the basic topologies of the SC converter.⁵⁶⁴ However, they need many switches and capacitors to make various voltage conversion ratios. The successive-approximation and recursive SC converter⁵⁶⁵⁻⁵⁶⁶ structure overcome the limitation of the number of the voltage conversion ratio by achieving the high-resolution SC converter with a small number of stages, but the complex switch and connection control need to be implemented by an integrated circuit (IC) for low-power consumption. However, the maximum operating voltage of the IC fabricated in the CMOS or BCDMOS process is smaller than 70 V and it becomes a limitation to track the MPP of the TENG.

5.2.2 Switched-Capacitor Converter for improving the charge extraction of the TENG

1
2
3
4 Figure 64(d) shows the power management of the TENG with the basic SC converter.⁵⁶⁷ The
5
6
7
8 operation of the system is very simple. In phase 1, the TENG charges capacitors in the series
9
10
11 connection through the full-wave rectifier. In phase 2, the mechanical switch controller
12
13
14 changes the capacitor connection from the series to the parallel and releases the charge to the
15
16
17
18 load.
19

20
21 A similar SC converter structure⁵⁶⁸ was applied to a sliding freestanding triboelectric-layer
22
23
24 mode TENG with a motion-triggered switch control (Figure 64(e)). In conjunction with the
25
26
27 theoretical analysis, the inductor-free power-management design improves the rate for
28
29
30 charging a super-capacitor by 5 times. Furthermore, this system also increases the output
31
32
33 charge of the TENG by increasing the conversion ratio of the SC converter. A wider voltage
34
35
36 conversion range is significant to cope with various input/output voltage conditions of the SC
37
38
39 converters. A fractal design-based switched-capacitor-convertors⁵⁶⁹(FSCC) that has a self-
40
41
42 similar geometrical structure was presented and the SC converter with the high voltage
43
44
45 conversion ratio can be easily implemented using this method. Figure 64(f) shows the fractal
46
47
48 design of 2^N . The number N is increased by replacing each capacitor with the 2^1 design
49
50
51 repeatably. The FSCC with 6-stages/96 voltage conversion ratio achieved 67 times higher
52
53
54
55
56
57
58 output charge compared to the output charge of the TENG with the direct connection.
59
60

1
2
3
4
5 The series/parallel connection of the capacitor can be also used to overcome the limitation
6
7
8 of the ICs by increasing the handling voltage over 70 V. A scalable multi-chip-stacked with
9
10
11 the switched capacitor technique⁵⁷⁰, as shown in Figure 64(g), was presented for enhancing
12
13
14 the charge extraction of the TENG. The proposed IC operated a synchronized switch
15
16
17 harvesting on the inductor (SSHI) method that reduces the charge loss caused by the internal
18
19
20 capacitor of the TENG during the rectification with the 130 V input voltage. The IC not only
21
22
23 achieved the 314% enhancement of the charge extraction of the TENG compared to the full-
24
25
26
27
28 bridge rectifier but also can increase the input voltage range with the additional stack of the
29
30
31
32 chip.
33
34
35
36
37
38
39
40
41
42
43
44
45
46
47
48
49
50
51
52
53
54
55
56
57
58
59
60

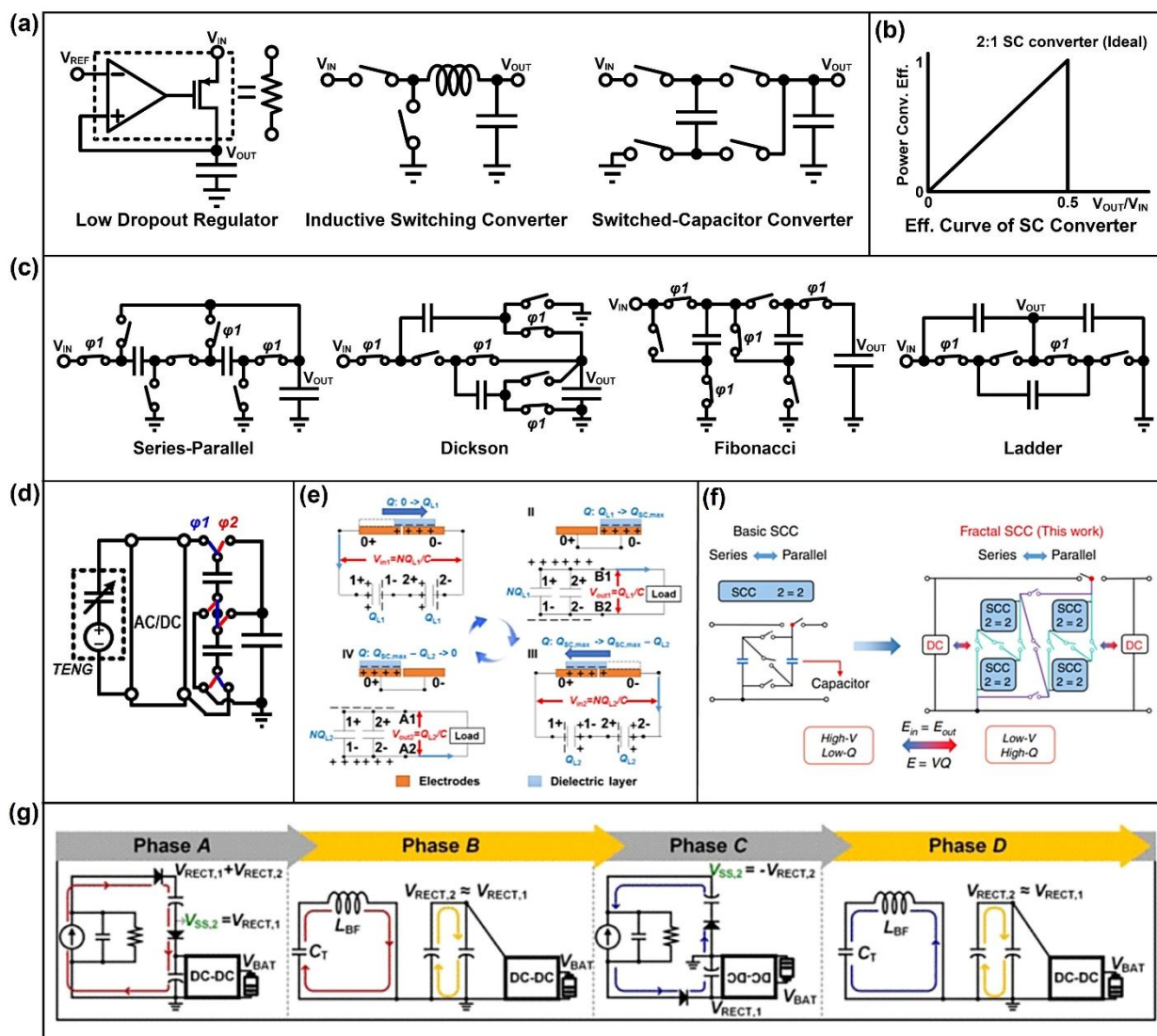


Figure 64. SC converter for the power management system for the TENG. **(a)** Types of the DC-DC converter. **(b)** power conversion efficiency of the 2:1 SC converter according to the output/input voltage ratio. **(c)** Structures of the basic SC converters. **(d)** TENG with the series-parallel SC converter. **(e)** The built-in SC converter of the sliding mode TENG. **Reprinted with permission from ref 568. Copyright 2017 Elsevier.** **(f)** A fractal design based switched-capacitor-converters. **Reprinted with permission under a Creative Commons CC BY license from ref. 569, Copyright 2020, Springer Nature.** **(g)** A scalable multi-chip-stacked with the SC technique. **Reprinted with permission from ref 570. Copyright 2022 IEEE.**

5.3 Power Management of TENG by Two-step Strategy

The AC/DC rectifier rectifies the AC voltage generated by the TENG to the DC voltage. The DC/DC converter converts the rectified DC voltage into a specific DC voltage to charge the output capacitor as depicted in Figure 65(a). It is important to select a diode for the AC/DC rectification that is also suitable for the TENG. Therefore, considering a proper reverse voltage (V_R) of the diode to withstand the high voltage of the TENG and selecting the small forward voltage drop (V_d) to minimize power loss are significant aspects of the AC/DC rectifier.^{446, 571} The power management system used for DC/DC power transfer includes a passive switch and proper automatic voltage regulation.

5.3.1 Full-Wave Diode Rectification

The equivalent circuit of the TENG is composed of a voltage source (V_{TENG}) and an internal impedance (Z_{TENG}) (Figure 65(b)).⁵⁷²⁻⁵⁷³ The TENG generating power transferred to the load (P_{IN}) can be expressed by impedance modeling and voltage division as follows⁵⁷¹ :

$$P_{IN} = \frac{Z_{in}}{Z_{TENG} + Z_{in} + 2Z_d} P_{TENG} \quad (26)$$

1
2
3
4 According to the maximum power transfer theory⁵⁷⁴, TENG power (P_{TENG}) can be transferred
5
6
7
8 up to 50%. Maximum power is possible when the sum of the impedances of two diodes (Z_d)
9
10
11 and Z_{TENG} is equal to the load impedance (Z_{in}).
12
13
14
15
16

17 **5.3.2 Passive Switched Circuit for Voltage Regulation**

18
19
20 According to equation (26), it is impossible to transfer P_{TENG} to the load because of
21
22
23 impedance imbalance.⁵⁷⁵⁻⁵⁷⁷ This unbalanced impedance prevents effective power transfer to
24
25
26 the load. However, it can be solved by using a coupler switch (Figure 65(c)-(i)).⁵⁷⁸ First, at
27
28 the charging mode, the TENG and rectifier are connected to a capacitor directly (Figure
29
30
31 65(c)-(ii)). Second, at the standby mode, it minimizes power loss by disconnecting the load
32
33
34 from the TENG (Figure 65(c)-(iii)). Third, at the power transfer mode, power can be supplied
35
36
37 to the load (Figure 65(c)-(iv)). However, due to the leakage of power and small P_{TENG}
38
39
40 generation, it takes a lot of time to charge the capacitance for DC/DC converter operation. In
41
42
43 addition, it has to be operated manually by using a switch.
44
45
46
47
48
49
50
51
52

53 **5.3.3 Automatic Voltage Regulation**

1
2
3
4
5 The proposed circuit diagram shows a load connection circuit using a comparator and a
6
7
8 PMOS switch (Figure 65(d)-(i)), which is called an Automatic Voltage Regulator (AVR).⁵⁷⁹
9

10
11 When the capacitor voltage (V_{Cap}) exceeds the driving voltage (V_{DR}), the load connection can
12
13
14 automatically transfer the energy stored in the capacitor to the load without the manual switch.
15
16
17

18 In this operation, to determine the voltage of V_{DR} for the load connection circuit, R_1 and R_2
19
20
21 can be simplified to the Thevenin equivalent circuit for V_{REF} (Figure 65(d)-(ii)). When V_{Cap}
22
23
24 exceeds 3.8 V, the PMOS switch turns on to transfer power to the load. When V_{Cap} is less
25
26
27 than 2.8 V, the PMOS switch turns off to disconnect power to the load (Figure 65(d)-(iii)).
28
29
30

31 However, it is difficult to apply it to an actual circuit due to loss caused by the driving power
32
33
34 (P_{DR}) of the elements. In other words, the sum of P_{DR} of the comparator, the driving power of
35
36
37 the PMOS switch, and the leakage power is higher than the total generated power from the
38
39
40 TENG. Therefore, a System-on-Chip (SoC) technology implemented by an IC is required for
41
42
43 high conversion efficiency in TENG-based energy harvesting applications.
44
45
46
47
48
49
50

51 **5.3.4 Enhanced AVR Circuit Implemented by SoC**

52
53

54
55 The small current consumption of the AVR circuit is necessary to increase the usefulness of
56
57
58 the TENG and the main DC paths of the AVR circuit that should be reduced are as follows: 1)
59
60

1
2
3
4 resistive feedback of V_{CAP} (R_1 , R_2); 2) positive feedback of the comparator (R_3 , R_4); 3) pull-
5
6
7
8 up resistor of the comparator (R_5); 4) bias current of the comparator and voltage reference
9
10
11 circuit. The current consumption caused by the resistors can be reduced by increasing the
12
13
14 resistance or applying the push-pull structure. However, it is difficult to reduce the total
15
16
17 quiescent current of the comparator and the voltage reference to less than $1 \mu\text{A}$ with discrete
18
19
20 components. On the other hand, IC design can not only achieve the sub- μA comparator⁵⁸⁰ or
21
22
23 sub-nA voltage reference circuit⁵⁸¹ but also reduce the switching power by implementing the
24
25
26
27
28 PMOS in the IC.
29
30
31
32
33
34
35
36
37
38
39
40
41
42
43
44
45
46
47
48
49
50
51
52
53
54
55
56
57
58
59
60

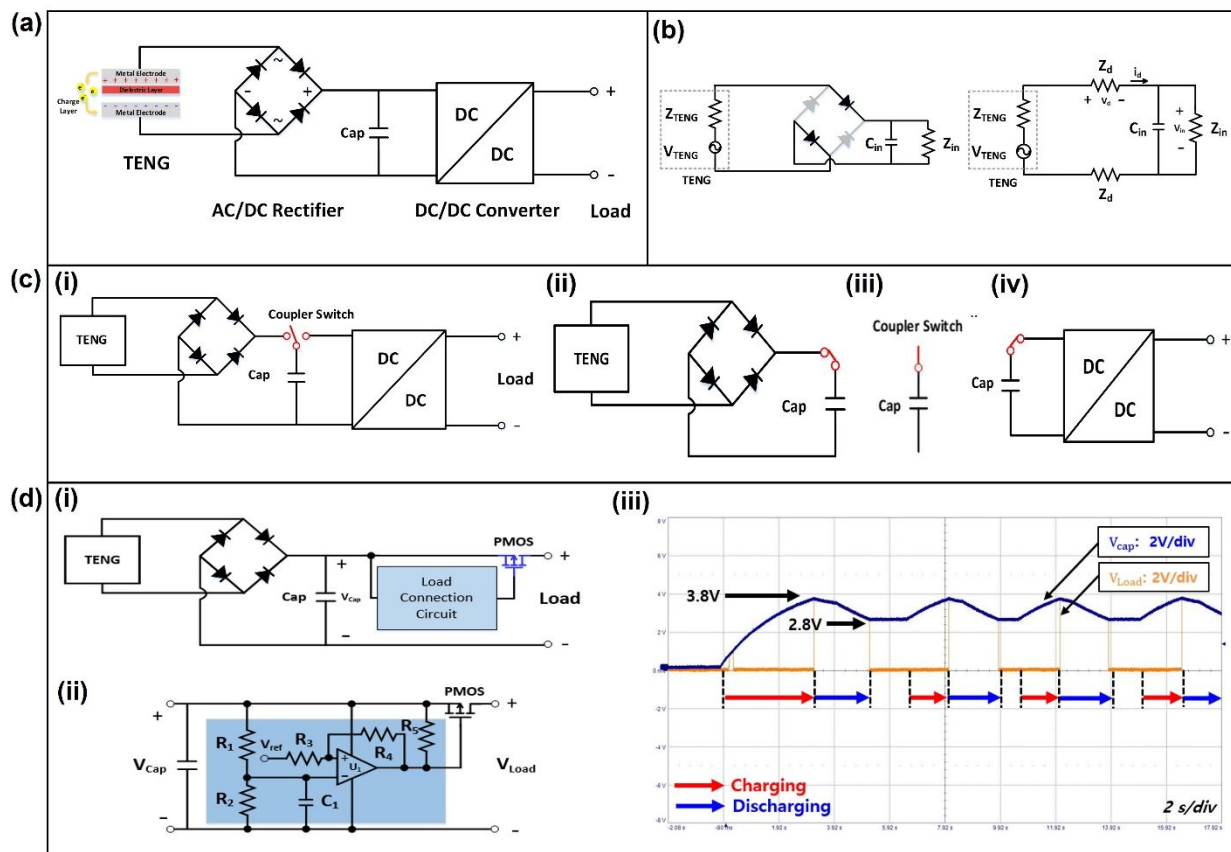


Figure 65. Two-step power management strategy. (a) TENG power conversion system. (b) Impedance modeling process for TENG. (c)-(i) Proposed three-stage power management system. (c)-(ii) Charging mode. (c)-(iii) Stand-by mode. (c)-(iv) Energy-usage mode. (d)-(i) Automatic voltage regulation circuit. (d)-(ii) Load connection circuit. (d)-(iii) Experimental waveform of load connection circuit.

5.4 Power management of TENG by MOSFET power converters

5.4.1 Theoretical basis of MOSFET-based power management

The basic unit of TENG is the contact separation between the polymer film sticking electrode and the metal film, so it has the characteristics of inherent high internal resistance. When the TENG parallel-connected with a load (Figure 66(a)-(i))¹¹⁵, the theoretical model is

$$R \frac{dQ}{dt} = V = -\frac{1}{C_{TENG}}Q + V_{OC}. \quad (27)$$

Simulation results show three different regions illustrating the output voltage and current (Figure 66(a)-(ii)). Through the simulation results, it is analyzed that the control equation of the optimal impedance of the contact-separation TENG is

$$R_{opt} = \frac{d_0^2}{F_{opt}^2 S v \epsilon_0} \approx \frac{(d_0 + x_{max})^2}{S v \epsilon_0} \quad (28)$$

From equation (28), the optimal impedance is related to the sum of the relative permittivity ratios of all dielectric materials (d_0), the maximum separation distance (x_{max}), the contact area (S), the average separation speed (v), and the permittivity of vacuum (ϵ_0). Figure 66(a)-(iii) depicts the variation of the TENG's output power with the contact speed and load resistance. As the velocity increases, the output power increases obviously as the accumulation of surface charge increases. The greater the contact speed, the smaller the internal resistance.

The V-Q curve can be used to describe the output energy of each cycle. When TENG is connected with different load resistors, the summary of the V-Q curve is shown in Figure 66(b)-(i).⁵⁸² To obtain the maximum output energy, a travel switch is connected with TENG for maximum short-circuit transferred charges and maximum open-circuit voltage (Figure 66(b)-(ii)). At this time, the V-Q curves obtained by connecting the TENG with different resistors are shown in Figure 66(b)-(iii). The results show that a larger external load can obtain a larger output power.

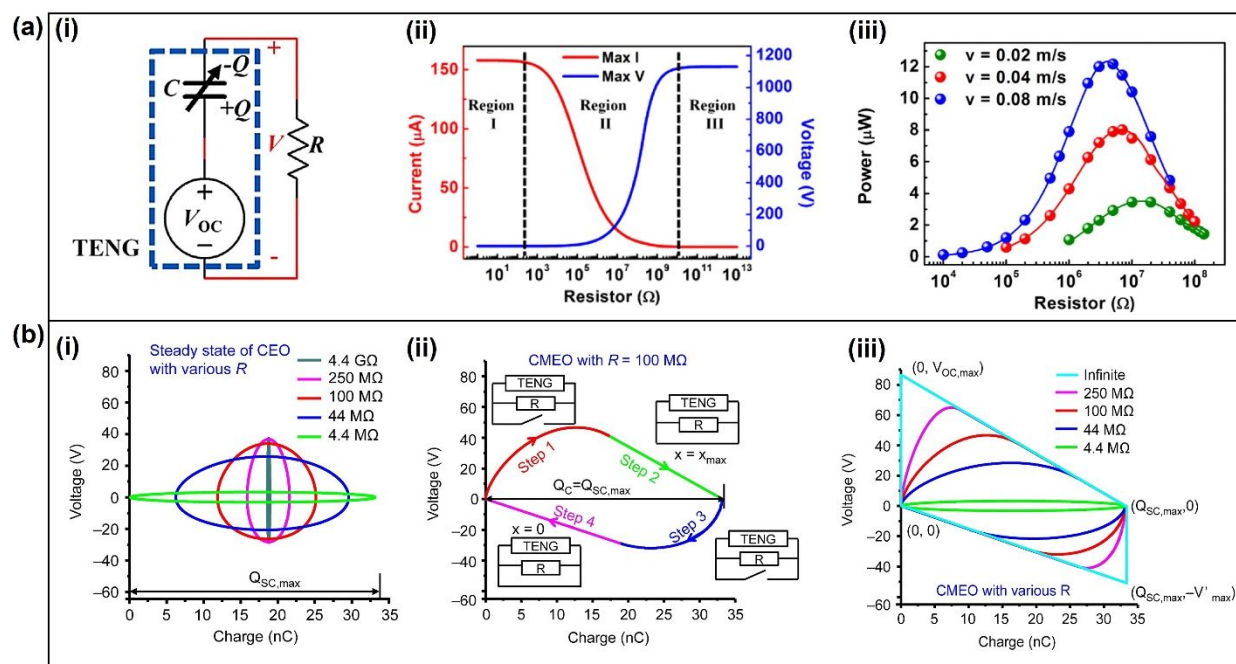


Figure 66. Theoretical model of MOSFET based power management for TENG. **(a)-(i)** The circuit schematic diagram of the parallel resistance of the TENG. **(a)-(ii)** The magnitude of the output current and voltage shown in the three regions is affected by the load. **(a)-(iii)** Output power variation with the velocity and load resistor. **Reprinted with permission from ref 115. Copyright 2015 Elsevier.** **(b)-(i)** The cycle for energy output with different loads in steady state. **(b)-(ii)** The cycles for maximized energy output with $R = 100 \text{ M}\Omega$. **(b)-(iii)** The

1
2
3
4 cycle for maximized energy output with different loads. **Reprinted with permission under a**
5 **Creative Commons CC BY license from ref. 582, Copyright 2015, Springer Nature.**
6
7
8
9
10
11
12
13
14
15
16
17
18
19
20
21
22
23
24
25
26
27
28
29
30
31
32
33
34
35
36
37
38
39
40
41
42
43
44
45
46
47
48
49
50
51
52
53
54
55
56
57
58
59
60

5.4.2 The circuit design of MOSFET-based power management for TENG

According to the theoretical model, Niu *et al.* designed a two-stage energy release as power management for TENG (Figure 67(a)-(i)).⁵⁸³ In this circuit, two switches controlled by a logic circuit periodically extract the energy from the snubber capacitor. Based on this management module, TENG has increased the conversion efficiency of AC power to DC power to 60% (Figure 67(a)-(ii)). The basic components of the switch signal circuit diagram are shown in Figure 67(b).⁵⁸⁴ The rectified signal is differentiated and fed to the non-inverting terminal of the comparator. The differential signal is compared with the zero potential of the inverting input terminal. The voltage peak can be detected accurately by this method. Song *et al.* designed a TENG power management module with both efficient energy output and maximized energy storage.⁵⁸⁵ To increase the energy output efficiency, a series switch controlled by logic circuits is designed. For the maximized energy storage parts, an LC oscillating system was employed to improve energy storage efficiency. The charging efficiency of different capacitors with and without power management is shown in Figure 67(c)-(i), which significantly increases the energy storage efficiency. The matched internal resistance decreased from 4.7 M Ω to 10 k Ω , and the whole efficiency for TENG is 69.3% (Figure 67(c)-(ii)). Xi *et al.* proposed a universal power management strategy using a

1
2
3
4
5 tribotronic energy extractor controlled by a MOSFET switch (Figure 67(d)-(i)).⁵⁸⁶ The
6
7
8 storage energy of directly charging is only 18.5 μJ , while the electrical energy is 2.37 mJ
9
10
11 after power management, which is increased about 128 times. Charging efficiency
12
13
14 comparison of direct charging and managed charging is shown in Figure 67(d)-(ii). At the
15
16
17 same time, the internal resistance decreased from 35 $\text{M}\Omega$ to 1 $\text{M}\Omega$ (Figure 67(d)-(iii)). The
18
19
20 first step in this power management strategy is maximum energy can be transferred from
21
22
23 TENG to the back-end circuit. The working mechanism is referred to the cycles for
24
25
26 maximized energy output of TENG⁵⁸², that is obtaining the maximum short-circuit
27
28
29 transferred charge and maximum open-circuit voltage. The second step is decreasing the
30
31
32 voltage and increasing the current by adding a parallel diode D1, a serial inductor L, and a
33
34
35 parallel capacitor C. Based on this circuit design, the energy conversion efficiency of
36
37
38 different forms of TENG has been significantly improved and verified in the application
39
40
41
42
43
44
45 demonstrations.

46
47
48 In cell simulation, drug release, and microenvironment regulation, small molecule drugs
49
50
51 are widely used because they easily penetrate cells to reach the internal environment and
52
53
54 participate in circulation. Sustained controlled release to the diseased site has always been a
55
56
57
58 common problem in the application of such drugs. Through this power management strategy,
59
60

1
2
3
4 combined with the organic electronic ion pumps, experiments for the controlled release of
5
6
7
8 small molecule drugs have been validated.⁵⁸⁷ TENG has advantages in harvesting low-
9
10
11 frequency ocean wave energy, but its harvested energy cannot be directly applied to
12
13
14 electronic devices. By combining this power management strategy, the charging capability of
15
16
17 TENG for capacitors is significantly improved.⁵⁸⁸ Other similar application examples have
18
19
20 also been verified in TENG to collect wind energy⁵⁸⁹⁻⁵⁹⁰ and biomechanical energy⁵⁹¹, which
21
22
23 reflects the versatility and universality of the power management strategy. Effective power
24
25
26 management strategies will surely play an indispensable role in future TENG-based self-
27
28
29 powered portable electronic devices, sensors, and implantable medical devices.
30
31
32
33
34
35
36
37
38
39
40
41
42
43
44
45
46
47
48
49
50
51
52
53
54
55
56
57
58
59
60

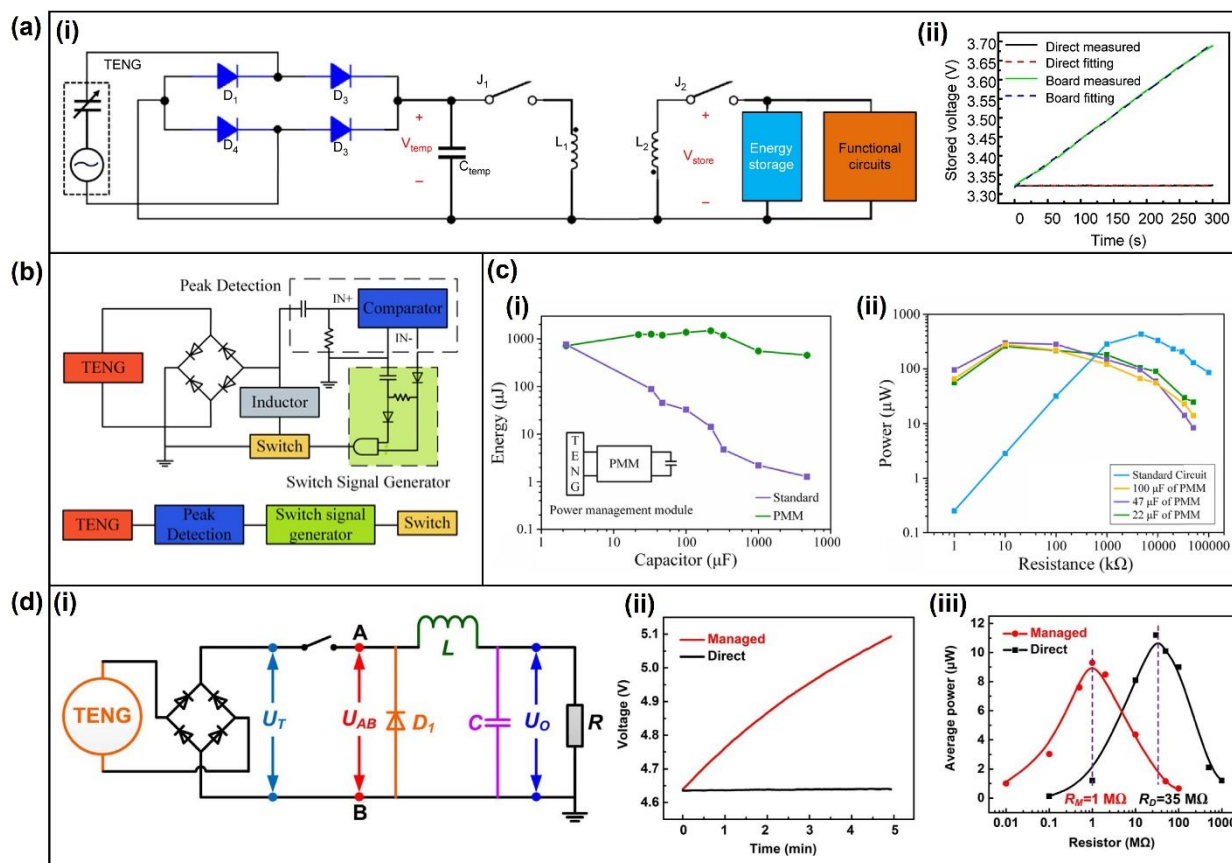


Figure 67. The circuit design of MOSFET based power management for TENG. **(a)-(i)** Design of management part. **(a)-(ii)** Intuitive TENG power management comparison. **Reprinted with permission under a Creative Commons CC BY license from ref. 583, Copyright 2015, Springer Nature.** **(b)** Basic components of switch signal circuit diagram. **Reprinted with permission under a Creative Commons CC BY license from ref. 584, Copyright 2022, MDPI.** **(c)-(i)** Charging ability comparison between standard circuit and power management circuit. **(c)-(ii)** Output power comparison. **Reprinted with permission from ref 585. Copyright 2019 Elsevier.** **(d)-(i)** Buck circuit-based power management strength for TENG. **(d)-(ii)** Charging efficiency comparison of direct charging and managed charging. **(d)-(iii)** After power management, the internal resistance decreases and average power increases. **Reproduced with permission from ref 586. Copyright 2017 Elsevier.**

6. Applications of TENGs

With the advent of internet of things, lightweight and sustainable power supply has become a key component to realize seamless human-machine interface. TENGs, directly convert mechanical energy into electrical energy, have been spotlighted as fascinating self-powered sensing system and power sources for wide range of devices (Figure 68). TENGs generating high voltage from ambient environmental change have been considered as one of ideal power sources for actuating robots, stimulating tissue, and purifying environments. Robust integration of flexible and lightweight TENGs into systems has been an attractive approach for devices pursuing sustainable energy^{592,60,68}. Self-powered sensing systems and power sources for electronics have been representative applications of TENGs. In this chapter, we discuss the progress in the development of self-powered sensing system and TENGs as power sources.

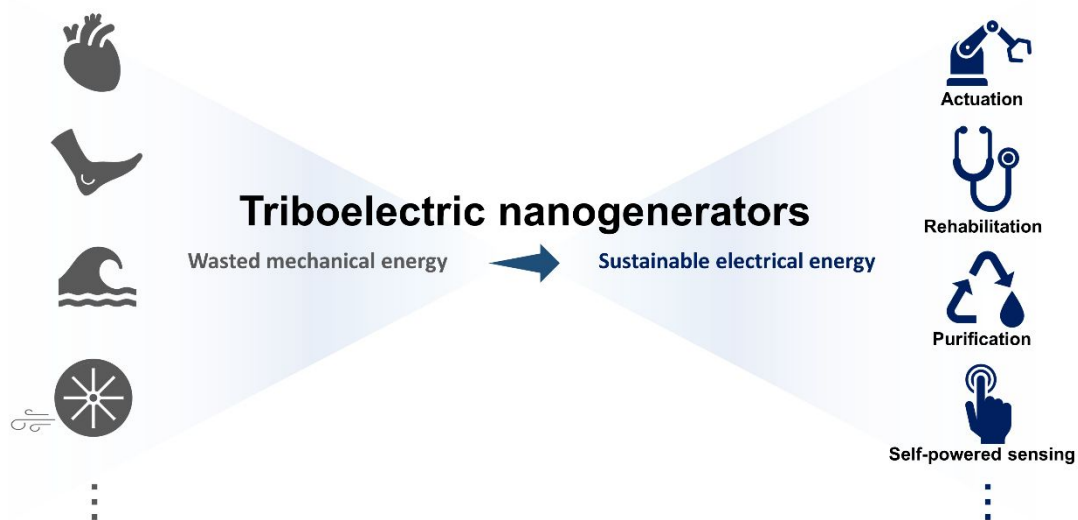


Figure 68. Triboelectric nanogenerators converting wasted mechanical energy to sustainable electrical energy for actuating robots, stimulating tissue, purifying environments, self-powered sensing system, and so on.

6.1. Robotic applications

6.1.1. Dielectric elastomer actuator

Dielectric elastomer actuators (DEAs) are electrically driven soft artificial muscles that have a wide range of potential applications including robotics⁵⁹³, haptics^{594,595}, prosthetics⁵⁹⁶, and microfluidics⁵⁹⁷. DEAs exhibit large deformation, high efficiency, long lifetime, and low fabrication costs⁵⁹⁸. These favorable properties make DEAs promising building blocks for future soft robotic systems.

DEAs consist of alternating compliant electrodes that are sandwiched by elastomeric materials of high dielectric strength. When a high voltage is applied to the electrodes, electrostatic attraction causes the elastomer to deform, which can be used to drive a robotic end effector. The electrostatic stress can be calculated as:

$$\sigma = \epsilon_0 \epsilon_r E^2 = \epsilon_0 \epsilon_r \left(\frac{V}{d}\right)^2 \quad (29)$$

where σ is the Maxwell stress, ϵ_0 is the permittivity of free space, ϵ_r is the elastomer dielectric constant, E is the applied electric field, V is the applied voltage, and d is the separation distance between alternating electrodes.⁶⁰⁰ If we assume the elastomer is linearly elastic at small strain (<15%), then the induced strain is approximated as:

$$\gamma = \frac{\sigma}{Y} = \frac{1}{Y} \epsilon_0 \epsilon_r \left(\frac{V}{d}\right)^2 \quad (30)$$

where γ is the strain and Y is the elastomer modulus. Based on Equations (29-30), the energy e and power density p of DEAs at small strains are given by:

$$e = \frac{1}{2} \sigma \gamma = \frac{1}{Y} \epsilon_0^2 \epsilon_r^2 \left(\frac{V}{d} \right)^4 \quad (31)$$

$$p = \frac{1}{2} \sigma \gamma f = \frac{1}{Y} \epsilon_0^2 \epsilon_r^2 \left(\frac{V}{d} \right)^4 f \quad (32)$$

where f is the actuation frequency.

Equations (31-32) shows the DEA energy and power density are proportional to the fourth power of applied voltage, which implies that it is critical to find elastomeric materials of a high dielectric strength. Acrylic based elastomers such as VHBs exhibit high dielectric strength (>100 V/ μm) and large strain ($>100\%$), which makes them ideal for creating energy-dense actuators. In recent works, researchers have reported energy density exceeding that of mammalian muscles^{596,599}. These types of DEAs have been applied in soft grippers⁶⁰¹ (Figure 69(a)) and jumping robots⁵⁹⁸ (Figure 69(b)).

In contrast to energy-dense applications, there is another class of robotic locomotion that requires high agility and controllability. To achieve animal-like agility, power-dense and high bandwidth DEAs^{602,603} have been developed to enable fast and controllable locomotion. Ji et al.⁶⁰² (Figure 69(c)) developed a power and sensing autonomous terrestrial robot whose speed exceeds 30 mm/s. Chen et al.⁶⁰⁴ (Figure 69(d)) developed a soft aerial robot whose flight speed exceeds 700 mm/s. In these examples, the DEAs are made of silicone elastomers. Although they have lower dielectric strength (<70 V/ μm), they exhibit low viscoelasticity which enable a high actuation frequency exceeding 500 Hz.

While we expect both acrylic and silicone DEAs to further improve performance and expand applications, both types of DEAs face a common challenge: achieving power autonomy and high efficiency as a standalone system. According to Equations (31-32), a DEA's energy and power density strongly depend on the maximum applied electric field, which relates to the

1
2
3
4 ratio between the applied voltage V to the elastomer thickness d . Existing fabrication
5
6 methods limit the elastomer thickness to be larger than 5 μm , which corresponds to a
7
8 minimum operating voltage of 500 V. In most cases, DEAs require 1- 10 kV and they are
9
10 tethered to offboard high-voltage power supplies. This is a main challenge for applying DEAs
11
12 in power autonomous systems. Recently, lightweight (<1 g) power electronics^{602,605,606} have
13
14 been developed to boost a low input voltage (3-10 V) into a high output voltage (200 – 500
15
16 V). However, these designs are limited to a low efficiency (<20%). Further, they cannot
17
18 generate output voltages higher than 800 V because of the limitations on lightweight
19
20 transistors and capacitors.
21
22
23
24

25
26 In our view, TENG is a promising technology for driving DEAs in future soft robotic
27
28 systems⁶⁰⁷ (Figure 69(e)). TENG can easily generate voltages higher than 1 kV, which is
29
30 sufficient for powering many of the existing DEAs. In a recent work, TENG is combined
31
32 with a DEA to develop a tunable optical modulator.⁵³ This example highlights the potential
33
34 benefits of using TENGs in high voltage soft robotic applications. There remain two research
35
36 directions. First, it is important to reduce DEA operating voltages and increase TENG's
37
38 maximum output voltage. This will allow TENGs to be applied in a variety of DEA-driven
39
40 systems. Second, TENGs need to improve their output power density in addition to having a
41
42 high output voltage. In most existing TENGs, the amount of induced charge is on the order of
43
44 microamps, which limits net current and power. For power-dense DEAs that require high
45
46 frequency actuations, existing TENGs cannot yet deliver sufficient power compared to a
47
48 battery of similar weight. From the perspective of driving agile soft robotic systems, we
49
50 believe increasing the net charge flow will be a critical and high impact direction.
51
52
53
54
55
56
57
58
59
60

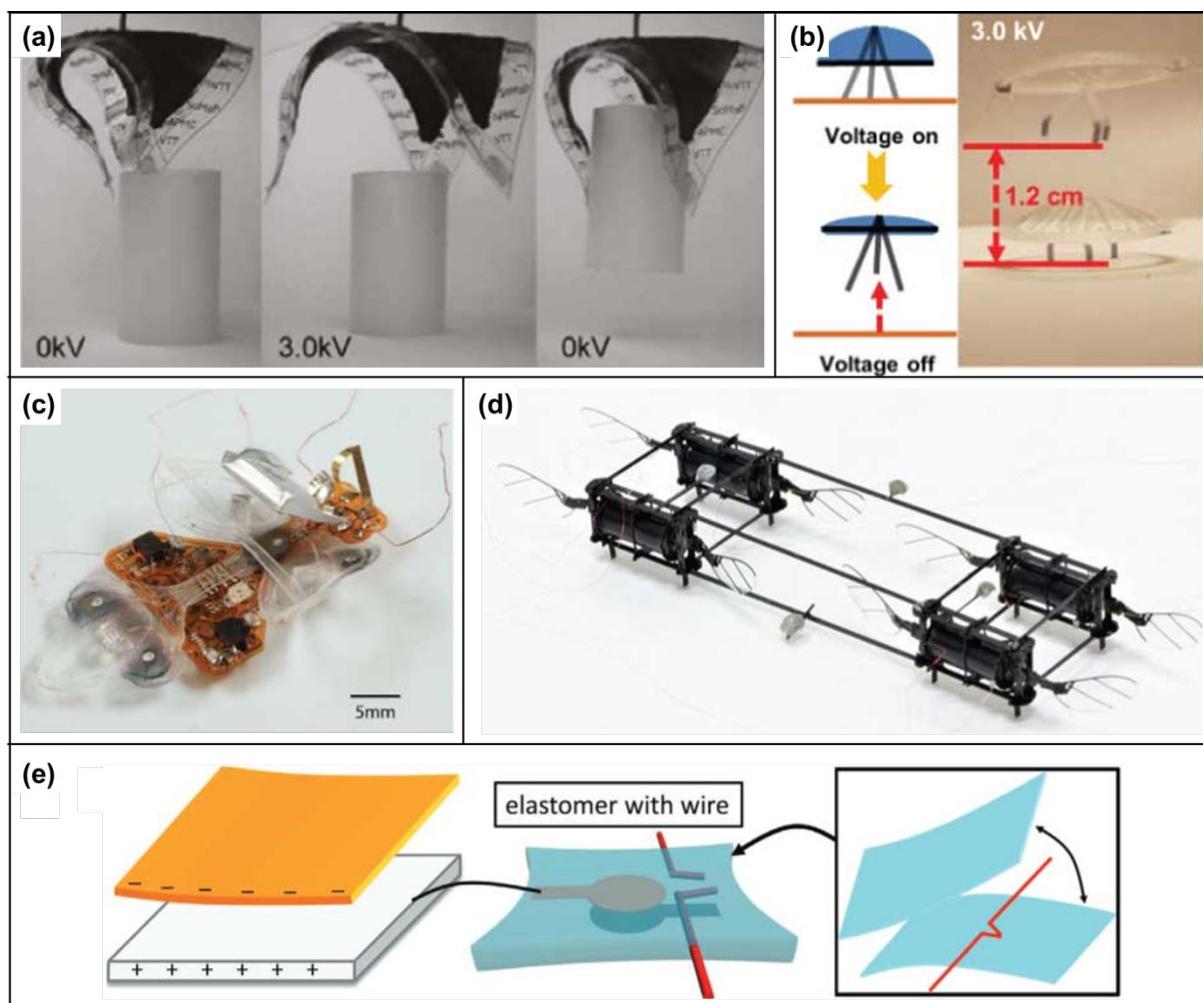


Figure 69. Structure and working mechanism of dielectric elastomer actuators (DEA). (a) soft grippers, **Reproduced from ref. 601. Copyright 2007, AIP Publishing.** and (b) jumping robots. **Reproduced from ref. 598. Copyright 2022, AAAP.** (c) A power and sensing autonomous terrestrial robot. **Reproduced from ref. 602. Copyright 2019, AAAP.** (d) A soft aerial robot whose flight speed exceeds 700 mm/s. **Reproduced from ref. 603. Copyright 2019, Springer Nature.** (e) TENGs for driving DEAs. **Reproduced from ref. 607. Copyright 2016, Wiley-VCH.**

6.1.2. Electrostatic adhesion gripper

In this section, we review the electrostatic adhesion grippers and manipulators based on the TENG. The high voltage provided by the TENG enhances electrostatic adhesion and provides a cost-effective solution to develop environmentally-stable adhesion and gripping. The high electric field induced polarization or electrostatic effect can produce a strong adhesion force on the electrode surface, which is called the electro-adhesive effect. Electrical adhesion effect can be widely used for gripping devices and the related electrical adhesion gripper have the advantages of precise control, fast response time and low energy consumption⁶⁰⁸. However, electrical adhesion usually requires high voltages, which limits electrostatic adhesion to a number of limited practical applications^{609,610}. As a device that effectively converts ambient mechanical energy into high voltage output, the TENG is a promising option for operating the electrical adhesion gripper. Xu L. et al⁶¹¹. propose a self-powered electrical adhesion gripper based on TENG with charge replenishment channels (CSC). Here, a CSC is designed to provide a replenishment for the dissipated charge occurring between electrodes, and then, resulting in an optimum charge distribution on the TENG electrodes and increasing the peak open circuit voltage of corona-charged individual TENG cells from 1000 V to an ultra-high level of 7000 V. Accordingly, with this self-powered electrical adhesion system consisting of

1
2
3
4 this enhanced TENG and an electro-adhesive sheet, the voltage can be increased to about
5
6
7
8 1500 V and an adhesion force of 6.7 N is generated to pick up a 0.35 kg metal block (Figure
9
10
11 70(a)). The same principle can also be applied to the adhesion of small objects, such as
12
13
14 microfluids. For example, Nie J H et al⁶¹². have designed a self-driven gripping probe for 3D
15
16
17 transfer of microdroplets based on TENG and photocontrol lable adhesion surface (PCAS).
18
19
20
21 With the help of UV irradiation and the electrostatic force, the water adhesion force of the
22
23
24 gripping probe allows microdroplets up to 25 μ L in volume to be carried in 3D space, which
25
26
27
28 greatly extends the range of applications for the adhesion gripper (Figure 70(b)).
29
30
31

32 For electro-adhesive devices, the chemical composition and structure of the device surface
33
34
35 has a strong influence on the generation of adhesion. To further enable rapid switching
36
37
38 between strong and weak electrostatic bonding states, Boutilier M S H et al⁶¹³. design a soft
39
40
41 nanocomposite electroadhesives (SNE) surface which applies electrostatic adhesion
42
43
44 mechanisms to mechanically flexible surfaces formed by dielectric-coated carbon nanotubes
45
46
47 (CNTs). The maximum adhesion force of the device is determined by the insulating coating
48
49
50 and surrounding air, while the maximum electro-adhesive pressure is \sim 20 kPa with an on/off
51
52
53 adhesion rate of \sim 700 in the millimetre region (Figure 70(c)). Sun Q et al⁶¹⁴. imprints
54
55
56 rewritable surface charge density gradients on superhydrophobic surfaces by chemical
57
58
59
60

1
2
3
4 modulation. The modulation of the surface charge density overcomes the resistance of water
5
6
7 droplets and with transforming the superhydrophobic region into a highly viscous region by
8
9
10
11 generating surface charge at predetermined locations, the water droplets can be absorbed and
12
13
14 placed without mass loss. In addition to air, electrostatic adhesion grippers can also be used
15
16
17 in different external environments such as underwater condition. Zheng H X et al⁶¹⁵. utilize a
18
19
20
21 patterned hybrid wettable adhesive surface design to selectively create space-constrained
22
23
24 monolithic air shells, which can protect the water bridge in underwater environment. With the
25
26
27 synergistic effect of the water bridge and the air shell, the adhesion with high pressure
28
29
30 difference is achieved. Then, the reversible reduction in adhesion is achieved by the
31
32
33 application of a small DC voltage, which can induce a rapid electrolytic process to rapidly
34
35
36 disturb the integrity of the protective air shell and the water bridge. Thus, with the help of
37
38
39 synergistic action and DC voltage inducing, a 200G metal load can be moved to any pre-
40
41
42 designed position at a DC supply voltage of 20V and released within a short time of 6s.
43
44
45
46
47

48 (Figure 70(d))
49
50
51
52
53
54
55
56
57
58
59
60

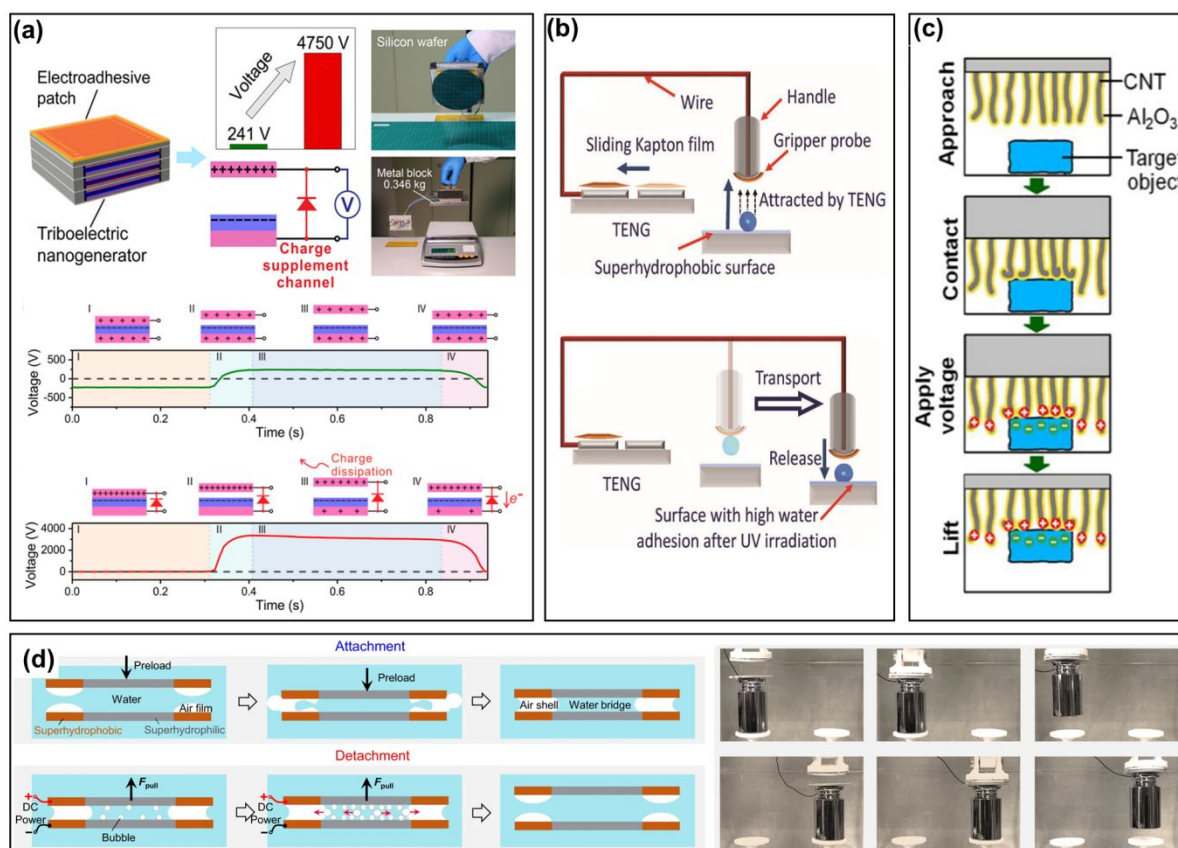


Figure 70. Application for electrostatic adhesion gripper. **(a)** A self-powered electroadhesion system with charge supplement channel. **Reprinted with permission from ref. 611, Copyright 2018, AMER CHEMICAL SOC.** **(b)** The combination of TENG and PCAS as a transport system structure for gripping probes. **Reprinted with permission from ref. 612, Copyright 2018, John Wiley and Sons.** **(c)** The electro-adhesive CNT surface contacts the target object and uses the electrostatic adhesion force to lift the object. **Reprinted with permission from ref. 613, Copyright 2021, John Wiley and Sons.** **(d)** Schematic illustration of the working mechanism for the electrically triggered reversible underwater adhesion and practical application. **Reprinted with permission under a Creative Commons CC BY license from ref. 615, Copyright 2022, Springer Nature.**

1
2
3
4
5 In addition, the electrostatic adhesion effect is also used in many other applications besides
6
7
8 gripping devices, such as the diverse manipulation of micro-droplets and micro-fluids⁶⁰⁷ (see
9
10
11 Figure 71). In 2021, Sun X et al⁶¹⁶. fabricate a functional nanowire triboelectric
12
13
14 nanogenerator (NW-TENG) based on polyaniline and polyvinylidene fluoride nanowires. The
15
16
17 TENG influences the electric field by varying the output signal to control the droplet
18
19
20 behavior. Thus, the mechanism of polarization deformation of droplets in a two-electrode
21
22
23 self-powered electrostatic manipulation system (EMS) is investigated. As shown in Figure
24
25
26
27
28 71(a), the increase in the TENG output voltage leads to the generation of polarized charge
29
30
31 and accordingly, the droplet starts to deform and move when the electric field strength
32
33
34 reaches 750 V/cm. Furthermore, when the voltage is reduced, the droplet becomes stable and
35
36
37 stops at the desired position. Compared to a normal DC stabilized power supply, the droplet
38
39
40 shows a faster response time under the drive of TENG for the same travel distance. (Figure
41
42
43
44 71(b)) Furthermore, the rupture process of droplets in an inhomogeneous high voltage field
45
46
47 proves the practicality and safety of EMS. With the output voltage of TENG, EMS can
48
49
50 maintain a voltage output above 1500 V, which ensures that the droplets move reciprocally at
51
52
53 high speed and gradually break up into smaller droplets. Meanwhile, no electrical faults occur
54
55
56
57
58 in the EMS during this process (Figure 71(c)). Another strategy for droplet manipulating is
59
60

1
2
3
4 human-motion-induced direct charge injection. Sun J F et al.⁶¹⁷ propose an effective droplet-
5
6
7 driven method using direct charge injection (DCI) provided by TENGs via human motion.
8
9

10
11 Because of no insulating layer separating the electrode from the droplet, the exposed
12
13
14 electrode can increase the electric field near the droplet and rapidly manipulate the droplet
15
16
17 movement. The DCI can drive a 10 μL droplet to have an average velocity of 0.25 nC and
18
19
20
21 255 mm/s, more than 6 times higher than conventional methods. Meanwhile, reciprocating
22
23
24 and jumping movements of the droplet are achieved by using alternating charge injection
25
26
27 (Figure 71(d)). In addition to direct adhesion, electrostatic forces have also been used as a
28
29
30 power source for grippers. Zheng L et al⁶¹⁸. combines TENG with vapor-excited responsive
31
32
33 smart materials to design a dual-stimulated flexible gripper. The two-finger gripper can grasp
34
35
36
37 and move objects weighing up to 6 g (Figure 71(e)).
38
39
40
41
42
43
44
45
46
47
48
49
50
51
52
53
54
55
56
57
58
59
60

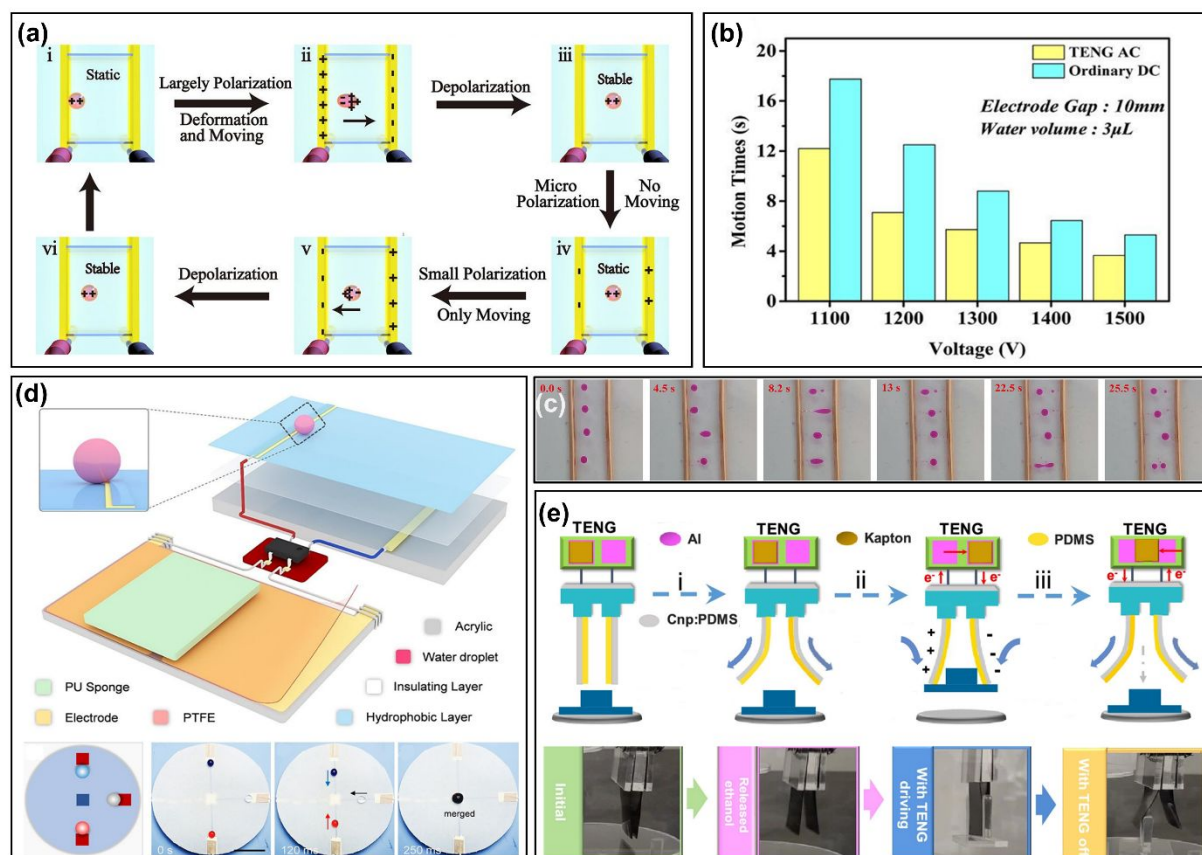


Figure 71. TENG-driven electrostatic manipulator. **(a)** Schematic diagram of the reciprocating motion of a water droplet in a TENG electric field. **(b)** Movement time of droplets in TENG AC field and ordinary DC field. **(c)** breaking process of water droplets controlled by TENG AC electric field. **Reprinted with permission from ref. 616, Copyright 2021, Elsevier.** **(d)** Three-dimensional schematic of the droplet-driven platform controlled by TENG and practical application. **Reprinted with permission from ref. 617, Copyright 2022, Elsevier.** **(e)** Working principle and working processes of Dual-stimulus flexible gripper based on TENG and vapor induction. **Reprinted with permission from ref. 618, Copyright 2019, AMER CHEMICAL SOC.**

6.1.3 Optical Actuator

To perceive the light conditions of the environment or make communication with human beings, optical actuators are considered indispensable components for future robots or artificial intelligence to conduct light switching or display missions⁶¹⁹. Generally, voltage-driven materials, such as liquid crystals and phosphor particles are commonly used to construct optical actuators. The working principles of liquid crystal-based optical actuators and the luminescence mechanism of phosphor particle are demonstrated in Figure 72(a), (b), respectively. For liquid crystal-based devices, applied voltage stimuli would switch the orientation and light-scattering properties of liquid crystal and therefore obtain an optical contrast or color change^{620,621}. For phosphor particle-based devices, take the ZnS:Cu as an example, some of the electrons in ZnS:Cu would be excited to the shallow electron trap states by an external voltage (or electric field) stimuli and then fall into the states of Cu impurity, which could generate luminescence at 510 nm wavelength⁶²². It is worth mentioning that the value of voltage stimuli to actuate these optical devices could reach several to thousand volts, while the current that flows through the devices could be none or very small^{623,624}. This makes TENG an attractive option to drive the optical actuators, due to its output characteristic (high voltage output and low current output)⁶²⁵. Moreover, TENG-driven optical actuators can get rid of traditional external power sources. The resulting devices can not only be self-powered, but more importantly the actuators could show optical responses based on the mechanical stimuli.

Recently, plenty of efforts have already been taken to develop various self-powered liquid crystal/phosphor particle based optical actuators. Here, some representative works will be briefly introduced. For the self-powered liquid crystal optical actuator, an all-in-one

1
2
3
4 dynamic optical transmittance modulator (OTM) has been developed, as shown in Figure
5
6
7
8 72(b)⁶²⁶. This OTM has a multilayer structure. When an external object (e.g., fingers)
9
10
11 contacts and slides on the top FEP film, an alternating electric field can be induced upon the
12
13 OTM. The polymer dispersed liquid crystal (PDLC) in the sliding area would be aligned
14
15 along the electric field, and switch to an instantaneous transparent state. However, when the
16
17 electric field disappears, PDLC will recover to the initial state. To obtain a steady device, the
18
19 cholesteric liquid crystals (CLC) were further selected to fabricate self-powered optical
20
21 actuator, as shown in Figure 72(c)⁶²⁷. A contact-separation mode TENG was used to convert
22
23 the mechanical stimuli to electricity and change the optical state of CLC-based actuator. Due
24
25 to the bistable characteristics of CLC, the optical actuator could maintain the optical states
26
27 even after removing the external stimuli. It is promising for long-term display applications.
28
29 For the self-powered phosphor particles based optical actuator, a triboelectrification-induced
30
31 electroluminescence device has been developed for visualized sensing, as illustrated in Figure
32
33 72(d), (e)⁶²⁸. This device has a sandwiched structure. When a separate object slides against
34
35 the electrification layer, transient light emission from the luminescent layer can be observed
36
37 along the trajectory due to the generated alternative electric field. Since the luminescent of
38
39 phosphor particles was essentially generated through an alternating electric field, the self-
40
41 powered phosphor particles-based optical actuator also could be operated by the non-contact
42
43 mode, as demonstrated in Figure 72(f)⁶²⁹. The movement of a floating conductive object on
44
45 the device will generate an AC-like electric field, which could modulate the emission of
46
47 phosphor particles. The morphology of the floating object could be sufficiently recognized
48
49 through the generated luminescence.
50
51
52
53
54
55
56
57
58
59
60

1
2
3
4 In addition to the above devices, other specific voltage-driven physical phenomenons or
5 materials also could be selected to fabricate self-powered optical actuators. For example,
6 electrowetting effect could be coupled with TENGs to form a self-powered optical switch, as
7 exhibited in Figure 72(g)⁶³⁰. By sliding the freestanding mode TENG, the generated voltage
8 will change the curvature of the electrowetting lens and the light propagation through the lens
9 could be switched. In addition, TENGs also could couple with the electrophoresis effect, and
10 on basis of this, a self-powered electronic paper (E-paper) was successfully developed.⁶³¹ The
11 AC voltage stimuli generated by a sliding mode TENG was covert to the DC signal through a
12 rectifier. Then, the different chromatic particles in the microcapsule of the E-paper would be
13 separated under the electrophoresis effect due to the disparate charges they carried.
14 Alternatively, by coupling the TENG and dielectric elastomer, a tunable optical modulator
15 has been reported, as illustrated in Figure 72(h).⁵³ At the initial state, the elastomer was
16 stretched, and the light could freely pass through. When the voltage generated from TENG
17 was applied to the elastomer, the light would be scattered due to the voltage-induced rippling
18 of the elastomer.

19
20
21
22
23
24
25
26
27
28
29
30
31
32
33
34
35
36
37
38
39
40
41 Despite the above progress, several aspects may still require future efforts. First, the
42 impedance matching between the TENG and optical devices should be sufficiently
43 considered. As we know, the impedance of TENGs is always very huge⁶³². The impedance of
44 optical devices might be small compared with TENGs. In this case, even if TENG could
45 generate tremendous voltage output, it still might fail to drive the optical device. Therefore,
46 low impedance and high output TENGs are urgently required. Second, although there already
47 have some bistable optical actuators that based on the cholesteric liquid crystals, most optical
48 actuators are instantaneous triggered. Efforts still need to be taken to develop bistable optical
49 actuators for the broader application scenario.

1
2
3
4
5
6
7
8
9
10
11
12
13
14
15
16
17
18
19
20
21
22
23
24
25
26
27
28
29
30
31
32
33
34
35
36
37
38
39
40
41
42
43
44
45
46
47
48
49
50
51
52
53
54
55
56
57
58
59
60

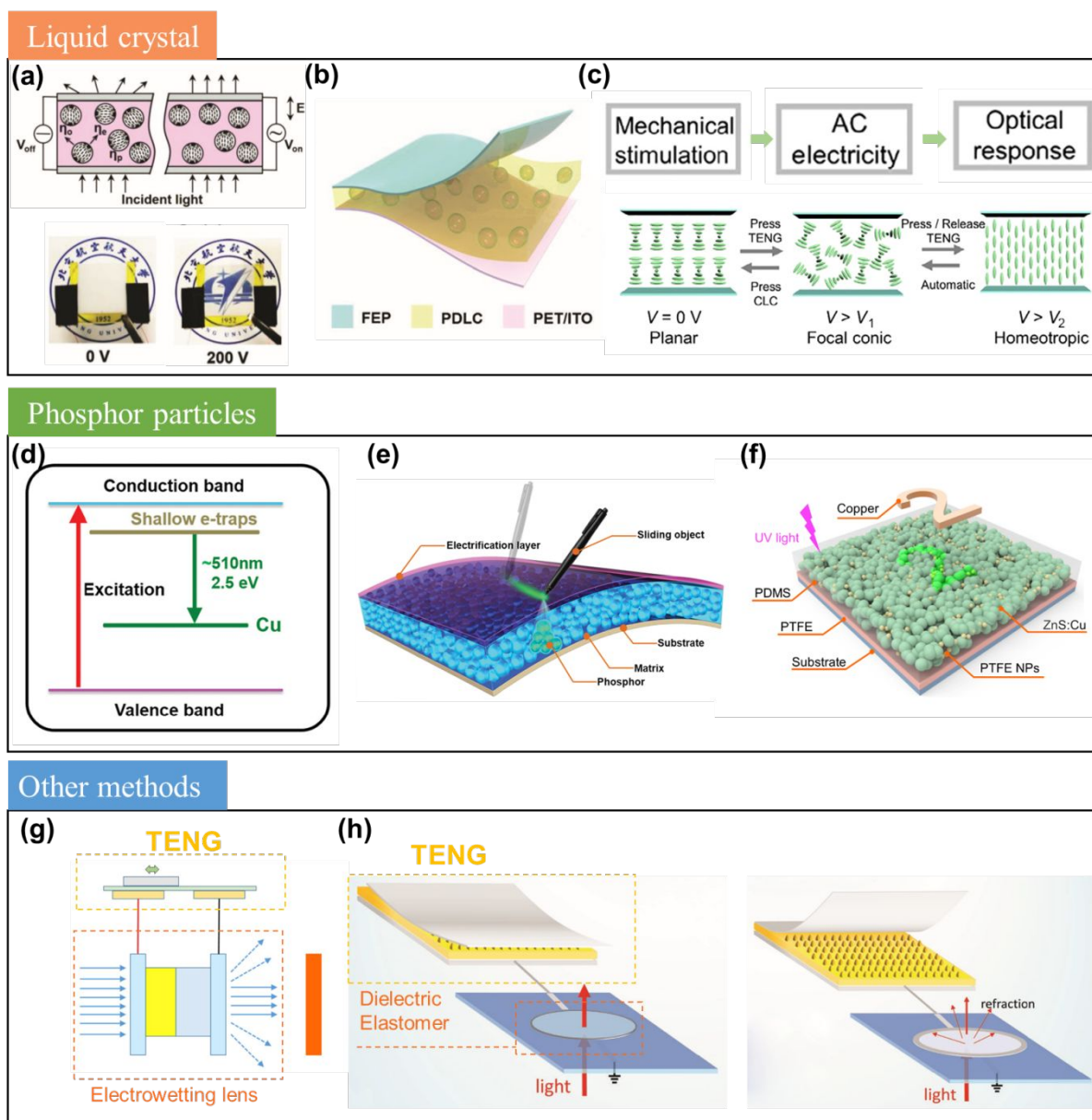


Figure 72. TENG-based optical actuators. (a) The working principle of liquid crystal based optical actuators. Reproduced from ref. 621. Copyright 2019, WILEY-VCH Verlag GmbH & Co. KGaA, Weinheim. (b) An all-in-one dynamic optical transmittance modulator that based on the polymer dispersed liquid crystal. Reproduced from ref. 626. Copyright 2020, WILEY-VCH Verlag GmbH & Co. KGaA, Weinheim. (c) A cholesteric liquid crystals based self-powered bistable optical actuator. Reproduced from ref. 627. Copyright 2021, Science China Press. (d) The luminescence mechanism of phosphor particles. Reproduced from ref. 628. Copyright 2016, WILEY-VCH Verlag GmbH & Co. KGaA, Weinheim. (e) A triboelectrification-induced electroluminescence device for the visualized sensing. Reproduced from ref. 628. 2016, WILEY-VCH Verlag GmbH & Co. KGaA, Weinheim. (f) A non-contact mode luminescence modulator for interactive visualized sensing. Reproduced from ref. 629. Copyright 2020, The Royal Society of Chemistry. (g) A self-powered electrowetting lens for light propagation switching. Reproduced from ref. 630. Copyright 2019, Elsevier Ltd. (h) A self-powered tunable

1
2
3
4 optical modulator based on dielectric elastomer. **Reproduced from ref. 53. Copyright 2017,**
5 **WILEY-VCH Verlag GmbH & Co. KGaA, Weinheim.**
6
7
8
9
10
11
12
13
14
15
16
17
18
19
20
21
22
23
24
25
26
27
28
29
30
31
32
33
34
35
36
37
38
39
40
41
42
43
44
45
46
47
48
49
50
51
52
53
54
55
56
57
58
59
60

6.2 Bio-medical applications

6.2.1. Healing

More than a decade ago, nanogenerator (NG) technology was developed as a concept for mechanical energy harvesting and conversion at the nano- or micrometer scale⁶³³. The operation principle was established on the piezoelectric effect and then extended to the triboelectric effect (i.e., TENGs), which substantially enriched the material selection and design opportunities, as well as brought in impressive sensitivity and efficiency to harvesting low-level mechanical energy^{634,8}. These features make TENGs a very promising candidate as an alternative power source for biomedical devices by utilizing available biomechanical energy. While majority applications are still focusing on battery charging for wearable or implantable devices (it is indeed a very promising application direction)^{635,636}, this section discusses another emerging application direction where the electricity from TENGs is directly used for providing biomedical functions, such as therapeutic electrostimulations (ES)^{637,638}.

Electricity is considered as the foundation of life, which is used predominately by all biological systems to achieve different physiological functions, such as communication, control, growth and repairing.⁶³⁹ Many clinical and cosmetic treatments use ES to achieve the targeted therapeutic pursues, including pain relief,⁶⁴⁰ tissue regeneration, wounds/skin healing,⁶⁴¹ bone recovery,⁶⁴² muscle restoration,⁶⁴³ and nerve stimulation^{644,645}. These conventional ES typically use high-frequency electrical pulses with at least microampere level current density and controlled by a large electrical system. Nevertheless, the fundamental correlation between the ES signals and the therapeutic effects are still largely unknown. Compared to these conventional ES systems, NG revolutionizes the delivery and control of ES through a more biomimetic fashion, which may substantially advance the

1
2
3
4 effectiveness of current ES technology and improve their adaptability. We term the ES
5 enabled by wearable or implantable NGs as *closed-loop ES*. As schematically shown in
6
7 Figure 73(a), the NG harvests the biomechanical energy from certain body motions and uses
8
9 the harvested energy to produce electricity for designed ES applications. This forms a closed
10
11 loop of energy conservation. Meanwhile, the ES treatments are only and automatically
12
13 responsive and synchronized to corresponding body motions as biofeedback without relying
14
15 on any external electronics. Therefore, this closed-loop ES is more natural (or biomimetic) in
16
17 signal delivery and manipulation, and thus may create less habituation and introduce more
18
19 effective therapeutic outcomes.
20
21
22
23
24

25 The closed-loop ES can be precisely exemplified by the implantable TENG-based vagus
26
27 nerve stimulator (VNS) used for diet and weight control³⁶⁵. The concept is schematically
28
29 illustrated in Figure 73(b) based on a rat model. The VNS device is made from a flexible
30
31 multilayer TENG, where polytetrafluoroethylene (PTFE) and copper electrodes were
32
33 encapsulated by polydimethylsiloxane (PDMS), Ecoflex, and polyimide tri-layer coatings.
34
35 The device has a size of 1 x 1 cm² and is implanted on the stomach out surface with its two
36
37 output leads connected to the anterior and posterior vagus nerves (AVNs and PVNs) at the
38
39 proximity of the gastro-esophageal junction. The VNS generates pulsed electrical signals in
40
41 response to the stomach motions with a typical amplitude of $\sim\pm 0.1V$ and pulse width of
42
43 $\sim 0.2s$. Through this design, the peristalsis of stomach after a certain amount of food intake
44
45 would activate the VNS to produce ES to the connected vagus nerves. These ES may provide
46
47 artificial fullness signal, and thereby the rat would stop eating so as to reduce the amount of
48
49 food intake. In this scenario, the closed loop is embodied by using “food intake”-related
50
51 stomach motions to power and activate VNS to control the “food intake” function. From the
52
53 weight control tests on adult rats, the experimental group (n=6) that received the VNS
54
55 implantation exhibited a constant lower amount of daily food intake ($\sim 2/3$ of the control
56
57
58
59
60

1
2
3
4 groups) over the entire testing period (75 days). As a result, the average weight of the
5
6 experimental group remained stably 38% less compared to the other control groups. This
7
8 study provides a promising alternative strategy of peripheral neuromodulation mechanism
9
10 that might be more effective for weight control compared to the implantable vagus nerve
11
12 blocker mechanism (such as vBloc[®]).⁶⁴⁶ More broadly, ES has been used to treat many
13
14 neurologic and psychiatric disorders, such as Parkinson's disease^{647,648,649}, essential
15
16 tremor^{650,651}, epilepsy^{652,653}, and major depression^{654,655}. Introducing the TENG concept to
17
18 achieve closed-loop ES may enable a strategy to improve the efficacy and adaptability. One
19
20 may envision that allowing the stimulation target to self-define the ES signal (e.g., on/off,
21
22 intensity, frequency) may directly reach the optimal stimulation conditions that are often
23
24 different from patient to patient.
25
26
27
28

29
30 In addition to nerve stimulation, externally applied ES could intervene many cellular
31
32 processes that lead to accelerated tissue growth, such as skins, muscles, and bones^{656,657}.
33
34 Specifically, ES can increase blood flow and decrease edema through the interaction with the
35
36 negatively charged protein, albumin – the major colloidal protein in blood^{658,659}. Electric
37
38 fields can control the migration of particular cells (e.g., neutrophils, macrophages, fibroblasts,
39
40 and epidermal cells) by inducing galvanotaxis responses^{660,661,662}. Electric cues and galvanic
41
42 stimulation can enhance multiple cellular activities such as deoxyribonucleic acid (DNA)
43
44 synthesis, cellular proliferation, cellular receptor expression for growth factors, calcium
45
46 uptake, and neurite growth and extension⁶⁶³. Similar to never stimulation discussed above,
47
48 current ES treatments for tissues are also primarily based on cumbersome electrical units to
49
50 provide power and modulate electric signals. Cutting edge research in this field continues to
51
52 look for alternative ES treatment approaches that are easy to implement and can promote
53
54 more significant outcomes⁶⁶⁴.
55
56
57
58
59
60

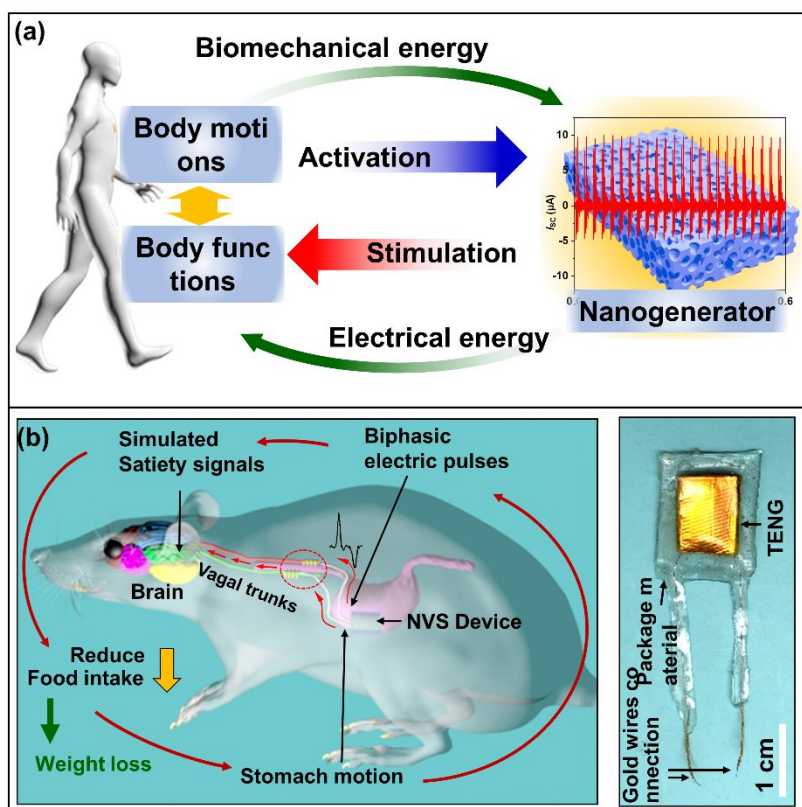


Figure 73. (a) A schematic diagram showing the concept of closed-loop ES. (b) Left: Schematics showing the operation concept of implantable NVS device for diet and weight control. The red arrows indicate the closed loop of biofeedback flow and control. Right: An optical photo of the VNS device. **Reprinted with permission under a Creative Commons CC BY license from ref. 365, Copyright 2018, Springer Nature.**

1
2
3
4 The electrical output generated by TENG is dependent on the limited amount of surface
5 charges. This feature is similar to the process of electric potential generation in biological
6 system, where displacement of oppositely charged ions induces bioelectricity. This similarity
7 may make NG ES particularly suitable for interfacing the biological system and stimulating
8 the physiological functions with minimal side effects. The recent successful results of skin
9 tissue (including hair follicles) resoration provided an excellent example, since the skin tissue
10 growth is directed by the endogenous electric field within the cellular matrix.⁶⁶⁵ The Wang
11 group developed an electrical bandage that integrates a TENG with a pair of dressing
12 electrodes.⁶⁶⁶ The TENG was designed to convert regular breathing into pulsed electrical
13 signals with a voltage output of ~0.1 to 1 V (Figure 74(a)). The voltage signal was directly
14 delivered to the interdigitated dressing electrodes that were fully covered a skin wound. From
15 the rat model, a 1 x 1 cm² full depth skin wound completely healed in just three days with the
16 help of TENG ES, compared to the controls that needed nearly 2 weeks. Similar effect has
17 also been obtained from human skin tissues that were grafted on mice as a preparatory step
18 towards a human subjects clinical trial. It was shown that a 4-mm full depth wound on human
19 skin tissue could fully healed in seven days while the control is still largely open.⁶⁶⁷ Cell-
20 level mechanism studies showed that proliferation of the fibroblast cells was enhanced by the
21 ES. The electric field could also influence the migration of fibroblast and facilitate their
22 ordering. The segregation of growth factors, including epidermal growth factor (EGF),
23 vascular endothelial growth factor (VEGF), keratinocyte growth factor (KGF) and
24 transforming growth factor beta (TGF- β) that are related to skin tissue growth, was also
25 enhanced under the influence of ES. Due to the charge-limited feature of the TENG output,
26 majority electricity could be quickly screened at the interface.⁶⁶⁸ Therefore, interfacial
27 electrochemical reaction is suppressed and substantially reduces the undesired reactive
28 oxygen species (ROS) generation in the tissue growth environment.
29
30
31
32
33
34
35
36
37
38
39
40
41
42
43
44
45
46
47
48
49
50
51
52
53
54
55
56
57
58
59
60

1
2
3
4 It was further discovered that hair follicles, an important functional component in skin
5 tissue, could as well be stimulated by ES dressing. The enhanced segregation of multiple
6 growth factors, such as KGF and VEGF, can facilitate the proliferation of hair follicles and
7 prolong their anagen stage, and therefore promote hair growth. The preliminary results were
8 demonstrated on both rats and genetically defective nude mice models. To fit in the head
9 area, an omnidirectional TENG was developed to produce electrical pulses from random head
10 motions, which were enabled by a concentric circular electrode design (Figure 74(b)).⁶⁶⁹ A
11 dressing electric field of 3 V/cm was found to be optimal to achieve the most significant hair
12 generation outcome, represented by fast hair shaft growth rates and a larger number of hair
13 follicles. The ~3 times higher hair follicle density obtained from nude mice showed the
14 potential of using TENG-enabled ES to overcome genetic defect, such as keratin disorder, to
15 promote hair growth. The outcomes from rodents outperformed controls treated with
16 Minoxidil, an FDA-approved medication for curing hair loss.
17
18
19
20
21
22
23
24
25
26
27
28
29
30
31
32
33

34 The last example we show here is the TENG-enabled ES for bone healing. Similar to
35 above two examples, bone fracture healing is another well-known biological process that is
36 influenced by the endogenous electric fields and can be facilitated by externally applied
37 ES.^{670,671,672,673,674} The challenge lies at how appropriate electric fields can be delivered to the
38 fracture area locally and consistently. To address this challenge, an implantable and
39 degradable TENG was developed.⁶⁷⁵ The device was created using a PLGA film, where
40 patterned micro-pyramids was fabricated to enable a sensitive interface paired with Mg
41 electrodes for in vivo biomechanical energy harvesting. The generated electrical signal was
42 directly applied to the interdigitated dressing electrodes wrapping around the fractured bone.
43 From the closed-fracture model of right tibia of rats, the in vivo TENG stimulation enabled a
44 rapid and complete bone fracture healing in just 6 weeks. The device could then degrade
45
46
47
48
49
50
51
52
53
54
55
56
57
58
59
60

1
2
3
4 naturally at the implantation site after the treatment without introducing any adverse effect to
5
6 the host.
7

8
9 The above examples are very encouraging to justify the applications of TENGs in
10
11 medical therapeutics. Given the broadness of how biological systems rely on endogenous
12
13 electric field, applications of NG-enabled closed-loop ES will be far beyond what have been
14
15 discussed in this section. It can be expected this strategy may become the next-generation
16
17 alternative to most clinical or cosmetic ES treatments, bring in higher efficacy, less adverse
18
19 effects, with excellent user friendliness.
20
21
22
23
24
25
26
27
28
29
30
31
32
33
34
35
36
37
38
39
40
41
42
43
44
45
46
47
48
49
50
51
52
53
54
55
56
57
58
59
60

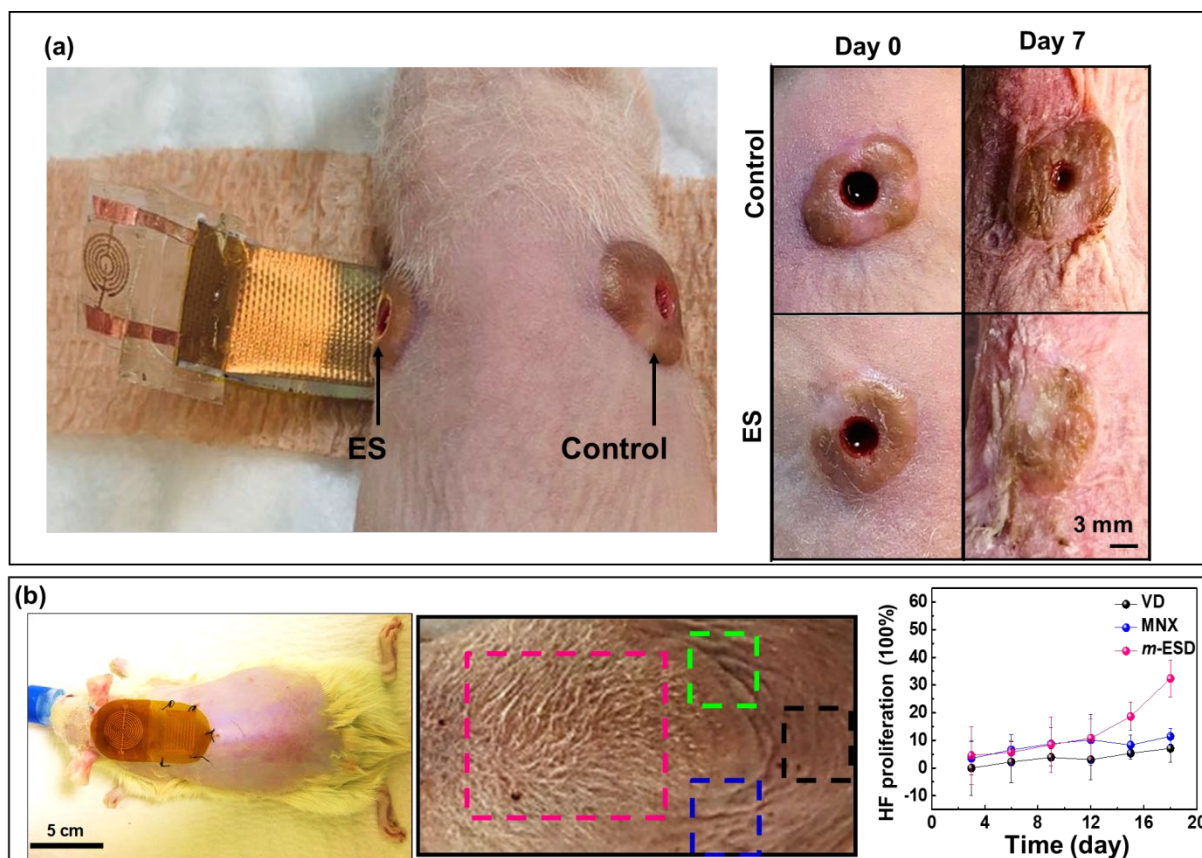


Figure 74. (a) Top: TENG-based electrical bandage for acute wound dressing on mice, where the mice received two grafted human skin tissues for ES treatment (left) and control (right). Bottom: Photos comparing the healing outcomes on the grafted human skin tissues with (ES) and without (control) ES dressing. **Reprinted with permission under a Creative Commons CC BY license from ref. 667, Copyright 2021, Springer Nature.** (b) Top: A rat received the hair regeneration device. Middle: Skin surface of a nude mice after being treated with TENG ES (m-ESD), comparing to the control area treated with Minoxidil (MNX), vitamin D3 (VD), and saline. Bottom: ratio of hair follicles (HF) increase at different days of treatment. **Reproduced from ref. 669. Copyright 2019, AMER CHEMICAL SOC.**

6.2.2 Drug delivery

Triboelectric nanogenerators enabled drug delivery devices that seamlessly interface with the human skin can deliver therapeutic agents in a convenient and self-administered manner^{676,677}.

Therefore, such wearable drug delivery devices can liberate patients with chronic diseases from dependency to centralized health facilities, which often lead to delayed treatment administration.⁶⁷⁸ To this end, TENGs can effectively harvest biomechanical energy around the human body and permit controllable and adaptive drug delivery.^{679,680,681}

To begin with, electroporation is a widely used mechanism for electrically-activated drug delivery devices, which relies on high-voltage electrical pulses to deliver therapeutic agents on the generated pores on the cell membrane.⁶⁸² TENGs can offer a transdermal drug delivery solution with decent stability and strong transmission efficiency because they can serve as on-body power sources and provide steady voltage pulses to drive these electroporation devices. A portable hand-powered wearable TENG assisted by nanoneedle-array of electrode was shown in Figure 75(a) to help with electroporation-induced transdermal drug delivery.⁶⁸³ By hand-cranking the disk TENG at 1 rpm, a 20 V output could be applied to the nanoneedle-array electrode, producing an electrical field of 2800 V/cm that was confined to the nanoneedle–cell interface. As the imposed localized electrical field is concentrated on a pointed tip, collateral cell damage is minimalized and imperceptible. Moreover, fluorescein isothiocyanate-labeled dextran was shown to effectively penetrate into the dorsal skin of nude mice as deep as 23 μm using the TENG-powered drug delivery system, which demonstrated a noninvasive and high-performance drug delivery method.

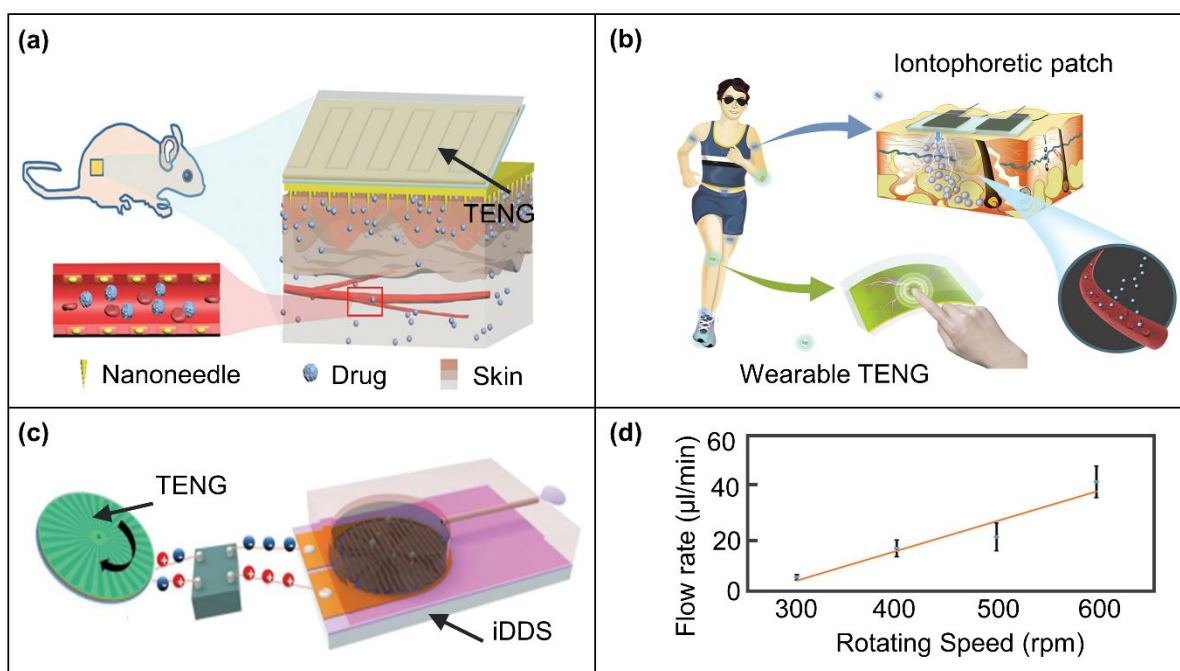
Furthermore, iontophoresis is a transdermal drug delivery strategy that is less painful than electroporation and allows controllable drug penetration. Figure 75(b) demonstrates a TENG-enabled iontophoretic transdermal drug delivery system for closed-loop biomechanical

1
2
3
4 sensing and therapy.⁶⁸⁴ The wearable TENG using PTFE and aluminum triboelectric layers
5 was integrated into an insole to harvest the gait energy, which generated an open circuit
6 voltage of 1200 V and a short-circuit current of 20 μA , at an operating frequency of 2 Hz.
7
8
9
10
11 Converting the generated electricity into direct current can activate a hydrogel drug patch
12 attached onto the skin of the ankle. The positive current drove the positively charged drug
13 molecules in the drug-maintaining hydrogel flowing from one side to another. Since the two
14 sides were insulated, drug molecules were transported through the skin by iontophoresis.
15
16
17
18
19
20 Moreover, TENG-powered iontophoretic drug delivery system effectively delivered the
21 modal drug R6G/MB into pig skin, proving its transdermal drug delivery abilities. This work
22 demonstrated a convenient, self-administrating, and safe drug delivery for ankle injury.
23
24
25
26

27
28 In addition, controlled and sustainable drug delivery systems are critical for chronic and
29 site-specific treatment. Electricity from TENGs can be applied for powering an on-demand
30 drug delivery system. The TENG-powered implantable drug-delivery system charged by the
31 human body's motion was presented in Figure 75(c).⁶⁸⁵ This device had a rotationally gating
32 structure where two layers of metal Cu patterned with radial arrayed strips were assembled as
33 a rotator and a stator. Output performance was controllably adjusted by optimizing the
34 rotation speed of the rotator. With an optimized setting, an output current and voltage of 1.5
35 mA and 15 V, were obtained with a rotating speed of 500 rpm. For the drug delivery process,
36 the electrical output of TENGs was rectified and applied to Au electrodes within the drug
37 reservoir where the water-splitting process occurred, pumping out the drug through a
38 microtube. Higher rotating speeds generally yielded higher delivery flow rates, resulting in
39 faster water-splitting rates. The output voltage reached about 5 V, and the delivery flow rate
40 was about 5.3 $\mu\text{L}/\text{min}$ with a 300-rpm rotating speed. Figure 75(d) plotted a higher flow rate
41 of 40 $\mu\text{L}\cdot\text{min}^{-1}$ was recorded at the rotating speed of 600 rpm. *In vitro* trans-sclera drug
42
43
44
45
46
47
48
49
50
51
52
53
54
55
56
57
58
59
60 delivery in porcine eyes was successfully realized with this implantable drug-delivery system.

1
2
3
4 Additionally, a TENG-based on-demand transdermal drug delivery system by the
5 iontophoresis effect was reported. The system was demonstrated on pig skin with R6G dye as
6 a model drug.⁶⁸⁴ Moreover, an electroporation intracellular drug delivery system was reported
7 that using wearable TENG as a power source by harvesting finger friction and hand
8 slapping.⁶⁸³ In another study, a TENG-based transdermal and non-invasive delivery system
9 was demonstrated for on-demand drug dosing.⁶⁸⁶ In 2020, the sustainable and controllable
10 release of salicylic acid from a flexible drug release device for potential wound healing was
11 demonstrated, which was powered by arm clapping using a wearable TENG.⁶⁸⁷

12
13
14
15
16
17
18
19
20
21
22
23 In summary, with a collection of compelling features, including light weight, low cost,
24 high voltage, TENGs are making a splash in the drug delivery community. Although the
25 wearability and efficiency of these drug delivery systems still needs further optimization, the
26 proof-of-concept demonstrations of using wearable TENGs for self-powered and on-demand
27 drug delivery emerges as compelling therapeutic approaches to treating chronic diseases.



1
2
3
4 **Figure 75. TENGs for drug delivery. (a)** Schematic illustration of in vivo TENG-driven
5 electroporation system. **Reproduced from ref. 683. Copyright 2019, John Wiley and Sons.**
6
7
8 **(b)** Schematic illustration of wearable TENG based self-powered iontophoretic transdermal
9 drug delivery system. **Reproduced from ref. 684. Copyright 2020, John Wiley and Sons.**
10
11
12 **(c)** Schematic configuration of TENG-based implantable drug delivery system. **Reproduced**
13 **from ref. 685. Copyright 2017, John Wiley and Sons. (d)** The flow rate of drug delivery
14 system as a function of TENG rotating speed. **Reproduced from ref. 685. Copyright 2017,**
15
16 **John Wiley and Sons.**
17
18
19
20
21
22
23
24
25
26
27
28
29
30
31
32
33
34
35
36
37
38
39
40
41
42
43
44
45
46
47
48
49
50
51
52
53
54
55
56
57
58
59
60

6.3 Environmental Applications

6.3.1 Water purification

In this section we review the pressing problems in water treatment that warrant the need for more solutions, discuss the advantages of TENGs for application in these sectors, and present examples of TENG driven systems being researched and developed for water treatment.

To treat water for safe human consumption, use, or discharge, many impurities need to be removed or inactivated, including waterborne pathogens⁶⁸⁸, organic pollutants⁶⁸⁹, industry contaminants like dyes⁶⁹⁰ and metals⁶⁹¹, as well as emerging contaminants like antibiotics⁶⁹² and micro/nano plastics⁶⁹³. The increasing complexity of pollutants and refractory contaminants in our waters continue to make the treatment process very difficult and energy intensive.⁶⁹⁴ With the growing population and overwhelming urbanization, more water is needing treatment than ever before, resulting in an enormous energy toll.^{695,696} Because of the high chemical and energy demands for water treatment, the current challenge is to reduce the economic and environmental implications by using more electricity and environmentally friendly energy sources.^{697,698} These challenges have sparked the development of various TENG powered devices for different focused areas of water treatment.

Waterborne pathogens are a massive threat to public health, especially in developing areas, rural regions, or disaster zones where people lack centralized sanitation facilities and have inconsistent access to grid power.^{688,699,700,701,702,703,704} Various TENG-powered devices have successfully been applied to inactivate pathogens in water using either the intense electric field generated directly or the electric current after transformation. Triboelectric energy harvesting devices have outputs regularly in the tens to thousands of volts, while only producing current in the order of nano/micro amps.⁷⁰⁵ Not only is this low current safe for

1
2
3
4 humans, but also this triboelectric power is perfect for electroporation based technologies, as
5
6 it can achieve a sufficient electric field for disinfection while reducing potential unwanted
7
8 electrochemical reactions from the low current.⁷⁰⁶ Liu et al. developed a triboelectric energy
9
10 harvester by harnessing the friction and built static energy between two sheets of aluminum
11
12 foil and a piece of plastic film.⁷⁰⁵ The foil was then connected to two parallel CuO nanowire-
13
14 modified electrodes to formulate a disinfection device. During operation, the microbes that
15
16 came in the vicinity of the nanowire tips were inactivated through electroporation of an
17
18 enhanced electric field powered by the generated static triboelectricity. However, for more
19
20 practical application, using hand motions to generate electricity is limited due to fragile
21
22 structure, low-frequency stimuli, and low output power density.⁶⁸⁸ Because of this, Tian et al.
23
24 reported a ball-in-ball TENG with rubber and aluminum foil to convert water wave energy to
25
26 electricity, which is applied to two carbon cloth electrodes modified with ZnO nanowires and
27
28 Ag nanoparticles (Figure 76(a)).⁷⁰⁶ Bacteria that passed through the TENG-powered device
29
30 were completely inactivated, and the operation sustained high disinfection performance due
31
32 to the charged electrodes slowly releasing electrons after being cut off from the power
33
34 supply. Huo et al. developed a rapid, self-powered disinfection device for both bacterial and
35
36 viral inactivation based on an oxidation-assisted electroporation mechanism driven by a
37
38 supercoiling-mediated rotational TENG that can achieve high speed rotation (Figure
39
40 76(b)).⁷⁰⁷ The high disinfection efficiency was attributed to both the nanowire-enhanced
41
42 electric field and the generated oxidative species.
43
44
45
46
47
48
49
50
51
52
53
54
55
56
57
58
59
60

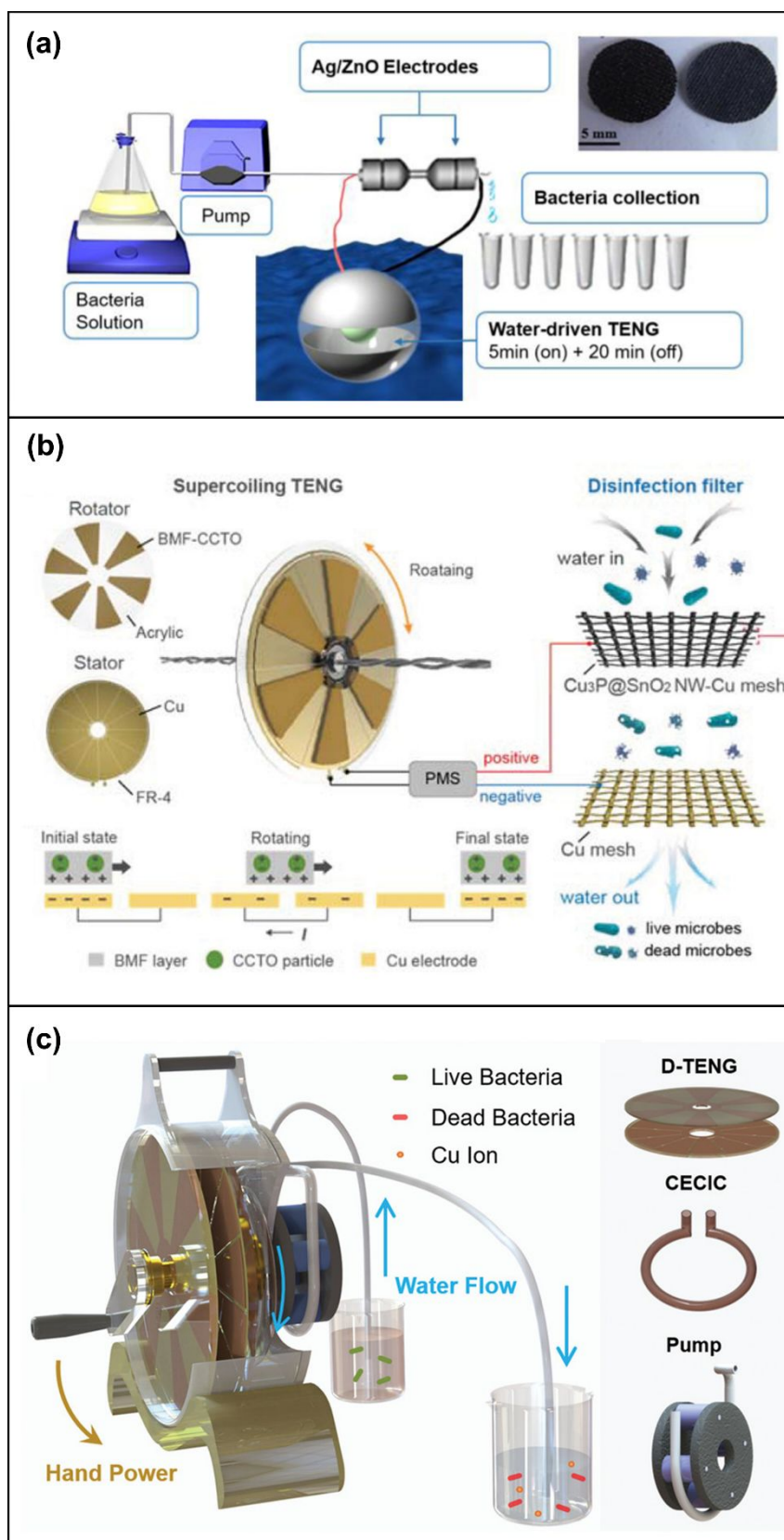


Figure 76. (a) Schematic of the experimental setup of the wave-driven ball-in-ball TENG water disinfection device with Ag/ZnO nanowires. **Reproduced from ref. 706. Copyright**

1
2
3
4 **2017, Elsevier. (b)** Supercoiling-mediated rotational TENG driven water disinfection system,
5 consisting of a supercoiling TENG, a power management system (PMS) with rectifiers, and a
6 disinfection filter for water-borne microbial inactivation. **Reproduced from ref. 707.**
7 **Copyright 2022, Wiley. (c)** Hand-powered TENG for self-powered disinfection based on the
8 coupling effect of a localized electric field and copper ion toxicity. Schematic of the proposed
9 TriboPump consisting of a hand-powered rotational TENG, a disinfection cell, and a water
10 pump. **Reproduced from ref. 708. Copyright 2019, Elsevier.**
11
12
13
14
15
16
17
18
19
20
21
22
23
24
25
26
27
28
29
30
31
32
33
34
35
36
37
38
39
40
41
42
43
44
45
46
47
48
49
50
51
52
53
54
55
56
57
58
59
60

1
2
3
4 With the assistance of power management systems, TENGs have also functioned as DC
5 powers to drive both electrochemical cells and UV radiation.⁶⁸⁸ When developing water
6 purification devices, pumps are often needed and require an external energy source,
7 especially in areas lacking consistent grid connection. Because of this, Ding et al. developed
8 a hand-powered disinfection device (TriboPump) with an integrated pump, driven by a
9 rotational TENG (Figure 76(c)).⁷⁰⁸ During operation, the TriboPump used hand power to
10 rotate, create energy, and drive water through a tubular coaxial electrode copper ionization
11 cell (CECIC) disinfection device. The CECIC used both the electric current to release copper
12 ions, and the locally enhanced electric field to enhance the uptake of copper ions by bacteria,
13 resulting in no live bacteria detection in the effluent with 6 log inactivation efficiency after
14 only 2.5 minutes. Jiang et al. used wave energy to self-power water disinfection systems that
15 coupled both TENGs and water electrolysis devices, achieving 6 log inactivation of three
16 model bacteria after only 60 seconds of operation.⁷⁰⁹ In another study, Wang et al. developed
17 a freestanding rotary TENG to power mobile UV light sources (Figure 77(a)).⁷¹⁰

18
19
20
21
22
23
24
25
26
27
28
29
30
31
32
33
34
35
36
37 Another limitation for large scale water treatment in rural, remote, or developing areas is
38 the lack of centralized facilities for chemical coagulation due to its high operating cost,
39 difficult management, and complex handling of bulky chemical sludge.⁷¹¹ Electrocoagulation
40 offers a promising alternative as it utilizes only simple electrodes and electrical power for a
41 lower cost, small sludge volume, and easy operating process.⁷¹² Because of this, Jeon et al.
42 designed a self-powered electrocoagulation cell for decentralized water treatment equipped
43 with a wind energy harvesting TENG (Figure 77(b)).⁷¹¹ The power supplied to the Al
44 electrodes inside the electrocoagulation unit induces electrochemical reactions, generating
45 aluminum hydroxide which acts as the coagulant to collect dissolved pollutants in untreated
46 water. This TENG powered electrocoagulation removed 90% of algae and 97% of organic
47
48
49
50
51
52
53
54
55
56
57
58
59
60

1
2
3
4 dye during a batch operation of 72 hours. Cho et al. proposed a waterwheel structured hybrid
5
6 generator to scavenge rotational energy from a disk-type TENG to power an
7
8 electrocoagulation cell (Figure 77(c)).⁷¹³ In their studies, the TENG demonstrated feasibility
9
10 as a power source for the electrocoagulation cell, which exhibited practical dye removal
11
12 around 60% under batch operation of 24 hours and superior microalgae removal of 95%
13
14 under 18-hour batch operation.
15
16
17
18

19 Electrochemical technologies have also gained increasing interest for their versatility,
20
21 environmental compatibility, lower potential cost, and higher effectiveness for refractory
22
23 pollutants.⁶⁹⁴ Liu et al. developed a water driven TENG with a DC output to power an
24
25 electrochemical cell, which generated free radicals for the degradation of organic pollutants
26
27 in wastewater treatment.⁶⁸⁹ With the electric field and electrons supplied by the TENG, the
28
29 fed phosphomolybdic acid and H₂O₂ were both activated, resulting in 100% removal of 4-CP
30
31 through dichlorination and mineralization by free radicals. Gao et al. designed a free-standing
32
33 rotary disc-structured TENG that can harvest various sources of vibrational energy to drive
34
35 an electrochemical cell to treat carcinogenic azo dye by controlling electrochemical oxidation
36
37 potential.⁶⁹⁰ The TENG was able to selectively treat 4-aminoazobenzene (AAB) to produce
38
39 CO₂, providing promising potential for TENG driven technologies to remove a variety of
40
41 dyes as most azo dyes popular to use in the industry are derivatives of AAB. Chen et al. also
42
43 fabricated a TENG-powered multifunctional system⁷¹⁴ that was capable of both the removal
44
45 of rhodamine B dye electrochemically, and Cu ions in water through metal electrodeposition
46
47 using the flow kinetic energy in the treatment cycle.⁶⁹⁴ When the TENG operated at a speed
48
49 of 600 rpm, the system removed almost 100% of rhodamine B within 15 minutes, while
50
51 97.3% of Cu ions were removed in 3 hours. The high-quality deposition of Cu makes the
52
53 system more promising for electroplating, while the high efficiency removal for rhodamine B
54
55
56
57
58
59
60

1
2
3
4 makes it feasible for removal of other contaminants in the water treatment process. This and
5
6 other previously discussed technologies show the promise of TENG driven technologies to
7
8 sustainably treat refractory pollutants like dyes and metals using self-powered
9
10 electrochemical processes with very low power consumption and little to no external
11
12 pollution.⁶⁹⁴
13
14

15
16 Other emerging contaminants of concerns include antibiotics, as one of the most relied
17
18 upon drugs in the world, and micro/nano-plastics, as plastic and plastic pollution have
19
20 become pervasive in our lives. To tackle these, Mo et al. designed a photocatalytic system
21
22 powered by crowned TENG to remove tetracycline from contaminated water as it is the most
23
24 widely-used antibiotic (Figure 77(d)).^{715,716} Using an iron-based metal framework, the TENG
25
26 collected water wave energy with an acceleration of 5 m/s^2 , resulting in a tetracycline
27
28 removal efficiency of 95.89% within 80 minutes. Furthermore, Park et al. demonstrated an
29
30 electrophoretic nanoparticle removal system using a porous-pyramid PDMS TENG whose
31
32 removal rate was 5.6 times higher than that for conventional flat TENG (Figure 77(e)).⁷¹⁷ The
33
34 PDMS TENG successfully removed nanoparticles of various materials including plastics,
35
36 heavy metal composites, metal oxides, and ceramics, showing great promise for TENGs to
37
38 power water treatment for both emerging contaminants and existing suspended/inorganic
39
40 pollutants.
41
42
43
44
45

46
47 Moving forward, some challenges remain the unstable and fluctuating conditions like
48
49 weather, temperature, and humidity, and their effects on the output power density and
50
51 reliability for energy harvesting with TENGs.⁶⁸⁸ This is critical as water treatment need to run
52
53 effectively and continuously to guarantee the public health and protect the environment.
54
55 Overall, TENG driven systems are very promising as efficient, self-powered, and sustainable
56
57 technologies to provide and increase the accessibility of clean water for people in remote,
58
59
60

1
2
3
4 developing, or disaster regions where there are inconsistent or unreliable power supplies.
5
6
7
8
9
10
11
12
13
14
15
16
17
18
19
20
21
22
23
24
25
26
27
28
29
30
31
32
33
34
35
36
37
38
39
40
41
42
43
44
45
46
47
48
49
50
51
52
53
54
55
56
57
58
59
60

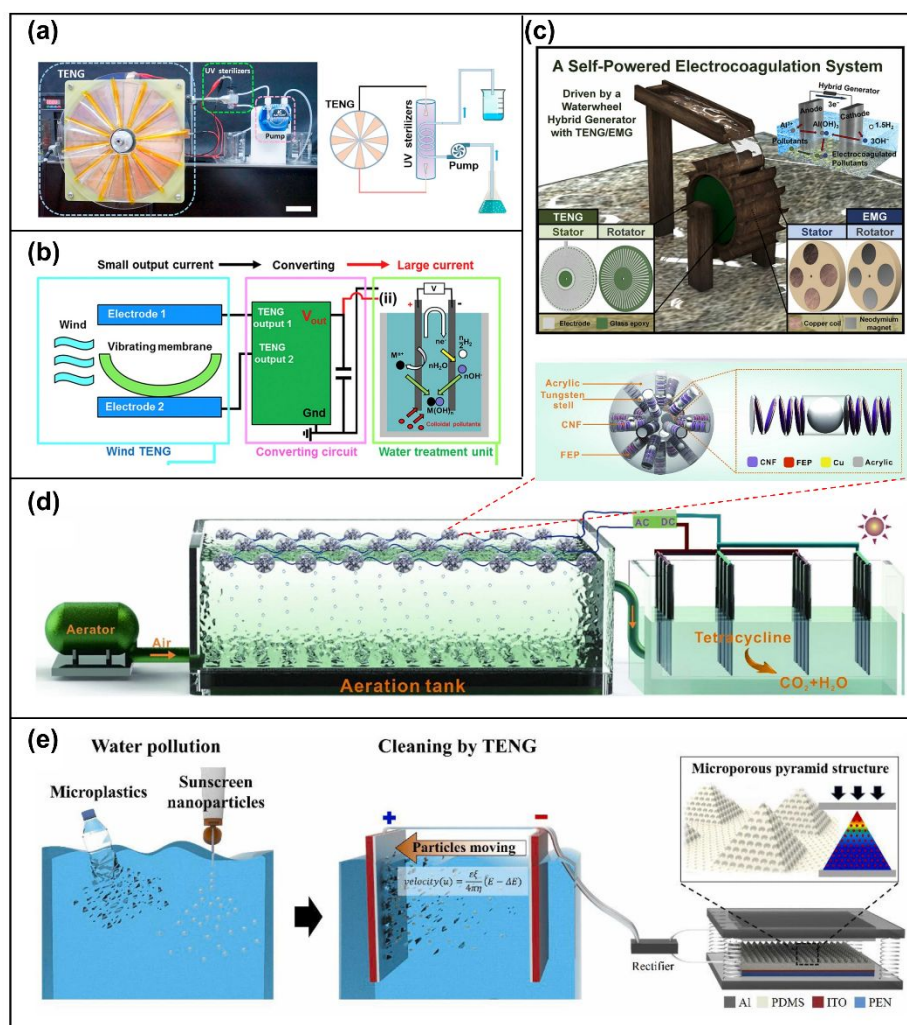


Figure 77. (a) Photograph and schematic diagram of a TENG powered UV water sterilization system (scale bar, 70 mm). **Reprinted with permission under a Creative Commons CC BY license from ref. 710, Copyright 2020, Elsevier.** (b) Schematic of a wind energy harvesting TENG for a self-powered electrocoagulation cell. Depicted are the TENG energy harvesting, the converting circuit, and the water treatment unit. **Reproduced from ref. 711. Copyright 2016, Elsevier.** (c) Schematic diagram of the waterwheel structured hybrid generator scavenging rotational energy from a disk-type TENG and an inset illustration of the electrochemical mechanism of the electrocoagulation method. **Reproduced from ref. 713. Copyright 2022, Elsevier.** (d) Self-powered photocatalytic system based on water wave driven crowned TENG for tetracycline removal. **Reproduced from ref. 716. Copyright 2022, Elsevier.** (e) Self-powered microplastics and nanoparticles removal system via high performance porous-pyramid TENG. **Reproduced from ref. 717. Copyright 2022, Elsevier.**

6.3.2. Air purification

Increasing air pollution is one of the factors impacting global health. COVID-19 and other respiratory viral evidence indicate that air pollution can affect respiratory defense mechanisms and cause infection to worsen. In the presence of such a pandemic, the need to eliminate air pollution becomes even more urgent.⁷¹⁸ Urban air pollution consists of a mixture of gaseous and particulate components, of which particulate matter (PM), nitrogen oxides (NO_x), and ozone (O_3) have been investigated extensively.^{719,720} Conventional air filters usually rely on tiny pore sizes to block contaminant particles but suffer from the drawbacks of large pore sizes and low porosity.⁷²¹ While electrostatic precipitators require an external power supply for long-term operation.⁷²² TENGs are an attractive option for producing high voltages for air purification with the benefit of self-sustainability. Various air filtration technologies coupling TENGs and mechanical filtration have achieved improved outcomes over classical filtration mechanisms.⁷²³ There is the strategy of harnessing the high voltage brought by TENGs to power the dust removal materials, such as the positively charged PI nanofiber filter in Figure 78(a), which provides an added electrostatic adsorption to mechanical filtration.⁷²⁴ Here are also approaches to achieving the adsorption of PM directly using components with large electrostatic charges of the TENGs, for instance, conductive sponges (CS) and electrospun fibers (nanofibrils, NFs) of the self-powered mask can generate

1
2
3
4 triboelectric charges with the breathing airflow (Figure 78(b)).⁷²⁵ In this section, we review
5
6
7
8 the applications of TENGs in air filtration.
9
10
11
12
13
14
15
16
17
18
19
20
21
22
23
24
25
26
27
28
29
30
31
32
33
34
35
36
37
38
39
40
41
42
43
44
45
46
47
48
49
50
51
52
53
54
55
56
57
58
59
60

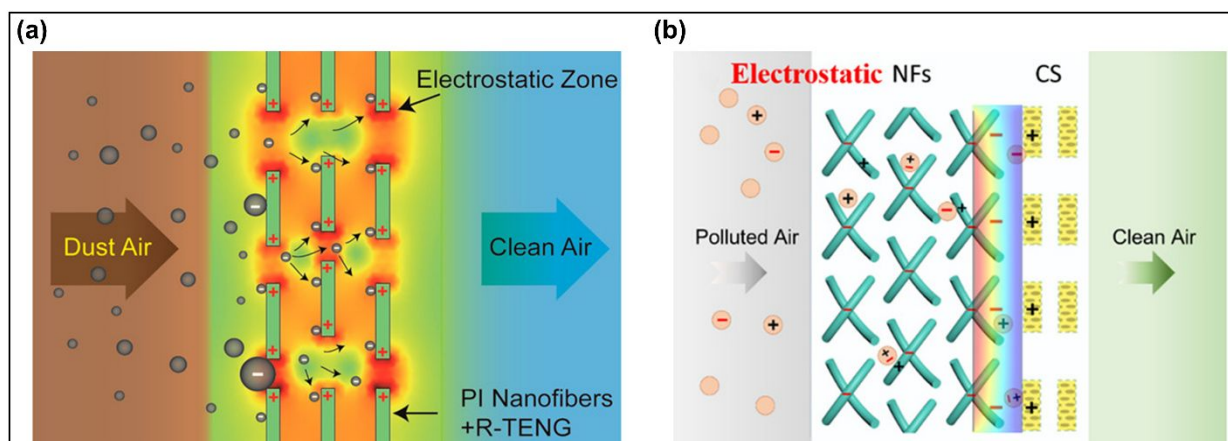


Figure 78. Different strategies of air filtration devices based on TENGs. **(a)** Schematic image of the filtration mechanism of the PI nanofibers charged by TENG. **Reprinted with permission from ref. 724, Copyright 2017, American Chemical Society.** **(b)** Schematic diagram of the self-powered triboelectric air filter based on the electrostatic force of filtration. **Reprinted with permission from ref. 725, Copyright 2021, American Chemical Society.**

1
2
3
4
5 For second-hand smoke pollution, Zhang et al. developed a high-voltage recharging
6
7
8 system that reduces PM concentration to World Health Organization (WHO) standards.⁷²⁶
9
10
11 The biomimetic hairy-contact triboelectric nanogenerator (BHC-TENG) can achieve an open-
12
13
14 circuit voltage of 8.42 kV by friction brought about by the rotation of a fluorinated ethylene
15
16
17 propylene (FEP) film and rabbit fur (Figure 79(a)-(i)). The high voltage generated by BHC-
18
19
20 TENG continuously injects charge to melt-blown fabrics through the tip discharge of the
21
22
23 microneedle array (Figure 79(a)-(ii)), which can solve the problem of charge loss when melt-
24
25
26 blown fabrics are exposed to high-humidity environments. Driven by BHC-TENGs, the
27
28
29 system maintains a removal efficiency of over 90% for PM 0.5-10. Further, Han et al.
30
31
32 achieved the removal of PMs from automobile exhaust by a high electric field generated by
33
34
35 friction between PTFE particles and aluminum electrodes.⁷²⁷ As shown in Figure 79(b)-(i),
36
37
38 when the chamber vibrates, the PTFE particles collide with two aluminum plates, resulting in
39
40
41 negative and positive charges of PTFE and aluminum, respectively. A current is formed when
42
43
44 the two electrodes are electrically connected, and when in open-circuit situation, the surface
45
46
47 charge density gradually saturates with the collision. Suspended particles will be removed
48
49
50 due to mechanical filtration and electrostatic adsorption while passing through the
51
52
53 triboelectric filter. The effective removal of exhaust particulate matter was verified by
54
55
56
57
58
59
60

1
2
3
4 installing the TENG-based filter on a commercial vehicle and testing the exhaust emissions
5
6
7
8 (Figure 79(b)-(ii)). The above two works implement the adsorption of PM from tobacco
9
10
11 smoke and vehicle exhaust through the TENG-powered external dust removal materials or
12
13
14 charged components of TENGs, respectively, and are essential for progress toward the
15
16
17 practical applications of self-powered PM cleaning.
18
19
20
21

22 In addition to particulate removal, there are studies dedicated to the degradation of
23
24
25 gaseous pollutants. Feng et al. exploited the high electrostatic field generated by the single
26
27
28 electrode triboelectric nanogenerator (SE-TENG) to inhibit the recombination of electron-
29
30
31 hole pairs in the photocatalytic process and enhance the photocatalytic effect.⁷²⁸ The
32
33
34 schematic diagram of the setup for degrading formaldehyde is shown in Figure 79(c)-(i). The
35
36
37 formaldehyde concentration was reduced to 60% within 250 min with SE-TENG as the driver,
38
39
40
41 which doubled the degradation efficiency compared to without the TENG (Figure 79(c)-(ii)).
42
43
44 Likewise targeting indoor formaldehyde degradation, Zheng et al. reported a rotation mode
45
46
47 high voltage TENG with direct current (RH-DC-TENG) that employs a rotating structure for
48
49
50 collecting wind energy.⁷²⁹ The RH-DC-TENG has an open circuit voltage range of 10 to 30
51
52
53 kV. The high electric field provided by RH-DC-TENG can promote photocatalytic
54
55
56 degradation and the experimental platform can be seen in Figure 79(d)-(i). The designed self-
57
58
59
60

1
2
3
4 powered air purifier formed by coupling the RH-DC-TENG with non-thermal plasma (NTP)
5
6
7
8 and photocatalytic oxidation (PCO) achieved a 94% reduction in formaldehyde concentration
9
10
11 in 10 minutes in a 13-liter airtight chamber (Figure 79(d)-(ii)). The above research provides
12
13
14
15 effective insights to solve the problem of high indoor formaldehyde concentration.
16
17

18 In summary, TENGs were designed to be applied to various air purification scenarios,
19
20
21 and initial experimental results proved impressive benefits. However, so far, research on the
22
23
24 degradation of gaseous pollutants has been less extensive than on particulate removal.
25
26
27
28 Besides, there are problems of relatively homogeneous structures and high dependence on the
29
30
31 external environment, so there is still need to consider the production details to enhance their
32
33
34
35 practicality.
36
37
38
39
40
41
42
43
44
45
46
47
48
49
50
51
52
53
54
55
56
57
58
59
60

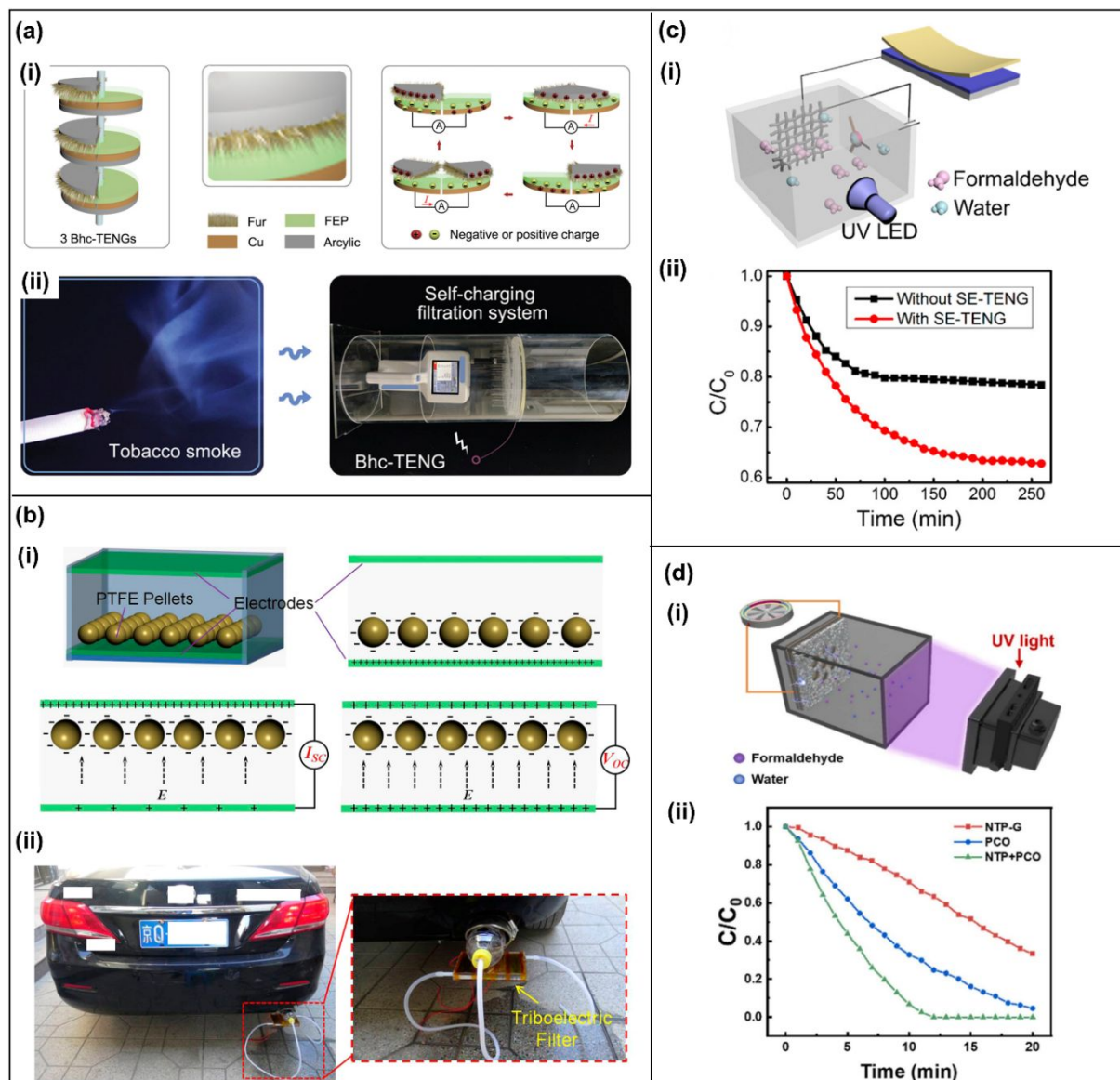


Figure 79. TENGs utilized in air purification devices and the corresponding application scenarios. **(a)-(i)** Material composition in the BHC-TENGs and the working mechanism. **(a)-(ii)** Photograph of the self-powered high-voltage recharging system for removing noxious tobacco smoke. **Reproduced from ref. 726, Copyright 2022, John Wiley and Sons.** **(b)-(i)** Three-dimensional structure and operating mechanism of the TENG. **(b)-(ii)** Picture of a car with a triboelectric filter on the tailpipe. Inset: Enlarged image of the device setting. **Reprinted with permission from ref. 727, Copyright 2015, American Chemical Society.** **(c)-(i)** Schematic diagram of the setup used for degrading formaldehyde driven by SE-TENG.

1
2
3
4 (c)-(ii) Concentration change during the photocatalytic degradation of formaldehyde with and
5 without SE-TENG. **Reproduced from ref. 728. Copyright 2017, American Chemical**
6
7
8 **Society. (d)-(i)** Schematic illustration of the experimental platform driven by RH-DC-TENG.
9
10
11 (d)-(ii) Variation of formaldehyde concentration in three degradation techniques. **Reprinted**
12
13 **with permission from ref. 729, Copyright 2022, Elsevier.**
14
15
16
17
18
19
20
21
22
23
24
25
26
27
28
29
30
31
32
33
34
35
36
37
38
39
40
41
42
43
44
45
46
47
48
49
50
51
52
53
54
55
56
57
58
59
60

6.4. Sensor applications

6.4.1. Tactile sensing

Tactile sensors serving for human-device interactive interfaces, robotic and prosthetic skins, and health monitoring are crucial components in a vast field of smart devices and wearable electronics. Conventional passive sensors, including resistive, capacitive, and optical-type ones, suffer from energy issues, complex device structures, and limited materials, impeding their applications.^{730,731,732} In contrast, TENGs offer advantages including self-powered sensing, diverse materials selection, simple structure, low cost and manufacturability, enabling many possibilities for tactile sensors that cannot be realized before.^{733,734,70}

The working mechanisms of the triboelectric tactile sensors are mainly founded on the single-electrode and contact-separation modes. For a single-electrode-mode TENG, skin touching would change the electric field created by the surface triboelectric charges, causing the flow of free electrons in the electrode accordingly and resulting in an active electrical signal.⁴²⁴ For a contact-separation-mode TENG, touching can bring contact of the two active components; thereby, the generating signals can respond touching.^{37,735} The actively-generating electrical signals in response to touching enable TENG self-powered tactile sensors.

Competing conventional passive tactile sensors suffer from a lack of flexibility and wearability as well as the issues of needing batteries and power dissipation. An electric eel's skin-inspired TENG is reported for energy harvesting and tactile sensing (Figure 80(a-c)).⁷³⁶ The device is designed using percolating silver nanowires networks as the electrode encapsulated in triboelectric silicone rubber. The device reveals intrinsic and mechanic durability and resilience, showing excellent biaxial stretchability, uniaxial stretchability of over 300% strain as well as abilities to multiple twists and folds (Figure 80(b)). It can convert energy from skin touching into electricity regardless of various extreme mechanical

1
2
3
4 conditions and deformations. Especially, even after experiencing tear damage, the device can
5
6 keep the capability to generate electricity. The devices are easy to scale up and shape as
7
8 desired, and the processes are cost-effective and suitable for industrial manufacture. With the
9
10 favorable mechanical tolerability, the skin-like device can be adapted to various non-planar
11
12 surfaces to scavenge touching energy. Furthermore, a fully autonomous and body-
13
14 conformable e-skin system with intuitively visual signals is realized by using the electric eel
15
16 skin-like device (Figure 80(c)). This work is expected to bring significant benefits to a wide
17
18 range of deformable electronics, and the demonstration of self-powered and adaptive human-
19
20 interactive system can advance the development of self-sufficient e-skin systems ranging
21
22 from self-powered interactive interfaces, to robotic and prosthetics skins.
23
24
25
26
27

28
29
30
31
32
33
34
35
36
37
38
39
40
41
42
43
44
45
46
47
48
49
50
51
52
53
54
55
56
57
58
59
60
Fibers, yarns, and textiles are ideal options for designing wearable and large-area tactile sensors. They offer advantages including flexibility, adaptability, breathability, and scalability. Therefore, tremendous efforts have been made to develop fiber-, yarn-, and textile-based TENG self-powered tactile sensors.^{37,737,738} For example, a single-thread-based wearable TENG is reported for human-motion energy harvesting and self-powered tactile sensing (Figure 80(d-e)).⁷³⁷ The single-electrode-mode TENG thread is fabricated by coating silicone rubber on a stainless-steel thread. It can extract energy during contact with skin. For a 5 cm-length TENG thread, the output open-circuit voltage and short-circuit current reached to ~15 V and ~7 μ A, respectively. By sewing the TENG thread on an elastic textile by a serpentine shape, a large-area and stretchable TENG textile can be realized. Because the effective contact area to the elastic and circular surface of outer silicone rubber depends on the contact force, the TENG thread exhibits the capability to actively sense different contact forces. It is demonstrated to serve as a human-device interface on a clothing to transmit Morse code from touches (Figure 80(e)). Moreover, the simplified single triboelectric thread

1
2
3
4 can be applied in a wide range of thread-based self-powered and sensing uses, including
5
6 gesture sensing, human-interactive interfaces, and human physiological signal monitoring.
7
8 With a good sensitivity, a wearable and self-powered pulse meter is realized by using the
9
10 TENG thread, realizing the real-time monitoring of human physiological signals on smart
11
12 clothing. Furthermore, by working with microcontrollers, more sophisticated tactile sensing
13
14 systems, such as wireless and wearable keyboards, are demonstrated.
15
16
17
18

19 A large-area waterproof textile-based TENG is reported for acting not only as a
20
21 wearable and implementable energy harvester but also a self-powered active tactile sensor
22
23 (Figure 80(f-g)).³⁷ The contact-separation-mode TENG textile is mainly comprised two
24
25 combined fabrics. The bottom one is composed of a conducting fabric sandwiched between a
26
27 roughened silicone rubber membrane and an ethylene-vinyl acetate (EVA) film as the
28
29 waterproof substrate. The upper one consisted of a conducting fabric sandwiched between a
30
31 mesh fabric and an EVA film. Finally, the TENG textile is completed by placing the mesh
32
33 side of the upper fabric onto the silicone rubber membrane of the bottom fabric and sealing
34
35 the borders by a waterproof adhesive. The contact and separation between the top conducting
36
37 fabric and bottom silicone rubber membrane enable to generate electricity. Particularly, it can
38
39 harvest energy from not only body motions but also natural tiny impacts (rains and winds).
40
41
42 Furthermore, touching the TENG textile can make the contact of two inner active fabrics and
43
44 generate electrical signals, enabling a self-powered textile-based tactile sensor. By
45
46 programming the actively responding signals, a system-level wearable tactile sensing system
47
48 such as a remote keypad for a music player has been demonstrated on a smart garment
49
50 (Figure 80(g)). The presented TENG textile exhibits advantages of both mechanical
51
52 compliance and waterproof, which are important for wearable tactile-sensing uses.
53
54
55
56
57
58
59
60

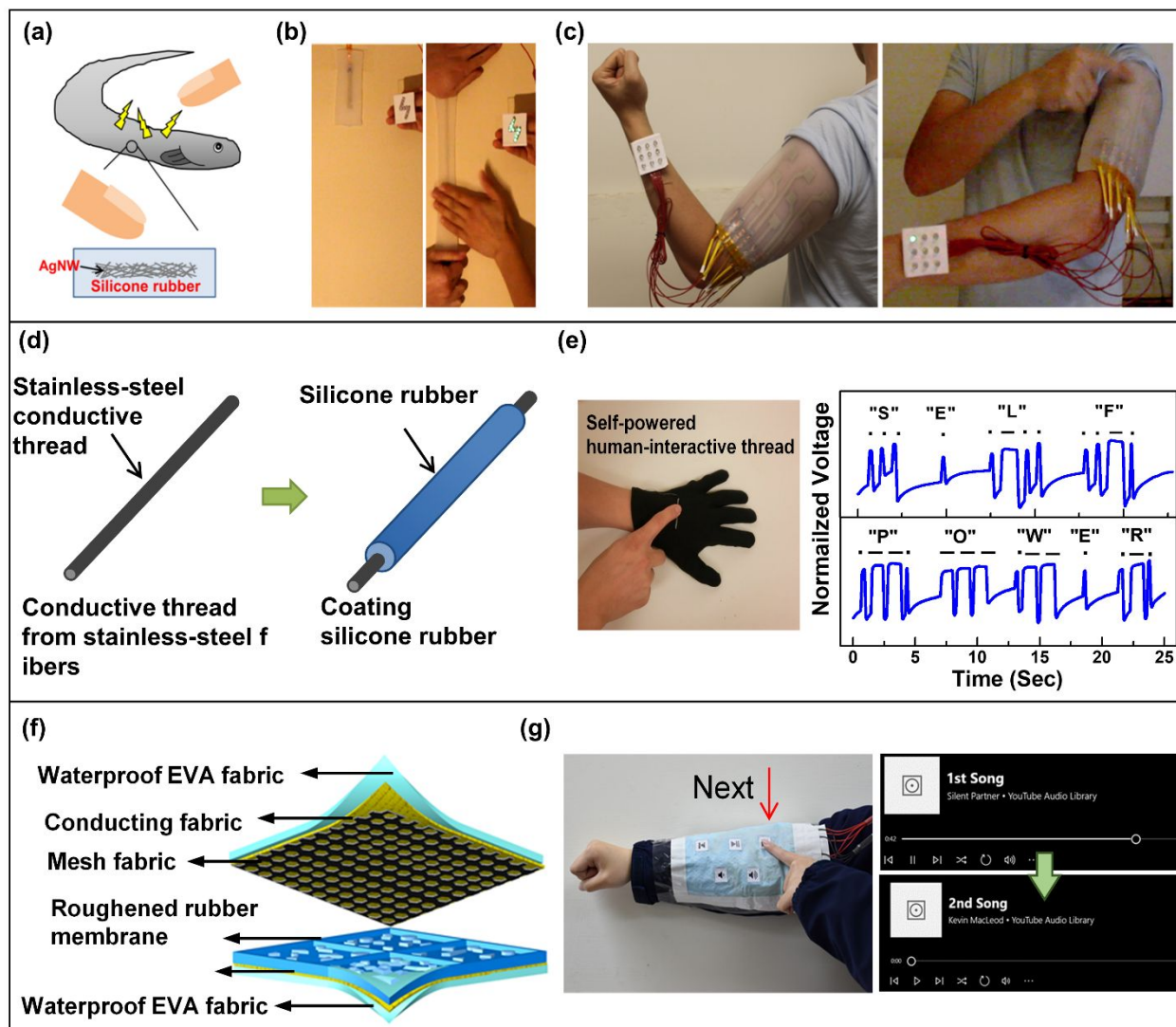


Figure 80. (a) Illustration of the concept of an electric eel skin-inspired nanogenerator. (b) Photograph demonstrating the stretchability of the electric eel skin-inspired TENG. (c) Photograph demonstrating that the self-powered electronic skin system. **Reproduced from ref. 736. Copyright 2016, John Wiley and Sons.** (d) Schematic diagram for the fabrication process of the TENG thread. (e) Left: Demonstration of the TENG threads using as a self-powered human-system interaction interface. Right: Morse codes produced by touching the TENG thread with finger, representing a phrase of “SELF-POWER”. **Reproduced from ref. 737. Copyright 2017, John Wiley and Sons.** (f) Device structure of a TENG textile. (g) Demonstrations of the TENG textile in use of fabric human-system interfaces. **Reprinted with permission under a Creative Commons CC BY license from ref. 37, Copyright 2019, John Wiley and Sons.**

1
2
3
4 Tactile sensors will inevitably experience repeated contacts and pressing, which may
5 cause physical damage.^{739,740,741} Mimicking the self-healing ability of human skin, self-
6 healable TENG tactile sensors have been intensively explored to gain the capability to
7 recover their mechanical properties and electrical functionality from damages for sustainable
8 and durable uses. Such self-healing abilities can be enabled by self-healable materials
9 through either physical (such as interchain diffusion, hydrogen bonding, shape-memory
10 behaviors and doping magnetic nanoparticles) or chemical (such as covalent, free-radical or
11 supramolecular dynamic bonds) processes or their combinations.^{742,743} The self-healing
12 TENG tactile sensors are developed based either on self-healing triboelectric materials,
13 current collectors or both.

14
15
16 An entirely and autonomously self-healable (30 min, 100% efficiency at 900% strain),
17 highly-transparent (~88.6% transparency), and super-stretchable (>900% stretchability)
18 TENG is developed as a durable power source and a self-powered active electronic skin
19 (Figure 81(a-b)).⁷³⁹ It is constructed by dynamic hydrogen-bonded ionic gel as the self-
20 healable electrode encapsulated by the dynamic metal-ligand-*coordinated*
21 polydimethylsiloxane (PDMS) as the self-healable triboelectric material. At ambient
22 conditions, the whole TENG can self-heal and regain its energy-harvesting ability from
23 complete bifurcation within 30 min. It works at the single-electrode mode. With an area of 4
24 × 2.5 cm², it offers an open-circuit voltage, short-circuit current density, and instantaneous
25 power to 20 V, 240 μA/m², and ~5 mW/m², respectively. Moreover, it retains functionality
26 even after 500 cutting-and-healing cycles or at 900 %-strain. The electricity triggered by
27 touching enables it to act as self-powered active electronic skins. Its capability to differentiate
28 different contact pressure is demonstrated at pristine, 25%-strained, and cut-and-healed conditions.

1
2
3
4 The pressure sensitivity originates from the soft materials of the device. The TENG tactile sensor
5
6
7 reveals autonomously self-healing, transparent, deformable, and energy-converting traits,
8
9
10 making it favorable for use in diverse human–device interfaces. The applicability of the self-
11
12 healing TENG tactile sensor has been demonstrated in smart glass, an epidermal controller,
13
14 and a mobile phone panel.
15
16

17 The superior in diverse materials selection and self-powered capability of TENGs
18
19 enables TENG-based self-powered tactile sensors to be used in many other fields where sense
20
21 of touch is needed. For example, tactile sensors are crucial components in the emerging soft
22
23 robotics. However, the integration of conventional tactile sensors into the continuously
24
25 deforming bodies of soft robots is challenging because conventional sensors suffer from
26
27 complicated device structures, scant stretchability, and incompatible moduli. Lai et al.
28
29 reported TENG-based self-powered, highly-stretchable, and highly sensitive robotic skins
30
31 that can be used in various kinds of soft robots (Figure 81(c-d)).⁷⁴⁴ The TENG robotic skins
32
33 are fabricated by silver nanoflakes as the electrode and the silicone rubber with triangular-
34
35 microprism surface as the triboelectric material. The robotic skins simultaneously possess
36
37 excellent stretchability to 100% strain and outstanding sensitivity to 0.29 kPa^{-1} (9.54 V/kPa)
38
39 in low-pressure regime ($< 5 \text{ kPa}$) with lowest-detection limit to 63 Pa . The TENG skins can
40
41 actively sense proximity and contact pressure to external stimuli by self-generating
42
43 electricity. With the aid of the TENG skins, soft robots enable to perform various actively
44
45 sensing tasks including perceiving their muscle motions and working states, detecting
46
47 moisture of a textile, and even monitoring slight human physiological signals. Furthermore,
48
49 the actively-generating signals can be processed by a computation module for diverse and
50
51 sophisticated reactions. For example, the human-soft robot interaction can be realized by
52
53 using a microcontroller (Figure 81(d)).
54
55
56
57
58
59
60

1
2
3
4 Although we can foresee the potential of TENG tactile sensors and their wide
5 applications, some challenges remain and need to be overcome to realize their full potential.
6
7 For example, environmental factors such as humidity and temperature could affect their
8 performances, which may hinder the applicability.^{744,745} Hence, the encapsulation technology
9 for such systems needs to be extensively investigated. Moreover, the development of machine
10 learning for TENG tactile sensors could be helpful to differentiate of the noise. On the other
11 hand, TENG-based slip and force vector sensors will be needed for more complete tactile
12 sensors. Furthermore, the interface connection and the match of elastic moduli would be
13 important for the integration of the TENG tactile sensors with other components and circuit
14 board. Last, for a large-area and multiplexing TENG tactile sensing array, high spatial
15 resolution requires to be ensured.
16
17
18
19
20
21
22
23
24
25
26
27
28
29
30
31
32
33
34
35
36
37
38
39
40
41
42
43
44
45
46
47
48
49
50
51
52
53
54
55
56
57
58
59
60

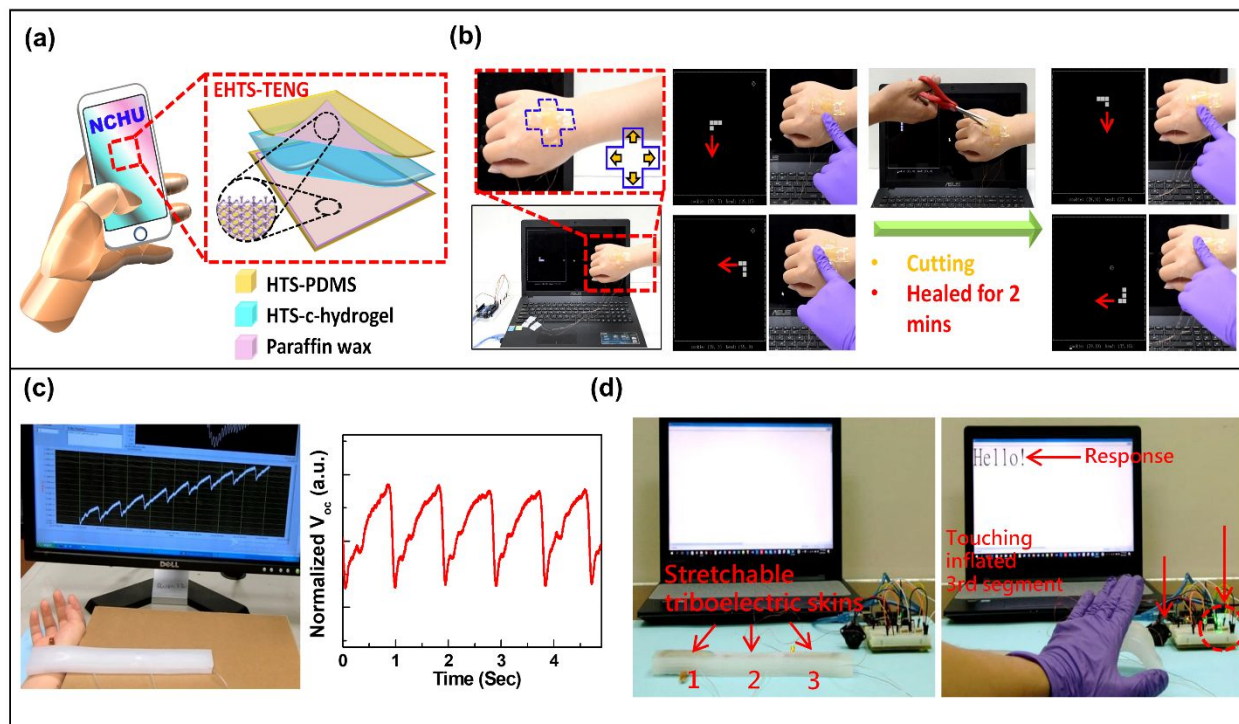


Figure 81. (a) Applications and schematic of a self-healing TENG. (b) Demonstration of a self-healing and self-powered epidermal controller used to play a video game before and after cutting and self-repair. **Reproduced from ref. 739. Copyright 2019, John Wiley and Sons.** (c) Left: demonstration of a soft robot with self-powered TENG sensing skin for detecting human pulses. Right: Real-time outputs of human pulses. (d) Photos for demonstrating the human-soft robot interaction. **Reproduced from ref. 744. Copyright 2018, John Wiley and Sons.**

6.4.2. Touch position sensing

With the advent of the IoT era, sensors equipping low-power consumption and lightweight have been gradually demanded⁷⁴⁶. It is expected that TENGs are readily capable to meet the needs. Because touches on TENGs can be directly converted into electrical signals based on electrostatic induction, electrical energy generated by TENGs have been utilized for sensing physical interaction^{52,51,50}. This ensures TENGs that can detect touches without additional power sources^{59,747}. This is called self-powered touch sensing. Simple structure (basically two layers of dielectric and conducting layers) of TENGs allows a wide range of material selection, and thus ensures TENGs to be fabricated with lightweight and flexible properties^{49,64,63}. The flexibility also contributes TENGs to be mounted on deformable substrates such as a human skin^{51,66,65}. The promising characteristics have allowed TENGs to be highlighted as self-powered touch sensors as well as energy harvesters.

A surface of TENGs can be charged based on contact electrification. The accumulated charges induce counter charges in the conductor of TENGs to maintain electrical equilibrium (Figure 82(a)). When an object approaches and contacts the TENG, the induced counter charges are released, and then electric current occurs. By measuring voltage across a connected external load, the touch by object can be readily detected (Figure 82(b)). Based on the sensing mechanism, self-powered sensing using TENG was demonstrated in 2012⁵². The TENG readily detected gentle touch of a piece of 20 mg bird feather with notable voltages induced in the TENG (Figure 82(c))⁵². Interestingly, sensing signals generated by the TENG readily distinguished not only first strong touch but also second weak touch during the falling process. This means the TENG is sensitive to applied touch pressure. Choi's group reported highly pressure sensitive triboelectric touch sensors (Figure 82(d), (e))⁷⁴⁸. The pressure sensitivity of the TENG was 22.3 V/kPa. Voltages induced at TENGs are dependent on the

1
2
3
4 contact surface⁷⁴⁸. Increased input pressure might lead to larger effective contact area,
5
6 resulting in increasing induced voltage. Even if the sensitivity was quite reduced beyond a
7
8 range of 20 kPa of applied pressure, it showed TENGs are fascinating candidates as pressure
9
10 sensors.
11
12

13
14 With the increasing demand of wearable sensors, stretchable and transparent TENGs have
15
16 been suggested based on ionic conductors^{51,66,749,750}, especially hydrogel containing ions
17
18 (Figure 82(f)). Thanks to its high transmittance (99%) and stretchability (340%), it was
19
20 robustly applied on human fingertips. Five TENGs attached on fingertips were programmed
21
22 to represent 2⁰, 2¹, 2², 2³, and 2⁴. Combinations of the touch signal from TENGs were
23
24 interpreted as an alphabet to be used as a wearable keyboard⁵¹.
25
26

27
28 Applying electrode grid layer as a conducting layer of TENG allows TENG to distinguish
29
30 touch position (Figure 82(g), (h))^{50,687,751}. By comparing voltages measured at each grid,
31
32 touch position is readily recognized. The touch points (α, β) are interpreted by the following
33
34 Equation (33)⁵⁰:
35
36

$$\begin{aligned} & \text{If } V_{xn} \text{ and } V_{ym} \neq 0, \text{ and } \textit{else} \approx 0, \\ & x_{2n-1} < \alpha < x_{2n}, y_{2m-1} < \beta < y_{2m} \end{aligned} \quad (33)$$

37
38
39
40
41
42
43
44
45
46
47 By increasing the density of the electrode grid, the spatial resolution can be enhanced.
48
49 However, the number of data lines and voltmeters corresponding to the electrode grid is also
50
51 increased, which causes the TENG to be complicated. To overcome the tradeoff, a gridless
52
53 touch position sensing mechanism was recently reported by Lee et al., which is called
54
55 triboresistive touch sensing (Figure 82(i), (j))⁵⁰. Touch point is recognized by comparing
56
57
58
59
60

1
2
3
4 voltages induced at each corner. The touch points are interpreted by following Equations (34-
5
6
7 35):
8
9

$$\alpha = \frac{V_2 + V_4}{V_1 + V_2 + V_3 + V_4} \quad (34)$$

$$\beta = \frac{V_1 + V_2}{V_1 + V_2 + V_3 + V_4} \quad (35)$$

10
11
12
13
14
15
16
17
18
19
20 **Where** V_1 , V_2 , V_3 , and V_4 are voltages induced at each corner, respectively. A comparison
21
22 of the voltages generated at each corner, which depend on the resistance between the touch
23
24 points and each corner, allows for estimation of the touch positions without the need for
25
26 electrode grid layers and external power sources.
27

28
29 In our view, there has been development in the research field of triboelectric touch sensors
30
31 over the last ten years. However, there are still a lot of issues we will have to explore to
32
33 enhance triboelectric touch sensors to be commercialized. Especially, even though the
34
35 sensing mechanisms of TENGs do not require power sources to be operated compared to
36
37 conventional touch sensing mechanisms such as capacitive and piezoresistive
38
39 sensing^{752,753,754}, an external power supply is still required to cover data acquisition and
40
41 processing. From the perspective of fully self-powered touch sensing systems, we believe
42
43 increasing power generation will be a critical and high impact direction to cover the energy
44
45 required for both data acquisition and processing.
46
47
48
49
50
51
52
53
54
55
56
57
58
59
60

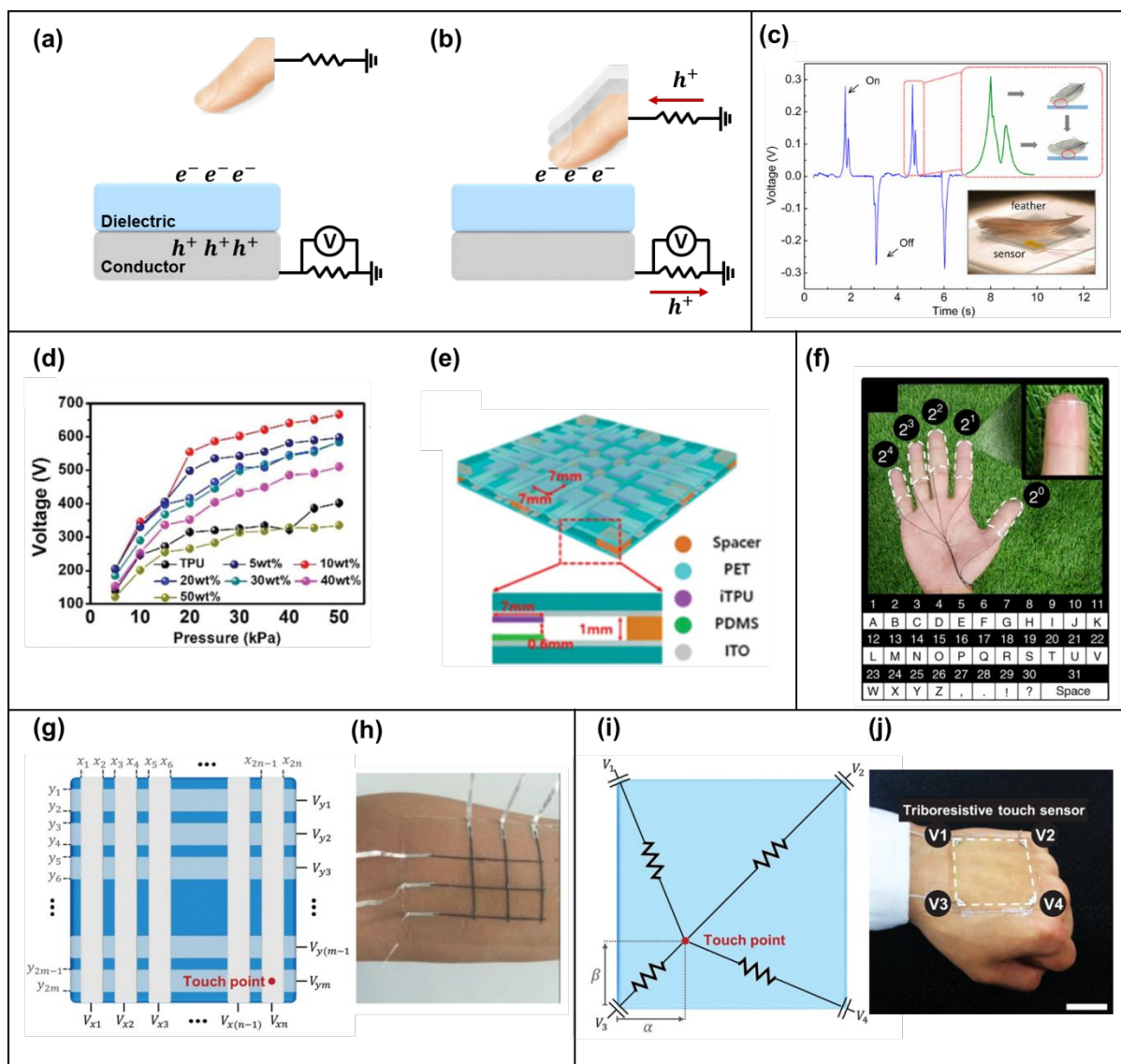


Figure 82. Self-powered touch sensing applications of TENGs. (a, b) Self-powered touch sensing mechanism. (c) Sensing signals generated when a bird feather touched on TENG. Reprinted with permission from ref. 52, Copyright 2012, American Chemical Society. (d, e) Transparent and soft touch sensor detecting touch pressure. Reprinted with permission from ref. 748, Copyright 2019, John Wiley and Sons. (f) Transparent and soft touch sensors based on combination of triboelectric touch signal. Reprinted with permission under a Creative Commons CC BY license from ref. 51, Copyright 2018, Springer Nature. (g) Schematic diagram of triboelectric touch point sensors. Reprinted with permission from ref. 50, Copyright 2022, WILEY-VCH VERLAG GMBH. (h) Photograph of triboelectric touch point sensor with electrode grid. Reprinted with permission from ref. 687, Copyright 2017, John Wiley and Sons. (i) Schematic diagram of triboresistive touch point sensor. (j) Photograph of triboresistive touch point sensor. Reprinted with permission from ref. 50, Copyright 2022, WILEY-VCH VERLAG GMBH.

6.4.3. Proximity sensing

Apart from detecting contact-induced motions and trajectories, TENGs are also capable of monitoring object movement in a non-contact manner, i.e., proximity sensing. Similar to the working mechanism of the free-standing mode, triboelectric proximity sensors work on the principle of electrostatic induction effect where the charged object approaches or departs from the electrode, creating electron flows to balance the local potential distribution. In general, the underlying working principles could be simplified into two cases, where the charged object moves in parallel to the electrode or perpendicular to it. Taking the perpendicular moving trajectory as an example, as the positively charged dielectric moves away from the bottom electrode, electrons on the electrode will be repelled to the ground due to electrostatic induction, thus generating a negative output current on the connected load. Conversely, the electrons will flow back once the dielectric approaches the bottom electrode, leading to a positive output current in the circuit. In the case of parallel moving patterns where the dielectric approaches or leaves the bottom electrode in a different manner, though the electric field distribution would be distinguished from the prior case, the output current has a similar relationship to the dielectric motions. Generally speaking, a single working electrode can detect the approaching or leaving of a charged object nearby through the

1
2
3
4 triboelectric output polarity and amplitude. Through specifically designed electrode arrays,
5
6
7
8 more sophisticated and comprehensive moving trajectories can be detected and differentiated
9
10
11 for diversified applications.
12
13

14
15 With an increasing demand for information exchange as well as reciprocal
16
17
18 interactions between the virtual and real world, TENG-based human-machine interfaces
19
20
21 (HMIs) in various forms have been vastly developed for diversified
22
23
24 applications.^{747,59,755,756,757,758} A growing interest has been observed in wearable HMIs with
25
26
27 noncontact attributes in recent years, especially during the current pandemic.⁷⁵⁹ Accordingly,
28
29
30 there are a few non-contact HMIs that have been reported for proximity sensing of
31
32
33 hand/finger on the basis of TENGs.^{760,553,761,762,763,764,765,744} Figure 83(a)-(i) shows a
34
35
36 triboelectric touch-free screen sensor (TSS) to recognize various gestures in the vicinity of it
37
38
39 in a noncontact working mode.⁷⁶¹ Based on a monolayer graphene and polyethylene
40
41
42 terephthalate (PET) substrate, the TSS is lightweight, flexible, and transparent, allowing it to
43
44
45 be easily integrated into screens of personal electronics. Considering that the human body is
46
47
48 usually negatively charged, when the fingers move above the TSS, the charge distribution on
49
50
51 the TSS surface will be changed due to the electrostatic induction, hence generating output
52
53
54 signals correspondingly. By embedding ten sensing units evenly distributed on the surface,
55
56
57
58
59
60

1
2
3
4 the TSS can detect several gestures including finger drop and lifting at different speeds,
5
6
7
8 making a fist, palm opening, and flipping in different directions. An intelligent non-contact
9
10
11 screen control system was further demonstrated, enabling contactless unlocking of the
12
13
14 smartphone interface (Figure 83(a)-(ii)). To detect the motion of a surface electrified object
15
16
17 across the plane parallel to the sensory interface, Zhang et al. designed and developed a self-
18
19
20 powered noncontact electronic skin based on the electrostatic induction and triboelectric
21
22
23 effect (Figure 83(b)-(i)).⁷⁶² A symmetric four-electrode configuration with quartered annulus
24
25
26 shapes was proposed and fabricated by depositing a thin layer of ITO on the PET substrate.
27
28
29 The object displacement under the polar coordinate system is determined by the ratios of
30
31
32 peak voltages from the four electrodes, which has greatly reduced the electrode number
33
34
35 compared to the conventional pixel-based sensory arrays. Through this approach, this
36
37
38 electronic skin can determine two key factors of the moving object: the distance between the
39
40
41 electronic skin center and projections of the stop point of the object, and the moving
42
43
44 direction. As presented in Figure 83(b)-(ii), the noncontact electronic skin has been
45
46
47 implemented as a real-time HMI for a Tetris game, demonstrating its promising prospect for
48
49
50 providing interactions between users and artificial intelligence with a degree of freedom.
51
52
53
54
55
56
57
58 Figure 83(c)-(i) shows a different design of electronic skin to track the object
59
60

1
2
3
4 motion/displacement above it, which contains stacked electrode-substrate layers with an
5 overlapped configuration.⁷⁶⁰ Each layer consists of five electrodes that are parallel to those on
6
7
8 the same layer but perpendicular to the ones on the other layer. Through spatial electrostatic
9
10
11 inductions, this transparent and stretchable electronic skin is capable of measuring an
12
13
14 electret's motion in the rectangular coordinate system with three degrees of freedom, as
15
16
17 illustrated in Figure 83(c)-(ii). A high accuracy (0.7498 mm, 1.0669 mm, 2.2003°) has been
18
19
20
21 achieved with this self-powered digital-analog hybrid device, which was demonstrated as an
22
23
24
25
26
27
28 HMI in a real-time game platform.

29
30
31 Recently, Lee et al. proposed a multimodal noncontact interaction interface by
32
33
34 combining a MEMS humidity sensor and a triboelectric sensor, which can provide a
35
36
37 continuous and steady response and recognize multidirectional finger motions simultaneously
38
39
40 (Figure 83(d)-(i)).⁵⁵³ The humidity level directly reflects the vertical distance between the
41
42
43 finger and the sensor. Meanwhile, the TENG sensor with a minimalist and electrode design
44
45
46 can easily differentiate the finger motion direction through the two-channel output voltages,
47
48
49 as indicated in Figure 83(d)-(ii). Leveraging the fused information from both sensors, this
50
51
52 noncontact interaction interface was implemented for virtual car control and 3D password
53
54
55 entering to a login system as proof of concept. On the basis of the proximity sensing of
56
57
58
59
60

1
2
3
4 TENG, Yuce et al. demonstrated a self-powered eye motion sensor for various application
5
6
7 scenarios, as shown in Figure 83(e)-(i).⁷⁶⁶ The whole sensing system is separated into two
8
9
10 parts: a stand-alone flexible polymer strip with a two-layer configuration and a metal
11
12
13 electrode fixed on the eyeglass lateral temple. As the Orbicularis Oculi (O.O) muscle
14
15
16 contracts or relaxes, charges will be generated on the polymer strip and affects the proximal
17
18
19 metal electrode through the near-field electrostatic induction. As a result, the subtle O.O
20
21
22 muscle movement can be monitored through the collected output signals. This eye motion
23
24
25 sensor was successfully demonstrated in an HMI prototype for hands-free cursor control, car
26
27
28 control, and VR drone control as shown in Figure 83(e)-(ii).
29
30
31
32
33
34
35
36
37
38
39
40
41
42
43
44
45
46
47
48
49
50
51
52
53
54
55
56
57
58
59
60

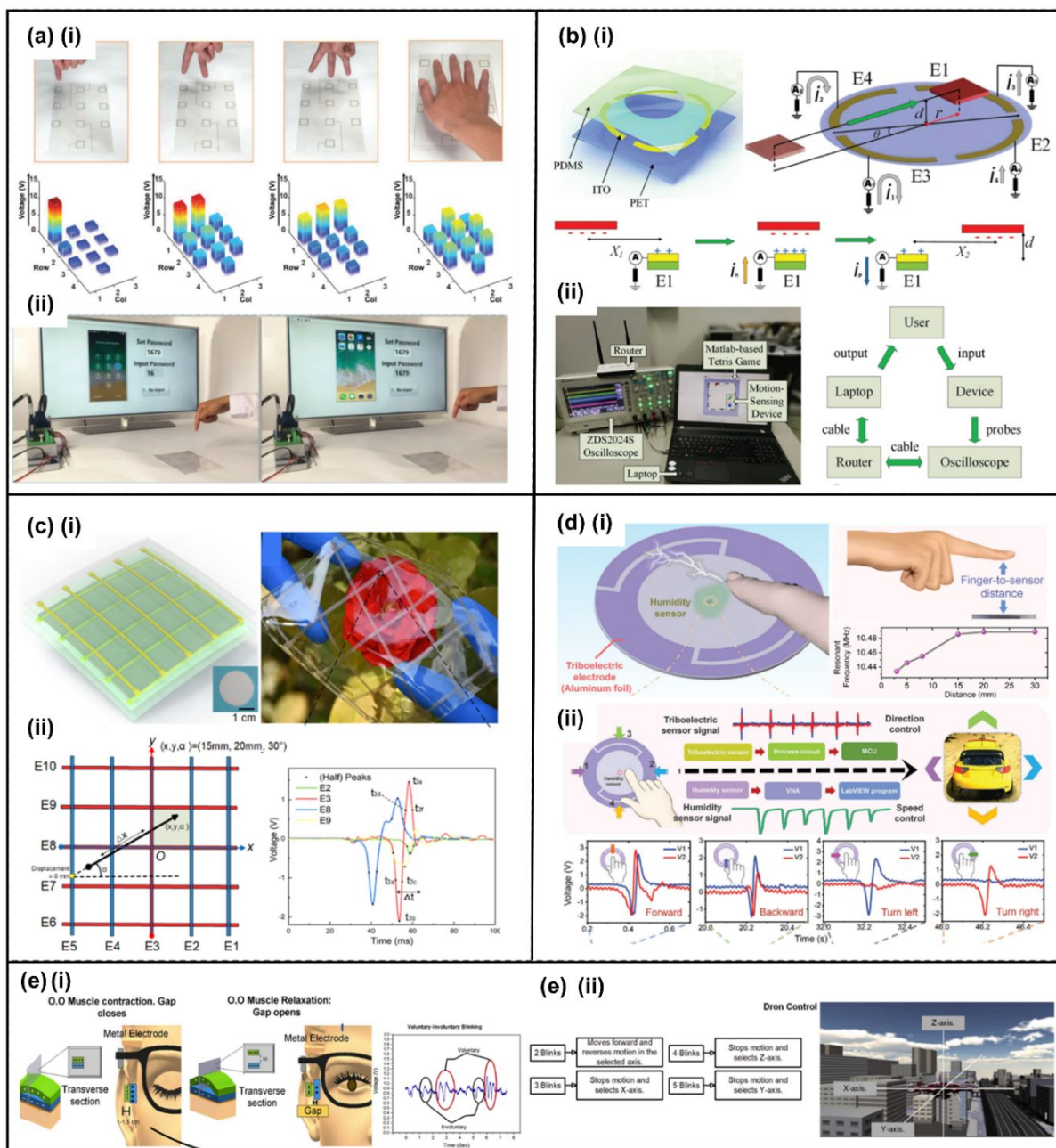


Figure 83. TENG-based proximity sensors for HMI applications. **(a)-(i)** Photos of one, two, three fingers, and a palm moved above the TSS unit array, and the corresponding peak voltages depicted by 3D diagram. **(a)-(ii)** Demonstration of smartphone interface unlocking after inputting the password through the TSS in a non-contact mode. **Reprinted with permission from ref. 761, Copyright 2020, WILEY-VCH.** **(b)-(i)** Schematics of the noncontact electronic skin and its working principle. **(b)-(ii)** A real-time HMI system with the electronic skin for the Tetris game. **Reprinted with permission from ref. 762 Copyright**

1
2
3
4
5 **2018, WILEY-VCH. (c)-(i)** Schematic and photo of the transparent and stretchable self-
6 powered electronic skin. **(c)-(ii)** An example moving trajectory of the electret and the
7 corresponding output signals from four electrodes. **Reprinted with permission from ref.**
8 **760, Copyright 2019, Elsevier. (d)-(i)** Schematic illustration of the multimodal noncontact
9 interaction interface, and the relationship between the humidity sensor resonant frequency
10 and the finger-to-sensor distance. **(d)-(ii)** Schematic diagram of the output flow for car
11 direction and speed control, and the corresponding two-channel triboelectric voltages
12 generated from the finger sliding motions. **Reprinted with permission from ref. 553,**
13 **Copyright 2022, WILEY-VCH. (e)-(i)** Working mechanism of the eye motion sensor and
14 output signals from eye blinks. **(e)-(ii)** Virtual drone control schemes with the eye motion
15 sensor. **Reprinted with permission from ref. 766, Copyright 2020, Elsevier.**
16
17
18
19
20
21
22
23
24
25
26
27
28
29
30
31
32
33
34
35
36
37
38
39
40
41
42
43
44
45
46
47
48
49
50
51
52
53
54
55
56
57
58
59
60

1
2
3
4
5 The proximity sensing enabled by TENG not only has introduced appealing features to the
6
7
8 next-generation HMIs but also is providing possibilities for intelligent smart home
9
10
11 applications.⁷⁶⁷⁻⁷⁷⁴ Gong et al. developed a self-powered sandwiched noncontact TENG
12
13
14 (NTENG) consisting of a graphene/shear-stiffening gel electrode and a shear-stiffening
15
16
17 elastomer shell, which is capable of detecting a vertically moving object's distance and
18
19
20 speed.⁷⁶⁹ The stretchable and shape-adaptive properties enable attachment of the NTENG
21
22
23 onto uneven surfaces as a touchless sensor for external environment monitoring, e.g., a
24
25
26 walking stick that assists the user move in darkness as shown in Figure 84(a). Three NTENG
27
28
29 units were assembled to the peripheral surface of the walking stick, and they are responsible
30
31
32 for left, forward, and right direction detection. Output signals will be generated when it is
33
34
35 adjacent to obstacles, with the three-channel triboelectric voltage helping the users to identify
36
37
38 the location of the barrier and hence guiding them to move freely even with no visual input.
39
40
41
42
43
44 In light of the COVID pandemic, the self-powered noncontact triboelectric would come in
45
46
47 handy in reducing the possible contact situations whenever and wherever possible. For
48
49
50 instance, it can be integrated with a hand sanitizer machine for touchless activation, which
51
52
53 shall break the virus transmission chain effectively by avoiding crossing contact through
54
55
56 conventional hand sanitizer devices. As presented in Figure 84(b), a touchless hand sanitizer
57
58
59
60

1
2
3
4 system was demonstrated and enabled by a triboelectric proximity sensor, which detects hand
5
6
7
8 approaching and hand leaving movement through the positive and negative output voltages.
9

10
11 ⁷⁶⁸ The proposed TENG sensor was equipped with a charge trapping interlayer to enhance its
12
13
14
15 output performance, maintaining a considerable output even under high-humidity conditions.
16
17

18
19 Human motion and its interaction with the environment are crucial for healthcare, which is
20
21
22 generally tracked through wearable sensors attached to multiple body parts. Considering the
23
24
25 human body is a naturally charged entity, a contactless sensing platform to distinguish and
26
27
28 monitor the diversified movements of human subjects can be developed based on TENG-
29
30
31 based proximity sensors, as shown in Figure 84(c)-(i).⁷⁶⁷ A flexible Non-Contact
32
33
34
35 Triboelectric Sensor (NCTS) was produced by simply attaching PDMS film onto the Al foil,
36
37
38 with the working principle of non-contact electrostatic induction. In other words, the
39
40
41
42 approaching or departing of any charged object (e.g., the human body) will induce electrons
43
44
45 to flow in or out to the Al electrode. Meanwhile, the electrification between the shoe and
46
47
48 floor should be taken into consideration as well when analyzing the charge distribution of the
49
50
51
52 whole system, which can largely affect the NCTS output signals. As presented in Figure
53
54
55
56 84(c)-(ii), the location of the sensor, the distance between the sensor and the subject,
57
58
59 shoe/floor materials, and motion types all exert influence on the sensor output, enabling
60

1
2
3
4 activity differentiation, walking speed /relative position estimation, and motion detection of
5
6
7
8 two individuals. In addition, two sensors fixed on specific parts of the house were used to
9
10
11 perform indoor location and tracking. A prototype system for assisting visually impaired and
12
13
14 elderly people to prevent accidents and detect falling events was then developed. In a similar
15
16
17 manner, Nie et al. demonstrated recognition of walking, approaching, running, falling, and
18
19
20 other moving activities through the proximity sensing of a polyvinylidene fluoride@Mxene
21
22
23 (Ti₃C₂T_x) composite film-based TENG (Figure 84(d)-(i)).⁷⁷¹ The peak-to-peak voltage
24
25
26 increases with the walking speed at the same distance with a sensitivity of 1.175 Vs/m, as
27
28
29 shown in Figure 84(d)-(ii). With two sensors fixed on the wall, different signals can be
30
31
32 detected when the user wearing a positive triboelectric material moves between them.
33
34
35 Accordingly, it can serve as an indoor human position recognition device to assist visually
36
37
38 impaired users to navigate in the near future. The proximity information of the human body
39
40
41 not only is useful for movement detection but also can serve as wake-up signals in smart
42
43
44 systems for energy conservation of electronic networks in unmanned areas. Figure 84(e)
45
46
47 presents a bionic triboelectric nanogenerator (bTENG) functioning as a self-powered motion
48
49
50 sensor in a wake-up circuit, which mimics the structure of plants with leaf-shaped tentacle
51
52
53
54
55
56
57
58
59
60

1
2
3
4 structures.⁷⁷⁰ The wake-up system can be triggered by the generated voltages of the bTENG
5
6
7
8 that may originate from both noncontact and contact mechanical disturbance.
9

10
11 Though broad application prospects of the TENG-based proximity sensors in various
12
13
14 forms have been demonstrated, there still exists a few limitations of current designs which
15
16
17
18 would require more effort to be devoted to this specified research discipline. Efficient and
19
20
21
22 stable proximity sensing depends upon sufficient charges on the detecting object, e.g., hand
23
24
25 or body. Charge dissipation over time becomes a critical issue limiting the long-term sensing
26
27
28 performance, especially under the non-contact mode where charge replenishment through
29
30
31
32 repetitive contact electrifications is lacking. Material modifications aiming at this specific
33
34
35 scenario could be applicable, such as the introduction of a charge trapping layer,⁷⁶⁸ material
36
37
38 optimization in terms of surface charge density and decay rate,⁷⁷² and utilizing electret
39
40
41 materials.⁷⁶⁰ Besides, due to the working principle of electrostatic induction, output voltages
42
43
44 in non-open-circuit (i.e., most cases) can only be generated by dynamic motions, while static
45
46
47 positions cannot be detected. Multimodal sensing could be a feasible solution where sensors
48
49
50
51 with different sensing mechanisms are introduced to the system, providing complementary
52
53
54 information for a more comprehensive proximal motion tracking. In addition, the triboelectric
55
56
57 output of the proximity sensor is affected by multiple aspects of the moving object, such as
58
59
60

1
2
3
4 material type, distance, speed, motion direction, etc., where the triboelectric output is difficult
5
6
7
8 and laborious to analyze by manual feature extractions. More advanced data analytics (e.g.,
9
10
11 machine learning) are used to adaptively learn features from the collected raw signals, which
12
13
14 may lay the foundation for intelligent proximity sensing systems for more broadened
15
16
17
18 applications than ever before.
19
20
21
22
23
24
25
26
27
28
29
30
31
32
33
34
35
36
37
38
39
40
41
42
43
44
45
46
47
48
49
50
51
52
53
54
55
56
57
58
59
60

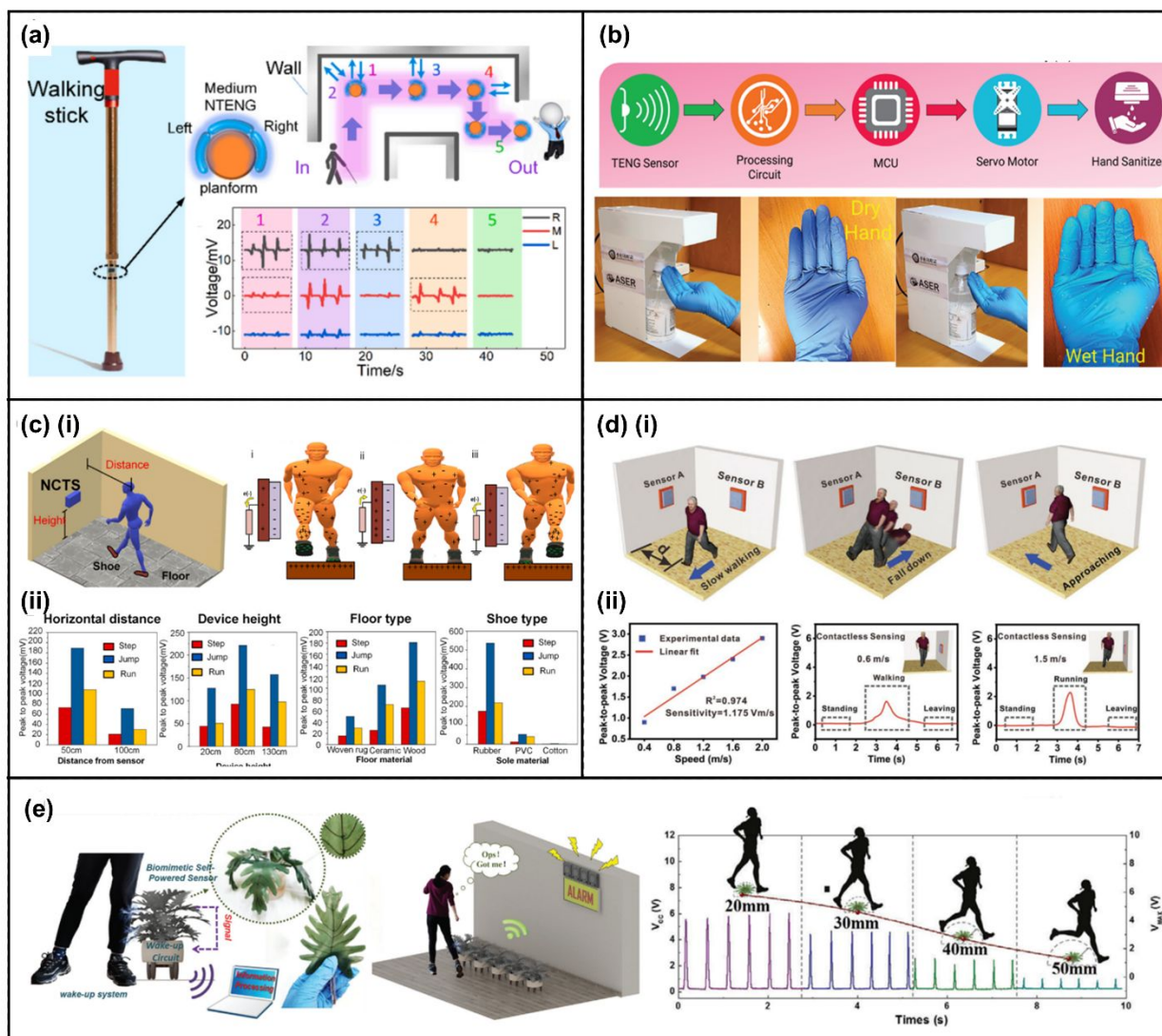


Figure 84. Proximity sensing for smart home applications. **(a)** A self-powered proximity sensing walking stick enabled by the three NTENG units to help users move in darkness through the three-channel triboelectric output voltages. **Reprinted with permission from ref. 769, Copyright 2021, Elsevier.** **(b)** The system architecture of a touchless hand sanitizer machine enabled by a triboelectric proximity sensor, and demonstration of activation of the system with both wet and dry hands. **Reprinted with permission from ref. 768, Copyright**

1
2
3
4 **2022, WILEY-VCH. (c)-(i)** Schematic illustration of the NCTS for non-contact motion
5
6
7
8 sensing and its working principle. **(c)-(ii)** Voltage outputs of the NCTS under various testing
9
10
11 conditions. **Reprinted with permission from ref. 767, Copyright 2021, Elsevier. (d)-(i)**
12
13
14 Contactless human motion detection through a self-powered proximity sensor. **(d)-(ii)** Sensor
15
16
17 response to different walking speeds. **Reprinted with permission from ref. 771, Copyright**
18
19
20 **2022, WILEY-VCH. (e)** A wake-up system with bTENG for mechanical disturbance
21
22
23 detection that can be applied for intruder alarm, and the output voltages at different sensing
24
25
26
27 distances. **Reprinted with permission under a Creative Commons CC BY license from**
28
29
30 **ref. 770, Copyright 2020, John Wiley and Sons.**
31
32
33
34
35
36
37
38
39
40
41
42
43
44
45
46
47
48
49
50
51
52
53
54
55
56
57
58
59
60

6.4.4. Defect Monitoring

Even tiny cracks in buildings, tunnels, bridges, railways, and maritime structures could be hazards because the growth of cracks is generally rapid and may cause disasters, including human injury and financial loss.^{775,776,777,778} Therefore, it is very important to detect cracks at an early stage, and crack monitoring systems are essential to prevent accidents. Cracks also could occur from ice surfaces located in rivers and streams, and it could be resulted in the accidents. These accidents can be considered as man-made and can cause enormous damage, so it is very important to prevent them early. Previously, piezo-resistive sensors, piezo-capacitive sensors, optical lasers, and acoustic source localization method were used for crack detection, but they have following limitations: high cost for installation and maintenance, low sensitivity, unstable response (easily affected by the environmental factors like temperature and humidity).^{779,780,781,782} As a self-powered monitoring system application, TENGs can be used as defect sensors for crack monitoring. TENG-based defect monitoring sensors have advantages as follows: small size (can be adapted to the environment for monitoring), light weight, and low cost (including both installation and maintenance costs). They can also be used without external power supplies or used with low power. Here we would like to introduce TENG-based defect monitoring systems.^{550,783,784}

1
2
3
4 In the field of structural health monitoring, the use of vibration is very powerful for
5
6
7
8 nondestructive investigation. Jung et al. proposed a wire-based triboelectric resonator
9
10
11 (WTER) for monitoring the crack initiation and widening.⁵⁵⁰ The authors obtained the
12
13
14 resonant frequency of the wire and used it to monitor crack initiation and widening, as shown
15
16
17
18 in Figure 85(a). They calculated the resonant frequency of the wire by Equation 36.
19

$$f = \frac{1}{2L} \sqrt{\frac{T}{\mu}} \quad (36)$$

20
21
22
23
24
25
26
27 The resonant frequency of a wire is determined by the tension (T), length (L), and linear
28
29
30 density (μ) of the wire. Since there is a consistency between the resonant frequency of
31
32
33 triboelectric signal and the resonant frequency of a wire, the initiation and widening of cracks
34
35
36
37 can be detected by change in resonant frequency, as shown in Figure 85(b). The authors
38
39
40 investigated the effects of tension, linear density, and length of wire on the resonant
41
42
43 frequency, and the experimental results showed well agreement with the equation. Generally,
44
45
46 TENG output is affected by environmental factors such as temperature and humidity. Since
47
48
49 WTER is a TENG-based system, it is essential to investigate environmental factors. The
50
51
52 authors designed a humidity chamber and measured the voltage output of WTER. As the
53
54
55 humidity increased from 10% to 80%, the voltage output and operating time decreased
56
57
58
59
60

1
2
3
4 dramatically. The change in the resonant frequency of WTER is determined by the influence
5
6
7
8 of thermal expansion coefficient, elastic modulus, linear density of wire, which is shown in
9
10
11 Equation 37.

$$f_T = \frac{1}{2L_0(1 + \alpha\Delta T)} \sqrt{\frac{T_0 - \alpha EA\Delta T}{\mu}} \quad (37)$$

12
13
14
15
16
17
18
19
20 Here, f_T is the resonant frequency, L_0 is the initial length of the wire, α is the thermal
21
22
23
24 expansion coefficient, ΔT is the temperature gradient, T_0 is the initial tension, E is the elastic
25
26
27 modulus, and A is the cross-sectional area of wire. In addition, the authors implemented A-
28
29
30 WTER using Arduino board and LCD display to implement a stand-alone, self-powered
31
32
33 crack monitoring WTER system, as shown in Figure 85(c). In the temperature range from 5
34
35
36 °C to 50 °C, Cu showed the least resonant frequency change, which is shown in Figure 85(d).
37
38
39
40 The relationship between elongation and frequency was investigated, and the sensitivity was
41
42
43
44 320 Hz/mm, which is sufficient to detect cracks, as shown in Figure 85(e). As a result of
45
46
47 comparing the resonant frequency of A-WTER with the resonant frequency measured
48
49
50 utilizing universal testing machine (UTM) by oscilloscope, the error was less than 1%. This
51
52
53
54 work showed the potential as a next-generation self-powered sensor for crack monitoring and
55
56
57 temperature monitoring in the social infrastructures.
58
59
60

1
2
3
4
5
6
7
8
9
10
11
12
13
14
15
16
17
18
19
20
21
22
23
24
25
26
27
28
29
30
31
32
33
34
35
36
37
38
39
40
41
42
43
44
45
46
47
48
49
50
51
52
53
54
55
56
57
58
59
60

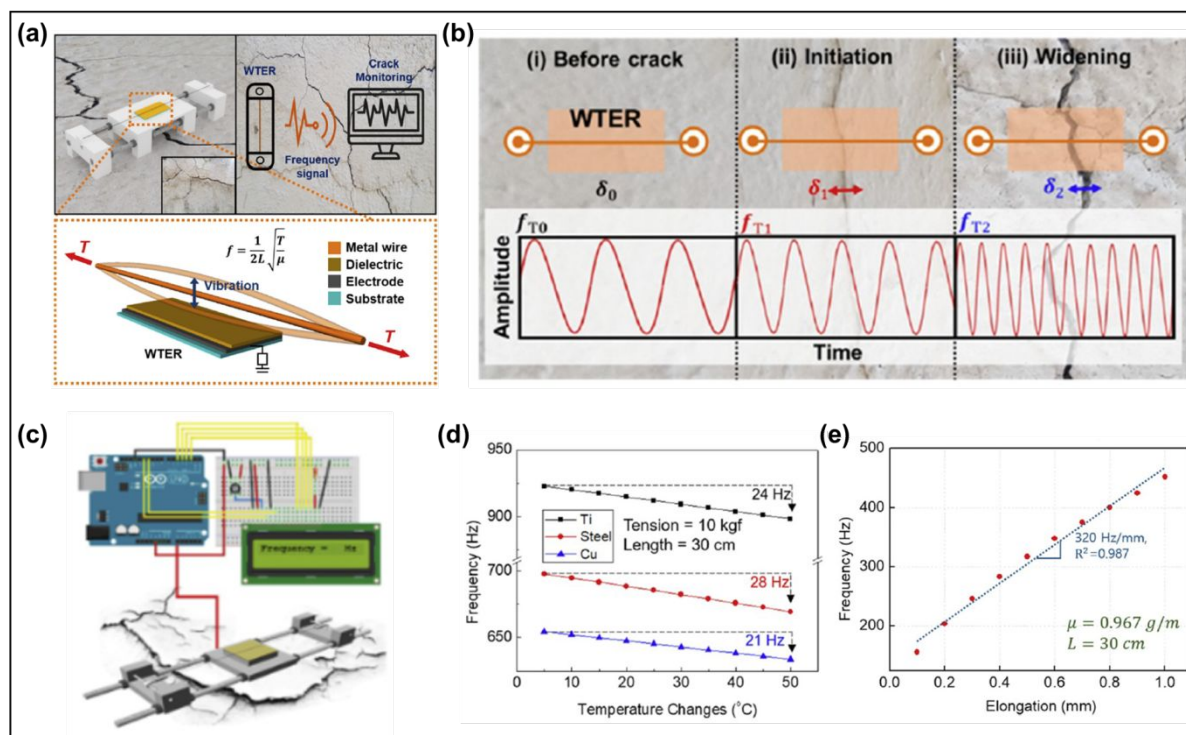


Figure 85. Wire-based triboelectric resonator for crack monitoring. **Reprinted with permission from ref. 550, Copyright 2020, Elsevier.** (a) Concept of the WTER used to monitor a crack. (b) Corresponding frequency behaviors according to crack initiation and widening. (c) Schematic of the integrated the WTER, arduino board, and LCD (A-WTER) (d) Frequency change caused by temperature for different metals (Ti, steel, and Cu) to understand the stability of the A-WTER, where the initial tension was 10 kgf and the length of wire was 30 cm. (e) Frequency measured by the A-WTER on a crack model for an elongation of 100 μm .

1
2
3
4
5 Early detection cracks in the ice surfaces are essential because even tiny cracks in the ice
6
7
8 surface can cause catastrophic accidents. Luo et al. proposed ice-based triboelectric
9
10
11 nanogenerator (ICE-TENG) to detect the cracks in the ice surfaces.⁷⁸³ The authors
12
13
14 investigated output performance of the ICE-TENG corresponding to the thickness of ice,
15
16
17 contact pressure, driven frequency, etc. They successfully demonstrated ice warning system
18
19
20 based on triboelectric interaction between an ice surface and human motion, as shown in
21
22
23 Figure 86(a), (b). When crack occurs on the ice surface, the output of ICE-TENG decreases,
24
25
26 as shown in Figure 86(c). We can recognize the occurrence of cracks in real-time through a
27
28
29 wireless warning system. As a self-powered crack monitoring system, durability is crucial
30
31
32 factor. Cracks on the ice surface leads to a decrease in TENG output due to surface damage,
33
34
35 which reduces system durability. However, self-healing is possible, which can improve the
36
37
38 system durability due to the low melting point and rapid phase transformation of ice, as
39
40
41 shown in Figure 86(d). Moreover, the coefficient of friction also affects the durability of the
42
43
44 system, and ICE-TENG has secured excellent durability due to the low coefficient of friction
45
46
47 of ice, as shown in Figure 86(e). These characteristics give ICE-TENGs a long lifespan and it
48
49
50 is expected to be used as a self-powered crack monitoring system. Finally, the authors
51
52
53
54
55
56
57
58
59
60

1
2
3
4 implemented a system that detects cracks occurring on the ice surface and provides a real-
5
6
7
8 time alarm, as shown in Figure 86(f), (g).
9

10
11
12 In modern society, since water is supplied through a pipe, it is very important and essential
13
14
15 to detect a crack or leakage of pipe. Vibration was used for structural health monitoring of
16
17
18 pipe⁷⁸⁴, and TENG-based vibration sensor can be applied in this field. Previously, it was
19
20
21 difficult to detect high-frequency ranges in TENG-based vibration sensors, and the structure
22
23
24 was not flexible. However, high-frequency range detection and flexible structure are very
25
26
27 important for various applications. Lin et al. proposed flexible ultrahigh-frequency
28
29
30 triboelectric vibration sensor (UTVS) for urban water pipeline leakage monitoring.⁷⁸⁵ The
31
32
33 authors optimized UTVS in terms of vibration frequency range, vibration response ability,
34
35
36 thermal stability, etc. UTVS has curved shape for structural health monitoring based on the
37
38
39 layer-particle-layer structure and utilization of flexible materials. To predict the leakage rate,
40
41
42 the authors measured the voltage output of UTVS according to various leakage rates. They
43
44
45 also simulated the situation of leakage in pipeline, and the turbulent flow occurs when there is
46
47
48 a leakage in the pipeline. A pipeline monitoring method in this work showed a possibility in
49
50
51 real-time leakage monitoring system for urban water supply. Machine learning is widely used
52
53
54 in various research fields nowadays, and it is also used in crack detection.^{786,787,788} In this
55
56
57
58
59
60

1
2
3
4 regard, surface cracks of TENGs can be detected and classified. Shen et al. proposed artificial
5
6
7
8 neural network (ANN) used for interface defect detection and an identification method.⁷⁸⁹
9

10
11 The electrical signals from TENGs are used as the training object to realize the non-contact
12
13
14 defect detection. The various defects could be detected such as edge fracture, unevenness of
15
16
17
18 substrate thickness, high surface roughness, noise, multiple defects, and sticky attachments.
19

20
21 The authors compared the accuracy and loss corresponding to the different number of pixels
22
23
24 and different number of neurons. They optimized the ANN model for high sensitivity and
25
26
27
28 low time consumption. ANN was used for the time through this work to detect TENG
29
30
31 defects, and it is expected that various follow-up studies and practical application
32
33
34 development will be possible in the near future based on machine learning in the TENG
35
36
37
38 defect monitoring field.
39
40
41

42 As above mentioned, defect monitoring systems are very important for the safety of social
43
44
45 infrastructures such as buildings, bridges, railways, maritime structures, pipes, etc. TENG
46
47
48 based self-powered defect monitoring systems are very useful due to the easy fabrication
49
50
51 process, low time-consuming, low cost for fabrication, etc. We introduced TENG-based
52
53
54 defect monitoring systems, and machine learning based TENG defect classification model.
55
56
57
58
59
60

1
2
3
4 These TENG-based defect monitoring technologies could be cornerstone for the next-
5
6
7
8 generation structural health monitoring of social infrastructures.
9
10
11
12
13
14
15
16
17
18
19
20
21
22
23
24
25
26
27
28
29
30
31
32
33
34
35
36
37
38
39
40
41
42
43
44
45
46
47
48
49
50
51
52
53
54
55
56
57
58
59
60

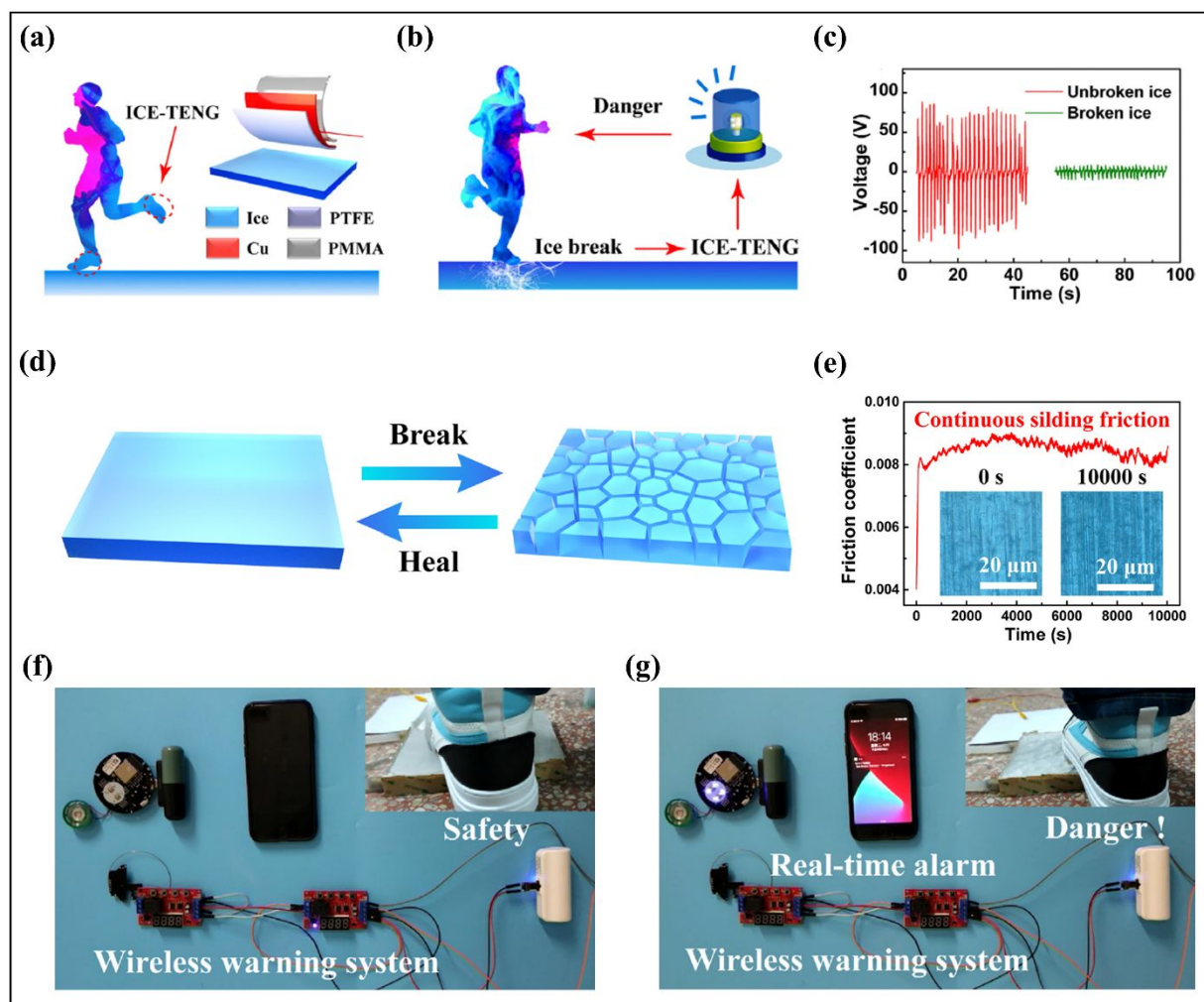


Figure 86. Ice-based triboelectric nanogenerator. Reprinted with permission from ref. 783, Copyright 2022, Elsevier. (a) Schematic illustration of the ICE-TENGs for energy harvesting during human motion on the ice surface. (b) Schematic illustration of the ICE-TENGs-based monitoring sensor. (c) The output voltage of the ICE-TENGs with unbroken and broken ice layers. (d) Schematic illustration of the reversible process from the broken ice to healable ice by regulating the temperature. (e) The long-time friction coefficient for 10,000 s. Photograph of the ICE-TENGs-based wireless warning system on the (f) unbroken and (g) broken ice layer.

6.5 Harvesting wasted mechanical energy

6.5.1. Harvesting ocean energy

The increasing severity of environmental problems has inspired active research on renewable energy. Among the various energy sources, blue energy (i.e., ocean energy) is receiving considerable attention, as it is known to contain abundant undeveloped renewable energy, including up to 1 billion kW of effective available water waves and tidal energy.⁷⁹⁰ To effectively harvest energy in an eco-friendly manner, not only the energy source but also the harvesting method is important. Although current harvesting devices such as electromagnetic generators, solar generators, and wind generators have the advantages of high output power and high efficiency on land, they are not applicable for continuously harvesting ocean energy because they require high-frequency stimulus or large supporting land. Therefore, TENGs hold great potential as the next-generation ocean energy harvesters because they are particularly efficient in harvesting at low-frequency mechanical motions and have extremely high design diversity and low manufacturing costs. For TENGs to be effectively used as an ocean energy harvester, in addition to the requirements of the conventional TENG, such as high performance and lightweight, the following conditions are required:^{19,791} i) harvesting capability against multi-frequency excitation, including low-frequency excitation, which is a

1
2
3
4 property of ocean waves; ii) waterproof or fully packaged devices to prevent performance
5
6
7 degradation due to corrosion or decomposition under water;^{792,149} iii) extreme mechanical
8
9
10 robustness so that it last for decades; and iv) low-cost, large-area, and mass-producible
11
12 fabrication processes to construct a harvester network with multiple TENGs in the ocean for
13
14 commercialization. Recently, TENGs for ocean energy harvesting satisfying these conditions
15
16 have been actively studied, particularly to improve harvesting efficiency because of their low
17
18 energy conversion rate and low power output, as well as their utilization in ocean monitoring
19
20 systems.^{793,794,795,22,796} In this section, we briefly summarize recent research on ocean-
21
22 harvesting TENGs in relation to the issues mentioned earlier and discuss associated
23
24 challenges and future research directions.
25
26
27
28
29
30
31
32
33
34
35
36
37
38
39

40 **6.5.1.1 Various types of TENGs for blue energy (ocean energy) harvesting**

41
42 The basic concept of ocean energy harvesting based on TENGs is constructing multiple
43
44 TENG networks on the ocean and harvesting tidal and wave energy (Figure 87(a)).⁷⁹⁷ Current
45
46 research is more focused on the development of structures for efficient energy harvesting
47
48 than just satisfying the abovementioned basic requirements for ocean energy harvesters.
49
50
51
52
53
54
55
56
57 TENGs for ocean energy harvesting are broadly classified as liquid–solid interface TENG
58
59
60

1
2
3
4 and solid–solid interface TENG. The liquid–solid interface TENG harvests energy from the
5
6
7
8 contact between the outer seawater and solid TENG surface or between the inner liquid and
9
10
11 solid TENG surface (Figure 87(b)).^{798,799} Although it is proposed to overcome the limitations
12
13
14 of solid–solid interface TENG, such as ambient humidity-sensitive performance, it is
15
16
17 premature to use them in real applications because of their low output power. Therefore,
18
19
20
21 solid–solid interface TENGs are still mainstream in ocean energy harvester research, and they
22
23
24 can also be classified into vertical contact-separation mode TENG (VC-TENG) and
25
26
27 freestanding mode TENG (FTENG) depending on their working mechanisms. In the VC-
28
29
30 TENG for ocean energy harvesting, various structures have been developed to enhance the
31
32
33 performance by increasing the contact layers and effectively utilizing irregular wave
34
35
36 excitations. For example, Liang et al. reported a spherical swing TENG based on the coupling
37
38
39 of a spring-assisted structure and a swing structure integrated with a charge excitation circuit
40
41
42 (Figure 87(c)).⁸⁰⁰ They claimed that this structure can convert low-frequency water wave
43
44
45 excitation to high-frequency motions, which can elevate the output performance. Wen et al.
46
47
48 demonstrated a flower-like triboelectric nanogenerator with six degrees of freedom, (Figure
49
50
51 87(d)).⁸⁰¹ The petals of the TENG can harvest energy with two degrees of freedom for
52
53
54 horizontal motion and with three degrees of freedom for rotational motion; the core can
55
56
57
58
59
60

1
2
3
4 harvest energy with one degree of freedom for the vertical motion, enabling the TENG to
5
6
7
8 fully harvest the kinetic energy from the wave. In another strategy, Wang et al. developed a
9
10
11 flag-like TENG for harvesting underwater ocean energy under extremely low-velocity
12
13
14 conditions, (Figure 87(e)).⁸⁰² The film-like TENG was fully sealed with a waterproof tape,
15
16
17 and a cylinder was designed to induce a vortex street that enhanced the vibration of the
18
19
20 TENG. However, the VC-TENG inevitably requires an excitation force above a certain
21
22
23 threshold to be in contact and separated from each other owing to the inside spring and mass.
24
25
26 Thus, FTENGs were developed to facilitate contact even under an extremely low wave input.
27
28
29 Liu et al. reported a nodding duck structured, multitrack directional FTENG for harvesting
30
31
32 low-frequency wave energy, as shown in Figure 87(f).⁷⁹⁷ They claimed that the synchronous
33
34
35 orbital movement of the inside nylon balls on an arc-shaped dielectric composite film
36
37
38 provided a stable and highly efficient power output. Gao et al. developed a gyroscope-
39
40
41 structured FTENG for harvesting multidirectional ocean wave energy, (Figure 87(g)).⁵³² Its
42
43
44 inner and outer generation units worked independently in different directions, enabling the
45
46
47 harvesting of multidirectional wave energy, and the multilayer structure increased the
48
49
50 effective power generation area. In addition, Wang et al. proposed an effective way to harvest
51
52
53 wave energy using sandwich-like TENG arrays connected to each other in parallel (Figure
54
55
56
57
58
59
60

1
2
3
4
5 87(h)).⁸⁰³ Studies have revealed that the energy output linearly increases with an increase in
6
7
8 the number of TENGs connected in parallel, and a sandwich-like structure can be one of the
9
10
11 best ways to effectively integrate several TENGs.
12

13
14 Overall, although TENGs for ocean energy harvesting face the problems of low energy
15
16 conversion and low output power, research is being actively conducted to improve the
17
18 harvesting efficiency through the design of materials and structures. State-of-the-art studies
19
20
21 have made great progress toward understanding the structures for the utilization of low-
22
23
24 frequency wave input. Therefore, TENGs have great potential for use in practical ocean
25
26
27 energy harvesting.
28
29
30
31
32
33
34
35
36
37
38
39
40
41
42
43
44
45
46
47
48
49
50
51
52
53
54
55
56
57
58
59
60

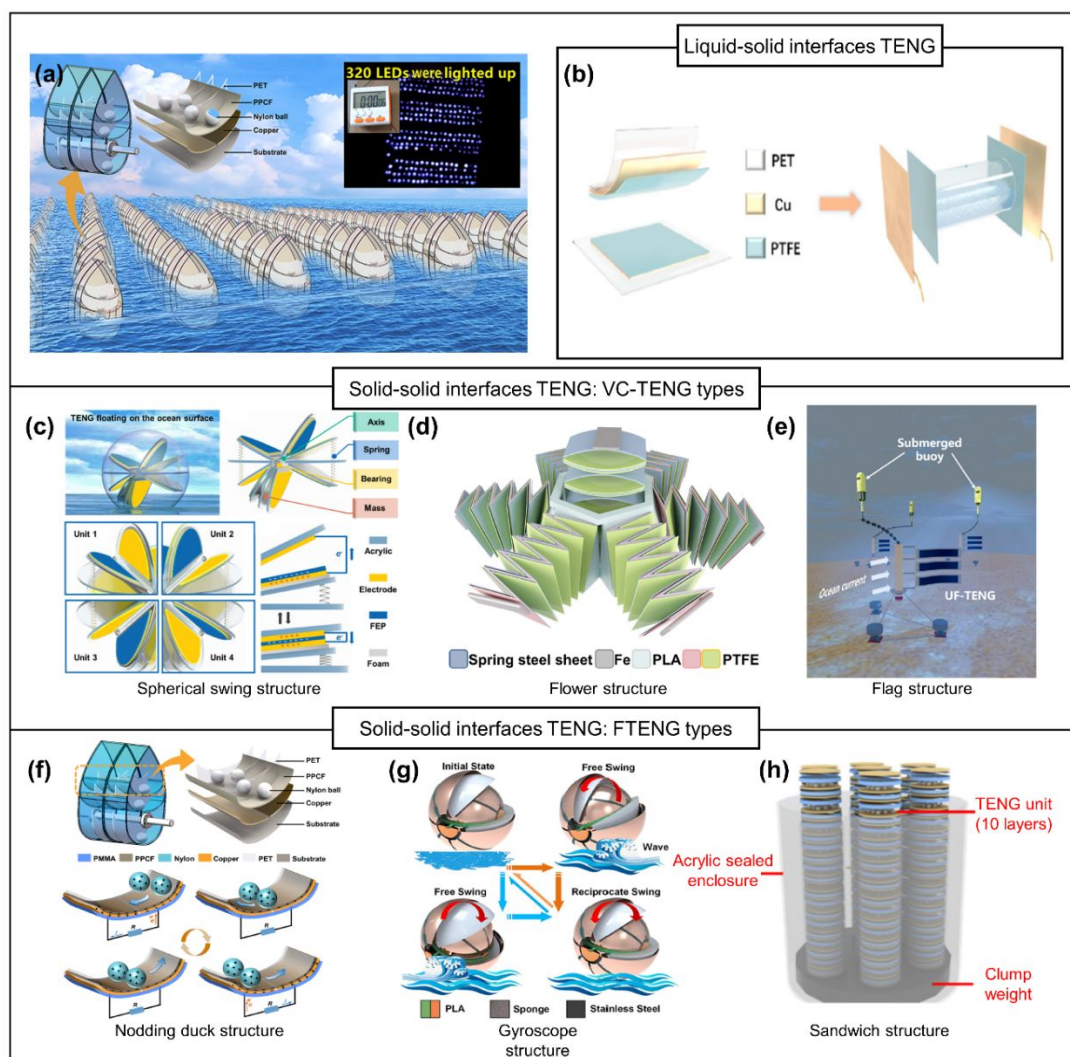


Figure 87. Various types of TENGs for blue energy harvesting (i.e., ocean energy harvesting). **(a)** Overall concept of ocean energy harvesting using multiple TENG networks. **Reprinted with permission from ref. 797, Copyright 2021, American Chemical Society.** **(b)** Schematic illustration of the liquid–solid interfaces TENG. **Reprinted with permission from ref. 798, Copyright 2021, Elsevier.** VC-TENGs with various structures for enhancing the harvesting efficiency: **(c)** Spherical swing structure for transforming low-frequency water wave vibrations to high-frequency motions. **Reprinted with permission from ref. 800, Copyright 2021, Elsevier.** **(d)** Flower structure for harvesting with six degrees of freedom. **reprinted with permission from ref. 801, Copyright 2022, Elsevier.** **(e)** Flag structure for harvesting underwater ocean energy with extremely low velocity. **Reprinted with permission from ref. 802, Copyright 2021, Elsevier.** FTENGs with various structures for enhancing the harvesting efficiency: **(f)** Nodding duck structure for harvesting low-frequency wave energy. **Reprinted with permission from ref. 797, Copyright 2021, American Chemical Society.** **(g)** Gyroscope structure for harvesting multidirectional energy. **Reprinted with permission from ref. 532, Copyright 2022, American Chemical Society.**

1
2
3
4 (h) Sandwich structure for harvesting energy from parallelly connected TENG array.
5 **Reprinted with permission from ref. 803, Copyright 2021, Elsevier.**

6 **6.5.1.2 Ocean monitoring systems based on TENGs**

7
8
9
10 With the increase in the demand and applicability of the ocean monitoring systems, the
11 meaning of “ocean monitoring systems” is becoming wider. In a conventional sense, it means
12 only monitoring ocean conditions (e.g., wave spectrum, temperature, salinity, and pH of sea
13 water) or weather. However, in a broader sense, it can include monitoring of all events that
14 occur in the ocean. The U.S. Integrated Ocean Observing System (IOOS) claims that several
15 sensors have been installed to support search and rescue operations, oil spill response, marine
16 shipping navigation, tracking of harmful algal blooms, and coastal water quality monitoring.
17 This implies that the role of ocean monitoring systems is becoming wider; therefore, various
18 systems need to be developed further to support them. TENGs are a promising candidate for
19 ocean monitoring systems because of their ocean energy harvesting capability and extremely
20 high design diversity. In general, there are two methods for monitoring systems using
21 TENGs.
22
23
24
25
26
27
28
29
30
31
32
33
34
35
36

37 First, TENGs can be directly utilized as self-powered sensors using their force-or contact
38 area-dependent output characteristics. For example, as a basic concept, Zhang et al. reported
39 a self-powered triboelectric wave spectrum sensor for quantifying ocean surface water waves
40 (Figure 88(a)).²³ Wave-height-dependent self-powered systems constructed with tubular
41 TENG and hollow ball buoys enable the measurement of six basic ocean wave parameters
42 (wave height, period, frequency, velocity, steepness, and wavelength), wave velocity
43 spectrum, and mechanical energy spectrum, eliminating the influence of seawater. Using a
44 similar concept, Xu et al. reported another wave sensor based on a liquid–solid interface
45 TENG (Figure 88(b)).⁸⁰⁴ They showed that the output voltage increases linearly with the
46 wave height with a sensitivity of 23.5 mV/mm. Second, TENGs can harvest energy from
47
48
49
50
51
52
53
54
55
56
57
58
59
60

1
2
3
4 ocean waves, and then later used to power various commercialized monitoring devices. Xu et
5 al. reported a simple strategy for monitoring ocean wave conditions using LED powered by
6 TENG (Figure 88(c)).⁵¹⁴ They claimed that the graded energy harvesting capability of TENG
7 changes the light intensity of LEDs with changes in the ocean wave conditions. Recently,
8 beyond simply driving simple devices, such as LED or thermocouples⁵³³, various electronic
9 devices for ocean monitoring have been powered by TENG-based systems.⁸⁰⁵ For example,
10 Jung et al. demonstrated TENG-based powering of an acoustic transmitter that can generate
11 acoustic vibrations to transmit data via water (Figure 88(d)).⁸⁰⁶ In addition, Ahn et al.
12 developed a wireless sustainable ocean monitoring system equipped with pH, salinity,
13 temperature, and oil leakage sensors (Figure 88(e)),⁵³¹ and an intelligent life jacket that could
14 activate a global positioning system sensor to send position information in an emergency to
15 land in real time (Figure 88(f)).⁵³¹ These demonstrate that TENG-based energy-harvesting
16 systems hold great promise for various ocean monitoring systems.

17
18
19
20
21
22
23
24
25
26
27
28
29
30
31
32
33
34 In summary, many studies have been conducted to develop sensing systems and to
35 demonstrate their monitoring capability. However, there are still some challenges caused by
36 the low energy harvesting performance of current TENGs, such as the difficulty of
37 continuous driving of multiple sensor arrays or difficulty in long-range wireless
38 communication. Therefore, we can conclude that although TENG-based ocean monitoring
39 systems clearly have great potential for use in practical applications, follow-up research
40 needs to be conducted to improve the system efficiency.
41
42
43
44
45
46
47
48
49
50
51
52
53
54
55
56
57
58
59
60

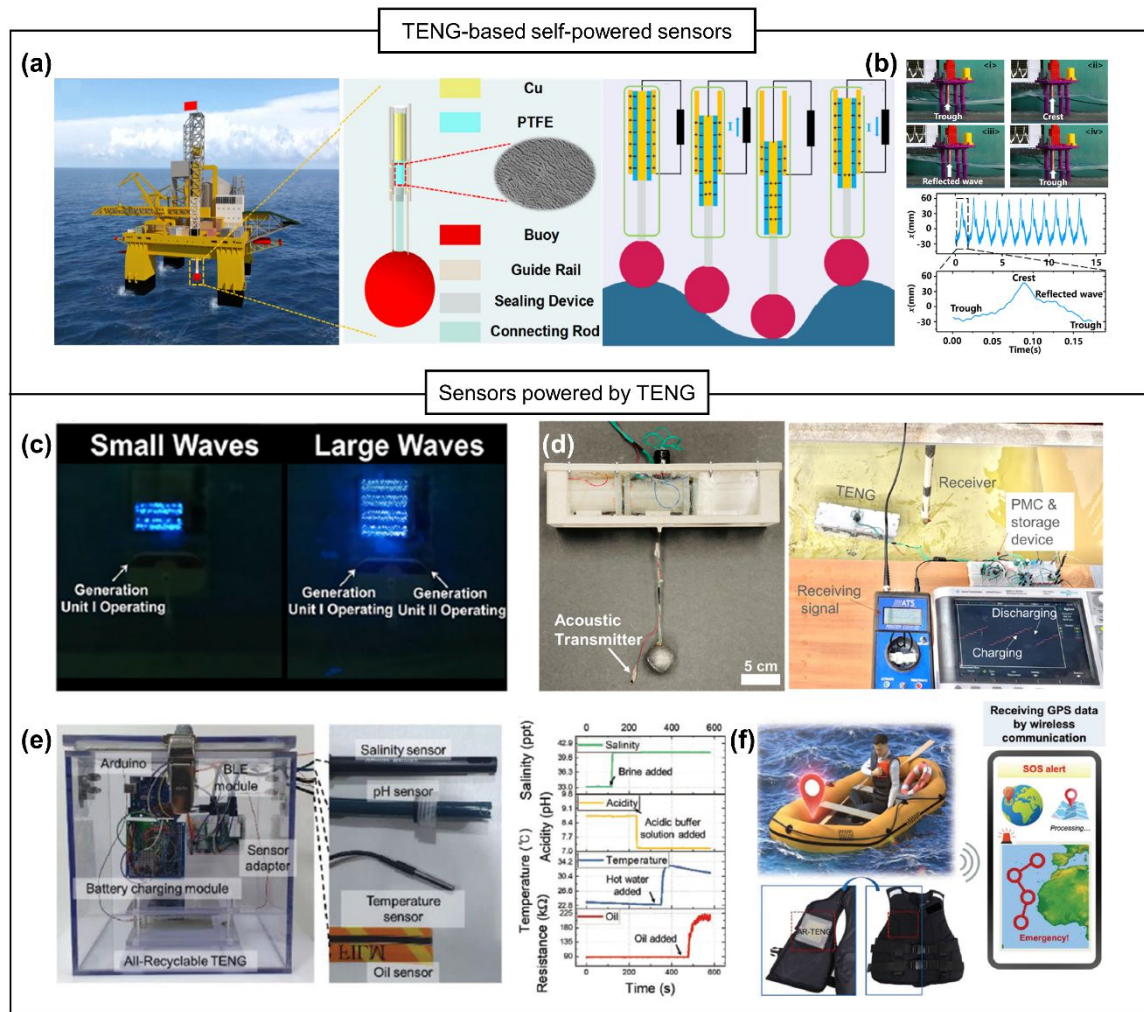


Figure 88. Ocean monitoring systems based on TENG. They are classified into two groups as TENG-based self-powered sensors and sensors powered by TENG depending on the role of TENG (e.g., TENG for directly measuring environmental parameters or for supplying energy). TENG-based self-powered sensors: TENG for quantifying ocean wave spectrum based on (a) the solid–solid interface tubular TENG. Reprinted with permission from ref. 23, Copyright 2020, American Chemical Society. (b) the liquid–solid interface TENG. Reprinted with permission from ref. 804, Copyright 2019, Elsevier. Commercialized sensors powered by TENG: (c) wave condition monitoring sensors using the brightness of LEDs. Reprinted with permission from ref. 514, Copyright 2021, American Chemical Society. (d) acoustic transmitter which can generate acoustic vibration via water. Reprinted with permission from ref. 806, Copyright 2022, Elsevier. (e) intelligent buoy equipped with pH, salinity, temperature, and oil leakage sensors. Reprinted with permission from ref. 531, Copyright 2022, Wiley-VCH GmbH. (f) intelligent life jacket equipped with a global positioning system sensor to send a position information signal in an emergency. Reprinted with permission from ref. 531, Copyright 2022, Wiley-VCH GmbH.

6.5.2 Harvesting wind energy

6.5.2.1 Cam-Based Integrated Windmill Kinematic Operatable

In this section, we review cam-based TENG assembled with the windmill system to harvest wind energy^{119, 807}. Among many kinds of cam-based TENG designs^{62,808,748,539}, the cam-based TENG integrated to the windmill^{119, 807} has a simple design compared to others structure. The cam-based TENG can be a sliding mechanical cam shape,^{748,62} or the bearing integrated cam shape^{119, 539, 808}, or magnetic - assembled cam⁸⁰⁷ to transfer the rotary motion into linear motion. Two kinds of cam-based TENG assembled with the windmill design (mechanical cam and magnet-assembled cam) are presented.

The photograph of a windmill assembled bearing cam driving TENG is shown in Figure 89(a)¹¹⁹. A windmill system driving TENG based on nanopillar-array architected polydimethylsiloxane (NpA-PDMS-based TENG) scavenge the wind flow through a windmill blade. The waste and non-bio-degradable plastic bottle is cut in the windmill blade shape. Afterward, it is fixed at the end of steel rod. In addition, to transfer the rotary motion by the windmill to linear motion of contact-separation mode TENG, the quad nose cam is fabricated with a 3D printer and located in the middle of the same steel rod. Finally, the axial steel rod together with the quad nose cam and windmill blade are hanged up the TENG unit by two 3D printed supporter. The TENG device consists of a 2 x 2 cm² of Al foil with the thickness of 80 μm serve as a top plate of TENG triboelectric layer, which attached to the polylactic acid (PLA) substrate by the double-sided foam tape. As the bottom plate, the same PLA substrate attached Al foil is utilized as an electrode, covered by the NpA-PDMS layers. For harvesting the wind energy by using this windmill NpA-PDMS-based TENG, the wind flow is varied from 0 – 14 or 15 m/s. The output voltage of the windmill integrated NpA-PDMS-based TENG at different wind speed is shown in Figure 89(b), (c). To demonstrate in

1
2
3
4 practical application, this windmill TENG is mounted on the moving car for scavenging the
5
6 wind flow energy.
7

8
9 In other designs of windmill energy harvester-based TENGs, Kim et al.⁸⁰⁷ propose a
10 magnet-assembled cam-based TENG design (MC-TENG). The advantage of this design is
11 able to enhance the output power and improve the sustainability by non-contact repulsive
12 force between magnets. The MC-TENG is then attached to the windmill to harvest the breeze
13 wind energy flow. The photograph of the MC-TENG-based windmill design is shown in
14 Figure 89(d). The MC-TENG uses three permanent magnets rare earth neodymium-iron-
15 boron (NdFeB) for replacing the mechanical interactions of mechanical cam-based TENG
16 (C-TENG). As the magnet attached to the edge of the cam (M_{cam}) approaches to the magnet
17 attached to upper surface of top plate (M_{top}) by cam rotation, the same polarity magnet of
18 these result in repulsive force between them. In the bottom plate, the magnet is attached to the
19 lower plate surface (M_{bottom}) with the same magnet polarity in facing toward the M_{top} . During
20 windmill shaft rotation, the repulsive force between M_{cam} and M_{top} induce the downward
21 movement of M_{top} and contact the bottom substrate. Afterward, the same polarity of M_{top} and
22 M_{bottom} cause the repulsive force and it is gradually increased as M_{top} approaches M_{bottom} . Due
23 to the barely contact between the same polarity magnet, the mechanical contact of C-TENG
24 disappears, leading to the sustainability of this design. In addition, to show the advantages of
25 MC-TENGs compared to C-TENGs, the charging curve performance of a 33 μF is depicted
26 in Figure 89(e). It shows the charging rate of MC-TENG is 2.59 times faster than that of C-
27 TENG. Finally, the MC-TENGs are utilized as a self-powered system for lighting 30 LEDs
28 connected in series instantaneously (Figure 89(f)).
29
30
31
32
33
34
35
36
37
38
39
40
41
42
43
44
45
46
47
48
49
50
51
52
53
54
55
56
57
58
59
60

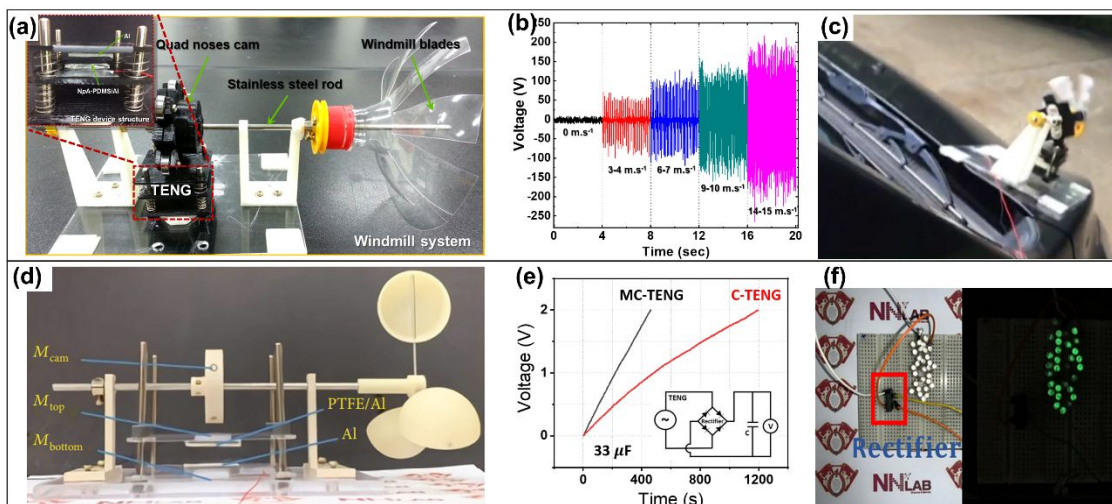


Figure 89. Cam-based TENG integrated windmill for wind energy harvesting. **(a)** Photograph image of windmill design assembled bearing cam driving TENG. **(b)** Output voltage measurement of the NpA-PDMS-based TENG mounted on windmill at different wind speed. **(c)** Photograph showing the NpA-PDMS-based TENG integrated windmill on a moving car for harvesting wind flow energy. **Reproduced with permission from ref 119. Copyright 2017, Elsevier.** **(d)** Photograph of the MC-TENG-based windmill design. **(e)** Capacitor charging curve by C-TENG and MC-TENG. **(f)** 30 LEDs illuminated by MC-TENG. **Reprinted with permission under a Creative Commons CC BY license from ref. 807, Copyright 2021, American Association for the Advancement of Science.**

6.5.2.2 Flutter-Based TENG for Wind Energy Harvesting

Along with the rotational structure-based TENG designs for wind energy scavenging, the non-rotational TENG design based on flutter is introduced in this section. Numerous works have been conducted on the flutter design-based TENG for wind energy harvesting^{809,810,811,812,813,814,815,816,817,818,819}. However, in this discussion, three significant flutter-based TENG designs are discussed. Firstly, the intercalated aluminum (Al) layer in between dielectric film based TENG is proposed by Cho et al.⁸²⁰. In the next, Son et al.⁸²¹ show the bidirectional fluttering TENG (WBF-TENG) through dual flagpole structure design for omnidirectional wind energy scavenging. Lastly, Sun et al.⁸²² display the double-flag flutter type TENG design for wind energy harvesting (FD-TENG). All of these kinds with a contact-separation friction mode provide a huge potential in wind direction recognition, self-powered wind sensing and monitoring system.

At first, the intercalated Al layer between dielectric film flutter based TENG designs for wind energy harvesting is presented by Cho et al.⁸²⁰. The schematic diagram and photographs of a single-contact friction mode PTFE-TENG and a double-contact friction mode inter-Al-TENG are shown in Figure 90(a), (b), respectively. Basically, it is composed of the polytetrafluoroethylene (PTFE) film acting as a dielectric and Al electrode. Both sides of the PTFE film with size of $2.5 \times 7.5 \text{ cm}^2$ are etched by using inductively coupled plasma-reactive ion etching (ICP-RIE) for enhance the roughness, leading the higher contact area during fluttering with top Al electrode. In the design of single-contact friction mode PTFE-TENG, the PTFE is bent toward the top Al electrode and leave a narrow gap between them, creating flutter movement during wind passing. The same small gap is also designed for inter-Al film in the double-contact friction unit for easy contact with bilateral Al top electrode, as shown in Figure 90(b). Under the wind speed of 15.1 m/s, the short-circuit

1
2
3
4 current performance of the single-contact friction mode PTFE-TENG and double-contact
5
6 friction mode inter-Al-TENG are illustrated in Figure 90(c), (d), respectively. Due to the
7
8 elastic modulus of Al is larger than PTFE, the flexibility during oscillation of the pure PTFE
9
10 film is also higher than the inter-Al film. Therefore, the oscillation frequency of pure PTFE-
11
12 TENG exhibits the higher frequency output than that of inter-Al-TENG, as shown in Figure
13
14 90(c), (d). In the case of single-contact PTFE-TENG, the output current shows about 5 peaks,
15
16 i.e., 5 oscillations contact, whereas the double-contact inter-Al-TENG flutters exhibit around
17
18 3.5 peaks in the same interval of 0.02 s. Finally, for practical application, 35 LEDs are lighted
19
20 by electricity connecting with the double-contact inter-Al-TENG at wind speed of 15.1 m/s,
21
22 as shown in Figure 90(e).
23
24
25

26
27 In the next discussion, the wind-driven bidirectional fluttering triboelectric nanogenerator
28
29 (WBF-TENG) is introduced. The WBF-TENG composes of slot structure and a dual flagpole
30
31 to scavenge the wind energy blowing in both directions. Figure 90(f) shows the schematic of
32
33 the WBF-TENG and two vertically stacked WBF-TENG with few inflow angles. The WBF-
34
35 TENG composes of a polyimide (PI) layer, acrylic sheet, flag poles at the both ends of the PI
36
37 layer, and the top-bottom Al electrodes. The high stiffness and electron affinity of PI
38
39 significantly affect the mechanical motion effect to the TENG performance. Due to the light-
40
41 weight of commercial straw, it is used for flagpole design. The schematic diagram of the
42
43 WBF-TENG mechanical motion is depicted in the left side and right side of Figure 90(g)
44
45 with the left-direction and right-direction wind flow induce flutter movement, respectively. In
46
47 the end, for real application design, the WBF-TENG is utilized for lighting 76 LEDs installed
48
49 on the swing during the left-to-right movement of swing. The real photograph of the WBF-
50
51 TENG and LEDs array attached on the swing is shown in Figure 90(h). Finally, the two
52
53 vertical stacked WBF-TENGs are introduced to harvest omnidirectional wind flow. The
54
55 voltage output of the of the lower and upper devices as the wind inflow of 3 m/s from 0°, 45°,
56
57
58
59
60

1
2
3
4 90° is illustrated in Figure 90(i). If the wind blows from 0° and 90° directions, only the upper
5 and lower devices generate the output. Whereas, in the case of wind blowing from a 45°
6
7 and lower devices generate the output. Whereas, in the case of wind blowing from a 45°
8 direction, both devices provide the same output voltage of 70.4 V. With this regard, the
9 WBF-TENG can produce electricity in omnidirectional wind by only two vertically stacked
10 devices, therefore, it can be used as a wind direction sensor.
11
12
13
14

15
16 Before closing the flutter type based TENG, the fluttering double-flag type TENG (FD-
17 TENG) is presented. Figure 90(j) introduces the structure design of the FD-TENG which
18 include two FEP films that fixed on the acrylic support that leaving a certain gap distance to
19 establish the internal and external flow areas. To make the electrode, 100 nm thickness of
20 silver is evaporated on FEP film by electron beam evaporation. The two ends of FEP with Ag
21 electrodes flag are attached on a “back-to-back” for contact-separation mode TENG, as
22 shown in bottom part of Figure 90(j). The real photograph of fabricated array-type of FD-
23 TENG in the ambient environment is shown in Figure 90(k) with the surrounding natural
24 wind speed of approximately 4.5 m/s. In the demonstration of the single FD-TENG, a wind
25 velocity of 10 m/s in the wind tunnel is applied to FD-TENG to lit up 205 green LEDs, as
26 shown in Figure 90(l). In addition, for powering the sensor the array-type FD-TENG is used
27 to drive a temperature-humidity sensor, as depicted in Figure 90(m). As the charging voltage
28 of capacitor reaches about 10 V, the temperature-humidity sensor is operated due to the
29 switch being closed. The charging/discharging curve of 100 μ F capacitor driving a
30 temperature-humidity sensor in 250 s by this array-type FD-TENG is illustrated in Figure
31 90(n). Through this practical application, the FD-TENG show a potential in acting as a power
32 supply for wireless sensor networks.
33
34
35
36
37
38
39
40
41
42
43
44
45
46
47
48
49
50
51
52
53
54
55
56
57
58
59
60

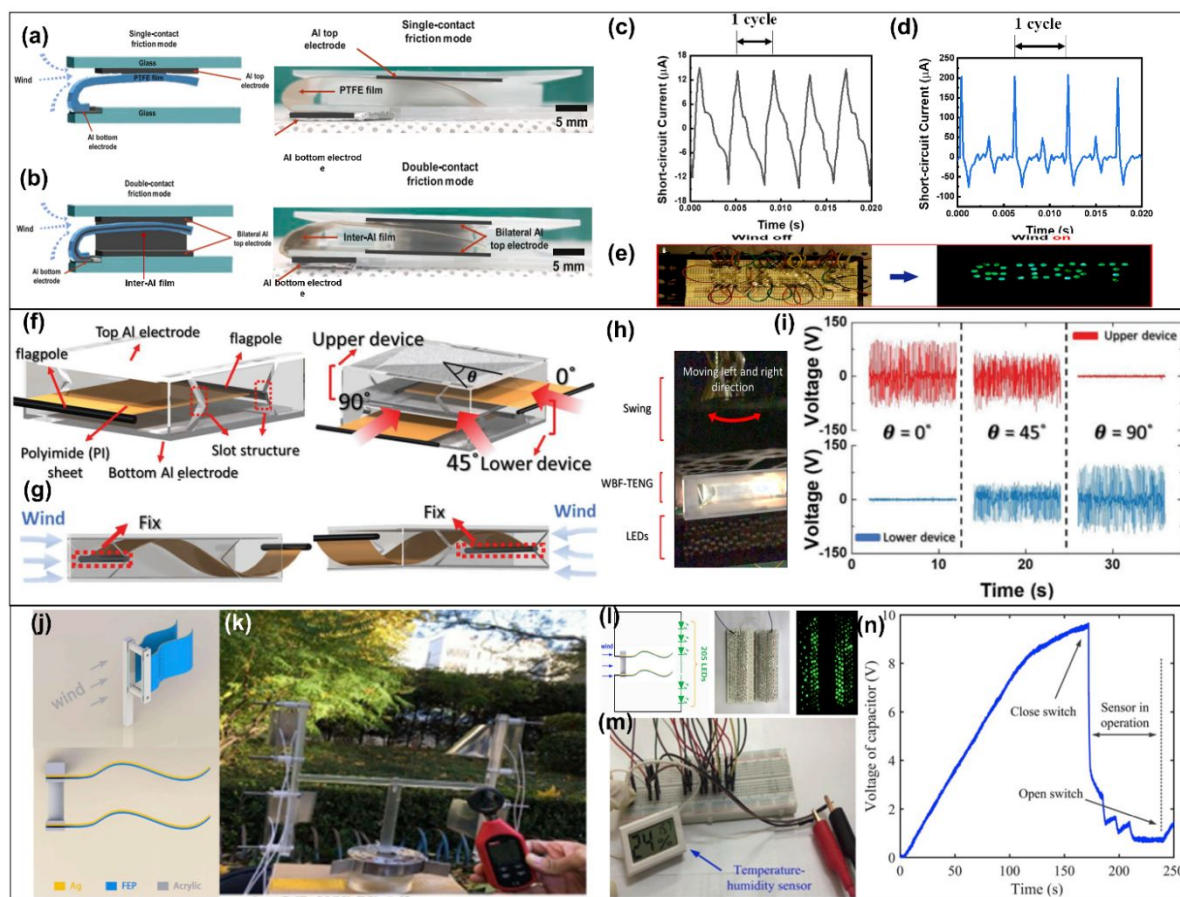


Figure 90. Intercalated Al layer between dielectric film flutter based TENG designs for wind energy harvesting. Schematic illustration and photographs of (a) a single-contact friction mode PTFE-TENG and (b) a double-contact friction mode inter-AI-TENG utilize bilateral Al top electrode for double friction contact. Short-circuit current of the (c) single-contact PTFE-TENG and (d) double-contact inter-AI-TENG under wind speed of 15.1 m/s. (e) Photograph of “GIST” letter using 35 LEDs lighting by a double-contact inter-AI-TENG wind energy harvester. **Reproduced with permission from ref. 820. Copyright 2020, Elsevier.** Wind-driven bidirectional fluttering TENG (WBF-TENG). Schematic illustration of (f) WBF-TENG and two vertical stacked WBF-TENG at various wind flow angle and (g) the flutter movement of WBF-TENG by left- and right- wind direction. (h) WBF-TENG light up LEDs during the swing to left and right direction. (i) Output voltage of lower and upper device of two vertical stacked WBF-TENG at wind inflow angle of 0° , 45° , and 90° . **Reproduced with permission from ref 821. Copyright 2022, Wiley.** Design of the fluttering double-flag type TENG. (j) Schematic diagram. (k) Fabricated array-type of FD-TENG in outdoor environment at wind velocity of 4.5 m/s. (l) Charging and discharging curve of 100 μF capacitor in 250 s. (m) Light up 205 LEDs connected in series by single FD-TENG at wind speed of 10.1 m/s. (n) FD-TENG array type powers the temperature-humidity sensor. **Reproduced with permission from ref 822. Copyright 2020, Elsevier.**

6.5.2.3 Advanced Structure Design for Wind Energy Harvesting

All the above reviewed works relate to rotational and fluttering type TENGs, and the TENGs used for harvesting wind energy still exhibit a large potential. In this section, the advanced structure design for wind energy scavenging is discussed with a focus on the wind energy harvester-based TENG design and application. Han et al.⁵²⁷ proposed a radial-engine-shaped TENG system to absorb NO_x and downgrade the enrichment forms of nitrate and nitrite in aqueous solution. In addition, Zhang et al.⁸²³ introduced a vortex-induced vibration based triboelectric nanogenerator (VIV-TENG) for efficient scavenging the wind energy at low speed.

In this work for wind energy scavenging is reported by Han et al.⁵²⁷. The as-fabricated radical-engine-shaped TENGs, an electrocatalytic system and one-way valves are used to design a self-powered NO_x absorption and downgrade system. To demonstrate the practical application, a simulation experiment system is verified in a sealed box, as shown in Figure 91(a). The radical-engine-shaped TENGs integrated one-way valves, electrolytic cell and power source motor together with 50 mL of pure water and NO_x detector are sealed. As shown in Figure 91(b), the radical-engine-shaped TENGs is attached with the wind cups and located on the top of a street light pole to absorb the NO_x pollution by wind energy. To stable the rotation, a plain bearing is utilized. The below inset figure is a photograph of the device installed with wind cups. Figure 91(c), (d) show the result detection of NO_2^- and NH_3 after 24 hours' degradation driven by the radical-engine-shaped TENGs, respectively. At the wind velocity of 6 m/s, the radical-engine-shaped TENGs drive the catalytic system and exhibit a decrease of NO_2^- concentration. In addition, the increasing of NH_3 concentration supports for explanation of the degradation reaction. This result provides a solution for solving and removing the pollution gas in surrounding air by a self-powered electrochemical system.

1
2
3
4 In the next discussion, a vortex-induced vibration based triboelectric nanogenerator (VIV-
5 TENG) for harvesting low wind speed and providing high average power output than other
6 previous studies. Figure 91(e) shows the scenario of harvesting wind energy from remote area
7 by using the VIV-TENG. The inset figure is the 3D schematic of the VIV-TENG, consists of
8 a lightweight cylinder and TENG device composed of polyaniline (PANI) and
9 polytetrafluoroethylene (PTFE), which act as the tribo-material pair. The tension springs are
10 utilized to hold the cylinder and TENG. Therefore, if the wind flows cross to the cylinder, it
11 can oscillate to transform to kinetic energy from the wind energy, leading to the TENG
12 electric power response from kinetic energy. In this work, the prediction results based on the
13 theoretical model are conducted and compared with the experimental results. However, in
14 this discussion, the output voltage of VIV-TENG at various wind velocities ranging from
15 1.66 – 3.38 m/s are shown in Figure 91(f), which show the optimal output voltage reaches
16 536 V at wind speeds of 2.78 m/s. In addition, the two VIV-TENG in tandem configuration
17 (T-VIV-TENG) is design for further practical application in wireless communication. To
18 operate the wireless data monitoring sensors, the T-VIV-TENG is used to charge the 1.22 mF
19 capacitor and power the wireless sensors, as described in Figure 91(g). The monitoring
20 sensor sends the data to a phone wirelessly via Bluetooth for recognizing the real-time
21 environment conditions.
22
23
24
25
26
27
28
29
30
31
32
33
34
35
36
37
38
39
40
41
42
43
44

45 Furthermore, the final discussion is about the TENG design that can harvest energy from
46 omnidirectional wind with a wide range of wind speeds. Ko et al.⁸²⁴ introduced a self-
47 suspended shell-based TENG (S³-TENG) for omnidirectional wind energy scavenging, as
48 shown in Figure 91(h). The S³-TENG composes of a rigid column with outside covered by a
49 flexible cylindrical shell. The outermost surface of the rigid column is covered by aluminum,
50 whereas the innermost surface of flexible cylindrical shell is attached with the PTFE to create
51 a tribo-material pair. Due to the Coulombic attraction between the tribo-material pair, the
52
53
54
55
56
57
58
59
60

1
2
3
4 flexible thin shell can form a self-suspended structure. Thus, the aluminum and ring-shape
5
6 electrode electrical connection is sustained and are deformed easily even by breeze wind.
7
8 Thanks to the cylindrical structure design of the S³-TENG, it leads to a uniform electrical
9
10 signal from omnidirectional wind. The real photograph of the fabricated S³-TENG is shown
11
12 in Figure 91(i) with described dimensions. Finally, to demonstrate the capability of S³-TENG
13
14 in wind energy harvesting at various wind velocity (2, 5, and 8 m/s), the root mean square
15
16 (RMS) output voltage of eight electrodes pairs is exhibited in Figure 91(j). The average
17
18 voltage output is increased with the higher wind speed and it is asymmetrically generated at a
19
20 steady wind speed in eight electrode pairs. Thus, the S³-TENG can be utilized as a nonlinear
21
22 self-powered wind direction and speed sensor concurrently. The real-time wind speed and
23
24 direction monitoring set up generated by the S³-TENG is shown in Figure 91(k). In this
25
26 observation, the RMS voltages from eight electrodes provide a symmetric signal as the wind
27
28 direction. Therefore, the wind direction depended eight electrode pairs RMS voltage
29
30 distribution can reveal the wind direction monitoring.
31
32
33
34
35
36
37
38
39
40
41
42
43
44
45
46
47
48
49
50
51
52
53
54
55
56
57
58
59
60

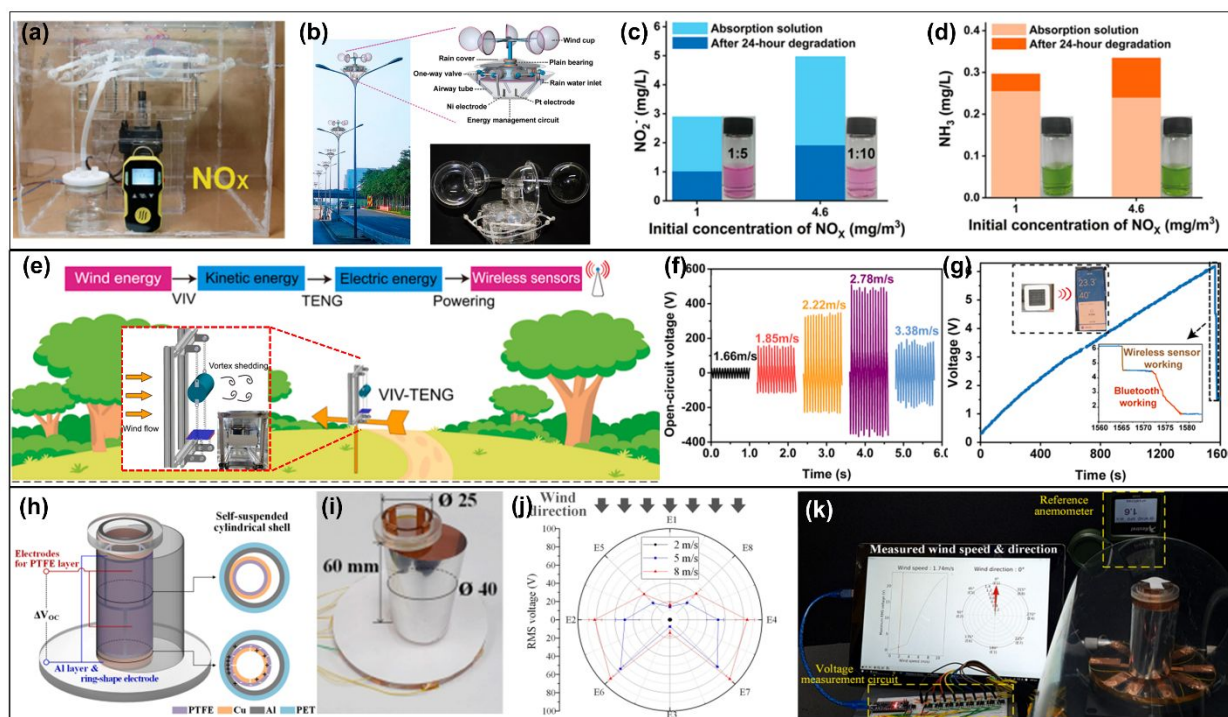


Figure 91. Self-powered NO_x degradation by the radial-engine-shaped TENGs. **(a)** Schematic diagram of the self-powered radial-engine shaped TENG system driven by wind power and photograph of the self-powered radial-engine-shaped TENGs. **(b)** NO_2^- and **(c)** NH_3 after 24-h of self-powered degradation using a 20 mL absorption solution from the simulation absorption experiment. **(d)** Photograph of the sealed box with electrolytic cell, NO_x detector, and the radial-engine-shaped TENGs driven by a motor. **Reproduced with permission from ref 527. Copyright 2020, American Chemical Society.** Vortex-induced vibration TENG at breeze wind energy **(e)** Potential application scenarios of designed VIV-TENGs for powering WSNs in remote field areas and 3D schematic diagram and photograph of the designed VIV-TENG. **(f)** open-circuit voltage at different values of wind speed. **(g)** wireless monitoring sensor. **Reproduced with permission from ref 823. Copyright 2022, Elsevier.** Self-suspended shell-based TENG for omnidirectional wind energy scavenging **(h)** Schematic design of self-suspended shell-based TENG and **(i)** the optical image of the proposed TENG device, **(j)** Root mean square voltage output triggers by eight electrode pairs in different wind speed ranging from 2 m/s – 5 m/s – 8 m/s, **(k)** Real-time measurement for wind speed and wind direction set up. **Reproduced with permission from ref 824. Copyright 2022, Elsevier.**

6.5.3 Harvesting human motion energy

The widespread use of wearable electronic devices has led to increasing demand for micro energy sources^{58,825}. The emergence of hybridized nanogenerators has provided a research direction for collecting various types of different forms of energy at the same time^{58,826,827,828,9,829}. Hybridized nanogenerators provide ideas to solve the energy demand of wearable electronic devices, and more and more hybridized nanogenerators are widely used in the field of wearable electronic devices^{828,362,830,831,832,833}. Common hybridized nanogenerators include photovoltaic cell-triboelectric nanogenerators (PVC-TENGs), electromagnetic-triboelectric nanogenerators (EMG-TENGs) and piezoelectric-triboelectric nanogenerators (TPiENGs)^{826,827,828,9,829,834,835,836}. Figure 92(a) shows a hybridized organic photovoltaic cell-triboelectric nanogenerator (OPV-TENG) system, which can collect light energy generated by indoor light sources and mechanical energy generated by human motion individually or simultaneously⁸³¹. The system has been tested to effectively and rapidly charge capacitors and has potential applications. A hybridized self-charging power textile system is introduced, also a solar cell- triboelectric nanogenerator, to collect energy generated by outdoor sunlight and body movement simultaneously⁸³⁷. This fiber structure can be used to prepare various types of e-textiles, smart clothes, etc., as wearable electronic devices. Figure 92(b) presents an electronic watch proposed by Quan et al⁸³⁸. Its power supply system consists of one triboelectric nanogenerator (TENG) and six electromagnetic generators (EMGs), which can effectively collect the energy generated by human movement. This electronic watch can be continuously powered while the wearer is moving, or it can be continuously and steadily powered by storing energy through capacitors. Zhang et al. also proposed a Hybridized EMG-TENG that can be applied in a commercial shoe to harvest energy from human movement while walking⁸³⁵. As shown in Figure 92(c), the energy generated during human movement can be converted into electrical energy to light up the

1
2
3
4 LED lights around the shoe, and in addition, it can provide electrical energy for a smart
5
6 pedometer and output and transmit relevant data, promoting the development of the field of
7
8 wearable electronics. Figure 92(d) also shows a flexible hybridized energy harvesting system,
9
10 which can collect human mechanical energy as well as external water droplet energy and
11
12 wave energy through two parts⁸³⁹. It has high flexibility, excellent wearability, large
13
14 scalability, and moisture resistance, and can power commercial electronic devices (e.g.,
15
16 calculators and clocks) without the need for an additional power supply. Hybridized
17
18 nanogenerators harvesting various forms of energy from the surrounding environment is a
19
20 very efficient and clean method with promising applications in wearable electronics to meet
21
22 the world's sustainable development and long-term energy needs.
23
24
25
26
27
28
29
30
31
32
33
34
35
36
37
38
39
40
41
42
43
44
45
46
47
48
49
50
51
52
53
54
55
56
57
58
59
60

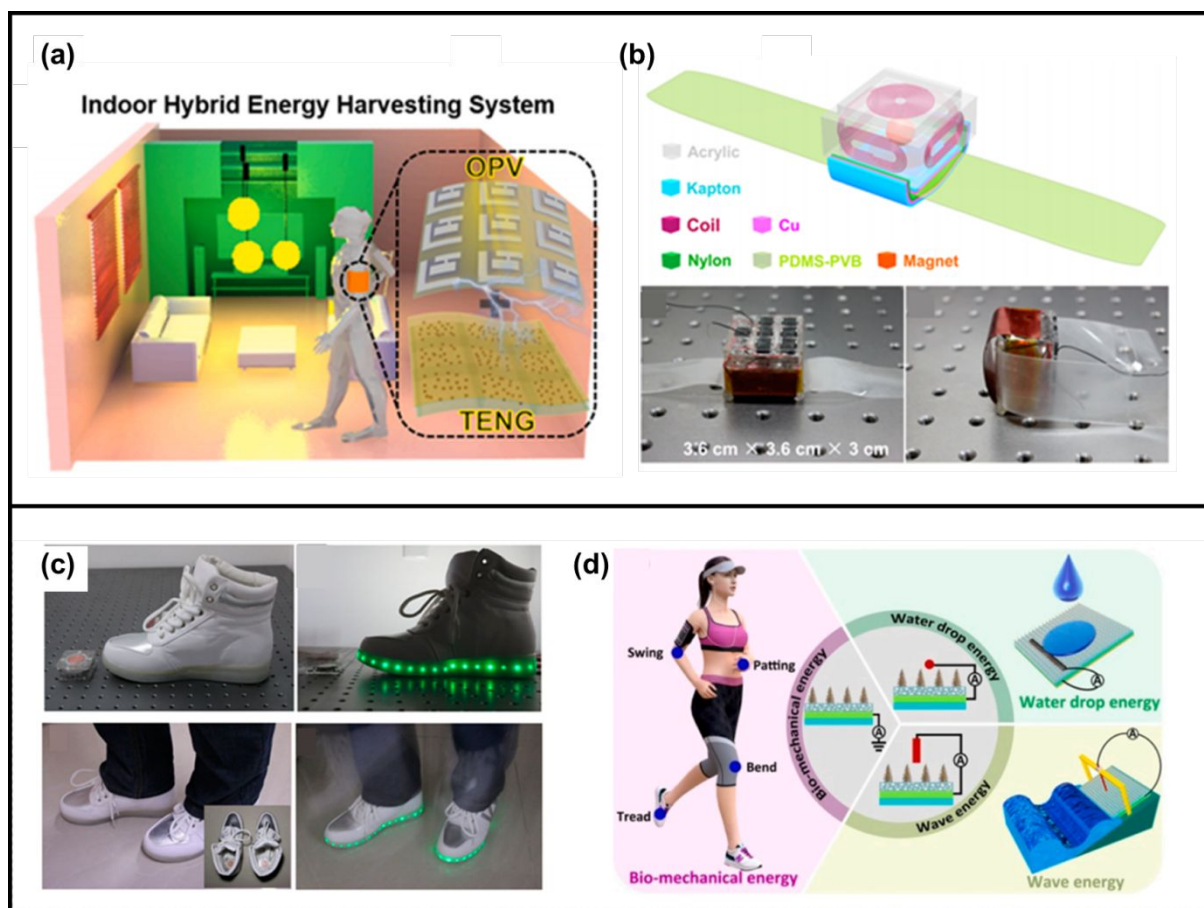


Figure 92. Hybridized nanogenerators for wearable applications. (a) A hybridized organic photovoltaic cell-triboelectric nanogenerator (OPV-TENG) system. **Reproduced with permission from ref. 831. Copyright 2020, Elsevier.** (b) A self-powered electronic watch. **Reproduced with permission from ref. 838. Copyright 2015, American Chemical Society.** (c) Hybridized nanogenerator applied to shoes. **Reproduced with permission from ref. 835. Copyright 2015, American Chemical Society.** (d) A hybridized dielectric-based TENG (HD-TENG). **Reproduced with permission from ref. 839. Copyright 2022, ELSEVIER SCIENCE SA.**

7. Summary and perspectives

Since TENGs are reported in 2012, they have been explosively developed and still developing in terms of materials (chapter 2), devices (chapter 3), systems (chapter 4), circuits (chapter 5), and applications (chapter 6). In this review, we would like to balance each topic's importance and cover all issues in each topic. The most important thing in this review is to understand that the target environment for TENG installation is the most critical to enhancing and optimizing the TENG systems, which is essential for commercializing TENGs. Due to the many applications of TENGs, we could not cover all applications of TENGs, but we believe that the readers can understand the promising possibility of TENG applications for next-generation life. In chapter 1, we introduced abundant wasting mechanical energies and TENG's advantages as one of many mechanical energy harvesters. Furthermore, we examined the governing equations for TENGs, which were induced by expanding maxwell's equations from Prof. Zhong Lin Wang. Still, we can expand those equations based on our own parametric functions and further design better tribomaterials and devices, systems, and circuits.

In chapter 2, we reviewed a range of the triboelectric materials, starting from the fundamentals of the charge transfer mechanism occurring on the surfaces of two materials

1
2
3
4 during the physical contact to the government strategies of the key materials technologies to
5 maximize the charge densities created on the surfaces. The charge transfer was commonly
6 explained via the transfer of electrons, ions, and materials, or two mores, and the contact
7 electrification of a solid surface and a liquid was also reviewed. To increase the charge
8 density, many studies about physical surface modifications by developing various
9 nanostructures via etching process and patterning processes have been conducted. The
10 chemical surface modification such as plasma treatment, neutral beam irradiation,
11 ultraviolet/ozone treatment, and chemical functionalization is also a good way to enhance the
12 output performance of the triboelectric nanogenerator. Besides the surface modification, the
13 materials' modification such as dielectric constant, mechanical properties could significantly
14 change the performance of the TENG. Here, various composites such as polymer-metal
15 inorganic nanomaterial composites, polymer-2D nanomaterial composites, ferroelectric
16 polymer-inorganic nanomaterial composites, and flexible/stretchable composites were
17 reviewed. As well as surface and bulk modifications, the intermediate layer engineering via
18 electron trapping layers and electron blocking layers /functional interlayers was a promising
19 approach for increasing the outputs of TENGs. A layer-by-layer self-assembly approach was
20 also reviewed, based on covalent bonding and weak electrostatic interactions. What should be
21 overcome in TENGs may be the stability of the materials and the noise during operation. As
22 functional tribomaterials, self-healing polymer materials to TENGs were suggested to
23 improve the durability of devices. To reduce the noise during operation, noise-canceling
24 TENG technologies were reported by introducing a porous metallic sponge. Finally,
25 Biological materials for TENGs were reviewed as energy sources for electronic devices such
26 as wearable, implantable, and environmentally friendly devices.
27
28
29
30
31
32
33
34
35
36
37
38
39
40
41
42
43
44
45
46
47
48
49
50
51
52
53
54
55
56
57
58
59
60

1
2
3
4 In chapter 3, we outlined triboelectric devices broken down by type of operation mode.
5
6 Although recent impressive progress has proven their potential as a fascinating energy
7
8 harvester, the field is still in its early stage and the devices are far from use for practical
9
10 application with regard to generated energy. Valuable efforts for instantaneous discharged
11
12 TENG design have contributed on TENGs to generate high peak power. However, the output
13
14 is generated relatively for a short time and no longer than a few milli-seconds per an input
15
16 contact, limiting their practical applications. Alternatively, charge pumping designs (sub-
17
18 TENG for main TENG) have been attractive approaches for enhancing amount of generated
19
20 electric energy. However, the design still requires additional pumping sub-TENG device,
21
22 causing the whole system to be bigger and heavier. Combining functions of the sub-TENG
23
24 into the main device might be an attractive approach. Furthermore, alternating current pulse
25
26 type outputs of conventional TENGs are not suitable as a power source for electronic devices
27
28 in real life. To address the above issue, research on TENGs generating direct currents has
29
30 been intensively highlighted. Even if it is fascinating research direction for utilizing TENGs
31
32 in real life, it still requires relatively high input frequency to get useful high power. It is
33
34 expected that strategies for minimized TENG generating stably high output energy is needed
35
36 to be explored, ensuring TENGs to be used in wide practical application in the future.
37
38
39
40
41
42
43
44
45
46

47 In chapter 4, we reviewed the various mechanical designs of energy harvesters based on the
48
49 TENGs for effective electrical generation considering the mechanical characteristics of the
50
51 input energy sources. There are a lot of purpose-built mechanical energy harvesting systems,
52
53 which can harvest a variety of input energy sources, such as ocean wave, wind,
54
55 biomechanical, and vibration energy. To understand the comprehensive mechanical design
56
57 guidelines of the energy harvester, we explained the TENG-based mechanical systems
58
59
60

1
2
3
4 capable of amplifying, reducing, and even modulating output frequencies through designs
5
6 incorporating various mechanical elements for energy transmission, such as gear train, spring,
7
8 and cam systems. As a result, it has successfully achieved the desired output performance,
9
10 long lifespan, and stable electricity generation from irregular input energy sources. In
11
12 addition, we have also reviewed a resonant system, which can harvest vibration energy with
13
14 dramatically increased amplitude by vibrating at resonant frequencies and resonant
15
16 wavelengths. Given that, the resonant system-based TENG can convert micro-vibration and
17
18 even acoustic vibration into useful electricity with the advantageous aspects of high
19
20 sensitivity. In this regard, the resonant system-based energy harvester can not only collect the
21
22 vibration energy to supply power micro nano-electronic devices, but also it can also play a
23
24 significant function in a self-powered and a wireless vibrations sensor in the surrounding
25
26 environment. Therefore, this review will provide mechanical design guidelines according to
27
28 the characteristics of the input energy source, thereby greatly contributing to the practical
29
30 applicability of the energy harvester in the future.
31
32
33
34
35
36
37
38
39

40 In chapter 5, we introduced circuit designs for power managements. The TENGs usually
41
42 exhibit low-energy transfer efficiency when directly either powering conventional electronics
43
44 or charging energy storage devices due to the impedance mismatch. TENGs offer high input
45
46 impedance ($\sim M\Omega$) while the impedances of conventional electronic devices and energy
47
48 storage units are relatively low. Furthermore, TENG output characteristics typically offer
49
50 high voltage at a few hundred volts, low output current at $\sim \mu A$ level, and limited output
51
52 power, which cannot satisfy the stable power supply requirements of electronic devices.
53
54 Therefore, an efficient power management circuit is required as an interface unit between the
55
56 TENG and external loads to facilitate impedance and voltage conversions for efficient energy
57
58
59
60

1
2
3
4 transfer and storage. Over the past years, several strategies of power management have been
5
6 proposed, such as inductive and capacitive transformers, switched-capacitors convertors, and
7
8 MOSFET power converters, which can be used for voltage regulation, impedance matching,
9
10 and efficiency improvements. Introducing inductive transformers is an effective strategy for
11
12 reducing voltage and the output impedance of TENGs. It typically consists of a rectifier,
13
14 capacitors, a regulator, and an electromagnetic transformer. However, inductive transformers
15
16 are relatively large and require high working frequency. Therefore, these transformers are
17
18 more suitable for rotary mode TENGs-based applications. Contrarily, capacitive transformers
19
20 are independent of the working frequency of the TENGs. Furthermore, capacitive
21
22 transformers can reduce the open circuit voltage and improve the transferred charge of TENG
23
24 multiple times. Similarly, switched-capacitor converters (SCC), based on MOSFETS and
25
26 capacitors, with easy integration capabilities can effectively perform step-down or step-up
27
28 voltage conversion by switching serial-to/from-parallel connections. SCC possess several
29
30 inherent advantages, including being magnets-free, lightweight, and offering high conversion
31
32 efficiency, which is quite suitable for wireless sensor networks, DC micro-grids, electric
33
34 vehicle, solar photovoltaic systems, etc. However, the number of capacitors cannot be
35
36 increased indefinitely due to the turn-on voltage drop of the diodes, which limits the ratio of
37
38 switched-capacitor conversion. The first step in the power management strategy maximizing
39
40 the energy transfer from the TENG to the back-end circuit. The second step is decreasing the
41
42 voltage and increasing the current by adding various circuit elements for powering
43
44 conventional electronics. For the maximum transfer of energy and DC conversions, the
45
46 sequential control of the switch is of paramount importance. To achieve the optimized
47
48 autonomous switching by the TENG, the switch can be realized by a logic circuit (e.g., a
49
50 micro-power voltage comparator) and a MOSFET. Due to this, internal resistance is reduced
51
52 and high energy can be extracted from the TENG and transferred to the back-end circuitry.
53
54
55
56
57
58
59
60

1
2
3
4
5
6
7
8 In chapter 6, we outlined applications of TENGs as power sources including robotic,
9 biomedical, and environmental applications and self-powered sensing including touch, touch
10 position, proximity, and crack sensing. With intensive attention during last ten years since the
11 paper was reported in 2012, the research field of TENGs have been notably growing in terms
12 of electric energy generation. The electrical energy generated by TENG has contributed on
13 suggesting the feasibility of TENGs to be used as power sources for various applications such
14 as actuation of robots, rehabilitation of biomedical, and purification of environments.
15 Furthermore, properties of electric signal generation under applied touch and movement of
16 targets allow TENG to be used as self-powered sensors. However, the both power sourcing
17 and self-powered sensing capability are still in proof-of-concept level due to lack of power
18 density and electrical stability. To actuate practical robots even with high frequency in real
19 time, the power conversion efficiency of TENGs is required to be improved. Existing TENGs
20 are lack of providing sufficient power yet compared to batteries and commercial power
21 sources. Furthermore, to realize ideal self-powered sensing systems based on TENGs, the
22 whole devices are required to be operated using triboelectric power generation without
23 depending on external power source for covering data acquisition and processing. We believe
24 increasing power generation density will be a critical and high impact direction.
25
26
27
28
29
30
31
32
33
34
35
36
37
38
39
40
41
42
43
44
45
46
47
48
49
50

51 As one of the promising electricity generation platforms, the TENGs are prosperously
52 developed in a variety of engineering fields since its proposal in 2012. In detail, the TENGs
53 have enabled us to realize a wide range of applications, which can be classified into four
54 areas: micro- and nano-power sources, self-powered sensing, high voltage (HV) power
55
56
57
58
59
60

1
2
3
4 source, and electrical stimulation. The roadmaps in Figure 93 tells us that so far, design
5 innovation and performance enhancement have been the major research areas for TENGs.
6
7 Recently, thanks to the efforts of researchers all over the world, the related technology has
8
9 matured a lot, and as a result, it has reached the stage of prototype development with
10
11 verification of performance in an actual driving environment beyond the lab scale
12
13 environment toward its commercialization.
14
15
16
17
18

19 Compared to the technology roadmap previously proposed in the early stage of the TENG
20
21 development, considerable technological advances have been made and it has had the effect
22
23 of advancing the timeline of achievements in the roadmap. For instance, self-powered
24
25 implantable electronics, smart and low-power human machine interfacing (HMI), in-vitro
26
27 bio-health monitoring, personal healthcare protection, air quality control (highlighted in red
28
29 letters in Figure 93) by means of the operation of the TENGs have been expected to be
30
31 implemented in the future, but thanks to unexpectedly rapid technological progress, the
32
33 implementation has already been achieved at this point. Such accelerated technological
34
35 advancement shows that the present TENGs are one step closer to commercialization, and it
36
37 is further expected that TENGs will serve as a key solution in the near future in line with
38
39 carbon reduction as well as energy-related environmental problems that are currently critical
40
41 issues worldwide.
42
43
44
45
46
47
48
49
50
51
52
53
54
55
56
57
58
59
60

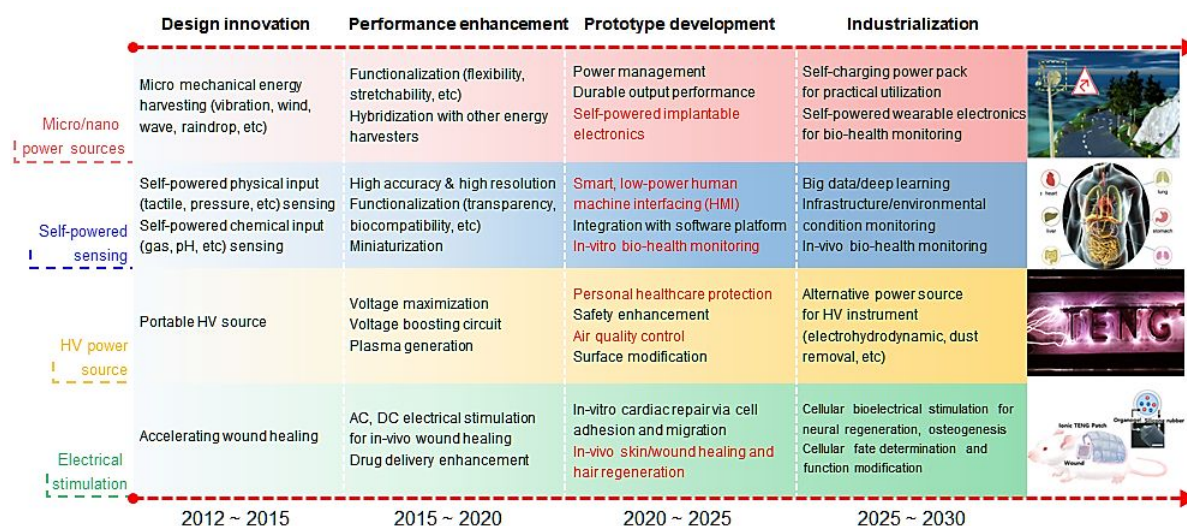


Figure 93. A roadmap of triboelectric nanogenerators (TENGs) with regard to key perspectives toward future commercialization development from 2012 to 2030. **Reproduced with permission from ref. 58, Copyright 2022 Wiley-VCH. Reproduced with permission from ref. 840, Copyright 2021 Elsevier B. V.**

1
2
3
4 **Author Information**
5

6
7 First Author
8

9 *E-mail: dongwhi.choi@khu.ac.kr
10

11 *E-mail: abcde@gachon.ac.kr
12

13 *E-mail: linzh@mx.nthu.edu.tw
14

15
16
17 Corresponding Author
18

19 *E-mail: zhong.wang@mse.gatech.edu
20

21 *E-mail: jbaik97@skku.edu
22

23 *E-mail: bred96@skku.edu
24

25
26
27 ORCID
28

29 Dongwhi Choi: 0000-0002-9286-2710
30

31 Zong-Hong Lin: 0000-0002-1793-7858
32

33 Younghoon Lee: 0000-0003-2436-9681
34

35 Zhong Lin Wang: 0000-0002-5530-0380
36

37 Jeong Min Baik: 0000-0002-3411-3981
38

39 Dukhyun Choi: 0000-0002-4788-0215
40

41 Miso Kim: 0000-0002-2323-4892
42

43 Siowling Soh: 0000-0002-4294-6772
44

45 Chi Kit Ao: 0000-0002-6474-0951
46

47 Chang Kyu Jeong: 0000-0001-5843-7609
48

49 Minbaek Lee: 0000-0003-3515-9647
50

51 Jungho Ryu: 0000-0002-4746-5791
52
53
54
55
56
57
58
59
60

1
2
3
4 Il-Doo Kim: 0000-0002-9970-2218

6
7 Jaewan Ahn: 0000-0002-0136-8427

9
10 Yujang Cho: 0000-0002-3772-5537

12
13 Pooi See Lee: 0000-0003-1383-1623

15
16 Feng Jiang: 0000-0001-7496-816X

18
19 Sang-Jae Kim: 0000-0002-5066-2622

21
22 Gaurav Khandelwal: 0000-0002-7698-4494

24
25 Hyun-Cheol Song: 0000-0001-5563-9088

27
28 Junghyo Nah: 0000-0001-9975-239X

30
31 Yong Tae Park: 0000-0001-9296-6790

33
34 Habtamu Gebeyehu Menge: 0000-0002-1023-0147

36
37 Jianhua Hao: 0000-0002-6186-5169

39
40 Ju-Hyuck Lee: 0000-0001-5383-5894

42
43 Sang-Woo Kim: 0000-0002-0079-5806

45
46 Dong-Min Lee: 0000-0002-5964-2636

48
49 Haixia Zhang: 0000-0003-4565-4123

51
52 Yunlong Zi: 0000-0002-5133-4057

54
55 Jia Cheng: 0000-0002-2557-0072

57
58 Ze Yang: 0000-0002-2062-7367

60
Yannan Xie: 0000-0002-6889-4288

Sangmin Lee: 0000-0002-6713-4797

Jihoon Chung: 0000-0002-4495-5998

1
2
3
4 Sumin Cho: 0000-0001-5168-3882
5

6
7 Il-Kwon Oh: 0000-0002-6705-7664
8

9
10 Tinghai Cheng: 0000-0003-0335-7614
11

12
13 Gang Cheng: 0000-0002-1242-8739
14

15
16 Guangqin Gu: 0000-0001-9508-1306
17

18
19 Minseob Shim: 0000-0001-6165-0320
20

21
22 Jeehoon Jung: 0000-0002-4055-3764
23

24
25 Changwoo Yun: 0000-0003-3747-7825
26

27
28 Chi Zhang: 0000-0002-7511-805X
29

30
31 Guoxu Liu: 0000-0001-8872-9979
32

33
34 Yufeng Chen: 0000-0001-6866-2623
35

36
37 Suhan Kim: 0000-0001-5407-3211
38

39
40 Xiangyu Chen: 0000-0002-0711-0275
41

42
43 Xiong Pu: 0000-0002-1254-8503
44

45
46 Zi Hao Guo: 0000-0002-0520-9837
47

48
49 Jun Chen: 0000-0002-3439-0495
50

51
52 Xing Xie: 0000-0002-2253-0964
53

54
55 Hulin Zhang: 0000-0003-4899-1491
56

57
58 Ying-Chih Lai: 0000-0002-3471-3290
59

60
Tianyi He: 0000-0003-0642-4894

Inkyu Park: 0000-0001-5761-7739

Junseong Ahn: 0000-0002-4090-5440

1
2
3
4
5
6
7
8
9
10
11
12
13
14
15
16
17
18
19
20
21
22
23
24
25
26
27
28
29
30
31
32
33
34
35
36
37
38
39
40
41
42
43
44
45
46
47
48
49
50
51
52
53
54
55
56
57
58
59
60

Notes

The authors declare no competing financial interest.

Acknowledgements

This work was supported by the National Research Foundation of Korea (NRF) grant funded by the Korea government (MSIT) (2019R1A2C2009822, 2022R1C1C1008831, 2021R1C1C2009703) and was supported by the Technology Innovation Program (20013794, Center for Composite Materials and Concurrent Design) funded by the Ministry of Trade, Industry & Energy (MOTIE, Korea).

VOCABULARY

Triboelectricity, the electric charge generation due to sequential contact and separation of two different materials; **mechanical energy**, the energy possessed by an object as a result of its mobility or position; **energy harvesting**, the conversion of ambient energy in the environment into electrical energy; **mechanical system**, a group of mechanical parts that change the motion or force of an input into the desired output; **work function**, The least amount of energy required for a free electron to leave the material's surface;

References

- (1) Kim, S.; Choi, J.; Seung, H. M.; Jung, I.; Ryu, K. H.; Song, H.-C.; Kang, C.-Y.; Kim, M., Gradient-index phononic crystal and Helmholtz resonator coupled structure for high-performance acoustic energy harvesting. *Nano Energy* **2022**, *101*, 107544.
- (2) Kim, M.; Dugundji, J.; Wardle, B. L., Efficiency of piezoelectric mechanical vibration energy harvesting. *Smart Materials and Structures* **2015**, *24* (5), 055006.
- (3) Beeby, S. P.; Tudor, M. J.; White, N., Energy harvesting vibration sources for microsystems applications. *Measurement science and technology* **2006**, *17* (12), R175.
- (4) Roundy, S.; Trolier-McKinstry, S., Materials and approaches for on-body energy harvesting. *MRS Bulletin* **2018**, *43* (3), 206-213.
- (5) Jiang, D.; Shi, B.; Ouyang, H.; Fan, Y.; Wang, Z. L.; Li, Z., Emerging implantable energy harvesters and self-powered implantable medical electronics. *ACS nano* **2020**, *14* (6), 6436-6448.
- (6) Wang, Z. L.; Song, J., Piezoelectric nanogenerators based on zinc oxide nanowire arrays. *Science* **2006**, *312* (5771), 242-246.
- (7) Kim, W.-G.; Kim, D.-W.; Tcho, I.-W.; Kim, J.-K.; Kim, M.-S.; Choi, Y.-K., Triboelectric nanogenerator: Structure, mechanism, and applications. *Acs Nano* **2021**, *15* (1), 258-287.
- (8) Wang, Y.; Yang, Y.; Wang, Z. L., Triboelectric nanogenerators as flexible power sources. *npj Flexible Electronics* **2017**, *1* (1), 1-10.
- (9) Zhang, T.; Yang, T.; Zhang, M.; Bowen, C. R.; Yang, Y., Recent Progress in Hybridized Nanogenerators for Energy Scavenging. *iScience* **2020**, *23* (11), 101689.
- (10) Ren, Z.; Wang, Z.; Liu, Z.; Wang, L.; Guo, H.; Li, L.; Li, S.; Chen, X.; Tang, W.; Wang, Z. L., Energy harvesting from breeze wind ($0.7\text{--}6\text{ m s}^{-1}$) using ultra-stretchable triboelectric nanogenerator. *Advanced Energy Materials* **2020**, *10* (36), 2001770.
- (11) Zhang, C.; Liu, Y.; Zhang, B.; Yang, O.; Yuan, W.; He, L.; Wei, X.; Wang, J.; Wang, Z. L., Harvesting wind energy by a triboelectric nanogenerator for an intelligent high-speed train system. *ACS Energy Letters* **2021**, *6* (4), 1490-1499.
- (12) Chen, P.; An, J.; Shu, S.; Cheng, R.; Nie, J.; Jiang, T.; Wang, Z. L., Super-durable, low-wear, and high-performance fur-brush triboelectric nanogenerator for wind and water energy harvesting for smart agriculture. *Advanced Energy Materials* **2021**, *11* (9), 2003066.

- 1
2
3
4
5 (13) Ren, Z.; Wu, L.; Pang, Y.; Zhang, W.; Yang, R., Strategies for effectively harvesting
6 wind energy based on triboelectric nanogenerators. *Nano Energy* **2022**, 107522.
7
8 (14) Chen, B.; Yang, Y.; Wang, Z. L., Scavenging wind energy by triboelectric
9 nanogenerators. *Advanced Energy Materials* **2018**, *8*(10), 1702649.
10
11 (15) Wang, Y.; Yu, X.; Yin, M.; Wang, J.; Gao, Q.; Yu, Y.; Cheng, T.; Wang, Z. L.,
12 Gravity triboelectric nanogenerator for the steady harvesting of natural wind energy. *Nano*
13 *Energy* **2021**, *82*, 105740.
14
15 (16) Zou, H.-X.; Zhao, L.-C.; Wang, Q.; Gao, Q.-H.; Yan, G.; Wei, K.-X.; Zhang, W.-M.,
16 A self-regulation strategy for triboelectric nanogenerator and self-powered wind-speed
17 sensor. *Nano Energy* **2022**, *95*, 106990.
18
19 (17) Liang, X.; Jiang, T.; Liu, G.; Feng, Y.; Zhang, C.; Wang, Z. L., Spherical triboelectric
20 nanogenerator integrated with power management module for harvesting multidirectional
21 water wave energy. *Energ Environ Sci* **2020**, *13*(1), 277-285.
22
23 (18) Xia, K.; Fu, J.; Xu, Z., Multiple-frequency high-output triboelectric nanogenerator
24 based on a water balloon for all-weather water wave energy harvesting. *Advanced Energy*
25 *Materials* **2020**, *10*(28), 2000426.
26
27 (19) Rodrigues, C.; Nunes, D.; Clemente, D.; Mathias, N.; Correia, J.; Rosa-Santos, P.;
28 Taveira-Pinto, F.; Morais, T.; Pereira, A.; Ventura, J., Emerging triboelectric nanogenerators
29 for ocean wave energy harvesting: state of the art and future perspectives. *Energ Environ Sci*
30 **2020**, *13*(9), 2657-2683.
31
32 (20) Liang, X.; Jiang, T.; Feng, Y.; Lu, P.; An, J.; Wang, Z. L., Triboelectric
33 nanogenerator network integrated with charge excitation circuit for effective water wave
34 energy harvesting. *Advanced Energy Materials* **2020**, *10*(40), 2002123.
35
36 (21) Zhang, C.; He, L.; Zhou, L.; Yang, O.; Yuan, W.; Wei, X.; Liu, Y.; Lu, L.; Wang, J.;
37 Wang, Z. L., Active resonance triboelectric nanogenerator for harvesting omnidirectional
38 water-wave energy. *Joule* **2021**, *5*(6), 1613-1623.
39
40 (22) Cheng, J.; Zhang, X.; Jia, T.; Wu, Q.; Dong, Y.; Wang, D., Triboelectric
41 nanogenerator with a seesaw structure for harvesting ocean energy. *Nano Energy* **2022**, *102*,
42 107622.
43
44 (23) Zhang, C.; Liu, L.; Zhou, L.; Yin, X.; Wei, X.; Hu, Y.; Liu, Y.; Chen, S.; Wang, J.;
45 Wang, Z. L., Self-powered sensor for quantifying ocean surface water waves based on
46 triboelectric nanogenerator. *Acs Nano* **2020**, *14*(6), 7092-7100.
47
48
49
50
51
52
53
54
55
56
57
58
59
60

- 1
2
3
4
5 (24) Deng, W.; Libanori, A.; Xiao, X.; Fang, J.; Zhao, X.; Zhou, Y.; Chen, G.; Li, S.;
6 Chen, J., Computational investigation of ultrasound induced electricity generation via a
7 triboelectric nanogenerator. *Nano Energy* **2022**, *91*, 106656.
8
9 (25) Liu, X.; Wang, Y.; Wang, G.; Ma, Y.; Zheng, Z.; Fan, K.; Liu, J.; Zhou, B.; Wang,
10 G.; You, Z., An ultrasound-driven implantable wireless energy harvesting system using a
11 triboelectric transducer. *Matter* **2022**.
12
13 (26) Lee, D.-M.; Rubab, N.; Hyun, I.; Kang, W.; Kim, Y.-J.; Kang, M.; Choi, B. O.; Kim,
14 S.-W., Ultrasound-mediated triboelectric nanogenerator for powering on-demand transient
15 electronics. *Science advances* **2022**, *8*(1), eabl8423.
16
17 (27) Kim, H. S.; Hur, S.; Lee, D.-G.; Shin, J.; Qiao, H.; Mun, S.; Lee, H.; Moon, W.; Kim,
18 Y.; Baik, J. M., Ferroelectrically augmented contact electrification enables efficient acoustic
19 energy transfer through liquid and solid media. *Energ Environ Sci* **2022**, *15*(3), 1243-1255.
20
21 (28) Hinchet, R.; Yoon, H.-J.; Ryu, H.; Kim, M.-K.; Choi, E.-K.; Kim, D.-S.; Kim, S.-W.,
22 Transcutaneous ultrasound energy harvesting using capacitive triboelectric technology.
23 *Science* **2019**, *365*(6452), 491-494.
24
25 (29) Zheng, J.; Yu, Z.; Wang, Y.; Fu, Y.; Chen, D.; Zhou, H., Acoustic Core–Shell
26 Resonance Harvester for Application of Artificial Cochlea Based on the Piezo-Triboelectric
27 Effect. *ACS nano* **2021**, *15*(11), 17499-17507.
28
29 (30) Zhao, H.; Xiao, X.; Xu, P.; Zhao, T.; Song, L.; Pan, X.; Mi, J.; Xu, M.; Wang, Z. L.,
30 Dual-tube helmholtz resonator-based triboelectric nanogenerator for highly efficient
31 harvesting of acoustic energy. *Advanced Energy Materials* **2019**, *9*(46), 1902824.
32
33 (31) Chen, F.; Wu, Y.; Ding, Z.; Xia, X.; Li, S.; Zheng, H.; Diao, C.; Yue, G.; Zi, Y., A
34 novel triboelectric nanogenerator based on electrospun polyvinylidene fluoride nanofibers for
35 effective acoustic energy harvesting and self-powered multifunctional sensing. *Nano energy*
36 **2019**, *56*, 241-251.
37
38 (32) Yuan, M.; Li, C.; Liu, H.; Xu, Q.; Xie, Y., A 3D-printed acoustic triboelectric
39 nanogenerator for quarter-wavelength acoustic energy harvesting and self-powered edge
40 sensing. *Nano Energy* **2021**, *85*, 105962.
41
42 (33) Chen, J.; Wang, Z. L., Reviving vibration energy harvesting and self-powered
43 sensing by a triboelectric nanogenerator. *Joule* **2017**, *1*(3), 480-521.
44
45 (34) Jin, L.; Zhang, S. L.; Xu, S.; Guo, H.; Yang, W.; Wang, Z. L., Free-fixed rotational
46 triboelectric nanogenerator for self-powered real-time wheel monitoring. *Advanced Materials*
47 *Technologies* **2021**, *6*(3), 2000918.
48
49
50
51
52
53
54
55
56
57
58
59
60

- 1
2
3
4
5 (35) Du, Y.; Tang, Q.; He, W.; Liu, W.; Wang, Z.; Wu, H.; Li, G.; Guo, H.; Li, Z.; Peng,
6 Y., Harvesting ambient mechanical energy by multiple mode triboelectric nanogenerator with
7 charge excitation for self-powered freight train monitoring. *Nano Energy* **2021**, *90*, 106543.
- 8
9 (36) Meng, Y.; Yang, J.; Liu, S.; Xu, W.; Chen, G.; Niu, Z.; Wang, M.; Deng, T.; Qin, Y.;
10 Han, M., Nano-fiber based self-powered flexible vibration sensor for rail fasteners tightness
11 safety detection. *Nano Energy* **2022**, *102*, 107667.
- 12
13 (37) Lai, Y. C.; Hsiao, Y. C.; Wu, H. M.; Wang, Z. L., Waterproof fabric-based
14 multifunctional triboelectric nanogenerator for universally harvesting energy from raindrops,
15 wind, and human motions and as self-powered sensors. *Advanced Science* **2019**, *6* (5),
16 1801883.
- 17
18 (38) Wang, L.; Liu, W.; Yan, Z.; Wang, F.; Wang, X., Stretchable and shape-adaptable
19 triboelectric nanogenerator based on biocompatible liquid electrolyte for biomechanical
20 energy harvesting and wearable human-machine interaction. *Advanced Functional Materials*
21 **2021**, *31* (7), 2007221.
- 22
23 (39) Wang, H.; Han, M.; Song, Y.; Zhang, H., Design, manufacturing and applications of
24 wearable triboelectric nanogenerators. *Nano Energy* **2021**, *81*, 105627.
- 25
26 (40) Yuan, W.; Zhang, C.; Zhang, B.; Wei, X.; Yang, O.; Liu, Y.; He, L.; Cui, S.; Wang,
27 J.; Wang, Z. L., Wearable, breathable and waterproof triboelectric nanogenerators for
28 harvesting human motion and raindrop energy. *Advanced Materials Technologies* **2022**, *7*
29 (6), 2101139.
- 30
31 (41) Ghosh, S. K.; Kim, J.; Kim, M. P.; Na, S.; Cho, J.; Kim, J. J.; Ko, H.,
32 Ferroelectricity-Coupled 2D-MXene-Based Hierarchically Designed High-Performance
33 Stretchable Triboelectric Nanogenerator. *ACS nano* **2022**, *16* (7), 11415-11427.
- 34
35 (42) Zhang, C.; Tang, W.; Han, C. B.; Fan, F. R.; Wang, Z. L., Theoretical Comparison,
36 Equivalent Transformation, and Conjunction Operations of Electromagnetic Induction
37 Generator and Triboelectric Nanogenerator for Harvesting Mechanical Energy. *Adv Mater*
38 **2014**, *26* (22), 3580-3591.
- 39
40 (43) Jiang, T.; Chen, X. Y.; Han, C. B.; Tang, W.; Wang, Z. L., Theoretical Study of
41 Rotary Freestanding Triboelectric Nanogenerators. *Advanced Functional Materials* **2015**, *25*
42 (19), 2928-2938.
- 43
44 (44) Niu, S. M.; Wang, S. H.; Lin, L.; Liu, Y.; Zhou, Y. S.; Hu, Y. F.; Wang, Z. L.,
45 Theoretical study of contact-mode triboelectric nanogenerators as an effective power source.
46 *Energ Environ Sci* **2013**, *6* (12), 3576-3583.
- 47
48
49
50
51
52
53
54
55
56
57
58
59
60

- 1
2
3
4
5 (45) Wang, Z. L., From contact electrification to triboelectric nanogenerators. *Rep Prog*
6 *Phys* **2021**, *84*(9).
7
8 (46) Wang, Z. L., On Maxwell's displacement current for energy and sensors: the origin of
9 nanogenerators. *Mater Today* **2017**, *20*(2), 74-82.
10
11 (47) Wang, Z. L., Maxwell's equations for a mechano-driven, shape-deformable, charged-
12 media system, slowly moving at an arbitrary velocity field $v(r, t)$. *J Phys Commun* **2022**,
13 6(8), 085013.
14
15 (48) Wang, Z. L., On the expanded Maxwell's equations for moving charged media
16 system-General theory, mathematical solutions and applications in TENG. *Mater Today*
17 **2022**, *52*, 348-363.
18
19 (49) Fan, F.-R.; Tian, Z.-Q.; Wang, Z. L., Flexible triboelectric generator. *Nano energy*
20 **2012**, *1*(2), 328-334.
21
22 (50) Lee, Y.; Lim, S.; Song, W. J.; Lee, S.; Yoon, S. J.; Park, J. M.; Lee, M. G.; Park, Y.
23 L.; Sun, J. Y., Triboresistive Touch Sensing: Grid-Free Touch-Point Recognition Based on
24 Monolayered Ionic Power Generators. *Adv Mater* **2022**, 2108586.
25
26 (51) Lee, Y.; Cha, S. H.; Kim, Y.-W.; Choi, D.; Sun, J.-Y., Transparent and attachable
27 ionic communicators based on self-cleanable triboelectric nanogenerators. *Nature*
28 *communications* **2018**, *9*(1), 1-8.
29
30 (52) Fan, F.-R.; Lin, L.; Zhu, G.; Wu, W.; Zhang, R.; Wang, Z. L., Transparent
31 triboelectric nanogenerators and self-powered pressure sensors based on micropatterned
32 plastic films. *Nano letters* **2012**, *12*(6), 3109-3114.
33
34 (53) Chen, X.; Pu, X.; Jiang, T.; Yu, A.; Xu, L.; Wang, Z. L., Tunable optical modulator
35 by coupling a triboelectric nanogenerator and a dielectric elastomer. *Advanced Functional*
36 *Materials* **2017**, *27*(1), 1603788.
37
38 (54) Chen, X.; Jiang, T.; Yao, Y.; Xu, L.; Zhao, Z.; Wang, Z. L., Stimulating acrylic
39 elastomers by a triboelectric nanogenerator—toward self-powered electronic skin and artificial
40 muscle. *Advanced Functional Materials* **2016**, *26*(27), 4906-4913.
41
42 (55) Chen, X.; Jiang, T.; Wang, Z. L., Modeling a dielectric elastomer as driven by
43 triboelectric nanogenerator. *Applied Physics Letters* **2017**, *110*(3), 033505.
44
45 (56) Li, J.; Long, Y.; Yang, F.; Wang, X., Respiration-driven triboelectric nanogenerators
46 for biomedical applications. *EcoMat* **2020**, *2*(3), e12045.
47
48
49
50
51
52
53
54
55
56
57
58
59
60

- 1
2
3
4
5 (57) Xiao, X.; Xiao, X.; Nashalian, A.; Libanori, A.; Fang, Y.; Li, X.; Chen, J.,
6 Triboelectric nanogenerators for self-powered wound healing. *Advanced Healthcare*
7 *Materials* **2021**, *10*(20), 2100975.
8
9 (58) Jeong, S.-H.; Lee, Y.; Lee, M.-G.; Song, W. J.; Park, J.-U.; Sun, J.-Y., Accelerated
10 wound healing with an ionic patch assisted by a triboelectric nanogenerator. *Nano Energy*
11 **2021**, *79*, 105463.
12
13 (59) Song, W. J.; Lee, Y.; Jung, Y.; Kang, Y.-W.; Kim, J.; Park, J.-M.; Park, Y.-L.; Kim,
14 H.-Y.; Sun, J.-Y., Soft artificial electroreceptors for noncontact spatial perception. *Science*
15 *advances* **2021**, *7*(48), eabg9203.
16
17 (60) Park, Y.; Jung, J.; Lee, Y.; Lee, D.; Vlassak, J. J.; Park, Y.-L., Liquid-metal micro-
18 networks with strain-induced conductivity for soft electronics and robotic skin. *npj Flexible*
19 *Electronics* **2022**, *6*(1), 1-10.
20
21 (61) Zou, Y.; Xu, J.; Chen, K.; Chen, J., Advances in Nanostructures for
22 High-Performance Triboelectric Nanogenerators. *Advanced Materials Technologies* **2021**, *6*
23 (3), 2000916.
24
25 (62) Lee, Y.; Kim, W.; Bhatia, D.; Hwang, H. J.; Lee, S.; Choi, D., Cam-based sustainable
26 triboelectric nanogenerators with a resolution-free 3D-printed system. *Nano Energy* **2017**, *38*,
27 326-334.
28
29 (63) Jiang, C.; Wu, C.; Li, X.; Yao, Y.; Lan, L.; Zhao, F.; Ye, Z.; Ying, Y.; Ping, J., All-
30 electrospun flexible triboelectric nanogenerator based on metallic MXene nanosheets. *Nano*
31 *Energy* **2019**, *59*, 268-276.
32
33 (64) Hinchet, R.; Seung, W.; Kim, S. W., Recent progress on flexible triboelectric
34 nanogenerators for selfpowered electronics. *ChemSusChem* **2015**, *8*(14), 2327-2344.
35
36 (65) Zhou, K.; Zhao, Y.; Sun, X.; Yuan, Z.; Zheng, G.; Dai, K.; Mi, L.; Pan, C.; Liu, C.;
37 Shen, C., Ultra-stretchable triboelectric nanogenerator as high-sensitive and self-powered
38 electronic skins for energy harvesting and tactile sensing. *Nano Energy* **2020**, *70*, 104546.
39
40 (66) Pu, X.; Liu, M.; Chen, X.; Sun, J.; Du, C.; Zhang, Y.; Zhai, J.; Hu, W.; Wang, Z. L.,
41 Ultrastretchable, transparent triboelectric nanogenerator as electronic skin for biomechanical
42 energy harvesting and tactile sensing. *Science advances* **2017**, *3*(5), e1700015.
43
44 (67) Yu, J.; Kim, W.; Oh, S.; Bhatia, D.; Kim, J.-G.; Choi, D., Toward Optimizing
45 Resonance for Enhanced Triboelectrification of Oscillating Triboelectric Nanogenerators.
46 *International Journal of Precision Engineering and Manufacturing-Green Technology* **2022**,
47 1-11.
48
49
50
51
52
53
54
55
56
57
58
59
60

- 1
2
3
4
5 (68) Kim, W.; Hwang, H. J.; Bhatia, D.; Lee, Y.; Baik, J. M.; Choi, D., Kinematic design
6 for high performance triboelectric nanogenerators with enhanced working frequency. *Nano*
7 *energy* **2016**, *21*, 19-25.
- 8
9 (69) Wang, Z. L., Triboelectric nanogenerators as new energy technology and self-powered
10 sensors—Principles, problems and perspectives. *Faraday discussions* **2014**, *176*, 447-458.
- 11
12 (70) Wang, Z. L., Triboelectric nanogenerator (TENG)—sparking an energy and sensor
13 revolution. *Advanced Energy Materials* **2020**, *10* (17), 2000137.
- 14
15 (71) Hwang, H. J.; Choi, D., The coupled effects of an electron blocking layer beneath
16 tribomaterials for boosted triboelectric nanogenerators. *Functional Composites and Structures*
17 **2021**, *3* (2), 025004.
- 18
19 (72) Jang, S.; Cho, S.; Lee, D.; Ra, Y.; Kam, D.; Lee, J.; Lee, G.; La, M.; Choi, D.,
20 Development of large-scale electret fabrication system for triboelectric nanogenerator
21 electrical output amplification. *Functional Composites and Structures* **2022**, *4* (4), 045004.
- 22
23 (73) Liu, Y.; Mo, J.; Fu, Q.; Lu, Y.; Zhang, N.; Wang, S.; Nie, S., Enhancement of
24 triboelectric charge density by chemical functionalization. *Advanced Functional Materials*
25 **2020**, *30* (50), 2004714.
- 26
27 (74) Choi, J. H.; Cha, K. J.; Ra, Y.; La, M.; Park, S. J.; Choi, D., Development of a
28 triboelectric nanogenerator with enhanced electrical output performance by embedding
29 electrically charged microparticles. *Functional Composites and Structures* **2019**, *1* (4),
30 045005.
- 31
32 (75) Ra, Y.; Choi, J. H.; La, M.; Park, S. J.; Choi, D., Development of a highly transparent
33 and flexible touch sensor based on triboelectric effect. *Functional Composites and Structures*
34 **2019**, *1* (4), 045001.
- 35
36 (76) Davies, D. K., Charge generation on dielectric surfaces. *Journal of Physics D:*
37 *Applied Physics* **1969**, *2* (11), 1533.
- 38
39 (77) Wåhlin, A.; Bäckström, G., Sliding electrification of Teflon by metals. *Journal of*
40 *Applied Physics* **1974**, *45* (5), 2058-2064.
- 41
42 (78) Gibson, H. W., Linear free energy relations. V. Triboelectric charging of organic
43 solids. *Journal of the American Chemical Society* **1975**, *97* (13), 3832-3833.
- 44
45 (79) Chun, S.; Choi, I. Y.; Son, W.; Jung, J.; Lee, S.; Kim, H. S.; Pang, C.; Park, W.; Kim,
46 J. K., High-output and bending-tolerant triboelectric nanogenerator based on an interlocked
47 array of surface-functionalized indium tin oxide nanohelices. *ACS Energy Letters* **2019**, *4*
48 (7), 1748-1754.
- 49
50
51
52
53
54
55
56
57
58
59
60

- 1
2
3
4
5 (80) Zhou, Y. S.; Wang, S.; Yang, Y.; Zhu, G.; Niu, S.; Lin, Z.-H.; Liu, Y.; Wang, Z. L.,
6 Manipulating nanoscale contact electrification by an applied electric field. *Nano letters* **2014**,
7 *14*(3), 1567-1572.
8
9 (81) Lin, S.; Xu, L.; Xu, C.; Chen, X.; Wang, A. C.; Zhang, B.; Lin, P.; Yang, Y.; Zhao,
10 H.; Wang, Z. L., Electron transfer in nanoscale contact electrification: effect of temperature
11 in the metal–dielectric case. *Advanced Materials* **2019**, *31*(17), 1808197.
12
13 (82) Xu, C.; Zi, Y.; Wang, A. C.; Zou, H.; Dai, Y.; He, X.; Wang, P.; Wang, Y. C.; Feng,
14 P.; Li, D., On the electron-transfer mechanism in the contact-electrification effect. *Advanced*
15 *Materials* **2018**, *30*(15), 1706790.
16
17 (83) Wang, A. C.; Zhang, B.; Xu, C.; Zou, H.; Lin, Z.; Wang, Z. L., Unraveling
18 temperature-dependent contact electrification between sliding-mode triboelectric pairs.
19 *Advanced Functional Materials* **2020**, *30*(12), 1909384.
20
21 (84) Xu, C.; Zhang, B.; Wang, A. C.; Cai, W.; Zi, Y.; Feng, P.; Wang, Z. L., Effects of
22 metal work function and contact potential difference on electron thermionic emission in
23 contact electrification. *Advanced Functional Materials* **2019**, *29*(29), 1903142.
24
25 (85) Wang, Z. L.; Wang, A. C., On the origin of contact-electrification. *Materials Today*
26 **2019**, *30*, 34-51.
27
28 (86) Li, D.; Xu, C.; Liao, Y.; Cai, W.; Zhu, Y.; Wang, Z. L., Interface inter-atomic
29 electron-transition induced photon emission in contact-electrification. *Science advances*
30 **2021**, *7*(39), eabj0349.
31
32 (87) Ao, C. K.; Jiang, Y.; Zhang, L.; Yan, C.; Ma, J.; Liu, C.; Jiang, Y.; Zhang, W.; Soh,
33 S., Balancing charge dissipation and generation: mechanisms and strategies for achieving
34 steady-state charge of contact electrification at interfaces of matter. *Journal of Materials*
35 *Chemistry A* **2022**, *10*(37), 19572-19605.
36
37 (88) Nie, J.; Ren, Z.; Xu, L.; Lin, S.; Zhan, F.; Chen, X.; Wang, Z. L., Probing
38 contact-electrification-induced electron and ion transfers at a liquid–solid interface.
39 *Advanced Materials* **2020**, *32*(2), 1905696.
40
41 (89) Lin, S.; Xu, L.; Chi Wang, A.; Wang, Z. L., Quantifying electron-transfer in liquid-
42 solid contact electrification and the formation of electric double-layer. *Nature*
43 *communications* **2020**, *11*(1), 1-8.
44
45 (90) Lin, S.; Zheng, M.; Luo, J.; Wang, Z. L., Effects of surface functional groups on
46 electron transfer at liquid–solid interfacial contact electrification. *ACS nano* **2020**, *14*(8),
47 10733-10741.
48
49
50
51
52
53
54
55
56
57
58
59
60

- 1
2
3
4
5 (91) Li, S.; Nie, J.; Shi, Y.; Tao, X.; Wang, F.; Tian, J.; Lin, S.; Chen, X.; Wang, Z. L.,
6 Contributions of different functional groups to contact electrification of polymers. *Advanced*
7 *Materials* **2020**, *32* (25), 2001307.
8
9 (92) Lin, S.; Chen, X.; Wang, Z. L., Contact electrification at the liquid–solid interface.
10 *Chemical Reviews* **2021**, *122* (5), 5209-5232.
11
12 (93) McCarty, L. S.; Winkleman, A.; Whitesides, G. M., Ionic electrets: electrostatic
13 charging of surfaces by transferring mobile ions upon contact. *Journal of the American*
14 *Chemical Society* **2007**, *129* (13), 4075-4088.
15
16 (94) Knoblauch, O., Versuche über die Berührungselektrizität. *Zeitschrift für*
17 *Physikalische Chemie* **1902**, *39* (1), 225-244.
18
19 (95) Medley, J., Fractional electrification of polar polymers. *Nature* **1953**, *171* (4363),
20 1077-1077.
21
22 (96) Diaz, A.; Wollmann, D.; Dreblow, D., Contact electrification: ion transfer to metals
23 and polymers. *Chem Mater* **1991**, *3* (6), 997-999.
24
25 (97) Wiles, J. A.; Fialkowski, M.; Radowski, M. R.; Whitesides, G. M.; Grzybowski, B.
26 A., Effects of surface modification and moisture on the rates of charge transfer between
27 metals and organic materials. *The Journal of Physical Chemistry B* **2004**, *108* (52), 20296-
28 20302.
29
30 (98) McCarty, L. S.; Whitesides, G. M., Electrostatic charging due to separation of ions at
31 interfaces: contact electrification of ionic electrets. *Angewandte Chemie International Edition*
32 **2008**, *47* (12), 2188-2207.
33
34 (99) Salaneck, W.; Paton, A.; Clark, D., Double mass transfer during polymer-polymer
35 contacts. *Journal of Applied Physics* **1976**, *47* (1), 144-147.
36
37 (100) Baytekin, H.; Patashinski, A.; Branicki, M.; Baytekin, B.; Soh, S.; Grzybowski, B.
38 A., The mosaic of surface charge in contact electrification. *Science* **2011**, *333* (6040), 308-
39 312.
40
41 (101) Piperno, S.; Cohen, H.; Bendikov, T.; Lahav, M.; Lubomirsky, I., The absence of
42 redox reactions for Palladium (II) and Copper (II) on electrostatically charged teflon:
43 Relevance to the concept of “Cryptoelectrons”. *Angewandte Chemie* **2011**, *123* (25), 5772-
44 5775.
45
46 (102) Baytekin, H. T.; Baytekin, B.; Incorvati, J. T.; Grzybowski, B. A., Material transfer
47 and polarity reversal in contact charging. *Angewandte Chemie International Edition* **2012**, *51*
48 (20), 4843-4847.
49
50
51
52
53
54
55
56
57
58
59
60

- 1
2
3
4
5 (103) Pandey, R. K.; Kakehashi, H.; Nakanishi, H.; Soh, S., Correlating material transfer
6 and charge transfer in contact electrification. *The Journal of Physical Chemistry C* **2018**, *122*
7 (28), 16154-16160.
8
9 (104) Sherrell, P. C.; Sutka, A.; Shepelin, N. A.; Lapcinskis, L.; Verners, O.; Germane, L.;
10 Timusk, M.; Fenati, R. A.; Malnieks, K.; Ellis, A. V., Probing contact electrification: a
11 cohesively sticky problem. *ACS Applied Materials & Interfaces* **2021**, *13* (37), 44935-44947.
12
13 (105) Clint, J.; Dunstan, T., Acid-base components of solid surfaces and the triboelectric
14 series. *EPL (Europhysics Letters)* **2001**, *54* (3), 320.
15
16 (106) Veregin, R. P.; McDougall, M. N.; Hawkins, M. S.; Vong, C.; Skorokhod, V.;
17 Schreiber, H. P., A bidirectional acid-base charging model for triboelectrification: Part 1.
18 Theory. *The Journal of imaging science and technology* **2006**, *50* (3), 282-287.
19
20 (107) Zhang, X.; Chen, L.; Jiang, Y.; Lim, W.; Soh, S., Rationalizing the triboelectric
21 series of polymers. *Chem Mater* **2019**, *31* (5), 1473-1478.
22
23 (108) Israelachvili, J. N., *Intermolecular and surface forces*. Academic press: 2011.
24
25 (109) Zimmermann, R.; Dukhin, S.; Werner, C., Electrokinetic measurements reveal
26 interfacial charge at polymer films caused by simple electrolyte ions. *The Journal of Physical*
27 *Chemistry B* **2001**, *105* (36), 8544-8549.
28
29 (110) Zangi, R.; Engberts, J. B., Physisorption of hydroxide ions from aqueous solution to
30 a hydrophobic surface. *Journal of the American Chemical Society* **2005**, *127* (7), 2272-2276.
31
32 (111) Kudin, K. N.; Car, R., Why are water- hydrophobic interfaces charged? *Journal of*
33 *the American Chemical Society* **2008**, *130* (12), 3915-3919.
34
35 (112) Zimmermann, R.; Freudenberg, U.; Schweiß, R.; Küttner, D.; Werner, C.,
36 Hydroxide and hydronium ion adsorption—A survey. *Current Opinion in Colloid & Interface*
37 *Science* **2010**, *15* (3), 196-202.
38
39 (113) Niu, S.; Wang, S.; Lin, L.; Liu, Y.; Zhou, Y. S.; Hu, Y.; Wang, Z. L., Theoretical
40 study of contact-mode triboelectric nanogenerators as an effective power source. *Energy &*
41 *Environmental Science* **2013**, *6* (12), 3576-3583.
42
43 (114) Lim, K.-W.; Peddigari, M.; Park, C. H.; Lee, H. Y.; Min, Y.; Kim, J.-W.; Ahn, C.-
44 W.; Choi, J.-J.; Hahn, B.-D.; Choi, J.-H., A high output magneto-mechano-triboelectric
45 generator enabled by accelerated water-soluble nano-bullets for powering a wireless indoor
46 positioning system. *Energy & Environmental Science* **2019**, *12* (2), 666-674.
47
48 (115) Niu, S.; Wang, Z. L., Theoretical systems of triboelectric nanogenerators. *Nano*
49 *Energy* **2015**, *14*, 161-192.
50
51
52
53
54
55
56
57
58
59
60

- 1
2
3
4
5 (116) Yoon, H.-J.; Kim, D.-H.; Seung, W.; Khan, U.; Kim, T. Y.; Kim, T.; Kim, S.-W.,
6 3D-printed biomimetic-villus structure with maximized surface area for triboelectric
7 nanogenerator and dust filter. *Nano Energy* **2019**, *63*, 103857.
- 8
9 (117) Xia, X.; Chen, J.; Liu, G.; Javed, M. S.; Wang, X.; Hu, C., Aligning graphene sheets
10 in PDMS for improving output performance of triboelectric nanogenerator. *Carbon* **2017**,
11 *111*, 569-576.
- 12
13 (118) Wang, H. S.; Jeong, C. K.; Seo, M.-H.; Joe, D. J.; Han, J. H.; Yoon, J.-B.; Lee, K. J.,
14 Performance-enhanced triboelectric nanogenerator enabled by wafer-scale nanogrates of
15 multistep pattern downscaling. *Nano Energy* **2017**, *35*, 415-423.
- 16
17 (119) Dudem, B.; Huynh, N. D.; Kim, W.; Kim, D. H.; Hwang, H. J.; Choi, D.; Yu, J. S.,
18 Nanopillar-array architected PDMS-based triboelectric nanogenerator integrated with a
19 windmill model for effective wind energy harvesting. *Nano Energy* **2017**, *42*, 269-281.
- 20
21 (120) Zhang, H.; Zhang, P.; Deng, L.; Fan, X., Enhancement of triboelectric
22 nanogenerators output performance by background paper-based hierarchical micro-structures
23 for energy harvesting. *Applied Physics Letters* **2022**, *121* (6), 063902.
- 24
25 (121) Qian, Y.; Nie, J.; Ma, X.; Ren, Z.; Tian, J.; Chen, J.; Shen, H.; Chen, X.; Li, Y.,
26 Octopus tentacles inspired triboelectric nanogenerators for harvesting mechanical energy
27 from highly wetted surface. *Nano Energy* **2019**, *60*, 493-502.
- 28
29 (122) Zheng, Q.; Fang, L.; Guo, H.; Yang, K.; Cai, Z.; Meador, M. A. B.; Gong, S.,
30 Highly porous polymer aerogel film-based triboelectric nanogenerators. *Advanced Functional*
31 *Materials* **2018**, *28* (13), 1706365.
- 32
33 (123) Lee, K. Y.; Chun, J.; Lee, J. H.; Kim, K. N.; Kang, N. R.; Kim, J. Y.; Kim, M. H.;
34 Shin, K. S.; Gupta, M. K.; Baik, J. M.; Kim, S. W., Hydrophobic sponge structure-based
35 triboelectric nanogenerator. *Adv Mater* **2014**, *26* (29), 5037-42.
- 36
37 (124) Chun, J.; Kim, J. W.; Jung, W.-s.; Kang, C.-Y.; Kim, S.-W.; Wang, Z. L.; Baik, J.
38 M., Mesoporous pores impregnated with Au nanoparticles as effective dielectrics for
39 enhancing triboelectric nanogenerator performance in harsh environments. *Energy &*
40 *Environmental Science* **2015**, *8* (10), 3006-3012.
- 41
42 (125) Zheng, J.; Wang, Y.; Yu, Z.; Fu, Y.; Chen, D.; Zhao, P.; Zhou, H., Integrated
43 nanospheres occupancy-removal and thermoforming into bulk piezoelectric and triboelectric
44 hybrid nanogenerators with inverse opal nanostructure. *Nano Energy* **2019**, *64*, 103957.
- 45
46
47
48
49
50
51
52
53
54
55
56
57
58
59
60

- 1
2
3
4
5 (126) Feng, Y.; Zheng, Y.; Ma, S.; Wang, D.; Zhou, F.; Liu, W., High output
6 polypropylene nanowire array triboelectric nanogenerator through surface structural control
7 and chemical modification. *Nano Energy* **2016**, *19*, 48-57.
- 8
9 (127) Huang, T.; Lu, M.; Yu, H.; Zhang, Q.; Wang, H.; Zhu, M., Enhanced power output
10 of a triboelectric nanogenerator composed of electrospun nanofiber mats doped with
11 graphene oxide. *Scientific reports* **2015**, *5*(1), 1-8.
- 12
13 (128) Nafari, A.; Sodano, H., Surface morphology effects in a vibration based triboelectric
14 energy harvester. *Smart Materials and Structures* **2017**, *27*(1), 015029.
- 15
16 (129) Muthu, M.; Pandey, R.; Wang, X.; Chandrasekhar, A.; Palani, I.; Singh, V.,
17 Enhancement of triboelectric nanogenerator output performance by laser 3D-surface pattern
18 method for energy harvesting application. *Nano Energy* **2020**, *78*, 105205.
- 19
20 (130) Huang, J.; Fu, X.; Liu, G.; Xu, S.; Li, X.; Zhang, C.; Jiang, L., Micro/nano-
21 structures-enhanced triboelectric nanogenerators by femtosecond laser direct writing. *Nano*
22 *Energy* **2019**, *62*, 638-644.
- 23
24 (131) Zhou, Y.; Deng, W.; Xu, J.; Chen, J., Engineering materials at the nanoscale for
25 triboelectric nanogenerators. *Cell Reports Physical Science* **2020**, *1*(8), 100142.
- 26
27 (132) Lee, H. E.; Park, J. H.; Jang, D.; Shin, J. H.; Im, T. H.; Lee, J. H.; Hong, S. K.;
28 Wang, H. S.; Kwak, M. S.; Peddigari, M., Optogenetic brain neuromodulation by stray
29 magnetic field via flash-enhanced magneto-mechano-triboelectric nanogenerator. *Nano*
30 *Energy* **2020**, *75*, 104951.
- 31
32 (133) Lee, C.; Yang, S.; Choi, D.; Kim, W.; Kim, J.; Hong, J., Chemically surface-
33 engineered polydimethylsiloxane layer via plasma treatment for advancing textile-based
34 triboelectric nanogenerators. *Nano Energy* **2019**, *57*, 353-362.
- 35
36 (134) Cheng, X.; Song, Z.; Miao, L.; Guo, H.; Su, Z.; Song, Y.; Zhang, H.-X., Wide range
37 fabrication of wrinkle patterns for maximizing surface charge density of a triboelectric
38 nanogenerator. *Journal of Microelectromechanical Systems* **2017**, *27*(1), 106-112.
- 39
40 (135) Wang, Y.; Duan, J.; Yang, X.; Liu, L.; Zhao, L.; Tang, Q., The unique dielectricity
41 of inorganic perovskites toward high-performance triboelectric nanogenerators. *Nano Energy*
42 **2020**, *69*, 104418.
- 43
44 (136) Wang, S.; Xie, Y.; Niu, S.; Lin, L.; Liu, C.; Zhou, Y. S.; Wang, Z. L., Maximum
45 surface charge density for triboelectric nanogenerators achieved by ionized-air injection:
46 methodology and theoretical understanding. *Adv Mater* **2014**, *26*(39), 6720-8.
- 47
48
49
50
51
52
53
54
55
56
57
58
59
60

- 1
2
3
4
5 (137) Yu, Y.; Li, Z.; Wang, Y.; Gong, S.; Wang, X., Sequential infiltration synthesis of
6 doped polymer films with tunable electrical properties for efficient triboelectric
7 nanogenerator development. *Advanced Materials* **2015**, *27*(33), 4938-4944.
- 8
9 (138) Du, W.; Han, X.; Lin, L.; Chen, M.; Li, X.; Pan, C.; Wang, Z. L., A Three
10 Dimensional Multi-Layered Sliding Triboelectric Nanogenerator. *Advanced Energy*
11 *Materials* **2014**, *4*(11), 1301592.
- 12
13 (139) Hedau, B.; Kang, B.-C.; Ha, T.-J., Enhanced Triboelectric Effects of Self-Poled
14 MoS₂-Embedded PVDF Hybrid Nanocomposite Films for Bar-Printed Wearable
15 Triboelectric Nanogenerators. *ACS nano* **2022**.
- 16
17 (140) Fang, Z.; Chan, K. H.; Lu, X.; Tan, C. F.; Ho, G. W., Surface texturing and
18 dielectric property tuning toward boosting of triboelectric nanogenerator performance.
19 *Journal of Materials Chemistry A* **2018**, *6*(1), 52-57.
- 20
21 (141) Kim, J.; Ryu, H.; Lee, J. H.; Khan, U.; Kwak, S. S.; Yoon, H.-J.; Kim, S.-W., High
22 Permittivity CaCu₃Ti₄O₁₂ Particle-Induced Internal Polarization Amplification for High
23 Performance Triboelectric Nanogenerators. *Advanced Energy Materials* **2020**, *10* (9),
24 1903524.
- 25
26 (142) Bhatta, T.; Maharjan, P.; Cho, H.; Park, C.; Yoon, S. H.; Sharma, S.; Salauddin, M.;
27 Rahman, M. T.; Rana, S. M. S.; Park, J. Y., High-performance triboelectric nanogenerator
28 based on MXene functionalized polyvinylidene fluoride composite nanofibers. *Nano Energy*
29 **2021**, *81*, 105670.
- 30
31 (143) Park, S.-J.; Seol, M.-L.; Kim, D.; Jeon, S.-B.; Choi, Y.-K., Triboelectric
32 nanogenerator with nanostructured metal surface using water-assisted oxidation. *Nano*
33 *Energy* **2016**, *21*, 258-264.
- 34
35 (144) Wang, S.; Zi, Y.; Zhou, Y. S.; Li, S.; Fan, F.; Lin, L.; Wang, Z. L., Molecular
36 surface functionalization to enhance the power output of triboelectric nanogenerators. *Journal*
37 *of Materials Chemistry A* **2016**, *4*(10), 3728-3734.
- 38
39 (145) Zhang, L.; Zhang, B.; Chen, J.; Jin, L.; Deng, W.; Tang, J.; Zhang, H.; Pan, H.; Zhu,
40 M.; Yang, W., Lawn structured triboelectric nanogenerators for scavenging sweeping wind
41 energy on rooftops. *Advanced Materials* **2016**, *28* (8), 1650-1656.
- 42
43 (146) Lee, S.; Chung, J.; Kim, D. Y.; Jung, J.-Y.; Lee, S. H.; Lee, S., Cylindrical water
44 triboelectric nanogenerator via controlling geometrical shape of anodized aluminum for
45 enhanced electrostatic induction. *ACS applied materials & interfaces* **2016**, *8* (38), 25014-
46 25018.
- 47
48
49
50
51
52
53
54
55
56
57
58
59
60

- 1
2
3
4
5 (147) Kwak, M. S.; Lim, K.-W.; Lee, H. Y.; Peddigari, M.; Jang, J.; Jeong, C. K.; Ryu, J.;
6 Yoon, W.-H.; Yi, S. N.; Hwang, G.-T., Multiscale surface modified magneto-mechano-
7 triboelectric nanogenerator enabled by eco-friendly NaCl imprinting stamp for self-powered
8 IoT applications. *Nanoscale* **2021**, *13* (18), 8418-8424.
- 11 (148) Mule, A. R.; Dudem, B.; Yu, J. S., High-performance and cost-effective triboelectric
12 nanogenerators by sandpaper-assisted micropatterned polytetrafluoroethylene. *Energy* **2018**,
13 *165*, 677-684.
- 16 (149) Ahn, J.; Zhao, Z.-J.; Choi, J.; Jeong, Y.; Hwang, S.; Ko, J.; Gu, J.; Jeon, S.; Park, J.;
17 Kang, M., Morphology-controllable wrinkled hierarchical structure and its application to
18 superhydrophobic triboelectric nanogenerator. *Nano Energy* **2021**, *85*, 105978.
- 21 (150) Choi, J.; Jo, W.; Lee, S. Y.; Jung, Y. S.; Kim, S.-H.; Kim, H.-T., Flexible and robust
22 superomniphobic surfaces created by localized photofluidization of azopolymer pillars. *ACS*
23 *nano* **2017**, *11* (8), 7821-7828.
- 26 (151) Ha, M.; Lim, S.; Cho, S.; Lee, Y.; Na, S.; Baig, C.; Ko, H., Skin-inspired
27 hierarchical polymer architectures with gradient stiffness for spacer-free, ultrathin, and highly
28 sensitive triboelectric sensors. *ACS nano* **2018**, *12* (4), 3964-3974.
- 31 (152) Zhu, G.; Pan, C.; Guo, W.; Chen, C.-Y.; Zhou, Y.; Yu, R.; Wang, Z. L.,
32 Triboelectric-generator-driven pulse electrodeposition for micropatterning. *Nano letters* **2012**,
33 *12* (9), 4960-4965.
- 36 (153) Bui, V.-T.; Chau, N. M.; Huynh, D. P.; Huynh, N. D.; Choi, D.; Nhat Do, H.,
37 Honeycomb-Patterned Polyimide-Based Triboelectric Nanogenerator with Excellent Thermal
38 Stability and Enhanced Electrification Performance. *ACS Applied Energy Materials* **2022**, *5*
39 (8), 9791-9800.
- 43 (154) Zhang, A.; Bai, H.; Li, L., Breath figure: a nature-inspired preparation method for
44 ordered porous films. *Chemical reviews* **2015**, *115* (18), 9801-9868.
- 46 (155) Vorobyev, A. Y.; Guo, C., Direct femtosecond laser surface nano/microstructuring
47 and its applications. *Laser & Photonics Reviews* **2013**, *7* (3), 385-407.
- 50 (156) Park, S.; Park, J.; Kim, Y.-g.; Bae, S.; Kim, T.-W.; Park, K.-I.; Hong, B. H.; Jeong,
51 C. K.; Lee, S.-K., Laser-directed synthesis of strain-induced crumpled MoS₂ structure for
52 enhanced triboelectrification toward haptic sensors. *Nano Energy* **2020**, *78*, 105266.
- 55 (157) Sohn, C.; Lee, J. J.; Kim, K.; Jeong, C. K., Communication—Power Enhancement
56 of Fabric Triboelectric Energy Harvesters Using Ultraviolet Light and Fluoro-Based
57 Treatment. *ECS Journal of Solid State Science and Technology* **2022**, *11* (5), 055006.
- 58
59
60

- 1
2
3
4
5 (158) Byun, K.-E.; Cho, Y.; Seol, M.; Kim, S.; Kim, S.-W.; Shin, H.-J.; Park, S.; Hwang,
6 S., Control of triboelectrification by engineering surface dipole and surface electronic state.
7 *ACS applied materials & interfaces* **2016**, *8*(28), 18519-18525.
8
9 (159) Shin, S. H.; Bae, Y. E.; Moon, H. K.; Kim, J.; Choi, S. H.; Kim, Y.; Yoon, H. J.;
10 Lee, M. H.; Nah, J., Formation of Triboelectric Series via Atomic-Level Surface
11 Functionalization for Triboelectric Energy Harvesting. *ACS Nano* **2017**, *11*(6), 6131-6138.
12
13 (160) Lapčinskis, L.; Linarts, A.; Mālnieks, K.; Kim, H.; Rubenis, K.; Pudzs, K.; Smits,
14 K.; Kovaļovs, A.; Kalniņš, K.; Tamm, A., Triboelectrification of nanocomposites using
15 identical polymer matrixes with different concentrations of nanoparticle fillers. *Journal of*
16 *Materials Chemistry A* **2021**, *9*(14), 8984-8990.
17
18 (161) Zhang, Q.; Jiang, C.; Li, X.; Dai, S.; Ying, Y.; Ping, J., Highly efficient raindrop
19 energy-based triboelectric nanogenerator for self-powered intelligent greenhouse. *ACS nano*
20 **2021**, *15*(7), 12314-12323.
21
22 (162) Kim, W.-S.; Cheong, H.-W.; Park, W.; Whang, K.-W., Effects of RF-Bias Power
23 Application in an Inductively Coupled CF 4 Plasma on the Nanoscale Morphology and
24 Chemical Bond Structure of Polyethylene Terephthalate Surface. *IEEE Transactions on*
25 *Plasma Science* **2014**, *42*(12), 4004-4009.
26
27 (163) Zou, H.; Zhang, Y.; Guo, L.; Wang, P.; He, X.; Dai, G.; Zheng, H.; Chen, C.; Wang,
28 A. C.; Xu, C., Quantifying the triboelectric series. *Nature communications* **2019**, *10*(1), 1-9.
29
30 (164) Samukawa, S.; Kubota, T.; Huang, C.-H.; Hashimoto, T.; Igarashi, M.; Nishioka,
31 K.; Takeguchi, M.; Uraoka, Y.; Fuyuki, T.; Yamashita, I., A new silicon quantum-well
32 structure with controlled diameter and thickness fabricated with ferritin iron core mask and
33 chlorine neutral beam etching. *Applied physics express* **2008**, *1*(7), 074002.
34
35 (165) Kim, W.; Okada, T.; Park, H.-W.; Kim, J.; Kim, S.; Kim, S.-W.; Samukawa, S.;
36 Choi, D., Surface modification of triboelectric materials by neutral beams. *Journal of*
37 *Materials Chemistry A* **2019**, *7*(43), 25066-25077.
38
39 (166) Yun, B. K.; Kim, J. W.; Kim, H. S.; Jung, K. W.; Yi, Y.; Jeong, M.-S.; Ko, J.-H.;
40 Jung, J. H., Base-treated polydimethylsiloxane surfaces as enhanced triboelectric
41 nanogenerators. *Nano Energy* **2015**, *15*, 523-529.
42
43 (167) Luo, N.; Feng, Y.; Li, X.; Sun, W.; Wang, D.; Ye, Q.; Sun, X.; Zhou, F.; Liu, W.,
44 Manipulating electrical properties of silica-based materials via atomic oxygen irradiation.
45 *ACS Applied Materials & Interfaces* **2021**, *13*(13), 15344-15352.
46
47
48
49
50
51
52
53
54
55
56
57
58
59
60

- 1
2
3
4
5 (168) Choi, K.-H.; Park, S.; Hyeong, S.-K.; Bae, S.; Hong, J.-M.; Kim, T.-W.; Lee, S. H.;
6 Ryu, S.; Lee, S.-K., Triboelectric effect of surface morphology controlled laser induced
7 graphene. *Journal of Materials Chemistry A* **2020**, *8* (38), 19822-19832.
- 8
9 (169) Akada, K.; Terasawa, T.-o.; Imamura, G.; Obata, S.; Saiki, K., Control of work
10 function of graphene by plasma assisted nitrogen doping. *Applied Physics Letters* **2014**, *104*
11 (13), 131602.
- 12
13 (170) Li, S.; Fan, Y.; Chen, H.; Nie, J.; Liang, Y.; Tao, X.; Zhang, J.; Chen, X.; Fu, E.;
14 Wang, Z. L., Manipulating the triboelectric surface charge density of polymers by low-energy
15 helium ion irradiation/implantation. *Energy & Environmental Science* **2020**, *13* (3), 896-907.
- 16
17 (171) Fan, Y.; Li, S.; Tao, X.; Wang, Y.; Liu, Z.; Chen, H.; Wu, Z.; Zhang, J.; Ren, F.;
18 Chen, X., Negative triboelectric polymers with ultrahigh charge density induced by ion
19 implantation. *Nano Energy* **2021**, *90*, 106574.
- 20
21 (172) Heidbrink, J. L.; Ramírez-Arizmendi, L. E.; Thoen, K. K.; Guler, L.; Kenttämä, H.
22 I., Polar effects control hydrogen-abstraction reactions of charged, substituted phenyl
23 radicals. *The Journal of Physical Chemistry A* **2001**, *105* (33), 7875-7884.
- 24
25 (173) Lapp, J.; Scheiner, S., Proximity effects of substituents on halogen bond strength.
26 *The Journal of Physical Chemistry A* **2021**, *125* (23), 5069-5077.
- 27
28 (174) Lee, J. H.; Kim, K. H.; Choi, M.; Jeon, J.; Yoon, H. J.; Choi, J.; Lee, Y.-S.; Lee, M.;
29 Wie, J. J., Rational molecular design of polymeric materials toward efficient triboelectric
30 energy harvesting. *Nano Energy* **2019**, *66*, 104158.
- 31
32 (175) Liu, Y.; Fu, Q.; Mo, J.; Lu, Y.; Cai, C.; Luo, B.; Nie, S., Chemically tailored
33 molecular surface modification of cellulose nanofibrils for manipulating the charge density of
34 triboelectric nanogenerators. *Nano Energy* **2021**, *89*, 106369.
- 35
36 (176) Roy, S.; Ko, H. U.; Maji, P. K.; Hai, L. V.; Kim, J., Large amplification of
37 triboelectric property by allicin to develop high performance cellulosic triboelectric
38 nanogenerator. *Chemical Engineering Journal* **2020**, *385*.
- 39
40 (177) Jung, Y. K.; Kim, K. N.; Baik, J. M.; Kim, B.-S., Self-powered triboelectric
41 aptasensor for label-free highly specific thrombin detection. *Nano Energy* **2016**, *30*, 77-83.
- 42
43 (178) Pao, Y.-P.; Yu, C.-C.; Lin, Y.-Z.; Chatterjee, S.; Saha, S.; Tiwari, N.; Huang, Y.-T.;
44 Wu, C.-C.; Choi, D.; Lin, Z.-H., Carbohydrate-protein interactions studied by solid-liquid
45 contact electrification and its use for label-free bacterial detection. *Nano Energy* **2021**, *85*,
46 106008.
- 47
48
49
50
51
52
53
54
55
56
57
58
59
60

- 1
2
3
4
5 (179) Fan, F. R.; Luo, J.; Tang, W.; Li, C.; Zhang, C.; Tian, Z.; Wang, Z. L., Highly
6 transparent and flexible triboelectric nanogenerators: performance improvements and
7 fundamental mechanisms. *Journal of Materials Chemistry A* **2014**, *2* (33), 13219-13225.
- 8
9 (180) Zhang, X.-S.; Han, M.-D.; Wang, R.-X.; Meng, B.; Zhu, F.-Y.; Sun, X.-M.; Hu, W.;
10 Wang, W.; Li, Z.-H.; Zhang, H.-X., High-performance triboelectric nanogenerator with
11 enhanced energy density based on single-step fluorocarbon plasma treatment. *Nano Energy*
12 **2014**, *4*, 123-131.
- 13
14 (181) Li, H. Y.; Su, L.; Kuang, S. Y.; Pan, C. F.; Zhu, G.; Wang, Z. L., Significant
15 enhancement of triboelectric charge density by fluorinated surface modification in nanoscale
16 for converting mechanical energy. *Advanced Functional Materials* **2015**, *25* (35), 5691-5697.
- 17
18 (182) Imaoka, T.; Okada, T.; Samukawa, S.; Yamamoto, K., Room-Temperature
19 Synthesis of GaN Driven by Kinetic Energy beyond the Limit of Thermodynamics. *ACS*
20 *applied materials & interfaces* **2017**, *9* (48), 41629-41633.
- 21
22 (183) Dong, J.; Huang, S.; Luo, J.; Zhao, J.; Fan, F. R.; Tian, Z.-Q., Supercapacitor-
23 Inspired Triboelectric Nanogenerator Based on Electrostatic Double Layer. *Nano Energy*
24 **2022**, *95*, 106971.
- 25
26 (184) Liu, Y.; Zheng, Y.; Wu, Z.; Zhang, L.; Sun, W.; Li, T.; Wang, D.; Zhou, F.,
27 Conductive elastic sponge-based triboelectric nanogenerator (TENG) for effective random
28 mechanical energy harvesting and ammonia sensing. *Nano Energy* **2021**, *79*.
- 29
30 (185) Haider, Z.; Haleem, A.; Ahmad, R. u. S.; Farooq, U.; Shi, L.; Claver, U. P.; Memon,
31 K.; Fareed, A.; Khan, I.; Mbogba, M. K.; Hossain, S. M. C.; Farooq, F.; Ali, W.; Abid, M.;
32 Qadir, A.; He, W.; Luo, J.; Zhao, G., Highly porous polymer cryogel based tribopositive
33 material for high performance triboelectric nanogenerators. *Nano Energy* **2020**, *68*.
- 34
35 (186) Kim, J.; Ryu, H.; Lee, J. H.; Khan, U.; Kwak, S. S.; Yoon, H. J.; Kim, S. W., High
36 permittivity CaCu₃Ti₄O₁₂ particle-induced internal polarization amplification for high
37 performance triboelectric nanogenerators. *Advanced Energy Materials* **2020**, *10* (9),
38 1903524.
- 39
40 (187) Niu, S.; Wang, S.; Lin, L.; Liu, Y.; Zhou, Y. S.; Hu, Y.; Wang, Z. L., Theoretical
41 study of contact-mode triboelectric nanogenerators as an effective power source. *Energy &*
42 *Environmental Science* **2013**, *6* (12), 3576.
- 43
44 (188) Wang, Z. L., On the first principle theory of nanogenerators from Maxwell's
45 equations. *Nano Energy* **2020**, *68*, 104272.
- 46
47
48
49
50
51
52
53
54
55
56
57
58
59
60

- 1
2
3
4
5 (189) Kim, M. P.; Um, D. S.; Shin, Y. E.; Ko, H., High-Performance Triboelectric
6 Devices via Dielectric Polarization: A Review. *Nanoscale research letters* **2021**, *16*(1), 35.
7
8 (190) Xi, Y. H.; Zhang, F.; Shi, Y. J., Effects of surface micro-structures on capacitances
9 of the dielectric layer in triboelectric nanogenerator: A numerical simulation study. *Nano*
10 *Energy* **2021**, *79*.
11
12 (191) Han, S. A.; Seung, W.; Kim, J. H.; Kim, S.-W., Ultrathin Noncontact-Mode
13 Triboelectric Nanogenerator Triggered by Giant Dielectric Material Adaption. *ACS Energy*
14 *Letters* **2021**, 1189-1197.
15
16 (192) Kim, Y. J.; Lee, J.; Park, S.; Park, C.; Park, C.; Choi, H. J., Effect of the relative
17 permittivity of oxides on the performance of triboelectric nanogenerators. *Rsc Adv* **2017**, *7*
18 (78), 49368-49373.
19
20 (193) Shi, K. M.; Zou, H. Y.; Sun, B.; Jiang, P. K.; He, J. L.; Huang, X. Y., Dielectric
21 Modulated Cellulose Paper/PDMS-Based Triboelectric Nanogenerators for Wireless
22 Transmission and Electropolymerization Applications. *Advanced Functional Materials* **2020**,
23 *30*(4).
24
25 (194) Cheon, S.; Kang, H.; Kim, H.; Son, Y.; Lee, J. Y.; Shin, H.-J.; Kim, S.-W.; Cho, J.
26 H., High-Performance Triboelectric Nanogenerators Based on Electrospun Polyvinylidene
27 Fluoride-Silver Nanowire Composite Nanofibers. *Advanced Functional Materials* **2018**, *28*
28 (2), 1703778.
29
30 (195) Ma, L.; Zhou, M.; Wu, R.; Patil, A.; Gong, H.; Zhu, S.; Wang, T.; Zhang, Y.; Shen,
31 S.; Dong, K.; Yang, L.; Wang, J.; Guo, W.; Wang, Z. L., Continuous and Scalable
32 Manufacture of Hybridized Nano-Micro Triboelectric Yarns for Energy Harvesting and
33 Signal Sensing. *ACS Nano* **2020**, *14*(4), 4716-4726.
34
35 (196) Nie, S.; Cai, C.; Lin, X.; Zhang, C.; Lu, Y.; Mo, J.; Wang, S., Chemically
36 functionalized cellulose nanofibrils for improving triboelectric charge density of a
37 triboelectric nanogenerator. *ACS Sustainable Chemistry & Engineering* **2020**, *8*(50), 18678-
38 18685.
39
40 (197) Chen, J.; Guo, H.; He, X.; Liu, G.; Xi, Y.; Shi, H.; Hu, C., Enhancing Performance
41 of Triboelectric Nanogenerator by Filling High Dielectric Nanoparticles into Sponge PDMS
42 Film. *ACS Appl Mater Interfaces* **2016**, *8*(1), 736-44.
43
44 (198) He, X.; Guo, H.; Yue, X.; Gao, J.; Xi, Y.; Hu, C., Improving energy conversion
45 efficiency for triboelectric nanogenerator with capacitor structure by maximizing surface
46 charge density. *Nanoscale* **2015**, *7*(5), 1896-903.
47
48
49
50
51
52
53
54
55
56
57
58
59
60

- 1
2
3
4
5 (199) Cha, S.; Cho, Y.; Kim, J. G.; Choi, H.; Ahn, D.; Sun, J.; Kang, D. S.; Pak, C.; Park,
6 J. J., Controllable Triboelectric Series Using Gradient Positive and Negative Charge-
7 Confinement Layer with Different Particle Sizes of Mesoporous Carbon Materials. *Small*
8 *Methods* **2022**, *6*(5).
- 9
10
11 (200) Wang, Z. L., Entropy theory of distributed energy for internet of things. *Nano*
12 *Energy* **2019**, *58*, 669-672.
- 13
14 (201) Shao, Y.; Feng, C.-p.; Deng, B.-w.; Yin, B.; Yang, M.-b., Facile method to enhance
15 output performance of bacterial cellulose nanofiber based triboelectric nanogenerator by
16 controlling micro-nano structure and dielectric constant. *Nano Energy* **2019**, *62*, 620-627.
- 17
18 (202) Qiu, Y. Q.; Fang, H.; Guo, J. J.; Wu, H., Fully nano/micro-fibrous triboelectric on-
19 skin patch with high breathability and hydrophobicity for physiological status monitoring.
20 *Nano Energy* **2022**, *98*.
- 21
22 (203) Chen, H. M.; Wang, J.; Ning, A. F., Optimization of a Rolling Triboelectric
23 Nanogenerator Based on the Nano-Micro Structure for Ocean Environmental Monitoring.
24 *Acs Omega* **2021**, *6*(32), 21059-21065.
- 25
26 (204) Zhao, L. M.; Zheng, Q.; Ouyang, H.; Li, H.; Yan, L.; Shi, B. J.; Li, Z., A size-
27 unlimited surface microstructure modification method for achieving high performance
28 triboelectric nanogenerator. *Nano Energy* **2016**, *28*, 172-178.
- 29
30 (205) Kim, D.; Lee, S.; Ko, Y.; Kwon, C. H.; Cho, J., Layer-by-layer assembly-induced
31 triboelectric nanogenerators with high and stable electric outputs in humid environments.
32 *Nano Energy* **2018**, *44*, 228-239.
- 33
34 (206) Meng, L. J.; Xu, Q. W.; Dan, L.; Wang, X. H., Single-Walled Carbon Nanotube
35 Based Triboelectric Flexible Touch Sensors. *J Electron Mater* **2019**, *48*(11).
- 36
37 (207) Han, L.; Peng, M. F.; Wen, Z.; Liu, Y. N.; Zhang, Y.; Zhu, Q. Q.; Lei, H.; Liu, S.
38 N.; Zheng, L.; Sun, X. H.; Li, H. X., Self-driven photodetection based on impedance
39 matching effect between a triboelectric nanogenerator and a MoS₂ nanosheets photodetector.
40 *Nano Energy* **2019**, *59*, 492-499.
- 41
42 (208) Zhang, X. S.; Han, M. D.; Wang, R. X.; Zhu, F. Y.; Li, Z. H.; Wang, W.; Zhang, H.
43 X., Frequency-Multiplication High-Output Triboelectric Nanogenerator for Sustainably
44 Powering Biomedical Microsystems. *Nano Letters* **2013**, *13*(3), 1168-1172.
- 45
46 (209) Palaniappan, V.; Masihi, S.; Zhang, X.; Emamian, S.; Bose, A. K.; Maddipatla, D.;
47 Hajian, S.; Panahi, M.; Narakathu, B. B.; Bazuin, B. J.; Atashbar, M. Z., A Flexible
48
49
50
51
52
53
54
55
56
57
58
59
60

1
2
3
4
5
6
7
8
9
10
11
12
13
14
15
16
17
18
19
20
21
22
23
24
25
26
27
28
29
30
31
32
33
34
35
36
37
38
39
40
41
42
43
44
45
46
47
48
49
50
51
52
53
54
55
56
57
58
59
60

Triboelectric Nanogenerator Fabricated Using Laser-Assisted Patterning Process. *Ieee Sensor* **2019**.

(210) Yan, Z. G.; Wang, L. L.; Xia, Y. F.; Qiu, R. D.; Liu, W. Q.; Wu, M.; Zhu, Y.; Zhu, S. L.; Jia, C. Y.; Zhu, M. M.; Cao, R. R.; Li, Z. L.; Wang, X., Flexible High-Resolution Triboelectric Sensor Array Based on Patterned Laser-Induced Graphene for Self-Powered Real-Time Tactile Sensing. *Advanced Functional Materials* **2021**, *31* (23).

(211) Nie, J. H.; Ren, Z. W.; Bai, Y.; Shao, J. J.; Jiang, T.; Xu, B.; Chen, X. Y.; Wang, Z. L., Long Distance Transport of Microdroplets and Precise Microfluidic Patterning Based on Triboelectric Nanogenerator. *Adv Mater Technol-Us* **2019**, *4* (1).

(212) Wen, R. M.; Feng, R.; Zhao, B.; Song, J. F.; Fan, L. M.; Zhai, J. Y., Controllable design of high-efficiency triboelectric materials by functionalized metal-organic frameworks with a large electron-withdrawing functional group. *Nano Research* **2022**.

(213) Vu, D. L.; Le, C. D.; Vo, C. P.; Ahn, K. K., Surface polarity tuning through epitaxial growth on polyvinylidene fluoride membranes for enhanced performance of liquid-solid triboelectric nanogenerator. *Compos Part B-Eng* **2021**, *223*.

(214) Song, G.; Kim, Y.; Yu, S.; Kim, M. O.; Park, S. H.; Cho, S. M.; Velusamy, D. B.; Cho, S. H.; Kim, K. L.; Kim, J.; Kim, E.; Park, C., Molecularly Engineered Surface Triboelectric Nanogenerator by Self-Assembled Monolayers (METS). *Chem Mater* **2015**, *27* (13), 4749-4755.

(215) Wang, C. C.; Chang, C. Y., Enhanced output performance and stability of triboelectric nanogenerators by employing silane-based self-assembled monolayers. *Journal of Materials Chemistry C* **2020**, *8* (13), 4542-4548.

(216) Xia, K. Q.; Zhu, Z. Y.; Zhang, H. Z.; Xu, Z. W., A triboelectric nanogenerator as self-powered temperature sensor based on PVDF and PTFE. *Appl Phys a-Mater* **2018**, *124* (8).

(217) Pu, X.; Zha, J. W.; Zhao, C. L.; Gong, S. B.; Gao, J. F.; Li, R. K. Y., Flexible PVDF/nylon-11 electrospun fibrous membranes with aligned ZnO nanowires as potential triboelectric nanogenerators. *Chemical Engineering Journal* **2020**, *398*.

(218) Lee, J. P.; Lee, J. W.; Baik, J. M., The Progress of PVDF as a Functional Material for Triboelectric Nanogenerators and Self-Powered Sensors. *Micromachines-Basel* **2018**, *9* (10).

- 1
2
3
4
5 (219) Kim, Y.; Wu, X. W.; Lee, C.; Oh, J. H., Characterization of PI/PVDF-TrFE
6 Composite Nanofiber-Based Triboelectric Nanogenerators Depending on the Type of the
7 Electrospinning System. *Acs Applied Materials & Interfaces* **2021**, *13*(31), 36967-36975.
- 8
9 (220) Liu, J. D.; Yu, D.; Zheng, Z. P.; Geng, H. F.; Guo, Y. P., Lead-free BiFeO₃ film on
10 glass fiber fabric: Wearable hybrid piezoelectric-triboelectric nanogenerator. *Ceram Int* **2021**,
11 *47*(3), 3573-3579.
- 12
13 (221) Zhang, P.; Zhang, W. K.; Deng, L.; Zhang, H. H., A triboelectric nanogenerator
14 based on temperature-stable high dielectric BaTiO₃-based ceramic powder for energy
15 harvesting. *Nano Energy* **2021**, *87*.
- 16
17 (222) Hajra, S.; Padhan, A. M.; Sahu, M.; Alagarsamy, P.; Lee, K.; Kim, H. J., Lead-free
18 flexible Bismuth Titanate-PDMS composites: A multifunctional colossal dielectric material
19 for hybrid piezo-triboelectric nanogenerator to sustainably power portable electronics. *Nano*
20 *Energy* **2021**, *89*.
- 21
22 (223) Küchler, A., *High Voltage Engineering: Fundamentals-Technology-Applications*.
23 Springer Vieweg: Berlin, Germany, 2018.
- 24
25 (224) Lee, J. W.; Cho, H. J.; Chun, J.; Kim, K. N.; Kim, S.; Ahn, C. W.; Kim, I. W.; Kim,
26 J.-Y.; Kim, S.-W.; Yang, C., Robust nanogenerators based on graft copolymers via control of
27 dielectrics for remarkable output power enhancement. *Science advances* **2017**, *3* (5),
28 e1602902.
- 29
30 (225) Jin, L.; Xiao, X.; Deng, W.; Nashalian, A.; He, D.; Raveendran, V.; Yan, C.; Su, H.;
31 Chu, X.; Yang, T., Manipulating relative permittivity for high-performance wearable
32 triboelectric nanogenerators. *Nano Letters* **2020**, *20*(9), 6404-6411.
- 33
34 (226) Shen, W.-W.; Mu, H.-B.; Zhang, G.-J.; Deng, J.-B.; Tu, D.-M., Identification of
35 electron and hole trap based on isothermal surface potential decay model. *Journal of Applied*
36 *Physics* **2013**, *113*(8), 083706.
- 37
38 (227) Takada, T.; Kikuchi, H.; Miyake, H.; Tanaka, Y.; Yoshida, M.; Hayase, Y.,
39 Determination of charge-trapping sites in saturated and aromatic polymers by quantum
40 chemical calculation. *IEEE Transactions on Dielectrics and Electrical Insulation* **2015**, *22*(2),
41 1240-1249.
- 42
43 (228) Feng, Y.; Zheng, Y.; Zhang, G.; Wang, D.; Zhou, F.; Liu, W., A new protocol
44 toward high output TENG with polyimide as charge storage layer. *Nano Energy* **2017**, *38*,
45 467-476.
- 46
47
48
49
50
51
52
53
54
55
56
57
58
59
60

- 1
2
3
4
5 (229) Park, D.; Lee, S.; Anh, C. V.; Park, P.; Nah, J., Role of a buried indium zinc oxide
6 layer in the performance enhancement of triboelectric nanogenerators. *Nano Energy* **2019**,
7 *55*, 501-505.
8
9 (230) Kim, D. W.; Lee, J. H.; You, I.; Kim, J. K.; Jeong, U., Adding a stretchable deep-
10 trap interlayer for high-performance stretchable triboelectric nanogenerators. *Nano Energy*
11 **2018**, *50*, 192-200.
12
13 (231) Xiong, J.; Cui, P.; Chen, X.; Wang, J.; Parida, K.; Lin, M.-F.; Lee, P. S., Skin-
14 touch-actuated textile-based triboelectric nanogenerator with black phosphorus for durable
15 biomechanical energy harvesting. *Nature Communications* **2018**, *9*(1), 4280.
16
17 (232) Park, H.-W.; Huynh, N. D.; Kim, W.; Lee, C.; Nam, Y.; Lee, S.; Chung, K.-B.;
18 Choi, D., Electron blocking layer-based interfacial design for highly-enhanced triboelectric
19 nanogenerators. *Nano Energy* **2018**, *50*, 9-15.
20
21 (233) Zhou, T.; Zhang, L.; Xue, F.; Tang, W.; Zhang, C.; Wang, Z. L., Multilayered
22 electret films based triboelectric nanogenerator. *Nano Research* **2016**, *9*(5), 1442-1451.
23
24 (234) Zi, Y. L.; Wu, C. S.; Ding, W. B.; Wang, Z. L., Maximized Effective Energy Output
25 of Contact-Separation Triggered Triboelectric Nanogenerators as Limited by Air Breakdown.
26 *Advanced Functional Materials* **2017**, *27*(24).
27
28 (235) Prada, T.; Harnchana, V.; Lakhonchai, A.; Chingsungnoen, A.; Poolcharuansin, P.;
29 Chanlek, N.; Klamchuen, A.; Thongbai, P.; Amornkitbamrung, V., Enhancement of output
30 power density in a modified polytetrafluoroethylene surface using a sequential O₂/Ar
31 plasma etching for triboelectric nanogenerator applications. *Nano Research* **2022**, *15* (1),
32 272-279.
33
34 (236) Shao, J. J.; Tang, W.; Jiang, T.; Chen, X. Y.; Xu, L.; Chen, B. D.; Zhou, T.; Deng,
35 C. R.; Wang, Z. L., A multi-dielectric-layered triboelectric nanogenerator as energized by
36 corona discharge. *Nanoscale* **2017**, *9*(27), 9668-9675.
37
38 (237) Nie, J. H.; Chen, X. Y.; Wang, Z. L., Electrically Responsive Materials and Devices
39 Directly Driven by the High Voltage of Triboelectric Nanogenerators. *Advanced Functional*
40 *Materials* **2019**, *29*(41).
41
42 (238) Han, K.; Luo, J. J.; Chen, J.; Chen, B. D.; Xu, L.; Feng, Y. W.; Tang, W.; Wang, Z.
43 L., Self-powered ammonia synthesis under ambient conditions via N₂ discharge driven by
44 Tesla turbine triboelectric nanogenerators. *Microsyst Nanoeng* **2021**, *7*(1).
45
46
47
48
49
50
51
52
53
54
55
56
57
58
59
60

- 1
2
3
4
5 (239) Firdous, I.; Fahim, M.; Daoud, W. A., Performance enhancement of triboelectric
6 nanogenerator through hole and electron blocking layers-based interfacial design. *Nano*
7 *Energy* **2021**, *82*.
- 8
9 (240) Choi, J. H.; Ra, Y.; Cho, S.; La, M.; Park, S. J.; Choi, D., Electrical charge storage
10 effect in carbon based polymer composite for long-term performance enhancement of the
11 triboelectric nanogenerator. *Compos Sci Technol* **2021**, *207*.
- 12
13 (241) Wang, H. L.; Guo, Z. H.; Zhu, G.; Pu, X.; Wang, Z. L., Boosting the Power and
14 Lowering the Impedance of Triboelectric Nanogenerators through Manipulating the
15 Permittivity for Wearable Energy Harvesting. *ACS Nano* **2021**, *15*(4), 7513-7521.
- 16
17 (242) Parida, K.; Xiong, J.; Zhou, X.; Lee, P. S., Progress on triboelectric nanogenerator
18 with stretchability, self-healability and bio-compatibility. *Nano Energy* **2019**, *59*, 237-257.
- 19
20 (243) Harnchana, V.; Ngoc, H. V.; He, W.; Rasheed, A.; Park, H.; Amornkitbamrung, V.;
21 Kang, D. J., Enhanced Power Output of a Triboelectric Nanogenerator using
22 Poly(dimethylsiloxane) Modified with Graphene Oxide and Sodium Dodecyl Sulfate. *ACS*
23 *Applied Materials & Interfaces* **2018**, *10*(30), 25263-25272.
- 24
25 (244) Lan, L.; Xiong, J.; Gao, D.; Li, Y.; Chen, J.; Lv, J.; Ping, J.; Ying, Y.; Lee, P. S.,
26 Breathable Nanogenerators for an On-Plant Self-Powered Sustainable Agriculture System.
27 *ACS Nano* **2021**, *15*(3), 5307-5315.
- 28
29 (245) Jiang, C.; Li, X.; Yao, Y.; Lan, L.; Shao, Y.; Zhao, F.; Ying, Y.; Ping, J., A
30 multifunctional and highly flexible triboelectric nanogenerator based on MXene-enabled
31 porous film integrated with laser-induced graphene electrode. *Nano Energy* **2019**, *66*,
32 104121.
- 33
34 (246) Jiang, F.; Zhou, X.; Lv, J.; Chen, J.; Chen, J.; Kongcharoen, H.; Zhang, Y.; Lee, P.
35 S., Stretchable, Breathable, and Stable Lead-Free Perovskite/Polymer Nanofiber Composite
36 for Hybrid Triboelectric and Piezoelectric Energy Harvesting. *Advanced Materials* **2022**, *34*
37 (17), 2200042.
- 38
39 (247) Jiang, F.; Lee, P. S., Performance optimization strategies of halide perovskite-based
40 mechanical energy harvesters. *Nanoscale Horizons* **2022**, *7*(9), 1029-1046.
- 41
42 (248) He, W.; Qian, Y.; Lee, B. S.; Zhang, F.; Rasheed, A.; Jung, J.-E.; Kang, D. J.,
43 Ultrahigh Output Piezoelectric and Triboelectric Hybrid Nanogenerators Based on ZnO
44 Nanoflakes/Polydimethylsiloxane Composite Films. *ACS Applied Materials & Interfaces*
45 **2018**, *10*(51), 44415-44420.
- 46
47
48
49
50
51
52
53
54
55
56
57
58
59
60

- 1
2
3
4
5 (249) Kim, D. H.; Dudem, B.; Yu, J. S., High-Performance Flexible Piezoelectric-Assisted
6 Triboelectric Hybrid Nanogenerator via Polydimethylsiloxane-Encapsulated Nanoflower-like
7 ZnO Composite Films for Scavenging Energy from Daily Human Activities. *ACS*
8 *Sustainable Chemistry & Engineering* **2018**, *6* (7), 8525-8535.
- 9
10
11 (250) Pu, X.; Zha, J.-W.; Zhao, C.-L.; Gong, S.-B.; Gao, J.-F.; Li, R. K. Y., Flexible
12 PVDF/nylon-11 electrospun fibrous membranes with aligned ZnO nanowires as potential
13 triboelectric nanogenerators. *Chemical Engineering Journal* **2020**, *398*, 125526.
- 14
15
16 (251) Khandelwal, G.; Chandrasekhar, A.; Pandey, R.; Maria Joseph Raj, N. P.; Kim, S.-
17 J., Phase inversion enabled energy scavenger: A multifunctional triboelectric nanogenerator
18 as benzene monitoring system. *Sensors and Actuators B: Chemical* **2019**, *282*, 590-598.
- 19
20
21 (252) Kim, M.-K.; Kim, M.-S.; Kwon, H.-B.; Jo, S.-E.; Kim, Y.-J., Wearable triboelectric
22 nanogenerator using a plasma-etched PDMS–CNT composite for a physical activity sensor.
23 *Rsc Adv* **2017**, *7* (76), 48368-48373.
- 24
25
26 (253) Deng, H.-T.; Zhang, X.-R.; Wang, Z.-Y.; Wen, D.-L.; Ba, Y.-Y.; Kim, B.; Han, M.-
27 D.; Zhang, H.-X.; Zhang, X.-S., Super-stretchable multi-sensing triboelectric nanogenerator
28 based on liquid conductive composite. *Nano Energy* **2021**, *83*, 105823.
- 29
30
31 (254) Shi, L.; Jin, H.; Dong, S.; Huang, S.; Kuang, H.; Xu, H.; Chen, J.; Xuan, W.; Zhang,
32 S.; Li, S.; Wang, X.; Luo, J., High-performance triboelectric nanogenerator based on
33 electrospun PVDF-graphene nanosheet composite nanofibers for energy harvesting. *Nano*
34 *Energy* **2021**, *80*, 105599.
- 35
36
37 (255) Gao, Y.; Liu, G.; Bu, T.; Liu, Y.; Qi, Y.; Xie, Y.; Xu, S.; Deng, W.; Yang, W.;
38 Zhang, C., MXene based mechanically and electrically enhanced film for triboelectric
39 nanogenerator. *Nano Research* **2021**, *14* (12), 4833-4840.
- 40
41
42 (256) Luo, X.; Zhu, L.; Wang, Y.-C.; Li, J.; Nie, J.; Wang, Z. L., A Flexible
43 Multifunctional Triboelectric Nanogenerator Based on MXene/PVA Hydrogel. *Advanced*
44 *Functional Materials* **2021**, *31* (38), 2104928.
- 45
46
47 (257) Chen, B. D.; Tang, W.; Zhang, C.; Xu, L.; Zhu, L. P.; Yang, L. J.; He, C.; Chen, J.;
48 Liu, L.; Zhou, T.; Wang, Z. L., Au nanocomposite enhanced electret film for triboelectric
49 nanogenerator. *Nano Research* **2018**, *11* (6), 3096-3105.
- 50
51
52 (258) Lee, B.-Y.; Kim, S.-U.; Kang, S.; Lee, S.-D., Transparent and flexible high power
53 triboelectric nanogenerator with metallic nanowire-embedded tribonegative conducting
54 polymer. *Nano Energy* **2018**, *53*, 152-159.
- 55
56
57
58
59
60

- 1
2
3
4
5 (259) Cheon, S.; Kang, H.; Kim, H.; Son, Y.; Lee, J. Y.; Shin, H.-J.; Kim, S.-W.; Cho, J.
6 H., High-Performance Triboelectric Nanogenerators Based on Electrospun Polyvinylidene
7 Fluoride–Silver Nanowire Composite Nanofibers. *Advanced Functional Materials* **2018**, *28*
8 (2), 1703778.
- 9
10
11 (260) Kim, S.-R.; Yoo, J.-H.; Park, J.-W., Using Electrospun AgNW/P(VDF-TrFE)
12 Composite Nanofibers to Create Transparent and Wearable Single-Electrode Triboelectric
13 Nanogenerators for Self-Powered Touch Panels. *ACS Applied Materials & Interfaces* **2019**,
14 *11* (16), 15088-15096.
- 15
16
17 (261) Chen, J.; Guo, H.; He, X.; Liu, G.; Xi, Y.; Shi, H.; Hu, C., Enhancing Performance
18 of Triboelectric Nanogenerator by Filling High Dielectric Nanoparticles into Sponge PDMS
19 Film. *ACS Applied Materials & Interfaces* **2016**, *8* (1), 736-744.
- 20
21
22 (262) Soin, N.; Zhao, P.; Prashanthi, K.; Chen, J.; Ding, P.; Zhou, E.; Shah, T.; Ray, S. C.;
23 Tsonos, C.; Thundat, T.; Siores, E.; Luo, J., High performance triboelectric nanogenerators
24 based on phase-inversion piezoelectric membranes of poly(vinylidene fluoride)-zinc stannate
25 (PVDF-ZnSnO₃) and polyamide-6 (PA6). *Nano Energy* **2016**, *30*, 470-480.
- 26
27
28 (263) Seung, W.; Yoon, H.-J.; Kim, T. Y.; Ryu, H.; Kim, J.; Lee, J.-H.; Lee, J. H.; Kim,
29 S.; Park, Y. K.; Park, Y. J.; Kim, S.-W., Boosting Power-Generating Performance of
30 Triboelectric Nanogenerators via Artificial Control of Ferroelectric Polarization and
31 Dielectric Properties. *Advanced Energy Materials* **2017**, *7* (2), 1600988.
- 32
33
34 (264) Kim, H. S.; Kim, D. Y.; Kim, J.-E.; Kim, J. H.; Kong, D. S.; Murillo, G.; Lee, G.-
35 H.; Park, J. Y.; Jung, J. H., Ferroelectric-Polymer-Enabled Contactless Electric Power
36 Generation in Triboelectric Nanogenerators. *Advanced Functional Materials* **2019**, *29* (45),
37 1905816.
- 38
39
40 (265) Šutka, A.; Mālnieks, K.; Lapčinskis, L.; Timusk, M.; Pudzs, K.; Rutkis, M.,
41 Matching the Directions of Electric Fields from Triboelectric and Ferroelectric Charges in
42 Nanogenerator Devices for Boosted Performance. *iScience* **2020**, *23* (4), 101011.
- 43
44
45 (266) Wen, R.; Guo, J.; Yu, A.; Zhai, J.; Wang, Z. l., Humidity-Resistive Triboelectric
46 Nanogenerator Fabricated Using Metal Organic Framework Composite. *Advanced*
47 *Functional Materials* **2019**, *29* (20), 1807655.
- 48
49
50 (267) Guo, Y.; Cao, Y.; Chen, Z.; Li, R.; Gong, W.; Yang, W.; Zhang, Q.; Wang, H.,
51 Fluorinated metal-organic framework as bifunctional filler toward highly improving output
52 performance of triboelectric nanogenerators. *Nano Energy* **2020**, *70*, 104517.
- 53
54
55
56
57
58
59
60

- 1
2
3
4
5 (268) Nallepalli, P.; Patel, T.; Kim, M. P.; Park, J.; Ye, Z.; Jung, H. W.; Ko, H.; Oh, J. K.,
6 Self-healable triboelectric nanogenerators based on ionic poly(hindered urea) network
7 materials cross-linked with fluorinated block copolymers. *Polymer Chemistry* **2022**, *13* (29),
8 4343-4351.
9
10
11 (269) Vu, D. L.; Vo, C. P.; Le, C. D.; Ahn, K. K., Enhancing the output performance of
12 fluid-based triboelectric nanogenerator by using poly(vinylidene fluoride-co-
13 hexafluoropropylene)/ionic liquid nanoporous membrane. *International Journal of Energy*
14 *Research* **2021**, *45* (6), 8960-8970.
15
16
17 (270) Dong, Y.; Mallineni, S. S. K.; Maleski, K.; Behlow, H.; Mochalin, V. N.; Rao, A.
18 M.; Gogotsi, Y.; Podila, R., Metallic MXenes: A new family of materials for flexible
19 triboelectric nanogenerators. *Nano Energy* **2018**, *44*, 103-110.
20
21
22 (271) Naguib, M.; Kurtoglu, M.; Presser, V.; Lu, J.; Niu, J.; Heon, M.; Hultman, L.;
23 Gogotsi, Y.; Barsoum, M. W., Two-Dimensional Nanocrystals Produced by Exfoliation of
24 Ti_3AlC_2 . *Adv. Mater.* **2011**, *23* (37), 4248-4253.
25
26
27 (272) Ghidui, M.; Lukatskaya, M. R.; Zhao, M. Q.; Gogotsi, Y.; Barsoum, M. W.,
28 Conductive two-dimensional titanium carbide 'clay' with high volumetric capacitance. *Nature*
29 **2014**, *516* (7529), 78-81.
30
31
32 (273) He, W.; Sohn, M.; Ma, R.; Kang, D. J., Flexible single-electrode triboelectric
33 nanogenerators with MXene/PDMS composite film for biomechanical motion sensors. *Nano*
34 *Energy* **2020**, *78*, 105383-105389.
35
36
37 (274) Bhatta, T.; Maharjan, P.; Cho, H.; Park, C.; Yoon, S. H.; Sharma, S.; Salauddin, M.;
38 Rahman, M. T.; Rana, S. M. S.; Park, J. Y., High-performance triboelectric nanogenerator
39 based on MXene functionalized polyvinylidene fluoride composite nanofibers. *Nano Energy*
40 **2021**, *81*, 105670-105682.
41
42
43 (275) Seol, M.; Kim, S.; Cho, Y.; Byun, K. E.; Kim, H.; Kim, J.; Kim, S. K.; Kim, S. W.;
44 Shin, H. J.; Park, S., Triboelectric Series of 2D Layered Materials. *Adv. Mater.* **2018**, *30* (39),
45 1801210-1801217.
46
47
48 (276) Sahatiya, P.; Kannan, S.; Badhulika, S., Few layer MoS_2 and in situ poled PVDF
49 nanofibers on low cost paper substrate as high performance piezo-triboelectric hybrid
50 nanogenerator: Energy harvesting from handwriting and human touch. *Appl. Mater. Today*
51 **2018**, *13*, 91-99.
52
53
54
55
56
57
58
59
60

- 1
2
3
4
5 (277) Wu, C.; Kim, T. W.; Park, J. H.; An, H.; Shao, J.; Chen, X.; Wang, Z. L., Enhanced
6 Triboelectric Nanogenerators Based on MoS₂ Monolayer Nanocomposites Acting as
7 Electron-Acceptor Layers. *ACS Nano* **2017**, *11* (8), 8356-8363.
- 8
9 (278) Kim, M.; Park, D.; Alam, M. M.; Lee, S.; Park, P.; Nah, J., Remarkable Output
10 Power Density Enhancement of Triboelectric Nanogenerators via Polarized Ferroelectric
11 Polymers and Bulk MoS₂ Composites. *ACS Nano* **2019**, *13*, 4640-4646.
- 12
13 (279) Karmakar, S.; Kumbhakar, P.; Maity, K.; Mandal, D.; Kumbhakar, P., Development
14 of flexible self-charging triboelectric power cell on paper for temperature and weight sensing.
15 *Nano Energy* **2019**, *63*, 103831-103843.
- 16
17 (280) Liu, J.; Zeng, Z.; Cao, X.; Lu, G.; Wang, L. H.; Fan, Q. L.; Huang, W.; Zhang, H.,
18 Preparation of MoS₂-Polyvinylpyrrolidone Nanocomposites for Flexible Nonvolatile
19 Rewritable Memory Devices with Reduced Graphene Oxide Electrodes. *Small* **2012**, *8* (22),
20 3517-3522.
- 21
22 (281) Duerloo, K.-A. N.; Ong, M. T.; Reed, E. J., Intrinsic Piezoelectricity in Two-
23 Dimensional Materials. *J. Phys. Chem. Lett.* **2012**, *3* (19), 2871-2876.
- 24
25 (282) Wu, W.; Wang, L.; Li, Y.; Zhang, F.; Lin, L.; Niu, S.; Chenet, D.; Zhang, X.; Hao,
26 Y.; Heinz, T. F.; Hone, J.; Wang, Z. L., Piezoelectricity of single-atomic-layer MoS₂ for
27 energy conversion and piezotronics. *Nature* **2014**, *514* (7523), 470-474.
- 28
29 (283) Lovinger, A. J., Ferroelectric Polymers. *SCIENCE* **1983**, *220* (4602), 1115-1121.
- 30
31 (284) Lee, K. Y.; Kim, S. K.; Lee, J.-H.; Seol, D.; Gupta, M. K.; Kim, Y.; Kim, S.-W.,
32 Controllable Charge Transfer by Ferroelectric Polarization Mediated Triboelectricity. *Adv.*
33 *Funct. Mater.* **2016**, *26* (18), 3067-3073.
- 34
35 (285) Seung, W.; Yoon, H.-J.; Kim, T. Y.; Ryu, H.; Kim, J.; Lee, J.-H.; Lee, J. H.; Kim,
36 S.; Park, Y. K.; Park, Y. J.; Kim, S.-W., Boosting Power-Generating Performance of
37 Triboelectric Nanogenerators via Artificial Control of Ferroelectric Polarization and
38 Dielectric Properties. *Adv. Energy Mater.* **2017**, *7* (2), 1600988-1600995.
- 39
40 (286) Cheon, S.; Kang, H.; Kim, H.; Son, Y.; Lee, J. Y.; Shin, H.-J.; Kim, S.-W.; Cho, J.
41 H., High-Performance Triboelectric Nanogenerators Based on Electrospun Polyvinylidene
42 Fluoride-Silver Nanowire Composite Nanofibers. *Adv. Funct. Mater.* **2018**, *28* (2), 1703778-
43 1703784.
- 44
45 (287) Park, Y.; Shin, Y. E.; Park, J.; Lee, Y.; Kim, M. P.; Kim, Y. R.; Na, S.; Ghosh, S.
46 K.; Ko, H., Ferroelectric Multilayer Nanocomposites with Polarization and Stress
47
48
49
50
51
52
53
54
55
56
57
58
59
60

1
2
3
4
5 Concentration Structures for Enhanced Triboelectric Performances. *ACS Nano* **2020**, *14* (6),
6 7101-7110.

7
8 (288) Pu, X.; Zha, J.-W.; Zhao, C.-L.; Gong, S.-B.; Gao, J.-F.; Li, R. K. Y., Flexible
9 PVDF/nylon-11 electrospun fibrous membranes with aligned ZnO nanowires as potential
10 triboelectric nanogenerators. *Chem. Eng. J.* **2020**, *398*, 125526-125534.

11
12 (289) Cao, V. A.; Lee, S.; Kim, M.; Alam, M. M.; Park, P.; Nah, J., Output power density
13 enhancement of triboelectric nanogenerators via ferroelectric polymer composite interfacial
14 layers. *Nano Energy* **2020**, *67*, 104300-104307.

15
16 (290) Kuang, X.; Gao, Q.; Zhu, H., Effect of calcination temperature of TiO₂ on the
17 crystallinity and the permittivity of PVDF-TrFE/TiO₂ composites. *J. Appl. Polym. Sci.* **2013**,
18 *129*(1), 296-300.

19
20 (291) Wu, L.; Jing, M.; Liu, Y.; Ning, H.; Liu, X.; Liu, S.; Lin, L.; Hu, N.; Liu, L., Power
21 generation by PVDF-TrFE/graphene nanocomposite films. *Compos. B. Eng.* **2019**, *164*, 703-
22 709.

23
24 (292) Wang, S.; Shao, H.-Q.; Liu, Y.; Tang, C.-Y.; Zhao, X.; Ke, K.; Bao, R.-Y.; Yang,
25 M.-B.; Yang, W., Boosting piezoelectric response of PVDF-TrFE *via* MXene for self-
26 powered linear pressure sensor. *Compos. Sci. Technol.* **2021**, *202*, 108600-108607.

27
28 (293) Wu, H.; He, W.; Shan, C.; Wang, Z.; Fu, S.; Tang, Q.; Guo, H.; Du, Y.; Liu, W.;
29 Hu, C., Achieving Remarkable Charge Density via Self-Polarization of Polar High-k Material
30 in a Charge-Excitation Triboelectric Nanogenerator. *Adv. Mater.* **2022**, *34* (13), 2109918-
31 2109927.

32
33 (294) Chamankar, N.; Khajavi, R.; Yousefi, A. A.; Rashidi, A.; Golestanifard, F., An
34 experimental model for predicting the piezo and dielectric constant of PVDF-PZT
35 nanocomposite fibers with 0–3 and 1–3 connectivity. *Ceram. Int.* **2020**, *46* (15), 23567-
36 23581.

37
38 (295) Ippili, S.; Jella, V.; Eom, S.; Hong, S.; Yoon, S. G., Light-Driven Piezo- and
39 Triboelectricity in Organic-Inorganic Metal Trihalide Perovskite toward Mechanical Energy
40 Harvesting and Self-powered Sensor Application. *ACS Appl. Mater. Interfaces* **2020**, *12* (45),
41 50472-50483.

42
43 (296) Jella, V.; Ippili, S.; Eom, J.-H.; Choi, J.; Yoon, S.-G., Enhanced output performance
44 of a flexible piezoelectric energy harvester based on stable MAPbI₃-PVDF composite films.
45 *Nano Energy* **2018**, *53*, 46-56.

- (297) Vacche, S. D.; Oliveira, F.; Leterrier, Y.; Michaud, V.; Damjanovic, D.; Månson, J.-A. E., The effect of processing conditions on the morphology, thermomechanical, dielectric, and piezoelectric properties of P(VDF-TrFE)/BaTiO₃ composites. *J. Mater. Sci.* **2012**, *47* (11), 4763-4774.
- (298) Zhou, T.; Zha, J. W.; Cui, R. Y.; Fan, B. H.; Yuan, J. K.; Dang, Z. M., Improving Dielectric Properties of BaTiO₃/Ferroelectric Polymer Composites by Employing Surface Hydroxylated BaTiO₃ Nanoparticles. *ACS Appl. Mater. Interfaces* **2011**, *3* (7), 2184-2188.
- (299) Guo, H.; Ma, C.; Liu, X.; Tan, X., Electrical poling below coercive field for large piezoelectricity. *Appl. Phys. Lett.* **2013**, *102* (9), 092902-092905.
- (300) Granzow, T.; Kouna, A. B.; Aulbach, E.; Rödel, J., Electromechanical poling of piezoelectrics. *Appl. Phys. Lett.* **2006**, *88* (25), 252907-252909.
- (301) Wu, J.; Xiao, D.; Wu, W.; Chen, Q.; Zhu, J.; Yang, Z.; Wang, J., Composition and poling condition-induced electrical behavior of (Ba_{0.85}Ca_{0.15})(Ti_{1-x}Zr_x)O₃ lead-free piezoelectric ceramics. *J. Eur. Ceram. Soc.* **2012**, *32* (4), 891-898.
- (302) Kamel, T. M.; de With, G., Poling of hard ferroelectric PZT ceramics. *J. Eur. Ceram. Soc.* **2008**, *28* (9), 1827-1838.
- (303) Bai, P.; Zhu, G.; Zhou, Y. S.; Wang, S.; Ma, J.; Zhang, G.; Wang, Z. L., Dipole-moment-induced effect on contact electrification for triboelectric nanogenerators. *Nano Res.* **2014**, *7* (7), 990-997.
- (304) Shin, K. S.; Kim, T. Y.; Yoon, G. C.; Gupta, M. K.; Kim, S. K.; Seung, W.; Kim, H.; Kim, S.; Kim, S.; Kim, S. W., Ferroelectric coupling effect on the energy-band structure of hybrid heterojunctions with self-organized P(VDF-TrFE) nanomatrices. *Adv. Mater.* **2014**, *26* (32), 5619-5625.
- (305) Cui, N.; Gu, L.; Lei, Y.; Liu, J.; Qin, Y.; Ma, X.; Hao, Y.; Wang, Z. L., Dynamic behavior of the triboelectric charges and structural optimization of the friction layer for a triboelectric nanogenerator. *ACS nano* **2016**, *10* (6), 6131-6138.
- (306) Kornfeld, M., Frictional electrification. *Journal of Physics D: Applied Physics* **1976**, *9* (8), 1183.
- (307) Chen, G.; Xu, Z., Charge trapping and detrapping in polymeric materials. *Journal of Applied Physics* **2009**, *106* (12), 123707.
- (308) Li, J.; Zhou, F.; Min, D.; Li, S.; Xia, R., The energy distribution of trapped charges in polymers based on isothermal surface potential decay model. *IEEE Transactions on Dielectrics and Electrical Insulation* **2015**, *22* (3), 1723-1732.

- 1
2
3
4
5 (309) Kim, Y. W.; Lee, H. B.; Yoon, J.; Park, S.-H., 3D customized triboelectric
6 nanogenerator with high performance achieved via charge-trapping effect and strain-
7 mismatching friction. *Nano Energy* **2022**, *95*, 107051.
- 8
9 (310) Wu, C.; Kim, T. W.; Choi, H. Y., Reduced graphene-oxide acting as electron-
10 trapping sites in the friction layer for giant triboelectric enhancement. *Nano Energy* **2017**, *32*,
11 542-550.
- 12
13 (311) Jiang, H.; Lei, H.; Wen, Z.; Shi, J.; Bao, D.; Chen, C.; Jiang, J.; Guan, Q.; Sun, X.;
14 Lee, S.-T., Charge-trapping-blocking layer for enhanced triboelectric nanogenerators. *Nano*
15 *Energy* **2020**, *75*, 105011.
- 16
17 (312) Hwang, H. J.; Hong, H.; Cho, B. G.; Lee, H. K.; Kim, J. S.; Lee, U. J.; Kim, W.;
18 Kim, H.; Chung, K.-B.; Choi, D., Band well structure with localized states for enhanced
19 charge accumulation on Triboelectrification. *Nano Energy* **2021**, *90*, 106647.
- 20
21 (313) Li, Z.; Zhu, M.; Qiu, Q.; Yu, J.; Ding, B., Multilayered fiber-based triboelectric
22 nanogenerator with high performance for biomechanical energy harvesting. *Nano Energy*
23 **2018**, *53*, 726-733.
- 24
25 (314) Chen, X.; Liu, Y.; Sun, Y.; Zhao, T.; Zhao, C.; Khattab, T. A.; Lim, E. G.; Sun, X.;
26 Wen, Z., Electron trapping & blocking effect enabled by MXene/TiO₂ intermediate layer for
27 charge regulation of triboelectric nanogenerators. *Nano Energy* **2022**, *98*, 107236.
- 28
29 (315) Salauddin, M.; Rana, S. S.; Sharifuzzaman, M.; Lee, S. H.; Zahed, M. A.; Do Shin,
30 Y.; Seonu, S.; Song, H. S.; Bhatta, T.; Park, J. Y., Laser-carbonized MXene/ZiF-67
31 nanocomposite as an intermediate layer for boosting the output performance of fabric-based
32 triboelectric nanogenerator. *Nano Energy* **2022**, 107462.
- 33
34 (316) Hwang, H. J.; Choi, D., The coupled effects of an electron blocking layer beneath
35 tribomaterials for boosted triboelectric nanogenerators. *Functional Composites and Structures*
36 **2021**, *3*(2), 025004.
- 37
38 (317) Xin, C.; Li, Z.; Zhang, Q.; Peng, Y.; Guo, H.; Xie, S., Investigating the output
39 performance of Triboelectric Nanogenerators with Single/Double-sided interlayer. *Nano*
40 *Energy* **2022**, 107448.
- 41
42 (318) Kim, W.; Park, J. H.; Hwang, H. J.; Rim, Y. S.; Choi, D., Interfacial molecular
43 engineering for enhanced polarization of negative tribo-materials. *Nano Energy* **2022**, *96*,
44 107110.
- 45
46 (319) Richardson, J. J.; Cui, J.; Bjornmalm, M.; Braunger, J. A.; Ejima, H.; Caruso, F.,
47 Innovation in layer-by-layer assembly. *Chemical reviews* **2016**, *116*(23), 14828-14867.
- 48
49
50
51
52
53
54
55
56
57
58
59
60

- 1
2
3
4
5 (320) Decher, G.; Hong, J. D. In *Buildup of ultrathin multilayer films by a self-assembly*
6 *process, 1 consecutive adsorption of anionic and cationic bipolar amphiphiles on charged*
7 *surfaces*, Makromolekulare Chemie. Macromolecular Symposia, Wiley Online Library: 1991;
8 pp 321-327.
9
10
11 (321) Menge, H. G.; Huynh, N. D.; Cho, C.; Choi, D.; Park, Y. T., Designable functional
12 polymer nanocomposites via layer-by-layer assembly for highly deformable power-boosted
13 triboelectric nanogenerators. *Composites Part B: Engineering* **2022**, *230*, 109513.
14
15 (322) Guo, X.; Helseth, L., Layer-by-layer polyelectrolyte films for contact electric energy
16 harvesting. *Journal of Physics D: Applied Physics* **2015**, *48* (7), 075302.
17
18 (323) Chung, I. J.; Kim, W.; Jang, W.; Park, H.-W.; Sohn, A.; Chung, K.-B.; Kim, D.-W.;
19 Choi, D.; Park, Y. T., Layer-by-layer assembled graphene multilayers on multidimensional
20 surfaces for highly durable, scalable, and wearable triboelectric nanogenerators. *Journal of*
21 *Materials Chemistry A* **2018**, *6* (7), 3108-3115.
22
23 (324) Lee, S.; Song, Y.; Ko, Y.; Ko, Y.; Ko, J.; Kwon, C. H.; Huh, J.; Kim, S. W.; Yeom,
24 B.; Cho, J., A Metal-Like Conductive Elastomer with a Hierarchical Wrinkled Structure.
25 *Advanced Materials* **2020**, *32* (7), 1906460.
26
27 (325) Huang, L.-B.; Han, J.-C.; Chen, S.; Sun, Z.; Dai, X.; Ge, P.; Zhao, C.-H.; Zheng, Q.-
28 Q.; Sun, F.-C.; Hao, J., 4D-printed self-recovered triboelectric nanogenerator for energy
29 harvesting and self-powered sensor. *Nano Energy* **2021**, *84*, 105873.
30
31 (326) Xu, W.; Huang, L.-B.; Hao, J., Fully self-healing and shape-tailorable triboelectric
32 nanogenerators based on healable polymer and magnetic-assisted electrode. *Nano Energy*
33 **2017**, *40*, 399-407.
34
35 (327) Xu, W.; Wong, M.-C.; Guo, Q.; Jia, T.; Hao, J., Healable and shape-memory dual
36 functional polymers for reliable and multipurpose mechanical energy harvesting devices.
37 *Journal of Materials Chemistry A* **2019**, *7* (27), 16267-16276.
38
39 (328) Xu, W.; Wong, M.-C.; Hao, J., Strategies and progress on improving robustness and
40 reliability of triboelectric nanogenerators. *Nano Energy* **2019**, *55*, 203-215.
41
42 (329) Dzhardimalieva, G. I.; Yadav, B. C.; Uflyand, I. E.; Oliva González, C. M.;
43 Kharisov, B. I.; Kharissova, O. V.; García, B. O., A review on the polymers with shape
44 memory assisted self-healing properties for triboelectric nanogenerators. *Journal of Materials*
45 *Research* **2021**, *36* (6), 1225-1240.
46
47
48
49
50
51
52
53
54
55
56
57
58
59
60

- 1
2
3
4
5 (330) Alabiso, W.; Hron, T. M.; Reisinger, D.; Bautista-Anguís, D.; Schlögl, S., Shape
6 memory-assisted self-healing of dynamic thiol-acrylate networks. *Polymer Chemistry* **2021**,
7 *12* (39), 5704-5714.
8
9 (331) Yang, Y.; Urban, M. W., Self-healing polymeric materials. *Chemical Society*
10 *Reviews* **2013**, *42* (17), 7446-7467.
11
12 (332) Thakur, V. K.; Kessler, M. R., Self-healing polymer nanocomposite materials: A
13 review. *Polymer* **2015**, *69*, 369-383.
14
15 (333) Terryn, S.; Langenbach, J.; Roels, E.; Brancart, J.; Bakkali-Hassani, C.; Poutrel, Q.-
16 A.; Georgopoulou, A.; George Thuruthel, T.; Safaei, A.; Ferrentino, P.; Sebastian, T.;
17 Norvez, S.; Iida, F.; Bosman, A. W.; Tournilhac, F.; Clemens, F.; Van Assche, G.;
18 Vanderborght, B., A review on self-healing polymers for soft robotics. *Materials Today* **2021**,
19 *47*, 187-205.
20
21 (334) Willocq, B.; Odent, J.; Dubois, P.; Raquez, J.-M., Advances in intrinsic self-healing
22 polyurethanes and related composites. *Rsc Adv* **2020**, *10* (23), 13766-13782.
23
24 (335) Luo, N.; Feng, Y.; Wang, D.; Zheng, Y.; Ye, Q.; Zhou, F.; Liu, W., New Self-
25 Healing Triboelectric Nanogenerator Based on Simultaneous Repair Friction Layer and
26 Conductive Layer. *ACS Applied Materials & Interfaces* **2020**, *12* (27), 30390-30398.
27
28 (336) Dai, X.; Huang, L.-B.; Du, Y.; Han, J.; Zheng, Q.; Kong, J.; Hao, J., Self-Healing,
29 Flexible, and Tailorable Triboelectric Nanogenerators for Self-Powered Sensors based on
30 Thermal Effect of Infrared Radiation. *Advanced Functional Materials* **2020**, *30* (16),
31 1910723.
32
33 (337) Sun, J.; Pu, X.; Liu, M.; Yu, A.; Du, C.; Zhai, J.; Hu, W.; Wang, Z. L., Self-
34 Healable, Stretchable, Transparent Triboelectric Nanogenerators as Soft Power Sources. *ACS*
35 *Nano* **2018**, *12* (6), 6147-6155.
36
37 (338) Gao, G.; Yang, F.; Zhou, F.; He, J.; Lu, W.; Xiao, P.; Yan, H.; Pan, C.; Chen, T.;
38 Wang, Z. L., Bioinspired Self-Healing Human–Machine Interactive Touch Pad with
39 Pressure-Sensitive Adhesiveness on Targeted Substrates. *Advanced Materials* **2020**, *32* (50),
40 2004290.
41
42 (339) Li, X.; Xiang, S.; Ling, D.; Zhang, S.; Li, C.; Dai, R.; Zhu, P.; Liu, X.; Pan, Z.,
43 Stretchable, self-healing, transparent macromolecular elastomeric gel and PAM/carrageenan
44 hydrogel for self-powered touch sensors. *Materials Science and Engineering B* **2022**, *283*,
45 115832.
46
47
48
49
50
51
52
53
54
55
56
57
58
59
60

- 1
2
3
4
5 (340) Huang, L.-B.; Dai, X.; Sun, Z.; Wong, M.-C.; Pang, S.-Y.; Han, J.; Zheng, Q.; Zhao,
6 C.-H.; Kong, J.; Hao, J., Environment-resisted flexible high performance triboelectric
7 nanogenerators based on ultrafast self-healing non-drying conductive organohydrogel. *Nano*
8 *Energy* **2021**, *82*, 105724.
9
10
11 (341) Dai, X.; Huang, L.-B.; Sun, Z.; Du, Y.; Xue, B.; Wong, M.-C.; Han, J.; Liang, Q.;
12 Wu, Y.; Dong, B.; Kong, J.; Hao, J., A phonic Braille recognition system based on a self-
13 powered sensor with self-healing ability, temperature resistance, and stretchability. *Materials*
14 *Horizons* **2022**.
15
16
17 (342) Zhang, P.; Guo, W.; Guo, Z. H.; Ma, Y.; Gao, L.; Cong, Z.; Zhao, X. J.; Qiao, L.;
18 Pu, X.; Wang, Z. L., Dynamically Crosslinked Dry Ion-Conducting Elastomers for Soft
19 Iontronics. *Advanced Materials* **2021**, *33* (31), 2101396.
20
21
22 (343) Li, G.; Li, L.; Zhang, P.; Chang, C.; Xu, F.; Pu, X., Ultra-stretchable and healable
23 hydrogel-based triboelectric nanogenerators for energy harvesting and self-powered sensing.
24 *Rsc Adv* **2021**, *11* (28), 17437-17444.
25
26
27 (344) Nevejans, S.; Ballard, N.; Fernández, M.; Reck, B.; García, S. J.; Asua, J. M., The
28 challenges of obtaining mechanical strength in self-healing polymers containing dynamic
29 covalent bonds. *Polymer* **2019**, *179*, 121670.
30
31
32 (345) Yoshie, N.; Yoshida, S.; Matsuoka, K., Self-healing of biobased furan polymers:
33 Recovery of high mechanical strength by mild heating. *Polymer Degradation and Stability*
34 **2019**, *161*, 13-18.
35
36
37 (346) Lai, Y.-C.; Wu, H.-M.; Lin, H.-C.; Chang, C.-L.; Chou, H.-H.; Hsiao, Y.-C.; Wu,
38 Y.-C., Entirely, Intrinsically, and Autonomously Self-Healable, Highly Transparent, and
39 Superstretchable Triboelectric Nanogenerator for Personal Power Sources and Self-Powered
40 Electronic Skins. *Advanced Functional Materials* **2019**, *29* (40), 1904626.
41
42
43 (347) Liu, P.; Sun, N.; Mi, Y.; Luo, X.; Dong, X.; Cai, J.; Jia, X.; Ramos, M. A.; Hu, T.
44 S.; Xu, Q., Ultra-low CNTs filled high-performance fast self-healing triboelectric
45 nanogenerators for wearable electronics. *Compos Sci Technol* **2021**, *208*, 108733.
46
47
48 (348) Du, Y.; Wang, X.; Dai, X.; Lu, W.; Tang, Y.; Kong, J., Ultraflexible, highly
49 efficient electromagnetic interference shielding, and self-healable triboelectric nanogenerator
50 based on Ti₃C₂T_x MXene for self-powered wearable electronics. *Journal of Materials*
51 *Science & Technology* **2022**, *100*, 1-11.
52
53
54 (349) Chen, H.; Koh, J. J.; Liu, M.; Li, P.; Fan, X.; Liu, S.; Yeo, J. C. C.; Tan, Y.; Tee, B.
55 C. K.; He, C., Super Tough and Self-Healable Poly(dimethylsiloxane) Elastomer via
56
57
58
59
60

Hydrogen Bonding Association and Its Applications as Triboelectric Nanogenerators. *ACS Applied Materials & Interfaces* **2020**, *12*(28), 31975-31983.

(350) Guan, Q.; Dai, Y.; Yang, Y.; Bi, X.; Wen, Z.; Pan, Y., Near-infrared irradiation induced remote and efficient self-healable triboelectric nanogenerator for potential implantable electronics. *Nano Energy* **2018**, *51*, 333-339.

(351) Patel, T.; Kim, M. P.; Park, J.; Lee, T. H.; Nallepalli, P.; Noh, S. M.; Jung, H. W.; Ko, H.; Oh, J. K., Self-Healable Reprocessable Triboelectric Nanogenerators Fabricated with Vitrimeric Poly(hindered Urea) Networks. *ACS Nano* **2020**, *14*(9), 11442-11451.

(352) Jia, Y.; Zhang, L.; Qin, M.; Li, Y.; Gu, S.; Guan, Q.; You, Z., Highly efficient self-healable and robust fluorinated polyurethane elastomer for wearable electronics. *Chemical Engineering Journal* **2022**, *430*, 133081.

(353) Liu, R.; Lai, Y.; Li, S.; Wu, F.; Shao, J.; Liu, D.; Dong, X.; Wang, J.; Wang, Z. L., Ultrathin, transparent, and robust self-healing electronic skins for tactile and non-contact sensing. *Nano Energy* **2022**, *95*, 107056.

(354) Lee, J. H.; Hinchet, R.; Kim, S. K.; Kim, S.; Kim, S.-W., Shape memory polymer-based self-healing triboelectric nanogenerator. *Energy & Environmental Science* **2015**, *8*(12), 3605-3613.

(355) Parida, K.; Thangavel, G.; Cai, G.; Zhou, X.; Park, S.; Xiong, J.; Lee, P. S., Extremely stretchable and self-healing conductor based on thermoplastic elastomer for all-three-dimensional printed triboelectric nanogenerator. *Nature communications* **2019**, *10*(1), 1-9.

(356) Yang, D.; Ni, Y.; Kong, X.; Li, S.; Chen, X.; Zhang, L.; Wang, Z. L., Self-healing and elastic triboelectric nanogenerators for muscle motion monitoring and photothermal treatment. *ACS nano* **2021**, *15*(9), 14653-14661.

(357) Lee, J. P.; Ye, B. U.; Kim, K. N.; Lee, J. W.; Choi, W. J.; Baik, J. M., 3D printed noise-cancelling triboelectric nanogenerator. *Nano Energy* **2017**, *38*, 377-384.

(358) Kim, S.; Kim, T. Y.; Lee, K. H.; Kim, T.-H.; Cimini, F. A.; Kim, S. K.; Hinchet, R.; Kim, S.-W.; Falconi, C., Rewritable ghost floating gates by tunnelling triboelectrification for two-dimensional electronics. *Nature Communications* **2017**, *8*(1), 1-7.

(359) Kim, J.-N.; Lee, J.; Go, T. W.; Rajabi-Abhari, A.; Mahato, M.; Park, J. Y.; Lee, H.; Oh, I.-K., Skin-attachable and biofriendly chitosan-diatom triboelectric nanogenerator. *Nano Energy* **2020**, *75*, 104904.

- 1
2
3
4
5 (360) Peng, X.; Dong, K.; Ye, C.; Jiang, Y.; Zhai, S.; Cheng, R.; Liu, D.; Gao, X.; Wang,
6 J.; Wang, Z. L., A breathable, biodegradable, antibacterial, and self-powered electronic skin
7 based on all-nanofiber triboelectric nanogenerators. *Science Advances* **2020**, *6* (26),
8 eaba9624.
9
10
11 (361) Hu, S.; Han, J.; Shi, Z.; Chen, K.; Xu, N.; Wang, Y.; Zheng, R.; Tao, Y.; Sun, Q.;
12 Wang, Z. L., Biodegradable, Super-Strong, and Conductive Cellulose Macrofibers for Fabric-
13 Based Triboelectric Nanogenerator. *Nano-micro letters* **2022**, *14* (1), 1-20.
14
15 (362) Guo, Y.; Zhang, X.-S.; Wang, Y.; Gong, W.; Zhang, Q.; Wang, H.; Brugger, J., All-
16 fiber hybrid piezoelectric-enhanced triboelectric nanogenerator for wearable gesture
17 monitoring. *Nano Energy* **2018**, *48*, 152-160.
18
19 (363) Wang, R.; Mu, L.; Bao, Y.; Lin, H.; Ji, T.; Shi, Y.; Zhu, J.; Wu, W., Holistically
20 engineered polymer–polymer and polymer–ion interactions in biocompatible polyvinyl
21 alcohol blends for high-performance triboelectric devices in self-powered wearable
22 cardiovascular monitorings. *Advanced Materials* **2020**, *32* (32), 2002878.
23
24 (364) Mariello, M.; Fachechi, L.; Guido, F.; De Vittorio, M., Conformal, Ultra-thin
25 Skin-Contact-Actuated Hybrid Piezo/Triboelectric Wearable Sensor Based on AlN and
26 Parylene-Encapsulated Elastomeric Blend. *Advanced Functional Materials* **2021**, *31* (27),
27 2101047.
28
29 (365) Yao, G.; Kang, L.; Li, J.; Long, Y.; Wei, H.; Ferreira, C. A.; Jeffery, J. J.; Lin, Y.;
30 Cai, W.; Wang, X., Effective weight control via an implanted self-powered vagus nerve
31 stimulation device. *Nature communications* **2018**, *9* (1), 1-10.
32
33 (366) Zheng, Q.; Zou, Y.; Zhang, Y.; Liu, Z.; Shi, B.; Wang, X.; Jin, Y.; Ouyang, H.; Li,
34 Z.; Wang, Z. L., Biodegradable triboelectric nanogenerator as a life-time designed
35 implantable power source. *Science advances* **2016**, *2* (3), e1501478.
36
37 (367) Li, Z.; Feng, H.; Zheng, Q.; Li, H.; Zhao, C.; Ouyang, H.; Noreen, S.; Yu, M.; Su,
38 F.; Liu, R., Photothermally tunable biodegradation of implantable triboelectric
39 nanogenerators for tissue repairing. *Nano Energy* **2018**, *54*, 390-399.
40
41 (368) Bettinger, C. J.; Bao, Z., Organic thin-film transistors fabricated on resorbable
42 biomaterial substrates. *Advanced materials* **2010**, *22* (5), 651-655.
43
44 (369) Qian, J.; He, J.; Qian, S.; Zhang, J.; Niu, X.; Fan, X.; Wang, C.; Hou, X.; Mu, J.;
45 Geng, W., A nonmetallic stretchable nylon-modified high performance triboelectric
46 nanogenerator for energy harvesting. *Advanced functional materials* **2020**, *30* (4), 1907414.
47
48
49
50
51
52
53
54
55
56
57
58
59
60

- 1
2
3
4
5 (370) Choi, Y. S.; Jing, Q.; Datta, A.; Boughey, C.; Kar-Narayan, S., A triboelectric
6 generator based on self-poled Nylon-11 nanowires fabricated by gas-flow assisted template
7 wetting. *Energy & Environmental Science* **2017**, *10*(10), 2180-2189.
- 8
9 (371) Feng, X.; Li, Q.; Wang, K., Waste plastic triboelectric nanogenerators using
10 recycled plastic bags for power generation. *ACS Applied Materials & Interfaces* **2020**, *13*(1),
11 400-410.
- 12
13 (372) Park, H.; Oh, S. J.; Kim, D.; Kim, M.; Lee, C.; Joo, H.; Woo, I.; Bae, J. W.; Lee, J.
14 H., Plasticized PVC-Gel Single Layer-Based Stretchable Triboelectric Nanogenerator for
15 Harvesting Mechanical Energy and Tactile Sensing. *Advanced Science* **2022**, 2201070.
- 16
17 (373) Su, Y.; Yang, Y.; Zhong, X.; Zhang, H.; Wu, Z.; Jiang, Y.; Wang, Z. L., Fully
18 enclosed cylindrical single-electrode-based triboelectric nanogenerator. *ACS applied*
19 *materials & interfaces* **2014**, *6*(1), 553-559.
- 20
21 (374) Zhang, H.; Yang, Y.; Su, Y.; Chen, J.; Adams, K.; Lee, S.; Hu, C.; Wang, Z. L.,
22 Triboelectric nanogenerator for harvesting vibration energy in full space and as self-powered
23 acceleration sensor. *Advanced Functional Materials* **2014**, *24*(10), 1401-1407.
- 24
25 (375) Wang, M.; Zhang, N.; Tang, Y.; Zhang, H.; Ning, C.; Tian, L.; Li, W.; Zhang, J.;
26 Mao, Y.; Liang, E., Single-electrode triboelectric nanogenerators based on sponge-like
27 porous PTFE thin films for mechanical energy harvesting and self-powered electronics.
28 *Journal of Materials Chemistry A* **2017**, *5*(24), 12252-12257.
- 29
30 (376) Dudem, B.; Kim, D. H.; Mule, A. R.; Yu, J. S., Enhanced performance of
31 microarchitected PTFE-based triboelectric nanogenerator via simple thermal imprinting
32 lithography for self-powered electronics. *ACS applied materials & interfaces* **2018**, *10*(28),
33 24181-24192.
- 34
35 (377) Sankar, P. R.; Supraja, P.; Mishra, S.; Prakash, K.; Kumar, R. R.; Haranath, D., A
36 novel triboelectric nanogenerator based on only food packaging aluminium foils. *Materials*
37 *Letters* **2022**, *310*, 131474.
- 38
39 (378) Liu, C.; Li, J.; Che, L.; Chen, S.; Wang, Z.; Zhou, X., Toward large-scale
40 fabrication of triboelectric nanogenerator (TENG) with silk-fibroin patches film via spray-
41 coating process. *Nano Energy* **2017**, *41*, 359-366.
- 42
43 (379) Niu, Q.; Huang, L.; Lv, S.; Shao, H.; Fan, S.; Zhang, Y., Pulse-driven bio-
44 triboelectric nanogenerator based on silk nanoribbons. *Nano Energy* **2020**, *74*, 104837.
- 45
46 (380) Zhang, X.-S.; Brugger, J.; Kim, B., A silk-fibroin-based transparent triboelectric
47 generator suitable for autonomous sensor network. *Nano Energy* **2016**, *20*, 37-47.
- 48
49
50
51
52
53
54
55
56
57
58
59
60

- 1
2
3
4
5 (381) Kim, H. J.; Kim, J. H.; Jun, K. W.; Kim, J. H.; Seung, W. C.; Kwon, O. H.; Park, J.
6 Y.; Kim, S. W.; Oh, I. K., Silk nanofiber-networked bio-triboelectric generator: silk bio-TEG.
7 *Advanced Energy Materials* **2016**, *6*(8), 1502329.
8
9 (382) Wang, R.; Gao, S.; Yang, Z.; Li, Y.; Chen, W.; Wu, B.; Wu, W., Engineered and
10 laser-processed chitosan biopolymers for sustainable and biodegradable triboelectric power
11 generation. *Advanced Materials* **2018**, *30*(11), 1706267.
12
13 (383) Jao, Y.-T.; Yang, P.-K.; Chiu, C.-M.; Lin, Y.-J.; Chen, S.-W.; Choi, D.; Lin, Z.-H.,
14 A textile-based triboelectric nanogenerator with humidity-resistant output characteristic and
15 its applications in self-powered healthcare sensors. *Nano Energy* **2018**, *50*, 513-520.
16
17 (384) Ma, C.; Gao, S.; Gao, X.; Wu, M.; Wang, R.; Wang, Y.; Tang, Z.; Fan, F.; Wu, W.;
18 Wan, H., Chitosan biopolymer-derived self-powered triboelectric sensor with optimized
19 performance through molecular surface engineering and data-driven learning. *InfoMat* **2019**,
20 *1*(1), 116-125.
21
22 (385) Fan, C.; Huang, J.; Mensah, A.; Long, Z.; Sun, J.; Wei, Q., A high-performance and
23 biodegradable tribopositive poly- ϵ -caprolactone/ethyl cellulose material. *Cell Reports*
24 *Physical Science* **2022**, *3*(8), 101012.
25
26 (386) Wang, T.; Li, S.; Tao, X.; Yan, Q.; Wang, X.; Chen, Y.; Huang, F.; Li, H.; Chen,
27 X.; Bian, Z., Fully biodegradable water-soluble triboelectric nanogenerator for human
28 physiological monitoring. *Nano Energy* **2022**, *93*, 106787.
29
30 (387) He, X.; Zou, H.; Geng, Z.; Wang, X.; Ding, W.; Hu, F.; Zi, Y.; Xu, C.; Zhang, S. L.;
31 Yu, H., A hierarchically nanostructured cellulose fiber-based triboelectric nanogenerator for
32 self-powered healthcare products. *Advanced Functional Materials* **2018**, *28*(45), 1805540.
33
34 (388) Zhang, R.; Dahlström, C.; Zou, H.; Jonzon, J.; Hummelgård, M.; Örtengren, J.;
35 Blomquist, N.; Yang, Y.; Andersson, H.; Olsen, M., Cellulose-based fully green triboelectric
36 nanogenerators with output power density of 300 W m⁻². *Advanced Materials* **2020**, *32*
37 (38), 2002824.
38
39 (389) Wu, H.; Chen, Z.; Xu, G.; Xu, J.; Wang, Z.; Zi, Y., Fully biodegradable water
40 droplet energy harvester based on leaves of living plants. *ACS Applied Materials &*
41 *Interfaces* **2020**, *12*(50), 56060-56067.
42
43 (390) Feng, Y.; Zhang, L.; Zheng, Y.; Wang, D.; Zhou, F.; Liu, W., Leaves based
44 triboelectric nanogenerator (TEG) and TENG tree for wind energy harvesting. *Nano Energy*
45 **2019**, *55*, 260-268.
46
47
48
49
50
51
52
53
54
55
56
57
58
59
60

- 1
2
3
4
5 (391) Ma, P.; Zhu, H.; Lu, H.; Zeng, Y.; Zheng, N.; Wang, Z. L.; Cao, X., Design of
6 biodegradable wheat-straw based triboelectric nanogenerator as self-powered sensor for wind
7 detection. *Nano Energy* **2021**, *86*, 106032.
- 8
9
10 (392) Han, Y.; Han, Y.; Zhang, X.; Li, L.; Zhang, C.; Liu, J.; Lu, G.; Yu, H.-D.; Huang,
11 W., Fish gelatin based triboelectric nanogenerator for harvesting biomechanical energy and
12 self-powered sensing of human physiological signals. *ACS applied materials & interfaces*
13 **2020**, *12*(14), 16442-16450.
- 14
15
16 (393) Pan, R.; Xuan, W.; Chen, J.; Dong, S.; Jin, H.; Wang, X.; Li, H.; Luo, J., Fully
17 biodegradable triboelectric nanogenerators based on electrospun polylactic acid and
18 nanostructured gelatin films. *Nano Energy* **2018**, *45*, 193-202.
- 19
20
21 (394) Park, I. W.; Choi, J.; Kim, K. Y.; Jeong, J.; Gwak, D.; Lee, Y.; Ahn, Y. H.; Choi, Y.
22 J.; Hong, Y. J.; Chung, W.-J., Vertically aligned cyclo-phenylalanine peptide nanowire-based
23 high-performance triboelectric energy generator. *Nano Energy* **2019**, *57*, 737-745.
- 24
25
26 (395) Chen, C.-H.; Tsao, Y.-H.; Lin, Z.-H., Development of biocompatible triboelectric
27 nanogenerators by using polypeptides as the contact materials. *ECS Transactions* **2016**, *72*
28 (6), 61.
- 29
30
31 (396) Mao, Y.; Zhang, N.; Tang, Y.; Wang, M.; Chao, M.; Liang, E., A paper triboelectric
32 nanogenerator for self-powered electronic systems. *Nanoscale* **2017**, *9*(38), 14499-14505.
- 33
34
35 (397) Zhang, X.-S.; Su, M.; Brugger, J.; Kim, B., Penciling a triboelectric nanogenerator
36 on paper for autonomous power MEMS applications. *Nano Energy* **2017**, *33*, 393-401.
- 37
38
39 (398) Jang, S.; Kim, H.; Oh, J. H., Simple and rapid fabrication of pencil-on-paper
40 triboelectric nanogenerators with enhanced electrical performance. *Nanoscale* **2017**, *9*(35),
41 13034-13041.
- 42
43
44 (399) Jiang, W.; Li, H.; Liu, Z.; Li, Z.; Tian, J.; Shi, B.; Zou, Y.; Ouyang, H.; Zhao, C.;
45 Zhao, L., Fully bioabsorbable natural-materials-based triboelectric nanogenerators. *Advanced*
46 *Materials* **2018**, *30*(32), 1801895.
- 47
48
49 (400) Luo, J.; Wang, Z.; Xu, L.; Wang, A. C.; Han, K.; Jiang, T.; Lai, Q.; Bai, Y.; Tang,
50 W.; Fan, F. R., Flexible and durable wood-based triboelectric nanogenerators for self-
51 powered sensing in athletic big data analytics. *Nature communications* **2019**, *10*(1), 1-9.
- 52
53
54 (401) Pang, Y.; Xi, F.; Luo, J.; Liu, G.; Guo, T.; Zhang, C., An alginate film-based
55 degradable triboelectric nanogenerator. *Rsc Adv* **2018**, *8*(12), 6719-6726.
- 56
57
58
59
60

- 1
2
3
4
5 (402) Sun, J.-G.; Yang, T. N.; Kuo, I.-S.; Wu, J.-M.; Wang, C.-Y.; Chen, L.-J., A leaf-
6 molded transparent triboelectric nanogenerator for smart multifunctional applications. *Nano*
7 *Energy* **2017**, *32*, 180-186.
- 8
9 (403) Liu, Z.; Ma, Y.; Ouyang, H.; Shi, B.; Li, N.; Jiang, D.; Xie, F.; Qu, D.; Zou, Y.;
10 Huang, Y., Transcatheter self-powered ultrasensitive endocardial pressure sensor. *Advanced*
11 *Functional Materials* **2019**, *29*(3), 1807560.
- 12
13 (404) Graham, S. A.; Patnam, H.; Manchi, P.; Paranjape, M. V.; Kurakula, A.; Yu, J. S.,
14 Biocompatible electrospun fibers-based triboelectric nanogenerators for energy harvesting
15 and healthcare monitoring. *Nano Energy* **2022**, *100*, 107455.
- 16
17 (405) Sardana, S.; Singh, Z.; Sharma, A. K.; Kaur, N.; Pati, P. K.; Mahajan, A., Self-
18 Powered Biocompatible Humidity Sensor Based on an Electrospun Anisotropic Triboelectric
19 Nanogenerator for Non-Invasive Diagnostic Applications. *Sensors and Actuators B:*
20 *Chemical* **2022**, 132507.
- 21
22 (406) Wu, Y.; Luo, Y.; Qu, J.; Daoud, W. A.; Qi, T., Nanogap and environmentally stable
23 triboelectric nanogenerators based on surface self-modified sustainable films. *ACS Applied*
24 *Materials & Interfaces* **2020**, *12*(49), 55444-55452.
- 25
26 (407) Le, T. H.; Mai, U. K. G.; Nguyen, H. T.; Luu, A. T.; Bui, V.-T., Surfactant-free GO-
27 PLA nanocomposite with honeycomb patterned surface for high power antagonistic bio-
28 triboelectric nanogenerator. *Journal of Science: Advanced Materials and Devices* **2022**, *7*(1),
29 100392.
- 30
31 (408) Mallineni, S. S. K.; Dong, Y.; Behlow, H.; Rao, A. M.; Podila, R., A wireless
32 triboelectric nanogenerator. *Advanced Energy Materials* **2018**, *8*(10), 1702736.
- 33
34 (409) Qiao, H.; Zhang, Y.; Huang, Z.; Wang, Y.; Li, D.; Zhou, H., 3D printing
35 individualized triboelectric nanogenerator with macro-pattern. *Nano Energy* **2018**, *50*, 126-
36 132.
- 37
38 (410) Song, Y.; Shi, Z.; Hu, G.-H.; Xiong, C.; Isogai, A.; Yang, Q., Recent advances in
39 cellulose-based piezoelectric and triboelectric nanogenerators for energy harvesting: a
40 review. *Journal of Materials Chemistry A* **2021**, *9*(4), 1910-1937.
- 41
42 (411) Nie, S.; Fu, Q.; Lin, X.; Zhang, C.; Lu, Y.; Wang, S., Enhanced performance of a
43 cellulose nanofibrils-based triboelectric nanogenerator by tuning the surface polarizability
44 and hydrophobicity. *Chemical Engineering Journal* **2021**, *404*, 126512.
- 45
46
47
48
49
50
51
52
53
54
55
56
57
58
59
60

- 1
2
3
4
5 (412) Graham, S. A.; Dudem, B.; Mule, A. R.; Patnam, H.; Yu, J. S., Engineering
6 squandered cotton into eco-benign microarchitected triboelectric films for sustainable and
7 highly efficient mechanical energy harvesting. *Nano Energy* **2019**, *61*, 505-516.
- 8
9 (413) Bai, Z.; Xu, Y.; Li, J.; Zhu, J.; Gao, C.; Zhang, Y.; Wang, J.; Guo, J., An eco-
10 friendly porous nanocomposite fabric-based triboelectric nanogenerator for efficient energy
11 harvesting and motion sensing. *ACS Applied Materials & Interfaces* **2020**, *12* (38), 42880-
12 42890.
- 13
14 (414) Adonijah Graham, S.; Dudem, B.; Patnam, H.; Mule, A. R.; Yu, J. S., Integrated
15 design of highly porous cellulose-loaded polymer-based triboelectric films toward flexible,
16 humidity-resistant, and sustainable mechanical energy harvesters. *ACS Energy Letters* **2020**,
17 *5*(7), 2140-2148.
- 18
19 (415) Oh, H.; Kwak, S. S.; Kim, B.; Han, E.; Lim, G. H.; Kim, S. W.; Lim, B., Highly
20 conductive ferroelectric cellulose composite papers for efficient triboelectric nanogenerators.
21 *Advanced Functional Materials* **2019**, *29*(37), 1904066.
- 22
23 (416) Pongampai, S.; Charoonsuk, T.; Pinpru, N.; Muanghlua, R.; Vittayakorn, W.;
24 Vittayakorn, N., High Performance Flexible Tribo/Piezoelectric Nanogenerators based on
25 BaTiO₃/Chitosan Composites. *Integrated Ferroelectrics* **2021**, *223*(1), 137-151.
- 26
27 (417) Khandelwal, G.; Joseph Raj, N. P. M.; Alluri, N. R.; Kim, S.-J., Enhancing
28 hydrophobicity of starch for biodegradable material-based triboelectric nanogenerators. *ACS*
29 *Sustainable Chemistry & Engineering* **2021**, *9*(27), 9011-9017.
- 30
31 (418) Zhang, X.-S.; Han, M.; Kim, B.; Bao, J.-F.; Brugger, J.; Zhang, H., All-in-one self-
32 powered flexible microsystems based on triboelectric nanogenerators. *Nano Energy* **2018**, *47*,
33 410-426.
- 34
35 (419) Wang, S.; Lin, L.; Xie, Y.; Jing, Q.; Niu, S.; Wang, Z. L., Sliding-triboelectric
36 nanogenerators based on in-plane charge-separation mechanism. *Nano letters* **2013**, *13* (5),
37 2226-2233.
- 38
39 (420) Lin, L.; Wang, S.; Xie, Y.; Jing, Q.; Niu, S.; Hu, Y.; Wang, Z. L., Segmentally
40 structured disk triboelectric nanogenerator for harvesting rotational mechanical energy. *Nano*
41 *letters* **2013**, *13*(6), 2916-2923.
- 42
43 (421) Bai, P.; Zhu, G.; Liu, Y.; Chen, J.; Jing, Q.; Yang, W.; Ma, J.; Zhang, G.; Wang, Z.
44 L., Cylindrical rotating triboelectric nanogenerator. *ACS nano* **2013**, *7*(7), 6361-6366.
45
46
47
48
49
50
51
52
53
54
55
56
57
58
59
60

- 1
2
3
4
5 (422) Meng, B.; Tang, W.; Too, Z.-h.; Zhang, X.; Han, M.; Liu, W.; Zhang, H., A
6 transparent single-friction-surface triboelectric generator and self-powered touch sensor.
7 *Energy & Environmental Science* **2013**, *6*(11), 3235-3240.
8
9 (423) Yang, Y.; Zhang, H.; Chen, J.; Jing, Q.; Zhou, Y. S.; Wen, X.; Wang, Z. L., Single-
10 electrode-based sliding triboelectric nanogenerator for self-powered displacement vector
11 sensor system. *Acs Nano* **2013**, *7*(8), 7342-7351.
12
13 (424) Yang, Y.; Zhang, H.; Lin, Z.-H.; Zhou, Y. S.; Jing, Q.; Su, Y.; Yang, J.; Chen, J.;
14 Hu, C.; Wang, Z. L., Human skin based triboelectric nanogenerators for harvesting
15 biomechanical energy and as self-powered active tactile sensor system. *ACS nano* **2013**, *7*
16 (10), 9213-9222.
17
18 (425) Wang, S.; Xie, Y.; Niu, S.; Lin, L.; Wang, Z. L., Freestanding
19 triboelectric-layer-based nanogenerators for harvesting energy from a moving object or
20 human motion in contact and non-contact modes. *Advanced materials* **2014**, *26* (18), 2818-
21 2824.
22
23 (426) Lin, L.; Wang, S.; Niu, S.; Liu, C.; Xie, Y.; Wang, Z. L., Noncontact free-rotating
24 disk triboelectric nanogenerator as a sustainable energy harvester and self-powered
25 mechanical sensor. *ACS applied materials & interfaces* **2014**, *6*(4), 3031-3038.
26
27 (427) Wang, Z.; Liu, W.; He, W.; Guo, H.; Long, L.; Xi, Y.; Wang, X.; Liu, A.; Hu, C.,
28 Ultrahigh electricity generation from low-frequency mechanical energy by efficient energy
29 management. *Joule* **2021**, *5*(2), 441-455.
30
31 (428) Wu, H.; Wang, S.; Wang, Z.; Zi, Y., Achieving ultrahigh instantaneous power
32 density of 10 MW/m² by leveraging the opposite-charge-enhanced transistor-like
33 triboelectric nanogenerator (OCT-TENG). *Nature communications* **2021**, *12*(1), 1-8.
34
35 (429) Chung, J.; Heo, D.; Shin, G.; Choi, D.; Choi, K.; Kim, D.; Lee, S., Ion-enhanced
36 field emission triboelectric nanogenerator. *Advanced Energy Materials* **2019**, *9* (37),
37 1901731.
38
39 (430) Yang, U. J.; Lee, J. W.; Lee, J. P.; Baik, J. M., Remarkable output power
40 enhancement of sliding-mode triboelectric nanogenerator through direct metal-to-metal
41 contact with the ground. *Nano Energy* **2019**, *57*, 293-299.
42
43 (431) Kim, J.; Cho, H.; Han, M.; Jung, Y.; Kwak, S. S.; Yoon, H. J.; Park, B.; Kim, H.;
44 Kim, H.; Park, J., Ultrahigh power output from triboelectric nanogenerator based on serrated
45 electrode via spark discharge. *Advanced Energy Materials* **2020**, *10*(44), 2002312.
46
47
48
49
50
51
52
53
54
55
56
57
58
59
60

- 1
2
3
4
5 (432) Zhang, Q.; Li, Y.; Cai, H.; Yao, M.; Zhang, H.; Guo, L.; Lv, Z.; Li, M.; Lu, X.; Ren,
6 C., A Single-Droplet Electricity Generator Achieves an Ultrahigh Output Over 100 V
7 Without Pre-Charging. *Advanced Materials* **2021**, *33* (51), 2105761.
- 8
9 (433) Fan, F. R.; Tian, Z.-q., Droplet-based nanogenerators for energy harvesting and self-
10 powered sensing. *Nanoscale* **2021**.
- 11
12 (434) Wu, H.; Mendel, N.; van Der Ham, S.; Shui, L.; Zhou, G.; Mugele, F., Charge
13 Trapping-Based Electricity Generator (CTEG): an ultrarobust and high efficiency
14 nanogenerator for energy harvesting from water droplets. *Advanced materials* **2020**, *32* (33),
15 2001699.
- 16
17 (435) Xu, W.; Zheng, H.; Liu, Y.; Zhou, X.; Zhang, C.; Song, Y.; Deng, X.; Leung, M.;
18 Yang, Z.; Xu, R. X., A droplet-based electricity generator with high instantaneous power
19 density. *Nature* **2020**, *578* (7795), 392-396.
- 20
21 (436) Zhang, N.; Gu, H.; Lu, K.; Ye, S.; Xu, W.; Zheng, H.; Song, Y.; Liu, C.; Jiao, J.;
22 Wang, Z., A universal single electrode droplet-based electricity generator (SE-DEG) for
23 water kinetic energy harvesting. *Nano Energy* **2021**, *82*, 105735.
- 24
25 (437) Dong, J.; Xu, C.; Zhu, L.; Zhao, X.; Zhou, H.; Liu, H.; Xu, G.; Wang, G.; Zhou, G.;
26 Zeng, Q., A high voltage direct current droplet-based electricity generator inspired by
27 thunderbolts. *Nano Energy* **2021**, *90*, 106567.
- 28
29 (438) Yu, A.; Jiang, P.; Wang, Z. L., Nanogenerator as self-powered vibration sensor.
30 *Nano Energy* **2012**, *1* (3), 418-423.
- 31
32 (439) Wang, J.; Pan, L.; Guo, H.; Zhang, B.; Zhang, R.; Wu, Z.; Wu, C.; Yang, L.; Liao,
33 R.; Wang, Z. L., Rational structure optimized hybrid nanogenerator for highly efficient water
34 wave energy harvesting. *Advanced Energy Materials* **2019**, *9* (8), 1802892.
- 35
36 (440) Zhang, H.; Quan, L.; Chen, J.; Xu, C.; Zhang, C.; Dong, S.; Lü, C.; Luo, J., A
37 general optimization approach for contact-separation triboelectric nanogenerator. *Nano
38 energy* **2019**, *56*, 700-707.
- 39
40 (441) Wang, H.; Shi, M.; Zhu, K.; Su, Z.; Cheng, X.; Song, Y.; Chen, X.; Liao, Z.; Zhang,
41 M.; Zhang, H., High performance triboelectric nanogenerators with aligned carbon
42 nanotubes. *Nanoscale* **2016**, *8* (43), 18489-18494.
- 43
44 (442) Chen, J.; Xu, J.; Zou, Y.; Nashalian, A., Leverage surface chemistry for high-
45 performance triboelectric nanogenerators. *Frontiers in Chemistry* **2020**, *8*, 959.
- 46
47
48
49
50
51
52
53
54
55
56
57
58
59
60

- 1
2
3
4
5 (443) Mahmud, M. P.; Lee, J.; Kim, G.; Lim, H.; Choi, K.-B., Improving the surface
6 charge density of a contact-separation-based triboelectric nanogenerator by modifying the
7 surface morphology. *Microelectronic Engineering* **2016**, *159*, 102-107.
- 8
9 (444) Wang, J.; Wu, C.; Dai, Y.; Zhao, Z.; Wang, A.; Zhang, T.; Wang, Z. L., Achieving
10 ultrahigh triboelectric charge density for efficient energy harvesting. *Nature communications*
11 **2017**, *8*(1), 1-8.
- 12
13 (445) Cheng, J.; Ding, W.; Zi, Y.; Lu, Y.; Ji, L.; Liu, F.; Wu, C.; Wang, Z. L.,
14 Triboelectric microplasma powered by mechanical stimuli. *Nature communications* **2018**, *9*
15 (1), 1-11.
- 16
17 (446) Liu, F.; Liu, Y.; Lu, Y.; Wang, Z.; Shi, Y.; Ji, L.; Cheng, J., Electrical analysis of
18 triboelectric nanogenerator for high voltage applications exemplified by DBD microplasma.
19 *Nano Energy* **2019**, *56*, 482-493.
- 20
21 (447) Yang, Z.; Yang, Y.; Liu, F.; Wang, Z.; Li, Y.; Qiu, J.; Xiao, X.; Li, Z.; Lu, Y.; Ji, L.,
22 Power backpack for energy harvesting and reduced load impact. *ACS nano* **2021**, *15* (2),
23 2611-2623.
- 24
25 (448) Guo, H.; Chen, J.; Yeh, M.-H.; Fan, X.; Wen, Z.; Li, Z.; Hu, C.; Wang, Z. L., An
26 ultrarobust high-performance triboelectric nanogenerator based on charge replenishment.
27 *ACS nano* **2015**, *9*(5), 5577-5584.
- 28
29 (449) Wang, H.; Zhang, M.; Yang, Z.; Wang, Z.; Liu, X.; Lu, Y.; Ji, L.; Wang, Z. L.;
30 Cheng, J., Energy from greenhouse plastic films. *Nano Energy* **2021**, *89*, 106328.
- 31
32 (450) Liu, X.; Zhang, M.; Yang, Z.; Wang, H.; Chen, J.; Wang, Z.; Lu, Y.; Chen, Y.; Ji,
33 L.; Cheng, J., Alternating Current Electroluminescent Device Powered by Triboelectric
34 Nanogenerator with Capacitively Driven Circuit Strategy. *Advanced Functional Materials*
35 **2022**, *32*(7), 2106411.
- 36
37 (451) Shen, J.; Li, B.; Yang, Y.; Yang, Z.; Liu, X.; Lim, K.-C.; Chen, J.; Ji, L.; Lin, Z.-H.;
38 Cheng, J., Application, challenge and perspective of triboelectric nanogenerator as micro-
39 nano energy and self-powered biosystem. *Biosensors and Bioelectronics* **2022**, 114595.
- 40
41 (452) Wang, J.; Yu, X.; Zhao, D.; Yu, Y.; Gao, Q.; Cheng, T.; Wang, Z. L., Enhancing
42 output performance of triboelectric nanogenerator via charge clamping. *Advanced Energy*
43 *Materials* **2021**, *11* (31), 2101356.
- 44
45 (453) Lone, S. A.; Lim, K. C.; Kaswan, K.; Chatterjee, S.; Fan, K.-P.; Choi, D.; Lee, S.;
46 Zhang, H.; Cheng, J.; Lin, Z.-H., Recent advancements for improving the performance of
47 triboelectric nanogenerator devices. *Nano Energy* **2022**, 107318.
- 48
49
50
51
52
53
54
55
56
57
58
59
60

- 1
2
3
4
5 (454) Cheng, L.; Xu, Q.; Zheng, Y.; Jia, X.; Qin, Y., A self-improving triboelectric
6 nanogenerator with improved charge density and increased charge accumulation speed.
7 *Nature communications* **2018**, *9*(1), 1-8.
8
9 (455) Xu, L.; Bu, T. Z.; Yang, X. D.; Zhang, C.; Wang, Z. L., Ultrahigh charge density
10 realized by charge pumping at ambient conditions for triboelectric nanogenerators. *Nano*
11 *Energy* **2018**, *49*, 625-633.
12
13 (456) Liu, W.; Wang, Z.; Wang, G.; Liu, G.; Chen, J.; Pu, X.; Xi, Y.; Wang, X.; Guo, H.;
14 Hu, C., Integrated charge excitation triboelectric nanogenerator. *Nature communications*
15 **2019**, *10*(1), 1-9.
16
17 (457) Wang, H.; Xu, L.; Bai, Y.; Wang, Z. L., Pumping up the charge density of a
18 triboelectric nanogenerator by charge-shuttling. *Nature communications* **2020**, *11*(1), 1-9.
19
20 (458) Yang, Z.; Yang, Y.; Wang, H.; Liu, F.; Lu, Y.; Ji, L.; Wang, Z. L.; Cheng, J.,
21 Charge Pumping for Sliding-mode Triboelectric Nanogenerator with Voltage Stabilization
22 and Boosted Current. *Advanced Energy Materials* **2021**, *11*(28), 2101147.
23
24 (459) Bai, Y.; Xu, L.; Lin, S.; Luo, J.; Qin, H.; Han, K.; Wang, Z. L., Charge pumping
25 strategy for rotation and sliding type triboelectric nanogenerators. *Advanced Energy*
26 *Materials* **2020**, *10*(21), 2000605.
27
28 (460) Yang, Z.; Yang, Y.; Liu, F.; Li, B.; Li, Y.; Liu, X.; Chen, J.; Wang, C.; Ji, L.; Wang,
29 Z. L., Thousandfold boosting instantaneous current of triboelectric nanogenerator based on
30 decoupled charge pump and discharge tube. *Nano Energy* **2022**, *98*, 107264.
31
32 (461) Zhang, Z.; Jiang, D.; Zhao, J.; Liu, G.; Bu, T.; Zhang, C.; Wang, Z. L., Tribovoltaic
33 effect on metal–semiconductor interface for direct-current low-impedance triboelectric
34 nanogenerators. *Advanced Energy Materials* **2020**, *10*(9), 1903713.
35
36 (462) Yang, Y.; Zhang, H.; Wang, Z. L., Direct-current triboelectric generator. *Advanced*
37 *Functional Materials* **2014**, *24*(24), 3745-3750.
38
39 (463) Liu, D.; Yin, X.; Guo, H.; Zhou, L.; Li, X.; Zhang, C.; Wang, J.; Wang, Z. L., A
40 constant current triboelectric nanogenerator arising from electrostatic breakdown. *Science*
41 *advances* **2019**, *5*(4), eaav6437.
42
43 (464) Yi, Z.; Liu, D.; Zhou, L.; Li, S.; Zhao, Z.; Li, X.; Wang, Z. L.; Wang, J., Enhancing
44 output performance of direct-current triboelectric nanogenerator under controlled
45 atmosphere. *Nano Energy* **2021**, *84*, 105864.
46
47
48
49
50
51
52
53
54
55
56
57
58
59
60

- 1
2
3
4
5 (465) Gao, Y.; Liu, D.; Zhou, L.; Li, S.; Zhao, Z.; Yin, X.; Chen, S.; Wang, Z. L.; Wang,
6 J., A robust rolling-mode direct-current triboelectric nanogenerator arising from electrostatic
7 breakdown effect. *Nano Energy* **2021**, *85*, 106014.
8
9 (466) Wang, J.; Li, Y.; Xie, Z.; Xu, Y.; Zhou, J.; Cheng, T.; Zhao, H.; Wang, Z. L.,
10 Cylindrical direct-current triboelectric nanogenerator with constant output current. *Advanced*
11 *Energy Materials* **2020**, *10*(10), 1904227.
12
13 (467) Xu, S.; Guo, H.; Zhang, S. L.; Jin, L.; Ding, W.; Wang, X.; Wang, Z. L., Theoretical
14 investigation of air breakdown direct current triboelectric nanogenerator. *Applied Physics*
15 *Letters* **2020**, *116*(26), 263901.
16
17 (468) Chen, P.; An, J.; Cheng, R.; Shu, S.; Berbille, A.; Jiang, T.; Wang, Z. L., Rationally
18 segmented triboelectric nanogenerator with a constant direct-current output and low crest
19 factor. *Energy & Environmental Science* **2021**, *14*(8), 4523-4532.
20
21 (469) Shao, H.; Fang, J.; Wang, H.; Dai, L.; Lin, T., Polymer–metal Schottky contact with
22 direct-current outputs. *Advanced Materials* **2016**, *28*(7), 1461-1466.
23
24 (470) Lin, S.; Lu, Y.; Feng, S.; Hao, Z.; Yan, Y., A high current density direct-current
25 generator based on a moving van der Waals Schottky diode. *Advanced Materials* **2019**, *31*
26 (7), 1804398.
27
28 (471) Liu, J.; Goswami, A.; Jiang, K.; Khan, F.; Kim, S.; McGee, R.; Li, Z.; Hu, Z.; Lee,
29 J.; Thundat, T., Direct-current triboelectricity generation by a sliding Schottky nanocontact
30 on MoS₂ multilayers. *Nature nanotechnology* **2018**, *13*(2), 112-116.
31
32 (472) Lin, S.; Chen, X.; Wang, Z. L., The tribovoltaic effect and electron transfer at a
33 liquid-semiconductor interface. *Nano Energy* **2020**, *76*, 105070.
34
35 (473) Ren, L.; Yu, A.; Wang, W.; Guo, D.; Jia, M.; Guo, P.; Zhang, Y.; Wang, Z. L.; Zhai,
36 J., pn Junction Based Direct-Current Triboelectric Nanogenerator by Conjunction of
37 Tribovoltaic Effect and Photovoltaic Effect. *Nano Letters* **2021**, *21*(23), 10099-10106.
38
39 (474) Zhang, Z.; He, T.; Zhao, J.; Liu, G.; Wang, Z.; Zhang, C., Tribo-thermoelectric and
40 tribovoltaic coupling effect at metal-semiconductor interface. *Materials Today Physics* **2021**,
41 *16*, 100295.
42
43 (475) Guo, H.; Jia, X.; Liu, L.; Cao, X.; Wang, N.; Wang, Z. L., Freestanding triboelectric
44 nanogenerator enables noncontact motion-tracking and positioning. *ACS nano* **2018**, *12*(4),
45 3461-3467.
46
47
48
49
50
51
52
53
54
55
56
57
58
59
60

- 1
2
3
4
5 (476) Kim, M.; Ra, Y.; Cho, S.; Jang, S.; Kam, D.; Yun, Y.; Kim, H.; Choi, D., Geometric
6 gradient assisted control of the triboelectric effect in a smart brake system for self-powered
7 mechanical abrasion monitoring. *Nano Energy* **2021**, *89*, 106448.
- 8
9 (477) Son, J.-h.; Heo, D.; Song, Y.; Chung, J.; Kim, B.; Nam, W.; Hwang, P. T.; Kim, D.;
10 Koo, B.; Hong, J., Highly reliable triboelectric bicycle tire as self-powered bicycle safety
11 light and pressure sensor. *Nano Energy* **2022**, *93*, 106797.
- 12
13 (478) Zhu, D.; Hu, Y.-Z., The study of transition from elastohydrodynamic to mixed and
14 boundary lubrication. *The advancing frontier of engineering tribology, Proceedings of the*
15 *1999 STLE/ASME HS Cheng Tribology Surveillance* **1999**, 150-156.
- 16
17 (479) Kim, D.; Chung, J.; Heo, D.; Chung, S. H.; Lee, G.; Hwang, P. T.; Kim, M. K.;
18 Jung, H.; Jin, Y.; Hong, J., AC/DC Convertible Pillar-Type Triboelectric Nanogenerator with
19 Output Current Amplified by the Design of the Moving Electrode. *Advanced Energy*
20 *Materials* **2022**, *12* (9), 2103571.
- 21
22 (480) Yang, B.; Tao, X.-m.; Peng, Z.-h., Upper limits for output performance of contact-
23 mode triboelectric nanogenerator systems. *Nano Energy* **2019**, *57*, 66-73.
- 24
25 (481) Dharmasena, R.; Silva, S., Towards optimized triboelectric nanogenerators. *Nano*
26 *Energy* **2019**, *62*, 530-549.
- 27
28 (482) Wei, X. Y.; Zhu, G.; Wang, Z. L., Surface-charge engineering for high-performance
29 triboelectric nanogenerator based on identical electrification materials. *Nano Energy* **2014**,
30 *10*, 83-89.
- 31
32 (483) Zhang, J.; Zheng, Y.; Xu, L.; Wang, D., Oleic-acid enhanced triboelectric
33 nanogenerator with high output performance and wear resistance. *Nano Energy* **2020**, *69*,
34 104435.
- 35
36 (484) Wu, J.; Xi, Y.; Shi, Y., Toward wear-resistive, highly durable and high performance
37 triboelectric nanogenerator through interface liquid lubrication. *Nano Energy* **2020**, *72*,
38 104659.
- 39
40 (485) Zhou, L.; Liu, D.; Zhao, Z.; Li, S.; Liu, Y.; Liu, L.; Gao, Y.; Wang, Z. L.; Wang, J.,
41 Simultaneously enhancing power density and durability of sliding-mode triboelectric
42 nanogenerator via interface liquid lubrication. *Advanced Energy Materials* **2020**, *10* (45),
43 2002920.
- 44
45 (486) Chung, J.; Chung, S.-H.; Lin, Z.-H.; Jin, Y.; Hong, J.; Lee, S., Dielectric liquid-
46 based self-operating switch triboelectric nanogenerator for current amplification via
47 regulating air breakdown. *Nano Energy* **2021**, *88*, 106292.
- 48
49
50
51
52
53
54
55
56
57
58
59
60

- 1
2
3
4
5 (487) Chung, S. H.; Chung, J.; Song, M.; Kim, S.; Shin, D.; Lin, Z. H.; Koo, B.; Kim, D.;
6 Hong, J.; Lee, S., Nonpolar liquid lubricant submerged triboelectric nanogenerator for current
7 amplification via direct electron flow. *Advanced Energy Materials* **2021**, *11* (25), 2100936.
8
9 (488) Song, M.; Chung, J.; Chung, S.-H.; Cha, K.; Heo, D.; Kim, S.; Hwang, P. T.; Kim,
10 D.; Koo, B.; Hong, J., Semisolid-lubricant-based ball-bearing triboelectric nanogenerator for
11 current amplification, enhanced mechanical lifespan, and thermal stabilization. *Nano Energy*
12 **2022**, *93*, 106816.
13
14 (489) Puppo, F.; Carrara, S.; De Micheli, G. *Silicon Nanowires for Biosensing*,
15 0128097396; Elsevier: 2018.
16
17 (490) Wang, Y.; Narayanan, S.; Wu, W., Field-assisted splitting of pure water based on
18 deep-sub-Debye-length nanogap electrochemical cells. *ACS nano* **2017**, *11* (8), 8421-8428.
19
20 (491) Watson, A. In *Quantitative estimates of characteristic values involved in*
21 *quasiparticle conduction in dielectric liquids*, IEEE 1997 Annual Report Conference on
22 Electrical Insulation and Dielectric Phenomena, IEEE: 1997; pp 718-721.
23
24 (492) Liu, X.; Zhang, J.; Zhang, L.; Feng, Y.; Feng, M.; Luo, N.; Wang, D., Influence of
25 interface liquid lubrication on triboelectrification of point contact friction pair. *Tribology*
26 *International* **2022**, *165*, 107323.
27
28 (493) Huynh, N. D.; Choi, D., Mechanical Conversion and Transmission Systems for
29 Controlling Triboelectric Nanogenerators. *Nanoenergy Advances* **2022**, *2* (1), 29-51.
30
31 (494) Kim, W.; Bhatia, D.; Jeong, S.; Choi, D., Mechanical energy conversion systems for
32 triboelectric nanogenerators: Kinematic and vibrational designs. *Nano Energy* **2019**, *56*, 307-
33 321.
34
35 (495) Lu, X.; Xu, Y.; Qiao, G.; Gao, Q.; Zhang, X.; Cheng, T.; Wang, Z. L., Triboelectric
36 nanogenerator for entire stroke energy harvesting with bidirectional gear transmission. *Nano*
37 *Energy* **2020**, *72*, 104726.
38
39 (496) Tang, Q.; Yeh, M.-H.; Liu, G.; Li, S.; Chen, J.; Bai, Y.; Feng, L.; Lai, M.; Ho, K.-
40 C.; Guo, H., Whirligig-inspired triboelectric nanogenerator with ultrahigh specific output as
41 reliable portable instant power supply for personal health monitoring devices. *Nano Energy*
42 **2018**, *47*, 74-80.
43
44 (497) Wang, J.; Jiang, Z.; Sun, W.; Xu, X.; Han, Q.; Chu, F., Yoyo-ball inspired
45 triboelectric nanogenerators for harvesting biomechanical energy. *Applied Energy* **2022**, *308*,
46 118322.
47
48
49
50
51
52
53
54
55
56
57
58
59
60

- 1
2
3
4
5 (498) Yin, M.; Lu, X.; Qiao, G.; Xu, Y.; Wang, Y.; Cheng, T.; Wang, Z. L., Mechanical
6 regulation triboelectric nanogenerator with controllable output performance for random
7 energy harvesting. *Advanced Energy Materials* **2020**, *10*(22), 2000627.
- 8
9 (499) Yoo, J.; Yoo, D.; Lee, S.; Sim, J.-Y.; Hwang, W.; Choi, D.; Kim, D. S., Extremely
10 high and elongated power output from a mechanical mediator-assisted triboelectric
11 nanogenerator driven by the biomechanical energy. *Nano energy* **2019**, *56*, 851-858.
- 12
13 (500) Yu, X.; Wang, Q.; Ke, M.; Ning, C.; Zhang, Y.; Han, S.; Cheng, T., Millivolt-Level
14 Stable Voltage Output of Triboelectric Nanogenerator Under Random Excitation by Double
15 Limiting. *Energy Technology* **2022**, *10*(9), 2200374.
- 16
17 (501) Zhang, B.; Chen, J.; Jin, L.; Deng, W.; Zhang, L.; Zhang, H.; Zhu, M.; Yang, W.;
18 Wang, Z. L., Rotating-disk-based hybridized electromagnetic-triboelectric nanogenerator for
19 sustainably powering wireless traffic volume sensors. *ACS nano* **2016**, *10*(6), 6241-6247.
- 20
21 (502) Zhong, X.; Yang, Y.; Wang, X.; Wang, Z. L., Rotating-disk-based hybridized
22 electromagnetic-triboelectric nanogenerator for scavenging biomechanical energy as a mobile
23 power source. *Nano Energy* **2015**, *13*, 771-780.
- 24
25 (503) Bhatia, D.; Jo, S. H.; Ryu, Y.; Kim, Y.; Kim, D. H.; Park, H.-S., Wearable
26 triboelectric nanogenerator based exercise system for upper limb rehabilitation post
27 neurological injuries. *Nano Energy* **2021**, *80*, 105508.
- 28
29 (504) Cho, S.; Hanif, Z.; Yun, Y.; Khan, Z. A.; Jang, S.; Ra, Y.; Lin, Z.-H.; La, M.; Park,
30 S. J.; Choi, D., Triboelectrification-driven microbial inactivation in a conductive cellulose
31 filter for affordable, portable, and efficient water sterilization. *Nano Energy* **2021**, *88*,
32 106228.
- 33
34 (505) Lee, S. H.; Cho, S.; Jang, S.; Lee, D.; Kam, D.; Choi, J. H.; Hanif, Z.; La, M.; Park,
35 S. J.; Choi, D., Fully Self-Powered Electrospray System via Triboelectric High Voltage
36 Generator and Its Use to Control Wettability of Various Surfaces. *International Journal of*
37 *Precision Engineering and Manufacturing-Green Technology* **2022**, 1-12.
- 38
39 (506) Liu, S.; Li, X.; Wang, Y.; Yang, Y.; Meng, L.; Cheng, T.; Wang, Z. L., Magnetic
40 switch structured triboelectric nanogenerator for continuous and regular harvesting of wind
41 energy. *Nano Energy* **2021**, *83*, 105851.
- 42
43 (507) Yang, W.; Wang, Y.; Li, Y.; Wang, J.; Cheng, T.; Wang, Z. L., Integrated flywheel
44 and spiral spring triboelectric nanogenerator for improving energy harvesting of intermittent
45 excitations/triggering. *Nano Energy* **2019**, *66*, 104104.
- 46
47
48
49
50
51
52
53
54
55
56
57
58
59
60

- 1
2
3
4
5 (508) Zhu, M.; Sun, Z.; Chen, T.; Lee, C., Low cost exoskeleton manipulator using
6 bidirectional triboelectric sensors enhanced multiple degree of freedom sensory system.
7 *Nature communications* **2021**, *12*(1), 1-16.
- 8
9 (509) Choi, S.; Cho, S.; Yun, Y.; Jang, S.; Choi, J. H.; Ra, Y.; La, M.; Park, S. J.; Choi,
10 D., Development of a high-performance handheld triboelectric nanogenerator with a
11 lightweight power transmission unit. *Advanced Materials Technologies* **2020**, *5*(4), 2000003.
- 12
13 (510) Kim, J. W.; Salauddin, M.; Cho, H.; Rasel, M. S.; Park, J. Y., Electromagnetic
14 energy harvester based on a finger trigger rotational gear module and an array of disc
15 Halbach magnets. *Applied Energy* **2019**, *250*, 776-785.
- 16
17 (511) Liu, G.; Chen, J.; Guo, H.; Lai, M.; Pu, X.; Wang, X.; Hu, C., Triboelectric
18 nanogenerator based on magnetically induced retractable spring steel tapes for efficient
19 energy harvesting of large amplitude motion. *Nano Research* **2018**, *11*(2), 633-641.
- 20
21 (512) Park, M.; Cho, S.; Yun, Y.; La, M.; Park, S. J.; Choi, D., A highly sensitive
22 magnetic configuration-based triboelectric nanogenerator for multidirectional vibration
23 energy harvesting and self-powered environmental monitoring. *International Journal of*
24 *Energy Research* **2021**, *45*(12), 18262-18274.
- 25
26 (513) Xie, Z.; Zeng, Z.; Wang, Y.; Yang, W.; Xu, Y.; Lu, X.; Cheng, T.; Zhao, H.; Wang,
27 Z. L., Novel sweep-type triboelectric nanogenerator utilizing single freewheel for random
28 triggering motion energy harvesting and driver habits monitoring. *Nano Energy* **2020**, *68*,
29 104360.
- 30
31 (514) Xu, Y.; Yang, W.; Lu, X.; Yang, Y.; Li, J.; Wen, J.; Cheng, T.; Wang, Z. L.,
32 Triboelectric nanogenerator for ocean wave graded energy harvesting and condition
33 monitoring. *ACS nano* **2021**, *15*(10), 16368-16375.
- 34
35 (515) Luo, Y.; Chen, P.; Cao, L. N.; Xu, Z.; Wu, Y.; He, G.; Jiang, T.; Wang, Z. L.,
36 Durability Improvement of Breeze-Driven Triboelectric-Electromagnetic Hybrid
37 Nanogenerator by a Travel-Controlled Approach. *Advanced Functional Materials* **2022**,
38 2205710.
- 39
40 (516) Yang, W.; Gao, Q.; Xia, X.; Zhang, X.; Lu, X.; Yang, S.; Cheng, T.; Wang, Z. L.,
41 Travel switch integrated mechanical regulation triboelectric nanogenerator with linear-
42 rotational motion transformation mechanism. *Extreme Mechanics Letters* **2020**, *37*, 100718.
- 43
44 (517) Tcho, I.-W.; Jeon, S.-B.; Park, S.-J.; Kim, W.-G.; Jin, I. K.; Han, J.-K.; Kim, D.;
45 Choi, Y.-K., Disk-based triboelectric nanogenerator operated by rotational force converted
46 from linear force by a gear system. *Nano Energy* **2018**, *50*, 489-496.
- 47
48
49
50
51
52
53
54
55
56
57
58
59
60

- 1
2
3
4
5 (518) Yun, Y.; Jang, S.; Cho, S.; Lee, S. H.; Hwang, H. J.; Choi, D., Exo-shoe
6 triboelectric nanogenerator: Toward high-performance wearable biomechanical energy
7 harvester. *Nano Energy* **2021**, *80*, 105525.
8
9 (519) Cho, S.; Yun, Y.; Jang, S.; Ra, Y.; Choi, J. H.; Hwang, H. J.; Choi, D.; Choi, D.,
10 Universal biomechanical energy harvesting from joint movements using a direction-
11 switchable triboelectric nanogenerator. *Nano Energy* **2020**, *71*, 104584.
12
13 (520) Gai, Y.; Bai, Y.; Cao, Y.; Wang, E.; Xue, J.; Qu, X.; Liu, Z.; Luo, D.; Li, Z., A
14 Gyroscope Nanogenerator with Frequency Up-Conversion Effect for Fitness and Energy
15 Harvesting. *Small* **2022**, *18* (14), 2108091.
16
17 (521) Choi, J. H.; Ra, Y.; Cho, S.; La, M.; Park, S. J.; Choi, D., Electrical charge storage
18 effect in carbon based polymer composite for long-term performance enhancement of the
19 triboelectric nanogenerator. *Composites Science and Technology* **2021**, *207*, 108680.
20
21 (522) He, S.; Wang, Z.; Zhang, X.; Yuan, Z.; Sun, Y.; Cheng, T.; Wang, Z. L., Self-
22 Powered Sensing for Non-Full Pipe Fluidic Flow Based on Triboelectric Nanogenerators.
23 *ACS Applied Materials & Interfaces* **2022**, *14* (2), 2825-2832.
24
25 (523) Liu, G.; Liu, R.; Guo, H.; Xi, Y.; Wei, D.; Hu, C., A novel triboelectric generator
26 based on the combination of a waterwheel-like electrode with a spring steel plate for efficient
27 harvesting of low-velocity rotational motion energy. *Advanced Electronic Materials* **2016**, *2*
28 (5), 1500448.
29
30 (524) Zhang, H.; Yang, Y.; Zhong, X.; Su, Y.; Zhou, Y.; Hu, C.; Wang, Z. L., Single-
31 electrode-based rotating triboelectric nanogenerator for harvesting energy from tires. *ACS*
32 *nano* **2014**, *8* (1), 680-689.
33
34 (525) Cheng, T.; Li, Y.; Wang, Y.-C.; Gao, Q.; Ma, T.; Wang, Z. L., Triboelectric
35 nanogenerator by integrating a cam and a movable frame for ambient mechanical energy
36 harvesting. *Nano Energy* **2019**, *60*, 137-143.
37
38 (526) Gao, Q.; Li, Y.; Xie, Z.; Yang, W.; Wang, Z.; Yin, M.; Lu, X.; Cheng, T.; Wang, Z.
39 L., Robust triboelectric nanogenerator with ratchet-like wheel-based design for harvesting of
40 environmental energy. *Advanced Materials Technologies* **2020**, *5* (1), 1900801.
41
42 (527) Han, K.; Luo, J.; Feng, Y.; Lai, Q.; Bai, Y.; Tang, W.; Wang, Z. L., Wind-driven
43 radial-engine-shaped triboelectric nanogenerators for self-powered absorption and
44 degradation of NOX. *ACS nano* **2020**, *14* (3), 2751-2759.
45
46
47
48
49
50
51
52
53
54
55
56
57
58
59
60

- 1
2
3
4
5 (528) Qian, J.; Wu, X.; Kim, D.-S.; Lee, D.-W., Seesaw-structured triboelectric
6 nanogenerator for scavenging electrical energy from rotational motion of mechanical
7 systems. *Sensors and Actuators A: Physical* **2017**, *263*, 600-609.
- 8
9 (529) Kim, J.-N.; Lee, J.; Lee, H.; Oh, I.-K., Stretchable and self-healable catechol-
10 chitosan-diatom hydrogel for triboelectric generator and self-powered tremor sensor targeting
11 at Parkinson disease. *Nano Energy* **2021**, *82*, 105705.
- 12
13 (530) Salauddin, M.; Rana, S. S.; Rahman, M. T.; Sharifuzzaman, M.; Maharjan, P.;
14 Bhatta, T.; Cho, H.; Lee, S. H.; Park, C.; Shrestha, K., Fabric-assisted MXene/silicone
15 nanocomposite-based triboelectric nanogenerators for self-powered sensors and wearable
16 electronics. *Advanced Functional Materials* **2022**, *32* (5), 2107143.
- 17
18 (531) Ahn, J.; Kim, J. S.; Jeong, Y.; Hwang, S.; Yoo, H.; Jeong, Y.; Gu, J.; Mahato, M.;
19 Ko, J.; Jeon, S., All-Recyclable Triboelectric Nanogenerator for Sustainable Ocean
20 Monitoring Systems. *Advanced Energy Materials* **2022**, 2201341.
- 21
22 (532) Gao, Q.; Xu, Y.; Yu, X.; Jing, Z.; Cheng, T.; Wang, Z. L., Gyroscope-Structured
23 Triboelectric Nanogenerator for Harvesting Multidirectional Ocean Wave Energy. *ACS nano*
24 **2022**, *16* (4), 6781-6788.
- 25
26 (533) Kim, J. S.; Kim, J.; Kim, J. N.; Ahn, J.; Jeong, J. H.; Park, I.; Kim, D.; Oh, I. K.,
27 Collectively Exhaustive Hybrid Triboelectric Nanogenerator Based on Flow-Induced
28 Impacting-Sliding Cylinder for Ocean Energy Harvesting. *Advanced Energy Materials* **2022**,
29 *12* (3), 2103076.
- 30
31 (534) Hu, S.; Yuan, Z.; Li, R.; Cao, Z.; Zhou, H.; Wu, Z.; Wang, Z. L., Vibration-Driven
32 Triboelectric Nanogenerator for Vibration Attenuation and Condition Monitoring for
33 Transmission Lines. *Nano Letters* **2022**, *22* (13), 5584-5591.
- 34
35 (535) Liu, Y.; Zheng, Y.; Wu, Z.; Zhang, L.; Sun, W.; Li, T.; Wang, D.; Zhou, F.,
36 Conductive elastic sponge-based triboelectric nanogenerator (TENG) for effective random
37 mechanical energy harvesting and ammonia sensing. *Nano Energy* **2021**, *79*, 105422.
- 38
39 (536) Zi, Y.; Guo, H.; Wen, Z.; Yeh, M.-H.; Hu, C.; Wang, Z. L., Harvesting low-
40 frequency (< 5 Hz) irregular mechanical energy: a possible killer application of triboelectric
41 nanogenerator. *ACS nano* **2016**, *10* (4), 4797-4805.
- 42
43 (537) Han, K. W.; Kim, J. N.; Rajabi-Abhari, A.; Bui, V. T.; Kim, J. S.; Choi, D.; Oh, I.
44 K., Long-lasting and steady triboelectric energy harvesting from low-frequency irregular
45 motions using escapement mechanism. *Advanced Energy Materials* **2021**, *11* (4), 2002929.
- 46
47
48
49
50
51
52
53
54
55
56
57
58
59
60

- 1
2
3
4
5 (538) He, G.; Luo, Y.; Zhai, Y.; Wu, Y.; You, J.; Lu, R.; Zeng, S.; Wang, Z. L.,
6 Regulating random mechanical motion using the principle of auto-winding mechanical watch
7 for driving TENG with constant AC output—An approach for efficient usage of high entropy
8 energy. *Nano Energy* **2021**, *87*, 106195.
9
10
11 (539) Pham, K. D.; Bhatia, D.; Huynh, N. D.; Kim, H.; Baik, J. M.; Lin, Z.-H.; Choi, D.,
12 Automatically switchable mechanical frequency regulator for continuous mechanical energy
13 harvesting via a triboelectric nanogenerator. *Nano Energy* **2021**, *89*, 106350.
14
15 (540) Albu-Schäffer, A.; Della Santina, C., A review on nonlinear modes in conservative
16 mechanical systems. *Annual Reviews in Control* **2020**, *50*, 49-71.
17
18 (541) Lu, S.; He, Q.; Wang, J., A review of stochastic resonance in rotating machine fault
19 detection. *Mechanical Systems and Signal Processing* **2019**, *116*, 230-260.
20
21 (542) Dykman, M. I.; Rastelli, G.; Roukes, M. L.; Weig, E. M., Resonantly induced
22 friction and frequency combs in driven nanomechanical systems. *Physical review letters*
23 **2019**, *122* (25), 254301.
24
25 (543) Wang, X.; Cong, L.; Zhu, D.; Yuan, Z.; Lin, X.; Zhao, W.; Bai, Z.; Liang, W.; Sun,
26 X.; Deng, G.-W., Visualizing nonlinear resonance in nanomechanical systems via single-
27 electron tunneling. *Nano Research* **2021**, *14* (4), 1156-1161.
28
29 (544) Khorasani, R. R.; Adib, E.; Farzanehfard, H., ZVT resonant core reset forward
30 converter with a simple auxiliary circuit. *IEEE Transactions on Industrial Electronics* **2017**,
31 *65* (1), 242-250.
32
33 (545) Silva, T. M. P.; Clementino, M. A.; de Sousa, V. C.; De Marqui, C., An
34 experimental study of a piezoelectric metastructure with adaptive resonant shunt circuits.
35 *IEEE/ASME Transactions on Mechatronics* **2020**, *25* (2), 1076-1083.
36
37 (546) Zhang, Q.; Xi, Z.; Wang, Y.; Liu, L.; Yu, H.; Wang, H.; Xu, M., Multi-Tube
38 Helmholtz Resonator Based Triboelectric Nanogenerator for Broadband Acoustic Energy
39 Harvesting. *Frontiers in Materials* **2022**, 259.
40
41 (547) Chen, J.; Zhu, G.; Yang, W.; Jing, Q.; Bai, P.; Yang, Y.; Hou, T. C.; Wang, Z. L.,
42 Harmonic-resonator-based triboelectric nanogenerator as a sustainable power source and a
43 self-powered active vibration sensor. *Advanced materials* **2013**, *25* (42), 6094-6099.
44
45 (548) Xu, X.; Wu, Q.; Pang, Y.; Cao, Y.; Fang, Y.; Huang, G.; Cao, C., Multifunctional
46 Metamaterials for Energy Harvesting and Vibration Control. *Advanced Functional Materials*
47 **2022**, *32* (7), 2107896.
48
49
50
51
52
53
54
55
56
57
58
59
60

- 1
2
3
4
5 (549) Wang, S.; Niu, S.; Yang, J.; Lin, L.; Wang, Z. L., Quantitative measurements of
6 vibration amplitude using a contact-mode freestanding triboelectric nanogenerator. *ACS nano*
7 **2014**, *8* (12), 12004-12013.
8
9 (550) Jung, Y.; Yu, J.; Hwang, H. J.; Bhatia, D.; Chung, K.-B.; Choi, D., Wire-based
10 triboelectric resonator for a self-powered crack monitoring system. *Nano Energy* **2020**, *71*,
11 104615.
12
13 (551) Tang, Y.; Xuan, W.; Zhang, C.; Xu, L.; Liu, F.; Chen, J.; Jin, H.; Ye, Z.; Cao, Z.; Li,
14 Y., Fully self-powered instantaneous wireless traffic monitoring system based on triboelectric
15 nanogenerator and magnetic resonance coupling. *Nano Energy* **2021**, *89*, 106429.
16
17 (552) Tan, X.; Zhou, Z.; Zhang, L.; Wang, X.; Lin, Z.; Yang, R.; Yang, J., A passive
18 wireless triboelectric sensor via a surface acoustic wave resonator (SAWR). *Nano Energy*
19 **2020**, *78*, 105307.
20
21 (553) Le, X.; Shi, Q.; Sun, Z.; Xie, J.; Lee, C., Noncontact Human–Machine Interface
22 Using Complementary Information Fusion Based on MEMS and Triboelectric Sensors.
23 *Advanced Science* **2022**, 2201056.
24
25 (554) Cheng, X.; Tang, W.; Song, Y.; Chen, H.; Zhang, H.; Wang, Z. L., Power
26 management and effective energy storage of pulsed output from triboelectric nanogenerator.
27 *Nano Energy* **2019**, *61*, 517-532.
28
29 (555) Zhu, G.; Chen, J.; Zhang, T.; Jing, Q.; Wang, Z. L., Radial-arrayed rotary
30 electrification for high performance triboelectric generator. *Nature Communications* **2014**, *5*
31 (1), 3426.
32
33 (556) Han, C.; Zhang, C.; Tang, W.; Li, X.; Wang, Z. L., High power triboelectric
34 nanogenerator based on printed circuit board (PCB) technology. *Nano Research* **2015**, *8* (3),
35 722-730.
36
37 (557) Zhang, K.; Wang, X.; Yang, Y.; Wang, Z. L., Hybridized Electromagnetic–
38 Triboelectric Nanogenerator for Scavenging Biomechanical Energy for Sustainably Powering
39 Wearable Electronics. *ACS Nano* **2015**, *9* (4), 3521-3529.
40
41 (558) Pu, X.; Liu, M.; Li, L.; Zhang, C.; Pang, Y.; Jiang, C.; Shao, L.; Hu, W.; Wang, Z.
42 L., Efficient Charging of Li-Ion Batteries with Pulsed Output Current of Triboelectric
43 Nanogenerators. *Advanced Science* **2016**, *3* (1), 1500255.
44
45 (559) Zhang, X.; Du, X.; Yin, Y.; Li, N.-W.; Fan, W.; Cao, R.; Xu, W.; Zhang, C.; Li, C.,
46 Lithium-Ion Batteries: Charged by Triboelectric Nanogenerators with Pulsed Output Based
47
48
49
50
51
52
53
54
55
56
57
58
59
60

1
2
3
4
5 on the Enhanced Cycling Stability. *ACS Applied Materials & Interfaces* **2018**, *10*(10), 8676-
6 8684.

7
8 (560) Tang, W.; Zhou, T.; Zhang, C.; Ru Fan, F.; Bao Han, C.; Lin Wang, Z., A power-
9 transformed-and-managed triboelectric nanogenerator and its applications in a self-powered
10 wireless sensing node. *Nanotechnology* **2014**, *25*(22), 225402.

11
12 (561) Maeng, J.; Shim, M.; Jeong, J.; Park, I.; Park, Y.; Kim, C., A Sub-fs-FoM Digital
13 LDO Using PMOS and NMOS Arrays With Fully Integrated 7.2-pF Total Capacitance. *IEEE*
14 *Journal of Solid-State Circuits* **2020**, *55*(6), 1624-1636.

15
16 (562) Park, I.; Maeng, J.; Shim, M.; Jeong, J.; Kim, C., A High-Voltage Dual-Input Buck
17 Converter Achieving 52.9% Maximum End-to-End Efficiency for Triboelectric Energy-
18 Harvesting Applications. *IEEE Journal of Solid-State Circuits* **2020**, *55*(5), 1324-1336.

19
20 (563) Maeng, J.; Park, I.; Shim, M.; Jeong, J.; Kim, C., A High-Voltage Dual-Input Buck
21 Converter With Bidirectional Inductor Current for Triboelectric Energy-Harvesting
22 Applications. *IEEE Journal of Solid-State Circuits* **2021**, *56*(2), 541-553.

23
24 (564) de Souza, A. F.; Tofoli, F. L.; Ribeiro, E. R. Switched Capacitor DC-DC
25 Converters: A Survey on the Main Topologies, Design Characteristics, and Applications
26 *Energies* [Online], 2021.

27
28 (565) Bang, S.; Blaauw, D.; Sylvester, D., A Successive-Approximation Switched-
29 Capacitor DC-DC Converter With Resolution of $V_{\text{IN}}/2^N$ for a Wide Range
30 of Input and Output Voltages. *IEEE Journal of Solid-State Circuits* **2016**, *51*(2), 543-556.

31
32 (566) Salem, L. G.; Mercier, P. P., A Recursive Switched-Capacitor DC-DC Converter
33 Achieving 2^N-1 Ratios With High Efficiency Over a Wide Output Voltage Range.
34 *IEEE Journal of Solid-State Circuits* **2014**, *49*(12), 2773-2787.

35
36 (567) Harmon, W.; Bangboje, D.; Guo, H.; Hu, T.; Wang, Z. L., Self-driven power
37 management system for triboelectric nanogenerators. *Nano Energy* **2020**, *71*, 104642.

38
39 (568) Zi, Y.; Guo, H.; Wang, J.; Wen, Z.; Li, S.; Hu, C.; Wang, Z. L., An inductor-free
40 auto-power-management design built-in triboelectric nanogenerators. *Nano Energy* **2017**, *31*,
41 302-310.

42
43 (569) Liu, W.; Wang, Z.; Wang, G.; Zeng, Q.; He, W.; Liu, L.; Wang, X.; Xi, Y.; Guo, H.;
44 Hu, C.; Wang, Z. L., Switched-capacitor-convertors based on fractal design for output power
45 management of triboelectric nanogenerator. *Nature Communications* **2020**, *11*(1), 1883.

46
47 (570) Lee, J.; Lee, S. H.; Kang, G. G.; Kim, J. H.; Cho, G. H.; Kim, H. S. In *A 130V*
48 *Triboelectric Energy-Harvesting Interface in $.18\mu\text{m}$ BCD with Scalable Multi-*
49

- 1
2
3
4
5 *Chip-Stacked Bias-Flip and Daisy-Chained Synchronous Signaling Technique*, 2022 IEEE
6 International Solid- State Circuits Conference (ISSCC), 20-26 Feb. 2022; 2022; pp 474-476.
7
8 (571) Chung, J.; Yong, H.; Moon, H.; Choi, S. T.; Bhatia, D.; Choi, D.; Kim, D.; Lee, S.,
9 Capacitor-Integrated Triboelectric Nanogenerator Based on Metal–Metal Contact for Current
10 Amplification. *Advanced Energy Materials* **2018**, *8*(15), 1703024.
11
12 (572) Dharmasena, R. D. I. G.; Deane, J. H. B.; Silva, S. R. P., Nature of Power
13 Generation and Output Optimization Criteria for Triboelectric Nanogenerators. *Advanced*
14 *Energy Materials* **2018**, *8*(31), 1802190.
15
16 (573) Lu, S.; Lei, W.; Gao, L.; Chen, X.; Tong, D.; Yuan, P.; Mu, X.; Yu, H., Regulating
17 the high-voltage and high-impedance characteristics of triboelectric nanogenerator toward
18 practical self-powered sensors. *Nano Energy* **2021**, *87*, 106137.
19
20 (574) Abdallah, M. N.; Sarkar, T. K.; Salazar-Palma, M. In *Maximum power transfer*
21 *versus efficiency*, 2016 IEEE International Symposium on Antennas and Propagation
22 (APSURSI), 26 June-1 July 2016; 2016; pp 183-184.
23
24 (575) Rasel, M. S.; Maharjan, P.; Salauddin, M.; Rahman, M. T.; Cho, H. O.; Kim, J. W.;
25 Park, J. Y., An impedance tunable and highly efficient triboelectric nanogenerator for large-
26 scale, ultra-sensitive pressure sensing applications. *Nano Energy* **2018**, *49*, 603-613.
27
28 (576) Zhu, Y.; Yang, B.; Liu, J.; Wang, X.; Wang, L.; Chen, X.; Yang, C., A flexible and
29 biocompatible triboelectric nanogenerator with tunable internal resistance for powering
30 wearable devices. *Scientific Reports* **2016**, *6*(1), 22233.
31
32 (577) He, T.; Shi, Q.; Wang, H.; Wen, F.; Chen, T.; Ouyang, J.; Lee, C., Beyond energy
33 harvesting - multi-functional triboelectric nanosensors on a textile. *Nano Energy* **2019**, *57*,
34 338-352.
35
36 (578) Yoon, B.-K.; , J.-Y. L.; , a. J.-H. J., Three-Stage Power Management System
37 Employing Impedance Coupler Switch for Triboelectric Nanogenerator. *The Transactions of*
38 *the Korean Institute of Power Electronics* **2020**, *25*(4), 243–250.
39
40 (579) Liu, Y.; Niu, S.; Wang, Z. L., Theory of Tribotronics. *Advanced Electronic*
41 *Materials* **2015**, *1*(9), 1500124.
42
43 (580) Isono, K.; Hirose, T.; Tsubaki, K.; Kuroki, N.; Numa, M. In *A 18.9-nA standby*
44 *current comparator with adaptive bias current generator*, IEEE Asian Solid-State Circuits
45 Conference 2011, 14-16 Nov. 2011; 2011; pp 237-240.
46
47
48
49
50
51
52
53
54
55
56
57
58
59
60

- 1
2
3
4
5 (581) Seok, M.; Kim, G.; Blaauw, D.; Sylvester, D., A Portable 2-Transistor Picowatt
6 Temperature-Compensated Voltage Reference Operating at 0.5 V. *IEEE Journal of Solid-*
7 *State Circuits* **2012**, *47*(10), 2534-2545.
- 8
9 (582) Zi, Y.; Niu, S.; Wang, J.; Wen, Z.; Tang, W.; Wang, Z. L., Standards and figure-of-
10 merits for quantifying the performance of triboelectric nanogenerators. *Nature*
11 *Communications* **2015**, *6*(1), 8376.
- 12
13 (583) Niu, S.; Wang, X.; Yi, F.; Zhou, Y. S.; Wang, Z. L., A universal self-charging
14 system driven by random biomechanical energy for sustainable operation of mobile
15 electronics. *Nature Communications* **2015**, *6*(1), 8975.
- 16
17 (584) Zhou, H.; Liu, G.; Zeng, J.; Dai, Y.; Zhou, W.; Xiao, C.; Dang, T.; Yu, W.; Chen,
18 Y.; Zhang, C. Recent Progress of Switching Power Management for Triboelectric
19 Nanogenerators *Sensors* [Online], 2022.
- 20
21 (585) Song, Y.; Wang, H.; Cheng, X.; Li, G.; Chen, X.; Chen, H.; Miao, L.; Zhang, X.;
22 Zhang, H., High-efficiency self-charging smart bracelet for portable electronics. *Nano Energy*
23 **2019**, *55*, 29-36.
- 24
25 (586) Xi, F.; Pang, Y.; Li, W.; Jiang, T.; Zhang, L.; Guo, T.; Liu, G.; Zhang, C.; Wang, Z.
26 L., Universal power management strategy for triboelectric nanogenerator. *Nano Energy* **2017**,
27 *37*, 168-176.
- 28
29 (587) Liu, G.; Xu, S.; Liu, Y.; Gao, Y.; Tong, T.; Qi, Y.; Zhang, C., Flexible Drug Release
30 Device Powered by Triboelectric Nanogenerator. *Advanced Functional Materials* **2020**, *30*
31 (12), 1909886.
- 32
33 (588) Liang, X.; Jiang, T.; Liu, G.; Xiao, T.; Xu, L.; Li, W.; Xi, F.; Zhang, C.; Wang, Z.
34 L., Triboelectric Nanogenerator Networks Integrated with Power Management Module for
35 Water Wave Energy Harvesting. *Advanced Functional Materials* **2019**, *29*(41), 1807241.
- 36
37 (589) Fu, X.; Xu, S.; Gao, Y.; Zhang, X.; Liu, G.; Zhou, H.; Lv, Y.; Zhang, C.; Wang, Z.
38 L., Breeze-Wind-Energy-Powered Autonomous Wireless Anemometer Based on Rolling
39 Contact-Electrification. *ACS Energy Letters* **2021**, *6*(6), 2343-2350.
- 40
41 (590) Liu, D.; Chen, B.; An, J.; Li, C.; Liu, G.; Shao, J.; Tang, W.; Zhang, C.; Wang, Z.
42 L., Wind-driven self-powered wireless environmental sensors for Internet of Things at long
43 distance. *Nano Energy* **2020**, *73*, 104819.
- 44
45 (591) Xu, F.; Dong, S.; Liu, G.; Pan, C.; Guo, Z. H.; Guo, W.; Li, L.; Liu, Y.; Zhang, C.;
46 Pu, X.; Wang, Z. L., Scalable fabrication of stretchable and washable textile triboelectric
47
48
49
50
51
52
53
54
55
56
57
58
59
60

nanogenerators as constant power sources for wearable electronics. *Nano Energy* **2021**, *88*, 106247.

(592) Hwang, H. J.; Lee, Y.; Lee, C.; Nam, Y.; Park, J.; Choi, D.; Kim, D., Mesoporous highly-deformable composite polymer for a gapless triboelectric nanogenerator via a one-step metal oxidation process. *micromachines* **2018**, *9*(12), 656.

(593) Gu, G.; Shea, H.; Seelecke, S.; Alici, G.; Rizzello, G., Soft Robotics Based on Electroactive Polymers. *Frontiers in Robotics and AI* **2021**, 122.

(594) Ji, X.; Liu, X.; Cacucciolo, V.; Civet, Y.; El Haitami, A.; Cantin, S.; Perriard, Y.; Shea, H., Untethered feel-through haptics using 18- μm thick dielectric elastomer actuators. *Advanced Functional Materials* **2021**, *31* (39), 2006639.

(595) Zhao, H.; Hussain, A. M.; Israr, A.; Vogt, D. M.; Duduta, M.; Clarke, D. R.; Wood, R. J., A wearable soft haptic communicator based on dielectric elastomer actuators. *Soft robotics* **2020**, *7*(4), 451-461.

(596) Duduta, M.; Hajiesmaili, E.; Zhao, H.; Wood, R. J.; Clarke, D. R., Realizing the potential of dielectric elastomer artificial muscles. *Proceedings of the National Academy of Sciences* **2019**, *116*(7), 2476-2481.

(597) Xu, S.; Chen, Y.; Hyun, N.-s. P.; Becker, K. P.; Wood, R. J., A dynamic electrically driven soft valve for control of soft hydraulic actuators. *Proceedings of the National Academy of Sciences* **2021**, *118*(34), e2103198118.

(598) Shi, Y.; Askounis, E.; Plamthottam, R.; Libby, T.; Peng, Z.; Youssef, K.; Pu, J.; Pelrine, R.; Pei, Q., A processable, high-performance dielectric elastomer and multilayering process. *Science* **2022**, *377*(6602), 228-232.

(599) Pei, Q.; Pelrine, R.; Rosenthal, M. A.; Stanford, S.; Prahlad, H.; Kornbluh, R. D., Recent progress on electroelastomer artificial muscles and their application for biomimetic robots. *Smart Structures and Materials 2004: Electroactive Polymer Actuators and Devices (EAPAD) 2004*, *5385*, 41-50.

(600) Li, T.; Li, G.; Liang, Y.; Cheng, T.; Dai, J.; Yang, X.; Liu, B.; Zeng, Z.; Huang, Z.; Luo, Y., Fast-moving soft electronic fish. *Science advances* **2017**, *3*(4), e1602045.

(601) Kofod, G.; Wirges, W.; Paajanen, M.; Bauer, S., Energy minimization for self-organized structure formation and actuation. *Applied Physics Letters* **2007**, *90*(8), 081916.

(602) Ji, X.; Liu, X.; Cacucciolo, V.; Imboden, M.; Civet, Y.; El Haitami, A.; Cantin, S.; Perriard, Y.; Shea, H., An autonomous untethered fast soft robotic insect driven by low-voltage dielectric elastomer actuators. *Science Robotics* **2019**, *4*(37), eaaz6451.

- 1
2
3
4
5 (603) Chen, Y.; Zhao, H.; Mao, J.; Chirarattananon, P.; Helbling, E. F.; Hyun, N.-s. P.;
6 Clarke, D. R.; Wood, R. J., Controlled flight of a microrobot powered by soft artificial
7 muscles. *Nature* **2019**, *575* (7782), 324-329.
- 8
9 (604) Chen, Y.; Xu, S.; Ren, Z.; Chirarattananon, P., Collision resilient insect-scale soft-
10 actuated aerial robots with high agility. *IEEE Transactions on Robotics* **2021**, *37* (5), 1752-
11 1764.
- 12
13 (605) James, J.; Iyer, V.; Chukewad, Y.; Gollakota, S.; Fuller, S. B. In *Liftoff of a 190 mg*
14 *laser-powered aerial vehicle: The lightest wireless robot to fly*, 2018 IEEE International
15 Conference on Robotics and Automation (ICRA), IEEE: 2018; pp 3587-3594.
- 16
17 (606) Jafferis, N. T.; Helbling, E. F.; Karpelson, M.; Wood, R. J., Untethered flight of an
18 insect-sized flapping-wing microscale aerial vehicle. *Nature* **2019**, *570* (7762), 491-495.
- 19
20 (607) Nie, J.; Chen, X.; Wang, Z. L., Electrically responsive materials and devices directly
21 driven by the high voltage of triboelectric nanogenerators. *Advanced Functional Materials*
22 **2019**, *29* (41), 1806351.
- 23
24 (608) Liu, S.; Li, Y.; Guo, W.; Huang, X.; Xu, L.; Lai, Y.-C.; Zhang, C.; Wu, H.,
25 Triboelectric nanogenerators enabled sensing and actuation for robotics. *Nano Energy* **2019**,
26 *65*, 104005.
- 27
28 (609) Rus, D.; Tolley, M. T., Design, fabrication and control of soft robots. *Nature* **2015**,
29 *521* (7553), 467-475.
- 30
31 (610) Graule, M. A.; Chirarattananon, P.; Fuller, S. B.; Jafferis, N. T.; Ma, K. Y.; Spenko,
32 M.; Kornbluh, R.; Wood, R. J., Perching and takeoff of a robotic insect on overhangs using
33 switchable electrostatic adhesion. *Science* **2016**, *352* (6288), 978-982.
- 34
35 (611) Xu, L.; Wu, H.; Yao, G.; Chen, L.; Yang, X.; Chen, B.; Huang, X.; Zhong, W.;
36 Chen, X.; Yin, Z., Giant voltage enhancement via triboelectric charge supplement channel for
37 self-powered electroadhesion. *ACS nano* **2018**, *12* (10), 10262-10271.
- 38
39 (612) Nie, J.; Ren, Z.; Bai, Y.; Shao, J.; Jiang, T.; Xu, L.; Chen, X.; Wang, Z. L., Long
40 distance transport of microdroplets and precise microfluidic patterning based on triboelectric
41 nanogenerator. *Advanced Materials Technologies* **2019**, *4* (1), 1800300.
- 42
43 (613) Boutilier, M. S.; Cao, C.; Nayakanti, N.; Kim, S.; Taheri-Mousavi, S. M.; Hart, A.
44 J., Limiting Mechanisms and Scaling of Electrostatically Controlled Adhesion of Soft
45 Nanocomposite Surfaces for Robotic Gripping. *ACS Applied Materials & Interfaces* **2020**, *13*
46 (1), 1192-1203.
- 47
48
49
50
51
52
53
54
55
56
57
58
59
60

- 1
2
3
4
5 (614) Sun, Q.; Wang, D.; Li, Y.; Zhang, J.; Ye, S.; Cui, J.; Chen, L.; Wang, Z.; Butt, H.-J.;
6 Vollmer, D., Surface charge printing for programmed droplet transport. *Nature materials*
7 **2019**, *18* (9), 936-941.
- 8
9 (615) Zheng, H.; Li, J.; Zhou, Y.; Zhang, C.; Xu, W.; Deng, Y.; Li, J.; Feng, S.; Yi, Z.;
10 Zhou, X., Electrically switched underwater capillary adhesion. *Nature communications* **2022**,
11 *13* (1), 1-8.
- 12
13 (616) Sun, X.; Feng, Y.; Wang, B.; Liu, Y.; Wu, Z.; Yang, D.; Zheng, Y.; Peng, J.; Feng,
14 M.; Wang, D., A new method for the electrostatic manipulation of droplet movement by
15 triboelectric nanogenerator. *Nano Energy* **2021**, *86*, 106115.
- 16
17 (617) Sun, J.; Zhang, L.; Zhou, Y.; Li, Z.; Libanori, A.; Tang, Q.; Huang, Y.; Hu, C.; Guo,
18 H.; Peng, Y., Highly efficient liquid droplet manipulation via human-motion-induced direct
19 charge injection. *Materials Today* **2022**, *58*, 41-47.
- 20
21 (618) Zheng, L.; Dong, S.; Nie, J.; Li, S.; Ren, Z.; Ma, X.; Chen, X.; Li, H.; Wang, Z. L.,
22 Dual-stimulus smart actuator and robot hand based on a vapor-responsive PDMS film and
23 triboelectric nanogenerator. *ACS applied materials & interfaces* **2019**, *11* (45), 42504-42511.
- 24
25 (619) KILIÇHAN, R.; YILMAZ, M., Artificial intelligence and robotic technologies in
26 tourism and hospitality industry. *Erciyes Üniversitesi Sosyal Bilimler Enstitüsü Dergisi* **2020**,
27 (50), 353-380.
- 28
29 (620) Higgins, D. A., Probing the mesoscopic chemical and physical properties of
30 polymer-dispersed liquid crystals. *Advanced Materials* **2000**, *12* (4), 251-264.
- 31
32 (621) Zhang, C.; Wang, H.; Guan, S.; Guo, Z.; Zheng, X.; Fan, Y.; Wang, Y.; Qu, T.;
33 Zhao, Y.; Chen, A., Self-powered optical switch based on triboelectrification-triggered liquid
34 crystal alignment for wireless sensing. *Advanced Functional Materials* **2019**, *29* (13),
35 1808633.
- 36
37 (622) Bol, A. A.; Ferwerda, J.; Bergwerff, J. A.; Meijerink, A., Luminescence of
38 nanocrystalline ZnS : CU²⁺. *Journal of Luminescence* **2002**, *99* (4), 325-334.
- 39
40 (623) Yang, C. H.; Chen, B.; Zhou, J.; Chen, Y. M.; Suo, Z., Electroluminescence of giant
41 stretchability. *Advanced Materials* **2016**, *28* (22), 4480-4484.
- 42
43 (624) Naseri, R.; Shoarinejad, S., Polarization grating based on liquid crystals doped with
44 ferroelectric nanoparticles. *Liquid Crystals* **2020**, *47* (12), 1863-1875.
- 45
46 (625) Li, Q.; Liu, W.; Yang, H.; He, W.; Long, L.; Wu, M.; Zhang, X.; Xi, Y.; Hu, C.;
47 Wang, Z. L., Ultra-stability high-voltage triboelectric nanogenerator designed by ternary
48
49
50
51
52
53
54
55
56
57
58
59
60

1
2
3
4
5 dielectric triboelectrification with partial soft-contact and non-contact mode. *Nano Energy*
6 **2021**, *90*, 106585.

7
8 (626) Zhang, C.; Guo, Z.; Zheng, X.; Zhao, X.; Wang, H.; Liang, F.; Guan, S.; Wang, Y.;
9 Zhao, Y.; Chen, A., A contact-sliding-triboelectrification-driven dynamic optical
10 transmittance modulator for self-powered information covering and selective visualization.
11 *Advanced Materials* **2020**, *32*(1), 1904988.

12
13 (627) Liu, H.; Guo, Z. H.; Xu, F.; Jia, L.; Pan, C.; Wang, Z. L.; Pu, X., Triboelectric-
14 optical responsive cholesteric liquid crystals for self-powered smart window, E-paper display
15 and optical switch. *Science Bulletin* **2021**, *66*(19), 1986-1993.

16
17 (628) Wei, X. Y.; Wang, X.; Kuang, S. Y.; Su, L.; Li, H. Y.; Wang, Y.; Pan, C.; Wang, Z.
18 L.; Zhu, G., Dynamic Triboelectrification-Induced Electroluminescence and its Use in
19 Visualized Sensing. *Advanced Materials* **2016**, *28*(31), 6656-+.

20
21 (629) Wang, H. L.; Su, L.; Li, H. Y.; Wang, Z. L.; Zhu, G., Electret-induced electric field
22 assisted luminescence modulation for interactive visualized sensing in a non-contact mode.
23 *Materials Horizons* **2020**, *7*(4), 1144-1149.

24
25 (630) Wang, J.; Wang, H.; Li, X.; Zi, Y., Self-powered electrowetting optical switch
26 driven by a triboelectric nanogenerator for wireless sensing. *Nano Energy* **2019**, *66*, 104140.

27
28 (631) Gu, Y.; Hou, T.; Chen, P.; Cao, J.; Pan, C.; Hu, W.; Yang, B.-R.; Pu, X.; Wang, Z.
29 L., Self-powered electronic paper with energy supplies and information inputs solely from
30 mechanical motions. *Photonics Research* **2020**, *8*(9), 1496-1505.

31
32 (632) Fang, C.; Tong, T.; Bu, T.; Cao, Y.; Xu, S.; Qi, Y.; Zhang, C., Overview of Power
33 Management for Triboelectric Nanogenerators. *Advanced Intelligent Systems* **2020**, *2*(2).

34
35 (633) Wang, X.; Song, J.; Liu, J.; Wang, Z. L., Direct-current nanogenerator driven by
36 ultrasonic waves. *Science* **2007**, *316*(5821), 102-105.

37
38 (634) Wang, X., Piezoelectric nanogenerators—Harvesting ambient mechanical energy at
39 the nanometer scale. *Nano Energy* **2012**, *1*(1), 13-24.

40
41 (635) Ouyang, H.; Liu, Z.; Li, N.; Shi, B.; Zou, Y.; Xie, F.; Ma, Y.; Li, Z.; Li, H.; Zheng,
42 Q., Symbiotic cardiac pacemaker. *Nature communications* **2019**, *10*(1), 1-10.

43
44 (636) Li, J.; Kang, L.; Long, Y.; Wei, H.; Yu, Y.; Wang, Y.; Ferreira, C. A.; Yao, G.;
45 Zhang, Z.; Carlos, C., Implanted battery-free direct-current micro-power supply from in vivo
46 breath energy harvesting. *ACS applied materials & interfaces* **2018**, *10*(49), 42030-42038.

- 1
2
3
4
5 (637) Wang, M.; Zhang, J.; Tang, Y.; Li, J.; Zhang, B.; Liang, E.; Mao, Y.; Wang, X.,
6 Air-flow-driven triboelectric nanogenerators for self-powered real-time respiratory
7 monitoring. *ACS nano* **2018**, *12* (6), 6156-6162.
- 8
9 (638) Li, J.; Long, Y.; Yang, F.; Wang, X., Degradable piezoelectric biomaterials for
10 wearable and implantable bioelectronics. *Current Opinion in Solid State and Materials*
11 *Science* **2020**, *24* (1), 100806.
- 12
13 (639) Levin, M.; Stevenson, C. G., Regulation of cell behavior and tissue patterning by
14 bioelectrical signals: challenges and opportunities for biomedical engineering. *Annu. Rev.*
15 *Biomed. Eng.* **2012**, *14*.
- 16
17 (640) Salazar, A.; Stein, C.; Marchese, R. R.; Plentz, R.; Pagnussat, A., Electric
18 Stimulation for Pain Relief in Patients with Fibromyalgia: A Systematic Review and Meta-
19 analysis of Randomized Controlled Trials. 2017.
- 20
21 (641) Hunckler, J.; De Mel, A., A current affair: electrotherapy in wound healing. *Journal*
22 *of multidisciplinary healthcare* **2017**, *10*, 179.
- 23
24 (642) Khalifeh, J. M.; Zohny, Z.; MacEwan, M.; Stephen, M.; Johnston, W.; Gamble, P.;
25 Zeng, Y.; Yan, Y.; Ray, W. Z., Electrical stimulation and bone healing: a review of current
26 technology and clinical applications. *IEEE reviews in biomedical engineering* **2018**, *11*, 217-
27 232.
- 28
29 (643) Gargiulo, P.; Vatnsdal, B.; Ingvarsson, P.; Knútsdóttir, S.; Gudmundsdóttir, V.;
30 Yngvason, S.; Helgason, T., Restoration of muscle volume and shape induced by electrical
31 stimulation of denervated degenerated muscles: qualitative and quantitative measurement of
32 changes in rectus femoris using computer tomography and image segmentation. *Artificial*
33 *organs* **2008**, *32* (8), 609-613.
- 34
35 (644) Bauer, S.; Baier, H.; Baumgartner, C.; Bohlmann, K.; Fauser, S.; Graf, W.;
36 Hillenbrand, B.; Hirsch, M.; Last, C.; Lerche, H., Transcutaneous vagus nerve stimulation
37 (tVNS) for treatment of drug-resistant epilepsy: a randomized, double-blind clinical trial
38 (cMPsE02). *Brain stimulation* **2016**, *9* (3), 356-363.
- 39
40 (645) Chakravarthy, K.; Nava, A.; Christo, P. J.; Williams, K., Review of recent advances
41 in peripheral nerve stimulation (PNS). *Current pain and headache reports* **2016**, *20* (11), 1-7.
- 42
43 (646) Hampton, T., Proposed rule seeks to safeguard against phased-out chemicals. *JAMA*
44 **2015**, *313* (8), 785-785.
- 45
46 (647) Priori, A.; Berardelli, A.; Inghilleri, M.; Accornero, N.; Manfredi, M., Motor
47 cortical inhibition and the dopaminergic system: pharmacological changes in the silent period
48
49
50
51
52
53
54
55
56
57
58
59
60

1
2
3
4
5 after transcranial brain stimulation in normal subjects, patients with Parkinson's disease and
6 drug-induced parkinsonism. *Brain* **1994**, *117*(2), 317-323.

7
8 (648) Kabay, S. C.; Kabay, S.; Yucel, M.; Ozden, H., Acute urodynamic effects of
9 percutaneous posterior tibial nerve stimulation on neurogenic detrusor overactivity in patients
10 with Parkinson's disease. *Neurourology and Urodynamics: Official Journal of the*
11 *International Continence Society* **2009**, *28*(1), 62-67.

12
13 (649) Farrand, A. Q.; Helke, K. L.; Gregory, R. A.; Gooz, M.; Hinson, V. K.; Boger, H.
14 A., Vagus nerve stimulation improves locomotion and neuronal populations in a model of
15 Parkinson's disease. *Brain stimulation* **2017**, *10*(6), 1045-1054.

16
17 (650) Pahwa, R.; Dhall, R.; Ostrem, J.; Gwinn, R.; Lyons, K.; Ro, S.; Dietiker, C.; Luthra,
18 N.; Chidester, P.; Hamner, S., An acute randomized controlled trial of noninvasive peripheral
19 nerve stimulation in essential tremor. *Neuromodulation: Technology at the Neural Interface*
20 **2019**, *22*(5), 537-545.

21
22 (651) Handforth, A.; Ondo, W.; Tatter, S.; Mathern, G.; Simpson, R.; Walker, F.; Sutton,
23 J.; Hubble, J.; Jankovic, J., Vagus nerve stimulation for essential tremor: a pilot efficacy and
24 safety trial. *Neurology* **2003**, *61*(10), 1401-1405.

25
26 (652) Berényi, A.; Belluscio, M.; Mao, D.; Buzsáki, G., Closed-loop control of epilepsy
27 by transcranial electrical stimulation. *Science* **2012**, *337*(6095), 735-737.

28
29 (653) Fisher, R. S.; Velasco, A. L., Electrical brain stimulation for epilepsy. *Nature*
30 *Reviews Neurology* **2014**, *10*(5), 261-270.

31
32 (654) Mayberg, H. S.; Lozano, A. M.; Voon, V.; McNeely, H. E.; Seminowicz, D.;
33 Hamani, C.; Schwalb, J. M.; Kennedy, S. H., Deep brain stimulation for treatment-resistant
34 depression. *Neuron* **2005**, *45*(5), 651-660.

35
36 (655) Jiménez, F.; Velasco, F.; Salin-Pascual, R.; Hernández, J. A.; Velasco, M.; Criales,
37 J. L.; Nicolini, H., A patient with a resistant major depression disorder treated with deep brain
38 stimulation in the inferior thalamic peduncle. *Neurosurgery* **2005**, *57*(3), 585-593.

39
40 (656) Thakral, G.; LaFontaine, J.; Najafi, B.; Talal, T. K.; Kim, P.; Lavery, L. A.,
41 Electrical stimulation to accelerate wound healing. *Diabetic foot & ankle* **2013**, *4*(1), 22081.

42
43 (657) Song, B.; Gu, Y.; Pu, J.; Reid, B.; Zhao, Z.; Zhao, M., Application of direct current
44 electric fields to cells and tissues in vitro and modulation of wound electric field in vivo.
45 *Nature protocols* **2007**, *2*(6), 1479-1489.

- 1
2
3
4
5 (658) Randall, B. F.; Imig, C.; Hines, H., Effect of electrical stimulation upon blood flow
6 and temperature of skeletal muscle. *American Journal of Physical Medicine & Rehabilitation*
7 **1953**, *32* (1), 22-26.
- 8
9 (659) Hecker, B.; Carron, H.; Schwartz, D., Pulsed galvanic stimulation: effects of current
10 frequency and polarity on blood flow in healthy subjects. *Archives of physical medicine and*
11 *rehabilitation* **1985**, *66* (6), 369-371.
- 12
13 (660) Winter, G., Movement of epidermal cells over the wound surface. *Dev Biol Skin*
14 **1964**, *5*, 113-127.
- 15
16 (661) Cooper, M.; Schliwa, M., Electrical and ionic controls of tissue cell locomotion in
17 DC electric fields. *Journal of neuroscience research* **1985**, *13* (1-2), 223-244.
- 18
19 (662) Orida, N.; Feldman, J. D., Directional protrusive pseudopodial activity and motility
20 in macrophages induced by extracellular electric fields. *Cell motility* **1982**, *2* (3), 243-255.
- 21
22 (663) Gentzkow, G. D.; Miller, K. H., Electrical stimulation for dermal wound healing.
23 *Clinics in podiatric medicine and surgery* **1991**, *8* (4), 827-841.
- 24
25 (664) Ud-Din, S.; Bayat, A., Electrical Stimulation and Cutaneous Wound Healing: A
26 Review of Clinical Evidence. *Healthcare (Basel)* **2014**, *2* (4), 445-467.
- 27
28 (665) Gentzkow, G. D., Electrical Stimulation to Heal Dermal Wounds. *The Journal of*
29 *Dermatologic Surgery and Oncology* **1993**, *19* (8), 753-758.
- 30
31 (666) Long, Y.; Wei, H.; Li, J.; Yao, G.; Yu, B.; Ni, D.; Gibson, A. L.; Lan, X.; Jiang, Y.;
32 Cai, W., Effective wound healing enabled by discrete alternative electric fields from wearable
33 nanogenerators. *ACS nano* **2018**, *12* (12), 12533-12540.
- 34
35 (667) Liu, A.; Long, Y.; Li, J.; Gu, L.; Karim, A.; Wang, X.; Gibson, A. L. F., Accelerated
36 complete human skin architecture restoration after wounding by nanogenerator-driven
37 electrostimulation. *Journal of Nanobiotechnology* **2021**, *19* (1), 280.
- 38
39 (668) Starr, M. B.; Shi, J.; Wang, X., Piezopotential-driven redox reactions at the surface
40 of piezoelectric materials. *Angewandte Chemie International Edition* **2012**, *51* (24), 5962-
41 5966.
- 42
43 (669) Yao, G.; Jiang, D.; Li, J.; Kang, L.; Chen, S.; Long, Y.; Wang, Y.; Huang, P.; Lin,
44 Y.; Cai, W., Self-activated electrical stimulation for effective hair regeneration via a wearable
45 omnidirectional pulse generator. *ACS nano* **2019**, *13* (11), 12345-12356.
- 46
47 (670) Fukada, E.; Yasuda, I., On the piezoelectric effect of bone. *Journal of the physical*
48 *society of Japan* **1957**, *12* (10), 1158-1162.
- 49
50
51
52
53
54
55
56
57
58
59
60

- 1
2
3
4
5 (671) Mattei, M. D.; Gagliano, N.; Moscheni, C.; Dellavia, C.; Calastrini, C.; Pellati, A.;
6 Gioia, M.; Caruso, A.; Stabellini, G., Changes in polyamines, c-myc and c-fos gene
7 expression in osteoblast-like cells exposed to pulsed electromagnetic fields.
8 *Bioelectromagnetics* **2005**, *26* (3), 207-214.
9
10
11 (672) Luben, R. A.; Cain, C. D.; Chen, M. C.-Y.; Rosen, D. M.; Adey, W. R., Effects of
12 electromagnetic stimuli on bone and bone cells in vitro: inhibition of responses to parathyroid
13 hormone by low-energy low-frequency fields. *Proceedings of the National Academy of*
14 *Sciences* **1982**, *79* (13), 4180-4184.
15
16
17 (673) Spadaro, J.; Bergstrom, W., In vivo and in vitro effects of a pulsed electromagnetic
18 field on net calcium flux in rat calvarial bone. *Calcified tissue international* **2002**, *70* (6).
19
20
21 (674) Schwartz, Z.; Simon, B.; Duran, M.; Barabino, G.; Chaudhri, R.; Boyan, B., Pulsed
22 electromagnetic fields enhance BMP-2 dependent osteoblastic differentiation of human
23 mesenchymal stem cells. *Journal of Orthopaedic Research* **2008**, *26* (9), 1250-1255.
24
25
26 (675) Yao, G.; Kang, L.; Li, C.; Chen, S.; Wang, Q.; Yang, J.; Long, Y.; Li, J.; Zhao, K.;
27 Xu, W., A self-powered implantable and bioresorbable electrostimulation device for
28 biofeedback bone fracture healing. *Proceedings of the National Academy of Sciences* **2021**,
29 *118* (28), e2100772118.
30
31
32 (676) Son, D.; Lee, J.; Qiao, S.; Ghaffari, R.; Kim, J.; Lee, J. E.; Song, C.; Kim, S. J.; Lee,
33 D. J.; Jun, S. W., Multifunctional wearable devices for diagnosis and therapy of movement
34 disorders. *Nature nanotechnology* **2014**, *9* (5), 397-404.
35
36
37 (677) Chen, G.; Xiao, X.; Zhao, X.; Tat, T.; Bick, M.; Chen, J., Electronic textiles for
38 wearable point-of-care systems. *Chemical Reviews* **2021**, *122* (3), 3259-3291.
39
40
41 (678) Libanori, A.; Chen, G.; Zhao, X.; Zhou, Y.; Chen, J., Smart textiles for personalized
42 healthcare. *Nature Electronics* **2022**, *5* (3), 142-156.
43
44
45 (679) Liu, Z.; Liang, X.; Liu, H.; Wang, Z.; Jiang, T.; Cheng, Y.; Wu, M.; Xiang, D.; Li,
46 Z.; Wang, Z. L., High-throughput and self-powered electroporation system for drug delivery
47 assisted by microfoam electrode. *ACS nano* **2020**, *14* (11), 15458-15467.
48
49
50 (680) Xiao, X.; Chen, G.; Libanori, A.; Chen, J., Wearable triboelectric nanogenerators for
51 therapeutics. *Trends in Chemistry* **2021**, *3* (4), 279-290.
52
53
54 (681) Zhang, S.; Bick, M.; Xiao, X.; Chen, G.; Nashalian, A.; Chen, J., Leveraging
55 triboelectric nanogenerators for bioengineering. *Matter* **2021**, *4* (3), 845-887.
56
57 (682) Amjadi, M.; Sheykhsari, S.; Nelson, B. J.; Sitti, M., Recent advances in wearable
58 transdermal delivery systems. *Advanced materials* **2018**, *30* (7), 1704530.
59
60

- 1
2
3
4
5 (683) Liu, Z.; Nie, J.; Miao, B.; Li, J.; Cui, Y.; Wang, S.; Zhang, X.; Zhao, G.; Deng, Y.;
6 Wu, Y., Self-powered intracellular drug delivery by a biomechanical energy-driven
7 triboelectric nanogenerator. *Advanced Materials* **2019**, *31* (12), 1807795.
- 8
9 (684) Wu, C.; Jiang, P.; Li, W.; Guo, H.; Wang, J.; Chen, J.; Prausnitz, M. R.; Wang, Z.
10 L., Self-powered iontophoretic transdermal drug delivery system driven and regulated by
11 biomechanical motions. *Advanced Functional Materials* **2020**, *30* (3), 1907378.
- 12
13 (685) Song, P.; Kuang, S.; Panwar, N.; Yang, G.; Tng, D. J. H.; Tjin, S. C.; Ng, W. J.;
14 Majid, M. B. A.; Zhu, G.; Yong, K. T., A self-powered implantable drug-delivery system
15 using biokinetic energy. *Advanced Materials* **2017**, *29* (11), 1605668.
- 16
17 (686) Ouyang, Q.; Feng, X.; Kuang, S.; Panwar, N.; Song, P.; Yang, C.; Yang, G.; Hemu,
18 X.; Zhang, G.; Yoon, H. S., Self-powered, on-demand transdermal drug delivery system
19 driven by triboelectric nanogenerator. *Nano Energy* **2019**, *62*, 610-619.
- 20
21 (687) Chen, X.; Wu, Y.; Shao, J.; Jiang, T.; Yu, A.; Xu, L.; Wang, Z. L., On-skin
22 triboelectric nanogenerator and self-powered sensor with ultrathin thickness and high
23 stretchability. *Small* **2017**, *13* (47), 1702929.
- 24
25 (688) Huo, Z. Y.; Lee, D. M.; Wang, S.; Kim, Y. J.; Kim, S. W., Emerging Energy
26 Harvesting Materials and Devices for Self-Powered Water Disinfection. *Small Methods*
27 **2021**, *5* (7), 2100093.
- 28
29 (689) Liu, X.; Mo, J.; Wu, W.; Song, H.; Nie, S., Triboelectric pulsed direct-current
30 enhanced radical generation for efficient degradation of organic pollutants in wastewater.
31 *Applied Catalysis B: Environmental* **2022**, *312*, 121422.
- 32
33 (690) Gao, S.; Su, J.; Wei, X.; Wang, M.; Tian, M.; Jiang, T.; Wang, Z. L., Self-powered
34 electrochemical oxidation of 4-aminoazobenzene driven by a triboelectric nanogenerator.
35 *ACS nano* **2017**, *11* (1), 770-778.
- 36
37 (691) Chen, G., Electrochemical technologies in wastewater treatment. *Separation and*
38 *purification Technology* **2004**, *38* (1), 11-41.
- 39
40 (692) Michael, I.; Rizzo, L.; McArdell, C.; Manaia, C.; Merlin, C.; Schwartz, T.; Dagot,
41 C.; Fatta-Kassinos, D., Urban wastewater treatment plants as hotspots for the release of
42 antibiotics in the environment: a review. *Water research* **2013**, *47* (3), 957-995.
- 43
44 (693) Moore, C. J., Synthetic polymers in the marine environment: A rapidly increasing,
45 long-term threat. *Environmental Research* **2008**, *108* (2), 131-139.
- 46
47
48
49
50
51
52
53
54
55
56
57
58
59
60

- 1
2
3
4
5 (694) Chen, S.; Wang, N.; Ma, L.; Li, T.; Willander, M.; Jie, Y.; Cao, X.; Wang, Z. L.,
6 Triboelectric nanogenerator for sustainable wastewater treatment via a self-powered
7 electrochemical process. *Advanced Energy Materials* **2016**, *6*(8), 1501778.
- 8
9 (695) Li, W.; Li, L.; Qiu, G., Energy consumption and economic cost of typical
10 wastewater treatment systems in Shenzhen, China. *Journal of Cleaner Production* **2017**, *163*,
11 S374-S378.
- 12
13 (696) Qu, J.; Wang, H.; Wang, K.; Yu, G.; Ke, B.; Yu, H.-Q.; Ren, H.; Zheng, X.; Li, J.;
14 Li, W.-W., Municipal wastewater treatment in China: Development history and future
15 perspectives. *Frontiers of Environmental Science & Engineering* **2019**, *13*(6), 1-7.
- 16
17 (697) Dong, F.; Pang, Z.; Yang, S.; Lin, Q.; Song, S.; Li, C.; Ma, X.; Nie, S., Improving
18 Wastewater Treatment by Triboelectric-Photo/Electric Coupling Effect. *ACS nano* **2022**, *16*
19 (3), 3449-3475.
- 20
21 (698) Ang, W. L.; Mohammad, A. W.; Johnson, D.; Hilal, N., Forward osmosis research
22 trends in desalination and wastewater treatment: A review of research trends over the past
23 decade. *Journal of Water Process Engineering* **2019**, *31*, 100886.
- 24
25 (699) Bogler, A.; Packman, A.; Furman, A.; Gross, A.; Kushmaro, A.; Ronen, A.; Dagot,
26 C.; Hill, C.; Vaizel-Ohayon, D.; Morgenroth, E., Rethinking wastewater risks and monitoring
27 in light of the COVID-19 pandemic. *Nature Sustainability* **2020**, *3*(12), 981-990.
- 28
29 (700) Pooi, C. K.; Ng, H. Y., Review of low-cost point-of-use water treatment systems for
30 developing communities. *NPJ Clean Water* **2018**, *1*(1), 1-8.
- 31
32 (701) Efstratiou, A.; Ongerth, J. E.; Karanis, P., Waterborne transmission of protozoan
33 parasites: review of worldwide outbreaks-an update 2011–2016. *Water research* **2017**, *114*,
34 14-22.
- 35
36 (702) Tien, J. H.; Earn, D. J., Multiple transmission pathways and disease dynamics in a
37 waterborne pathogen model. *Bulletin of mathematical biology* **2010**, *72*(6), 1506-1533.
- 38
39 (703) Huo, Z.-Y.; Du, Y.; Chen, Z.; Wu, Y.-H.; Hu, H.-Y., Evaluation and prospects of
40 nanomaterial-enabled innovative processes and devices for water disinfection: A state-of-the-
41 art review. *Water Research* **2020**, *173*, 115581.
- 42
43 (704) Datar, A.; Liu, J.; Linnemayr, S.; Stecher, C., The impact of natural disasters on
44 child health and investments in rural India. *Social Science & Medicine* **2013**, *76*, 83-91.
- 45
46 (705) Liu, C.; Xie, X.; Zhao, W.; Yao, J.; Kong, D.; Boehm, A. B.; Cui, Y., Static
47 electricity powered copper oxide nanowire microbicidal electroporation for water
48 disinfection. *Nano letters* **2014**, *14*(10), 5603-5608.
- 49
50
51
52
53
54
55
56
57
58
59
60

- 1
2
3
4
5 (706) Tian, J.; Feng, H.; Yan, L.; Yu, M.; Ouyang, H.; Li, H.; Jiang, W.; Jin, Y.; Zhu, G.;
6 Li, Z., A self-powered sterilization system with both instant and sustainable anti-bacterial
7 ability. *Nano Energy* **2017**, *36*, 241-249.
8
9 (707) Huo, Z.-Y.; Lee, D.-M.; Jeong, J.-M.; Kim, Y.-J.; Kim, J.; Suh, I.-Y.; Xiong, P.;
10 Kim, S.-W., Microbial Disinfection with Supercoiling Capacitive Triboelectric
11 Nanogenerator. *Advanced Energy Materials* **2022**, *12* (15), 2103680.
12
13 (708) Ding, W.; Zhou, J.; Cheng, J.; Wang, Z.; Guo, H.; Wu, C.; Xu, S.; Wu, Z.; Xie, X.;
14 Wang, Z. L., TriboPump: a low-cost, hand-powered water disinfection system. *Advanced*
15 *Energy Materials* **2019**, *9* (27), 1901320.
16
17 (709) Jiang, Q.; Jie, Y.; Han, Y.; Gao, C.; Zhu, H.; Willander, M.; Zhang, X.; Cao, X.,
18 Self-powered electrochemical water treatment system for sterilization and algae removal
19 using water wave energy. *Nano Energy* **2015**, *18*, 81-88.
20
21 (710) Wang, Z.; Shi, Y.; Liu, F.; Wang, H.; Liu, X.; Sun, R.; Lu, Y.; Ji, L.; Wang, Z. L.;
22 Cheng, J., Distributed mobile ultraviolet light sources driven by ambient mechanical stimuli.
23 *Nano Energy* **2020**, *74*, 104910.
24
25 (711) Jeon, S.-B.; Kim, S.; Park, S.-J.; Seol, M.-L.; Kim, D.; Chang, Y. K.; Choi, Y.-K.,
26 Self-powered electro-coagulation system driven by a wind energy harvesting triboelectric
27 nanogenerator for decentralized water treatment. *Nano Energy* **2016**, *28*, 288-295.
28
29 (712) Emanjomeh, M. M.; Sivakumar, M., Review of pollutants removed by
30 electrocoagulation and electrocoagulation/flotation processes. *Journal of Environmental*
31 *Management* **2009**, *90* (5), 1663-1679.
32
33 (713) Cho, H.; Kim, I.; Park, J.; Kim, D., A waterwheel hybrid generator with disk
34 triboelectric nanogenerator and electromagnetic generator as a power source for an
35 electrocoagulation system. *Nano Energy* **2022**, *95*, 107048.
36
37 (714) Cheng, G.; Lin, Z.-H.; Du, Z.-l.; Wang, Z. L., Simultaneously harvesting
38 electrostatic and mechanical energies from flowing water by a hybridized triboelectric
39 nanogenerator. *Acs Nano* **2014**, *8* (2), 1932-1939.
40
41 (715) Daghrir, R.; Drogui, P., Tetracycline antibiotics in the environment: a review.
42 *Environmental chemistry letters* **2013**, *11* (3), 209-227.
43
44 (716) Mo, J.; Liu, Y.; Fu, Q.; Cai, C.; Lu, Y.; Wu, W.; Zhao, Z.; Song, H.; Wang, S.; Nie,
45 S., Triboelectric nanogenerators for enhanced degradation of antibiotics via external electric
46 field. *Nano Energy* **2022**, *93*, 106842.
47
48
49
50
51
52
53
54
55
56
57
58
59
60

- 1
2
3
4
5 (717) Park, B.-G.; Lee, C.; Kim, Y.-J.; Park, J.; Kim, H.; Jung, Y.; Ko, J. S.; Kim, S.-W.;
6 Lee, J.-H.; Cho, H., Toxic micro/nano particles removal in water via triboelectric
7 nanogenerator. *Nano Energy* **2022**, *100*, 107433.
- 8
9 (718) Brauer, M.; Casadei, B.; Harrington, R. A.; Kovacs, R.; Sliwa, K.; Group, W. A. P.
10 E., Taking a stand against air pollution—The impact on cardiovascular disease: A joint
11 opinion from the world heart federation, american college of cardiology, american heart
12 association, and the european society of cardiology. *Circulation* **2021**, *143* (14), e800-e804.
- 13
14 (719) Seinfeld, J. H., Urban air pollution: state of the science. *Science* **1989**, *243* (4892),
15 745-752.
- 16
17 (720) Liao, K.; Huang, X.; Dang, H.; Ren, Y.; Zuo, S.; Duan, C., Statistical approaches for
18 forecasting primary air pollutants: a review. *Atmosphere* **2021**, *12* (6), 686.
- 19
20 (721) Liu, H.; Liu, L.; Yu, J.; Yin, X.; Ding, B., High-efficiency and super-breathable air
21 filters based on biomimetic ultrathin nanofiber networks. *Composites Communications* **2020**,
22 *22*, 100493.
- 23
24 (722) Chen, B.; Li, S.; Guo, Y.; Li, H.; Zhou, W.; Liu, B., Research on electrostatic
25 shielding characteristics of electrostatic precipitator. *Journal of the Air & Waste Management*
26 *Association* **2022**, *72* (4), 331-345.
- 27
28 (723) Liu, J.; Jiang, T.; Li, X.; Wang, Z. L., Triboelectric filtering for air purification.
29 *Nanotechnology* **2019**, *30* (29), 292001.
- 30
31 (724) Gu, G. Q.; Han, C. B.; Lu, C. X.; He, C.; Jiang, T.; Gao, Z. L.; Li, C. J.; Wang, Z.
32 L., Triboelectric nanogenerator enhanced nanofiber air filters for efficient particulate matter
33 removal. *ACS nano* **2017**, *11* (6), 6211-6217.
- 34
35 (725) Hao, R.; Yang, S.; Yang, K.; Zhang, Z.; Wang, T.; Sang, S.; Zhang, H., Self-
36 Powered Air Filter Based on an Electrospun Respiratory Triboelectric Nanogenerator. *ACS*
37 *Applied Energy Materials* **2021**, *4* (12), 14700-14708.
- 38
39 (726) Zhang, J.; Chen, P.; Zu, L.; Yang, J.; Sun, Y.; Li, H.; Chen, B.; Wang, Z. L.,
40 Self-Powered High-Voltage Recharging System for Removing Noxious Tobacco Smoke by
41 Biomimetic Hairy-Contact Triboelectric Nanogenerator. *Small* **2022**, *18* (33), 2202835.
- 42
43 (727) Han, C. B.; Jiang, T.; Zhang, C.; Li, X.; Zhang, C.; Cao, X.; Wang, Z. L., Removal
44 of particulate matter emissions from a vehicle using a self-powered triboelectric filter. *ACS*
45 *nano* **2015**, *9* (12), 12552-12561.
- 46
47
48
49
50
51
52
53
54
55
56
57
58
59
60

- 1
2
3
4
5 (728) Feng, Y.; Ling, L.; Nie, J.; Han, K.; Chen, X.; Bian, Z.; Li, H.; Wang, Z. L., Self-
6 powered electrostatic filter with enhanced photocatalytic degradation of formaldehyde based
7 on built-in triboelectric nanogenerators. *ACS nano* **2017**, *11* (12), 12411-12418.
- 8
9 (729) Zheng, Q.; Sun, T.; Fang, L.; Zheng, L.; Li, H., Self-powered air purifier with
10 coupling of non-thermal plasma and photocatalytic oxidation for formaldehyde degradation
11 based on triboelectric nanogenerator. *Nano Energy* **2022**, *102*, 107706.
- 12
13 (730) Chortos, A.; Liu, J.; Bao, Z., Pursuing prosthetic electronic skin. *Nature materials*
14 **2016**, *15* (9), 937-950.
- 15
16 (731) Ra, Y.; Choi, J. H.; La, M.; Park, S. J.; Choi, D., Development of a highly
17 transparent and flexible touch sensor based on triboelectric effect. *Functional Composites and*
18 *Structures* **2019**, *1* (4), 045001.
- 19
20 (732) Kim, W.; Bhatia, D.; Hwang, H. J.; Choi, K.; Choi, D., Double impact triboelectric
21 nanogenerators for harvesting broadband vibrations from vehicles. *Functional Composites and*
22 *Structures* **2019**, *1* (3), 035003.
- 23
24 (733) Wang, S.; Lin, L.; Wang, Z. L., Triboelectric nanogenerators as self-powered active
25 sensors. *Nano Energy* **2015**, *11*, 436-462.
- 26
27 (734) Zhu, G.; Peng, B.; Chen, J.; Jing, Q.; Wang, Z. L., Triboelectric nanogenerators as a
28 new energy technology: from fundamentals, devices, to applications. *Nano Energy* **2015**, *14*,
29 126-138.
- 30
31 (735) Li, M.; Lu, H.-W.; Wang, S.-W.; Li, R.-P.; Chen, J.-Y.; Chuang, W.-S.; Yang, F.-S.;
32 Lin, Y.-F.; Chen, C.-Y.; Lai, Y.-C., Filling the gap between topological insulator
33 nanomaterials and triboelectric nanogenerators. *Nature communications* **2022**, *13* (1), 1-11.
- 34
35 (736) Lai, Y. C.; Deng, J.; Niu, S.; Peng, W.; Wu, C.; Liu, R.; Wen, Z.; Wang, Z. L.,
36 Electric eel-skin-inspired mechanically durable and super-stretchable nanogenerator for
37 deformable power source and fully autonomous conformable electronic-skin applications.
38 *Advanced Materials* **2016**, *28* (45), 10024-10032.
- 39
40 (737) Lai, Y. C.; Deng, J.; Zhang, S. L.; Niu, S.; Guo, H.; Wang, Z. L.,
41 Single-thread-based wearable and highly stretchable triboelectric nanogenerators and their
42 applications in cloth-based self-powered human-interactive and biomedical sensing.
43 *Advanced Functional Materials* **2017**, *27* (1), 1604462.
- 44
45 (738) Paosangthong, W.; Torah, R.; Beeby, S., Recent progress on textile-based
46 triboelectric nanogenerators. *Nano Energy* **2019**, *55*, 401-423.
- 47
48
49
50
51
52
53
54
55
56
57
58
59
60

- 1
2
3
4
5 (739) Lai, Y. C.; Wu, H. M.; Lin, H. C.; Chang, C. L.; Chou, H. H.; Hsiao, Y. C.; Wu, Y.
6 C., Entirely, intrinsically, and autonomously self-healable, highly transparent, and
7 superstretchable triboelectric nanogenerator for personal power sources and self-powered
8 electronic skins. *Advanced Functional Materials* **2019**, *29*(40), 1904626.
- 11 (740) Deng, J.; Kuang, X.; Liu, R.; Ding, W.; Wang, A. C.; Lai, Y. C.; Dong, K.; Wen, Z.;
12 Wang, Y.; Wang, L., Vitriimer elastomer-based jigsaw puzzle-like healable triboelectric
13 nanogenerator for self-powered wearable electronics. *Advanced Materials* **2018**, *30* (14),
14 1705918.
- 18 (741) Khan, A.; Ginnaram, S.; Wu, C.-H.; Lu, H.-W.; Pu, Y.-F.; Wu, J. I.; Gupta, D.; Lai,
19 Y.-C.; Lin, H.-C., Fully self-healable, highly stretchable, and anti-freezing supramolecular
20 gels for energy-harvesting triboelectric nanogenerator and self-powered wearable electronics.
21 *Nano Energy* **2021**, *90*, 106525.
- 25 (742) Hager, M. D.; Greil, P.; Leyens, C.; van der Zwaag, S.; Schubert, U. S., Self-healing
26 materials. *Advanced Materials* **2010**, *22* (47), 5424-5430.
- 28 (743) Song, T.; Jiang, B.; Li, Y.; Ji, Z.; Zhou, H.; Jiang, D.; Seok, I.; Murugadoss, V.;
29 Wen, N.; Colorado, H., Self-healing Materials: a review of recent developments. *ES*
30 *Materials & Manufacturing* **2021**, *14*, 1-19.
- 33 (744) Lai, Y. C.; Deng, J.; Liu, R.; Hsiao, Y. C.; Zhang, S. L.; Peng, W.; Wu, H. M.;
34 Wang, X.; Wang, Z. L., Actively perceiving and responsive soft robots enabled by
35 self-powered, highly extensible, and highly sensitive triboelectric proximity-and
36 pressure-sensing skins. *Advanced Materials* **2018**, *30*(28), 1801114.
- 40 (745) Wen, X.; Su, Y.; Yang, Y.; Zhang, H.; Wang, Z. L., Applicability of triboelectric
41 generator over a wide range of temperature. *Nano Energy* **2014**, *4*, 150-156.
- 43 (746) 이영훈. A study on electrostatic soft ionic sensors and generators based on
44 tribotronics. 서울대학교 대학원, 2021.
- 46 (747) Lee, Y.; Song, W. J.; Jung, Y.; Yoo, H.; Kim, M.-Y.; Kim, H.-Y.; Sun, J.-Y., Ionic
47 spiderwebs. *Science Robotics* **2020**, *5*(44), eaaz5405.
- 50 (748) Hwang, H. J.; Kim, J. S.; Kim, W.; Park, H.; Bhatia, D.; Jee, E.; Chung, Y. S.; Kim,
51 D. H.; Choi, D., An ultra-mechanosensitive visco-poroelastic polymer ion pump for
52 continuous self-powering kinematic triboelectric nanogenerators. *Advanced Energy Materials*
53 **2019**, *9*(17), 1803786.
- 56 (749) Lee, Y.; Song, W.; Sun, J.-Y., Hydrogel soft robotics. *Materials Today Physics*
57 **2020**, *15*, 100258.
- 59
60

- 1
2
3
4
5 (750) Park, J.-M.; Park, J.; Kim, Y.-H.; Zhou, H.; Lee, Y.; Jo, S. H.; Ma, J.; Lee, T.-W.;
6 Sun, J.-Y., Aromatic nonpolar organogels for efficient and stable perovskite green emitters.
7 *Nature communications* **2020**, *11* (1), 1-10.
8
9 (751) Ba, Y.-Y.; Bao, J.-F.; Wang, Z.-Y.; Deng, H.-T.; Wen, D.-L.; Zhang, X.-R.; Tu, C.;
10 Zhang, X.-S., Self-powered trajectory-tracking microsystem based on electrode-miniaturized
11 triboelectric nanogenerator. *Nano Energy* **2021**, *82*, 105730.
12
13 (752) Jin, M. L.; Park, S.; Lee, Y.; Lee, J. H.; Chung, J.; Kim, J. S.; Kim, J. S.; Kim, S. Y.;
14 Jee, E.; Kim, D. W., An ultrasensitive, visco-poroelastic artificial mechanotransducer skin
15 Inspired by piezo2 protein in mammalian merkel cells. *Advanced Materials* **2017**, *29* (13),
16 1605973.
17
18 (753) Hwang, B.-U.; Zabeeb, A.; Trung, T. Q.; Wen, L.; Lee, J. D.; Choi, Y.-I.; Lee, H.-
19 B.; Kim, J. H.; Han, J. G.; Lee, N.-E., A transparent stretchable sensor for distinguishable
20 detection of touch and pressure by capacitive and piezoresistive signal transduction. *NPG*
21 *Asia Materials* **2019**, *11* (1), 1-12.
22
23 (754) Rao, Z.; Ershad, F.; Almasri, A.; Gonzalez, L.; Wu, X.; Yu, C., Soft electronics for
24 the skin: from health monitors to human-machine interfaces. *Advanced Materials*
25 *Technologies* **2020**, *5* (9), 2000233.
26
27 (755) Ding, W.; Wang, A. C.; Wu, C.; Guo, H.; Wang, Z. L., Human-machine interfacing
28 enabled by triboelectric nanogenerators and tribotronics. *Advanced Materials Technologies*
29 **2019**, *4* (1), 1800487.
30
31 (756) Pu, X.; An, S.; Tang, Q.; Guo, H.; Hu, C., Wearable triboelectric sensors for
32 biomedical monitoring and human-machine interface. *Iscience* **2021**, *24* (1), 102027.
33
34 (757) Sun, Z.; Zhu, M.; Lee, C., Progress in the triboelectric human-machine interfaces
35 (HMIs)-Moving from smart gloves to AI/haptic enabled HMI in the 5G/IoT era. *Nanoenergy*
36 *Advances* **2021**, *1* (1).
37
38 (758) Zhu, M.; He, T.; Lee, C., Technologies toward next generation human machine
39 interfaces: From machine learning enhanced tactile sensing to neuromorphic sensory systems.
40 *Applied Physics Reviews* **2020**, *7* (3), 031305.
41
42 (759) Lu, L.; Jiang, C.; Hu, G.; Liu, J.; Yang, B., Flexible noncontact sensing for human-
43 machine interaction. *Advanced Materials* **2021**, *33* (16), 2100218.
44
45 (760) Guo, H.; Wu, H.; Song, Y.; Miao, L.; Chen, X.; Chen, H.; Su, Z.; Han, M.; Zhang,
46 H., Self-powered digital-analog hybrid electronic skin for noncontact displacement sensing.
47 *Nano Energy* **2019**, *58*, 121-129.
48
49
50
51
52
53
54
55
56
57
58
59
60

- 1
2
3
4
5 (761) Tang, Y.; Zhou, H.; Sun, X.; Diao, N.; Wang, J.; Zhang, B.; Qin, C.; Liang, E.;
6 Mao, Y., Triboelectric touch-free screen sensor for noncontact gesture recognizing.
7 *Advanced Functional Materials* **2020**, *30*(5), 1907893.
8
9 (762) Wu, H.; Su, Z.; Shi, M.; Miao, L.; Song, Y.; Chen, H.; Han, M.; Zhang, H.,
10 Self-powered noncontact electronic skin for motion sensing. *Advanced Functional Materials*
11 **2018**, *28*(6), 1704641.
12
13 (763) Lee, J. W.; Jung, S.; Jo, J.; Han, G. H.; Lee, D.-M.; Oh, J.; Hwang, H. J.; Choi, D.;
14 Kim, S.-W.; Lee, J. H., Sustainable highly charged C 60-functionalized polyimide in a non-
15 contact mode triboelectric nanogenerator. *Energy & Environmental Science* **2021**, *14*(2),
16 1004-1015.
17
18 (764) Wang, F.; Ren, Z.; Nie, J.; Tian, J.; Ding, Y.; Chen, X., Self-powered sensor based
19 on bionic antennae arrays and triboelectric nanogenerator for identifying noncontact motions.
20 *Advanced Materials Technologies* **2020**, *5*(1), 1900789.
21
22 (765) Chen, S.; Wang, Y.; Yang, L.; Guo, Y.; Wang, M.; Sun, K., Flexible and transparent
23 sensors with hierarchically micro-nano texture for touchless sensing and controlling. *Nano*
24 *Energy* **2021**, *82*, 105719.
25
26 (766) Anaya, D. V.; He, T.; Lee, C.; Yuce, M. R., Self-powered eye motion sensor based
27 on triboelectric interaction and near-field electrostatic induction for wearable assistive
28 technologies. *Nano Energy* **2020**, *72*, 104675.
29
30 (767) Anaya, D. V.; Zhan, K.; Tao, L.; Lee, C.; Yuce, M. R.; Alan, T., Contactless
31 tracking of humans using non-contact triboelectric sensing technology: Enabling new
32 assistive applications for the elderly and the visually impaired. *Nano Energy* **2021**, *90*,
33 106486.
34
35 (768) Shrestha, K.; Sharma, S.; Pradhan, G. B.; Bhatta, T.; Maharjan, P.; Rana, S. S.; Lee,
36 S.; Seonu, S.; Shin, Y.; Park, J. Y., A Siloxene/Ecoflex Nanocomposite-Based Triboelectric
37 Nanogenerator with Enhanced Charge Retention by MoS₂/LIG for Self-Powered Touchless
38 Sensor Applications. *Advanced Functional Materials* **2022**, 2113005.
39
40 (769) Yuan, F.; Liu, S.; Zhou, J.; Wang, S.; Wang, Y.; Xuan, S.; Gong, X., Smart
41 touchless triboelectric nanogenerator towards safeguard and 3D morphological awareness.
42 *Nano Energy* **2021**, *86*, 106071.
43
44 (770) Zhang, C.; Dai, K.; Liu, D.; Yi, F.; Wang, X.; Zhu, L.; You, Z., Ultralow Quiescent
45 Power-Consumption Wake-Up Technology Based on the Bionic Triboelectric
46 Nanogenerator. *Advanced Science* **2020**, *7*(12), 2000254.
47
48
49
50
51
52
53
54
55
56
57
58
59
60

- 1
2
3
4
5 (771) Zhang, W.; Lu, Y.; Liu, T.; Zhao, J.; Liu, Y.; Fu, Q.; Mo, J.; Cai, C.; Nie, S.,
6 Spheres Multiple Physical Network-Based Triboelectric Materials for Self-Powered
7 Contactless Sensing. *Small* **2022**, 2200577.
- 8
9 (772) Rana, S. S.; Zahed, M. A.; Rahman, M. T.; Salauddin, M.; Lee, S. H.; Park, C.;
10 Maharjan, P.; Bhatta, T.; Shrestha, K.; Park, J. Y., Cobalt-Nanoporous Carbon Functionalized
11 Nanocomposite-Based Triboelectric Nanogenerator for Contactless and Sustainable
12 Self-Powered Sensor Systems. *Advanced Functional Materials* **2021**, 31 (52), 2105110.
- 13
14 (773) Shiwei, A.; Gao, X.; Lu, C.; Yao, D.; Lu, M.; Zhang, M.; Sun, Y.; Fang, H.; Li, D.,
15 Self-Powered Flexible Sensor Based on Triboelectric Nanogenerators for Noncontact Motion
16 Sensing. *IEEE Sensors Journal* **2022**, 22 (13), 12547-12559.
- 17
18 (774) Xi, Y.; Hua, J.; Shi, Y., Noncontact triboelectric nanogenerator for human motion
19 monitoring and energy harvesting. *Nano Energy* **2020**, 69, 104390.
- 20
21 (775) Tan, H.; Hu, X.; Wu, X.; Zeng, Y.; Tu, X.; Xu, X.; Qian, J., Initial crack
22 propagation of integral joint in steel truss arch bridges and its fatigue life accession.
23 *Engineering Failure Analysis* **2021**, 130, 105777.
- 24
25 (776) Gao, Y.; Sun, H., Influence of initial defects on crack propagation of concrete under
26 uniaxial compression. *Construction and Building Materials* **2021**, 277, 122361.
- 27
28 (777) Gledić, I.; Mikulić, A.; Parunov, J., Improvement of the Ship Emergency Response
29 Procedure in Case of Collision Accident Considering Crack Propagation during Salvage
30 Period. *Journal of Marine Science and Engineering* **2021**, 9(7), 737.
- 31
32 (778) Fang, X.-Y.; Zhang, H.-N.; Ma, D.-W.; Wu, Z.-J.; Huang, W., Influence of welding
33 residual stress on subsurface fatigue crack propagation of rail. *Engineering Fracture*
34 *Mechanics* **2022**, 271, 108642.
- 35
36 (779) Gu, J.; Ahn, J.; Jung, J.; Cho, S.; Choi, J.; Jeong, Y.; Park, J.; Hwang, S.; Cho, I.;
37 Ko, J., Self-powered strain sensor based on the piezo-transmittance of a mechanical
38 metamaterial. *Nano Energy* **2021**, 89, 106447.
- 39
40 (780) Li, D.; Nie, J.-H.; Ren, W.-X.; Ng, W.-H.; Wang, G.-H.; Wang, Y., A novel
41 acoustic emission source location method for crack monitoring of orthotropic steel plates.
42 *Engineering Structures* **2022**, 253, 113717.
- 43
44 (781) Zhou, Z.; Cui, Z.; Yin, S.; Kundu, T., A rapid acoustic source localization technique
45 for early warning of building material damage. *Construction and Building Materials* **2022**,
46 325, 126840.
- 47
48
49
50
51
52
53
54
55
56
57
58
59
60

- 1
2
3
4
5 (782) Hao, Q.; Shen, Y.; Wang, Y.; Liu, J., An adaptive extraction method for rail crack
6 acoustic emission signal under strong wheel-rail rolling noise of high-speed railway.
7 *Mechanical Systems and Signal Processing* **2021**, *154*, 107546.
8
9
10 (783) Luo, N.; Xu, G.; Feng, Y.; Yang, D.; Wu, Y.; Dong, Y.; Zhang, L.; Wang, D., Ice-
11 based triboelectric nanogenerator with low friction and self-healing properties for energy
12 harvesting and ice broken warning. *Nano Energy* **2022**, *97*, 107144.
13
14 (784) Sharma, V. B.; Singh, K.; Gupta, R.; Joshi, A.; Dubey, R.; Gupta, V.; Bharadwaj,
15 S.; Zafar, M. I.; Bajpai, S.; Khan, M. A., Review of structural health monitoring techniques in
16 pipeline and wind turbine industries. *Applied System Innovation* **2021**, *4*(3), 59.
17
18 (785) Lin, Z.; Sun, C.; Zhang, G.; Fan, E.; Zhou, Z.; Shen, Z.; Yang, J.; Liu, M.; Xia, Y.;
19 Si, S., Flexible triboelectric nanogenerator toward ultrahigh-frequency vibration sensing.
20 *Nano Research* **2022**, 1-8.
21
22 (786) Ali, R.; Chuah, J. H.; Talip, M. S. A.; Mokhtar, N.; Shoaib, M. A., Structural crack
23 detection using deep convolutional neural networks. *Automation in Construction* **2022**, *133*,
24 103989.
25
26 (787) Müller, A.; Karathanasopoulos, N.; Roth, C. C.; Mohr, D., Machine learning
27 classifiers for surface crack detection in fracture experiments. *International Journal of*
28 *Mechanical Sciences* **2021**, *209*, 106698.
29
30 (788) Zhang, L.; Wang, Z.; Wang, L.; Zhang, Z.; Chen, X.; Meng, L., Machine learning-
31 based real-time visible fatigue crack growth detection. *Digital Communications and*
32 *Networks* **2021**, *7*(4), 551-558.
33
34 (789) Shen, F.; Li, Z.; Xin, C.; Guo, H.; Peng, Y.; Li, K., Interface Defect Detection and
35 Identification of Triboelectric Nanogenerators via Voltage Waveforms and Artificial Neural
36 Network. *ACS Applied Materials & Interfaces* **2022**, *14*(2), 3437-3445.
37
38 (790) Shen, F.; Li, Z.; Guo, H.; Yang, Z.; Wu, H.; Wang, M.; Luo, J.; Xie, S.; Peng, Y.;
39 Pu, H., Recent advances towards ocean energy harvesting and self-powered applications
40 based on triboelectric nanogenerators. *Advanced Electronic Materials* **2021**, *7*(9), 2100277.
41
42 (791) Wu, X.; Li, X.; Ping, J.; Ying, Y., Recent advances in water-driven triboelectric
43 nanogenerators based on hydrophobic interfaces. *Nano Energy* **2021**, *90*, 106592.
44
45 (792) Jung, Y.; Ahn, J.; Kim, J. S.; Ha, J. H.; Shim, J.; Cho, H.; Oh, Y. S.; Yoon, Y. J.;
46 Nam, Y.; Oh, I. K., Spherical Micro/Nano Hierarchical Structures for Energy and Water
47 Harvesting Devices. *Small Methods* **2022**, 2200248.
48
49
50
51
52
53
54
55
56
57
58
59
60

- 1
2
3
4
5 (793) Chen, H.; Xing, C.; Li, Y.; Wang, J.; Xu, Y., Triboelectric nanogenerators for a
6 macro-scale blue energy harvesting and self-powered marine environmental monitoring
7 system. *Sustainable Energy & Fuels* **2020**, *4* (3), 1063-1077.
- 8
9 (794) Zaw, N. Y. W.; Yun, J.; Goh, T. S.; Kim, I.; Kim, Y.; Lee, J. S.; Kim, D., All-
10 polymer waterproof triboelectric nanogenerator towards blue energy harvesting and self-
11 powered human motion detection. *Energy* **2022**, *247*, 123422.
- 12
13 (795) Wu, Y.; Zeng, Q.; Tang, Q.; Liu, W.; Liu, G.; Zhang, Y.; Wu, J.; Hu, C.; Wang, X.,
14 A teeterboard-like hybrid nanogenerator for efficient harvesting of low-frequency ocean
15 wave energy. *Nano Energy* **2020**, *67*, 104205.
- 16
17 (796) Rodrigues, C.; Ramos, M.; Esteves, R.; Correia, J.; Clemente, D.; Gonçalves, F.;
18 Mathias, N.; Gomes, M.; Silva, J.; Duarte, C., Integrated study of triboelectric nanogenerator
19 for ocean wave energy harvesting: Performance assessment in realistic sea conditions. *Nano*
20 *Energy* **2021**, *84*, 105890.
- 21
22 (797) Liu, L.; Yang, X.; Zhao, L.; Hong, H.; Cui, H.; Duan, J.; Yang, Q.; Tang, Q.,
23 Nodding duck structure multi-track directional freestanding triboelectric nanogenerator
24 toward low-frequency ocean wave energy harvesting. *ACS nano* **2021**, *15* (6), 9412-9421.
- 25
26 (798) Sun, W.; Zheng, Y.; Li, T.; Feng, M.; Cui, S.; Liu, Y.; Chen, S.; Wang, D., Liquid-
27 solid triboelectric nanogenerators array and its applications for wave energy harvesting and
28 self-powered cathodic protection. *Energy* **2021**, *217*, 119388.
- 29
30 (799) Sun, M.; Lu, Q.; Wang, Z. L.; Huang, B., Understanding contact electrification at
31 liquid–solid interfaces from surface electronic structure. *Nature communications* **2021**, *12*
32 (1), 1-11.
- 33
34 (800) Liang, X.; Liu, Z.; Feng, Y.; Han, J.; Li, L.; An, J.; Chen, P.; Jiang, T.; Wang, Z. L.,
35 Spherical triboelectric nanogenerator based on spring-assisted swing structure for effective
36 water wave energy harvesting. *Nano Energy* **2021**, *83*, 105836.
- 37
38 (801) Wen, H.; Yang, P.; Liu, G.; Xu, S.; Yao, H.; Li, W.; Qu, H.; Ding, J.; Li, J.; Wan,
39 L., Flower-like triboelectric nanogenerator for blue energy harvesting with six degrees of
40 freedom. *Nano Energy* **2022**, *93*, 106796.
- 41
42 (802) Wang, Y.; Liu, X.; Chen, T.; Wang, H.; Zhu, C.; Yu, H.; Song, L.; Pan, X.; Mi, J.;
43 Lee, C., An underwater flag-like triboelectric nanogenerator for harvesting ocean current
44 energy under extremely low velocity condition. *Nano Energy* **2021**, *90*, 106503.
- 45
46
47
48
49
50
51
52
53
54
55
56
57
58
59
60

- 1
2
3
4
5 (803) Wang, H.; Fan, Z.; Zhao, T.; Dong, J.; Wang, S.; Wang, Y.; Xiao, X.; Liu, C.; Pan,
6 X.; Zhao, Y., Sandwich-like triboelectric nanogenerators integrated self-powered buoy for
7 navigation safety. *Nano Energy* **2021**, *84*, 105920.
- 8
9 (804) Xu, M.; Wang, S.; Zhang, S. L.; Ding, W.; Kien, P. T.; Wang, C.; Li, Z.; Pan, X.;
10 Wang, Z. L., A highly-sensitive wave sensor based on liquid-solid interfacing triboelectric
11 nanogenerator for smart marine equipment. *Nano Energy* **2019**, *57*, 574-580.
- 12
13 (805) Rui, P.; Zhang, W.; Zhong, Y.; Wei, X.; Guo, Y.; Shi, S.; Liao, Y.; Cheng, J.;
14 Wang, P., High-performance cylindrical pendulum shaped triboelectric nanogenerators
15 driven by water wave energy for full-automatic and self-powered wireless hydrological
16 monitoring system. *Nano Energy* **2020**, *74*, 104937.
- 17
18 (806) Jung, H.; Ouro-Koura, H.; Salalila, A.; Salalila, M.; Deng, Z. D., Frequency-
19 multiplied cylindrical triboelectric nanogenerator for harvesting low frequency wave energy
20 to power ocean observation system. *Nano Energy* **2022**, *99*, 107365.
- 21
22 (807) Kim, H.; Hwang, H. J.; Huynh, N. D.; Pham, K. D.; Choi, K.; Ahn, D.; Choi, D.,
23 Magnetic force enhanced sustainability and power of cam-based triboelectric nanogenerator.
24 *Research* **2021**, *2021*.
- 25
26 (808) Bhatia, D.; Lee, J.; Hwang, H. J.; Baik, J. M.; Kim, S.; Choi, D., Design of
27 mechanical frequency regulator for predictable uniform power from triboelectric
28 nanogenerators. *Advanced Energy Materials* **2018**, *8*(15), 1702667.
- 29
30 (809) Hu, J.; Pu, X.; Yang, H.; Zeng, Q.; Tang, Q.; Zhang, D.; Hu, C.; Xi, Y., A flutter-
31 effect-based triboelectric nanogenerator for breeze energy collection from arbitrary directions
32 and self-powered wind speed sensor. *Nano Research* **2019**, *12*(12), 3018-3023.
- 33
34 (810) Tcho, I.-W.; Kim, W.-G.; Kim, J.-K.; Kim, D.-W.; Yun, S.-Y.; Son, J.-H.; Choi, Y.-
35 K., A flutter-driven triboelectric nanogenerator for harvesting energy of gentle breezes with a
36 rear-fixed fluttering film. *Nano Energy* **2022**, *98*, 107197.
- 37
38 (811) Bae, J.; Lee, J.; Kim, S.; Ha, J.; Lee, B.-S.; Park, Y.; Choong, C.; Kim, J.-B.; Wang,
39 Z. L.; Kim, H.-Y., Flutter-driven triboelectrification for harvesting wind energy. *Nature*
40 *communications* **2014**, *5*(1), 1-9.
- 41
42 (812) Li, Z.; Zhou, S.; Yang, Z., Recent progress on flutter-based wind energy harvesting.
43 *International Journal of Mechanical System Dynamics* **2022**, *2*(1), 82-98.
- 44
45 (813) Yu, X.; Fu, S.; Zuo, X.; Zeng, J.; Shan, C.; He, W.; Li, W.; Hu, C., Moisture
46 Resistant and Stable Wireless Wind Speed Sensing System Based on Triboelectric
47
48
49
50
51
52
53
54
55
56
57
58
59
60

1
2
3
4
5 Nanogenerator with Charge-Excitation Strategy. *Advanced Functional Materials* **2022**, *32*
6 (44), 2207498.

7
8 (814) Phan, H.; Shin, D.-M.; Jeon, S. H.; Kang, T. Y.; Han, P.; Kim, G. H.; Kim, H. K.;
9 Kim, K.; Hwang, Y.-H.; Hong, S. W., Aerodynamic and aeroelastic flutters driven
10 triboelectric nanogenerators for harvesting broadband airflow energy. *Nano Energy* **2017**, *33*,
11 476-484.

12
13 (815) Yao, Y.; Zhou, Z.; Wang, K.; Liu, Y.; Lu, X.; Cheng, T., Arc-shaped flutter-driven
14 wind speed sensor based on triboelectric nanogenerator for unmanned aerial vehicle. *Nano*
15 *Energy* **2022**, *104*, 107871.

16
17 (816) Phan, T. K.; Wang, S.; Wang, Y.; Wang, H.; Xiao, X.; Pan, X.; Xu, M.; Mi, J., A
18 self-powered and low pressure loss gas flowmeter based on fluid-elastic flutter driven
19 triboelectric nanogenerator. *Sensors* **2020**, *20*(3), 729.

20
21 (817) Moon, H.; Chung, J.; Kim, B.; Yong, H.; Kim, T.; Lee, S.; Lee, S., Stack/flutter-
22 driven self-retracting triboelectric nanogenerator for portable electronics. *Nano Energy* **2017**,
23 *31*, 525-532.

24
25 (818) Zhang, Y.; Fu, S. C.; Chan, K. C.; Shin, D. M.; Chao, C. Y. H., Boosting power
26 output of flutter-driven triboelectric nanogenerator by flexible flagpole. *Nano Energy* **2021**,
27 *88*.

28
29 (819) Zhu, Z.; Xiang, H.; Zeng, Y.; Zhu, J.; Cao, X.; Wang, N.; Wang, Z. L.,
30 Continuously harvesting energy from water and wind by pulsed triboelectric nanogenerator
31 for self-powered seawater electrolysis. *Nano Energy* **2022**, *93*, 106776.

32
33 (820) Cho, S.; Shin, Y.; Choi, J.; Eom, J.; Oh, B. S.; Lee, J.; Jung, G. Y., Triboelectric
34 nanogenerator based on intercalated Al layer within fluttering dielectric film. *Nano Energy*
35 **2020**, *77*, 105184.

36
37 (821) Son, J. h.; Heo, D.; Goh, D.; Lee, M.; Chung, J.; Choi, S.; Lee, S., Wind-Driven
38 Bidirectional Fluttering Triboelectric Nanogenerator Via Dual Flagpole and Slot Structure
39 Design. *Advanced Materials Technologies* **2022**, 2200453.

40
41 (822) Sun, W.; Ding, Z.; Qin, Z.; Chu, F.; Han, Q., Wind energy harvesting based on
42 fluttering double-flag type triboelectric nanogenerators. *Nano Energy* **2020**, *70*, 104526.

43
44 (823) Zhang, L.; Meng, B.; Tian, Y.; Meng, X.; Lin, X.; He, Y.; Xing, C.; Dai, H.; Wang,
45 L., Vortex-induced vibration triboelectric nanogenerator for low speed wind energy
46 harvesting. *Nano Energy* **2022**, *95*, 107029.

- 1
2
3
4
5 (824) Ko, H.-J.; Kwon, D.-S.; Bae, K.; Kim, J., Self-suspended shell-based triboelectric
6 nanogenerator for omnidirectional wind-energy harvesting. *Nano Energy* **2022**, *96*, 107062.
7
8 (825) Lee, S.; Lee, Y.; Park, J.; Choi, D., Stitchable organic photovoltaic cells with textile
9 electrodes. *Nano Energy* **2014**, *9*, 88-93.
10
11 (826) Chen, C.; Zhao, S.; Pan, C.; Zi, Y.; Wang, F.; Yang, C.; Wang, Z. L., A method for
12 quantitatively separating the piezoelectric component from the as-received "Piezoelectric"
13 signal. *Nat Commun* **2022**, *13* (1), 1391.
14
15 (827) Fan, X.; He, J.; Mu, J.; Qian, J.; Zhang, N.; Yang, C.; Hou, X.; Geng, W.; Wang, X.;
16 Chou, X., Triboelectric-electromagnetic hybrid nanogenerator driven by wind for self-
17 powered wireless transmission in Internet of Things and self-powered wind speed sensor.
18 *Nano Energy* **2020**, *68*, 104319.
19
20 (828) Guo, Y.; Chen, Y.; Ma, J.; Zhu, H.; Cao, X.; Wang, N.; Wang, Z. L., Harvesting
21 wind energy: A hybridized design of pinwheel by coupling triboelectrification and
22 electromagnetic induction effects. *Nano Energy* **2019**, *60*, 641-648.
23
24 (829) Zhang, Y.; Zeng, Q.; Wu, Y.; Wu, J.; Yuan, S.; Tan, D.; Hu, C.; Wang, X., An
25 Ultra-Durable Windmill-Like Hybrid Nanogenerator for Steady and Efficient Harvesting of
26 Low-Speed Wind Energy. *Nano-Micro Letters* **2020**, *12* (1).
27
28 (830) Jiang, K.; Hong, S.-H.; Tung, S.-H.; Liu, C.-L., Effects of cation size on
29 thermoelectricity of PEDOT:PSS/ionic liquid hybrid films for wearable thermoelectric
30 generator application. *Journal of Materials Chemistry A* **2022**, *10* (36), 18792-18802.
31
32 (831) Jung, S.; Oh, J.; Yang, U. J.; Lee, S. M.; Lee, J.; Jeong, M.; Cho, Y.; Kim, S.; Baik,
33 J. M.; Yang, C., 3D Cu ball-based hybrid triboelectric nanogenerator with non-fullerene
34 organic photovoltaic cells for self-powering indoor electronics. *Nano Energy* **2020**, *77*.
35
36 (832) Rahman, M. T.; Salauddin, M.; Maharjan, P.; Rasel, M. S.; Cho, H.; Park, J. Y.,
37 Natural wind-driven ultra-compact and highly efficient hybridized nanogenerator for self-
38 sustained wireless environmental monitoring system. *Nano Energy* **2019**, *57*, 256-268.
39
40 (833) Ren, Z.; Zheng, Q.; Wang, H.; Guo, H.; Miao, L.; Wan, J.; Xu, C.; Cheng, S.;
41 Zhang, H., Wearable and self-cleaning hybrid energy harvesting system based on
42 micro/nanostructured haze film. *Nano Energy* **2020**, *67*.
43
44 (834) Xie, L.; Zhai, N.; Liu, Y.; Wen, Z.; Sun, X., Hybrid Triboelectric Nanogenerators:
45 From Energy Complementation to Integration. *Research (Wash D C)* **2021**, *2021*, 9143762.
46
47
48
49
50
51
52
53
54
55
56
57
58
59
60

- 1
2
3
4
5 (835) Zhang, K.; Wang, X.; Yang, Y.; Wang, Z. L., Hybridized electromagnetic-
6 triboelectric nanogenerator for scavenging biomechanical energy for sustainably powering
7 wearable electronics. *ACS Nano* **2015**, *9*(4), 3521-9.
8
9 (836) Zhang, Q.; Li, L.; Wang, T.; Jiang, Y.; Tian, Y.; Jin, T.; Yue, T.; Lee, C., Self-
10 sustainable flow-velocity detection via electromagnetic/triboelectric hybrid generator aiming
11 at IoT-based environment monitoring. *Nano Energy* **2021**, *90*.
12
13 (837) Wen, Z.; Yeh, M. H.; Guo, H.; Wang, J.; Zi, Y.; Xu, W.; Deng, J.; Zhu, L.; Wang,
14 X.; Hu, C.; Zhu, L.; Sun, X.; Wang, Z. L., Self-powered textile for wearable electronics by
15 hybridizing fiber-shaped nanogenerators, solar cells, and supercapacitors. *Sci Adv* **2016**, *2*
16 (10), e1600097.
17
18 (838) Quan, T.; Wang, X.; Wang, Z. L.; Yang, Y., Hybridized Electromagnetic-
19 Triboelectric Nanogenerator for a Self-Powered Electronic Watch. *ACS Nano* **2015**, *9* (12),
20 12301-12310.
21
22 (839) Wang, J.; Ma, L.; He, J.; Yao, Y.; Zhu, X.; Peng, L.; Yang, J.; Li, K.; Qu, M.,
23 Superwetable hybrid dielectric based multimodal triboelectric nanogenerator with superior
24 durability and efficiency for biomechanical energy and hydropower harvesting. *Chemical*
25 *Engineering Journal* **2022**, *431*.
26
27 (840) Su, Y.; Chen, G.; Chen, C.; Gong, Q.; Xie, G.; Yao, M.; Tai, H.; Jiang, Y.; Chen, J.,
28 Self-powered respiration monitoring enabled by a triboelectric nanogenerator. *Advanced*
29 *Materials* **2021**, *33*(35), 2101262.
30
31
32
33
34
35
36
37
38
39
40
41
42
43
44
45
46
47
48
49
50
51
52
53
54
55
56
57
58
59
60